15 July 1995 Volume A198 Nos. 1–2 ISSN 0921-5093

MATERIALS SCIENCE & ENGINEERING

A

Structural Materials: Properties, Microstructure and Processing

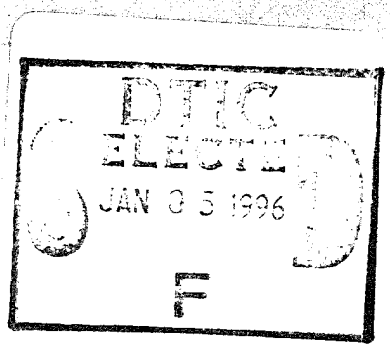

Containing papers presented at the 3rd US–Japan Seminar on Development and Environmental Characteristics of New Materials, June 7–9, 1994, Mt. Hood, OR, USA

Guest Editors: R.M. Latanision and K. Hashimoto

ELSEVIER

MATERIALS SCIENCE AND ENGINEERING A

The journal provides an international medium for the publication of theoretical and experimental studies and reviews of the properties and behavior of a wide range of materials, related both to their structure and to their engineering application. The varied topics comprising materials science and engineering are viewed as appropriate for publication: these include, but are not limited to, the properties and structure of crystalline and non-crystalline metals and ceramics, polymers and composite materials.

Types of contributions
Original research work not already published; plenary lectures and/or individual papers given at conferences; reviews of specialized topics within the scope of the journal; engineering studies; letters to the editor.

Subscriptions
Volumes 189–204, each volume containing 2 issues, are scheduled for publication. Prices are available from the publishers upon request. Subscriptions are accepted on a prepaid basis only. Issues are sent by SAL (Surface Air Lifted) mail wherever this service is available. Airmail rates are available upon request. Please address all requests regarding orders and subscription queries to

ELSEVIER SCIENCE SA

P.O. Box 564, 1001 Lausanne, Switzerland
Telephone: (21) 3 20 73 81
Telex: 450620 ELSA CH Telefax: (21) 3 235 444

Issues are sent by surface mail after air delivery to Argentina, Australia, Brazil, Canada, China, Hong Kong, India, Israel, Japan, Malaysia, Mexico, New Zealand, Pakistan, Singapore, South Africa, South Korea, Taiwan, Thailand and the USA. Airmail rates for other countries are available on request.
For advertising rates apply to the publishers. A specimen copy will be sent on request.

US and Canadian customers may obtain information from the following.

ELSEVIER SCIENCE INC.
Attn.: Journal Information Center, 655 Avenue of the Americas New York, NY 10010, USA.
Telephone: (212) 633 3750 Telex: 420 643 AEP UI
Telefax: (212) 633 3764.

Abstracting and/or Indexing Services
American Ceramic Society; Cambridge Scientific Abstracts; Chemical Abstracts; Current Contents; Engineering Index; FIZ Karlsruhe; Fluid Abstracts; Fluidex; Glass Technology Abstracts; Inspec/Physics Abstracts; Metals Abstracts; Pascal (Centre National de la Recherche Scientifique); Physikalische Berichte; Research Alert™; Science Citation Index.

MATERIALS SCIENCE & ENGINEERING

A

Structural Materials: Properties, Microstructure and Processing

Owing to a printing error, the Publisher regrets that the Author and Subject Indexes were omitted from Volume 196. They are therefore reproduced here.

ELSEVIER

Materials Science and Engineering A196 (1995) 275

MATERIALS SCIENCE & ENGINEERING A

Author Index of Volume 196

Elsevier Science S.A.

ELSEVIER

Materials Science and Engineering A196 (1995) 277–280

MATERIALS SCIENCE & ENGINEERING A

Subject Index of Volume 196

Elsevier Science S.A.

MATERIALS SCIENCE & ENGINEERING

A

Structural Materials: Properties, Microstructure and Processing

Volume A198 (1995)

Containing papers presented at the 3rd US–Japan Seminar on Development and Environmental Characteristics of New Materials, June 7–9, 1994, Mt. Hood, OR, USA.

Guest Editors: R.M. Latanision and K. Hashimoto

ELSEVIER AMSTERDAM—LAUSANNE—NEW YORK—OXFORD—SHANNON—TOKYO

International Standard Serial Number 0921-5093

 0921-5093/95/$9.50

Printed in The Netherlands

ELSEVIER

Materials Science and Engineering A198 (1995) v–vi

MATERIALS SCIENCE & ENGINEERING A

Contents

ELSEVIER

Materials Science and Engineering A198 (1995) vii

MATERIALS SCIENCE & ENGINEERING A

Preface

This meeting at Mt. Hood is the third US–Japan seminar on corrosion. The first, chaired by Roger Staehle and Hideya Okada, was held in Hawaii 19 years ago. The second, at Nikko, was chaired by Shiro Haruyama and Henry Leidheiser. Professor Koji Hashimoto and I are grateful to the Japan Society for the Promotion of Science and to the National Science Foundation and the Office of Naval Research in the United States for their continuing interest and support. I hope that this spirit of collaboration between corrosion scientists and engineers in Japan and in the United States, in which we can all take pleasure, will continue for a very long time.

I feel certain that our collaboration will continue because corrosion—the environmental degradation of materials—is so intimately associated with the development of new materials and new engineering systems. The motivation for the present seminar is the realization that if new materials are to become incorporated into engineering systems, their chemical behavior must be determined before exposure to service environments. More often, however, the corrosion resistance or chemical stability of materials is considered only after a field failure has occurred. It is clear, therefore, that the otherwise attractive properties of a material may not be successfully exploited if that material is not chemically stable (or cannot be made stable) in service. This seminar brought together leaders in the corrosion science and engineering communities (university, industry, and national laboratories) from Japan and the US with the objective of establishing a shared research agenda that will lead to the more timely and effective introduction of new materials into engineering systems which serve society throughout the world.

Finally, it is important to mention that while the seminar was technically rich, it will be remembered as well for the presence of many of the spouses of the participants and for the early June snowstorm which greeted us upon our arrival at the spectacular Mt. Hood.

R.M. Latanision
Guest Editor

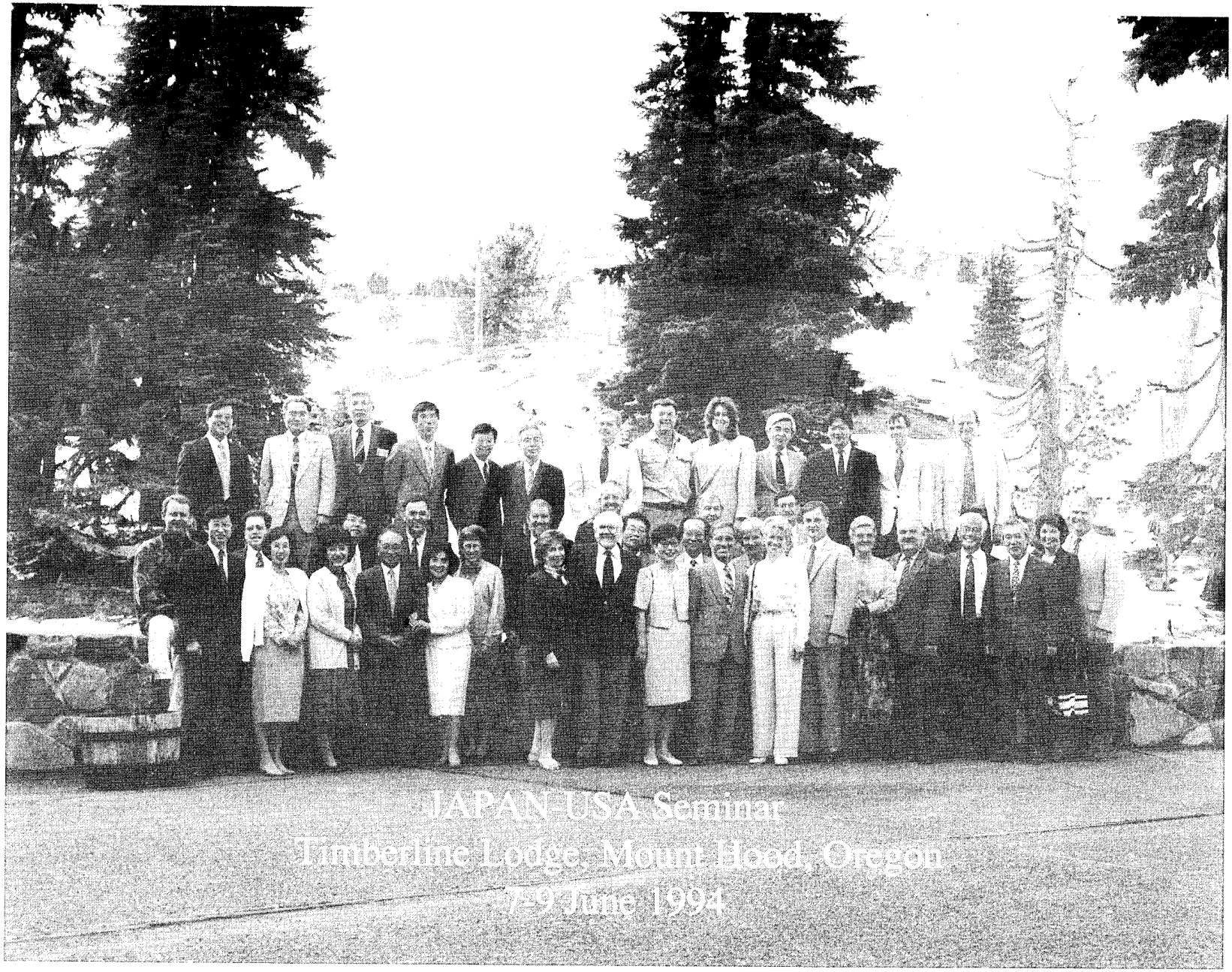
JAPAN-USA Seminar
Timberline Lodge, Mount Hood, Oregon
7-9 June 1994

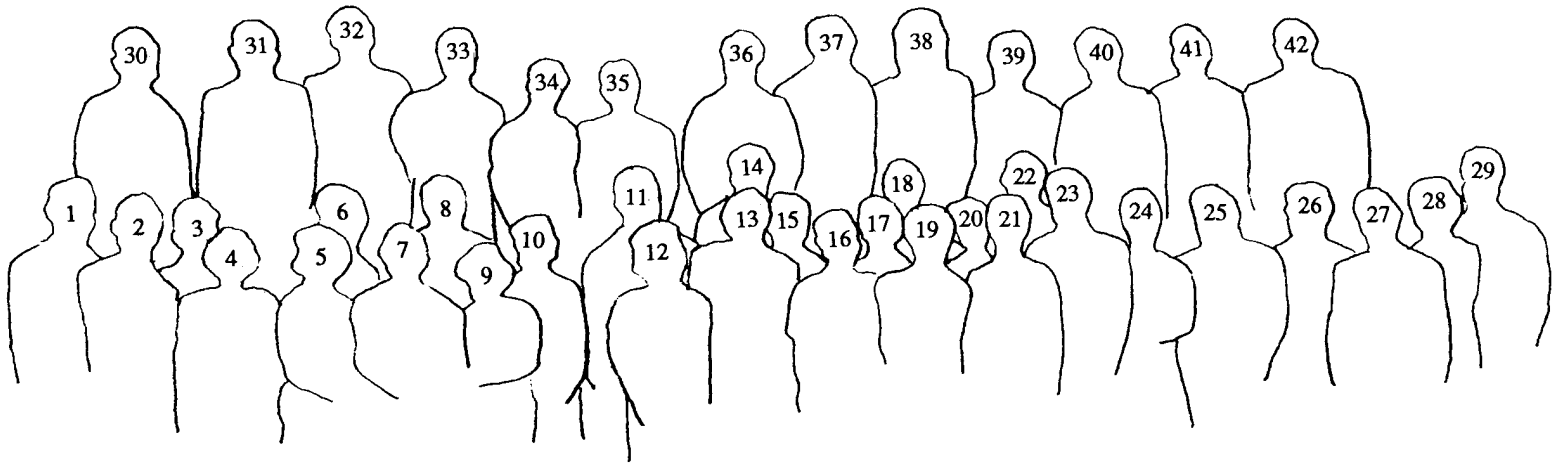

1. Florian Mansfeld
2. Misao Hashimoto
3. Mark Buonanno
4. Machiko Yamamoto
5. Mionako Hayashi
6. Takenori Nakayama
7. Kenzo Kobayashi
8. J. Doug Sinclair
9. Yoshiko Kobayashi
10. Ginny Sinclair
11. David Duquette
12. Mollee Kruger
13. Jerry Kruger
14. Richard Ricker
15. Masahiro Seo
16. Yasuko Hashimoto
17. Toshio Shibata
18. Roger Staehle
19. Koji Hashimoto
20. Judy Pickering
21. Carolyn Latanision
22. Howard Pickering
23. Ron Latanision
24. Eileen Wilde
25. Bryan Wilde
26. Katsuhisa Sugimoto
27. Hiroo Nagano
28. Catherine Jones
29. Russell Jones
30. Yoshio Takizawa
31. Yasunori Hayaski
32. Iwao Matsushima
33. Katsumi Yamamoto
34. Toshiaki Ohtsuka
35. Koji Yamakawa
36. Jesse Lumsden
37. Joe Payer
38. Constance Beal
39. Tooru Tsuru
40. Lloyd Hihara
41. Clive Clayton
42. William Smyrl

ELSEVIER

Materials Science and Engineering A198 (1995) 1–10

MATERIALS SCIENCE & ENGINEERING A

Recent progress in corrosion-resistant metastable alloys

Koji Hashimoto[a], Pyeong-Yeol Park[a], Jin-Han Kim[a], Hideaki Yoshioka[a], Hiroyuki Mitsui[a], Eiji Akiyama[a], Hiroki Habazaki[a], Asahi Kawashima[a], Katsuhiko Asami[a], Zbigniew Grzesik[b], Stanislaw Mrowec[b]

[a]*Institute for Materials Research, Tohoku University, Sendai 980-77, Japan*
[b]*Department of Physical Chemistry, Academy of Mining and Metallurgy, Mickiewicza 30, 30-059 Cracow, Poland*

Abstract

Tailoring new corrosion-resistant alloys has recently been performed mostly by the sputter deposition technique. This technique is suitable for forming a single-phase solid solution even when the boiling point of one component is lower than the melting points of the other components and/or when one component is immiscible with another component in the liquid state. Aluminium–refractory metal, chromium–valve metal and molybdenum–chromium–nickel alloys have been successfully prepared in a single amorphous phase. Amorphous aluminium–refractory metal alloys are corrosion resistant in 1 M HCl and chromium–valve metal alloys are spontaneously passive in 12 M HCl, showing a better corrosion resistance in comparison with the alloy components. The amorphous aluminium–refractory metal alloys also have an extraordinarily high hot corrosion resistance. Their sulphidation resistance at higher temperatures is far higher than any other known metallic materials and their oxidation resistance is comparable to chromia- or alumina-forming alloys.

Keywords: Al–refractory metal alloys; Cr–valve metal alloys; Cr–Ni–Mo alloys; Sulfide corrosion; Oxidation; Spontaneous passivation

1. Introduction

Since the extremely high corrosion resistance of amorphous Fe–Cr–P–C alloys was reported in 1974 [1], a variety of corrosion-resistant amorphous alloys have been prepared. When sufficient amount of passivating elements are present they show extremely high corrosion resistance, particularly in strong acids. They are characterized by the formation of a homogeneous, single solid solution phase exceeding the solubility limits of alloying elements in the equilibrium state. The homogeneous single-phase nature leads to the formation of a uniform passive film and hence is responsible for high corrosion resistance. The formation of a single solid solution alloy regardless of alloying elements and their concentrations is attractive and suitable for tailoring new alloys having specific properties.

Recent efforts in the preparation of new corrosion-resistant alloys have mostly involved the use of sputter deposition techniques. The composition range amorphizable by sputtering is the widest among the various methods for the preparation of amorphous alloys. Even if single amorphous phase alloys are not formed, the alloys thus prepared are always composed of microcrystals with very fine grains and sometimes behave similarly to solid solution alloys. This technique is particularly suitable for forming alloys when the boiling point of one component is lower than the melting points of the other components and/or when one component is immiscible with another component in the liquid state, because sputter deposition does not require melting for alloy formation.

This paper reviews our recent results with corrosion-resistant metastable alloys prepared by sputtering.

Elsevier Science S.A.
SSDI 0921-5093(94)04501-1

2. Apparatus

D.c. magnetron sputtering was used for the preparation of alloys [2,3]. In general, targets were composed of an alloy component disc 100 mm in diameter and several mm thick and other alloy component discs of smaller sizes which were placed in the sputter erosion region of the 100 mm diameter disc. The composition of sputter deposits was controlled by changing the number of smaller discs placed on the larger disc. Glass and various metal plates were used as substrates. For the purpose of homogenization of the sputter deposits, the water-cooled substrates were revolved around a central axis of the sputtering chamber, in addition to revolution of the substrates themselves around a central axis of each substrate disc. Before sputtering, the sputtering chamber was evacuated to about 10^{-7} Torr (1 Torr = 133.3 Pa). After pre-sputtering of the target, sputtering was carried out at about 10^{-3} Torr of argon gas, which was prepared by removal of oxygen, water and dust from high-purity (99.9995%) argon.

The composition of the sputter deposits was determined by electron probe microanalysis and the structure of the sputter deposits was mostly identified by X-ray diffraction in the θ–2θ mode with Cu Kα radiation. The apparent grain size of the sputter deposits was estimated from the full width at half maximum (FWHM) of the main diffraction peaks.

3. Corrosion resistance in acids

3.1. Al alloys

A variety of new corrosion-resistant amorphous alloys were prepared, such as Al–Ta [3], Al–Nb [3], Al–Ti [4–7], Al–Zr [4, 8], Al–Cr [9], Al–Mo [4,10], Al–W [4,10] and Al–Mg–Ti [11]. Fig. 1 shows the structure of various aluminium–transition metal alloys [12]. These alloys become amorphous single phases in

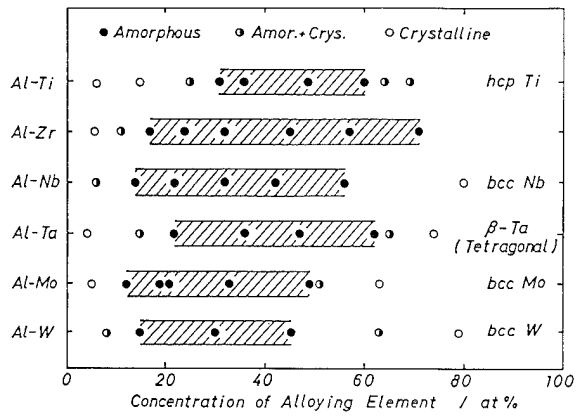

Fig. 1. Structure of sputter-deposited aluminium alloys identified by X-ray diffraction [12].

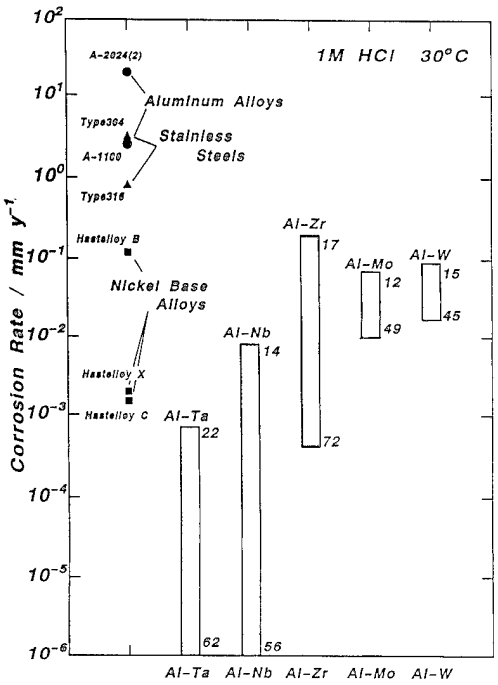

Fig. 2. Corrosion rates of various aluminium alloys and conventional corrosion-resistant alloys measured in 1 M HCl at 30 °C [13].

wide composition ranges. Alloy formation is significantly effective in enhancing the corrosion resistance. Fig. 2 shows a comparison of the corrosion rates of the various aluminium alloys with those of conventional corrosion-resistant alloys measured in 1 M HCl at 30 °C [13]. The use of aluminium alloys in 1 M HCl has not previously been considered. However, when aluminium is alloyed with various refractory elements, the alloys possess sufficiently high corrosion resistance even in 1 M HCl. Except for Al–Ti alloys, the corrosion resistance in 1 M HCl increases with increasing alloying additions. Al–Ti alloys dissolve actively, but other amorphous aluminium alloys are spontaneously passive even in 1 M HCl. Amorphous Al–Ta and Al–Nb alloys are especially corrosion resistant.

X-ray photelectron spectroscopic (XPS) analysis revealed that passive films formed on the amorphous alloys are composed of cations of both aluminium and corrosion-resistant elements. As shown in Table 1, the cationic composition in the passive film is almost the same as the alloy composition and the passive film consists of oxyhydroxide in which cations of aluminium and alloying elements are homogeneously distributed. Although aluminium oxyhydroxide is easily dissolved in acids, the formation of a double oxyhydroxide of aluminium and refactory metals provides high corrosion resistance. On the other hand, if the alloys consist of a refractory element and an element with low passivating ability, such as amorphous Ta–Ni [16] and Ta–Cu [17] alloys, the passive films formed in concentrated acids are composed mostly of valve metal cations and the

alloys have very high corrosion resistance even in concentrated acids. By contrast, the passive films formed on the aluminium–refractory metal alloys contain high concentrations of aluminium ions which do not form stable passive films in strong acids. This restricts further enhancement of the corrosion resistance of Al–refractory metal alloys and is responsible for pitting corrosion of the amorphous alloys by anodic polarization in chloride-containing solutions, although the pitting potentials are much higher than that of aluminium.

3.2. Cr alloys

Chromium and valve metals such as titanium, zirconium, niobium and tantalum are all passivated in strong acids. Consequently, if one succeeds in preparing chromium alloys with these valve metals, they seem to be ideal corrosion-resistant alloys in aqueous environments. An attempt to produce these alloys was made by sputtering.

Fig. 3 shows X-ray diffraction patterns of binary chromium–niobium alloys [18]. The alloys containing 29–63 at.% niobium show halo patterns typical of the amorphous structure. The Cr–21 Nb and Cr–73 Nb alloys, however, show sharp peaks corresponding to 110 reflection of bcc chromium and niobium phases. The characteristic interatomic spacing, d, corresponding to the lattice spacing in the crystalline materials was estimated for the first peak or halo position of the X-ray diffraction patterns of the alloys shown in Fig. 3 [18]. The apparent grain size was also estimated from the FWHM of the first peak or halo in the X-ray diffraction patterns, although amorphous alloys are not composed of grains. Fig. 4 shows the characteristic interatomic spacing and the apparent grain size as a function of the alloy niobium content. The characteristic interatomic spacing of alloys with 29–63 at.% niobium increases with increasing alloy niobium content, just as in a binary solid solution. This indicates that the amorphous alloys consist of a single-phase solid solution. Since the Goldschmidt radius of niobium is larger than that of chromium, the change in d with niobium concentration in the alloy can be reasonably explained. As the characteristic interatomic spacing of amorphous alloys is situated between the 110 lattice spacings of bcc chromium and niobium, it can be said that the amorphous alloys are closely packed similarly to crystalline solid solutions. The apparent grain size of the alloy with 29–63 at.% niobium is of the order of 1 nm. This is almost the same as the size of atom groups assumed to exist in liquid metals, and hence these alloys are regarded as amorphous alloys. Accordingly, sputter-deposited Cr–Nb alloys form a single amorphous solid solution phase in a wide composition range from 29 to 63 at.% niobium. The formation of a single amorphous phase composed of two elements belonging to neighboring groups in the Periodic Table is a new finding, and indicates the advantage of the use of the sputtering technique to produce amorphous alloys.

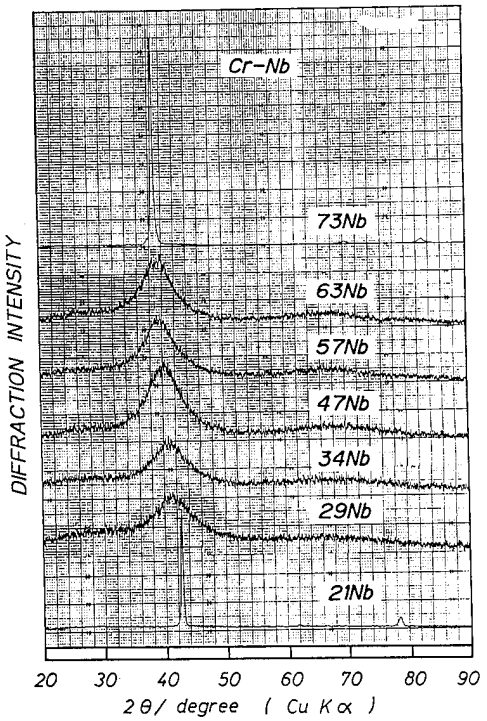

Fig. 3. X-ray diffraction patterns of sputter-deposited Cr–Nb alloys [16].

Table 1
Cationic composition of surface films formed on binary Al–refractory metal alloys by immersion in 1 M HCl

Alloy (at.%)	Cations in the film		Ref.
	Al	Alloying (at.%)	
Al–24 Zr	70	30 Zr	14
Al–57 Zr	37	63 Zr	14
Al–56 Nb	52	48 Nb	3
Al–22 Ta	68	32 Ta	3
Al–49 Mo	65	35 Mo	4
Al–15 W	78	22 W	15
Al–45 W	55	45 W	15

Fig. 5 shows the structure of sputter-deposited chromium–valve metal alloys as a function of alloying additions [12]. These alloys show an amorphous single solid solution structure over wide composition ranges. These were all new amorphous alloys. Their corrosion resistance in concentrated hydrochloric acid is remarkably high.

Fig. 6 shows the change in the corrosion rate of Ti–Cr and Zr–Cr alloys in 6 M HCl solution at 30 °C as a function of the chromium content of the alloy [19,20]. In 6 M HCl solution chromium and titanium

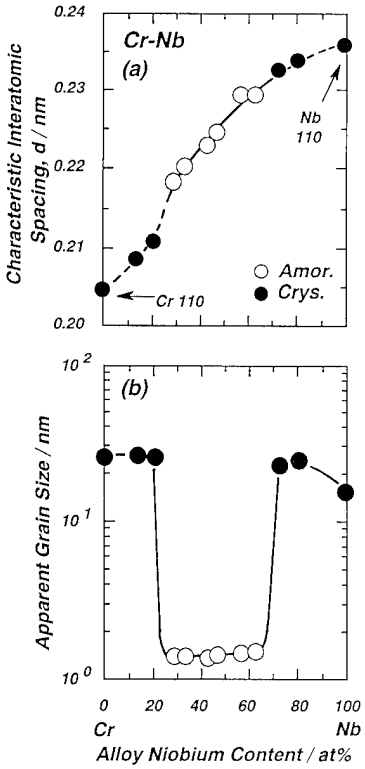

Fig. 4. Characteristic interatomic spacing estimated from the peak positions in X-ray diffraction patterns and the apparent grain size estimated from the FWHM for the most intense reflection in X-ray diffraction patterns as a function of the alloy niobium content [16].

dissolve actively. However, the Cr–Ti alloys show very low corrosion rates which are several orders of magnitude lower than those of alloy components. Binary Zr–Cr alloys also show low corrosion rates. In spite of the fact that the corrosion rate of chromium metal is five orders of magnitude higher than that of Zr metal, the corrosion rate of the alloys decreases with increasing alloy chromium content.

Fig. 7 shows corrosion rates of Cr–Nb [18], Cr–Ta [18] and Cu–Ta [17] alloys in 12 M HCl at 30 °C. Amorphous Cu–Ta alloys also have high corrosion resistance in 12 M HCl. However, because copper itself does not form a stable passive film in 12 M HCl, the

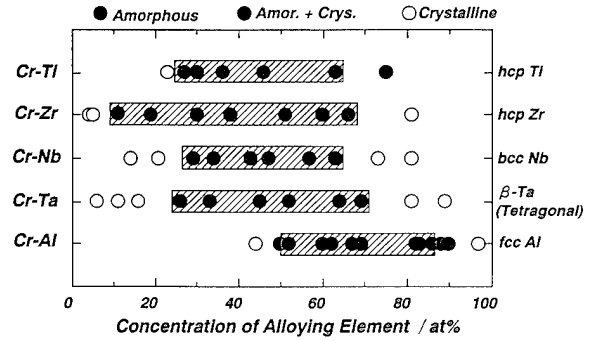

Fig. 5. Structure of sputter-deposited chromium alloys identified by X-ray diffraction [12].

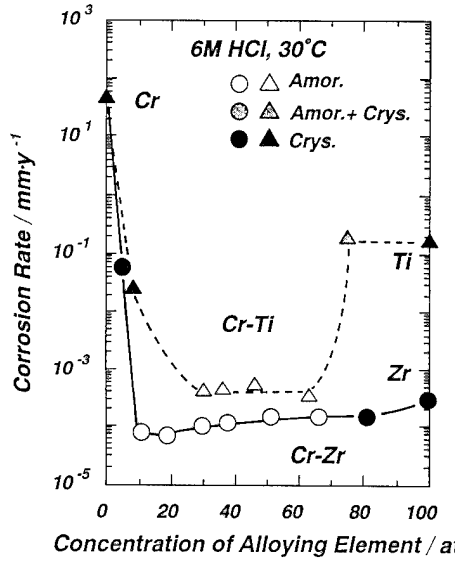

Fig. 6. Changes in the corrosion rates of Ti–Cr and Zr–Cr alloys in 6 M HCl solution at 30 °C as a function of alloy chromium content. Corrosion rates of chromium, titanium and zirconium are also shown for comparison [19,20].

corrosion resistance of the Cu–Ta alloy cannot exceed that of tantalum metal, and dilution of tantalum with copper decreases the corrosion resistance. By contrast, Cr–Nb and Cr–Ta alloys show very high corrosion resistance which is higher than that of the alloy components. These results indicate that if both components of binary alloys have a strong passivating ability, the alloys are able to possess better corrosion resistance than the alloy components. The corrosion rate of Cr–

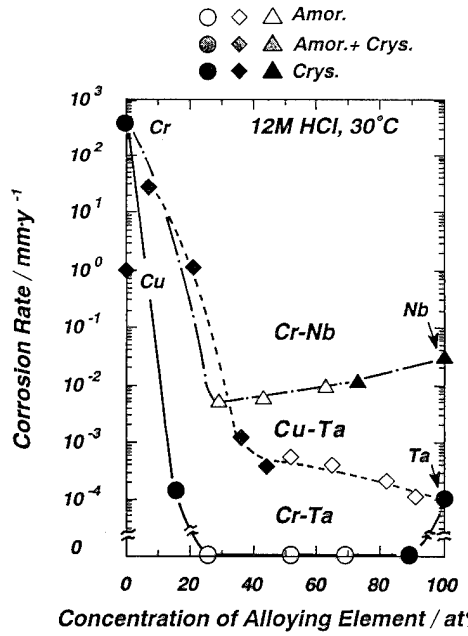

Fig. 7. Changes in the corrosion rates of Cr–Nb [18], Cr–Ta [18] and Cu–Ta [17] alloys in 12 M HCl solution at 30 °C as a function of concentration of alloying element. Corrosion rates of chromium, niobium and tantalum are shown for comparison.

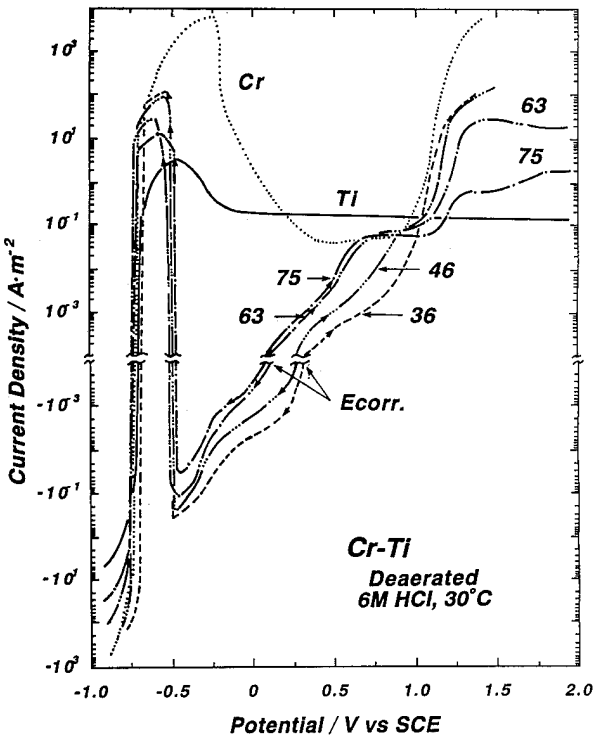

Fig. 8. Potentiodynamic polarization curves for sputter-deposited Ti–Cr alloys, titanium and chromium measured in deaerated 6 M HCl solution at 30 °C [19].

Nb alloys tends to decrease with increasing chromium content. The corrosion rates of Cr–Ta alloys are extremely low and are lower than the level measurable by inductively coupled plasma (ICP) spectrometry, 2×10^{-5} mm per year. It can therefore be said that the amorphous Cr–Ta alloys are immune to corrosion even in 12 M HCl. Athough Cr–16 Ta alloy is crystalline, the corrosion rate of this alloy is very low and of the same order as that of tantalum. Cr–89 Ta alloy, another crystalline alloy, shows a lower corrosion rate than that of tantalum. These results may come from the fact that Cr–16 Ta alloy consists of a single bcc chromium phase supersaturated with tantalum whereas Cr–89 Ta alloy is a single β-tantalum phase supersaturated with chromium.

Fig. 8 shows potentiodynamic polarization curves of sputter-deposited Ti–Cr alloys measured in deaerated 6 M HCl solution at 30 °C [19]. Both chromium and titanium dissolve actively but the Ti–Cr alloys are spontaneously passive owing to dissolved oxygen, the concentration of which is of the order of several tens of ppb. Increasing the chromium content of the alloy decreases the anodic current density. An interesting fact is that an increase in the chromium content of the alloy increases the cathodic current densities of both oxygen and hydrogen reductions. Because there are no spontaneously passive chromium-containing alloys in this aggressive acid, the fact that chromium has such high activities for cathodic reactions has not previously been known. However, the high open-circuit potential and low corrosion rate of the Cr–Ti alloys are mostly dependent upon the chromium content of the alloy. Cathodic polarization results in depassivation in the active region of chromium and the active dissolution current is high when the chromium content of the alloy is high.

Fig. 9 shows potentiodynamic polarization curves of sputter-deposited Cr–Ta alloys measured in 12 M HCl solution at 30 °C [18]. Cr–Ta alloys are also spontaneously passive in 12 M HCl. Cathodic polarization does not result in depassivation in the active region of chromium. In 12 M HCl chromium dissolves actively and the passive current density of chromium is of the order of 10–100 A m^{-2}. Nevertheless, an increasing alloy chromium content decreases the anodic current density and enhances the cathodic oxygen reduction and hydrogen evolution. In this manner, the most significant fact in enhancing the corrosion resistance is that, if spontaneous passivation occurs, the presence of chromium enhances the cathodic oxygen and hydrogen reductions.

Fig. 10 shows cationic fractions of niobium and tantalum in the surface film formed on Cr–Nb and Cr–Ta alloys immersed or polarized for 1 h in 12 M HCl solution at 30 °C [21]. Table 2 shows the fractions of cations in the passive films formed on chromium–valve metal alloys. Although valve metal cations are apt to be concentrated in the passive film, except for Cr–

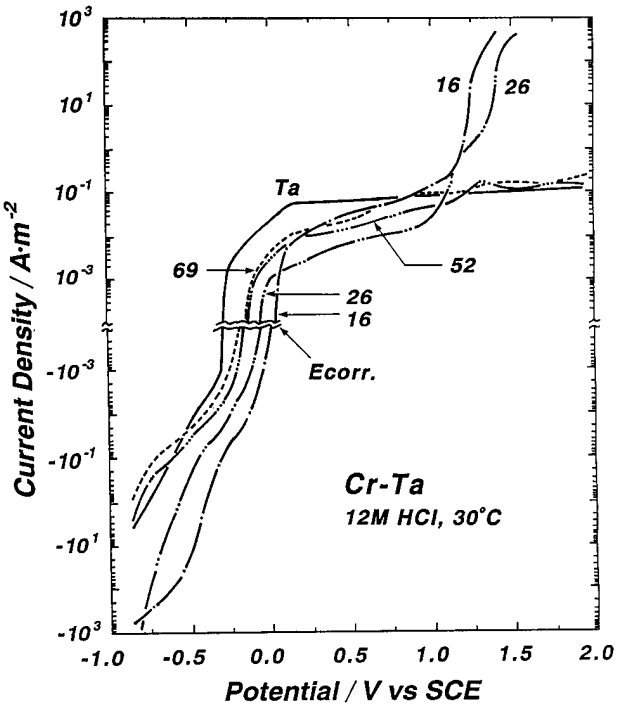

Fig. 9. Potentiodynamic polarization curves for sputter-deposited Cr–Ta alloys and tantalum measured in 12 M HCl solution at 30 °C [18].

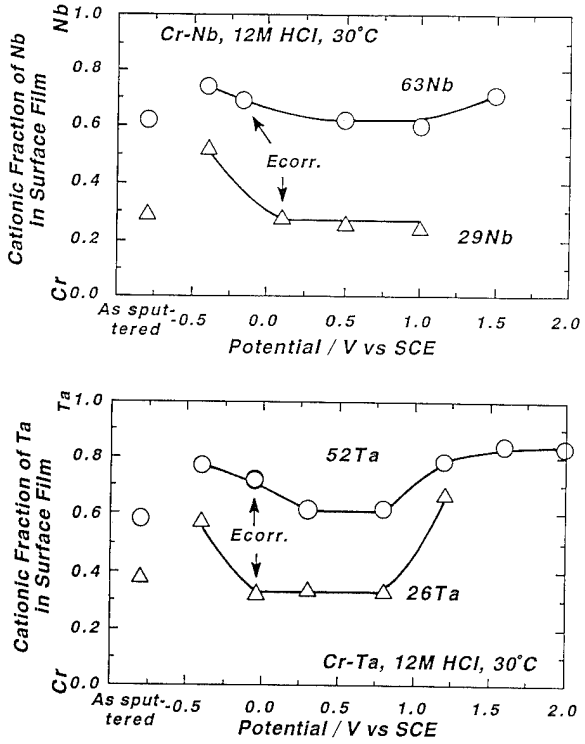

Fig. 10. Cationic fractions of niobium and tantalum in the surface film formed on Cr–Nb and Cr–Ta alloys immersed or polarized for 1 h in 12 M HCl solution at 30 °C [21].

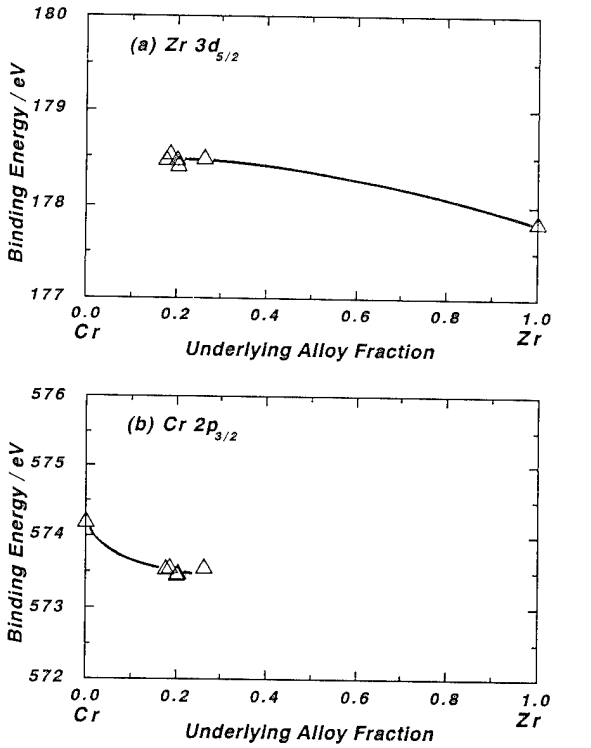

Fig. 11. Correlation of the binding energies of the Cr $2p_{3/2}$ and Zr $3d_{5/2}$ electrons with the fraction of zirconium in the alloy surface under the surface film.

Nb alloys, it is clear that the film consists of both chromium and valve metal cations. As can be seen in Fig. 10, the composition of the stable passive film is not appreciably different from the composition of the air-formed film. In other words, immersion or anodic polarization in the passive region does not change the film composition from that of the air-formed film. It can therefore be said that the air-formed films on these alloys are stable in 12 M HCl. Because of the presence of the air-formed film, spontaneous passivation occurs without reconstruction of the air-formed film.

An interesting fact can be seen with regard to the binding energy of inner shell electrons. Fig. 11 shows the correlation of the binding energies of the Cr $2p_{3/2}$ and Zr $3d_{5/2}$ electrons with the fraction of zirconium in the alloy surface under the surface film. Alloy formation leads to an increase in the binding energy of Zr $3d_{5/2}$ electrons and to a decrease in the binding energy of Cr $2p_{3/2}$ electrons. This indicates that the electronic interaction occurs between chromium and zirconium by alloying, that is, charge transfer from zirconium atoms to more electronegative chromium atoms. This kind of charge transfer from valve metal atoms to more electronegative chromium atoms by alloying has been found for other amorphous alloys such as Cr–Ti, Cr–Nb and Cr–Ta alloys.

Table 2
Cationic composition of passive films formed on binary Cr valve metal alloys in concentrated hydrochloric acids

Alloy (at.%)	HCl concentration (M)	Cations in the film		Ref.
		Cr	Alloying element (at.%)	
Cr–46 Ti	6	44	56 Ti	18
Cr–63 Ti		30	70 Ti	18
Cr–30 Zr		48	52 Zr	20
Cr–29 Nb	12	73	27 Nb	21
Cr–63 Nb		38	62 Nb	21
Cr–26 Ta		68	32 Ta	21
Cr–52 Ta		39	61 Ta	21

Fig. 12 shows the correlation of the binding energies of the Cr^{3+} $2p_{3/2}$ and Ta^{5+} $4f_{7/2}$ electrons with the cationic fraction of tantalum in the surface film formed on Cr–Ta alloys [21]. In contrast to that found in the underlying alloys, formation of a film containing both tantalum and chromium results in charge transfer from chromium to tantalum. Similar charge transfer from chromium (III) ions to valve metal cations has been found for Cr–Ti, Cr–Zr and Cr–Nb alloys. The charge transfer between different cations indicates that these cations locate very closely to show the electronic interaction. This means that the passive film does not consist of a simple mixture of chromium oxyhydroxide and valve metal oxide, but is composed of a double oxyhydroxide of chromium and valve metal cations.

It can therefore be said that if the double oxyhydroxide films of chromium and valve metal cations are formed by uniform distribution of cations, increasing the film chromium content lowers the anodic dissolution current and enhances the cathodic oxygen reduction and hydrogen evolution. Although the roles of chromium and valve metal cations in enhancing the passivity are still unclear, chromium has a better passivating ability than valve metals in spite of the fact that chromium itself dissolves actively in aggressive concentrated hydrochloric acid. The resultant double oxyhydroxide films are more protective than valve metal oxide films in these aggressive solutions, and increasing the alloy chromium content increases the corrosion resistance of the binary chromium–valve metal alloys.

3.3. Cr–Mo alloys

Molybdenum is also an effective alloying element, enhancing the corrosion resistance of the alloys in less oxidizing environments. Fig. 13 shows potentiostatic polarization curves of molybdenum and tungsten metals in 6 M HCl solution at 30 °C [22]. At a potential of 100 mV (vs. SCE) or less, molybdenum is in the passive state where a passive tetravalent molybdenum oxide film is formed. Anodic polarization of molybdenum leads to a sharp increase in the anodic current density due to transpassive dissolution as molybdate ions. This behaviour is easily understood by measuring the amount of molybdenum dissolved during polarization. Fig. 14 shows the amounts of molybdenum and tungsten dissolved during polarization for 1 h at each potential in 6 M HCl solution at 30 °C obtained by ICP solution analysis [22]. These are true anodic polarization curves of molybdenum and tungsten. No dissolution of molybdenum and tungsten occurs in the passive region. However, cathodic polarization results in depassivation of molybdenum showing the active dissolution current, whereas tungsten shows no depassivation.

Although it is impossible to prepare amorphous binary Cr–Mo alloys, in order to examine the synergistic effect of chromium and molybdenum, amorphous ternary Cr–Ni–Mo alloys were prepared by sputter deposition [23]. Fig. 15 shows the change in the corrosion rate of Cr–Ni–Mo alloys in 12 M HCl solution at 30 °C as a function of alloy molybdenum content [23].

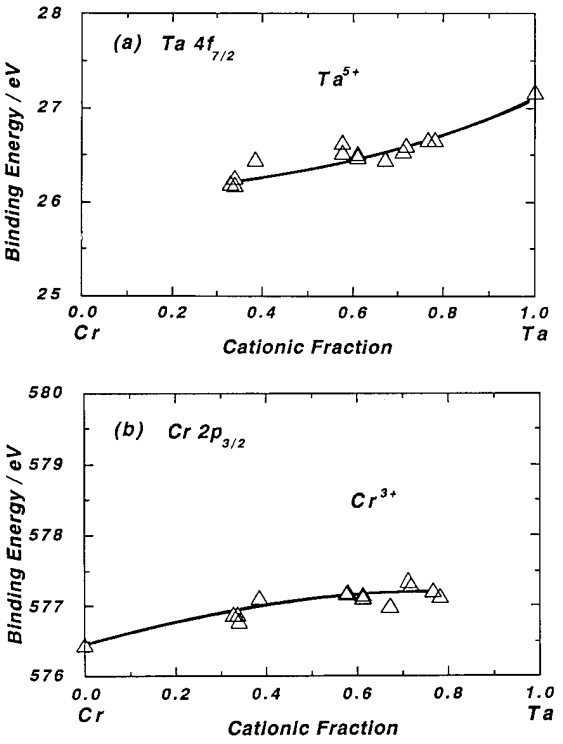

Fig. 12. Correlation of the binding energies of the Cr^{3+} $2p_{3/2}$ and Ta^{5+} $4f_{7/2}$ electrons with the cationic fraction of tantalum in the surface film formed on Cr–Ta alloys [21].

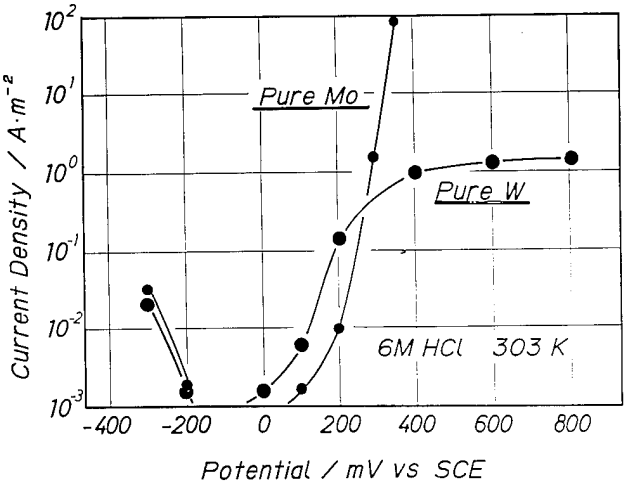

Fig. 13. Potentiostatic polarization curves for molybdenum and tungsten metals in 6 M HCl solution at 30 °C. The current density was measured after polarization for 1 h at each potential [22].

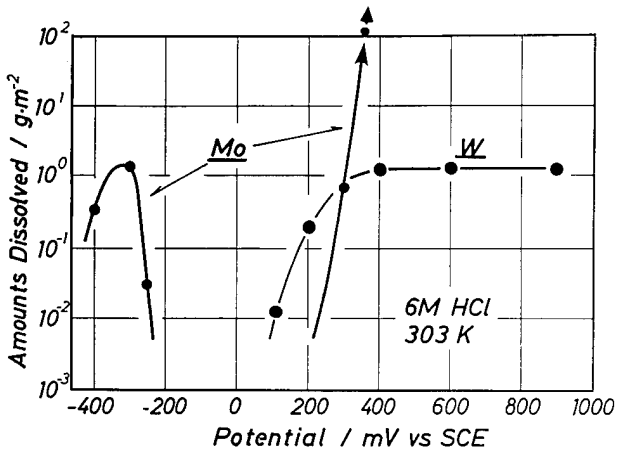

Fig. 14. Amounts dissolved from molybdenum and tungsten metals after polarization for 1 h at each potential in 6 M HCl solution at 30 °C obtained by ICP solution analysis [22].

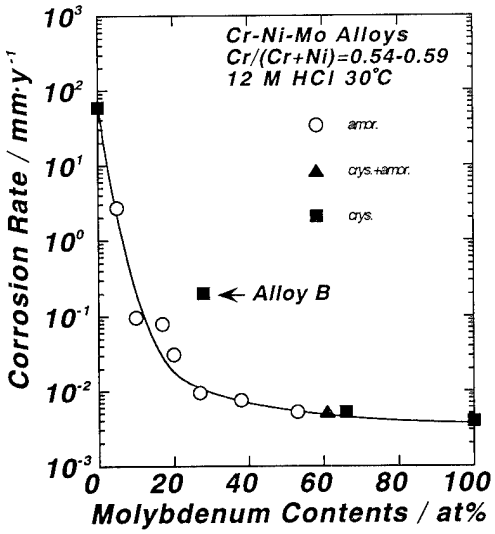

Fig. 15. Change in the corrosion rate of sputter-deposited Cr–Ni–Mo alloys in 12 M HCl solution at 30 °C as a function of alloy molybdenum content. The Cr/(Cr + Ni) atomic ratio in the alloy is 0.54–0.59 [23].

When the ratio of Cr to Ni in ternary Cr–Ni–Mo alloys is almost fixed, an increase in alloy molybdenum content simply decreases the corrosion rate regardless of the alloy structure.

Fig. 16 shows potentiodynamic anodic and cathodic polarization curves of Cr–Ni–Mo alloys measured in 12 M HCl solution at 30 °C [23]. The potentiodynamic polarization curve of molybdenum in 12 M HCl indicates that the passive tetravalent molybdenum film has a high activity for both oxygen and hydrogen reductions. The cathodic polarization curves of ternary Cr–Ni–Mo alloys are almost the same as that of molybdenum. The molybdenum addition decreases the anodic dissolution current and raises the open-circuit potential in the passive region of chromium.

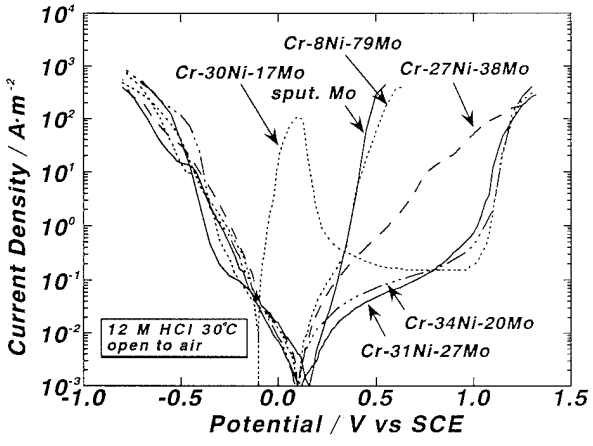

Fig. 16. Potentiodynamic anodic and cathodic polarization curves for Cr–Ni–Mo alloys measured in 12 M HCl solution at 30 °C [23].

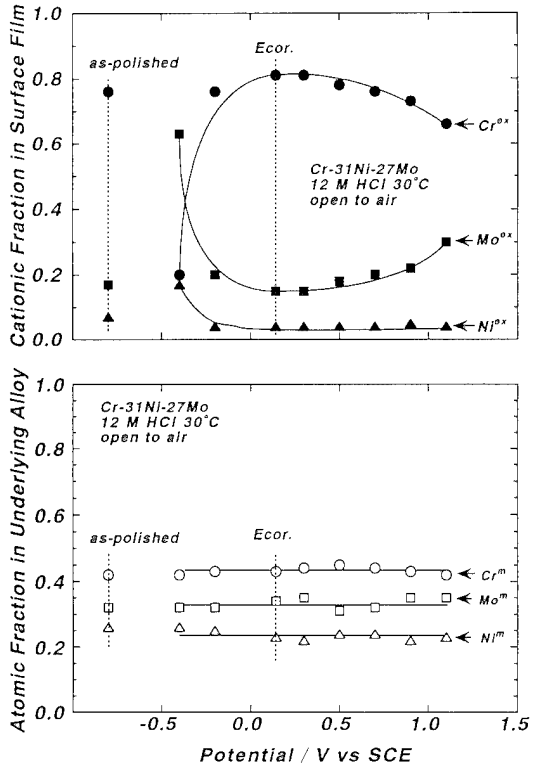

Fig. 17. Cationic fractions in the surface film and atomic fractions in the underlying alloy surface for the amorphous Cr–31 Ni–27 Mo alloy polarized or immersed for 1 h in 12 M HCl at 30 °C [23].

Fig. 17 shows cationic fractions in the surface film and atomic fractions in the underlying alloy surface for amorphous Cr–31 Ni–27 Mo alloy polarized or immersed for 1 h in 12 M HCl at 30 °C [23]. The chromium content of the alloy is 42% but the chromium content of the film after open-circuit immersion exceeds 80%. Nickel is deficient in both the surface film and underlying alloy, and the underlying alloy surface is enriched in molybdenum. Consequently, molybdenum contained in the alloy supresses alloy dissolution, raises the open-circuit potential and leads to the formation of the chromium-enriched passive film. It can therefore be said that an increase in molybdenum content of Cr–Ni–Mo alloys increases the corrosion resistance owing to enhancement of the formation of a chromium-enriched passive film.

4. Resistance against sulphidation and oxidation

Another interesting fact is the extremely high resistance of Al–refractory metal alloys against high-temperature corrosion in sulphadizing and oxidizing environments. Conventional oxidation-resistant alloys suffer catastrophic corrosion in sulphur-containing atmospheres at high temperatures, because of the poor protective properties of sulphide scales. For instance,

the non-stoichiometry of sulphide scales formed on these alloys is often 10%. Because of rapid diffusion of cations through the sulphide scale they are sulphidized very rapidly. Some refractory metals such as molybdenum and niobium are, however, resistant to sulphide corrosion and their sulphidation rates are almost comparable to the oxidation rate of chromium [24–26]. These metals, however, have very low resistance against high-temperature oxidation in spite of the fact that sulphidizing atmospheres in industry are often oxidizing. On the other hand, the best alloying element to form a protective scale in oxidizing environments is aluminium. Consequently, Al–refractory metal alloys must be the best materials having high resistance against both oxidation and sulphidation.

Fig. 18 shows the temperature dependence of sulphidation (solid lines) and oxidation (dotted lines) rates for Al–Mo [27], Al–Mo–Si [28] and Al–Nb alloys [29]. The sulphidation rates of Al–Mo alloys are significantly lower than that of molybdenum metal and are comparable to the oxidation rate of chromia-forming alloys. The sulphidation rates of Al–Nb alloys are lowered further and are lower than that of niobium metal.

The better protective properties of the sulphide scale formed on the Al–Mo alloys in comparison with those of the MoS_2 scale on pure molybdenum result from lower defect concentration in the aluminium-droped MoS_2 phase, constituting the major part of the inner barrier layer [30,31]. The reason why the sulphide scale

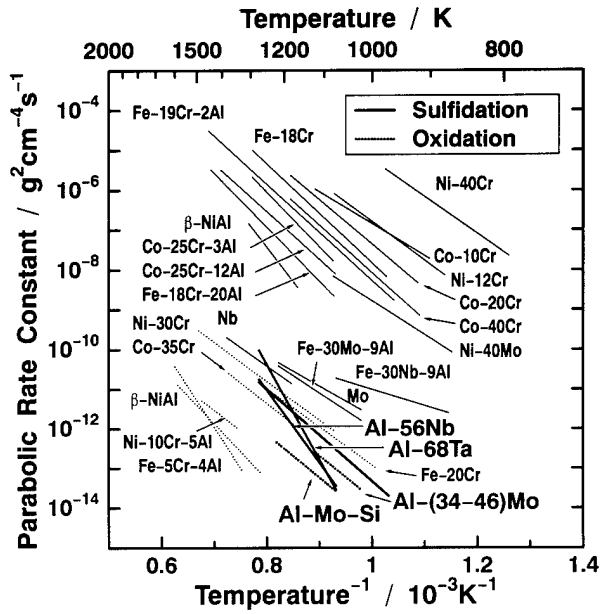

Fig. 18. Temperature dependence of the sulphidation (solid lines) and oxidation (dotted lines) rates for Al–Mo, Al–Mo–Si and Al–Nb alloys [27–29] and analogous dependence of the rates for several binary and ternary alloys [25,30].

formed on the Al–Nb alloys is more protective than that formed on pure niobium is different from that for the Al–Mo alloys. The X-ray diffraction patterns show the formation of the niobium sulphide scale with a strongly preferred orientation on both niobium metal and Al–Nb alloys. The 2 s-NbS_2 scale grows perpendicular to the c-axis during sulphidation. The 2 s-NbS_2 scale is composed of two-dimensional sulphur layers perpendicular to the c-axis. Nb atoms between two sulphur layers are bonded strongly to S atoms. However, only weak van der Waals bonding exists between S atoms in each adjacent sulphur layer without Nb atoms [32,33], and hence transportation of atoms or ions along the sulphur layers without Nb atoms occurs relatively easily. Therefore, the NbS_2 barrier layer grows with the strongly preferred orientation. When aluminium is added, the aluminium-containing niobium sulphide scale is formed, in which aluminium ions locate between the niobium-free sulphur layers and hence the outward diffusion of niobium through the niobium sulphides scale is obstructed. This is the reason why the Al–Nb alloys have a better sulphidation resistance than niobium metal, in spite of the fact that the same niobium sulphide scale with the same preferred orientation is formed on both niobium metal and Al–Nb alloys.

The oxidation rate of Al–Mo alloys is comparable to that of chromia-forming alloys although it is higher than that of aluminia-forming alloys. However, the oxidation rate at temperatures higher than 900 °C is very high. The scale consists mostly of alumina, but because of high alloy molybdenum contents, molybdenum is also oxidized, forming volatile MoO_3. Since the melting point of MoO_3 is 793 °C, the formation of low-melting MoO_3 is responsible for relatively low oxidation resistance of Al–Mo alloys. Accordingly, an attempt to improve the oxidation resistance was made by adding silicon to Al–Mo alloys. The ternary Al–Mo–Si alloys have high sulphidation resistance similar to that of the Al–Mo alloys and have a higher oxidation resistance than Al–Mo alloys. This is attributable to the formation of molybdenum silicide, which is stable against oxidation. During sulphidation and oxidation, amorphous alloys are crystallized, forming intermetallics. Al–Mo alloys form Al_8Mo_3 and Mo_3Al phases. The molybdenum-rich Mo_3Al phase is readily oxidized, forming volatile MoO_3. Accordingly, when the alumina scale surface on the Al–Mo alloys was analysed by XPS, a low concentration of molybdenum was always found. By contrast, Al–Mo–Si alloys are crystallized to Al_8Mo_3 and Mo_5Si_3 phases without forming the easily oxidizable molybdenum-rich Mo_3Al phase. The Mo_5Si_3 phase is very stable against oxidation. Accordingly, any Mo and Si were detected in the top-most surface of the alumina scale.

5. Conclusion

The corrosion behaviour of newly tailored amorphous alloys prepared by sputtering has been interpreted briefly. Different alloy families exhibit different characteristics, although they all have extremely high corrosion resistance. In this manner, sputtering is suitable for tailoring new corrosion-resistant alloys. In addition, sputtering is effective for preparing supersaturated solid solution alloys which are suitable for studying the effects of various alloying elements dissolved in the alloy matrix. Attempts will be continued to prepare new alloys which have high resistance against both wet corrosion and high-temperature corrosion.

References

[1] M. Naka, K. Hashimoto and T. Masumoto, *J. Jpn. Inst. Met.*, *38* (1974) 835.

[2] K. Shimamura, K. Miura, A. Kawashima, K. Asami and K. Hashimoto in R.B. Diegle and K. Hashimoto (eds.), *Corrosion, Electrochemistry and Catalysis of Metallic Glasses*, Electrochemical Society, Pennington, NJ, 1988, p. 232.

[3] H. Yoshioka, A. Kawashima, K. Asami and K. Hashimoto, in R.B. Diegle and K. Hashimoto (eds.), *Corrosion, Electrochemistry and Catalysis of Metallic Glasses*, Electrochemical Society, Pennington, NJ, 1988, p. 242.

[4] H. Yoshioka, H. Habazaki, A. Kawashima, K. Asami and K. Hashimoto, *Corros. Sci.*, *31* (1990) 349.

[5] Q. Yan, H. Yoshioka, H. Habazaki, A. Kawashima, K. Asami and K. Hashimoto, *Corros. Sci.*, *31* (1990) 401.

[6] Q. Yan, H. Yoshioka, H. Habazaki, A. Kawashima, K. Asami and K. Hashimoto, *J. Non-Cryst. Solids*, *125* (1990) 25.

[7] Q. Yan, H. Yoshioka, H. Habazaki, A. Kawashima, K. Asami and K. Hashimoto, *Corros. Sci.*, *32* (1990) 327.

[8] H. Yoshioka, H. Habazaki, A. Kawashima, K. Asami and K. Hashimoto, *Electrochim. Acta*, *36* (1991) 1227.

[9] J.H. Kim, H. Yoshioka, H. Habazaki, A. Kawashima, K. Asami and K. Hashimoto, in C.R. Clayton and K. Hashimoto (eds.), *Corrosion, Electrochemistry and Catalysis of Metastable Metals and Intermetallics*, Electrochemical Society, Pennington, NJ, 1993, p. 48.

[10] H. Yoshioka, A. Kawashima, K. Asami and K. Hashimoto, in *Proc. MRS International Meeting on Advanced Materials, Tokyo, May 30–June 3, 1988* Vol. 3, Materials Research Society, Pittsburgh, PA, 1988, p. 429.

[11] E. Akiyama, J.H. Kim, H. Yoshioka, H. Habazaki, A. Kawashima, K. Asami and K. Hashimoto, *Corros. Sci.*, *34* (1993) 27.

[12] K. Hashimoto, N. Kumagai, H. Yoshioka, J.H. Kim, E. Akiyama, H. Habazaki, A. Kawashima, K. Asami and K. Hasimoto, *Corros. Sci.*, *35* (1993) 363.

[13] H. Yoshioka, H. Habazaki, A. Kawashima, K. Asami and K. Hashimoto, in C.R. Clayton and K. Hashimoto (eds.), *Corrosion, Electrochemistry and Catalysis of Metastable Metals and Intermetallics*, Electrochemical Society, Pennington, NJ, 1993, p. 72.

[14] H. Yoshioka, H. Habazaki, A. Kawashima, K. Asami and K. Hashimoto, *Corros. Sci.*, *33* (1992) 425.

[15] H. Yoshioka, H. Habazaki, A. Kawashima, K. Asami and K. Hashimoto, *Corros. Sci.*, *32* (1991) 313.

[16] A. Mitsuhashi, H. Habazaki, A. Kawashima, K. Asami and K. Hashimoto, in R.B. Diegle and K. Hashimoto (eds.), *Corrosion, Electrochemistry and Catalysis of Metallic Glasses*, Electrochemical Society, Pennington, NJ, 1988, p. 191.

[17] J.H. Kim, H. Yoshioka, H. Habazaki, A. Kawashima, K. Asami and K. Hashimoto, *Corros. Sci.*, *33* (1992) 1507.

[18] J.H. Kim, E. Akiyama, H. Habazaki, A. Kawashima, K. Asami and K. Hashimoto, *Corros. Sci.*, *34* (1993) 1947.

[19] J.H. Kim, E. Akiyama, H. Yoshioka, H. Habazaki, A. Kawashima, K. Asami and K. Hashimoto, *Corros. Sci.*, *34* (1993) 975.

[20] J.H. Kim, E. Akiyama, H. Habazaki, A. Kawashima, K. Asami and K. Hashimoto, *Corros. Sci.*, *34* (1993) 1817.

[21] J.H. Kim, E. Akiyama, H. Habazaki, A. Kawashima, K. Asami and K. Hashimoto, *Corros. Sci.*, *36* (1994) 511.

[22] H. Habazaki, A. Kawashima, K. Asami and K. Hashimoto, *Corros. Sci.*, *33* (1992) 225.

[23] P.Y. Park, E. Akiyama, H. Habazaki, A. Kawashima, K. Asami and K. Hashimoto, *Corros. Sci.*, *36* (1994) 1395.

[24] P. Kofstad, *High Temperature Corrosion*, Elsevier, London, 1988.

[25] S. Mrowec and K. Przybylski, *High Temp. Mater. Processes*, *6* (1984) 1.

[26] S. Mrowec and K. Przybylski, *Oxid. Met.*, *23* (1985) 107.

[27] H. Habazaki, J. Dabek, K. Hashimoto, S. Mrowec and M. Danielewski, *Corros. Sci.*, *34* (1993) 183.

[28] H. Habazaki, J. Dabek, K. Hashimoto, S. Mrowec and M. Danielewski, in C.R. Clayton and K. Hashimoto (eds.), *Corrosion, Electrochemistry and Catalysis of Metastable Metals and Intermetallics*, Electrochemical Society, Pennington, NJ, 1993, p. 224.

[29] H. Mitsui, H. Habazaki, K. Asami, K. Hashimoto and S. Mrowec, in *Proc. MRS International Meeting on Advanced Materials, Tokyo, August 30–September 3, 1993*, Trans. Mater. Research Soc. Jpn., 14A (1994) 309.

[30] B. Gleeson, D.L. Douglass and F. Gesmundo, *Oxid. Met.*, *31* (1989) 209.

[31] Z. Grzesik, H. Habazaki, K. Hashimoto and S. Mrowec, *Corros. Sci.*, *36* (1994) 1499.

[32] F. Kadijk and F. Jellinek, *J. Less-Common Met.*, *19* (1969) 421.

[33] F. Gesmundo, F. Viani and Y. Niu, *Oxid. Met.*, *38* (1992) 465.

ELSEVIER

Materials Science and Engineering A198 (1995) 11–18

MATERIALS SCIENCE & ENGINEERING A

Effect of microstructure on passive film formation and breakdown in sputter-deposited Al–Ta alloy films

Jerome Kruger[a], R. Scott Lillard[a], Christopher C. Streinz[a], Patrick J. Moran[b]

[a]*The Johns Hopkins University, Baltimore, MD 21218, USA*
[b]*United States Naval Academy, Annapolis, MD 21402, USA*

Abstract

The role played by microstructural features in the passivation and breakdown processes which lead to pitting has been examined for the first time by the new techniques of dynamic imaging microellipsometry (DIM) and local electrochemical impedance spectroscopy (LEIS). Contrary to expectations, an examination of the passivation of sputter-deposited Al–Ta alloy films found that the film on the Al_3Ta precipitates formed a thicker passive layer than that on the solid solution matrix surrounding the precipitates. The LEIS study of the microstructural effects under breakdown conditions found that the film on the Al_3Ta precipitate had a higher capacitance than the dealloyed region surrounding it, indicating that the film on the precipitate has different properties from the dealloyed region in its vicinity. This difference in film thickness and properties, found by both DIM and LEIS, may be responsible for the breakdown which leads to pitting initiated in the region adjacent to the precipitates.

Keywords: Microstructure; Pitting; Passivation; Breakdown; Al–Ta alloy films

1. Introduction

It has been shown in recent years [1–5] that sputter-deposited, solid solution, aluminum–transition metal (Cr, Mo, Ta, W and others) alloy films have dramatically high pitting potentials E_{pit}. The objective of this study was to try to gain a better understanding of the origins of the enhanced passivity and resistance to pitting exhibited by these non-equilibrium materials. For example, solid solution additions of 8 at.% Ta increase E_{pit} by approximately 0.8 V (-0.7 to 0.1 V vs. a saturated calomel electrode (SCE)) [5]. The mechanism(s) responsible for these improvements is by no means understood and remains somewhat controversial. An X-ray photoelectron spectroscopy (XPS) study by Davis et al. [5] of the Al–Ta system (the alloys considered in this paper) demonstrated that the passive film remains thin throughout a polarization sequence and that it is enriched in Ta_2O_5 compared with the bulk alloy concentration. They proposed that this thin Ta_2O_5-rich film resists Cl^- penetration, enhancing the localized corrosion resistance of the alloy. In situ ellipsometric measurements [6] verified that Al–8Ta forms a thinner passive film than pure Al. There have been a number of other suggested mechanisms, e.g. by Natishan et al. [2] and Szklarska-Smialowska [7]. Missing from these proposed mechanisms is the role of the oxide film, which forms on the matrix and precipitate materials, in the initiation of pits; this was the purpose of the present study.

This paper describes the application of two in situ techniques, local electrochemical impedance spectroscopy (LEIS) [8] and dynamic imaging microellipsometry (DIM) [9], to a study of the effect of a microstructural feature (the Al_3Ta precipitates formed in Al–Ta alloys) on passive film formation and breakdown. (More detailed descriptions of the application of these techniques to studies of the Al–Ta system are given elsewhere [10–13].) Although these precipitates are not observed in solid solution sputtered alloy films, exceedingly small precipitate nuclei may serve as sites for pit initiation. This paper seeks to examine the role, if any, played by Al_3Ta precipitates in the pitting process using LEIS and DIM. To do this, bulk Al–Ta alloys with large precipitates have been used. The microstructural studies are correlated with electrochemical and ellipsometric measurements made on solid solution alloys to form the basis for a discussion concerning the

SSDI 0921-5093(94)04502-X

role of precipitates in the initiation of pitting in Al–Ta alloys.

2. Experimental approach and details

2.1. Techniques

2.1.1. Local electrochemical impedance spectroscopy

Electrochemical impedance spectroscopy (EIS), which is also known as a.c. impedance, is a non-destructive in situ technique which has been used extensively to investigate electrochemical systems [14]. The current response of the whole electrode is used to produce the impedance data. This results in a surface-averaged measurement that may not be relevant if interest is focused on the determination of the effects of microstructural features on local phenomena such as localized corrosion processes. The non-uniformity arises because the frequency dependence of the current distribution in the vicinity of a corrosion site is markedly different from that near an inactive or passive area. EIS has been applied to localized corrosion systems, but data analysis for these systems is complex [15]. For this reason, a technique (LEIS) for generating local a.c. impedance data has been developed [8] to investigate localized corrosion due to multiphases, grain boundary effects or other surface heterogeneities which may occur on an electrode surface. The basis for this technique depends on the premise that the a.c. solution current densities near the working electrode, in a conventional three-electrode a.c. impedance measurement, are proportional to the local impedance properties of the electrode.

It has been demonstrated that the current distribution near an electrode may be mapped in three dimensions; each, or any combination, may be mapped for an electrode surface by choosing the correct probe geometry [16]. This technique, in order to simplify data analysis, only measures the component of the a.c. current normal to the electrode. Because the current and potential lines are perpendicular to one another, it is necessary to measure the a.c. potential drop between planes parallel to the electrode to determine the a.c. solution current density normal to the electrode. An effective map of the local impedance properties of an electrode requires that this a.c. potential drop measurement must be made on a relatively small scale. To accomplish this, the two-electrode microprobe, shown in Fig. 1, was designed (see Ref. [8] for more details).

2.1.2. Dynamic imaging microellipsometry

Traditional ellipsometry, an optical technique that enables the thickness and complex refractive index of thin films on metal surfaces to be measured in situ [17], has been a valuable tool for studying corrosion processes [18], but it is by nature a surface averaging technique and is limited in its ability to study localized corrosion processes, such as the effects of microstructure on passive film growth and breakdown.

Cohn and Wagner [9] developed dynamic imaging microellipsometry (DIM) in order to overcome this limitation. In contrast with other techniques [19,20] aimed at acquiring high spatial resolution ellipsometric data, DIM is a radiometric full field imaging approach to ellipsometry. Good spatial resolution (approximately 20 μm) and precision, in addition to good temporal resolution (minutes), have been demonstrated. The DIM approach uses the standard polarizer, specimen, compensator, analyzer (PSCA) ellipsometry configuration in combination with an imaging lens, a charged coupled device (CCD) video camera and digital image processing techniques to acquire high spatial resolution ellipsometric data with good temporal resolution. DIM produces digitized grey scale maps (called ellipsograms) of the ellipsometric parameters Δ (change in phase) and Ψ (change in relative amplitude) that enable the determination of the film thickness with a resolution of approximately 0.1 nm and film and substrate refractive indices. The ellipsograms are produced by acquiring

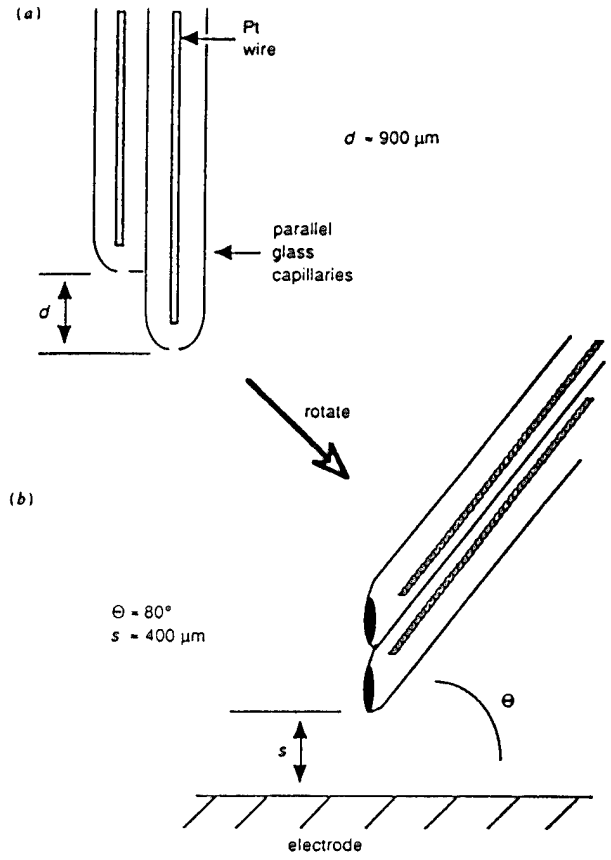

Fig. 1. The two-electrode microprobe used to make LEIS measurements (from Ref. [8]).

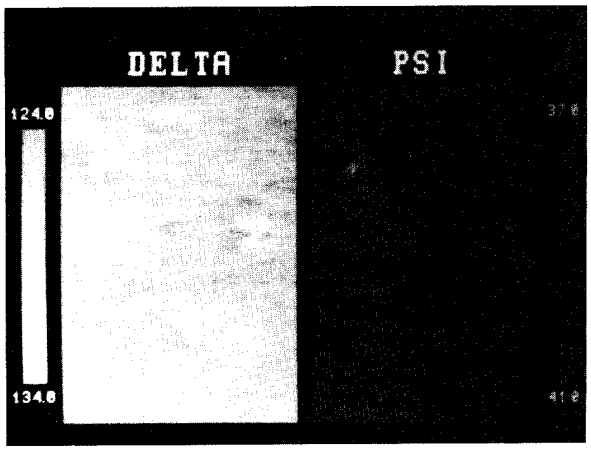

Fig. 2. Ellipsogram for the Al_3Ta precipitate/Al matrix system at $E_{corr} = -0.750$ V vs. SCE. The bright regions in the Δ map and the dark regions in the Ψ map are the precipitates. The grey levels are proportional to Δ and Ψ (from Ref. [12]).

four digitized intensity maps each at a distinct polarizer setting and then calculating the Δ and Ψ maps point by point using the appropriate algorithms.

A third-generation DIM system [21] has recently been developed and applied to the in situ study of passivation. Ellipsogram to ellipsogram temporal resolution for this system is approximately 20 s. A sample in situ ellipsogram of a passivated Al–Ta alloy with large microstructural features is illustrated in Fig. 2. The grey levels observed are linearly proportional to Δ and Ψ. The grain structure is "observed" in the Δ map but not in the Ψ map, indicating differences in the passive film thickness over the respective grains.

2.2. Materials

2.2.1. Alloy fabrication and characterization

2.2.1.1. *Sputtered films.* Al–Ta alloys of composition Al–4at.%Ta, Al–8at.%Ta and Al–25at.%Ta, 99.999% Al and 99.9% Ta were deposited on single-crystal (orientation 100 or 110) silicon substrates via magnetron cosputter deposition. These compositions will hereafter be referred to as Al–4Ta, Al–8Ta and Al–25Ta respectively. Specimens were sputtered for 1 h to a final thickness of approximately 400 nm. Glancing angle X-ray analysis and transmission electron microscopy showed no evidence of second phase Al_3Ta precipitates in either of the sputtered alloys.

2.2.1.2. *Alloys with large Al_3Ta precipitates.* To explore the capability of DIM and LEIS to examine in situ passive film formation and breakdown processes at a resolution level of the microstructures existing in an Al–Ta alloy, it was necessary to prepare an alloy that contained Al_3Ta precipitates whose size was within the detectability of the two techniques (20 μm for DIM and 300 μm for LEIS). An Al–1.5at.%Ta alloy was prepared and heat treated at a temperature above the solidus line for 12 days to produce large (approximately 50 μm) Al_3Ta precipitates surrounded by essentially pure Al. (The equilibrium concentration of Ta in Al is approximately 0.02at.%Ta [22].) The specimens provided two of the microstructural features existing in Al–Ta alloys that are relevant to the study of localized passive film formation and breakdown: Al_3Ta and the dealloyed region adjacent to the Al_3Ta precipitates. To examine the areas where no dealloying occurred, sputter-deposited Al–Ta films were also examined by DIM.

2.3. Electrochemical experiments

2.3.1. Procedure

Potentiodynamic polarization and EIS curves of thin sputtered Al–4Ta and Al–8Ta alloy films (as well as bulk Al and Ta) were generated in deaerated 0.1 M NaCl, pH 7.5 (abbreviated as NaCl), aerated 0.1 M NaCl, pH 4.5–5.5 (NaCl5), aerated 0.5 M boric acid/0.05 M sodium tetraborate, pH 7.2 (Borate7), aerated 0.1 M NaCl/0.5 M boric acid/0.05 M sodium tetraborate, pH 7.2 (NaClBor7) and aerated 0.1 M NaCl/0.5 M NaAc, pH 7–8 (NaClAce7) solutions. LEIS experiments on alloys containing large Al_3Ta precipitates were performed in the borate/boric acid solution given above.

2.4. Ellipsometric experiments

2.4.1. Procedure (sputtered alloy films)

Passive film growth on Al, solid solution Al–8Ta and Al–25Ta and Ta was studied via ellipsometry in a solution buffered to pH 7.2 with 0.5 M boric acid/0.05 M sodium tetraborate. Solutions were neither aerated nor deaerated. Samples of approximately 1 cm^2 area were cleaved from the sputtered wafers and mounted on a Teflon™ sleeve working electrode assembly. Samples were allowed to equilibrate for 4 h to achieve a stable E_{corr} and to allow gas bubbles to disperse from the solution.

In these experiments, the DIM system was used as a conventional ellipsometer. Streinz et al. [11] describes the determination of film thicknesses and optical constants from the raw ellipsometric data. As expected, all the ellipsograms were uniform with no microstructural features.

Samples were polarized to 0.0, 1.0, 2.0 and 5.0 V vs. SCE for 15 min. Two specimens of each alloy were polarized to each of the anodic potentials. Ellipsograms were obtained at 1 min intervals during polarization. Additional specimens were polarized for 20 h at 0.0 V

vs. SCE to monitor long-term film formation. Ellipsograms were obtained at 1 min intervals for the first 15 min, 15 min intervals for the first hour and 1 h intervals until completion of the experiment.

XPS was used to determine the composition of the passive films on Al–8Ta and Al–25Ta polarized at 0.0 V vs. SCE for 15 min.

2.4.2. Procedure (alloys with Al_3Ta precipitates)

Specimens were stepped anodically to 0.0, 1.0, 2.0 or 5.0 V vs. SCE for 15 min. Ellipsograms were obtained at 1 min intervals during polarization. By obtaining ellipsograms at different times at a potential in the passive region of the anodic polarization curve, we were able to determine the rate of passive film formation for each of the microstructural features. Passive film growth on Al–1.5Ta alloys containing large Al_3Ta precipitates was measured via DIM in a solution buffered to pH 7.2 with 0.05 M sodium tetraborate and 0.5 M boric acid. All ellipsometric measurements were made at an angle of incidence of 71.0°. The DIM system has been described in detail in a previous paper [21].

As with the DIM measurements on the sputtered alloy films, samples were then allowed to stabilize for 4 h to achieve a steady E_{corr} and to allow gas bubbles to disperse from the solution. It was important for the solution to be free from all macroscopic and microscopic bubbles. The presence of even a few small bubbles in the solution interfered greatly with DIM data acquisition by blocking the path of either the incident or reflected radiation. It was especially important in the microellipsometry experiments for the solution to be free of bubbles since they induced heterogeneities in the ellipsograms that could be mistaken for heterogeneities on the electrode surface. No significant changes were observed in the ellipsometric parameters for the matrix or the precipitate during the stabilization period.

2.5. Pitting experiments

2.5.1. Procedure

In order to relate the LEIS and DIM experimental results to sites where breakdown, leading to pit initiation, takes place, an Al–1.5Ta alloy containing large Al_3Ta precipitates was polarized potentiostatically to 0.0 V vs. SCE for 15 min to form a barrier layer passive film. After polarization, the alloy was open-circuited and returned to E_{corr}. This took approximately 15 min. The sample was then removed from the buffered borate (pH 7.2) solution and immersed in an identical solution containing 0.1 M NaCl. Following potential stabilization in the solution containing NaCl, the alloy was polarized to −0.5 V (approximately 0.25 V above the pitting potential). Pits were allowed to initiate and propagate until specimen current densities on the order of several hundred microamperes per square centimeter were observed. The alloy was then removed from the solution, rinsed and the pit location and morphology were examined by scanning electron microscopy (SEM). After SEM examination, the sample was repolished and passivated at 1.0 V for 15 min, allowed to pit as before and re-examined by SEM.

3. Results and discussion

3.1. Electrochemical studies

3.1.1. Single-phase alloy films

To determine whether or not the sputter deposition process affects the corrosion properties of metals (by creating a very small grain size, for example), the pitting potential of sputter-deposited Al was compared with that of bulk Al. Polarization results of thin film and bulk Al generated in the solutions described in Section 2.3 are given in Table 1.

Table 1 provides ample evidence to indicate that, although additions of Ta to Al create alloys with improved pitting potentials when produced with a non-equilibrium method such as sputter deposition, Ta additions to Al do not decrease the rate of metal dissolution. As can be seen in Table 1, the results of the potentiodynamic polarization experiments demonstrate that the passive current density for Al in aerated 0.5 M boric acid/0.05 M sodium borate solution (pH 7.2) (Borate7) is approximately 1.4 μA cm^{-2}. In this same solution, the passive current densities of Al–4Ta and Al–8Ta are larger, 6.5 and 6.9 μA cm^{-2} respectively. This same trend is also found in chloride-containing

Table 1
Summary of pitting potentials and passive current densities for bulk Al, sputtered Al, Ta, Al–4Ta and Al–8Ta (from Ref. [13])

Sample (solution)	$i_{pass} \times 10^{-6}$ (cm^{-2})	E_{pit} vs. SCE (mV)
Bulk Al		
(NaCl)	0.30 ± 0.1	−691 ± 18
Thin film Al		
(NaCl)	0.28 ± 0.05	−687 ± 13
(Borate)	1.40	N.A.
Ta		
(NaClBor7)	2.0 ± 0.5	N.A.
Al–4Ta		
(NaCl5)	58 ± 8	−433 ± 9
(NaClBor7)	2.5 ± 0.24	> +200
(Borate 7)	6.5	N.A.
(NaClAce7)	1.9	> +200
Al–8Ta		
(NaCl5)	79 ± 16	−278 ± 13
(NaClBor7)	2.36 ± 0.32	+132 ± 20.8
(NaClAce7)	3.0	+190
(Borate7)	7.0	N.A.

Table 2
Summary of EIS data for 99.999% Al, Al–4Ta and Al–8Ta. All experiments were performed at a potential in the passive range. Bessone [25] components: R_t = polarization resistance; C_b = capacitance of oxide film; t = film thickness determined from C_b (from Ref. [13])

Sample (solution)	Passive potential vs. SCE(mV)	R_t (Ω cm^2)	C_b (F $\times 10^{-6}$ cm^{-2})	t (m $\times 10^{-10}$)
Al				
(Borate7)	−300	1.18×10^5	2.68	28
(NaCl)	−900	1.72×10^5	5.00	15
Al–4Ta				
(Borate 7)	−240	5.55×10^4	15.1	7.1
(NaCl5)	−700	1.14×10^3	11.8	7.3
Al–8Ta				
(Borate7)	−240	3.08×10^4	31.2	3.1
(NaCl5)	−500	1.60×10^3	13.0	7.3

solutions. In 0.1 M NaCl buffered to pH 7 with boric acid and sodium borate (NaClBor7), the passive current density of Al is approximately 0.3 μA cm^{-2}. In the same solution, the passive current densities of Al–4Ta, Al–8Ta and Ta are 2.5, 2.4 and 2.0 μA cm^{-2} respectively. These findings agree with those of Davis et al. [5] who found that the passive current densities for Ta and Al–Ta alloys were higher than the passive current density for pure Al in the same solution.

From the results shown in Table 1 it can be concluded that Ta and an alloy with a non-equilibrium structure do not result in a decrease in the i_{pass} value of Al but lead to an increase in the E_{pit} value of Al. Therefore it appears that an increase in E_{pit} is not related to the conductivity of ions through the passive film below E_{pit}. A possible explanation may be found using the concept of the pH of zero charge (pH_{pzc}) [23,24] which determines whether an oxide will adsorb a Lewis base such as Cl^-. Thus the pH_{pzc} of the oxide film will determine whether Cl^- will adsorb at or above E_{pit}. Ta raises the pH_{pzc}.

EIS experiments were carried out to relate the passive film properties to the polarization data of the sputtered alloy films. The EIS data were interpreted on the basis of the model of Bessone et al. [25], which was proposed for a metal bearing dielectric films of the type formed in our study. Values for each of the components of the Bessone model were established for Al, Al–4Ta and Al–8Ta and are given in Table 2. The dielectric constant used for Al oxide was 8.5 and is an average of the dielectric constants for this material [26]. Because no values for the dielectric constant of the alloys have yet been reported in the literature, a value for the Al–4Ta and Al–8Ta alloy was assumed using the simple rule of mixtures.

The EIS data given in Table 2 support the polarization data in Table 1. Thus the corrosion rate (R_t) increases and the film thickness (t) decreases when Ta is alloyed with Al. This may indicate, according to Davis et al. [5], that Ta^{5+} ions act as a barrier to oxygen, resulting in thinner films, and to Cl^-, resulting in a higher E_{pit}.

3.1.2. Alloys with large Al_3Ta precipitates

The Al–1.5Ta specimen shown in Fig. 3 was studied by LEIS. The Al_3Ta precipitates in this sample were on the order of 10–100 μm in diameter, although one large precipitate measuring approximately 1 mm in diameter was found. The segregation of the precipitates to one side of the sample, as shown in Fig. 3, was due to gravity. This sample was studied in an aerated 0.1 M sodium chloride solution buffered to pH 7.2 with 0.5 M boric acid/0.05 M sodium borate and held at $E_{corr} = -750$ mV vs. SCE. LEIS line scans of this sample were generated by stepping the probe in increments of 250 μm from the precipitate-depleted region to the precipitate-rich region (see Fig. 3) and were conducted over the frequency range of 1–10 000 Hz.

Two LEIS line scans at 2.4 and 2400 Hz were carried out to plot the magnitude of the impedance as a function of position and the results are given in Fig. 4. In Fig. 4, position 0.0 is in a region of the sample which is mostly Al; the large precipitate is centered at about the 4.5 position and position 6.0 is in a region of high precipitate density. It can be seen that regions of high precipitate concentration have low impedance values. The dip in the high frequency impedance data, between 1000 and 10 000 Hz, results from changes in the current density distribution as discussed elsewhere [8]. The lowest impedance in these line scans is that of the large precipitate, which is approximately 500 Ω cm^{-2} lower than the impedance of the Al portion of the sample at 2.4 Hz. This point is re-emphasized in Fig. 5, a Bode magnitude plot generated from LEIS by plotting the logarithm of the magnitude of the impedance from one position, either over Al or the Al_3Ta precipitate, as a function of frequency. Although the LEIS data were not generated at frequencies low enough to enable the

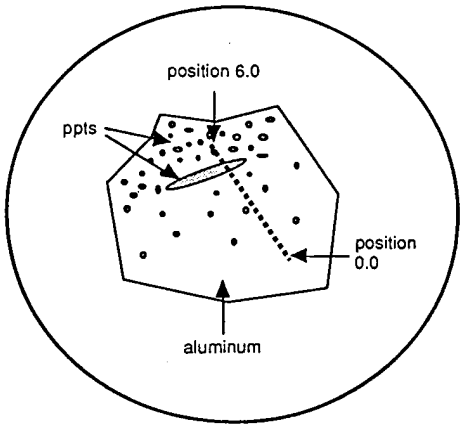

Fig. 3. The Al–1.5Ta alloy used for the LEIS experiments (from Ref. [10]).

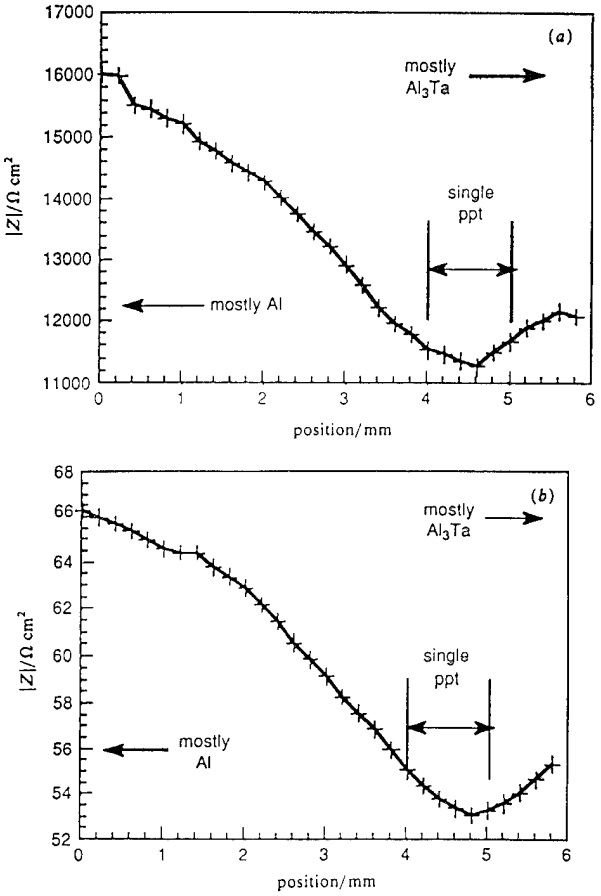

Fig. 4. LEIS line scans of the specimen shown in Fig. 3: (a) at 2.4 Hz; (b) at 2400 Hz. From Ref. [10].

charge transfer impedance for the precipitate and Al to be resolved, it is clear from Fig. 5 that the capacitance of the film over the precipitate is slightly larger than the capacitance of the film over Al. This indicates that the two films differ somewhat in composition and/or thickness. This will be shown, more positively, in the DIM results described below.

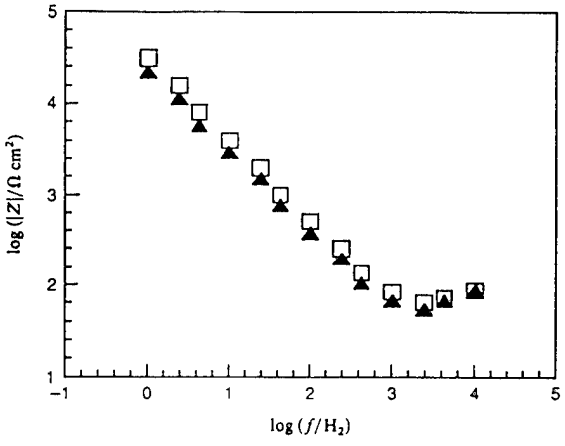

Fig. 5. Bode magnitude plot generated from LEIS data for the Al_3Ta precipitate (▲) and the Al matrix (□). From Ref. [10].

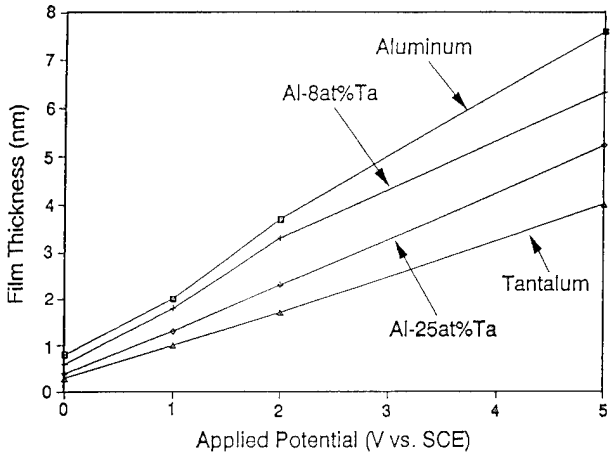

Fig. 6. Change in barrier layer film thickness vs. applied potential for Al, Al 8Ta, Al–25Ta and Ta. Increasing concentrations of solid solution Ta decrease the film thickness. From Ref. [11].

3.2. Ellipsometric studies

3.2.1. Single-phase alloy films

These experiments sought to determine the barrier layer thickness of the passive films on solid solution Al–8Ta, Al–25Ta, Al and Ta. The indices of refraction for the films were in the ranges 1.59–1.62 and 2.17–2.22 for the films on Al and Ta respectively. These indices are consistent with literature values [27,28].

A decrease in the thickness of the anodic oxide films on Al, Al–8Ta, Al–25Ta and Ta at applied potentials of 0.0, 1.0, 2.0 and 5.0 V vs. SCE occurred with an increase in the concentration of Ta in the solid solution alloy films (Fig. 6), indicating the formation of a more protective film. This may suggest an enrichment of the barrier layer film with Ta_2O_5 with increasing applied potential, as observed by Davis et al. [5].

The X-ray photoelectron spectrum for Al–25Ta polarized at 0.0 V vs. SCE for 15 min showed that the composition of the passive film on Al–25Ta was approximately 30% oxidized Ta. Analysis of the film on Al–8Ta polarized at 0.0 V vs. SCE for 15 min showed a film composition of approximately 10% oxidized Ta.

The results found in the ellipsometric studies of the non-equilibrium alloys may be related to the improved pitting resistance of the Al–Ta system. First, the fact that the film on the alloys is thinner indicates that it has a higher ionic resistivity. This is consistent with the model of Davis et al. [5], who proposed that the thin layer impedes the migration of Cl^- through the passive film, as pointed out above in the discussion of the electrochemical experiments. However, the observation of thinner passive films does not eliminate the possibility that another mechanism may be responsible for the improved pitting resistance of these alloys.

3.2.2. Alloys containing large Al_3Ta precipitates

Fig. 7 plots the change in film thickness vs. the applied potential. At 0.0 V, the thickness of the passive film on the precipitate is approximately twice that of the passive film on the matrix; at around 0.0 V the thicknesses are approximately equal, and at 2.0 V the film thickness over the matrix is greater than that over the precipitate. The average indices of refraction of the films formed on the Al matrix and Al_3Ta precipitate were 1.60 and $1.78 + 0.055i$ respectively. An examination of the film formation on sputtered Al–25Ta and Al–8Ta revealed film thicknesses less than those measured for the matrix or the Al_3Ta precipitate.

It is expected that the precipitate should form thinner films at all applied potentials owing to the enrichment of highly protective Ta_2O_5 in the passive layer and, indeed, thinner films do form on the precipitate at high potentials (2.0 V and above), but not at low potentials (below 0.0 V). At present this is not understood. The index of refraction of the film over the matrix is consistent with that formed on pure Al [12]. The real portion of the index of the film over the precipitate is consistent with a film containing both Al_2O_3 and Ta_2O_5. Muth [29] has shown that the index of Ta_2O_5 is 2.22 and that an Al–Ta alloy forms a film whose index is between that of Al_2O_3 and Ta_2O_5 depending on the alloy composition. A first approximation using the law of mixtures indicates that Al_3Ta would be expected to form a film with an index of 1.75. It should also be noted that the film over Al_3Ta has a small absorption coefficient. The physical basis for this is not presently understood since the indices of the passive layers on Al and Ta are entirely real. A small absorption coefficient indicates that the passive film probably has a limited electrical conductivity (unlike Al_2O_3 and Ta_2O_5 which are insulators). This is consistent with the observation in this study and in Ref. [21] that at high overpotentials (several volts) oxygen is evolved at the precipitates.

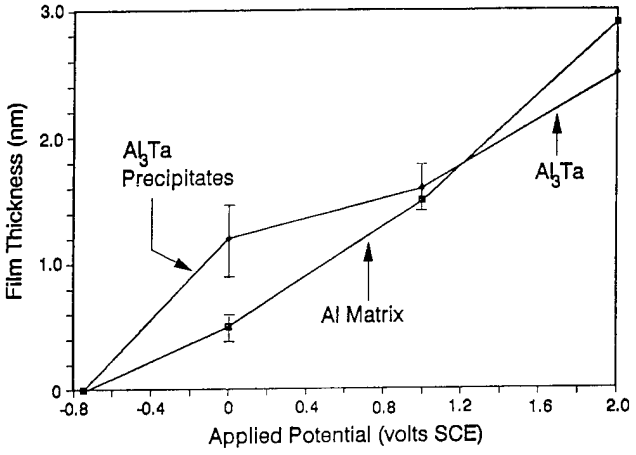

Fig. 7. Change in barrier layer thickness vs. applied potential for the Al_3Ta precipitate and the Al matrix. The thicknesses become equal at around 1.0 V. From Ref. [12].

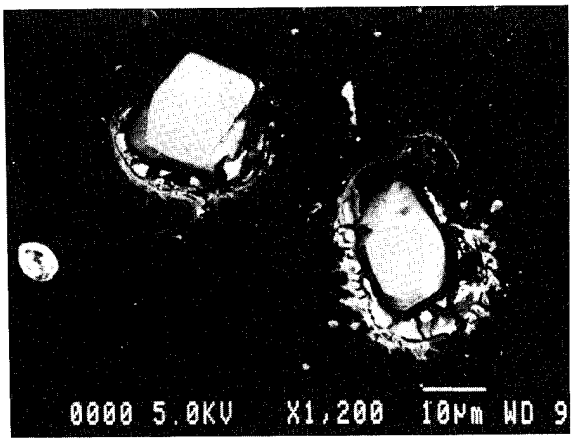

Fig. 8. Scanning electron photomicrograph of the preferential dissolution of Al around Al_3Ta precipitates after 48 h immersion in aerated 0.1 M NaCl, pH 5, at E_{corr} (a potential that is less than 1.0 V vs. SCE, where the films on Al_3Ta and Al have unequal thicknesses). The bright white "specks" are the result of charging and not additional precipitates or impurities. From Ref. [13].

3.3. Pitting experiments

The above LEIS and DIM measurements indicate that the precipitate film and the dealloyed region film differ in thickness (except at a potential of around 1.0 V) as well as in composition and/or structure. Therefore it is probable that there is an incoherent interface between the two films which is susceptible to localized attack [30]. Local strains or flaws, such as dislocations at the interface, may promote Cl^- adsorption or ingress that leads to breakdown. This hypothesis is supported by Fig. 8, a scanning electron micrograph of two of the precipitates in this alloy after immersion in 0.1 M NaCl at E_{corr} for 48 h. This micrograph clearly shows the preferential dissolution of Al around an Al_3Ta precipitate. It is apparent that the interface between the two films serves as a site for local attack, although a cathodic precipitate may provide the driving force for propagation [31]. However, when Al–1.5Ta samples containing large Al_3Ta precipitates were polarized potentiostatically at 1.0 V, the precipitate and matrix films were nearly equal in thickness and the flaw density at the precipitate–matrix interface was probably lower than for the film sample polarized at 0.0 V. When these specimens were immersed in a solution containing 0.1 M NaCl passivated at 0.0 V vs. SCE, where the passive films on both the precipitate and matrix surfaces are nearly equal, approximately half of the pits were located at the interfaces between the matrix and the Al_3Ta precipitates (Fig. 9). Therefore, for samples passivated at 1.0 V, the vast majority of pits were observed in the Al matrix material. Only two pits were observed at the interface between the matrix and precipitates,

indicating that when their respective passive films are nearly the same thickness the interface is less susceptible to breakdown. Many pits were observed near precipitates, but not at the interface. However, for specimens passivated at potentials where the film thicknesses are unequal, e.g. at 0.0 V, pitting occurs at the precipitate–matrix interface (Fig. 8).

4. Concluding remarks

The following conclusions can be drawn from this study of the effect of microstructure on the passivity and breakdown of sputtered Al–Ta alloy films.

4.1. Effect of the non-equilibrium microstructure

(1) The non-equilibrium structure does not increase E_{pit}.
(2) The non-equilibrium structure inhibits the formation of Al_3Ta precipitates. Breakdown initiates at defects in the passive film formed at the precipitate–matrix boundary. This is so because the thickness of the film on the precipitate differs from that on the matrix. At potentials at which the films have equal thicknesses, breakdown usually occurs at sites away from the precipitate–matrix interface.

4.2. Effect of Ta additions

(1) Below E_{pit} the addition of Ta to Al does not decrease the corrosion rate.
(2) Ta raises the pH_{pzc} of the passivated alloy surface. This, in turn, raises the potential of Cl^- ion adsorption and thereby E_{pit}.

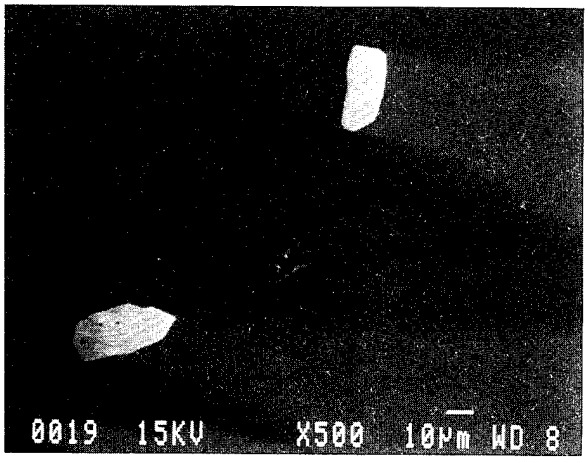

Fig. 9. Scanning electron photomicrograph of pitted sample held at 1.0 V vs. SCE, a potential at which the films on Al_3Ta and Al have equal thicknesses. Pitting occurs in the Al matrix at sites away from the precipitates. From Ref. [12].

Acknowledgments

The authors are grateful to Dr. John Sedriks and the Office of Naval Research (Contract No. N00014-89-J-1180) who supported this work. We also thank Frank Biancaniello of the National Institute of Standards and Technology who produced, using great ingenuity, the Al–Ta specimens with large precipitates.

References

[1] B.A. Shaw, T.L. Fritz, G.D. Davis and W.C. Moshier, *J. Electrochem. Soc., 137* (1990) 1317.
[2] P.M. Natishan, E. McCafferty and G.K. Hubler, *J. Electrochem. Soc., 135* (1988) 321.
[3] W.C. Moshier, G.D. Davis and G.O. Cote, *J. Electrochem. Soc., 136* (1989) 356.
[4] G.S. Frankel, M.A. Russak, C.V. Jahnes, M. Mirzamaani and V.A. Brusic, *J. Electrochem. Soc., 136* (1989) 1243.
[5] G.D. Davis, W.C. Moshier, T.L Fritz and G.O. Cote, *J. Electrochem. Soc., 137* (1990) 422.
[6] C.C. Streinz, *J. Electrochem. Soc., 139* (1992) 70C.
[7] Z. Szklarska-Smialowska, in G.S. Frankel and R.C. Newman (eds.), *Critical Factors in Localized Corrosion*, The Electrochemical Society, Princeton, NJ, 1992.
[8] R.S. Lillard, P.J. Moran and H.S. Issacs, *J. Electrochem. Soc., 139* (1992) 1007.
[9] R.F. Cohn and J.W. Wagner, *Appl. Opt., 28* (1989) 3187.
[10] J. Kruger, R.S. Lillard, C.C. Streinz and P.J. Moran, *Faraday Discuss., 94* (1993) 127.
[11] C.C. Streinz, J. Kruger and P.J. Moran, *J. Electrochem. Soc., 141* (1994) 1126.
[12] C.C. Streinz, P.J. Moran, J.W. Wagner and J. Kruger, *J. Electrochem. Soc., 141* (1994) 1132.
[13] R.S. Lillard, *Ph.D. Dissertation*, The Johns Hopkins University, Baltimore, MD, 1993.
[14] D.D. Macdonald (ed.), *Impedance Spectroscopy*, Wiley, New York, 1987.
[15] K. Juttner, W.J. Lorenz, M.W. Kendig and F. Mansfeld, *J. Electrochem. Soc., 135* (1988) 332.
[16] C. Scheffey, *Rev. Sci. Instrum., 50* (1988) 787.
[17] R.M.A. Azzam and N.M. Bashara, *Ellipsometry and Polarized Light*, Elsevier, New York, 1987.
[18] J. Kruger, *J. Phys. (Paris) Colloq., 38* (C5) (1977) 129.
[19] K. Sugimoto and S. Matsuda, *J. Electrochem. Soc., 130* (1983) 2323.
[20] A.J. Hurd and C.J. Brinker, *J. Phys. (Paris), 49* (1988) 1017.
[21] C.C. Streinz, J.W. Wagner, J. Kruger and P.J. Moran, *J. Electrochem. Soc., 139* (1992) 711.
[22] *Metals Handbook, Metallography, Structures and Phase Diagrams*, Vol. 8, American Society for Metals, 8th edn., 1973.
[23] G.A. Parks, *Chem. Rev., 65* (1965) 177.
[24] P.M. Natishan, E. McCafferty and G.K. Hubler, *J. Electrochem. Soc., 135* (1988) 321.
[25] J. Bessone, C. Mayer, K. Juttner and W.J. Lorenz, *Electrochim. Acta, 28* (1983) 171.
[26] T.D. Burleigh and A.T. Smith, *J. Electrochem. Soc., 138* (1991) L34.
[27] L. Young, *Anodic Oxide Films*, Academic Press, New York, 1961.
[28] D.G. Smith and L. Young, *Thin Solid Films, 101* (1983) 11.
[29] D.G. Muth, *J. Vac. Sci. Technol., 6* (1969) 749.
[30] W. Ostwald, *Z. Phys. Chem., 34* (1900) 495.
[31] V.M. Glazov, M.V. Maltsev and U.D. Chistyakov, *Izv. Akad. Nauk. USSR, Otd. Tekhn. Nauk., 4* (1957) 131.

ELSEVIER

Materials Science and Engineering A198 (1995) 19–24

MATERIALS SCIENCE & ENGINEERING A

Structure and corrosion properties of Al/Si and Fe/Zr multilayers

Takenori Nakayama[a,*], Kenji Yamamoto[a], Hiroshi Satoh[a], Toyohiko J. Konno[b], Bruce M. Clemens[b], Robert Sinclair[b]

[a]*Materials Research Laboratory, Kobe Steel, Ltd., 5-5, Takatsukadai, 1-chome, Nishi-ku, Kobe, Hyogo 651-22, Japan*
[b]*Department of Materials Science and Engineering, Stanford University, CA 94305, USA*

Abstract

Al/Si and Fe/Zr multilayer films were synthesized by sputter deposition. Modulation wavelengths (Λ) were varied from 3 to 35 nm for Al/Si multilayers and from 0.8 to 92 nm for Fe/Zr multilayers. Their structure and corrosion properties depend on Λ. In Al/Si multilayers, the corrosion resistance increased significantly with decreasing Λ. In Fe/Zr multilayers, the samples with Λ around 4 nm, in which a crystalline to amorphous transition was exhibited, appeared to be the most corrosion resistant. This behavior is discussed in connection with the multilayer structure.

Keywords: Multilayers; Corrosion; Modulation wavelength; Al–Si; Fe–Zr

1. Introduction

Artificially produced metallic superlattices and multilayers are of interest from both the scientific and practical points of view [1–5]. In particular, much attention has been devoted to the electronic and magnetic properties. However, in practice, the corrosion resistance can be equally important, because any devices must be reliable and corrosive failure must not occur. However, the corrosion properties of such nanometer-scale multilayers are unknown. Such parameters are also of great interest from a scientific point of view.

This paper aims to clarify the relationship between the modulation wavelength and corrosion properties of sputter-deposited Al/Si and Fe/Zr multilayers in connection with their structure, using X-ray diffraction (XRD), high- resolution transmission electron microscopy (HRTEM), X-ray photoelectron spectroscopy (XPS), electrochemical techniques, and so on. Al/Si is one of the most well-known systems for microelectronic materials, and Fe/Zr is a typical magnetic material. Hence there are good reasons for studying these multilayer systems.

2. Experimental details

Films (thickness, 1 μm) of Al/Si multilayers ($Al_{1-x}Si_x$; $x = 0.29–0.44$) and films (thickness, 2 μm) of Fe/Zr multilayers ($Fe_{1-x}Zr_x$; $x = 0.40–0.52$) were synthesized on cleaned glass slides by d.c./r.f. sputter deposition in a system with a rotating sample stage and high-purity dual targets (99.999% Al, 99.999% Si, 99.9% Fe, 99.9% Zr). The sputter deposition chamber was evacuated to a base pressure of less than 5×10^{-7} Torr by a cryo pump, and the depositions were performed at a pressure of 3×10^{-3} Torr of Ti- getter-cleaned Ar. Fig. 1 shows a schematic diagram of the sputter deposition apparatus for the formation of these multilayers. The layer thicknesses were varied from 3 to 35 nm for the Al/Si system and from 0.8 to 92 nm for the Fe/Zr system. Pure Al and Si films, 1 μm thick, and pure Fe and Zr films, 2 μm thick, were also synthesized by sputter deposition for comparison.

The structures of the films were characterized by low- and high-angle XRD and cross-sectional HRTEM. The compositions were examined by inductively coupled plasma mass spectrometry (ICP-MS).

Potentiodynamic anodic polarization scans were made in an aerated 0.1 M HCl aqueous solution at 25 °C for Al/Si multilayers and in an aerated 0.1 M H_2SO_4 aqueous solution at 25 °C for Fe/Zr multilayers, using

* Corresponding author.

SSDI 0921-5093(94)04503-8

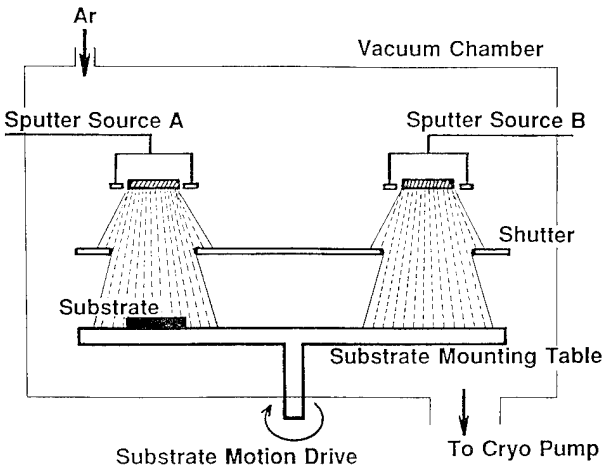

Fig. 1. Schematic diagram of the sputter deposition apparatus for the formation of multilayers.

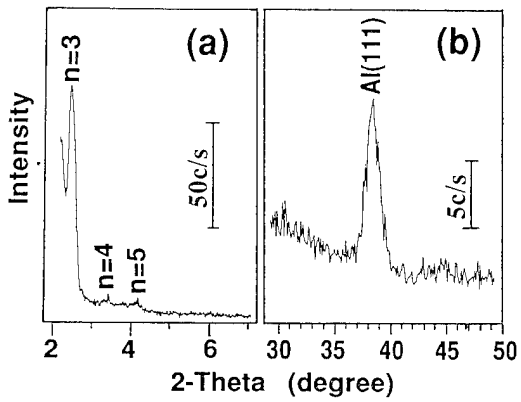

Fig. 2. XRD patterns of an Al/Si multilayer with a modulation wavelength Λ of 10 nm: (a) low-angle reflection; (b) high-angle reflection.

a PAR 273 potentiostat and a K0235 flat cell, to examine the corrosion properties of the films. The scan rate was 10 mV s^{-1} for the former and 2 mV s^{-1} for the latter. The potentials were referred to an Ag/AgCl electrode. Electrochemical testing of Al/Si multilayers at a constant potential of −0.2 V vs. Ag/AgCl in 0.1 M HCl solution was also conducted to monitor the anodic current density as a function of time. The compositions of the surface films before and after the corrosion tests were analyzed by XPS. Surface morphologies after the corrosion test were also observed with a metallurgical microscope.

3. Results and discussion

3.1. Al/Si multilayers

3.1.1. Structure of the films

Fig. 2 shows the low- and high-angle XRD patterns obtained from the Al/Si multilayer with a modulation wavelength (Λ) of 10 nm. At low angles, superlattice lines due to scattering from the composition modulation are clearly seen. These superlattice lines were used to determine the modulation wavelength of the samples. At high angles, the (111) reflection of Al can be distinguished, indicating that Al layers are crystalline and oriented in the (111) direction. The Al(111) texture was also observed in the as-sputtered pure Al film and an amorphous structure was recognized in the Si film.

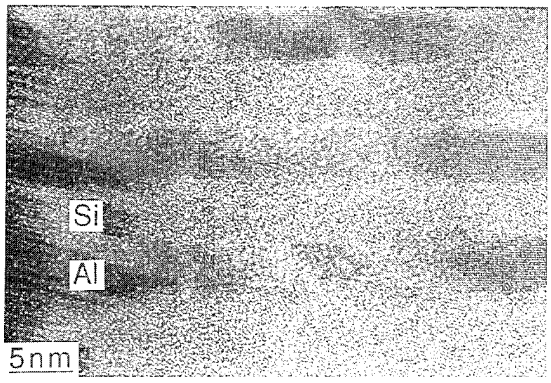

Fig. 3. Cross-sectional high- resolution transmission electron micrograph of an Al Si multilayer with a modulation wavelength Λ of 12 nm.

Fig. 3 presents a cross-sectional high- resolution transmission electron micrograph of the Al/Si multilayer with Λ = 12 nm, confirming the multilayered structure, the presense of a crystalline Al texture and amorphous Si. Other selected samples showed equivalent HRTEM results.

It is concluded from the above that as-sputtered Al/Si multilayers with Λ = 3–35 nm are composed of (111)-oriented crystalline Al layers and amorphous Si layers.

3.1.2. Corrosion properties of the films

Anodic polarization curves were measured in 0.1 M HCl solution. They showed that the anodic current density decreased with decreasing Λ. Fig. 4 shows the relationship between the pitting potential, which was defined as the potential reaching the current density of 1 A m^{-2} in each anodic polarization curve, and Λ. It is clear that the pitting potential is dependent on Λ and the corrosion resistance significantly increases with decreasing Λ.

Fig. 5 shows the time dependence of the anodic current density at −0.2 V vs. Ag/AgCl in 0.1 M HCl solution for Al/Si multilayers with Λ = 5, 10 and 35 nm. It is clear that the multilayers with smaller Λ tend to have lower anodic current density and the corrosion resistance increases with decreasing Λ.

Fig. 6 presents the surface morphologies of Al/Si multilayers with Λ = 5 and 35 nm after corrosion tests at −0.2 V vs. Ag/AgCl in 0.1 M HCl solution. This

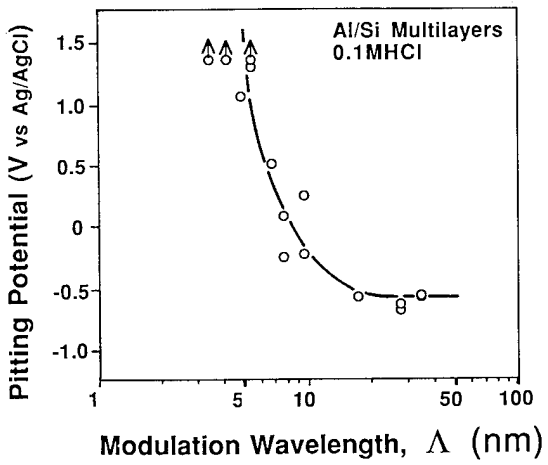

Fig. 4. Relation between pitting potential and modulation wavelength for Al/Si multilayers.

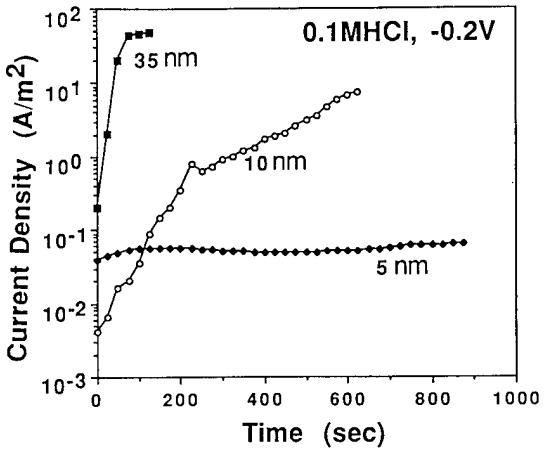

Fig. 5. Time dependence of the anodic current density of selected Al/Si multilayers.

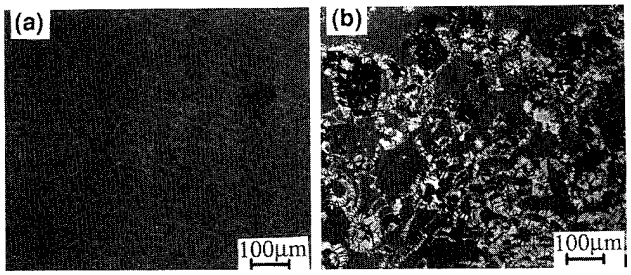

Fig. 6. Surface morphologies of Al/Si multilayers after polarization test at −0.2 V vs. Ag/AgCl in 0.1 M HCl solution: (a) Λ = 5 nm; (b) Λ = 35 nm.

microscopic observation indicates that Al layers are preferentially corroded through defects in the Si layers and the Si layers are delaminated. In addition, Al corrosion products were recognized by XPS analysis of

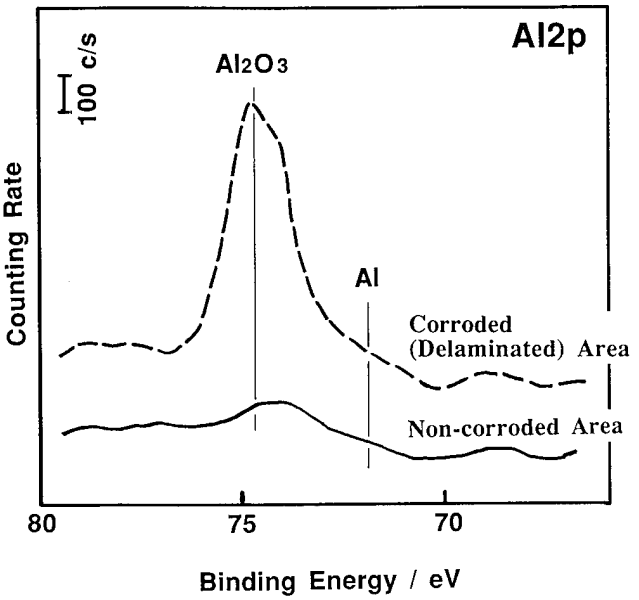

Fig. 7. X-Ray photoelectron Al 2p spectra of corroded area and non-corroded area of Al/Si multilayer with Λ = 35 nm after polarization test at −0.2 V vs. Ag/AgCl in 0.1 M HCl solution.

the surface of the films as shown in Fig. 7. These observations suggest the following corrosion mechanism as illustrated schematically in Fig. 8: (1) entrance of the solution into the Al layer through the defects in the Si layer; (2) corrosion of Al and the formation of corrosion products; (3) delamination of the Si layer due to the increase in volume of the corrosion products in

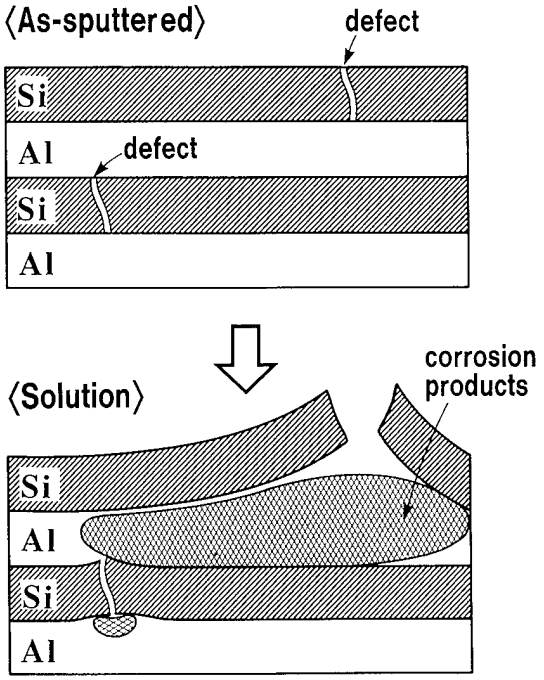

Fig. 8. Schematic diagram of the corrosion process for the Al/Si multilayer.

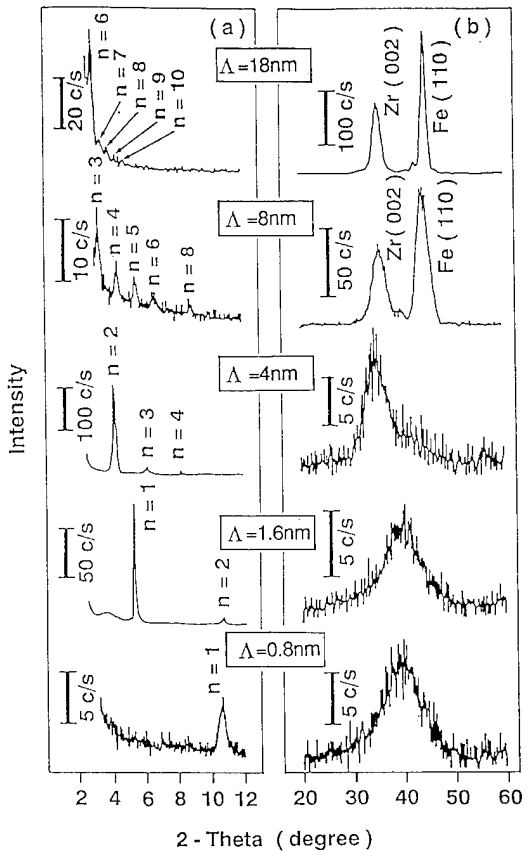

Fig. 9. XRD patterns of selected Fe/Zr multilayers: (a) low-angle reflection; (b) high-angle reflection.

the Al layer; (4) repetition of the above processes. Considering the above model, one of the possible reasons for the dependence of the corrosion resistance on Λ seems to be related to the diffusivity of the solution in the Al layer. Thus the smaller Λ is on a nanometer scale, the more difficult it is for the solution to diffuse into the narrower crevice formed by dissolution of the Al layer, resulting in an increasing corrosion resistance with decreasing Λ.

3.2. Fe/Zr multilayers

3.2.1. Structure of the films

Fig. 9 shows the low- and high-angle XRD patterns of samples with different modulation wavelengths (Λ). At low angles, superlattice lines are seen for all samples in the figure, indicating that these samples are periodic multilayers. These superlattice lines were used to determine the modulation wavelength of the samples. High-angle X-ray reflections from samples with Λ smaller than 4 nm show a broad peak, indicating an amorphous state. For larger Λ, however, Fe(110) and Zr(001) reflections can be distinguished, indicating that these samples are crystalline and oriented in the film plane.

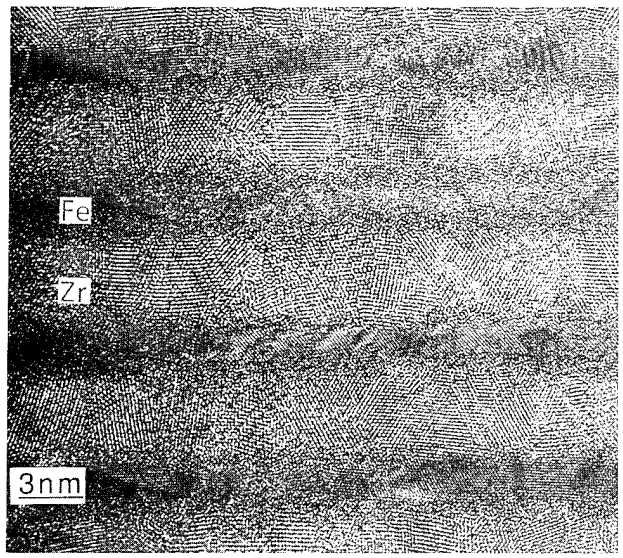

Fig. 10. High-resolution transmission electron micrograph of Fe/Zr multilayer with Λ = 8 nm.

Fig. 10 presents a cross-sectional high- resolution transmission electron micrograph of the sample with Λ = 8 nm. The composition modulation is clear. Small grains are visible in both Fe and Zr layers, indicating that the sample is crystalline. This agrees with the results of XRD. A small amount of amorphous phase is also seen along the interface between Fe and Zr layers. On the other hand, XRD and HRTEM show no layered structure for Λ smaller than 0.8 nm, suggesting that these samples contain homogeneous amorphous alloy.

From the above, the structure of Fe/Zr multilayers synthesized in this study is summarized in Fig. 11. The results are consistent with equivalent metal multilayer systems [1].

3.2.2. Corrosion properties of the films

Fig. 12 presents the anodic polarization curves of pure Fe, pure Zr and selected Fe/Zr multilayers measured in 0.1 M H_2SO_4 solution. It shows that the anodic current density of the Fe/Zr multilayer greatly depends on Λ. The anodic current of the Fe/Zr multilayer rapidly decreases to a minimum with decreasing Λ for Λ greater than 4 nm. It is noticeable that the corrosion resistance of the Fe/Zr multilayer with Λ = 4 nm is greater than that of pure Zr, whereas the corro-

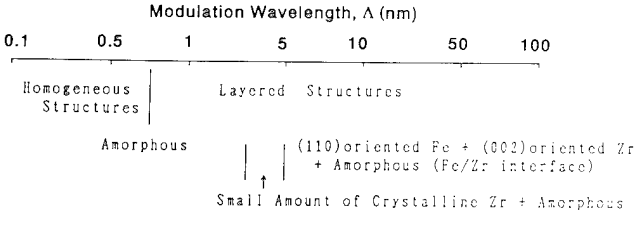

Fig. 11. Summary of the structure of Fe/Zr multilayers.

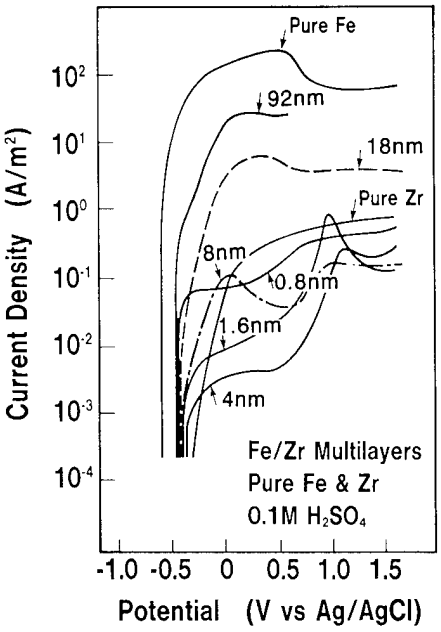

Fig. 12. Anodic polarization curves of pure Fe, pure Zr and selected Fe/Zr multilayers tested in H_2SO_4 solution.

sion resistance of the Fe/Zr multilayer with $\Lambda = 92$ nm is poor and close to that of pure Fe. In contrast, the corrosion resistance of Fe/Zr multilayers with Λ smaller than 4 nm seems to deteriorate with decreasing Λ.

Fig. 13 summarizes the relationship between the anodic current density obtained from the value at 0 mV vs. Ag/AgCl in each anodic polarization curve in Fig. 12 and Λ, showing that the corrosion resistance varies with Λ. For Λ greater than 4 nm, the corrosion resistance increases significantly with decreasing Λ. The samples with $\Lambda = 4$ nm are the most corrosion resistant. In films with Λ smaller than 4 nm, the corrosion resistance deteriorates with decreasing Λ.

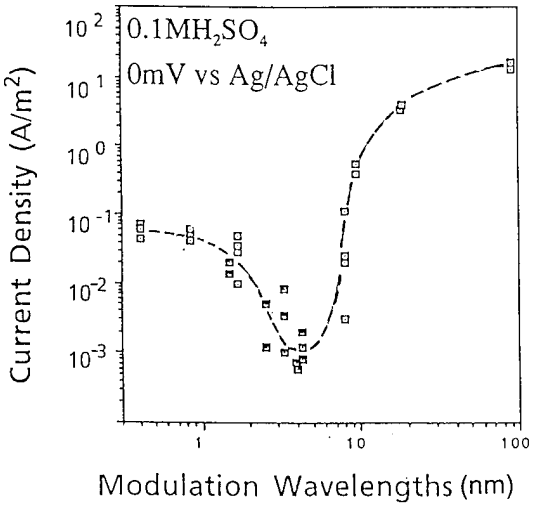

Fig. 13. Relation between anodic current density and modulation wavelength of Fe/Zr multilayers.

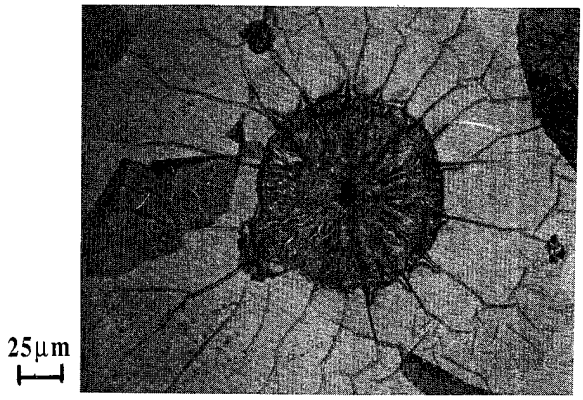

Fig. 14. Surface morphology of the Fe/Zr multilayer with a modulation wavelength Λ of 18 nm after polarization test in H_2SO_4 solution.

Fig. 14 shows the surface morphology of the Fe/Zr multilayer with $\Lambda = 18$ nm after the polarization test in 0.1 M H_2SO_4 solution. This observation of the specimen surface after the corrosion test indicates that the Fe layers are preferentially corroded through pin-hole-type defects in the Zr layers and the Zr layers are fractured and delaminated. These observations suggest the following corrosion mechanism as discussed for Al/Si multilayers: (1) entrance of the solution into the Fe layer through defects in the Zr layer; (2) corrosion of Fe and the formation of corrosion products; (3) delamination of the Zr layer due to an increase in the volume of corrosion products in the Fe layer; (4) repetition of the above processes. Considering the above model, possible reasons for the dependence of the corrosion resistance on Λ may be related to the diffusivity of the solution in the Fe layers and the structure of the films. Thus in films with Λ greater than 4 nm, the smaller Λ is, the more difficult it is for the solution to diffuse into the narrower crevice formed by dissolution of the Fe layers, resulting in an increase in corrosion resistance with decreasing Λ. The presence of an amorphous layer at the interface between the Fe and Zr layers also contributes to the increase in the corrosion resistance, because the amount of pure crystalline Fe decreases due to the increase in the amorphous interface with decreasing wavelength. However, in order to understand better the deterioration of the corrosion resistance with decreasing Λ in films with Λ smaller than 4 nm, further consideration of the dependence of the structure of the Fe/Zr multilayer on Λ is required.

4. Conclusions

(1) Sputter-deposited Al/Si multilayers are composed of amorphous Si layers and (111)-oriented crystalline Al layers. The corrosion properties vary with the modulation wavelength. With decreasing modulation wavelength, the corrosion resistance significantly increases.

XPS and microscopic observations indicate that the Al layers are preferentially corroded through defects in the Si layers.

(2) Sputter-deposited Fe/Zr multilayers with modulation wavelengths (Λ) greater than 8 nm are composed of (110)-oriented Fe and (002)-oriented Zr crystalline layers, and the interface between Fe and Zr is amorphous. The samples with Λ between 4 and 0.8 nm contain compositionally modulated amorphous multilayers. The corrosion properties vary with Λ. In films with Λ greater than 4 nm, the corrosion resistance increases significantly with decreasing Λ. The samples with $\Lambda = 4$ nm appear to be the most corrosion resistant. In films with Λ less than 4 nm, the corrosion resistance deteriorates with decreasing Λ. It is suggested that the Fe layers are preferentially corroded through defects in the Zr layers. This behavior was discussed in connection with the multilayer structure.

References

[1] T.W. Barbee, B.M. Clemens, R. Sinclair, I.K. Schuller, J. Guimpel and Y. Bruynseraede, *Mater. Res. Soc. Bull., 15* (2) (1990) 17.
[2] M.N. Baibich, J.M. Broto, A. Fert, F. Nguyen Van Dau, F. Petroff, P. Estienne, G. Creuzet, A. Friederich and J. Chazelas, *Phys. Rev. Lett., 61* (1988) 2472.
[3] T. Shinjo and T. Takada, *Metallic Superlattices*, Elsevier, 1987.
[4] B.M. Clemens and D.L. Williamson, *Mater. Res. Soc. Symp. Proc., 103* (1988) 159.
[5] T.J. Konno and R. Sinclair, *Mater. Res. Soc. Symp. Proc., 230* (1992) 189.

ELSEVIER

Materials Science and Engineering A198 (1995) 25–34

MATERIALS SCIENCE & ENGINEERING A

Corrosion of rapidly solidified neodymium–iron–boron (Nd–Fe–B) permanent magnets and protection via sacrificial zinc coatings

S.A. Attanasio, R.M. Latanision

H.H. Uhlig Corrosion Laboratory, Department of Materials Science and Engineering, Massachusetts Institute of Technology, Cambridge, MA 02139, USA

Abstract

Rapidly solidified Nd–Fe–B alloys were found to corrode actively at open circuit in aerated Na_2SO_4 and NaCl at 30 °C and 80 °C. Estimated penetration rates (greater than 27 mil year^{-1}) indicate the need for corrosion control methods.

The use of sacrificial zinc coatings in controlling the corrosion of Nd–Fe–B alloys may have previously been overlooked because of two potential limitations: incomplete protection and hydrogen damage. The electrochemical activity of Nd may prevent zinc from providing complete sacrificial protection to Nd–Fe–B at breaks in the coating, and cracking could occur when hydrogen production is galvanically stimulated on Nd–Fe–B at breaks in the coating.

This study focuses on the evaluation of the protection conferred to Nd–Fe–B when a Zn/Nd–Fe–B galvanic couple is formed due to coating penetration. Quantitative solution analysis was used to demonstrate that the dissolution of Nd, Fe and B is essentially prevented by the galvanic coupling of Nd–Fe–B to zinc in NaCl at 25 °C. Galvanic coupling to zinc also reduces the rate of environmentally assisted cracking of Nd–Fe–B. Sacrificial zinc coatings appear to be a viable, cost-effective corrosion control method for Nd–Fe–B, and the limitations described above should not preclude their use in this application.

Keywords: Corrosion; Nd–Fe–B; Permanent magnets; Sacrificial zinc coatings

1. Introduction

Nd–Fe–B is the most powerful permanent magnet currently known to man. The alloy can be prepared either by sintering or by a rapid solidification processing (RSP) technique pioneered by General Motors. In the RSP technique, rapidly quenched Nd–Fe–B ribbons are compacted at elevated temperature into a fully dense body known as a hot pressed (h.p.) magnet. The microstructure of h.p. magnets generally consists of isotropic, polygonal $Nd_2Fe_{14}B$ grains (80–100 nm in diameter) surrounded by a continuous 1–5 nm wide Nd-rich grain boundary phase [1–3], as shown schematically in Fig. 1. Despite intense investigation, the identity of the Nd-rich phase has not been confirmed. The phase appears to be stabilized by oxygen and can crystallize either in the hexagonal close packed or face-centered cubic structure, depending on the amount of

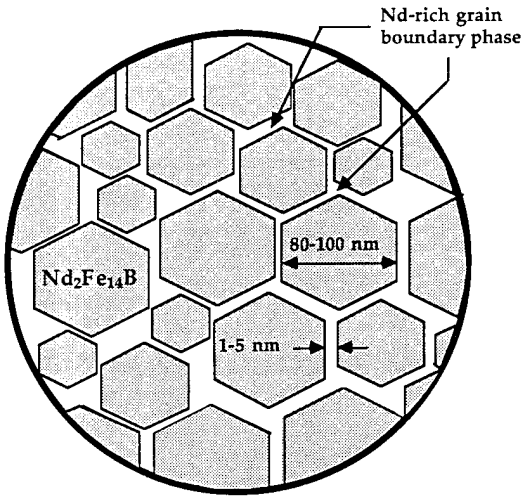

Fig. 1. Schematic microstructure of the hot pressed (h.p.) rapidly solidified Nd–Fe–B alloy.

SSDI 0921-5093(94)04504-6

oxygen admitted to the system during processing [4,5]. The addition of elements other than Nd, Fe and B to the alloy can also influence the composition and structure of this phase.

The energy product of the magnet can be increased by subjecting the h.p. alloy to a thermomechanical treatment known as die upsetting, which crystallographically aligns the axis of easy magnetization (*c*-axis) of the ferromagnetic $Nd_2Fe_{14}B$ grains in a common direction, with the Nd-rich phase still present at the grain boundaries. Further details relating to the h.p. and die upset (d.u.) magnets can be found elsewhere [6–10].

The possibility of preferential grain boundary corrosion in Nd–Fe–B alloys prepared by the RSP technique is a concern because Nd is an electrochemically active element, and because intergranular corrosion has been observed in sintered Nd–Fe–B [11]. Although the microstructure of the alloy may be detrimental to its corrosion resistance, it is believed that the isolation of the $Nd_2Fe_{14}B$ grains by the paramagnetic Nd-rich phase improves the demagnetization resistance of the alloy by forcing each grain to reverse its magnetization independently [12].

Permanent magnets are important materials in many industries. Their numerous applications in automobiles, for example, are shown in Fig. 2. The powerful Nd–Fe–B alloy can provide significantly more magnetic flux per unit weight than previous permanent magnetic materials. A marked reduction in the weight, bulkiness and cost of parts, such as electric motors, can be achieved through the use of Nd–Fe–B permanent magnets [6].

Despite the many benefits of employing the Nd–Fe–B magnet, its poor corrosion resistance has been cited as a potential problem with its use in many applications [14–16]. Since the magnetic flux is directly dependent on the volume of the magnetic material present [17], loss of metal by corrosion decreases the power of a permanent magnet. A 25% loss in magnetic flux, for example, was found to result from a 72 h exposure of sintered Nd–Fe–B to an autoclave environment (120 °C, 2 atm) [18].

The majority of previous electrochemical testing on Nd–Fe–B has been performed using alloys prepared by sintering rather than by RSP. Testing has been conducted in electrolytes such as H_3PO_4 [19,20], H_2SO_4 [20,21], NaH_2PO_4 [19], NaOH [19] and Ringer's solution [20], primarily under deaerated conditions. Since the corrosion of Nd–Fe–B is of concern in industrial and marine environments as well as automotive environments which contain de-icing salts, tests performed in aerated, near-neutral electrolytes, such as Na_2SO_4 and NaCl, will probably be more relevant to actual service conditions than tests performed in the above electrolytes [22]. Testing has generally been performed at room temperature [19–21], even though the alloy can be subjected to a wide range of temperatures in service (−40 to 170 °C) [23].

1.1. Corrosion control via sacrificial zinc coatings

Although sacrificial zinc coatings may represent a cost-effective corrosion control method for Nd–Fe–B, their use may have previously been overlooked because of two potential limitations: incomplete protection and hydrogen damage. Zinc coatings may be incapable of providing complete sacrificial protection to Nd–Fe–B at breaks in the coating, because Nd is an electrochemically active element and its anodic dissolution can therefore occur at potentials much more negative than the corrosion potential of the Nd–Fe–B alloy [24]. However, since the rate of Nd dissolution cannot be predicted using thermodynamics, the degree of protection provided at breaks in the coating can only be determined by testing. Hydrogen production will be galvanically stimulated on the alloy at breaks in the coating, and the rate of cracking of Nd–Fe–B could be accelerated by hydrogen uptake. Although hydrogen degradation of Nd–Fe–B has been observed under strong cathodic polarization ($i_c \approx 0.4$–1.3 A cm^{-2}) in H_2SO_4 (pH 0–1) [24], the relevance of these results may be limited due to the severe testing conditions employed.

Zinc generally exhibits good resistance to atmospheric corrosion because of the formation of sparingly soluble corrosion products [25]. The life of a zinc coating can additionally be extended by covering it with a paint or a similar organic in order to delay its exposure to the corrosive environment.

Corrosion control of Nd–Fe–B via zinc and/or organic coatings does not present an inherent problem, since the coating material(s) will not affect the magnetic field produced by the alloy. The coating should not be excessively thick, however, since the magnetic flux decreases with the square of the distance from the magnet [18]. Coatings of 75 μm or more can be used without adversely affecting magnetic performance [26]. Zinc coatings of this thickness can be applied using hot-dip galvanizing, electroplating or vapor deposition.

2. Experimental procedure

Rapidly solidified Nd–Fe–B alloys were produced by the Magnequench® Division of the General Motors Corporation. Zinc metal (greater than 99.9 wt.%) was purchased from Johnson Matthey Chemicals. Samples for polarization and galvanic corrosion tests were polished to a 1200 grit finish, degreased with acetone and masked with a thin layer of silicone rubber adhesive (16 h cure). Polarization was conducted at 0.16 mV s^{-1}.

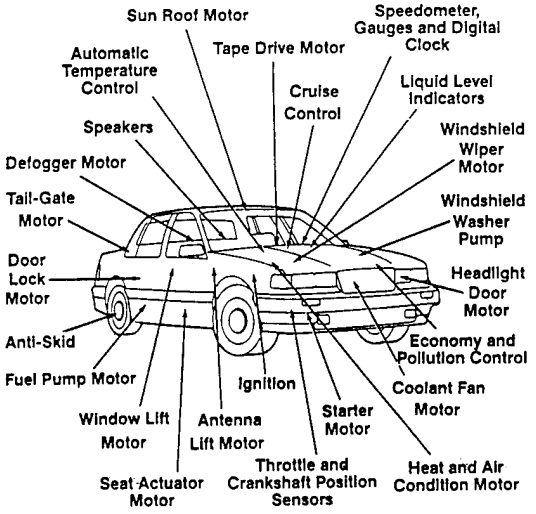

Fig. 2. Automotive applications involving permanent magnets (after Croat and Herbst [13]).

Test electrolytes were aerated, non-agitated 0.5 M Na_2SO_4 and 0.5 M NaCl (pH $\approx$ 6) at both 30 ± 0.5 °C and 80 ± 1 °C. A saturated calomel reference electrode (SCE) was used at 30 °C, and a silver/silver chloride reference electrode (Ag/AgCl) at 80 °C.

3. Results and discussion

3.1. Polarization testing

The corrosion of Nd–Fe–B was initially investigated by measuring the polarization behavior of h.p. and d.u. alloys in aerated Na_2SO_4 and NaCl solutions, because of the scarcity of previous electrochemical testing in relevant electrolytes. The anodic and cathodic polarization behavior of the alloys prepared by RSP at 30 °C are shown in Figs. 3(a) and 3(b) in Na_2SO_4 and in Figs. 4(a) and 4(b) in NaCl. The anodic and cathodic polarization behavior at 80 °C are shown in Figs. 5(a) and 5(b) in Na_2SO_4 and in Figs. 6(a) and 6(b) in NaCl. Due to the anisotropic nature of the d.u. magnets, two orthogonal planes were tested. One test plane was approximately perpendicular to the c-axis of the elongated $Nd_2Fe_{14}B$ grains (d.u.$\perp c$), and the other plane was approximately parallel to the c-axis of the grains (d.u.$\parallel c$).

Nd–Fe–B was found to exhibit Tafel kinetics (active corrosion) at low anodic overpotentials in all four test solutions, as shown in Figs. 3(a)–6(a). Regions of higher anodic overpotential were not shown in order to enhance the clarity of Figs. 3(a)–6(a). Mass transfer control was generally found to exist up to +1.5 V (SCE), although a slight reduction in current density was observed at potentials noble to −0.2 V (SCE) in Na_2SO_4 at 30 °C. An active–passive transition was observed in Na_2SO_4 at 80 °C (Fig. 5(a)), as discussed below. The alloy was found to exhibit diffusion-limited oxygen reduction kinetics at low cathodic overpotentials in all test solutions, as shown in Figs. 3(b)–6(b). The linear regions observed at higher cathodic overpotentials correspond to the reduction of water to hydrogen. The rate-controlling reaction in the corrosion of Nd–Fe–B in the test solutions appears to be diffusion-limited oxygen reduction.

Although passivation was induced by anodic polarization at 80 °C in Na_2SO_4, the usefulness of the passive film obtained appears to be limited. Since the alloy exhibits active dissolution at open circuit, the corrosion rate of the alloy is substantial (approximately 110 μA cm^{-2}) despite the presence of the active–passive transition. Both the passive current density (approximately 100 μA cm^{-2}) and the critical current density for passivation (approximately 20 mA cm^{-2}) are relatively high, and the passive region is very narrow (less than 0.1 V).

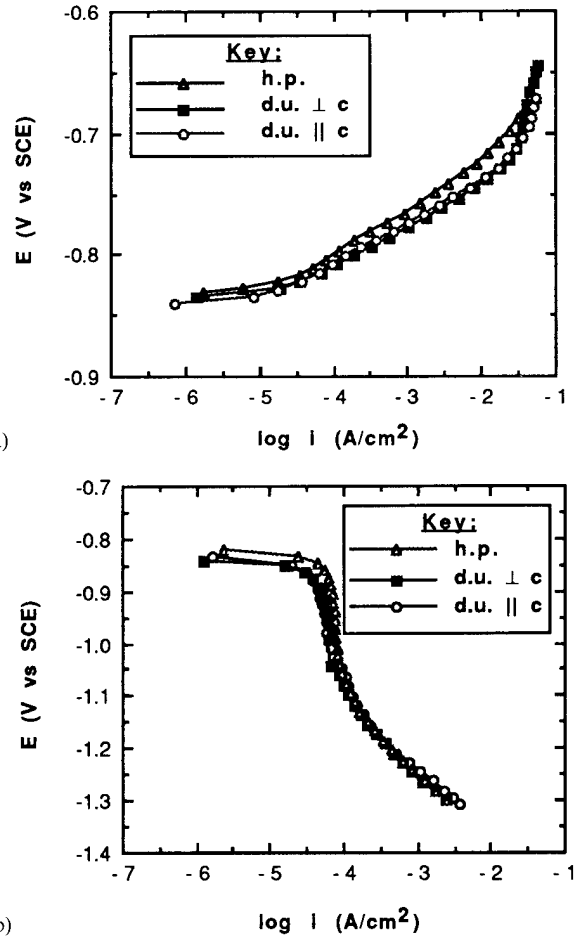

Fig. 3. Anodic (a) and cathodic (b) polarization of hot pressed (h.p.) and die upset (d.u.) Nd–Fe–B alloys in 0.5 M Na_2SO_4 at 30 °C. The anisotropic d.u. samples were tested on two orthogonal planes: a plane perpendicular to the c-axis of the $Nd_2Fe_{14}B$ grains (d.u.$\perp c$) and a plane parallel to the c-axis of the grains (d.u.$\parallel c$).

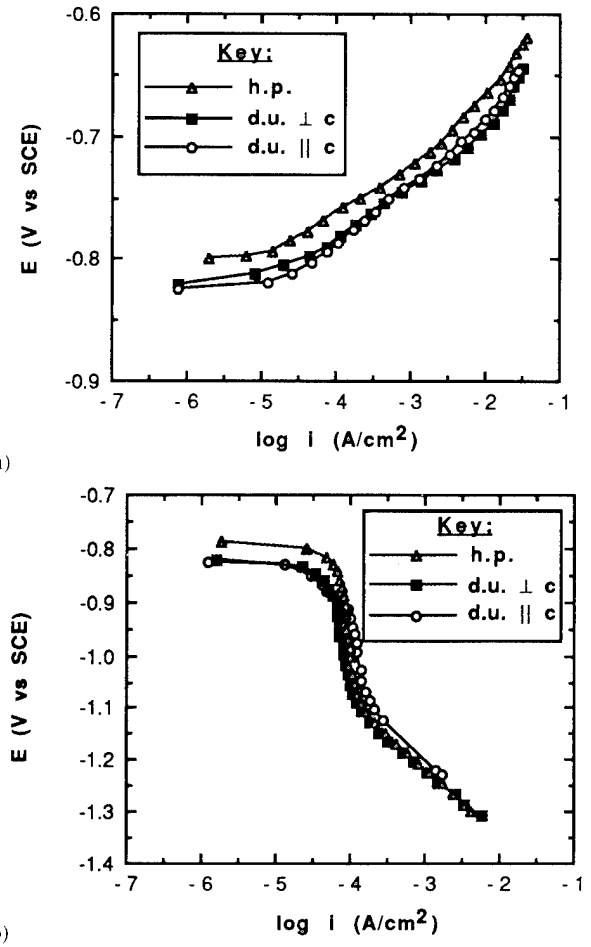

Fig. 4. Anodic (a) and cathodic (b) polarization of hot pressed (h.p.) and die upset (d.u.$\perp c$, d.u. $\|c$) Nd–Fe–B alloys in 0.5 M NaCl at 30 °C.

No significant effect of the magnetic flux on the polarization behavior of Nd–Fe–B was observed (Figs. 3–6), as the magnetic flux lines emerging from the d.u. samples are perpendicular to the test plane of the d.u.$\perp c$ samples and parallel to the test plane of the d.u.$\|c$ samples. In addition, the microstructural changes which result from subjecting the h.p. alloy to the die upsetting process were found to exert only a slight effect on the polarization behavior of Nd–Fe–B (Figs. 3–6). No electrochemical basis was observed for the results of Jacobsen and Kim [27], who reported that the weight loss of magnetized (sintered) Nd–Fe–B in aerated salt water was significantly less than that of non-magnetized samples.

3.1.1. Rate of metal loss

The corrosion current density (i_{corr}) can be estimated by extrapolating both the anodic and cathodic polarization curves to the corrosion potential. For h.p. Nd–Fe–B in NaCl at 30 °C, for example, the average i_{corr} was estimated to be 58 μA cm^{-2}. Faraday's law can be used to convert this value into a penetration rate in mils per year (mpy) using the following equation [28]

$$\text{Penetration rate (mpy)} = (0.129) \times \frac{i_{corr}(\mu\text{A cm}^{-2}) \times \text{atomic weight (g mol}^{-1})}{\text{number of electrons transferred} \times \text{density (g cm}^{-3})} \quad (1)$$

The density of h.p. samples is 7.6 g cm^{-3}. The atomic weight was estimated to be 66 g mol^{-1} and the number of electrons transferred as 2.2, using weighted averages based on the standard alloy composition of 15 at.% Nd, 77 at.% Fe and 8 at.% B. Using these parameters in Eq. (1), the rate of metal loss was estimated to be 29 mpy (0.74 mm year^{-1}), assuming general corrosion to be operative. Similar values (27–55 mpy) were estimated for the other three test solutions.

A significant limitation of polarization testing is that it does not provide information regarding the morphology of corrosive attack. If localized corrosion is taking place, the penetration rates calculated above are likely to be a significant underestimate of the actual metal loss rate of the alloy.

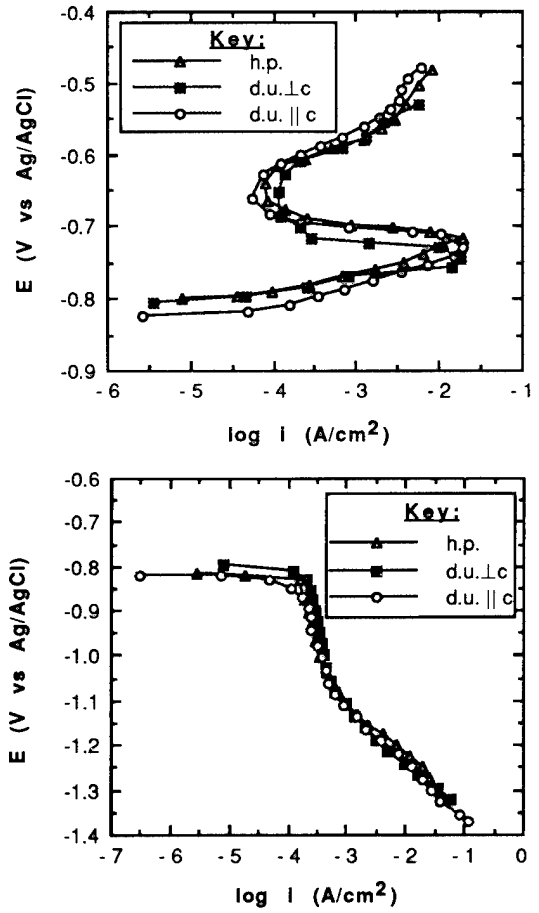

Fig. 5. Anodic (a) and cathodic (b) polarization of hot pressed (h.p.) and die upset (d.u.$\perp c$, d.u.$\|c$) Nd–Fe–B alloys in 0.5 M Na_2SO_4 at 80 °C.

A complete analysis of the morphology of attack is currently in progress. Preliminary work has revealed definitive evidence of pitting attack in NaCl at 25 °C at short immersion times (15–60 min). Although measured pit depths (approximately 1 μm) from these tests were extrapolated to penetration rates greater than 200 mpy (5 mm year^{-1}), it is not yet known whether this type of attack propagates over longer periods of time. An investigation of preferential grain boundary corrosion is planned, although this analysis is expected to require significant effort as a result of the extremely fine scale of the phases present in the alloys prepared by RSP.

The effects of preferential grain boundary corrosion can be estimated by recalculating the penetration rates assuming that the anodic current at E_{corr} is derived solely from the corrosion of the Nd-rich phase. The density of this phase was estimated as 7.3 g cm^{-3}, the atomic weight as 118 g mol^{-1} and the number of electrons transferred as 2.7, based on an approximate grain boundary composition of Nd_7Fe_3 [2,29]. The grain to grain boundary area ratio was estimated as 95 : 5 [30]. It was assumed that undercutting of grains can continue indefinitely due to the interconnection of the grain boundary phase. The penetration rate in NaCl at 30 °C was estimated as 890 mpy (23 mm year^{-1}), and similar values were estimated for the other test solutions.

The estimated penetration rates demonstrate how strongly localized attack, such as pitting or intergranular corrosion, would affect the overall metal loss rate. Weight loss testing could not be used to determine the accuracy of the estimated penetration rates since cracking of several samples precluded the measurement of useful weight loss data, as described later.

The results of the polarization tests are compatible with previous reports of the poor corrosion resistance for Nd–Fe–B [14–16]. Since penetration rates greater than 5–20 mpy are usually considered excessive for expensive alloys such as Nd–Fe–B [28], the penetration rates estimated indicate that corrosion control methods are needed to improve the viability of Nd–Fe–B as an engineering material.

3.2. Corrosion control via sacrificial zinc coatings

Since the barrier properties of zinc coatings have been characterized in the past [31–34], the current study is focused on evaluating whether or not protection will be conferred to Nd–Fe–B when it is exposed to the corrosive environment due to penetration of the sacrificial zinc coating. A sacrificial coating must be electrochemically active to the base metal in order to provide cathodic protection. The coating supplies protection by acting as the anode of the coating/base metal galvanic couple which is formed once the coating is penetrated. The effectiveness of a sacrificial coating can therefore be evaluated by studying the galvanic properties of the sacrificial coating/base metal system. An established technique for analyzing galvanic systems involves the use of the mixed potential theory, usually in combination with galvanic corrosion testing [35–39]. Only one test solution was utilized in this evaluation (NaCl, 30 °C) due to the limited number of samples available.

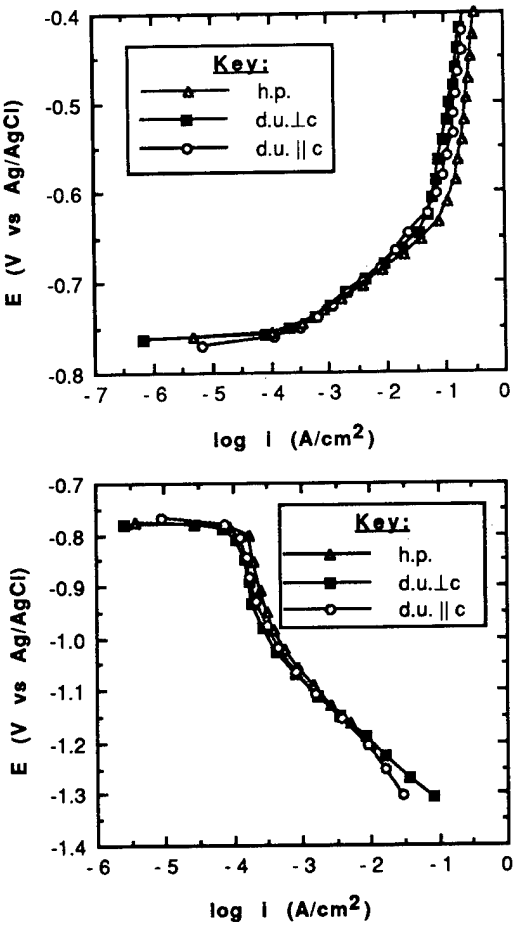

Fig. 6. Anodic (a) and cathodic (b) polarization of hot pressed (h.p.) and die upset (d.u.$\perp c$, d.u.$\| c$) Nd–Fe–B alloys in 0.5 M NaCl at 80 °C.

3.2.1. Mixed potential theory and galvanic corrosion testing

Polarization tests were performed on both h.p. Nd–Fe–B and zinc in NaCl at 30 °C. The results are shown in Fig. 7 using a Zn to Nd–Fe–B area ratio of 1.8 : 1. The area ratio was greater than 1 : 1 in order to simulate the area ratio obtained when a small area of base metal is exposed to an electrolyte due to cracking or corrosion of the coating metal. According to the mixed potential theory, the intersection of the total oxidation curve and the total reduction curve is the predicted

couple potential (E_{couple}) of the coating/base metal system, and the reaction rate for each of the individual anodic and cathodic reactions can be predicted by calculating the current density at E_{couple}.

Galvanic exposures of zinc and h.p. Nd–Fe–B were conducted at 30 °C in NaCl, using a Zn to Nd–Fe–B area ratio of 1.8 : 1. Zinc was found to be the anodic member of the couple in all cases. Measured values of both E_{couple} and the galvanic current density relative to the area of the cathode ($i_{g(c)}$) over the 20 h test period are shown in Fig. 8. The average values of E_{couple} and $i_{g(c)}$ were −1.06 V (SCE) and 120 μA cm^{-2} respectively, which correlated well with the E_{couple} and $i_{g(c)}$ values predicted by the mixed potential theory (−1.04 V (SCE), 110 μA cm^{-2}). The galvanic current density is reported with respect to the area of the cathode (Nd–Fe–B), since the parameter $i_{g(c)}$ is relevant to the cathodic protection requirements of the Nd–Fe–B alloy.

3.2.2. Preliminary evaluation of sacrificial zinc coatings

Nd–Fe–B was cathodically polarized by 0.27 V on galvanic coupling to zinc ($E_{corr} = -0.79$ V, $E_{couple} = -1.06$ V). The mixed potential theory was used to predict the anodic current density on coupled Nd–Fe–B by extrapolating the Tafel region of the h.p. anodic polarization curve in Fig. 4(a) to E_{couple}. The anodic dissolution rate of coupled Nd–Fe–B was predicted to be negligible (2×10^{-6} μA cm^{-2}). The penetration rates calculated from this value were also predicted to be negligible (less than 10^{-4} mpy), regardless of whether general or intergranular corrosion was assumed to take place. The mixed potential theory thus predicts that sacrificial zinc coatings may be capable of reducing the corrosion of Nd–Fe–B to an acceptable level, even if localized corrosion is considered.

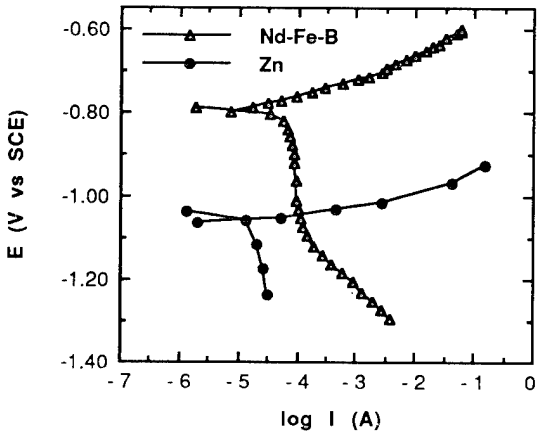

Fig. 7. Anodic and cathodic polarization of hot pressed Nd–Fe–B and Zn in 0.5 M NaCl at 30 °C. The diagram corresponds to an Nd–Fe–B electrode with an area of 1 cm^2 and a Zn electrode of 1.8 cm^2.

3.2.3. Evaluation of sacrificial zinc coatings via long-term immersion tests

Long-term immersion tests were performed in order to evaluate whether the significant reduction in the Nd–Fe–B dissolution rate predicted to occur on galvanic coupling to zinc would actually be obtained in practice. Immersion tests were also performed to determine whether incomplete protection, alkaline damage and/or hydrogen damage would occur if Nd–Fe–B was subjected to cathodic polarization for an extended period of time.

The long-term immersion tests (1 month) were performed in 0.5 M NaCl at 25 °C with the h.p. Nd–Fe–B samples either immersed at open circuit (uncoupled) or galvanically coupled to zinc using a Zn to Nd–Fe–B area ratio of 1.8 : 1. Average potential values of −0.82 V (SCE) and −1.06 V (SCE) were measured for uncoupled and coupled samples respectively. Although the potential of the coupled samples became slightly noble with time, measured values were active to −1.04 V (SCE) at all times during the 29 day test period. The measured pH of all bulk solutions was approximately 6.0 both before and after testing.

It was initially planned to evaluate the degree of protection provided by galvanic coupling to zinc by comparing the weight loss measured for Nd–Fe–B in both the uncoupled and coupled conditions. However, weight loss testing was precluded by the cracking of several test samples. The degree of protection could therefore only be evaluated by comparing the amount of insoluble and soluble corrosion products formed by both uncoupled and coupled samples. A second set of uncoupled samples was used in this determination due to cracking of the original test specimens.

The uncoupled samples were found to be completely covered by an insoluble, rust-colored corrosion product in less than 5 days, as shown in Fig. 9(a). The coupled samples, however, exhibited no rust-colored products even after 29 days in solution, as shown in Fig. 9(b). The very thin white covering found to exist on the coupled samples (Fig. 9(b)) is believed to be a zinc corrosion product which precipitated in the solution and settled onto the Nd–Fe–B surfaces. Although this product was too thin to be removed for conclusive analysis, the presence of zinc on the coupled Nd–Fe–B surfaces was verified by energy dispersive X-ray spectroscopy (EDX).

The absence of any rust-colored product on the coupled samples after 29 days of immersion (Fig. 9(b)) indicates that the dissolution rate of Fe atoms may have been significantly reduced by galvanic coupling of Nd–Fe–B to zinc. A reduction in the rate of Fe dissolution is consistent with the fact that cathodic polarization of Nd–Fe–B to E_{couple} moves the alloy into the immunity region of the Fe Pourbaix diagram [40], as shown in Fig. 10(a).

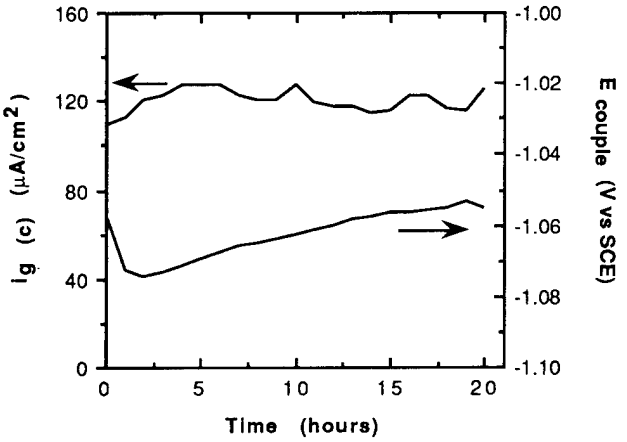

Fig. 8. Galvanic current density (relative to the area of the cathode) and couple potential values measured during the galvanic exposure of hot pressed Nd–Fe–B and Zn in 0.5 M NaCl at 30 °C, using a Zn to Nd–Fe–B area ratio of 1.8 : 1. Zinc was the anodic member of the couple.

The dissolution of Nd and B cannot be evaluated by an examination of insoluble corrosion products, since Nd–Fe–B is in the stability region of soluble Nd and B corrosion products at both E_{corr} and E_{couple}, as indicated in Figs. 10(b) and 10(c). The possibility of forming soluble Fe products at E_{corr} also exists, as shown in Fig. 10(a). It was therefore necessary to measure the amount of soluble Nd, Fe and B corrosion products in solution.

Solutions from both uncoupled and coupled tests were quantitatively analyzed using inductively coupled plasma atomic emission spectroscopy (ICP-AES), as shown in Table 1. Significant amounts of soluble Nd and Fe corrosion products were present in the solution containing the uncoupled sample after only 5 days of immersion. Conversely, the amount of soluble Nd, Fe and B in the solution containing the coupled sample was below the detection limit of the spectrometer, even after 29 days of immersion.

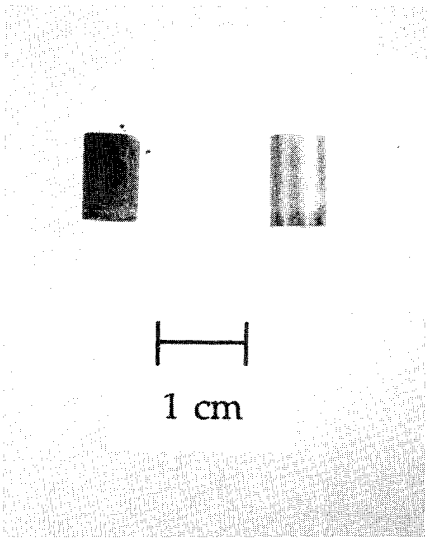

Fig. 9. Hot pressed Nd–Fe–B samples which were (a) left at open circuit (uncoupled) and (b) galvanically coupled to zinc in 0.5 M NaCl at 25 °C. The uncoupled sample was removed after 5 days in solution and the coupled sample was removed after 29 days in solution. The dark, insoluble corrosion product on (a) is rust colored.

The results of quantitative solution analysis provide conclusive evidence that the dissolution of Nd, Fe and B is essentially prevented by galvanic coupling to zinc. Maximum penetration rates for coupled Nd–Fe–B were calculated using the detection limits in Table 1. A penetration rate of 0.04 mpy was calculated when general corrosion was assumed to be operative. If all metal loss was assumed to come from the grain boundary phase, a maximum penetration rate of 0.7 mpy was calculated. Sacrificial zinc coatings therefore appear to be capable of reducing the corrosion of Nd–Fe–B to a negligible level, even if the possibility of localized corrosion is considered.

The marked reduction in the dissolution rate of Nd on coupling (Table 1) indicates that the electrochemical activity of Nd should not be a barrier to the use of zinc coatings as a corrosion control method for Nd–Fe–B. The observed reduction in Nd dissolution may be attributed to either thermodynamic or kinetic factors, as discussed below.

When the Nd–Fe–B alloy is galvanically coupled to zinc, the anodic dissolution of Nd will be thermodynamically impossible if E_{couple} (-1.06 V (SCE)) is active to the equilibrium half-cell potential for Nd ($E_{Nd/Nd^{3+}}$) [41]. However, the standard potential of Nd ($E^{\circ}_{Nd/Nd^{3+}} = -2.67$ V (SCE)) is so electronegative that the decrease in the dissolution of Nd on coupling almost certainly cannot be attributed to thermodynamic considerations (see Fig. 10(c)).

Since cathodic polarization of the Nd–Fe–B alloy from E_{corr} to E_{couple} is expected to reduce the anodic overvoltage for the Nd dissolution reaction, it is possible that the corrosion rate of Nd could be markedly reduced by coupling to zinc. Although the anodic Tafel slope for Nd dissolution is not known, Tafel slopes for metal dissolution are typically 100 mV per decade or less [41]. Cathodic polarization from E_{corr} to E_{couple} (270 mV) can thus be predicted to reduce the Nd dissolution rate by more than two orders of magnitude. Therefore kinetic considerations may be capable of explaining the observed reduction in Nd dissolution on coupling.

3.2.4. Environmentally assisted cracking

Several Nd–Fe–B samples cracked unexpectedly during long-term immersion in the absence of external loading, most probably due to a combination of residual stresses and environmental effects. Two uncoupled samples each cracked after 9 days in solution, one sample which was coupled to zinc cracked after 23 days

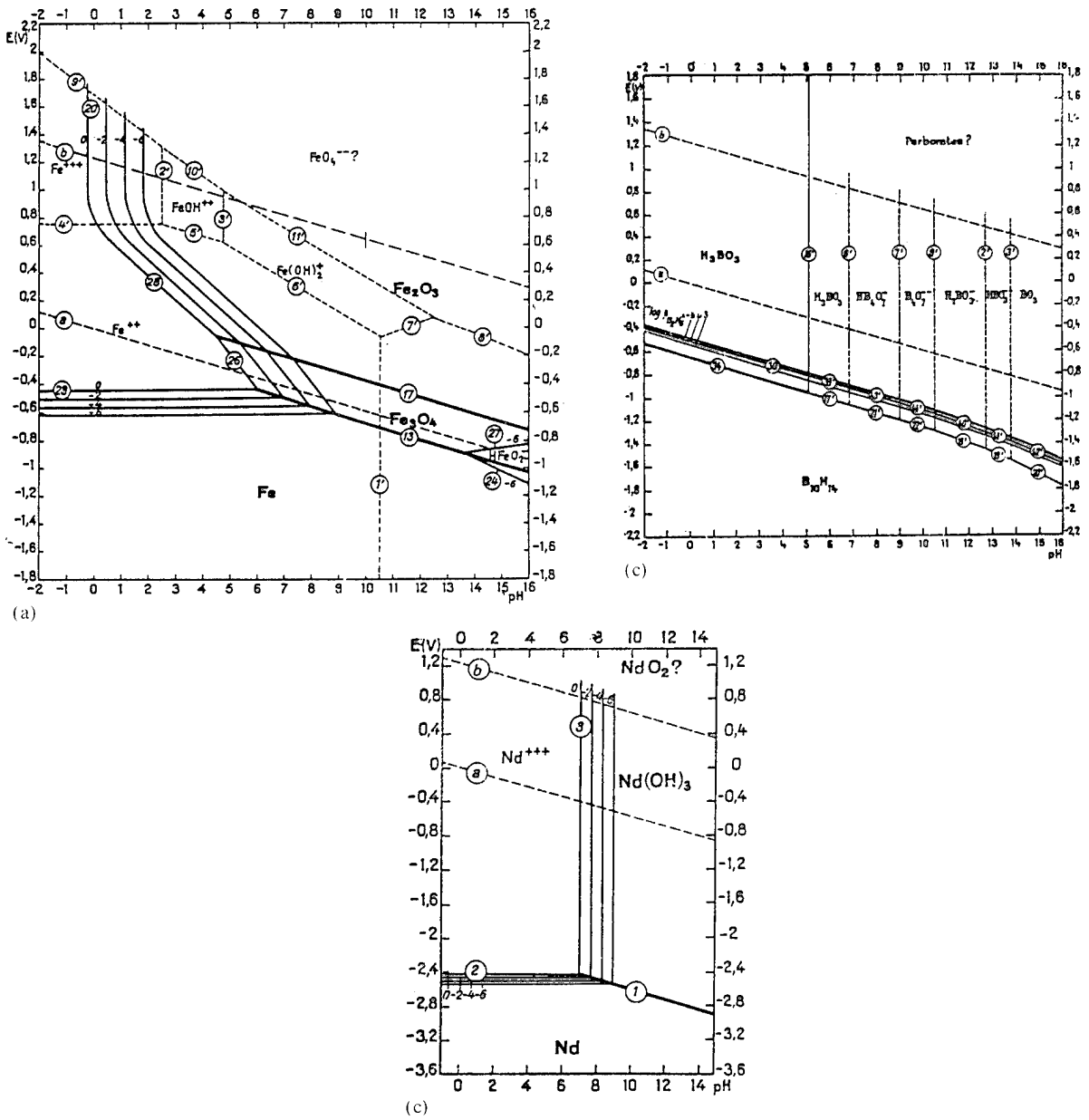

Fig. 10. The Pourbaix diagrams for (a) Fe, (b) B and (c) Nd at 25 °C. Insoluble corrosion products appear in bold type and soluble corrosion products in standard type. The average E_{corr} in the uncoupled tests (− 0.82 V vs. SCE) corresponds to − 0.58 V on the diagrams, and the average E_{couple} (− 1.06 V vs. SCE) corresponds to − 0.82 V. The bulk pH was approximately 6.0 in both cases.

in solution and the other coupled sample had not cracked on removal at 29 days, as shown in Fig. 11.

The extent of cracking in the uncoupled tests was substantial, as shown in Fig. 12(a). Both uncoupled samples were found to crack catastrophically into several fragments after 9 days of immersion. The damage suffered by the coupled sample which cracked after 23 days in solution was much less severe, as shown in Fig. 12(b), as only a small fraction of the sample was lost due to cracking. The coupled sample which did not crack during 29 days of immersion is also shown in Fig. 12(b). The initial dimensions of the cracked samples were similar to the dimensions of the uncracked specimen.

One concern regarding the use of sacrificial zinc coatings as a corrosion control method for Nd–Fe–B is the fact that hydrogen production will be galvanically stimulated on the alloy at breaks in the coating. In the presence of an applied or residual stress, the rate of cracking of Nd–Fe–B could be accelerated by the resulting hydrogen uptake. However, increased damage

Table 1
Results of the quantitative ICP-AES solution analysis for coupled and uncoupled long-term immersion tests in NaCl at 25 °C. All values were measured in milligrams per liter and the volume of the test solution analyzed was 0.65 l in both cases. The exposed area of the Nd–F–B samples was approximately 2.1 cm^2 in both the uncoupled and coupled tests. The uncoupled samples were removed after 5 days in solution, and the coupled samples after 29 days of immersion

Element	Uncoupled	Coupled
Neodymium	2.55	<0.10
Iron	3.99	<0.05
Boron	0.15	<0.05
Zinc	<0.05	20.30

of Nd–Fe–B on coupling was not found to occur as galvanic coupling to zinc was found to reduce rather than accelerate the rate of cracking (Fig. 11).

The increase in cracking resistance obtained on coupling should be viewed in a comparative rather than an absolute sense, since cracking was not completely eliminated by coupling to zinc. Since the coupled sample which cracked during testing underwent essentially no anodic dissolution (Table 1), it apparently was damaged by hydrogen. The appearance of hydrogen damage on coupling does not appear to be a barrier to the use of sacrificial zinc coatings, however, since both the rate and extent of cracking were much less than in the absence of coupling.

Although the cause of fracture in the uncoupled samples would seem to be an anodic phenomenon, such as stress corrosion cracking or corrosion product wedging, the cause of environmentally assisted fracture cannot be assessed on the basis of potential alone [42–45]. For example, the presence of pitting indicates the possibility of extensive localized hydrogen generation under open-circuit conditions. Electrochemical permeation testing will be used to investigate the cause of fracture.

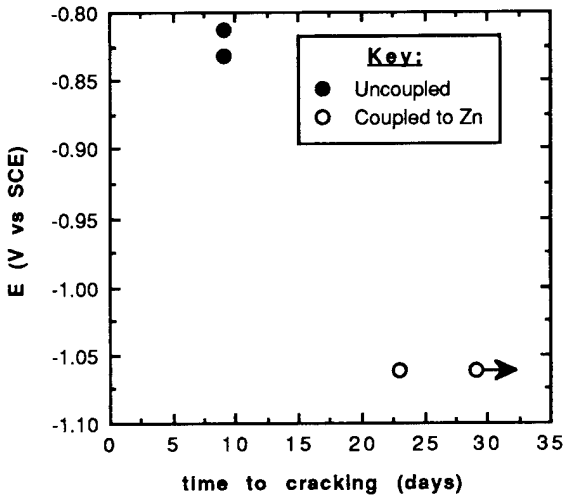

Fig. 11. Time to cracking for hot pressed Nd–Fe–B samples in aerated 0.5 M NaCl at 25 °C. The sample marked with an arrow did not exhibit cracking on removal from the test solution after 29 days of immersion. The extent of cracking of the remaining samples is shown in Fig. 12.

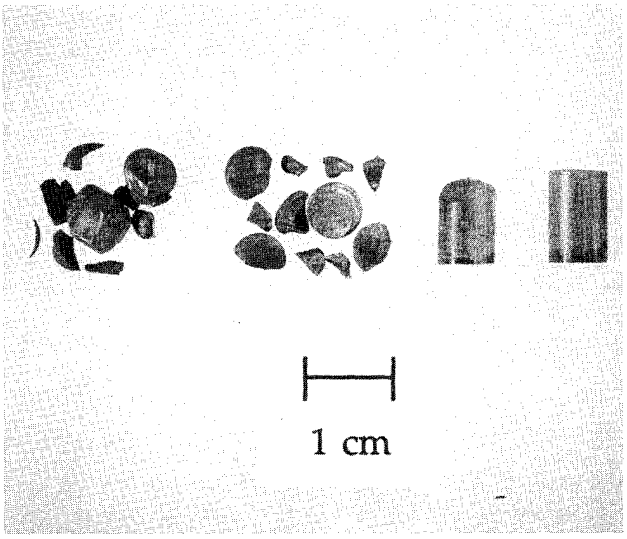

Fig. 12. Extent of cracking exhibited by (a) uncoupled samples and (b) coupled samples after immersion in 0.5 M NaCl at 25 °C. The uncoupled samples were removed (on cracking) after 9 days in the test solution, and the coupled samples were removed after 29 days of immersion.

The source of the stress which contributed to the observed cracking is under investigation, but has not yet been identified. Residual stresses might have been imparted to the samples during the machining treatment used to produce specimens with a common diameter. The stress could also have been provided by the wedging action of anodically formed corrosion products.

An analysis of the crack path is in progress, but has been impeded thus far by the extremely fine grain size of the alloy. Immersion tests are being performed in Na_2SO_4 to investigate the effect of Cl^- on the cracking process.

4. Conclusions

(1) Nd–Fe–B alloys prepared by RSP were found to corrode actively at open circuit in all test solutions, with estimated metal loss rates of at least 27 mpy.

(2) The anodic dissolution of Nd, Fe and B was essentially prevented by galvanic coupling of Nd–Fe–B to zinc in NaCl at 25 °C. The maximum metal loss rate of coupled Nd–Fe–B was calculated to be less than 1 mpy.

(3) Galvanic coupling to zinc was found to reduce the rate of environmentally assisted cracking of Nd–Fe–B in NaCl at 25 °C.

(4) Sacrificial zinc coatings appear to be a viable corrosion control method for Nd–Fe–B, based on results obtained in NaCl at 25–30 °C.

Acknowledgements

The financial support of both the National Science Foundation (NSF) and the American Society for Engineering Education (ASEE) is gratefully acknowledged. Test samples were provided by Magnequench®. The many useful contributions of Dr. D.B. Mitton of the Massachusetts Institute of Technology are also acknowledged.

References

[1] T. Chu, *J. Appl. Phys.*, *69* (1991) 6046.
[2] R.K. Mishra, *J. Appl. Phys.*, *61* (1987) 3778.
[3] R.K. Mishra, *J. Appl. Phys.*, *64* (1988) 5562.
[4] W. Tang, S. Zhou, R. Wang and C.D. Graham, *J. Appl. Phys.*, *64* (1988) 5516.
[5] R. Ramesh, J.K. Chen and G. Thomas, *J. Appl. Phys.*, *61* (1987) 2993.
[6] J.F. Herbst, R.W. Lee and F.E. Pinkerton, *Annu. Rev. Mater. Sci.*, *16* (1986) 467.
[7] J.J. Croat, *IEEE Trans. Magn.*, *25* (1989) 3550.
[8] J.F. Herbst and J.J. Croat, *J. Magn. Magn. Mater.*, *100* (1991) 57.
[9] R.W. Lee, *Appl. Phys. Lett.*, *46* (1985) 790.
[10] R.W. Lee, E.G. Brewer and N.A. Schaffel, *IEEE Trans. Magn.*, *21* (1985).
[11] K. Ohashi, Y. Tawara, T. Yokoyama and N. Kobayashi, in C. Herget and R. Poerschke (eds.), *Proc. 9th Int. Workshop on Rare-Earth Magnets and their Applications, Bad Soden, Germany, August, 1987*, Deutsche Physikalische Gesellschaft, Bad Honef, 1987, p. 355.
[12] J. Fidler and K.G. Knoch, *J. Magn. Magn. Mater.*, *80* (1989) 48.
[13] J.J. Croat and J.F. Herbst, *Mater. Res. Soc. Bull.*, *13* (1988) 37.
[14] S.G. Sankar, *J. Met.*, *43* (2) (1991) 30.
[15] H.H. Stadelmaier and E.-T.H. Henig, *J. Mater. Eng.*, *00* (1992) 12.
[16] P. Tenaud, H. Lemaire and F. Vial, *J. Magn. Magn. Mater.*, *101* (1991) 328.
[17] D. Hatfield, *Permanent Magnets and Magnetism*, Iliffe Books, London, 1962, pp. 29–39.
[18] T. Minowa, M. Yoshikawa and M. Honshima, *IEEE Trans. Magn.*, *25* (1989) 3776.
[19] G.W. Warren, G. Gao and Q. Li, *J. Appl. Phys.*, *70* (10) (1991) 6609.
[20] T.S. Chin, R.T. Chang, W.T. Tsai and M.P. Hung, *IEEE Trans. Magn.*, *24* (2) (1988) 1927.
[21] H. Bala, S. Szymura and J.J. Wysłocki, *J. Mater. Sci.*, *25* (1990) 571.
[22] J. Shain, Magnequench®, personal communication, May, 1993.
[23] E. Welker, Magnequench®, personal communication, May, 1993.
[24] H. Bala and S. Szymura, *Corrosion Sci.*, *32* (1991) 953.
[25] J.H. Payer, in R. Baboian (ed.), *Electrochemical Techniques in Corrosion Engineering*, NACE, Houston, 1977, p. 61.
[26] R. Mason, Magnequench®, personal communication, September, 1994.
[27] J. Jacobsen and A.S. Kim, *J. Appl. Phys.*, *61* (1987) 3765.
[28] M.G. Fontana and N.D. Greene, *Corrosion Engineering*, McGraw-Hill, 1978, pp. 378–379.
[29] A. Hütten and P. Haasen, *Scr. Metall.*, *21* (1987) 407.
[30] R.K. Mishra, *J. Magn. Magn. Mater.*, *54–57* (1986) 450.
[31] C.G. Munger, *Corrosion Prevention by Protective Coatings*, NACE, Houston, 1984, pp. 129–131.
[32] A.R. Cook, in H. Leidheiser, *Corrosion Control by Coatings*, Science Press, Princeton, 1979, p. 49.
[33] K. Barton, *Protection Against Atmospheric Corrosion*, Wiley, London, pp. 97–98.
[34] F.N. Speller, *Corrosion Causes and Prevention*, McGraw-Hill, New York, 1951, pp. 335–341.
[35] F. Mansfeld and E.P. Parry, *Corrosion Sci.*, *13* (1973) 605.
[36] L.H. Hihara and R.M. Latanision, *Corrosion*, *48* (1992) 546.
[37] K. Hosoya, R. Ballinger, J. Pryblowski and I.S. Hwang, *Corrosion*, *44* (1988) 838.
[38] J.R. Galvele and S.M. De Micheli, *Corrosion Sci.*, *10* (1970) 795.
[39] J.C. Rowlands, *Corrosion Sci.*, *2* (1962) 89.
[40] M. Pourbaix, *Atlas of Electrochemical Equilibria in Aqueous Solutions*, NACE, Houston, 1974, pp. 163, 193, 312.
[41] D.A. Jones, *Principles and Prevention of Corrosion*, MacMillan, New York, 1992, pp. 80, 455, 456.
[42] B.E. Wilde, *Corrosion*, *27* (1971) 326.
[43] J.H. Shively, R.F. Hehemann and A.R. Troiano, *Corrosion*, *23* (1967) 215.
[44] R.J. Gest and A.R. Troiano, *Corrosion*, *30* (1974) 274.
[45] R.M. Latanision, O.H. Gastine and C.R. Compeau, in Z.A. Foroulis (ed.), *Environment-Sensitive Fracture of Engineering Materials*, TMS-AIME Meeting, Chicago, IL, October, 1977.

ELSEVIER

Materials Science and Engineering A198 (1995) 35–41

MATERIALS SCIENCE & ENGINEERING A

Oxidation of an amorphous $Ni_{77}P_{23}$ alloy in air and dry oxygen at 300 °C

K. Shimizu[a], K. Kobayashi[a], P. Skeldon[b], G.E. Thompson[b], G.C. Wood[b]

[a]*Department of Chemistry, Faculty of Science and Technology, Keio University, 3-14-1 Hiyoshi, Yokohama 223, Japan*
[b]*Corrosion and Protection Centre, University of Manchester Institute of Science and Technology, Manchester M60 1QD, UK*

Abstract

The oxidation behaviour of an amorphous $Ni_{77}P_{23}$ alloy, prepared by electrodeposition, was investigated in air and in dry oxygen at 300 °C. The morphology, structure and composition of the oxide developed on the alloy were examined by X-ray photoelectron spectrometry, secondary-ion mass spectrometry (SIMS), and by high resolution transmission electron microscopy of ultramicrotomed sections. With successful preparation of extremely thin ultramicrotomed sections, between 5 and 10 nm thick, the microstructure of the oxide grown on the alloy and the oxide–alloy interface were revealed clearly, at atomic scale resolution, for the first time. SIMS depth profiling analysis has shown that the oxide films, grown in air and dry oxygen, consist mainly of NiO. However, the oxide growth rate in air was found to be considerably less than that in dry oxygen. High resolution cross-sectional transmission electron microscopy has shown that the difference in oxidation rates appears to be due to the distinctly different mosaic structure of the oxide films grown in air and dry oxygen which, in turn, affects the length of easy paths for Ni^{2+} diffusion during oxide growth.

Keywords: Amorphous Ni–P alloy; Oxidation; XPS; SIMS; Cross-sectional TEM

1. Introduction

Amorphous nickel–phosphorus alloys, prepared by electrolytic or electroless deposition, are of great commercial interest. Thus, these alloys are often applied over various substrates, aluminium alloys for example, to enhance corrosion resistance, and to improve hardness, wear properties, and solderability. More recently, these alloys are also receiving considerable interest as catalysts and as potential materials for making ohmic contact to III–V devices. The understanding of the oxidation behaviour of these alloys at relatively low temperatures, below 300 °C, is of practical importance, since they are subjected to such temperatures during processing or use. Thus, the thermal oxidation of an amorphous $Ni_{81}P_{19}$ alloy, prepared by electroless deposition, has been investigated in air at temperatures below 350 °C by Siconolfi and Frankentahl [1] using X-ray photoelectron spectrometry (XPS) and Auger electron spectroscopy (AES) combined with argon sputtering for depth analysis. It has been reported that the oxidation in air at 300 °C, for example, results in the growth of a layer of oxidation product consisting of three distinct layers. Next to the Ni–P substrate, there is a thin layer of $Ni_3(PO_4)_2$, seperating the Ni–P substrate from a layer of NiO which constitutes the bulk of the oxide. Over the NiO layer and adjacent to the air, there is a thin layer of $Ni(OH)_2$.

In order to obtain further insight into this complex, but interesting, behaviour of the oxide growth on amorphous nickel–phosphorus alloys, high resolution cross-sectional transmission electron microscopy has been employed here, yielding various pieces of important information, as described below, on the structure of the oxide films, which cannot be obtained readily by other techniques for surface analysis.

2. Experimental details

High purity annealed copper sheets, of dimensions $10 \times 20 \times 0.5\ mm^3$, were electropolished in a phosphoric acid solution to obtain a mirror finished surface. After electropolishing, the specimens were rinsed thoroughly in distilled water and dried in a cold air stream.

SSDI 0921-5093(94)04505-4

An amorphous nickel–phosphorus alloy, with an atomic composition of $Ni_{77}P_{23}$, was electrodeposited onto the electropolished copper substrate in a bath containing 240 g l^{-1} of $NiSO_4 \cdot 6H_2O$, 45 g l^{-1} of $NiCl_2 \cdot 6H_2O$, 30 g l^{-1} of H_3BO_3 and 40 g l^{-1} of H_3PO_3 at 70 °C with a constant current density of 5 A dm^{-2} for 2 min [2]. After electrodeposition, the specimens were rinsed thoroughly in distilled water, dried in a cold air stream, and stored in a desiccator for 30 min before oxidation in air or in dry oxygen at 300 °C for times ranging from 5 to 120 min.

The oxidised specimens were analysed using a JPS-90SX X-ray photoelectron spectrometer with a non-monochromated Mg Kα X-ray source. The core-level photoelectron spectra were recorded for Ni $2p_{3/2}$, O 1s, C 1s and P 2p regions after various oxidation times. All binding energies were corrected for charge shift by taking the C 1s spectrum from the adventitious carbon at 284.6 eV. The oxidized specimens were also analysed by secondary-ion mass spectrometry (SIMS) depth profiling with particular attention to the distribution of OH^- and phosphorus in the oxide. SIMS depth profiling was carried out in a Perkin-Elmer Atomica 6500 ion microprobe. The primary ion beam for sputtering was Cs^+ of 3 keV with a beam current of 5 nA, rastered across the surface area of 300 × 300 μm^2; the secondary ions were collected only from a central area, about 30 × 30 μm^2. The incident angle of the primary ion beam was set to 60 °C.

Ultramicrotomed sections of the Ni–P alloys and attached copper substrate were prepared in the usual way, using an RMC 6000 XL ultramicrotome [3]. Briefly, encapsulated specimens were trimmed initially with a glass knife and suitably thin sections, between 5 and 10 nm, were prepared by sectioning, in the direction approximately parallel to the (Ni–P)–copper interface, with a diamond knife. The sections were then examined in a Philips EM430 or JEM 4000EX high resolution transmission electron microscope operated at 300 kV and 400 kV respectively.

3. Results

3.1. Examination of the initial $Ni_{77}P_{23}$ alloy

Fig. 1 shows a transmission electron micrograph of an ultramicrotomed section of the $Ni_{77}P_{23}$ alloy and the copper substrate. The copper substrate is observed at the bottom of the micrograph and shows a flat and smooth surface. The $Ni_{77}P_{23}$ layer is observed above the flat copper substrate as a darker band of material of uniform thickness, about 390 nm. The $Ni_{77}P_{23}$ alloy appears featureless and uniform in contrast in the transmission electron microscope. No diffracting regions, indicative of the presence of crystalline regions,

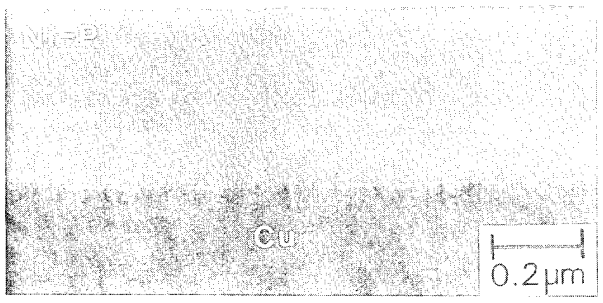

Fig. 1. Transmission electron micrograph of an ultramicrotomed section of the $Ni_{77}P_{23}$ alloy and the copper substrate.

are readily evident, indicating that the $Ni_{77}P_{23}$ alloy is largely amorphous. However, close examination of the alloy at higher resolution revealed the presence of ordered regions, a few nanometres in size [2,4]. This suggests that the $Ni_{77}P_{23}$ alloy is not totally amorphous as has been believed previously [5], but appears to have a more ordered structure which is related to the atomistic processes of electrodeposition.

Fig. 2 shows the Ni $2p_{3/2}$ and O 1s spectral regions obtained from the as-deposited $Ni_{77}P_{23}$ alloy which had been rinsed thoroughly in distilled water after electrodeposition, dried in a cool air stream and subsequently stored in a desiccator for 30 min at room temperature before XPS analysis. The P 2p region is shown in Fig. 3 separately. Deconvolution of the Ni $2p_{3/2}$ region gave two peaks at 852.9 and 856.5 eV. Similarly, deconvolution of the P 2p region gave two peaks at 129.5 and 133.2 eV, while the O 1s peak is a singlet with a binding energy of 531.4 eV. Of these peaks, the Ni $2p_{3/2}$ component at 852.9 eV and the P 2p component at 129.5 eV are associated with the substrate $Ni_{77}P_{23}$ alloy. Thus, the remaining peaks are associated with the presence of a thin surface layer formed, over the electrodeposited $Ni_{77}P_{23}$ surface, during rinsing in distilled water or exposure to air at room temperature before XPS analysis. The P 2p component at 133.2 eV is a clear indica-

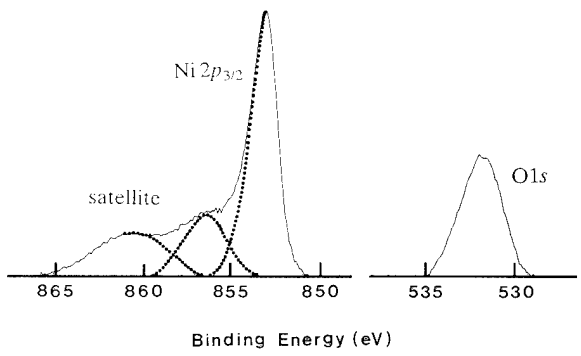

Fig. 2. The Ni $2p_{3/2}$ and O 1s photoelectron spectra obtained from the surface of as-deposited $Ni_{77}P_{23}$ alloy.

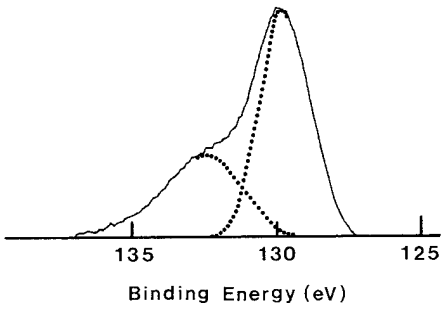

Fig. 3. The P 2p photoelectron spectrum obtained from the surface of as-deposited $Ni_{77}P_{23}$ alloy.

tion that the phosphorus is oxidised and present as P^{5+} in the surface layer, as expected from the fact that both nickel and phosphorus are thermodynamically unstable in air. Interpretation of the Ni $2p_{3/2}$ at 856.5 eV and O 1s at 531.3 eV depends on the form of P^{5+} in the thin surface film. Recent work by Sicinolfi and Frankentahl [1] has shown that the Ni–P alloy of similar composition, but prepared by electroless deposition, is covered with an $Ni(OH)_2$–$Ni_3(PO_4)_2$ layer only 6 Å thick. There is no reason to suppose that the surface film covering the $Ni_{77}P_{23}$ should be any different. Thus, the Ni $2p_{3/2}$ peak at 856.5 eV and O 1s peak at 531.4 eV are interpreted as the sum of contributions from $Ni(OH)_2$ and $Ni_3(PO_4)_2$.

3.2. Oxide film developed on the alloy in air at 300 °C

Fig. 4 shows the X-ray photoelectron spectra for the Ni $2p_{3/2}$ and O 1s regions for specimens oxidized in air at 300 °C for 5 min (Fig. 4(a)) and 30 min (Fig. 4(b)). No signal was detected from either component of the alloy or from P^{5+} due to the growth of a relatively thick layer of NiO, as will be shown later by SIMS depth profiling. Deconvolution of the Ni $2p_{3/2}$ region

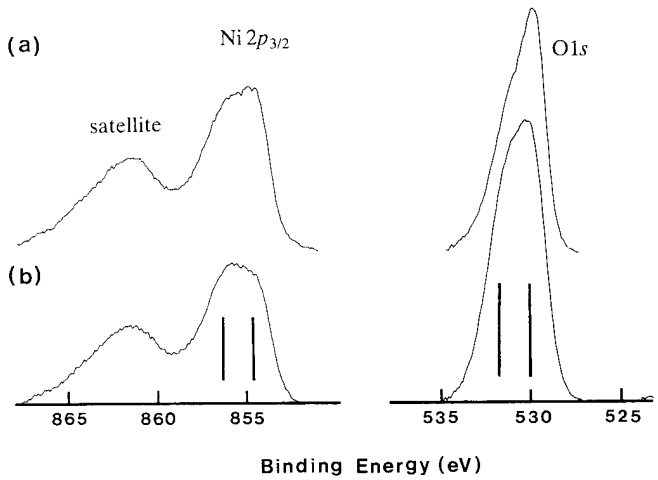

Fig. 4. The Ni $2p^{3/2}$ and O 1s photoelectron spectra obtained from the specimens oxidised in air at 300 °C for (a) 5 min and (b) 30 min.

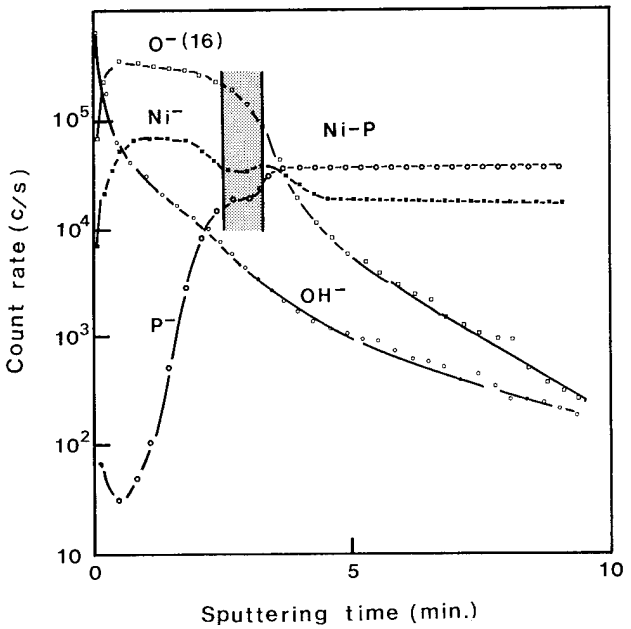

Fig. 5. SIMS depth profile of the oxide film grown on the $Ni_{77}P_{23}$ alloy by oxidation in air at 300 °C for 30 min.

gave two peaks at 845.5 and 856.5 eV. The higher-binding-energy components in the Ni $2p^{3/2}$ and O 1s spectra are from $Ni(OH)_2$, while the lower-binding-energy components are from NiO [1]. Comparing the spectra in Figs. 4(a) and 4(b), an increasing contribution from $Ni(OH)_2$ is evident as oxidation time increases. At face value, this suggests that $Ni(OH)_2$ is present as a discrete layer which thickens with increasing oxidation time in agreement with the results of Siconolfi and Frankentahl [1].

Fig. 5 shows a SIMS depth profile of the oxide grown over the $Ni_{77}P_{23}$ alloy by heating in air at 300 °C for 30 min, revealing the approximate distributions of Ni, O, P, and OH through the film thickness. It is evident that NiO is the major component of the oxide film. Adjacent to the Ni–P substrate, however, there appears to be a thin layer (shaded in Fig. 5) in which Ni, O and P are present. It is most likely that the layer corresponds to the $Ni_3(PO_4)_2$ layer detected, by Siconolfi and Frankentahl using AES depth profiling, for the oxide grown over the $Ni_{81}P_{19}$ alloy under similar oxidation conditions (see Fig. 6 in Ref. [1]). A further interesting point which emerges from SIMS depth profiling is that the outermost $Ni(OH)_2$ layer, which has been detected by XPS and shown to grow as oxidation time increases, cannot be clearly revealed here as a discrete layer. Rather, the depth profile suggests that the OH is present only at the surface of the NiO.

Fig. 6 shows a transmission electron micrograph of an ultramicrotomed section of the $Ni_{77}P_{23}$ alloy and its thermal oxide grown by heating in air at 300 °C for 30 min. The oxide film is observed clearly over the alloy which appears to have been crystallized, mostly to

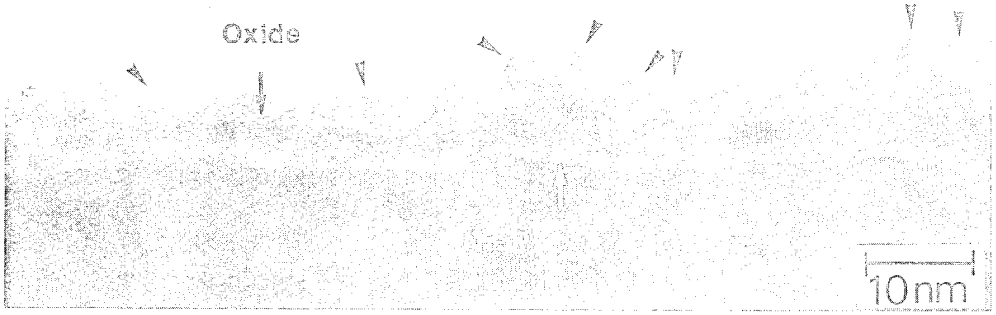

Fig. 6. Transmission electron micrograph of an ultramicrotomed section of the $Ni_{77}P_{23}$ alloy and the oxide film, which was formed by oxidising in air at 300 °C for 30 min.

Ni_3P, during oxidation [6,7]. The oxide layer is not microscopically uniform in thickness. The thickness of the oxide layers varies from about 5 nm, in thinner regions, to about 10 nm, in thicker regions. It is evident that the oxide layer consists mainly of fine NiO crystals, only a few nanometres in size, which appear to be randomly oriented. Lattice fringes of spacings about 0.24 nm and 0.21 nm are observed clearly within these crystals, which correspond to the (111) and (200) planes of NiO respectively. Close examination of the oxide surface indicates that the lattice fringes associated with NiO extend up to the outermost surface. Facetting is also observed clearly at locations indicated by the arrows. The $Ni(OH)_2$ layer, which has been detected by XPS and shown to grow as oxidation time increases, cannot be readily observed here. Between the NiO layer and Ni–P alloy, on the other hand, there appears to be a thin lighter layer, a few nanometres thick, which is thought to be the $Ni_3(PO_4)_2$ layer suggested by the AES and SIMS depth profiling analyses described above.

3.3. Oxide film developed on the alloy in dry oxygen at 300 °C

The oxide film growth in dry oxygen was found to be considerably different from that in air. The difference in thickness of the oxide was evident immediately even from examination of the oxidized specimens by the naked eye. Thus no significant changes were observed in the appearance of the specimen after oxidation in air at 300 °C for 30 min, while the specimen oxidized in dry oxygen at 300 °C for 30 min exhibited a brown shade, indicating the growth of thicker oxide.

Fig. 7 shows a SIMS depth profile of the oxide developed on the $Ni_{77}P_{23}$ alloy by heating in dry oxygen at 300 °C for 30 min. Comparing Figs. 6 and 7, thicker oxide growth is evident in dry oxygen. From the time needed to remove completely the oxide by sputtering, the thickness of the oxide developed in dry oxygen is estimated to be about twice that grown in air. No significant differences are, however, observed in the composition of the oxide grown in air and in dry oxygen. It appears that the oxide consists mainly of NiO. Next to the alloy, a thin layer is formed in which Ni, O and P are present. However, the layer, which is thought to be $Ni_3(PO_4)_2$, is not revealed as clearly as in the oxide grown in air (Fig. 5).

Fig. 8 shows a transmission electron micrograph of an ultramicrotomed section of the $Ni_{77}P_{23}$ alloy and its thermal oxide film developed by heating in dry oxygen at 300 °C for 30 min. The oxide film, about 20 nm thick, is observed clearly over the $Ni_{77}P_{23}$ alloy which appears to have been crystallized during oxidation. It is evident that the microstructure of the oxide layer is considerably different from that grown in air (Fig. 6) where the oxide layer consists of fine, randomly oriented NiO crystals, only a few nanometres in size. It appears that the oxide film developed in dry oxygen

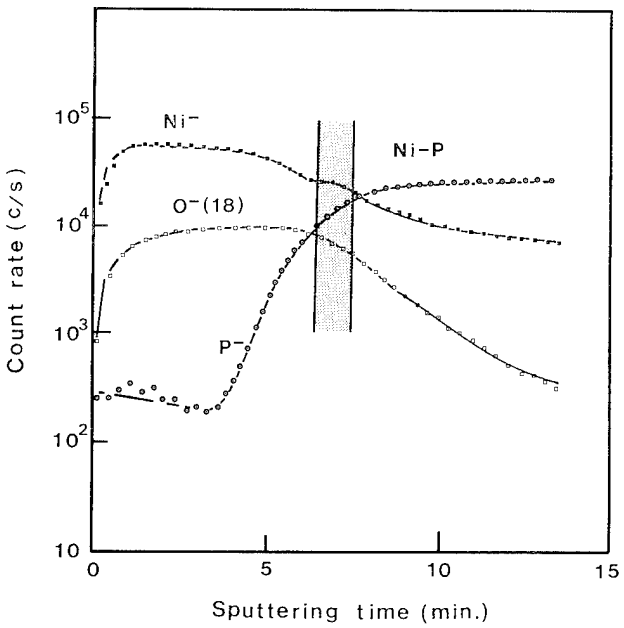

Fig. 7. SIMS depth profile of the oxide grown on the $Ni_{77}P_{23}$ alloy by oxidation in dry oxygen at 300 °C for 30 min.

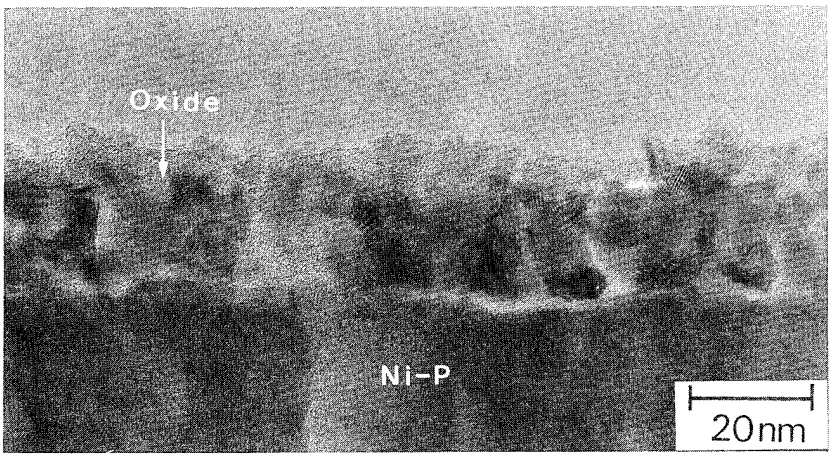

Fig. 8. As Fig. 6 but after oxidation in dry oxygen at 300 °C for 30 min.

consists of larger, columnar crystals with diameters up to 10 nm. Fig. 9 is an enlargement of a local area in Fig. 8. Lattice fringes of spacings about 0.24 nm and 0.21 nm, which correspond respectively to the (111) and (200) planes of NiO, are observed within the crystals. An NiO crystal in [001] projection is observed at the location indicated by the arrow, showing crossed (200) fringes of spacing about 0.21 nm. Close examination of the interface between the oxide and the Ni–P substrate also reveals a thin lighter layer, a few nanometres thick, as in the oxide grown in air. Given the SIMS depth profile shown in Fig. 7, the layer is thought to represent the layer of $Ni_3(PO_4)_2$.

4. Discussion

The understanding of many problems associated with the growth of thin surface films on metals, like the oxide on the $Ni_{77}P_{23}$ alloy of interest here, has become increasingly dependent on gaining precise knowledge of the morphologies, compositions and structures of the films, as well as the film–metal interfaces involved. It is clear that both the structural and chemical characterization of the films and film–metal interfaces can best be done by examining cross-sectional specimens in the analytical and high resolution transmission electron microscope. However, the preparation of the cross-sectional specimens is not routine. Without experience, the preparation of cross-sectional specimens can be an extremely frustrating and time-consuming process. Ion beam milling is now the best-established technique for reducing specimen thickness to electron transparency and has been widely used for semiconductors and ceramics. However, the technique cannot be applied successfully for many of the surface films on metals because of vastly different thinning rates experienced across the film–metal interfaces. A further problem is that the specimen suffers damage by ion beam as well as becoming chemically active.

The problems associated with ion beam milling can be avoided by the novel use of ultramicrotomy. Ultramicrotomy, a technique of mechanically cutting thin slices for electron microscopy, has been used widely in biological studies. However, the application of the technique for materials science was very rare. The work at the Corrosion and Protection Centre, University of Manchester Institute of Science and Technology, has shown [2,8,9] that ultramicrotomy is an extremely powerful technique for the preparation of cross-section-al specimens of metals and their surface films. It has been shown that ultramicrotomed sections can be prepared successfully for aluminium and aluminium alloys, copper, and even for harder and tougher metals such as zirconium, titanium and stainless steels. With an improved materials' ultramicrotomy approach, it is now possible to prepare ultramicrotomed sections, between 5 and 10 nm thick, with negligible damage to the film material and the film–metal interface.

With successful preparation of extremely thin ultramicrotomed sectons, between 5 and 10 nm thick, the microstructure of the oxide developed on the $Ni_{77}P_{23}$ alloy and the oxide–alloy interface have been revealed clearly, at atomic-scale resolution, for the first time. It has been shown that the microstructures of the oxides developed in air and in dry oxygen are considerably different. The oxide developed in air appears to consist of fine, randomly oriented NiO crystals, a few nanometres in size. In comparison, the oxide developed in dry oxygen consists of larger, columnar NiO crystals with diameters up to about 10 nm. In either case, a thin lighter layer, which is thought to be $Ni_3(PO_4)_2$, has been observed between the NiO layer and Ni–P substrate. At the relatively low oxidation temperature concerned here, i.e. 300 °C, the oxide growth on the amorphous $Ni_{77}P_{23}$ alloy is thought to proceed, like that on nickel, by migration of Ni^{2+} ions along grain boundaries in the oxide film which act as paths for easy diffusion. Thus, it appears that the difference in oxida-

Fig. 9. An enlargement of a local area in Fig. 8.

tion rates in air and in dry oxygen is closely related to the difference in the mosaic structure of the oxide films which, in turn, affects the length of easy paths for Ni^{2+} diffusion.

A further interesting point is the behaviour of phosphorus during oxidation. As shown in Fig. 6, oxidation in air at 300 °C for 30 min results in the growth of the oxide film which consists of an outer NiO layer, about 8 nm in average thickness, and an inner $Ni_3(PO_4)_2$ layer, about 1 nm thick. Assuming the density of NiO and $Ni_3(PO_4)_2$ to be 6.67 and 4.40 respectively, the amount of phosphorus in the oxide film (or more precisely the layer of oxidation products) is estimated to be only about one-tenth of that expected from the alloying composition. This suggests that most phosphorus atoms, if not all diffuse into the bulk alloy during oxidation.

The distinct difference in the microstructure of the oxide grown in air and in dry oxygen deserves particular attention. The difference could be due to the presence or absence of water vapour in the oxidizing environments, to the differing oxygen pressure, or to the combination of both. Using ellipsometry, Gupta et al. [10] studied oxidation of Ni, Ni–Cr and $Ni_{81}P_{14}$ alloys in the temperature range 100–400 °C in different environments including air, water vapour, and O_2-N_2 mixtures in which the partial pressure of oxygen was varied form 0.05 to 0.5 atm. They found that the rate of oxide growth for all three metals in water vapour is considerably less than that in air. At 400 °C, for instance, oxidation of the $Ni_{86}P_{14}$ alloy in air for 30 min resulted in the growth of an oxide, about 6 nm thick. In contrast, in water vapour, no significant oxide growth was detected on the alloy until the oxidation time exceeded about 60 min. They also found that the oxidation rate increases as the partial pressure of oxygen increases for all three metals studied. Following oxidation at 400 °C for 100 min, for example, the thicknesses of the oxides grown on the $Ni_{86}P_{14}$ alloy are estimated to be about 45 nm and 70 nm for oxygen pressures of 0.2 atm (which roughly corresponds to that in air) and 1 atm respectively (Fig. 6 in Ref. [10]). Unfortunately, data at 300 °C, the temperature employed in the present work, are not available in Ref. [10], preventing comparison with the present work. However, it is reasonable to assume that the difference in the microstructure of the oxide grown in air and in dry oxygen is due to the combined effects of water vapour and oxygen pressure which affect the nucleation of NiO crystals and subsequent development of the mosaic structure. The oxide growth on the amorphous $Ni_{77}P_{23}$ alloy appears complex, involving not only short circuit diffusion of Ni^{2+}, but also transport of Ni^{2+} through the $Ni_3(PO_4)_2$ layer, separating the NiO layer from the alloy, and crystallization of the amorphous alloy. Thus, the role of water vapour and oxygen pressure on the nucleation of NiO crystals and subsequent development of the mosaic structure will be best addressed by studying a simple system, which exhibits a similar oxidation behaviour. The oxidation of nickel seems ideal, since the oxide growth on nickel is known to be affected by water vapour and oxygen partial pressure in ways similar to those observed for $Ni_{86}P_{14}$ alloy [10]. Work along this line is now in progress and the results will be published in due course.

Finally, the cause for the discrepancy between the XPS, transmission electron microscopy concerning the presence or absence of the outermost $Ni(OH)_2$ layer is discussed only briefly. XPS analysis of the specimens oxidized in air has shown clearly the presence of

$Ni(OH)_2$ at the outermost surface of the oxidized specimens. An increasing contribution from $Ni(OH)_2$ is also evident in the Ni $2p_{3/2}$ and O 1s spectra as the oxidation time increases. At face value, this suggests that the $Ni(OH)_2$ is present as a discrete layer, covering the NiO layer, and its thickness increases with oxidation time. However, the $Ni(OH)_2$ layer is not revealed by high resolution transmission electron microscopy of ultramicrotomed sections, while SIMS depth profiling analysis has also suggested that OH is present only at the surface of NiO rather than as a discrete layer. The discrepancy between the XPS, transmission electron microscopy and SIMS results may result from the assumption in the XPS analysis of thin films that the films are uniform, whereas in reality the oxide grown on the $Ni_{77}P_{23}$ alloy is microscopically non-uniform. Thus, the analysis of XPS results based on a uniform, layered model of the oxide is not valid here. The surface of the oxide film is noticeably rough at a microscopic scale, since the film consists of fine, randomly orientated NiO crystals. As the oxidation time increases, more NiO crystals are formed, and the roughness at the oxide surface increases. Thus, it is most likely that XPS has simply detected surface OH groups which increase in number with oxidation time as a result of the increasing surface area. Using the uniform layer model, an erroneous interpretation is made that the $Ni(OH)_2$ is present as a discrete layer which thickens with increasing oxidation time.

Various surface analytical techniques, such as XPS, AES, SIMS, ion scattering spectroscopy (ISS) etc., are now available for compositional and structural analysis of thin surface films, less than 10 nm thick, on metals. The results obtained by these techniques are analysed normally with the assumption (implicit or explicit) that the films are microscopically uniform in thickness. In certain cases, the film is very thin, less than 10 nm, has been taken to imply that the film is microscopically uniform. It now appears that such views are too naive and, in certain cases, could well lead to an erroneous interpretation of results. The present work indicates clearly that high resolution cross-sectional transmission electron microscopy, allied with a novel technique of specimen preparation using ultramicrotomy, has an enormous potential for the structural and compositional analysis of thin surface films on metals, even when the thicknesses of the films are less than 10 nm.

Acknowledgements

Thanks are due to the Royal Society for the provision of a Guest Research Fellowship to one of the authors (K. Shimizu). Thanks are also due to Professor K. Hiraga of the Institute for Materials, Tohoku University, for the provision of time on a JEM 4000EX transmission electron microscope.

References

[1] D. Siconolfi and R.P. Frankentahl, *J. Electrochem. Soc.*, *136* (1989) 2475.
[2] K. Shimizu, K. Kobayashi, G.E. Thompson and G.C. Wood, *Philos. Mag. Lett.*, *61* (1990) 43.
[3] R.C. Furneaux, G.E. Thompson and G.C. Wood, *Corros. Sci.*, *18* (1978) 853.
[4] K. Shimizu, K. Kobayashi, G.E. Thompson and G.C. Wood, *J. Surf. Finish. Soc. Jpn.*, *42* (1991) 122.
[5] G.S Cargil, *J. Appl. Phys.*, *41* (1970) 12; *Solid State Phys.*, *30* (1975) 227.
[6] S.T. Pai, J.P. Marton and J.D. Brown, *J. Appl. Phys.*, *43* (1972) 282.
[7] M.R. Lambert and D.J. Duquette, *Thin Solid Films*, *177* (1989) 202.
[8] G.E. Thompson, K. Shimizu, B. Bethune and G.C. Wood, *Microsc. Anal.*, (September 1991) 41.
[9] K. Shimizu, K. Kobayashi, G.E. Thompson and G.C. Wood, in B.R. MacDougal, R.S. Alwitt and T.A. Rammanarayaran (eds.), *Oxide Films on Metals and Alloys*, Electrochemical Society, Pennington, NJ PV 92-22, 1992, pp. 23–38.
[10] K. Gupta, J.P. Marton and J. Shewchen, *J. Electrochem. Soc.*, *121* (1974) 118.

ELSEVIER

Materials Science and Engineering A198 (1995) 43–49

MATERIALS SCIENCE & ENGINEERING A

The influence of laser surface melting on the resistance of AISI 4135 low alloy steel to hydrogen-induced brittle fracture

B.E. Wilde[a], M. Manohar[b], C.E. Albright[c]

[a]*Fontana Corrosion Center, Department of Materials Science and Engineering, The Ohio State University, Columbus, OH 43210, USA*
[b]*Homer Research Laboratories, Bethlehem Steel Corporation, Bethlehem, PA 18016, USA*
[c]*Department of Welding Engineering, The Ohio State University, Columbus, OH 43210, USA*

Abstract

Flat and cylindrical heat-treated AISI 4135 low alloy steel specimens were surface treated using power levels of 50, 100 and 200 W. The results of hydrogen permeation and slow strain rate tension (SSRT) tests show the following.

(1) Laser surface treatment of AISI 4135 low alloy steel results in a reduction in the hydrogen absorption kinetics as measured by the permeation test, and also an improved resistance to hydrogen-induced fracture in the SSRT test under galvanostatic charging conditions.

(2) The degree of effectiveness in reducing the hydrogen absorption rate is shown to occur at all power levels, and is greatest at the 50 W level.

(3) A clear qualitative relationship is described between the hydrogen absorption rate and the time to failure in the SSRT test. This relation was even more striking in terms of the fractographic detail of the fracture face.

(4) A possible explanation for the reduced hydrogen absorption as a result of low power laser surface melting treatment is the influence of the rapidly quenched metal surface on the steady state degree of hydrogen adatom coverage or the absorption kinetic rate constant or both.

(5) Reverse membrane permeation experiments indicated that the effect of laser surface melting on the permeation flux at constant charging current was not due to barriers in the metal which alter the hydrogen flux gradient across the membrane.

Keywords: Hydrogen embrittlement; Permeation; Absorption; Kinetics; Low alloy steels

1. Introduction

One limitation to the widespread use of high strength steels is their susceptibility to hydrogen-induced fracture (HIF) under conditions in which exposure involves corrosion in aqueous media. It is recognized that, for HIF to occur, hydrogen atoms must enter the steel through the surface in contact with the corrosive environment, and recent efforts have been directed at impeding the entry of hydrogen by suitably modifying the corroding surface of the steel as described elsewhere [1,2].

The amount of hydrogen generated on the surface by the corrosion reaction decreases with decreasing corrosion rate; therefore it is argued that any method of reducing the latter should reduce the amount of hydrogen absorbed. Surface modification using laser beams has been found to be successful in reducing corrosion rates in several alloy systems [3–17], and this work is a continuation of that of Wilde and Shimada [18], who found that laser surface melting (LSM) reduced hydrogen absorption into AISI 1018 steel.

However, in this work, in addition to the LSM of flat permeation membrane specimens, equivalent LSM of round slow strain rate tension (SSRT) test specimens of a low alloy steel (AISI 4135) was carried out to evaluate directly whether the susceptibility to HIF could be correlated with the hydrogen permeation test results.

2. Theoretical background

It is well known that the hydrogen evolution reaction on metal surfaces is a multistep reaction involving the

SSDI 0921-5093(94)04506-2

following steps [19–23]:

(1) hydrogen adsorption

$$M(e)^- + H_3O^+ \rightarrow MH_{ads} + H_2O \text{ (in acid solutions)} \quad (1)$$

$$M(e)^- + H_2O \rightarrow MH_{ads} + OH^- \text{ (in alkaline solutions)} \quad (2)$$

(2) hydrogen recombination

$$MH_{ads} + MH_{ads} \rightarrow 2M + H_2 \quad (3)$$

(3) electrode desorption

$$MH_{ads} + H_3O^+ + M(e)^- \rightarrow 2M + H_2O + H_2 \quad (4)$$

(4) hydrogen absorption

$$MH_{ads} \rightarrow MH_{abs} \quad (5)$$

where MH_{ads} and MH_{abs} refer to the hydrogen adatom and the hydrogen absorbed by the metal respectively.

As far as HIF is concerned, the hydrogen absorption reaction (Eq. (5)) is the most important and involves the incorporation of a surface adatom in the metal lattice. The amount of hydrogen adsorbed on the surface is represented by the surface coverage θ, which is defined as [21]

$$\theta = \frac{\text{number of adsorption sites filled}}{\text{total number of adsorption sites available}} \quad (6)$$

The rate at which the adsorbed hydrogen is absorbed into the metal surface can be represented as

$$\text{rate of absorption} = k_{abs}\theta - k_{des}C_0 \quad (7)$$

where k_{abs} is the absorption rate constant and k_{des} is the desorption rate constant.

The absorbed hydrogen builds up a concentration C_o just beneath the metal surface which controls the permeation of the absorbed hydrogen into the metal membrane according to the boundary conditions shown in Fig. 1.

The permeation rate of the absorbed hydrogen through the membrane is given by

$$J = \frac{D(C_o - C_L)}{L} \quad (8)$$

where D is the diffusivity of hydrogen in the metal, C_L is the fugacity of hydrogen at the exit side of the metallic membrane and L is the membrane thickness.

Kim and Wilde [24] have shown that the absorption kinetics follow a first-order reaction path, and the higher the surface coverage θ, the greater will be the amount of hydrogen entering the steel with the concomitant higher risk of HIF. However, little work is found in the literature attempting to correlate data obtained from hydrogen absorption experiments with susceptibility to HIF. One of the objectives of this study was to determine whether such a correlation existed in the case of laser surface melted AISI 4135 high strength low alloy steel.

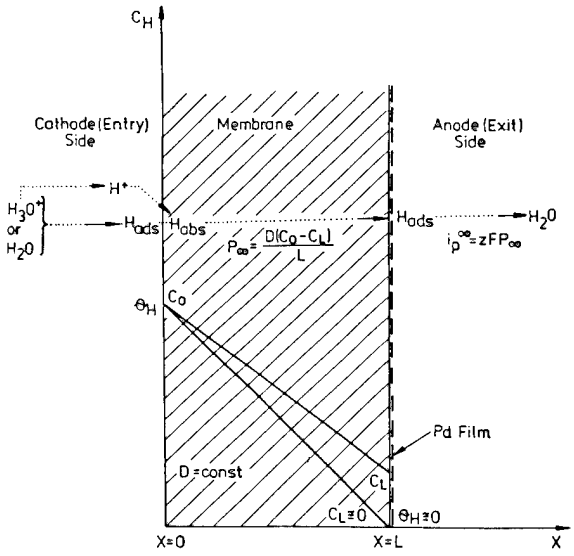

Fig. 1. Schematic representation of the boundary conditions involved in the absorption of hydrogen into a membrane.

3. Experimental procedure

The composition of the steel used in this study and the heat treatment employed to obtain a yield (0.2% offset) strength of 183 ksi are given in Table 1. Hydrogen permeation membranes (size, 40 mm × 40 mm × 1.7 mm) and SSRT specimens (diameter, 3.75 mm) were prepared by machining. After heat treatment, the specimens were ground to 320 grit finish and washed with detergent and acetone. LSM was then carried out using a Coherent Everlase M53 CO_2 laser machine. A Laserdyne 410 CNC machine was used to control the movement of the workpiece. The arrangement used for the LSM of the permeation membranes is shown in Fig. 2 and the LSM conditions employed are summarized in Table 2.

The SSRT test specimens were surface treated using a rotary fixture. LSM was carried out by focusing a stationary laser beam on the surface of the cylindrical specimen rotating at a constant speed and moving axially at a constant rate. In order to keep the LSM conditions as close as possible to those employed for the permeation membrane specimens used in the hydrogen absorption studies, the travel speed was maintained at 100 in min^{-1} by rotating the specimen at 248 rev min^{-1}, and an interval of 0.005 in between passes was obtained by providing an axial movement of 1.24 in

Table 1
Composition and heat treatment of the steel used

Element	C	Mn	Si	Cr	Mo	S	P
Content (wt.%)	0.33	0.75	0.30	1.09	0.185	0.013	0.003

Heat treatment: austenitize at 870 °C for 1 h, followed by an oil quench; temper at 425 °C for 30 min, followed by air cool.

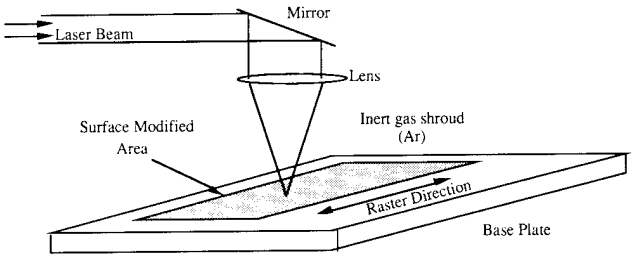

Fig. 2. Diagram of LSM arrangement.

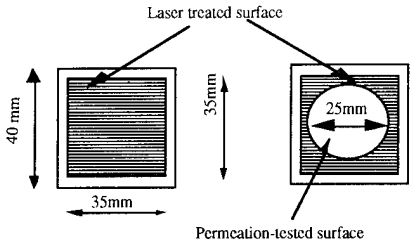

Fig. 3. Location of LSM and permeation testing on membranes.

min^{-1}. Power levels of 50, 100 and 200 W were once again employed. Fig. 3 shows the specimen and the location where LSM and permeation testing were carried out on the membrane specimens.

Hydrogen absorption rate experiments were carried out at room temperature using the Devanathan–Stachurski electrochemical technique described elsewhere [22] and shown schematically in Fig. 4. The permeation cell consisted of two identical Pyrex glass chambers with the membrane fixed between them using clamps. The electrode potentials in both circuits were measured using saturated calomel electrodes (SCEs) mounted through Luggin capillary probes. NaOH (1 N) was used as electrolyte since the steel is passive in this environment and is virtually immune to corrosion effects such as stress corrosion cracking. The solution was prepared using reagent grade NaOH and double-distilled, demineralized water, and was used as the electrolyte in both chambers. In the anodic cell, the membrane (working electrode) was maintained at a potential of $+100$ mV_{SCE} using a potentiostat. After the specimen had been degassed (which was indicated by the attainment of a low background current), hydrogen was evolved galvanostatically on the cathodic side at a rate of 197 μA cm^{-2}. This value was chosen to correspond to the rate of hydrogen evolution that a low alloy steel surface would experience when corroding under natural conditions in acidified brine. Nitrogen was bubbled through the electrolyte in both chambers. The current in the anodic circuit was recorded as a function of time using a strip-chart recorder and the steady state permeation current was obtained for each specimen. The difference between the steady state permeation current density and the background current density yielded the hydrogen permeation flux J_∞ which was used as the criterion for comparison.

Microhardness measurements (Knoop 25 g load) were made in the base steel and in the laser surface melted regions of the membranes and the results are shown schematically in Fig. 9 (see Section 4) together with the metallurgical microstructures developed.

SSRT testing was carried out on the 3.175 mm diameter cylindrical specimens in both the untreated and laser surface melted conditions using a strain rate of 2×10^{-6}. The electrolyte used and the charging current density were once again 1 N NaOH and 197 μA cm^{-2} respectively. A load cell was used to monitor the stress (and hence the strain) and its output was connected to a strip-chart recorder. Thus the test involved obtaining the stress–time relationship for a specimen strained at a constant rate on which hydrogen was galvanostatically evolved at a predetermined rate. In order to exclude brittle fracture and stress corrosion effects, one specimen was tested in air and another in 1 N NaOH without hydrogen charging. The fracture surfaces were examined using a scanning electron microscope. The time to failure and the fracture mode were used as assessment criteria.

Table 2
LSM conditions employed

Laser	CO_2, 10.6 μm
Beam diameter	330 μm
Lens	ZnSe, 5 in focal length
Power levels	50, 100 and 200 W
Power densities	5.73, 11.46 and 22.9×10^4 W cm^{-2}
Travel speed	42.3 min s^{-1}
Shielding gas	Argon
Interval	0.127 mm (0.005 in)
Dwell time	3 s

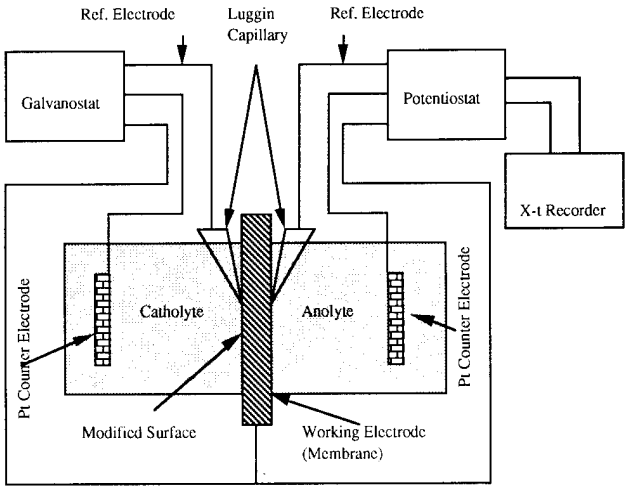

Fig. 4. Schematic diagram of the hydrogen permeation cell.

Table 3
Results of hydrogen permeation experiments

Condition	Permeation flux J, ($\mu A\ cm^{-2}$)
Base steel	0.60
LSM 50 W	0.38
LSM 100 W	0.40
LSM 200 W	0.51
Charging current density	197 $\mu A\ cm^{-2}$
Anodic potential	0.100 V_{sce}
Electrolyte	1 N NaOH

LSM 50 W refers to laser treatment using 50 W power.

4. Results and discussion

The results of the permeation experiments (Table 3) reveal that LSM treatment resulted in reduced hydrogen absorption, with the 50 W treatment being the most effective. The 200 W treatment, which gave the highest permeation flux of the laser surface melted specimens, was also seen to reduce the hydrogen absorption to some extent compared with the untreated condition.

The kinetics of hydrogen absorption into a ferrous metal surface have been discussed in Section 2 and have a first-order dependence on θ, which in turn dictates the value of C_o. In view of the experimental data showing a decrease in absorption rate in the LSM experiments, it is clear that the LSM treatment influences either k_{abs} or θ, or the LSM treatment changes the hydrogen flux gradient across the membrane (see Fig. 1).

To explore these possibilities, permeation experiments were conducted as previously described by Chattoraj and Wilde [25], in which the treated surface was reversed and made the oxidation side of the membrane and the hydrogen fugacity was maintained at zero with an applied anodic potential. Under these conditions, it was rationalized that the now untreated input surface would absorb hydrogen at a high rate (like the base steel, see Table 3) if the LSM treatment affected the surface absorption kinetics, e.g. θ or k_{abs}. However, if the measured flux was less than that measured at constant current on a non-treated surface, this would imply that the LSM treatment affected the hydrogen flux gradient inside the steel.

In the event, the data obtained in the reverse membrane experiments all gave permeation fluxes similar in magnitude to that obtained on a base steel surface, indicating that the LSM affected the basic hydrogen absorption kinetics, i.e. similar to that observed in the presence of compressive stresses imposed by shot peening.

The SSRT test results presented in Table 4 and Figs. 5–8 reveal that the LSM 50 W treatment, in addition to decreasing the absorption rate of hydrogen under the charging conditions used, resulted in a significant improvement in the HIF behavior. While the base steel failed in 14.5 h in a 100% brittle, intergranular (IG) mode in the untreated condition (Fig. 5), the LSM 50 W treatment resulted in a 100% ductile fracture by

Table 4
Results of the SSRT tests

Condition	Time to failure (h)
Base steel in air	27.5
Base steel in NaOH (no H_2 charging)	27.5
Base steel in NaOH with H_2 charging	14.5
LSM 50 W in NaOH with H_2 charging	27
LSM 100 W in NaOH with H_2 charging	20
LSM 200 W in NaOH with H_2 charging	16.5
Cathodic charging current	197 $\mu A\ cm^{-2}$
Strain rate	$2 \times 10^{-6}\ s^{-1}$

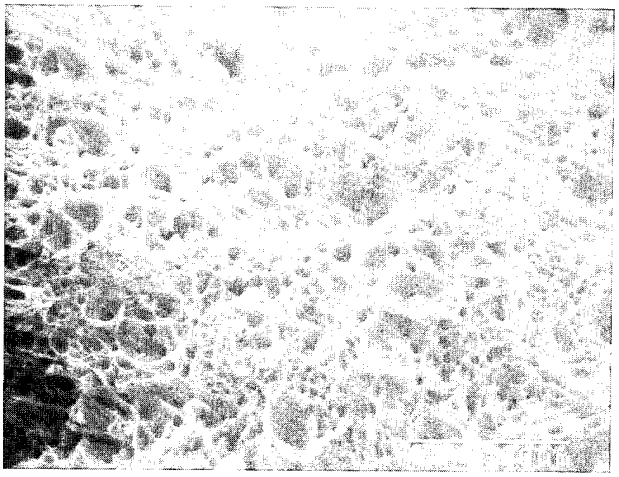

a) Base steel fractured in air

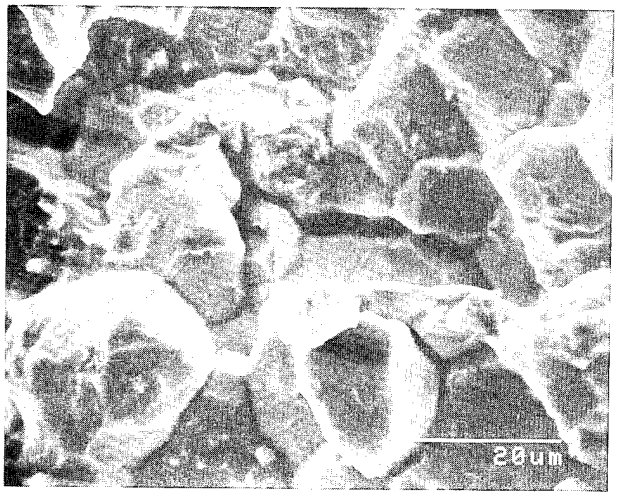

b) Base steel with cathodic charging

Fig. 5. Scanning electron microscopy fractograph of the base steel SSRT specimen (1500 × magnification).

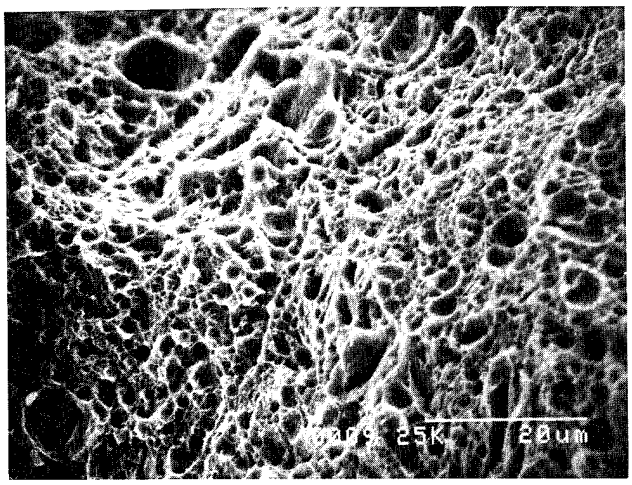

Fig. 6. Scanning electron microscopy fractograph of LSM 50 W SSRT specimen (1500 × magnification).

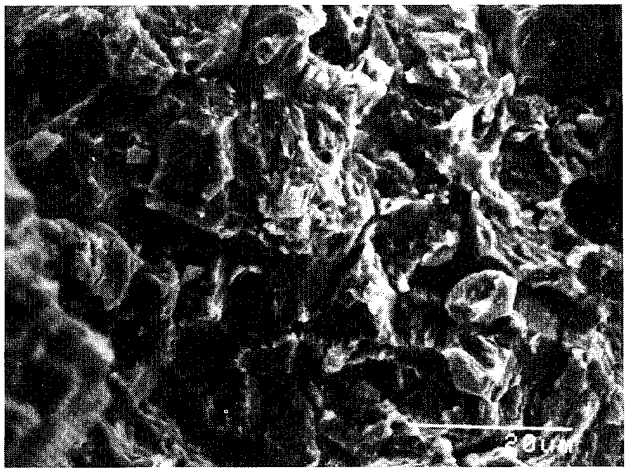

Fig. 8. Scanning electron microscopy fractograph of LSM 200 W SSRT specimen (1500 × magnification).

microvoid coalescence (MVC) and took almost as long to fail as the specimen in air (Fig. 6). The LSM 100 W and LSM 200 W treatments gave intermediate results, but both showed longer times to failure and less brittle fractures compared with the untreated condition (Figs. 7 and 8). The observation that the time to failure of the untreated specimen in 1 N NaOH without hydrogen charging was the same as that in air rules out stress corrosion effects.

According to the hydrogen-assisted cracking model proposed by Beachem [26], IG fracture is generally favored at low stresses and high hydrogen levels. The fact that IG features were observed in the untreated base steel fracture surface suggests that the amount of hydrogen absorbed by the steel was relatively high under the charging conditions employed. On the other hand, the MVC type of fracture observed in the LSM 50 W specimen indicates that the fracture occurred under (relatively) high stress and low hydrogen conditions. This indicates that less hydrogen was absorbed in the LSM 50 W specimen compared with the untreated base steel specimen. The LSM 100 W and LSM 200 W specimens showed the effects of increasing hydrogen and decreasing stress conditions.

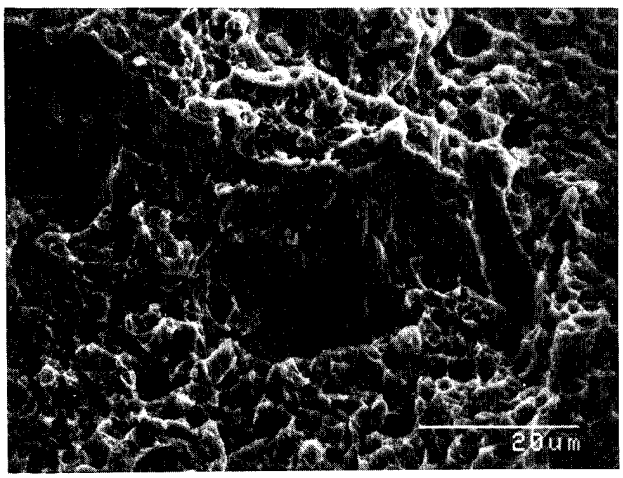

Fig. 7. Scanning electron microscopy fractograph of LSM 100 W SSRT specimen (1500 × magnification).

The hydrogen permeation and SSRT test results presented in Tables 3 and 4 indicate clearly that low power LSM improves the HIF resistance of the steel by reducing the rate of hydrogen absorption at the steel surface. However, these effects could not definitely be correlated with the hardness in the laser surface melted region. As shown in Fig. 9, the LSM 50 W and LSM 100 W specimens showed higher hardness levels in the laser surface melted regions and lower permeation fluxes than the untreated base steel. However, the LSM 200 W specimen showed a lower hardness and a lower permeation flux than the untreated base steel. Thus the hardness of the microstructure by itself does not appear to play a significant role in hydrogen absorption.

One possible explanation for the diminished effect of the higher power levels could be that the tempered heat-affected zone (HAZ) of each pass, which was observed as a dark etching region of relatively low hardness (see Fig. 9), acted as a pipe for hydrogen diffusion into the substrate. Although not experimentally verified, it is possible that the stress fields associated with the martensitic transformation or dislocations, or both, might play a role. The portion of each pass unaffected by the next pass can be expected to retain a compressive stress as a result of the martensitic transformation and the associated expansion which is resisted by the underlying substrate.

It appears that the best situation would be obtained if the width of the fusion pass is minimized, which can be achieved by increasing the cooling rate following the heating cycle by reducing the laser power or increasing the travel speed and by optimizing the pass overlap.

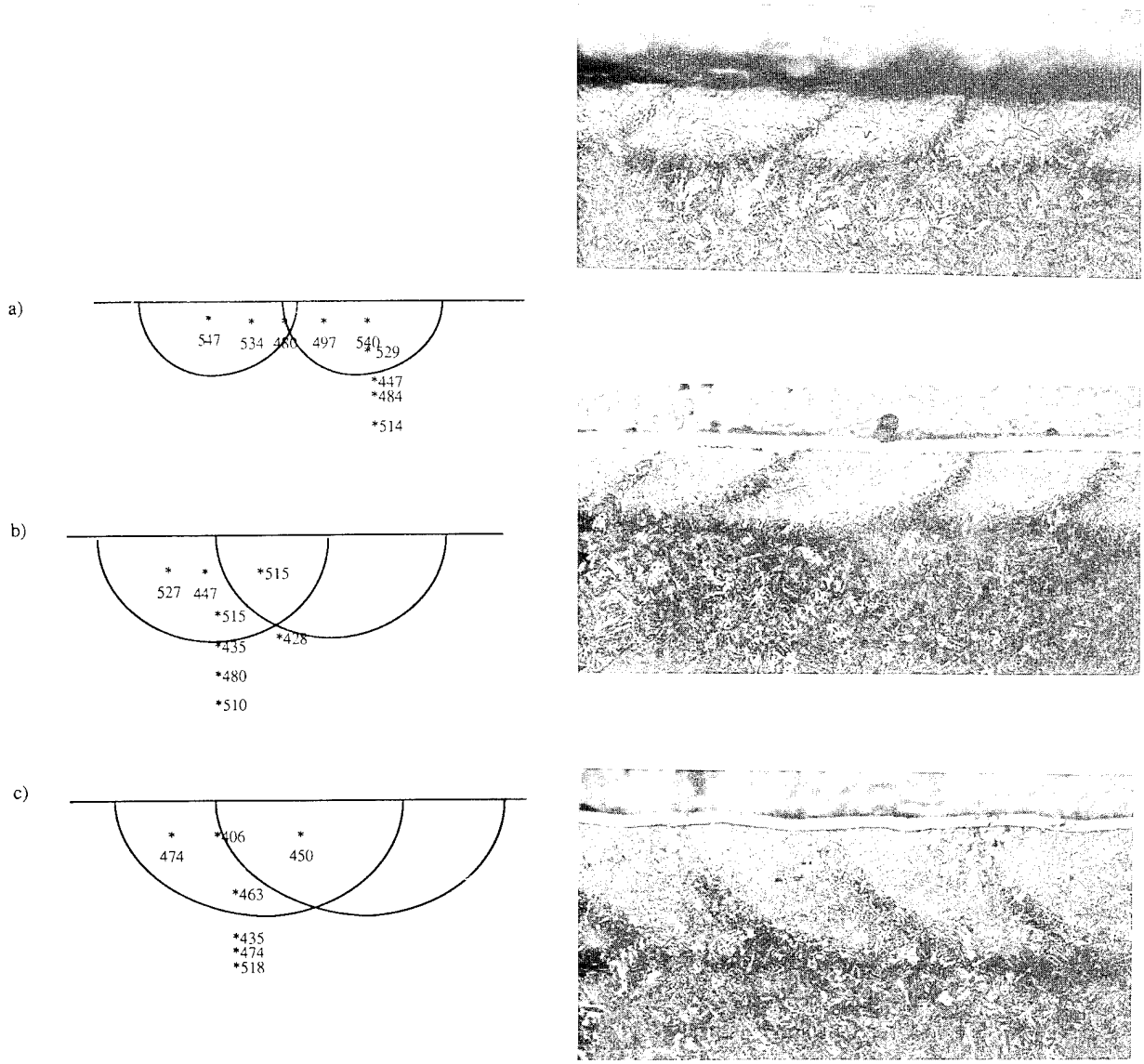

Fig. 9. Results of Knoop microhardness measurements with corresponding microstructures: (a) LSM 50 W; (b) LSM 100 W; (c) LSM 200 W.

The present results, indicating a correlation between the hydrogen absorption kinetics and the performance in the SSRT tests, although qualitatively valid, should be treated with some caution from a quantitative point of view. Because of the dynamic nature of the interaction of hydrogen with dislocations, the lower the diffusivity of hydrogen in the steel, the lower the strain rate that should be employed in the SSRT test. Either SSRT testing using slower strain rates or constant load testing with hydrogen charging might resolve this issue and is recommended for future investigation.

Also, while correlating the permeation and SSRT test results, it should be borne in mind that, even though the composition, heat treatment, charging conditions, etc. were reproduced within practical limits, the hydrogen diffusion flux profile in the two cases may be different because of differences in the geometry of the specimens. In the permeation specimen, hydrogen is allowed to diffuse freely across the specimen and attain a steady state concentration profile, whereas in the SSRT specimen, hydrogen is charged all around the cylindrical surface. Thus the results should only be seen as indicating a trend.

5. Conclusions

On the basis of the data presented in this investigation, the following conclusions can be drawn.

(1) Laser surface treatment of AISI 4135 low alloy steel results in a reduction in the hydrogen absorption kinetics as measured by the permeation test, and also an improved resistance to hydrogen-induced fracture in the SSRT test.

(2) The degree of effectiveness in reducing the hydrogen absorption rate, which occurs at all power levels, is greatest at the 50 W level.

(3) A clear qualitative relationship is found between the hydrogen absorption rate and the time to failure in the SSRT test. This relation is even more striking in terms of the fractographic detail of the fracture face.

(4) A possible explanation for the reduced hydrogen absorption as a result of low power laser surface melting treatment is the influence of the rapidly quenched metal surface on the steady state degree of hydrogen adatom coverage or the absorption kinetic rate constant or both.

(5) Reverse membrane permeation experiments indicate that the effect of laser surface melting on the permeation flux at constant charging current is not due to barriers in the metal which alter the hydrogen flux gradient across the membrane.

References

[1] M. Manohar, *Ph.D. Dissertation*, The Ohio State University, 1990.

[2] I. Chattoraj, *Ph.D. Dissertation*, The Ohio State University, 1991.

[3] E. McCafferty, P.G. Moore and G.T. Peace, *J. Electrochem. Soc., 129* (1982) 9–17.

[4] C.W. Draper, R.E. Woods and L.S. Meyer, *Corrosion, 36* (1980) 405–408.

[5] W.M. Steen, Zhen da Chen and D.R.F. West, in D. Belforte and M. Levitt (eds.), *Industrial Laser Materials Processing—The Best of 1986/1987 Industrial Laser Annual Handbook*, PennWell Books, 1988, pp. 183–199.

[6] T.R. Anthony and H.E. Cline, *J. Appl. Phys., 49* (1978) 1248–1255.

[7] E. McCafferty, C.R. Clayton and J. Oudar (eds.), *Fundamental Aspects of Corrosion Protection by Surface Modification*, The Electrochemical Society, Pennington, NJ, 1984.

[8] J.B. Lumsden, D.S. Gnanamuthu and R.J. Moore, in E. McCafferty, C.R. Clayton and J. Oudar (eds.), *Fundamental Aspects of Corrosion Protection by Surface Modification*, The Electrochemical Society, Pennington, NJ, 1984.

[9] E. McCafferty and P.G. Moore, in E. McCafferty, C.R. Clayton and J. Oudar (eds.), *Fundamental Aspects of Corrosion Protection by Surface Modification*, The Electrochemical Society, Pennington, NJ, 1984, pp. 112–121.

[10] C.W. Draper and S.P. Sharman, *Thin Solid Films, 84* (1981) 333.

[11] P.L. Bonora, M. Basssoli, P.L. DeAnna, G. Battaglia, P. Della Mea, P. Mazzoldi and E. Jannitti, *Mater. Chem., 5* (1980) 73.

[12] J.D. Ayers, R.J. Schaefer, F.D. Bogar and E. McCafferty, *Corrosion, 37* (1981) 55–57.

[13] P.T. Cottrell, R.P. Frankenthal, G.W. Kammlott, D.J. Siconolfi and C.W. Draper, *J. Electrochem. Soc., 130* (1983) 998–1001.

[14] P.G. Moore and E. McCafferty, *J. Electrochem. Soc., 128* (1981) 1391–1393.

[15] K. Mukherjee and J. Mazumder (eds.), *Laser Processing of Materials*, TMS/AIME, Warrendale, PA, 1985.

[16] T. Chande and A. Ghose, in K. Mukherjee and J. Mazumder (eds.), *Laser Processing of Materials*, TMS/AIME, Warrendale, PA, 1985.

[17] E. McCafferty and P.G. Moore, *J. Electrochem. Soc., 133* (1986) 1090–1096.

[18] B.E. Wilde and T. Shimada, *Scr. Metall., 22* (1988) 551–556.

[19] J.O.M. Bockris and A.K.N. Reddy, *Modern Electrochemistry*, Vol. 2, Plenum, New York, 1970, pp. 1232–1251.

[20] H. Kaesche, *Metallic Corrosion*, translated by R.A. Rapp, NACE, Houston, 1985, Chapters 5 and 90.

[21] P.W. Atkins, *Physical Chemistry*, W.H. Freeman, San Francisco, 2nd edn., 1982, p. 1013.

[22] M.A. Devanathan and Z. Stachurski, *Proc. R. Soc. London, Ser. A, 270* (1962) 690.

[23] P.K. Subramanyan, Electrochemical aspects of hydrogen in metals, in J.O.M. Bockris et al. (eds.), *Comprehensive Treatise of Electrochemistry*, Plenum, New York, 1981, pp. 411–461.

[24] C.D. Kim and B.E. Wilde, *J. Electrochem. Soc., 118* (1971) 202.

[25] I. Chattoraj and B.E. Wilde, *Scr. Metall., 26* (1992) 89.

[26] C.D. Beachem, *Metall. Trans., 3* (1972) 437–451.

ELSEVIER

Materials Science and Engineering A198 (1995) 51–61

MATERIALS SCIENCE & ENGINEERING A

Development of "stainless" aluminum alloys by surface modification

F. Mansfeld, Y. Wang

Corrosion and Environmental Effects Laboratory (CEEL), Department of Materials Science and Engineering, University of Southern California, Los Angeles, CA 90089-0241, USA

Abstract

In a research project devoted to the elimination of toxic materials in methods of corrosion protection, surface modification processes have been developed to improve the pitting resistance of aluminum alloys without the use of chromates. These processes use chemical treatments in various cerium salt solutions and an electrochemical treatment in a molybdate solution. The details of the surface modification method depend on alloy composition. For Al 6061 and Al 6013 treated by immersion in hot $Ce(NO_3)_3$ and $CeCl_3$ followed by anodic polarization in Na_2MoO_4, pitting did not occur during immersion in 0.5 M NaCl for 60 days. Surface modification of Al 7075-T6 and Al 2024-T3 involves immersion in boiling $Ce(NO_3)_3$, anodic polarization in Na_2MoO_4 and immersion in boiling $CeCl_3$. Very corrosion-resistant surfaces were produced on Al 7075-T6 after applying an electrochemical pretreatment step which removes copper from the outer surface layers. During exposure of Al 7075 in 0.5 M NaCl for 30 days no measurable corrosion was indicated by continuous monitoring with electrochemical impedance spectroscopy and by visual observation. For Al 2024, significant improvements in the resistance to localized corrosion were also obtained with these processes. A further modification of the Ce–Mo process which is very effective for Al 2024 consists of immersion in hot cerium acetate, anodic polarization in Na_2MoO_4 and immesion in hot $Ce(NO_3)_3$. Impedance data collected in 0.5 M NaCl remained capacitive for 30 days, which is indicative of lack of localized corrosion. Surface anlaysis showed increased levels of Ce and Mo at sites where Cu-containing compounds are located. Apparently local cathodes are eliminated during the surface modification process, thereby reducing the driving force for pitting.

Keywords: Aluminium alloys; Surface modification; Corrosion protection; Pitting

1. Introduction

For more than 40 years, chromate conversion coatings have been widely applied for corrosion protection of Al alloys. Major reasons for the widespread use of chromate conversion coatings are their self-healing nature, the ease of application and their high electric conductivity. However, chromium is amoung the US Environmental Protection Agency's top toxic substances, since in its hexavalent form it is a known carcinogen and is environmentally hazardous as a waste product [1]. Because current environmental legislation is moving towards total exclusion of Cr^{6+} and because of tightening regulatory pressure to reduce the hazardous waste of chromium, many attempts are being made to develop non-toxic alternative methods of corrosion protection. Early work centered on metal oxyanion analogs of chromate such as molybdates, tungstates, vanadates and permanganates. The most widely investigated compound in this group has been molybdate, possibly because of its non-toxic nature [2,3] and its known ability to reduce the susceptibility to pitting of stainless steels. Progress in developing Cr^{6+}-free methods of corrosion protection has been discussed in a recent workshop on chromate replacements in light metal finishing [4]. It is apparent that at present no simple process is available which can completely replace chromate conversion coatings at equal corrosion resistance of the coated alloy and equal ease of application.

Research in this laboratory has focused on the concept of "corrosion protection by surface modification" with emphasis on elimination of hazardous chemicals used in corrosion protection of Al alloys. The Ce–Mo process (US Patent No. 5 194 138) for surface modification of Al alloys consists of a combination of chemical (immersion in boiling $CeCl_3$ followed by immersion in boiling $Ce(NO_3)_3$) and electrochemical (anodic polarization in Na_2MoO_4) process steps [5–11]. This process was successfully applied to corrosion protection of Al

SSDI 0921-5093(94)04507-0

Table 1
Minor alloying elements of Al 7075 and Al 2024 (wt.%)

Alloy	Cu	Si	Fe	Mn	Mg	Zn	Cr
Al 2024	3.8/4.9	<0.5	<0.5	0.3/0.9	1.2 1.8	<0.25	<0.1
Al 7075	1.2/2.0	<0.4	<0.5	<0.3	2.1/2.9	5.1/6.1	0.18/0.28

6061-T6, which did not show any signs of corrosion during immersion in 0.5 M NaCl for 30 days, and Al 6013-T6, which passed the salt spray test according to ASTM B 117 [11]. The experimental results suggest that the exceptional resistance of these alloys to localized corrosion is due to synergistic effects of Ce and Mo.

When the Ce–Mo process was applied to Al alloys with higher Cu content such as Al 7075-T6 and Al 2024-T3, less satisfactory results were obtained. Cu-containing intermetallic compounds in the outer surface layer apparently affect the corrosion behavior of modified surfaces, weakening their resistance of localized corrosion. Therefore, in the studies reported below, a Cu removal process was used as pretreatment step in order to avoid deleterious effects of Cu-containing intermetallics [12]. Cu is removed only from the outer surface layers without affecting the mechanical properties of the alloy. In addition, it was found necessary to modify the original Ce–Mo process slightly for these alloys. The corrosion behavior of modified surfaces on Al 2024 and Al 7075 was investigated using polarization measurements, electrochemcial impedance spectroscopy (EIS), microscopic observation and surface analysis.

2. Experimental

2.1. Materials

The materials studied were Al 7075-T6 with about 1.6 wt.% Cu and Al 2024-T3 with about 4.4 wt.% Cu. The minor alloying elements are listed in Table 1.

2.2. Methods

2.2.1. Cu removal process

The Cu removal process consists of deoxidizing the sample in Diversey 560 (Diversified Chemical Sales, USA) for 10 min at room temperature followed by anodic polarization in an acidic solution (Table 2). The deoxidizer Diversey 560 contains approximately 25% H_2SO_4, 15% HNO_3 and 2% H_2SiF_6. In the polarization step, different operation parameters and solutions were used for Al 2024 and Al 7075. Al 2024 was polarized at −55 mV (vs. SCE) in 0.5 M $NaNO_3$ + 0.67 M HNO_3, while for Al 7075 a potential of −248 mV was applied in 0.5 M $NaNO_3$ (pH 1, adjusted with HCl). At these potentials, pure Cu was found to dissolve at very high rates. Whereas pure Al was passive. Anodic polarization curves for Al 7075 showed a current peak in the Cu removal solution at −248 mV. For Al 2024 it has been observed that Cu removal can also be achieved in the same solution using a galvanostatic technique or coupling to a graphite electrode [13].

2.2.2. Surface modification

The surface modification process for Al 2024 and Al 7075 involves immersion in boiling 10 mM $Ce(NO_3)_3$ at 100 °C for 2 h, anodic polarization in 0.1 M Na_2MoO_4 at +500 mV vs. SCE for 2 h and immersion in boiling 5 mM $CeCl_3$ at 100 °C for 2 h. This modification of the original Ce–Mo process for Al 6061 [5–12] is described in Table 3. For Al 7075, the modified Ce–Mo process was applied after Cu removal (Table 2) and to as-received samples, which were degreased by wiping with Alconox detergent. For Al 2024, surface modification was applied after Cu removal.

2.2.3. Evaluation of corrosion resistance

The corrosion resistance of samples with different surface treatments was evaluated by immersion in 0.5 M NaCl (open to air). Changes in surface properties were monitored periodically with EIS. The exposed area was $A = 20\ cm^2$. The test period was based on the observed degree of corrosion. For untreated Al 7075 (Al 7075/as-received) and for Al 2024 after Cu removal (Al 2024/Cu removal), tests were carried out for 7 days, whereas for the corresponding modified surfaces corrosion tests were performed for 30 days. EIS data were collected at the open-circuit potential E_{corr}. The software packages BASICS and PITFIT [14,15] were used for the analysis of EIS data. For passive surfaces, EIS data were analyzed using BASICS based on the equivalent circuit shown in Fig. 1(a), where R_p is the polarization resistance of the passive surface and C_p is its capacitance. PITFIT was utilized when pitting corrosion was observed. In the pitting model described in Fig. 1(b), R_p and C_p are the properties of the passive surface, R_{pit} and C_{pit} are the corresponding parameters of the pitted area, F is the area fraction on which pitting occurs and $W = (K/F)(j\omega)^n$ describes a transmission line element with $-1 < n < 0$ [16]. Analysis of experimental impedance spectra with PITFIT results in the values of $R_p(1-F)$, R_{pit}/F and $C_t = C_p(1-F) + FC_{pit}$ and also of K/F and n as a function of exposure time. Polariza-

Table 2
Copper removal processes for Al 2024-T3 and Al 7075-T6

Step	Al 2024-T3	Al 7075-T6
1. Cleaning and degreasing	Immersion in Alconox for 1 min Wipe with Alconox Rinse	Immersion in Alconox for 1 min Wipe with Alconox Rinse
2. Deoxidizing	Diversey 560 for 10 min Rinse	Diversey 560 for 10 min Rinse
3. Copper removal	Polarization in 0.5 M $NaNO_3$ + 0.67 M HNO_3 at −55 mV (vs. SCE) for 30 min Rinse	Polarization in 0.5 M $NaNO_3$ (pH 1, adjusted by HCl) at −248 mV (vs. SCE) for 30 min Rinse

tion curves in 0.5 M NaCl were measured at a scan rate 0.2 mV s^{-1} for untreated and modified samples of Al 7075-T6.

Surface analysis

Surface analysis was performed by EDS for Al 7075/as-received treated in the modified Ce–Mo process. The chemical composition of the surface layer was analyzed for both exposed and unexposed surfaces. For selected samples, surface morphologies were determined by scanning electron microscopy (SEM) and elemental mapping by EDS was employed to determine the distribution of Ce and Mo in the modified oxide layers and its relation to localized corrosion events.

3. Results and discussion

3.1. Untreated Al 7075

The impedance spectra for Al 7075/as-received in 0.5 M NaCl in Fig. 2 clearly indicate that localized corrosion occurred already in the early stages of exposure. For passive surfaces, impedance spectra show only one time constant and the phase angle approaches zero degree at the lowest frequencies. Spectra for pitting corrosion such as those in Fig. 2 are characterized by a transmission line type impedance and a minimum of the phase angle at lower frequencies. The occurrence of a second time constant can be seen clearly in Bode plots of phase angle in the low-frequency region (Fig. 2). Another characteristic change of the impedance spectra due to development of localized corrosion is the increase of C_t at intermediate frequencies (Fig. 2). Pit initiation was observed visually in less than 1 day for as-received samples. EIS data were not collected for such samples during the early stage of pit initiation owing to experimental problems as discussed elsewhere [17–19].

Electrochemical parameters obtained by fitting of the experimental data in Fig. 2 to the pitting model (Fig. 1(b)) are plotted in Fig. 3 as a function of exposure time, where R_p^0 is the polarization resistance of passive surface normalized to the total exposed area A, and C_t contains contributions from the capacitances of the passive and pitted surface fractions. R_p^0 decreased slightly with increasing exposure time, whereas C_t increased continuously. The observed increase in C_t is due to the increase in the capacitance of the pitted area $C_{pit,exp} = FC_{pit}$ assuming that $C_p(1-F) = C_p$ for $F \rightarrow 0$ remains constant during the test period. $C_{pit,exp}$ is obtained as $C_{pit,exp} = C_t - C_p$. Assuming further that pits are hemispherical, the pitted area can be calculated as a function of exposure time as $A_{pit} = 2AF$. The value of F at the end of the test is determined by microscopic observation. Based on this value a specific pit capacitance $C_{pit}^0 = C_{pit,exp}/A_{pit}$ is then calculated, which is assumed to remain constant during the test. F is calculated as a function of exposure time as

$$F = C_{pit,exp}/2AC_{pit}^0 \quad (1)$$

For the data in Fig. 3, $C_{pit}^0 = 634\ \mu F\ cm^{-2}$ was used.

The increase in F and the polarization resistance of the pits $R_{pit}^0 = R_{pit}A_{pit}$ with exposure time as shown in Fig. 4. F increased from about 0.6% ($A_{pit} = 0.024\ cm^2$) to about 2% (0.08 cm^2) in 5 days. The increase in R_{pit}^0 with time suggests that pit growth rates decrease with time. The dependence of R_{pit}^0 on exposure time t was further evaluated by plotting log $(1/R_{pit}^0)$ vs. log t (Fig. 5). The linear dependence observed in Fig. 5 allows a pit growth law to be established which can be described by [20,21]

$$1/R_{pit}^0 = at^b \quad (2)$$

where a and b are experimentally determined parameters. For most Al alloys studied during exposure to NaCl, b (Eq. (2)) was close to −1 [20,21], which means that pit growth rates decrease linearly with exposure time. It has to be considered that contrary to other evaluations of pit growth laws with electrochemical techniques in which an external potential was applied, the present data have been obtained at E_{corr}.

Table 3
Surface modification procedures

Step	Treatment
1. Surface modification by $Ce(NO_3)_3$	Immersion in 10 mM $Ce(NO_3)_3$ at 100 °C for 2 h, then rinsing in distilled water
2. Surface modification by Na_2MoO_4	Polarization in 0.1 M Na_2MoO_4 at +100 mV (vs. mercury sulfate reference electrode) for 2 h, then rinsing in distilled water
3. Suface modification by $CeCl_3$	Immersion in 5 mM $CeCl_3$ at 100 °C for 2 h, then rinsing in distilled water

3.2. Al 7075/Ce–Mo process

The impedance spectra for Al 7075 treated with the modified Ce–Mo process described in Table 3 indicate that the modified surface remained passive during the test period of 30 days (Fig. 6). R_p^0 was nearly constant at about 5×10^5 ohm cm^2 and C_p^0 increased slowly from 7.5 to 9.5 μF cm^{-2}, which is a typical range for a thin film of hydrated aluminum oxide [21] (Fig. 7). Visually, a few spots of local dissolution were observed after 4 days, which grew very slowly with increasing exposure time. After exposure to NaCl for 30 days, the surface morphology was examined by SEM. It was found that the morphology of these spots was different from the pitting corrosion phenomena usually occurring on Al alloys. A circular area, typically about 60 μm in diameter, with cracks in the oxide layer was observed (Fig. 8(a)). Some areas of very small dimensions with localized attack can be found at the periphery of these circular features. Fig. 8(b) shows more detailed information from the center of the spot in Fig. 8(a). Cracks radiating from the center can be identified ending at a short distance. The chemical composition of the surface in Fig. 8 was analyzed by EDS for a portion of the sample which had not been exposed and an area which had been exposed to NaCl for 30 days. The results are given in Fig. 9(a) for the unexposed surface and in Fig. 9(b) for the corrosion spot shown in Fig. 8. In both cases Ce and Mo were detected in the surface layer; however, Ce and Mo showed increased levels around the observed spot (Fig. 9(b)).

Elemental mapping was employed to determine the distribution of Ce and Mo in the modified surfaces in more detail. Results for the area shown in Fig. 8(a) are presented in Fig. 10. It is interesting that the chemical

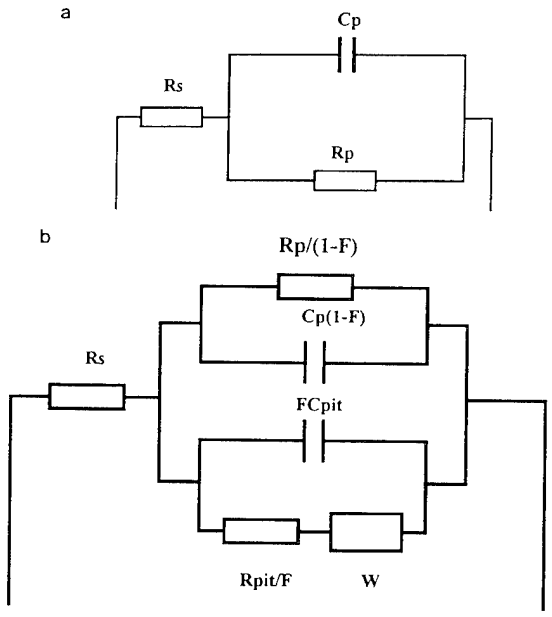

Fig. 1. Equivalent circuit for Al alloys exposed to NaCl: (a) for a passive surface; (b) for a pitted surface.

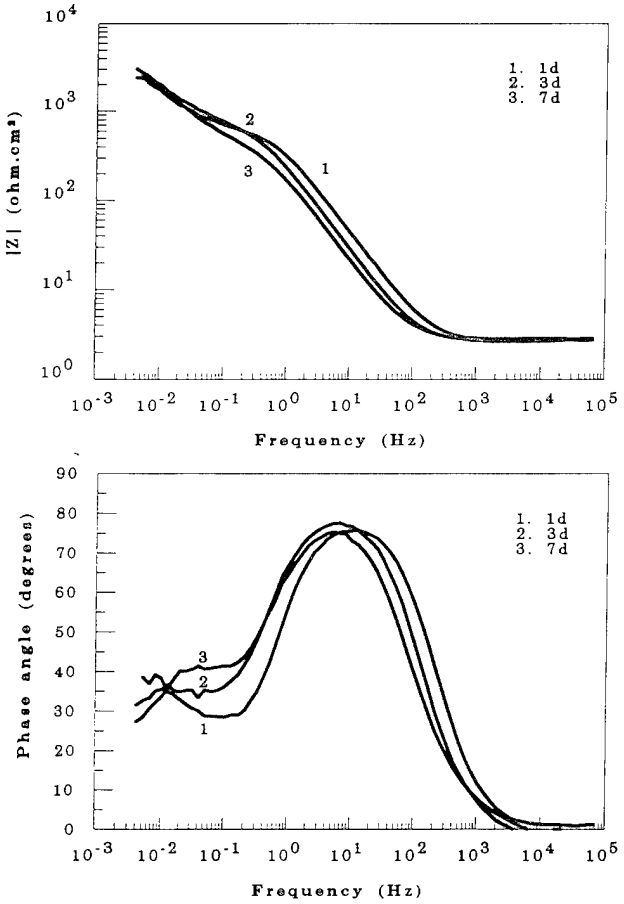

Fig. 2. Bode plots for Al 7075-T6 as-received as a function of exposure time to 0.5 M NaCl.

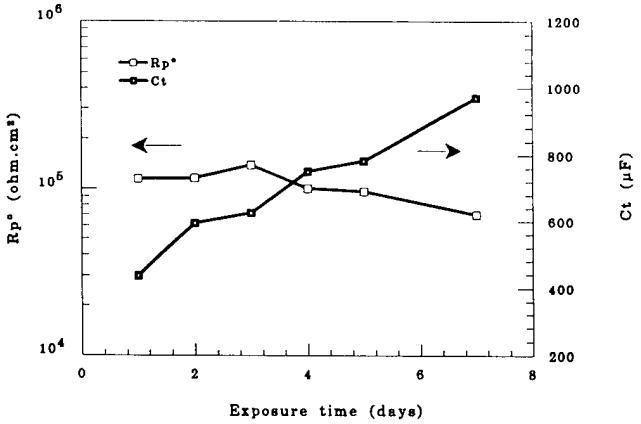

Fig. 3. R_p^0 and C_t for Al 7075-T6/as-received as a function of exposure time to 0.5 M NaCl.

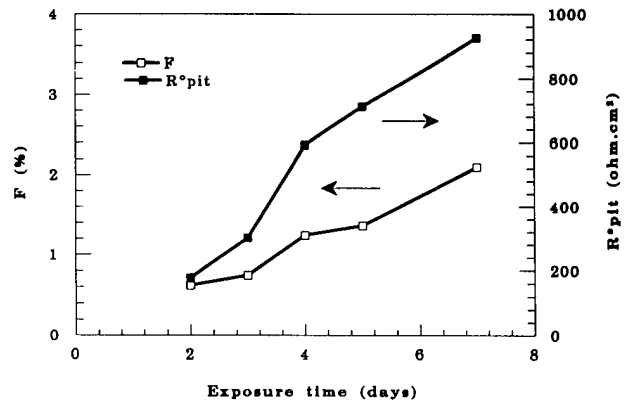

Fig. 4. F and R_{pit}^0 for Al 7075-T6/as-received as a function of exposure time to 0.5 M NaCl.

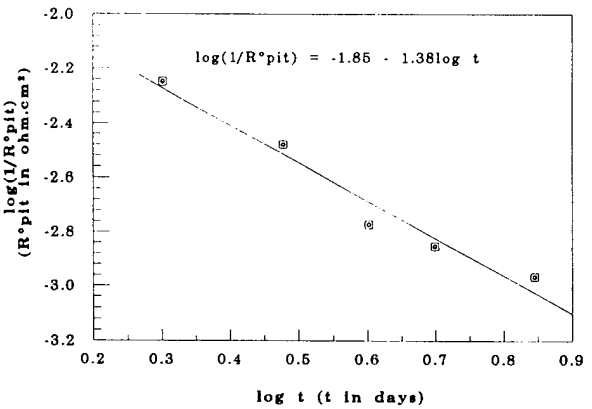

Fig. 5. Pit growth law for Al 7075-T6/as-received exposed to 0.5 M NaCl.

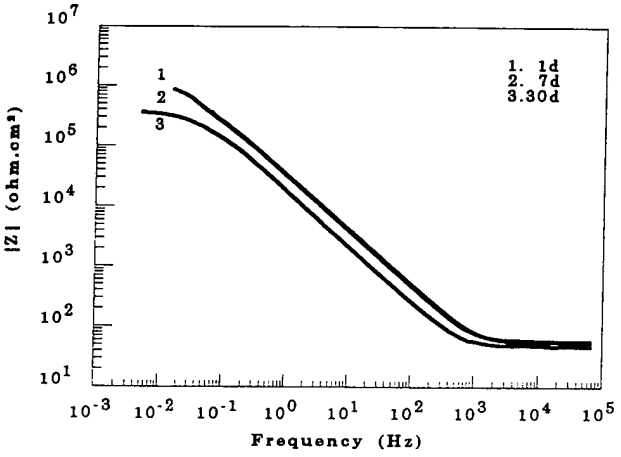

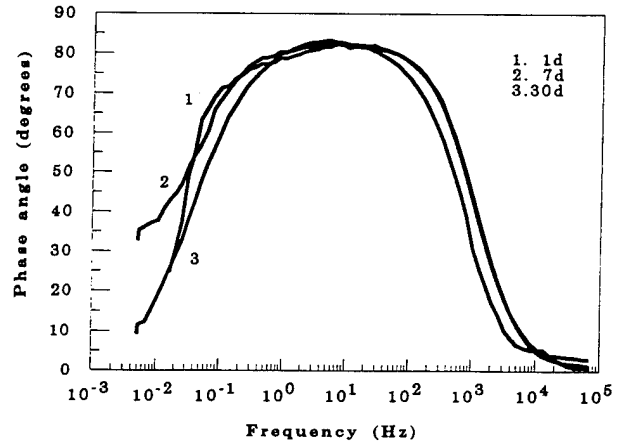

Fig. 6. Impedance spectra of Al 7075-T6/as-received, modified by the Ce–Mo process, during exposure to 0.5 M NaCl.

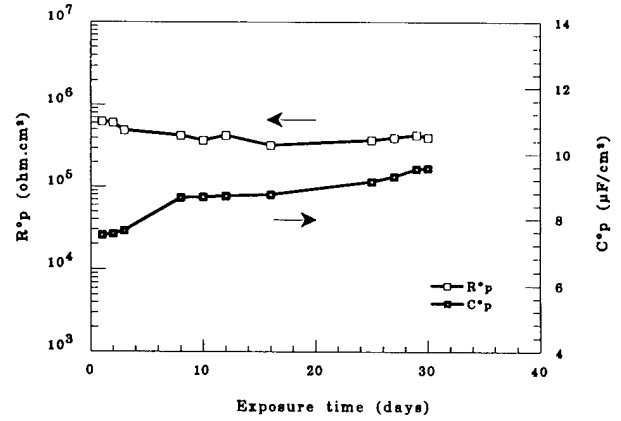

Fig. 7. R_p^0 and C_p^0 for Al 7075-T6/as-received, modified by the Ce–Mo process, as a function of exposure time to 0.5 M NaCl.

composition of the surface layer is different in the inner circle and an outer ring. Ce is concentrated in the inner circle which also contains Mo in the region where Cu was also identified. Very little Al is detected in the inner circle. These results can be explained by assuming that during surface modification in the Ce–Mo process, Cu-containing intermetallic compounds served as cathodes, creating an alkaline environment in their vicinity, thereby accelerating local dissolution of Al and leading to precipitation of Ce oxide and/or Ce hydroxide around these compounds [22,23]. Incorporation of Mo into the surface film occurred during anodic polarization in Na_2MoO_4, probably by interaction between molybdate and aluminium oxide [24–26]. The observed

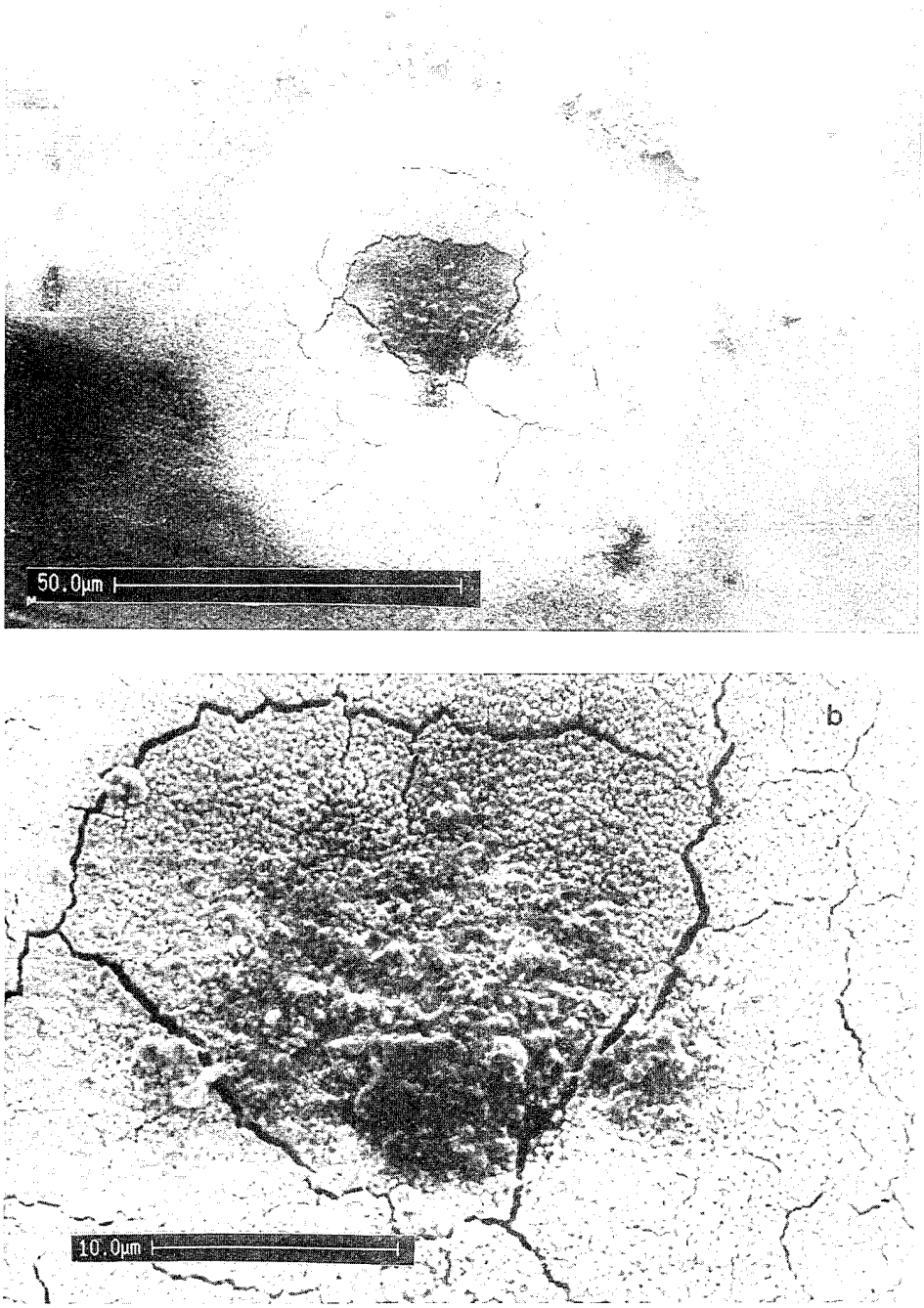

Fig. 8. Surface morphology of Al 7075-T6/as-received, modified by the Ce–Mo process, after exposure to 0.5 M NaCl for 30 days.

cracks occurred during exposure to NaCl and not during treatment in the modified Ce–Mo process.

In order to evaluate further the effects of surface modification on the resistance to localized corrosion, anodic polarization curves were recorded in 0.5 M NaCl (open to air) for Al 7075 which was untreated or treated in the modified Ce–Mo process in Table 3. The polarization behavior in NaCl showed that the increased pitting resistance of the modified surface was due to the increase of the pitting potential E_{pit} at constant E_{corr}. The anodic polarization curve for Al 7075/as-received modified by the Ce–Mo process shows a passive region of approximately 200 mV (Fig. 11). During anodic polarization, sudden jumps of the current were observed accompanied by the formation of new single pits. The passive current densities ranged from 1 to 5 $\mu A\ cm^{-2}$. This polarization behavior is very different from that for Al 7075-T6/as-received, for which E_{pit} and E_{corr} coincide (Fig. 11). With increasing anodic polarization, the current dramatically increased, as shown in Fig. 11, as pits

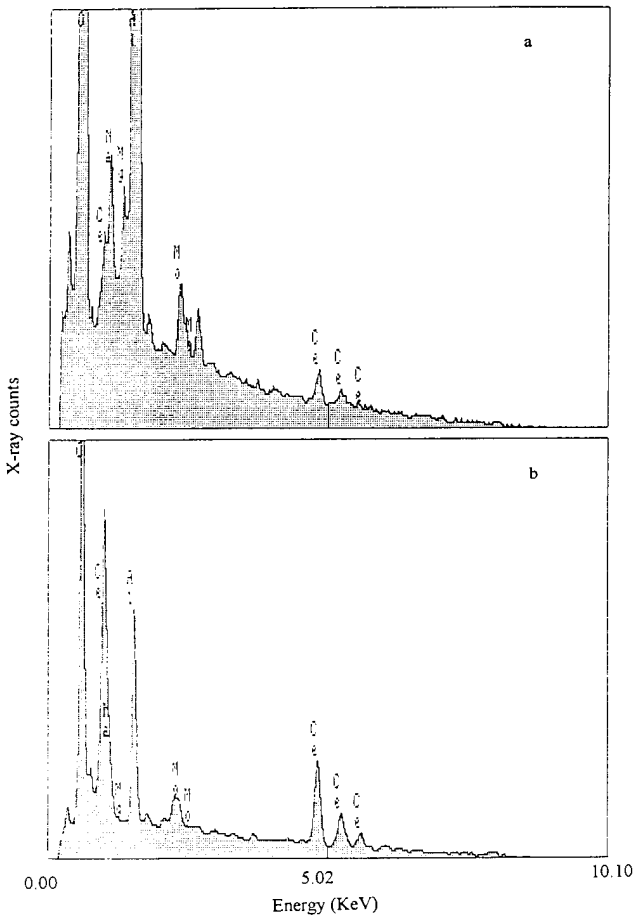

Fig. 9. Chemical composition of surface layers on Al 7075-T6/as-received, modified by the Ce–Mo process: (a) unexposed surface; (b) corrosion spot after exposure to 0.5 M NaCl for 30 days.

nucleated and grew. The observed increase in E_{pit} is most likely the result of changes in the surface chemistry of the modified surface layers, on which weak spots, which would lead to pit initiation for untreated surfaces, have been passivated during the surface modification process by the formation of Ce oxide/hydroxides and incorporation of Mo species.

3.3. Al 2024/Cu removal

Experimental impedance spectra obtained for Al 2024 treated with the Cu removal step according to Table 2 are presented in Fig. 12, and R_p^0 and C_t are shown as a function of exposure time in Fig. 13. Similar corrosion behavior was determined as for Al 7075 (Fig. 3), but the pitted area seemed to increase faster than for Al 7075, as can be seen from the increase in C_t from 525 to 1450 μF within 6 days (Fig. 13) (Eq. (1)).

3.4. Cu removal/Ce–Mo process

The results in Figs. 9 and 10 demonstrated that Ce and Mo can be incorporated into the outer surface

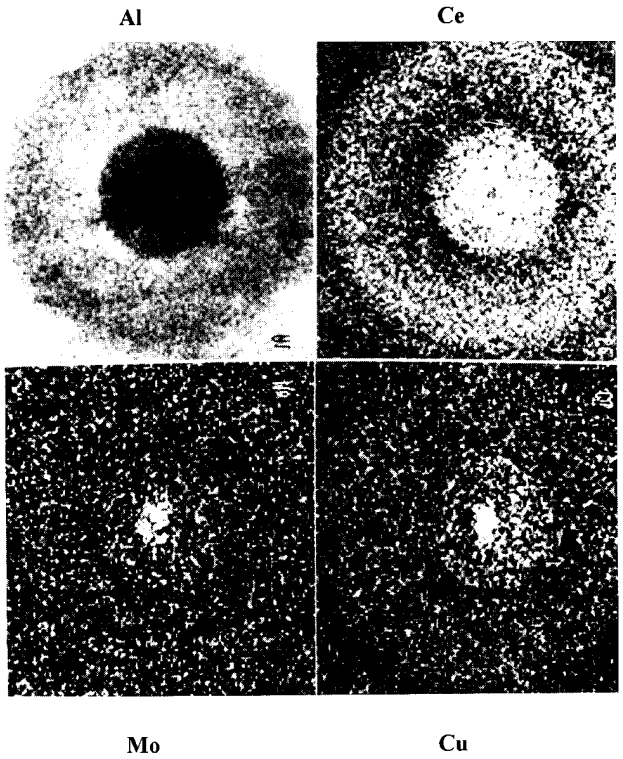

Fig. 10. Elemental mapping for Al 7075-T6 (sample of Fig. 8).

layers of Al 7075 by the modified Ce–Mo process, leading to reduced pit initiation and propagation rates. However, localized dissolution due to the presence of Al_2Cu intermetallic compounds could not be eliminated to the extent achieved previously for Al 6061 [5–11]. In order to eliminate completely localized corrosion for Al 7075 and Al 2024, Cu removal (Table 2) was applied as a pretreatment step before the Ce–Mo process. It had been demonstrated earlier by surface analysis that Cu-containing compounds had been removed from the outer surface after applying the Cu removal process [12]. The surface morphology of Al 7075 after Cu removal in Fig. 14 shows some holes from which Cu compounds had been removed; however, the remaining surface was fairly smooth.

Following Cu removal, the modified Ce–Mo process was applied to Al 7075 and Al 2024. Impedance spectra for Al 7075 are shown in Fig. 15. For a test period of 30 days, no measurable corrosion was indicated and the impedance remained capacitive. R_p^0 and C_p^0 did not change significantly with exposure time (Fig. 16). The constant values of R_p^0 (about 10^6 ohm cm^2) and C_p^0 (about 3 μF cm^{-2}) demonstrate that the modified surface is resistant to pitting in 0.5 M NaCl.

For Al 2024, a significant improvement of the corrosion resistance was obtained by applying the modified Ce–Mo process after Cu removal. For a sample treated in this manner, the impedance spectra in Fig. 17 were entirely different from those for the sample from which Cu had been removed but the Ce–Mo Process had not

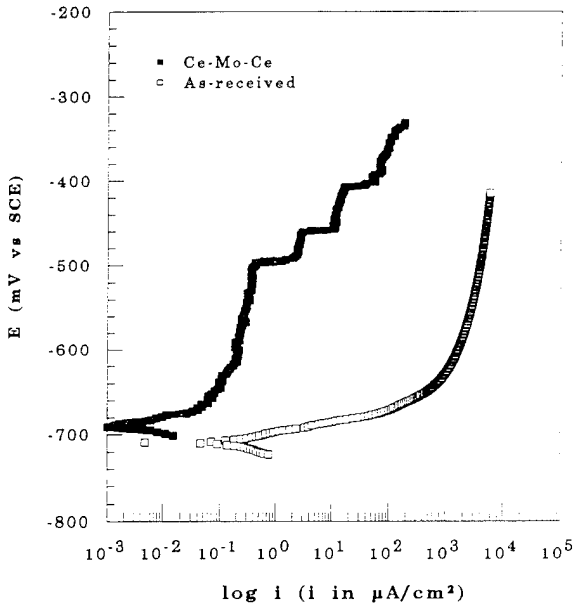

Fig. 11. Polarization curves in 0.5 M NaCl for Al 7075-T6, untreated and modified by the Ce–Mo process.

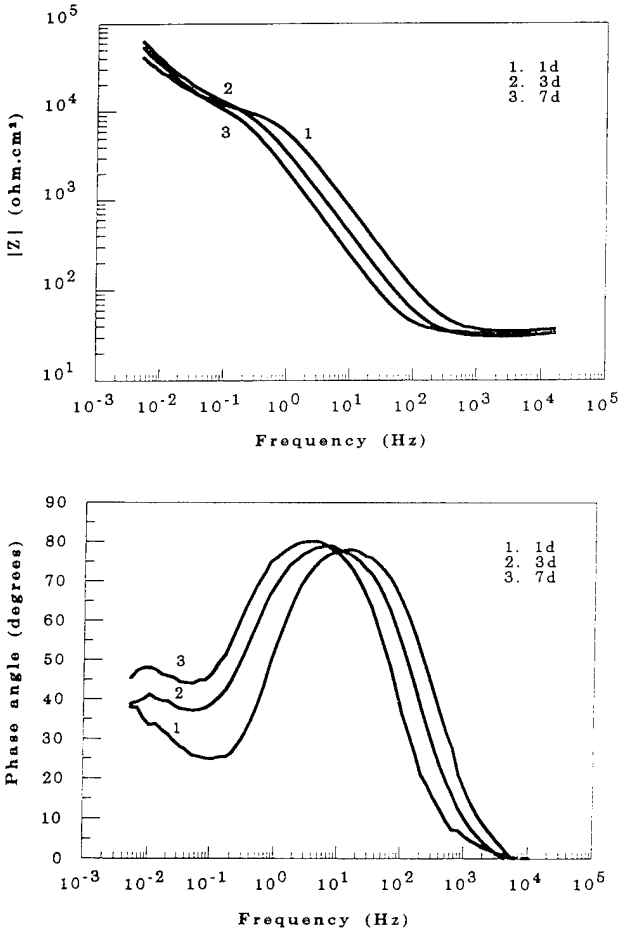

Fig. 12. Impedance spectra for Al 2024-T3/Cu removal as a function of exposure time to 0.5 M NaCl.

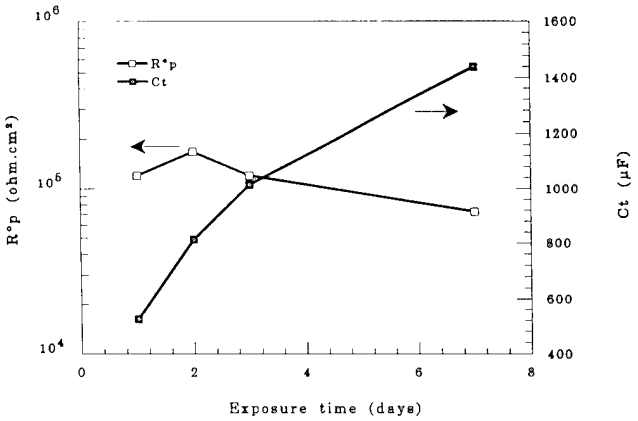

Fig. 13. R_p^0 and C_t for Al 2024-T3 Cu removal as a function of exposure time to 0.5 M NaCl.

been applied (Fig. 12). For an exposure period of 30 days, no changes in the surface properties due to corrosion were indicated by EIS (Fig. 17). It should be mentioned that a few, very small pits initiated between 4 and 7 days. However, after 1 week, no additional pit initiation was observed visually. At the end of the test, 13 small pits were identified and F was about $6.5 \times 10^{-2}\%$ ($A_{pit} = 0.026\ cm^2$). This value is much smaller than that for the sample with Cu removal only for which F was determined as 8% after exposure to 0.5 M NaCl for only 7 days (Fig. 12). For Al 2024-T3/as-received or after Cu removal, the pit initiation time was determined as less than 2 h and pits spread out over the surface within 3 days. In terms of pit initiation time, resistance of localized corrosion was increased considerably through application of the Ce–Mo process after Cu removal.

A further modification of the Ce–Mo process consists in immersion in hot Ce acetate ($(CH_3CO_2)_3Ce$), anodic polarization in Na_2MoO_4 and immersion in hot $Ce(NO_3)_3$ (Table 4). Excellent results were obtained for Al 2024 after the Cu removal step during immersion in 0.5 M NaCl for 30 days (Fig. 18). The impdance data did not show any significant changes between the first and the last day of exposure, remaining capacitive, which is typical of passive surfaces. R_p^0 remained close to 4×10^7 ohm cm^2 and C_p^0 increased slightly from 7 to 9 μF cm^{-2} (Fig. 19). Anodic polarization curves showed that E_{pit} for Al 2024 increased after Cu removal at constant E_{corr} and treatment according to Table 4 with $i_{pass} < 1\ \mu A\ cm^{-2}$ (Fig. 20). It is obvious that the surface modification procedure in Table 4 produces oxides layers on Al 2024 of outstanding resistance to a very aggressive solution such as 0.5 M NaCl (open to air).

4. Conclusions

"Stainless" aluminum alloys with exceptional resistance to localized corrosion can be prepared by surface

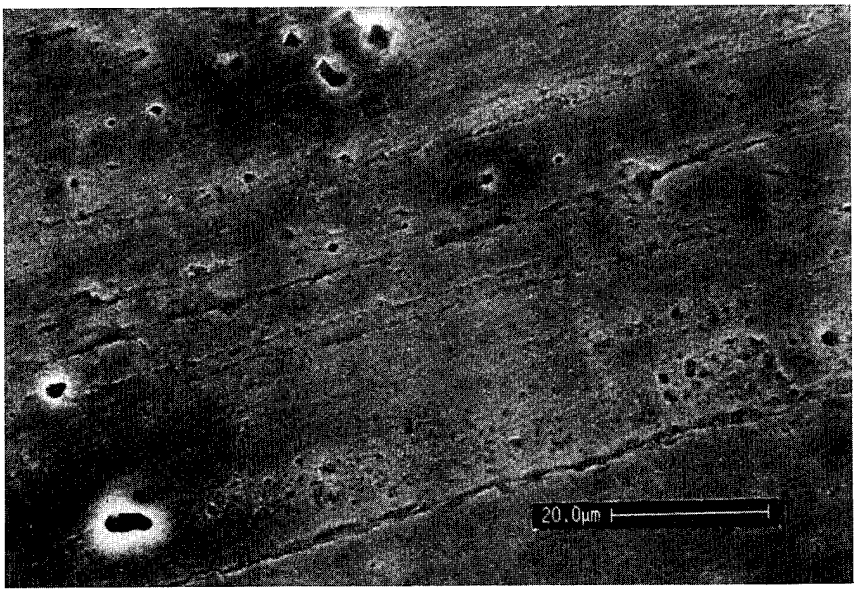

Fig. 14. Surface morphology of Al 7075-T6/Cu removal.

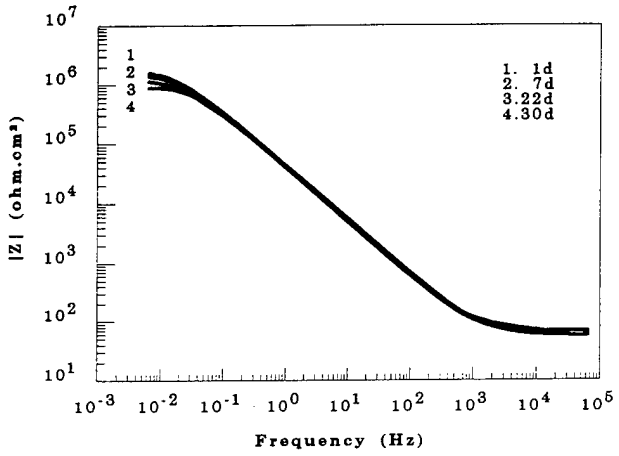

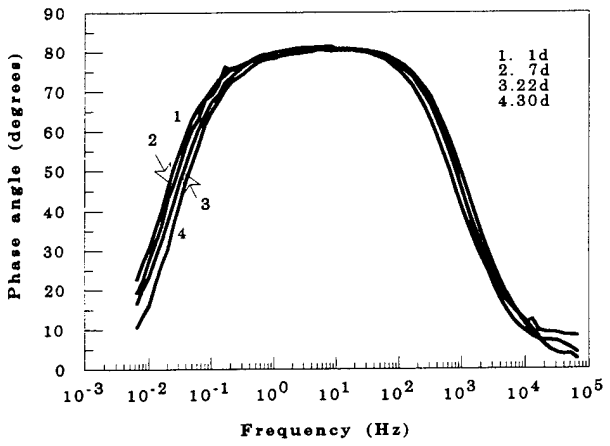

Fig. 15. Impedance spectra of Al 7075-T6/Cu removal, treated by the Ce–Mo process, during exposure to 0.5 M NaCl.

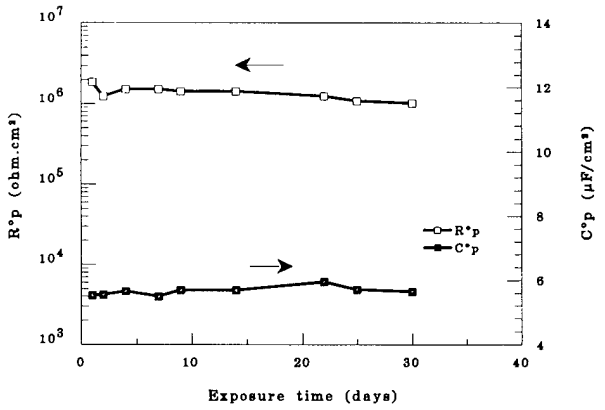

Fig. 16. R_p^0 and C_p^0 for Al 7075-T6/Cu removal, treated by the Ce–Mo process, as a function of exposure to 0.5 M NaCl.

modification. For Al 6061 and 6013, the original Ce–Mo process $(Ce(NO)_3)_3$–$CeCl_3$–Na_2MoO_4 was very successful in preventing pit initiation and growth for extended time periods. The modified Ce–Mo process improves the pitting resistance of high-Cu Al alloys such as Al 2024 and 7075. Very corrosion-resistant surfaces were produced for Al 7075-T6. However, owing to the presence of Al_2Cu intermetallic compounds, pitting corrosion could not be eliminated completely and localized corrosion still occurred to a minor extent. By applying a Cu removal pretreatment step, which removes Cu-containing compounds from the outer surface layers without affecting the mechanical properties, modified surfaces of Al 7075-T6 were produced for

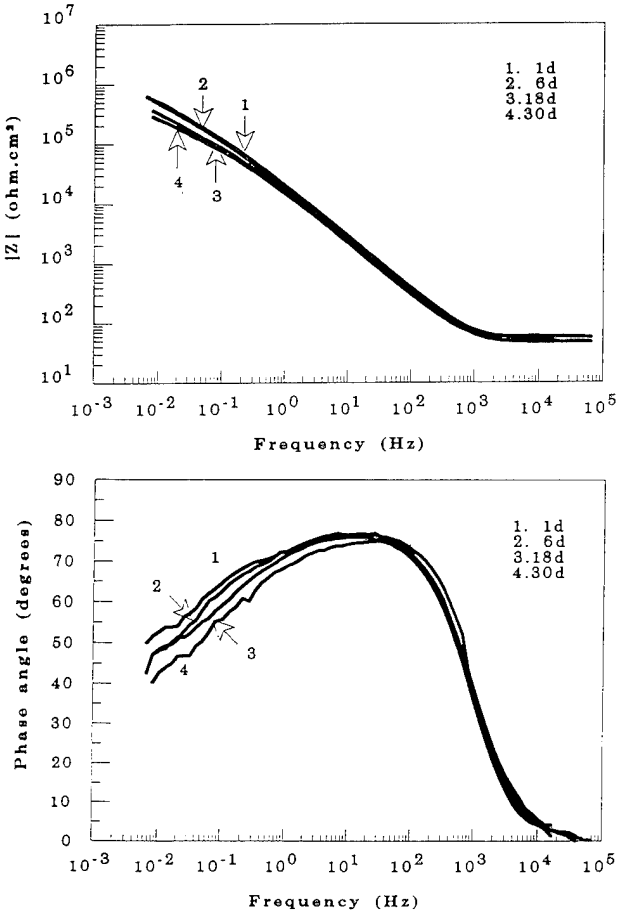

Fig. 17. Impedance spectra of Al 2024-T3/Cu removal, treated by the Ce–Mo process, during exposure to 0.5 M NaCl.

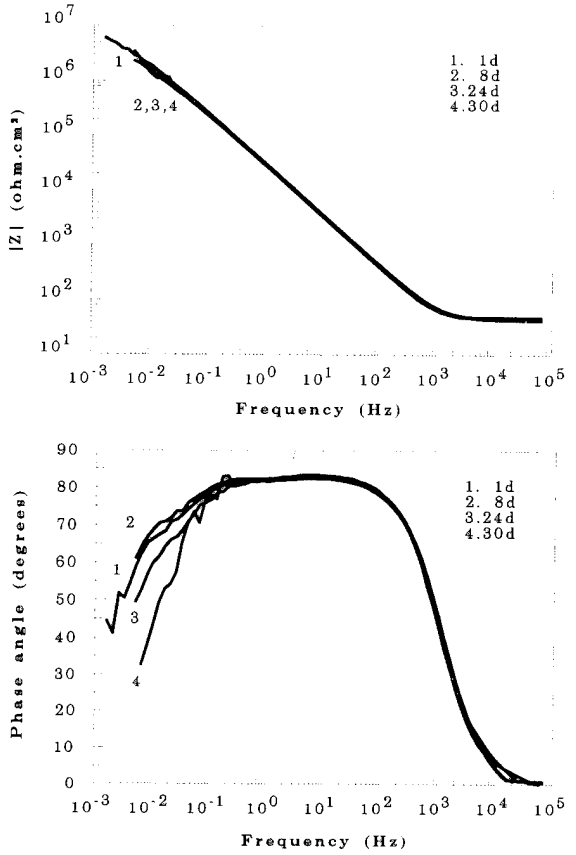

Fig. 18. Impedance spectra of Al 2024-T3/Cu removal, treated by the Ce–Mo process according to Table 4, during exposure to 0.5 M NaCl.

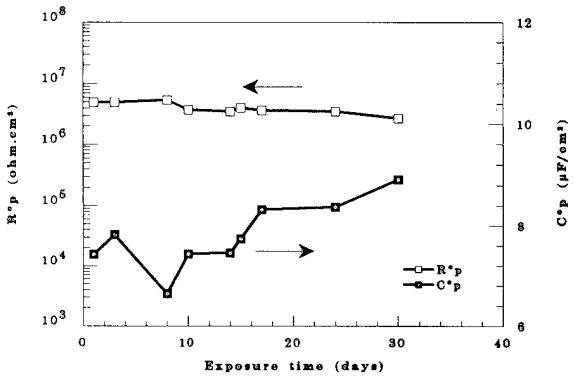

Fig. 19. R_p^0 and C_p^0 for Al 2024-T3/Cu removal, treated by the Ce–Mo process according to Table 4, as a function of exposure time to 0.5 M NaCl.

which no measurable corrosion was observed during a period of exposure of 30 days to 0.5 M NaCl.

For Al 2024-T3, significant improvements in the resistance to localized corrosion were obtained when the Cu removal pretreatment was applied. Use of Ce acetate as the first step of the surface modification process and replacement of $CeCl_3$ with $Ce(NO_3)_3$ resulted in excellent resistance of pitting in 0.5 M NaCl. The incorporation of Ce and Mo in the outer surface layers reduces the susceptibility to localized corrosion. Mo and Ce are concentrated at sites where Cu precipitates were located, thereby reducing the extent and activity of local cathodes. Ce and Mo seem to produce

Table 4
Surface modification for Al 2024-T3

Step	Treatment
1. Surface modification by $(CH_3CO_2)_3Ce$	Immersion in 4 mH $(CH_3CO_2)_3$ Ce at 100 °C for 1.5 h, then rinsing in distilled water
2. Surface modification by Na_2MoO_4	Polarization in 0.1 M Na_2MoO_4 at +100 mV (vs. mercury sulfate reference electrode) for 2 h, then rinsing in distilled water
3. Surface modification by $Ce(NO_3)_3$	Immersion in 10 mM $Ce(NO_3)_3$ at 100 °C for 2 h, then rinsing in distilled water

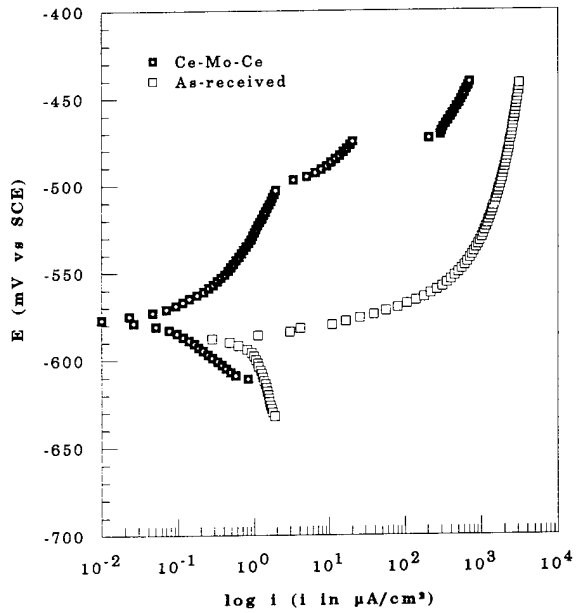

Fig. 20. Polarization curves in 0.5 M NaCl for Al 2024-T3, untreated and after Cu removal and surface modification by the Ce–Mo process according to Table 4.

synergistic effects by a mechanism which is still unclear. Further work in defining the roles of Ce and Mo in achieving the remarkable improvements in corrosion resistance reported here for two high-Cu Al alloys is being carried out.

Acknowledgement

This work was funded by the Office of Naval Research (Dr. A.J. Sedriks) under Contracts Nos. N00014-88-0034 and N00014-91-1041.

References

[1] D.J. McCoy, presented at the *Second AESF/EPA Chromium Colloquium, Miami, FL, February 1990.*

[2] N.J. Sax, *Dangerous Properties of Industrial Materials*, Van Nostrand Reinhold, New York, 5th edn., 1979.

[3] G.D. Wilcox, D.R. Gabe and M.E. Warwick, *Corros. Sci., 28* (1988) 577.

[4] *Minutes of the Third Annual Workshop on Chromate Replacements in Light Metal Finishing, Sandia National Laboratory, Albuquerque, New Mexico, 15–16 September 1993.*

[5] F. Mansfeld, H. Shih and Y. Wang, presented at the *178th Meeting of the Electrochimical Society Seattle, WA, October 1990,* paper No. 228.

[6] F. Mansfeld, Y. Wang and H. Shih, *J. Electrochem. Soc., 138* (1991) L74.

[7] F. Mansfeld, Y. Wang and H. Shih, *Electrochim. Acta, 37* (1992) 2277.

[8] F. Mansfeld, Y. Wang and H. Shih, *Met. Forum, 111–112* (1992) 191.

[9] F. Mansfeld, H. Shih and Y. Wang, paper presented at *Corrosion/91*, paper No. 136, NACE, Houston, TX, 1991.

[10] F. Mansfeld, Y. Wang and H. Shih, Corrosion protection of Al-based materials by surface modification, *Proc. 1st Pan-American Corrosion and Protection Congress, Mar del Plata, Argentina, 25–30 October 1992,* NACE, Houston, TX, 1992.

[11] F. Mansfeld, Y. Wang, S.H. Lin and L. Kwiatkowski, in *Proc. 12th Int. Corrosion Congress, Houston, TX, September 1993,* NACE, Houston, TX, 1993, p. 219.

[12] F. Mansfeld, S.H. Lin and L. Kwiatkowski, unpublished results.

[13] F. Mansfeld and S.H. Lin, unpublished results.

[14] F. Mansfeld, C.H. Tsai and H. Shih, *ASTM STP, 1154* (1992) 186.

[15] H. Shih and F. Mansfeld, *Corrosion, 45* (1989) 610.

[16] J.R. Macdonald (Ed.), *Impedance Spectroscopy*, Wiley, New York, 1987.

[17] F. Mansfeld, *Electrochim. Acta, 38* (1993) 1891.

[18] F. Mansfeld and J.C.S. Fernandes, *Corros. Sci., 34* (1993) 2105.

[19] F. Mansfeld and J.C.S. Fernandes, *Port. Electrochim. Acta, 11* (1993) 245.

[20] F. Mansfeld, Y. Wang, H. Xiao and H. Shih in *Proc. Symp Critical Factors in Localized Corrosion*, Electrochemical Society, Proc. Vol. 92-9, 1992, p. 469.

[21] F. Mansfeld, Y. Wang, S.H. Lin, H. Xiao and H. Shih, *ASTM STP, 1188* (1993) 297.

[22] B.R.W. Hinton, *J. Alloys Compd., 180* (1992) 15.

[23] D.R. Arnott, B.R.W. Hinton and N.E. Ryan, *Met. Forum, 9* (1986) 162.

[24] Y. Okamoto and T. Imanaka, *J. Phys. Chem., 92* (1988) 7102.

[25] G.H. Cartledge, *Corrosion, 24* (1968) 223.

[26] W.C. Moshier and G.D. Davis, *Corrosion, 46* (1990) 43.

ELSEVIER

Materials Science and Engineering A198 (1995) 63–69

MATERIALS SCIENCE & ENGINEERING A

Corrosion characteristics of Fe_2O_3–Cr_2O_3 artificial passivation films under potentiostatic control

Shigeaki Tanaka, Nobuyoshi Hara, Katsuhisa Sugimoto

Department of Metallurgy, Faculty of Engineering, Tohoku University, Sendai 980-77, Japan

Abstract

Fe_2O_3–Cr_2O_3 composite oxide thin films, that is, artificial passivation films, with various Cr_2O_3 content were formed on Pt substrates by a MOCVD method. The rate of change of film thickness as a function of potential was examined in 1 kmol m^{-3} H_2SO_4 using in-situ ellipsometry under potentiostatic control. The rate of thinning can be divided into four characteristic ranges according to potential; i.e. the range of the reduction dissolution of Fe_2O_3 component, the range of no dissolution, the range of the field-assisted dissolution of Fe_2O_3 component, and the range of the oxidation dissolution of Cr_2O_3 component. The range of no dissolution of $Fe_2O_3Cr_2O_3$ composite films was named the intrinsic passivity. The anodic polarization curve for an Fe–18Cr alloy in passive and transpassive potentials was also divided into four characteristic ranges which correspond to the ranges for the artificial passivation films. The dissolution behavior of passive and transpassive films can be explained based on the origin of the four ranges. It was presumed that passive films on Fe–Cr alloys exhibit their intrinsic nature in the potential range of the intrinsic passivity.

Keywords: Artificial passivation film; Fe_2O_3–Cr_2O_3 film; MOCVD; Ellipsometry; Potentiostatic control; Passivity; Transpassivity

1. Introduction

A knowledge of the electrochemical properties of passive films is indispensable for the analysis of corrosion characteristics of stainless steels. It is hard, however, to get exact information on those properties, because most passive films have some defects resulting from the steel matrices, and the information from passivated steels contains not only the information from the passive films but also that from the steel matrices.

A means to overcome this difficulty is to use artificial passivation films. Artificial passivation films are the films which are formed to simulate the composition and nature of real passive films on metals and alloys [1]. The films can be used for simulation experiments to estimate the dissolution rate of passive films in corrosive environments. The authors synthesized $Fe_2O_3Cr_2O_3$, NiO–Cr_2O_3, and Fe_2O_3–Cr_2O_3–NiO artificial passivation films using a metal–organic chemical vapor deposition (MOCVD) method, and reported quantitative relationships between the dissolution rate and the composition of the films in 5 kmol m^{-3} HCl [2,3].

It is well known that the dissolution rate of stainless steels changes with potential, and this has been explained by the potential-dependent dissolution of passive films on the steels. The purpose of the present study is to obtain quantitative relationships between the dissolution rates and the electrode potential on Fe_2O_3–Cr_2O_3 artificial passivation films in 1 kmol m^{-3} H_2SO_4. Based on those relationships, correlations between the potential-dependent dissolution characteristics of the artificial passivation films and the passivation behavior of Fe–Cr alloys are discussed.

2. Experimental details

2.1. MOCVD

Fe_2O_3–Cr_2O_3 composite oxide films were made by a MOCVD technique. Fe(III) and Cr(III) acetylacetonate compounds, i.e. $Fe(O_2C_5H_7)_3$ and $Cr(O_2C_5H_7)_3$, were used as vapor sources and heated to 423 K and 438 K, respectively [4,5]. Water vapor was used as reaction gas and N_2 was used as carrier gas. A Pt plate of 25 mm × 15 mm × 0.5 mm was used as a substrate. The surface of the Pt plate was finished with 1-μm diamond paste and degreased ultrasonically in ethanol.

Elsevier Science S.A.
SSDI 0921-5093(94)04508-9

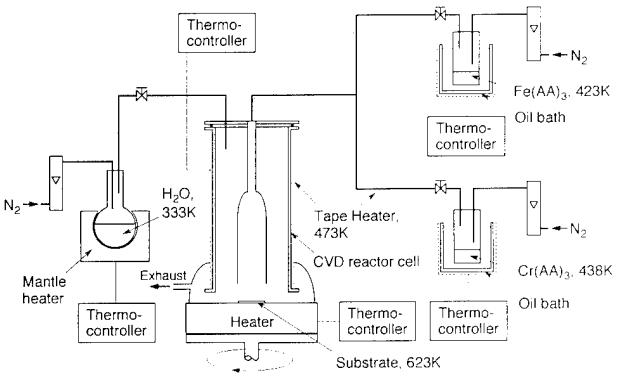

Fig. 1. Apparatus for MOCVD.

Fig. 1 shows the schematic of the MOCVD system. Each source was heated in an oil bath, and the source vapor and water vapor were carried into a reactor cell by the carrier gas. Line pipes and the reactor cell were heated to 473 K by tape heaters to avoid condensation of vapor source in the system. The substrate was heated to 623 K on a heater and horizontally rotated with a moving device to get a homogeneous flow of the vapor sources on the substrate. As a result, oxide films with homogeneous composition in depth were obtained. The composition of the films was controlled by the flow rate of the carrier gas. The thickness of the films was adjusted to 15–30 nm by controlling the deposition time.

2.2. Ellipsometry

The thickness and optical constant of the films were determined by ellipsometry. A rotating-analyzer-type automatic ellipsometer, which has the conventional polarizer–compensator–specimen analyzer configuration, was used. Fig. 2 shows the schematic of the ellipsometer system combined with an electrochemical polarization system. Monochromatic light of wavelength 546.1 nm was used for the measurements. The angle of

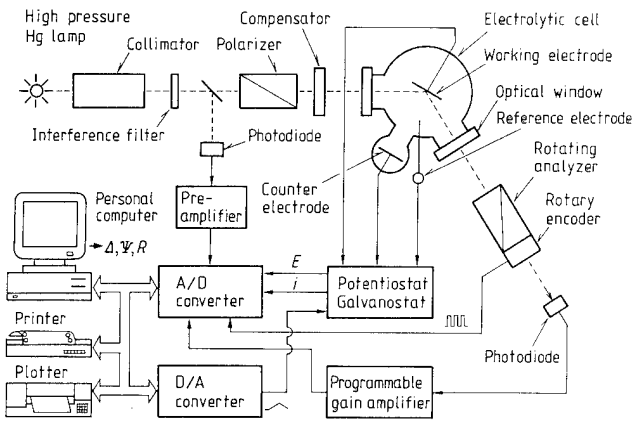

Fig. 2. Apparatus for electrochemical ellipsometric measurement.

incidence of the monochromatic light was 60.00°. The polarizer was fixed at an angle of 45°. The analyzer was rotated at an angular velocity of 360 deg s^{-1}. The intensity of light through the analyzer was measured by a photodiode and recorded with a computer as a function of rotation angle.

In the measurements of ellipsometric parameters, three-parameter ellipsometry was employed [6]. That is, the relative phase retardation Δ, the relative amplitude reduction $\tan\psi$ and the relative reflectivity change $\Delta R/R$ were measured. From these parameters obtained, the thicknesses and optical constants of the films were calculated using Drude's exact optical equations.

2.3. Inductively coupled plasma-emission spectroscopy (ICPS) analysis

The chemical composition of composite oxide films was determined by chemical analysis: the films were dissolved under anodic polarization in 5×10^{-3} m^3 of 1 kmol m^{-3} H_2SO_4, and this solution was analyzed by ICPS, which gave the content of the Fe and Cr in the films, W_{Fe} and W_{Cr}. The cationic mass fraction of Fe and Cr, X_{Fe} and X_{Cr}, of the films were calculated from W_{Fe} and W_{Cr}, for example, $X_{CR} = W_{CR}/(W_{Fe} + W_{CR})$; $X_{Fe} + X_{Cr} = 1$.

2.4. XPS analysis

The oxidation states of the constituent elements of the films were examined by X-ray photoelectron spectroscopy (XPS). A Mg $K\alpha_{1,2}$ X-ray source (1253.6 eV) was operated at 5 kV and 30 mA. The photoelectron spectra of the $2p_{3/2}$ level for Fe and Cr, and the 1s level for C and O were measured. The measurement of the spectra was carried out under a pressure of 5×10^{-5} Pa at room temperature. For calibration of the photoelectron binding energy, the C1s peak appearing at 285.0 eV in the background spectra was used.

2.5. Electrochemical polarization test

Electrochemical polarization tests of the films were done using the system shown in Fig. 2. The electrolytic solution was 1 kmol m^{-3} H_2SO_4 at 298 K. A Ag/AgCl (3.33 kmol m^{-3} KCl) electrode (0.206 V vs. SHE) was used as a reference electrode.

Changes in ellipsometric parameters as a function of time were measured on the films at each set potential. The set potential was increased or decreased at intervals of 0.1 V from the corrosion potential. Continuous measurements as a function of potential on the same specimen were performed on Fe_2O_3 or Cr_2O_3 single oxide films. On the other hand, discontinuous measurements were done on Fe_2O_3–Cr_2O_3 composite oxide films; i.e. specimens were exchanged at each set poten-

tial because of the change in the surface composition of specimens. Holding times at each set potential were 2 and 4 ks for single and composite oxide films, respectively.

Potentiodynamic anodic and cathodic polarization curves were also measured on single and composite oxide films under a dark room light illumination. The scan rate was 0.38 mV s^{-1}.

3. Results

3.1. XPS analysis of Fe_2O_3–Cr_2O_3 composite films

The XPS spectra of Fe $2p_{3/2}$, Cr $2p_{3/2}$, and O 1s levels for a Fe_2O_3–Cr_2O_3 ($X_{Cr} = 0.43$) composite oxide film are shown in Figs. 3(a), 3(b) and 3(c), respectively. The Fe $2p_{3/2}$ spectrum of the film exhibits a main peak at 711.2 ± 0.1 eV, which is close to the peaks of α- and γ-Fe_2O_3 (711.0–711.2 eV) in the literature [7,8]. There is no peak component at 708.3–709.7 eV which is ascribed to Fe^{2+} species in the film [7,8]. Therefore, Fe exists in the film as Fe^{3+} ions. The Cr $2p_{3/2}$ spectrum of the film exhibits a main peak at 577.2 ± 0.1 eV, which is close to the peak of α-Cr_2O_3 (576.52 eV) [9] and $Cr(OH)_3$ (577.03 eV) [9]. This means Cr exists in the film as Cr^{3+} ions. The O 1s spectrum of the film exhibits a strong peak at 530.2 eV and weak shoulders at about 531.8 eV and about 533.4 eV, which are assigned to O^{2-}, OH^- and H_2O species, respectively [7–10]. This indicates O in the film exists as O^{2-}, OH^-, and H_2O.

From XPS analysis of passive films on Fe–Cr and Fe–Cr–Ni alloys in acid solutions, it has been shown that Fe, Cr, and O in the films exist as Fe^{2+} and Fe^{3+}, Cr^{3+}, and O^{2-} and OH^-, respectively [11–16]. While in the passive films formed in neutral solutions, Fe mostly exists as Fe^{3+} [17]. Therefore, the oxidation states of constituent elements in the Fe_2O_3–Cr_2O_3 composite oxide films are analogous to those in passive films on Fe–Cr and Fe–Cr–Ni alloys. The OH^- and

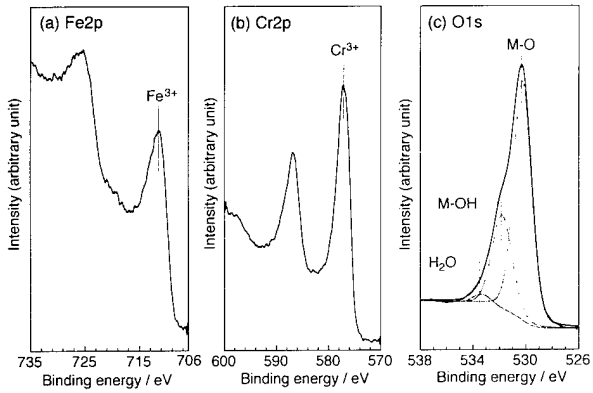

Fig. 3. XPS spectra for Fe_2O_3–Cr_2O_3 ($X_{Cr} = 0.43$) composite film.

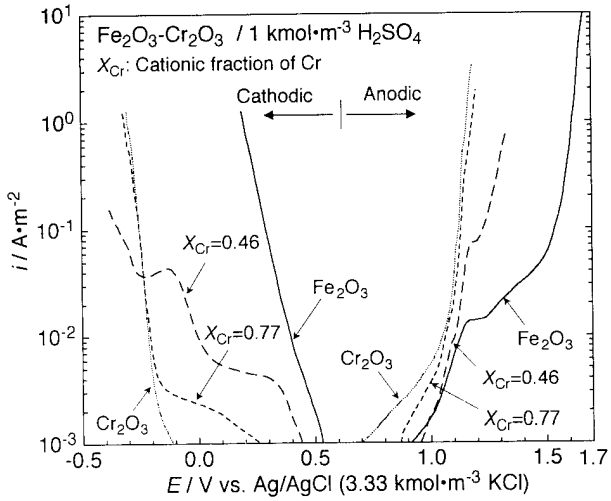

Fig. 4. Anodic and cathodic polarization curves for Fe_2O_3, Cr_2O_3 and Fe_2O_3–Cr_2O_3 films in 1 kmol m^{-3} H_2SO_4.

H_2O contents of the composite oxide films are, however, substantially lower than those of passive films on the alloys.

3.2. Polarization curves of Fe_2O_3–Cr_2O_3 composite films

Potentiodynamic anodic and cathodic polarization curves for Fe_2O_3, Cr_2O_3 and Fe_2O_3–Cr_2O_3 films in 1 kmol m^{-3} H_2SO_4 are shown in Fig. 4. The anodic polarization curve for the Fe_2O_3 film has a very low current region between 0.5 V and 1.0 V which reflects the nature of an n-type semiconductor [18]. The current sharply increases because of oxygen evolution at potentials higher than 1.5 V. The cathodic polarization curve for the Fe_2O_3 film shows a large current increase due to the reduction of the film at potentials lower than 0.5 V. The anodic polarization curve for the Cr_2O_3 film shows a large current increase due to the oxidation of the film to $Cr_2O_7^{2-}$ ions at potentials higher than 0.9 V. The cathodic polarization curve for the Cr_2O_3 film has a very low current region between -0.1 V and $+0.7$ V which reflects the nature of a p-type semiconductor [18]. The current begins to increase owing to the hydrogen evolution at potentials lower than -0.1 V. The anodic and cathodic polarization curves for the Fe_2O_3–Cr_2O_3 films move toward the anodic and the cathodic polarization curves for the Cr_2O_3 film, respectively, with increasing X_{Cr} of the films. This reflects changes in the conduction type and the chemical nature of the films.

3.3. Ellipsometric analysis of Fe_2O_3–Cr_2O_3 films under potentiostatic polarization

Changes in the complex optical constant $n - ki$ and thickness d as a function of time t for the Fe_2O_3 film at a cathodic potential of 0.3 V in 1 kmol m^{-3} H_2SO_4 are

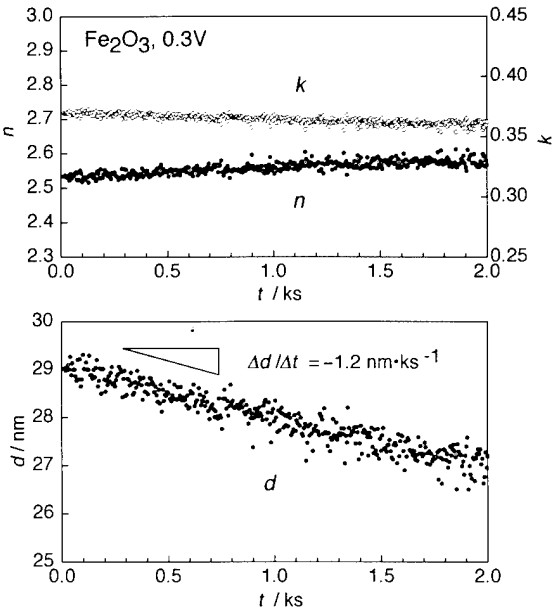

Fig. 5. Changes in optical constant $n-ki$ and thickness d as a function of time t for Fe_2O_3 film at 0.3 V in 1 kmol m^{-3} H_2SO_4.

shown in Fig. 5. The values of n and k were almost constant, and the value of d decreased linearly with time. This means that the film can be reduced homogeneously without any change in the film composition.

The decrease in the thickness of the Cr_2O_3 film due to oxidation dissolution at potentials higher than 1.1 V was also homogeneous and proportional with time.

Changes in the complex optical constant $n-ki$ and thickness d as a function of time t for the Fe_2O_3–Cr_2O_3 ($X_{Cr}=0.58$) film at a cathodic potential of 0.2 V in

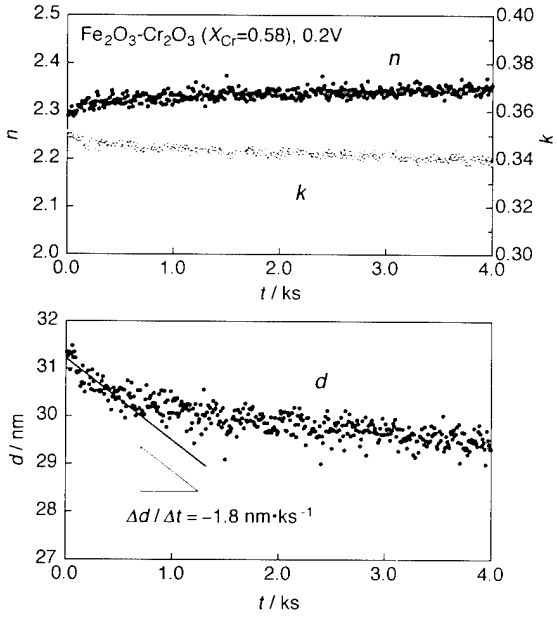

Fig. 6. Changes in optical constant, $n-k\,i$, and thickness, d, as a function of time, t, for Fe_1O_3–Cr_2O_3 film ($X_{Cr}=0.58$) at 0.2 V in 1 kmol m^{-3} H_2SO_4.

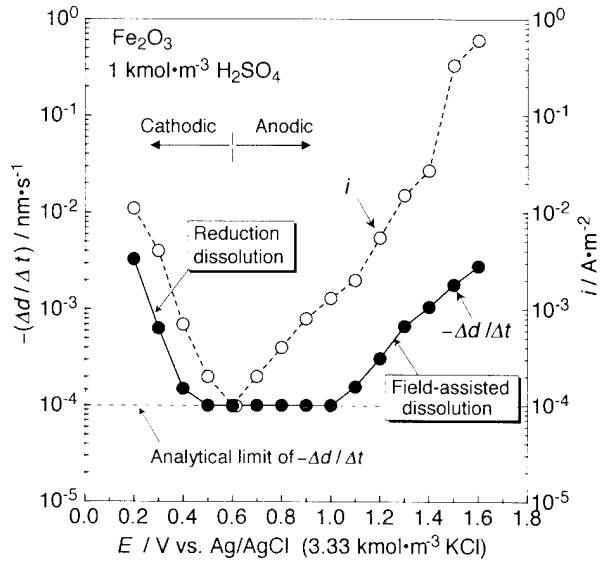

Fig. 7. Change in decrease rate of film thickness, $-\Delta d/\Delta t$, and current density, i, as a function of potential, E, for Fe_2O_3 film in 1 kmol m^{-3} H_2SO_4.

1 kmol m^{-3} H_2SO_4 are exhibited in Fig. 6. The value of n increased and that of k decreased slightly with time. The value of d decreased sharply at the beginning of reduction and then gradually at the end of reduction. This means that selective reduction takes place, accompanying the change in film composition. Therefore, the average gradient of the d vs. t curve at the beginning of reduction was taken for the thinning rate of film thickness, $-\Delta d/\Delta t$.

The thinning rates of film thickness $-\Delta d/\Delta t$, thus obtained as a function of potential E for Fe_2O_3, Cr_2O_3 and Fe_2O_3–Cr_2O_3 films in 1 kmol m^{-3} H_2SO_4 are shown in Figs. 7, 8 and 9, respectively. Potentiostatic

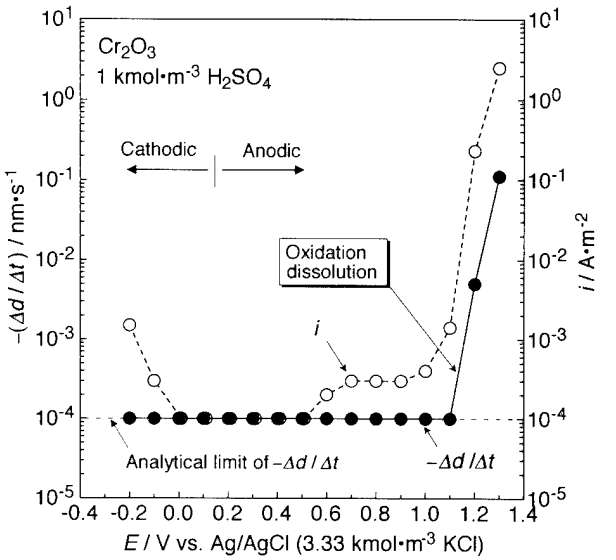

Fig. 8. Change in decrease rate of film thickness, $-\Delta d/\Delta t$, and current density, i, as a function of potential, E, for Cr_2O_3 film in 1 kmol m^{-3} H_2SO_4.

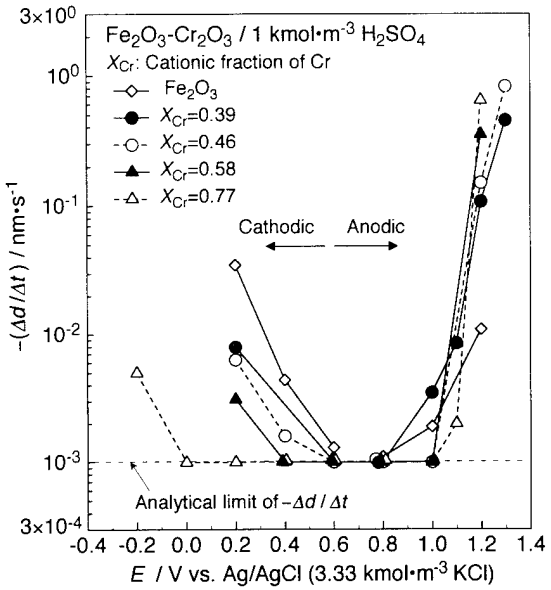

Fig. 9. Change in decrease rate of film thickness, $-\Delta d/\Delta t$, as a function of potential, E, for Fe_2O_3–Cr_2O_3 films in 1 kmol m^{-3} H_2SO_4.

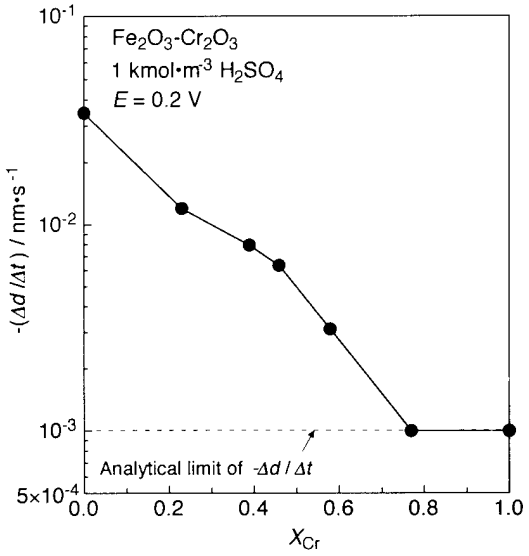

Fig. 10. Change in decrease rate of film thickness, $-\Delta d/\Delta t$, as a function of cationic fraction of Cr, X_{Cr}, for Fe_2O_3–Cr_2O_3 film at 1.2 V in 1 kmol m^{-3} H_2SO_4.

anodic and cathodic polarization curves obtained at the same time under the illumination of monochromatic light for ellipsometry are also given in the figures.

Fig. 7 shows that increases in $-\Delta d/\Delta t$, which are due to field-assisted dissolution and reduction dissolution, occur on the Fe_2O_3 film at potentials higher than 1.0 V and lower than 0.5 V, respectively. The current density of the anodic polarization curve, which contains photocurrent, is larger than that in Fig. 4.

Fig. 8 shows an increase in $-\Delta d/\Delta t$, which is due to oxidation dissolution, occurs on the Cr_2O_3 film at po-

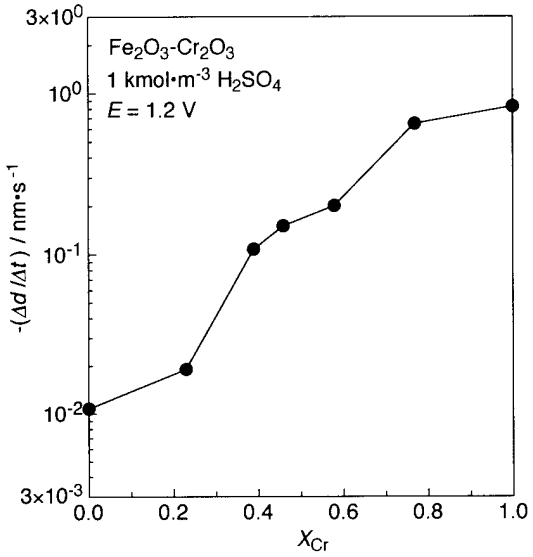

Fig. 11. Change in decrease rate of film thickness, $-\Delta d/\Delta t$, as a function of cationic fraction of Cr, X_{Cr}, for Fe_2O_3–Cr_2O_3 film at 1.2 V in 1 kmol m^{-3} H_2SO_4.

tentials higher than 1.1 V. There is a slight increase in current between 0.6 V and 1.0 V. This increase in current is not due to dissolution because there is no increase in $\Delta d/\Delta t$.

Fig. 9 shows that both field-assisted and reduction dissolution can be suppressed by increasing X_{Cr} of Fe_2O_3–Cr_2O_3 films. Oxidation dissolution is, however, promoted with increasing X_{Cr}. The decrease in the rate of reduction dissolution is shown in Fig. 10 as a function of X_{Cr} for the Fe_2O_3–Cr_2O_3 films. Reduction dissolution disappears at X_{Cr} values larger than 0.8. The increase in the rate of oxidation dissolution is shown in Fig. 11 as a function of X_{Cr} for the Fe_2O_3–Cr_2O_3 films. Oxidation dissolution is suppressed up to $X_{Cr} = 0.2$ and then increases exponentially with increasing X_{Cr}.

4. Discussion

4.1. Reduction dissolution of Fe_2O_3 film

Reduction dissolution of the Fe_2O_3 film is thought to occur according to following reactions [19] :

$$2Fe^{2+} + 3H_2O = Fe_2O_3 + 6H^+ + 2e \quad (1)$$

$$E_{eq} = 0.728 - 0.1773pH - 0.0591 \log[Fe^{2+}] \quad (V \textit{ vs. } NHE) \quad (2)$$

The value of E_{eq} calculated by assuming $[Fe^{2+}] = 1$ in 1 kmol m^{-3} H_2SO_4 (pH $\approx$ 0) is about 0.52 V (vs. Ag/AgCl, 3.33 kmol m^{-3} KCl). This value corresponds

well with the potential at the onset of the increase in $-\Delta d/\Delta t$ in the cathodic region of Fig. 7.

4.2. Field-assisted dissolution of Fe_2O_3 film

The dissolution of oxides under a high field has been explained by the field-assisted ion transfer mechanism given by Mott and Cabrera [20,21] and/or the Helmholtz-layer potential-difference mechanism given by Vermilyea [22]. The dissolution rate of oxides can be expressed by the Mott and Cabrera mechanism as follows:

$$i_{Fe}(ox) = i_{Fe,0}(ox)\exp\left(\frac{z\alpha F}{RT}\frac{\Delta E}{d_{ox}}\right) \quad (3)$$

where $i_{Fe}(ox)$ is the dissolution rate of Fe_2O_3, $i_{Fe,0}(ox)$ is the exchange current, z is the valence of the ion, α is the transfer coefficient of the ion, F is the Faraday constant, R is the gas constant, T is the absolute temperature, ΔE is the potential difference across the film, and d_{ox} is the film thickness. The dissolution rate of oxides expressed by the Vermilyea's mechanism is as follows:

$$i_{Fe}(ox) = i_{Fe,0}(ox)\exp\left(\frac{z\alpha F}{RT}\phi_{H.L.}\right) \quad (4)$$

where $\phi_{H.L.}$ is the potential difference across the Helmholtz layer. Both mechanisms suggest that the increase in film dissolution occurs without the oxidation of Fe ions. The increase in $-\Delta d/\Delta t$ at high potentials in Fig. 7 should correspond to this. Field-assisted dissolution of the Fe_2O_3 film begins at 0.8 V, as shown in Fig. 9, which shows results obtained using fresh specimens at each potential.

4.3. Oxidation dissolution of Cr_2O_3 film

The anodic oxidation dissolution of the Cr_2O_3 film can be expressed by the following reaction [23]:

$$Cr_2O_3 + 4H_2O = Cr_2O_7^{2-} + 8H^+ + 6e \quad (5)$$

$$E_{eq} = 1.168 - 0.0788pH + 0.0098\log[CR_2O_7^{2-}] \quad (V\ vs.\ NHE) \quad (6)$$

The value of E_{eq} calculated by assuming $[Cr_2O_7^{2-}] = 1$ in 1 kmol m^{-3} H_2SO_4 (pH $\approx$ 0) is about 0.96 V (vs. Ag/AgCl, 3.33 kmol m^{-3} KCl). This value corresponds well with the potential at the onset of the increase in $-\Delta d/\Delta t$ in the anodic region of Fig. 8.

4.4. Dissolution ranges of Fe_2O_3–Cr_2O_3 artificial passivation films

A $-\Delta d/\Delta t$ vs. E curve for a Fe_2O_3–Cr_2O_3 ($X_{Cr} = 0.39$) film has four characteristic ranges, as shown in Fig. 9; i.e. the ranges which correspond to

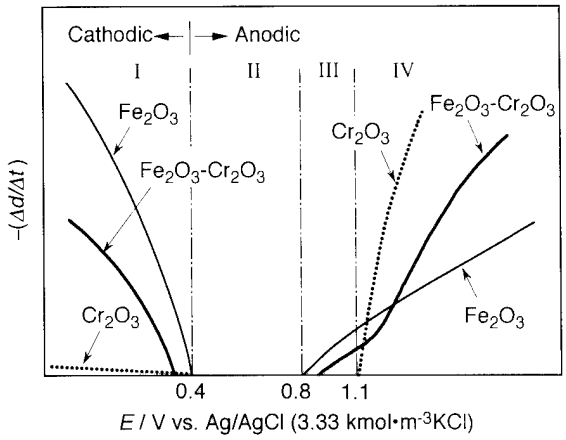

I : Passivity with reduction dissolution
II : Intrinsic passivity
III : Passivity with field-assisted dissolution
IV : Passivity with oxidation dissolution (transpassivity)

Fig. 12. Four ranges of decrease rate of film thickness, $-\Delta d/\Delta t$, vs. potential, E, curve.

reduction dissolution of Fe_2O_3 below 0.4 V, no dissolution between 0.4 V and 0.8 V, field-assisted dissolution of Fe_2O_3 between 0.8 V and 1.1 V, and oxidation dissolution of Cr_2O_3 above 1.1 V. These ranges are labeled here: (a) passivity with reduction dissolution (range I), (b) intrinsic passivity (range II), (c) passivity with field-assisted dissolution (range III), and (d) passivity with oxidation dissolution (transpassivity, range IV), respectively, and are shown schematically in Fig. 12. Such dissolution behavior of Fe_2O_3–Cr_2O_3 artificial passivation films should reflect the behavior of in-situ passive films on Fe–Cr alloys.

4.5. Dissolution range of real passive film on Fe–Cr alloy

The four characteristic dissolution ranges of Fe_2O_3–Cr_2O_3 artificial passivation films were superimposed on the anodic polarization curve of a high-purity Fe-18Cr alloy (C, 0.0054 wt.%; N, 0.0005 wt.%; Mn, less than 0.001 wt.%; Si, 0.003 wt.%) in de-aerated 1 kmol m^{-3} H_2SO_4 at 298 K. The result is shown in Fig. 13. The change of the i vs. E curve in the passivity and transpassivity regions in Fig. 13 is very similar to that of the $-\Delta d/\Delta t$ vs. E curve for the artificial passivation films shown in Figs. 9 and 12. A small increase of i in range I can be explained by the degradation of the passive film owing to reduction dissolution of the Fe_2O_3 component of the film. The passive film in this range should be slightly porous. A current minimum is observed in range II, where there is no dissolution. The passive film in this range should be compact. A gradual increase of i with potential in range III can be assigned to field-

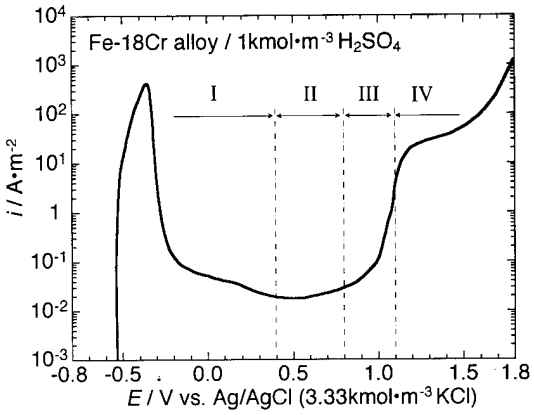

I : Passivity with reduction dissolution
II : Intrinsic passivity
III : Passivity with field-assisted dissolution
IV : Passivity with oxidation dissolution (transpassivity)

Fig. 13. Four ranges of anodic polarization curve for Fe–18Cr alloy in 1 kmol m^{-3} H_2SO_4.

assisted dissolution of the Fe_2O_3 component of the film. The passive film should become slightly porous. A large increase of i in range IV is due to oxidation dissolution of the Cr_2O_3 component of the film. The passive film (transpassive film) here should be very porous. Such supposed structures of passive films on Fe–18Cr alloy are schematically given in each range of Fig. 14. The passive films on Fe–Cr alloys should exhibit their intrinsic nature in the intrinsic passivity range (range II) where there is no dissolution of Fe_2O_3–Cr_2O_3 films.

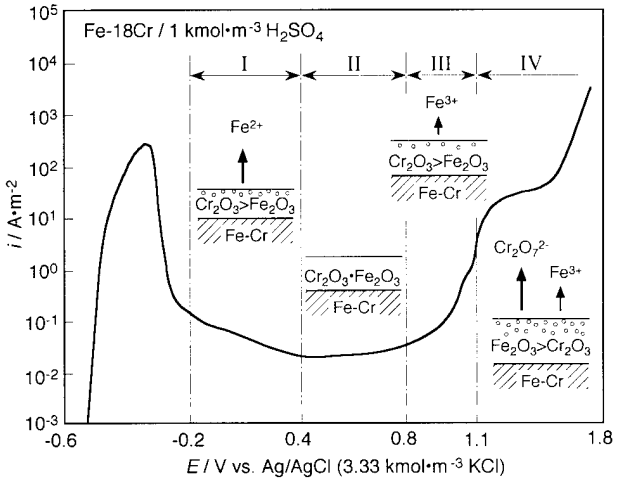

I: Film is porous due to reduction dissolution of Fe_2O_3
II: Film is compact without dissolution of both Cr_2O_3 and Fe_2O_3
III: Film is slightly porous due to field-assisted dissolution of Fe_2O_3
IV: Film is porous due to oxidation dissolution of Cr_2O_3

Fig. 14. Supposed structure of passive films on Fe–18Cr alloy in four potential ranges in 1 kmol m^{-3} H_2SO_4.

5. Conclusions

(1) Fe_2O_3 films show reduction dissolution at potentials lower than 0.4 V and field-assisted dissolution at potentials higher than 0.8 V.

(2) Cr_2O_3 films show no reduction dissolution at potentials in the cathodic region, and oxidation dissolution at potentials higher than 1.1 V.

(3) Fe_2O_3–Cr_2O_3 composite films show reduction dissolution at potentials lower than 0.4 V and field-assisted and oxidation dissolution at potentials higher than 0.8 V and 1.1 V, respectively.

(4) Reduction dissolution can be suppressed with increasing Cr_2O_3 content of Fe_2O_3–Cr_2O_3 composite films.

(5) The intrinsic passivity range was recognized for Fe_2O_3–Cr_2O_3 composite films in the potential region between 0.4V and 0.8 V.

(6) The passive current of Fe–Cr alloy exhibits a minimum in the potential range corresponding to the intrinsic passivity of Fe_2O_3–Cr_2O_3 composite film.

References

[1] K. Sugimoto, *Tetsu-To-Hagane*, *77* (1991) 1116.
[2] K. Sugimoto, M. Seto, S. Tanaka and N. Hara, *J. Electrochem. Soc.*, *140* (1993) 1586.
[3] S. Tanaka, N. Hara and K. Sugimoto, in M.W. Kendig, K. Sugimoto and N.R. Sorensen (eds.), *Proc. Symp. on Corrosion Protection by Coatings and Surface Modification*, Electrochemical Society, Pennington, NJ, 1994, p. 54.
[4] K.L. Hardee and A.J. Bard, *J. Electrochem. Soc.*, *123* (1976) 1024.
[5] K.L. Hardee and A.J. Bard, *J. Electrochem. Soc.*, *124* (1977) 215.
[6] W.-K. Paik and J.O'M. Bockris, *Surf. Sci.*, *28* (1971) 61.
[7] N.S. McIntyre and D.G. Zetaruk, *Anal. Chem.*, *49* (1977) 1521.
[8] C.R. Brundle, T.J. Chuang and K. Wandelt, *Surf. Sci.*, *68* (1977) 459.
[9] K. Asami and K. Hashimoto, *Corros. Sci.*, *17* (1977) 559.
[10] K.S. Kim and N. Winograd, *Surf. Sci.*, *43* (1974) 625.
[11] K. Hashimoto, K. Asami and K. Teramoto, *Corros. Sci.*, *19* (1979) 3.
[12] I. Olefjord and B. Brox, in M. Froment (ed.), *Passivity of Metals and Semiconductors*, Elsevier, Amsterdam, 1983, p.61.
[13] C.R. Clayton and Y.C. Lu, *J. Electrochem. Soc.*, *133* (1986) 2465.
[14] M. Ben-Haim, U. Atzmong and N. Shamir, *Corrosion*, *44* (1988) 461.
[15] I. Olefjord, *Corros. Sci.*, *31* (1990) 89.
[16] I. Olefjord and B.O. Elfstrom, *Corrosion*, *38* (1982) 46.
[17] S.C. Tjong, R.W. Hoffman and E.B. Yeager, *J. Electrochem. Soc.*, *129* (1982) 1662.
[18] N. Hara, A. Yamada and K. Sugimoto, *J. Jpn. Inst. Metals*, *49* (1985) 640.
[19] M. Pourbaix, *Atlas of Electrochemical Equilibria in Aqueous Solution*, NACE, Houston, TX, 1974, p. 309.
[20] N.F. Mott, *Trans. Faraday Soc.*, *36* (1940) 472.
[21] H. Cabrera and N.F. Mott, *Rep. Progr. Phys.*, *12* (1949) 163.
[22] D.A. Vermilyea, *J. Electrochem. Soc.*, *113* (1966) 1067.
[23] Ref. [19], p. 256.

ELSEVIER

Materials Science and Engineering A198 (1995) 71–74

MATERIALS SCIENCE & ENGINEERING A

Study on corrosion properties of sputter coating of oxides on stainless steels

Y. Hayashi, M. Masuda, J. Lee, M. Kojima

Department of Materials Science and Engineering, Faculty of Engineering, Kyushu University, Fukuoka 812, Japan

Abstract

To improve the corrosion resistivity of steels, the effect of oxide coating has been studied. Various oxides were coated on stainless steels by r.f. sputtering and corrosion properties of the steels were examined in acidic solutions. Structural defects, pinholes, were inevitable in the sputter-coated oxides. The defect probability was determined by electrochemical measurements and direct observations using a liquid crystal. The anodic current was analyzed assuming current flow through the defects. The corrosion properties were discussed, taking the electrical charge on the surface of oxides in solutions into account.

Keywords: Oxide coating; Pinhole; pH of zero charge; Stainless steel; Corrosion

1. Introduction

Stainless steel with its passivation film has high corrosion resistivity, and has been used without surface coatings. In recent years, however, various surface coatings were developed also for stainless steel with various intentions [1]. Oxide coating is one of the interesting treatments for realizing high corrosion resistivity and good surface appearance. Oxides or hydroxides are naturally formed on stainless steels, but their composition and structure are determined mostly by the nature of the steel, and are not easily modified. By a dry process of coating any kind of oxide film can be formed on any substrate. Studies of the preformances of artificially formed surface films are sometimes useful for understanding the nature of natural surface films. An oxide surface in solution has its specific electrical charge [2], and the excess surface charge has been known to play an important role in corrosion. Natishan et al. [3] studied the corrosion properties of oxides on Al formed by ion implantation, and showed the importance of the pH of zero charge of the oxide. Sato [4] discussed the properties of passivity referring to the ion selectivity of the bilayered structure of the passivation film. Sugimoto [5] formed oxide films as an artificial passivation film to study the nature of corrosion resistivity. Oxide coating is, therefore, interesting both from the technical viewpoint of improving the corrosion resistivity of steels and the scientific viewpoint of studying the passivation and corrosion resistivity of materials.

R.f. sputtering is a useful way of forming any kind of oxide film on any substrate. In this study single- and double-layered oxide films were formed on stainless steels by r.f. sputtering, and the structural defects in the films and the effect of the oxide coating on the corrosion properties were studied. The effect of pH of zero charge of the oxides in solutions on the corrosion properties was examined.

2. Experimental details

Various oxide films were coated on sheets of stainless steel, types 410 and 304, by r.f. sputtering. The sputtering targets were oxides, Al_2O_3, SiO_2, Ta_2O_5, TiO_2 and ZrO_2. The substrate temperature was 573 K, and the sputtering gas was Ar at 5.3 Pa. The X-ray diffraction peaks were not observed from most of the oxide films except for TiO_2 and ZrO_2. The thicknesses of the oxide films were adjusted to about 1 μm. Pairs of double-layered oxide films were also prepared by changing the coating sequence of the two different oxides.

SSDI 0921-5093(94)04509-7

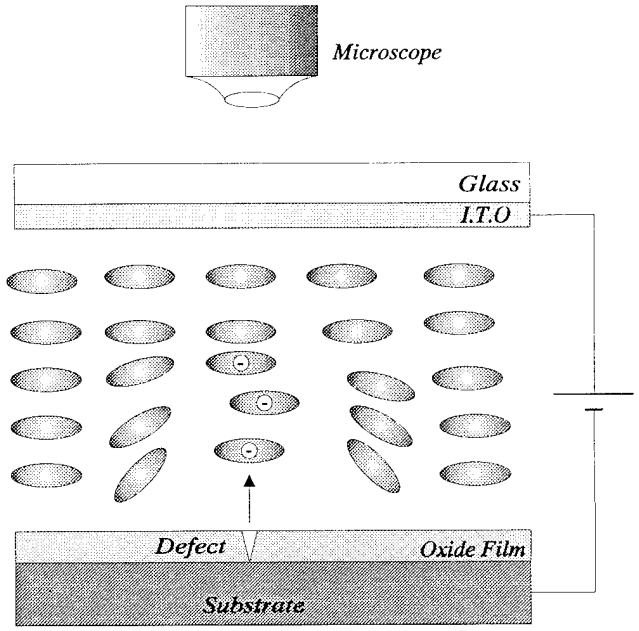

Fig. 1. Schematic representation of the defect observation method using a nematic liquid crystal.

Since structural defects were inevitable in the sputter coating films, the pinhole defect was observed using dynamical scattering of a nematic liquid crystal [6,7]. As shown in Fig. 1 a thin layer of nematic liquid crystal was inserted between the coating film and a transparent electrode, and an electrical field was applied between the substrate and the transparent electrode. When pinholes exist in the insulating oxide film, electrical current flows through the pinholes and the liquid crystal. The current disturbs the alignment of the molecules of the liquid crystal, and this disturbance can be observed by an optical microscope from the transparent electrode side.

The probability of the pinhole defects was also determined by an electrochemical method proposed by Sugimoto [8], which measures the critical passivation current density in a solution of 0.5 kmol m^{-3} H_2SO_4 containing 0.05 kmol m^{-3} potassium thiocyanate (KSCN).

The effect of coatings on corrosion was studied by measuring anodic polarization curves in sulphuric acid solutions.

3. Results

The anodic polarization curves measured in the solution containing KSCN are shown in Figs. 2 and 3 for the substrate steels of type 410 and type 304 respectively. The polarization curves showed distinct active dissolution peaks before passivation. The peak current density is used as a measure of defect probability. The defect density was obtained from the number of disturbance points counted in the observation of the dynamic

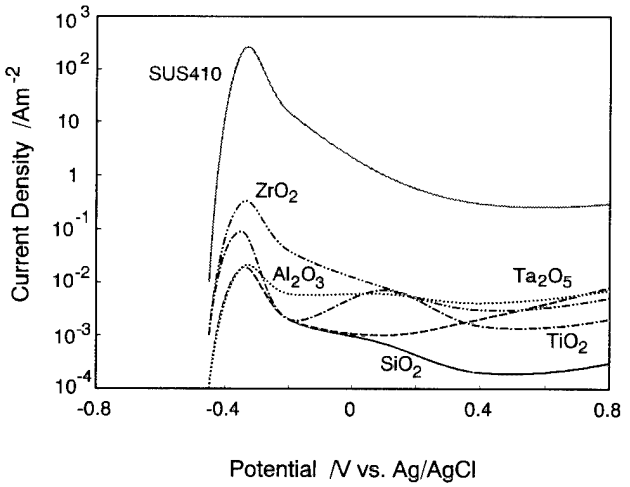

Fig. 2. Anodic polarization curves of oxide-coated 410 stainless steel measured in the solution of 0.5 kmol m^{-3} H_2SO_4 containing KSCN.

scattering of the liquid crystal. The relation between the critical passivation current density and the defect density is shown in Fig. 4. A good linear relation is obtained. Since the defect probability is very sensitive to the condition of the r.f. sputter coating, it exhibits scatter from specimen to specimen but the linear relationship of Fig. 4 remains.

The peak current densities for the specimens are shown in Fig. 5 referred to the values of pH of zero charge of the oxides [9–15]. There seems no correlation between the critical passivation current density and pH of zero charge.

Anodic polarization curves were measured in 0.5 kmol m^{-3} H_2SO_4 for specimens with a single layer of oxide films. The passive current densities are shown in Fig. 6 as a function of the pH of zero charge of the oxides. The passive current density, compared to the critical passivation current density, shows rather a good correlation with the pH of zero charge: the passive current is lower for a specimen coated with an oxide

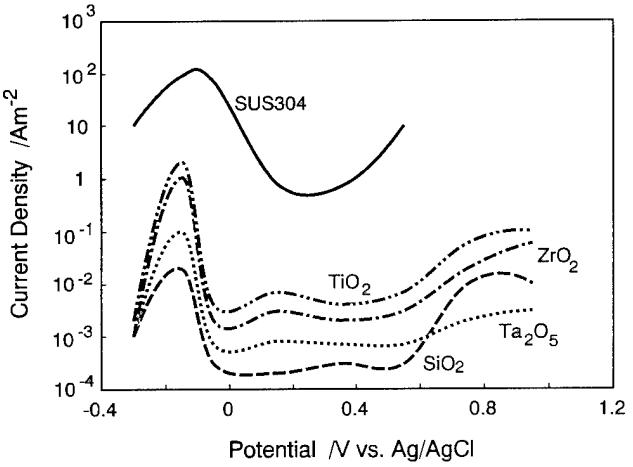

Fig. 3. Anodic polarization curves of oxide-coated 304 stainless steel measured in the solution of 0.5 kmol m^{-3} H_2SO_4 containing KSCN.

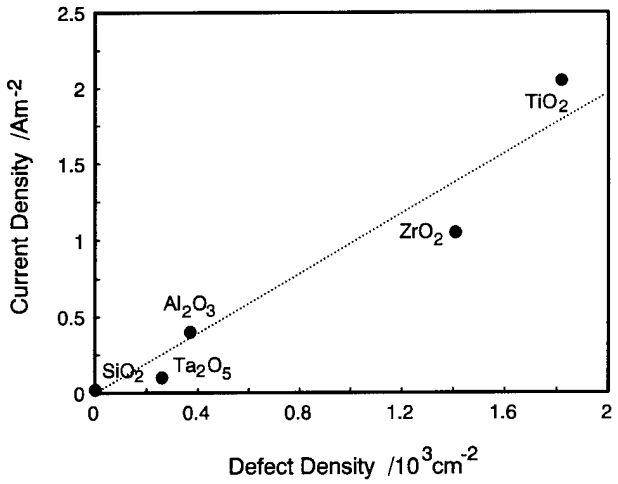

Fig. 4. Relation between the two types of defect observation methods: critical passivation current density measured in a solution containing KSCN and observation of the dynamical scattering of the liquid crystal.

with a lower value of pH of zero charge, although the results are not compared for the specimens with equal defect probability.

Anodic polarization curves were also measured for specimens with double-layered oxide coatings. Pairs of double-layered oxides were prepared by changing the coating sequence of the oxides. The passive current densities are shown in Fig. 7. The current density is low for the specimen with an oxide of higher value of pH of zero charge as an inner coating and an oxide of lower value of it as an outer coating. Though there is no good correlation with the difference between the values of pH of zero charge of the two oxides, the coating order has a distinct effect on the passive current density. The passive current densities for the double-layered coatings were measured as a function of the pH of the measuring solution. The results are shown in Figs. 8 and 9 for

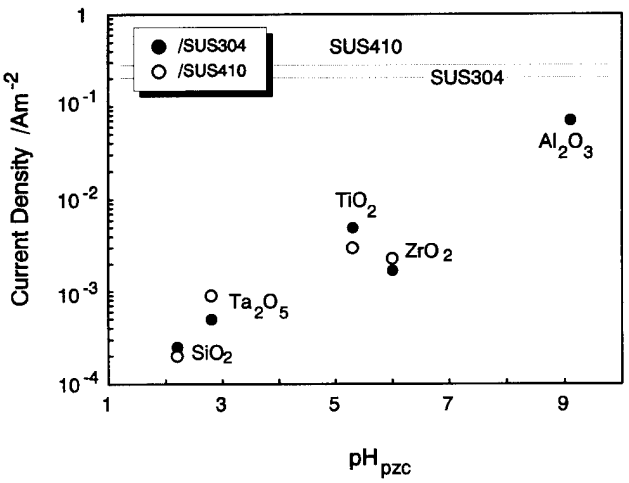

Fig. 5. Relation between the critical passivation current density of the oxide-coated steels and pH of zero charge of the oxide.

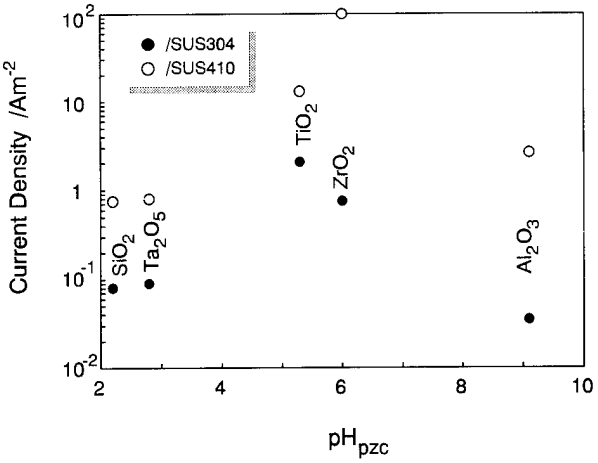

Fig. 6. Relation between the passive current density of the oxide-coated steels and pH of zero charge of the oxide.

the pairs of oxides SiO_2/Al_2O_3 and Ta_2O_5/Al_2O_3. The difference in passive current decreases as the pH value of the solution increases, and for some pH values the difference is not observable.

4. Discussion

Since the oxides coated in this experiment are insulators, the current measured at the potential of anodic polarization is the current from the substrate steel. Electrochemical reactions at the surface of the oxide need not be considered. The current in the active region is very high, and the nature of the inner wall of the pinhole of the oxide has little influence on the rate of electrochemical reactions. The results of Fig. 4 may be understood by considering only pinhole defects in the coating films. The electrochemical method of determining defect probability proposed by Sugimoto has a

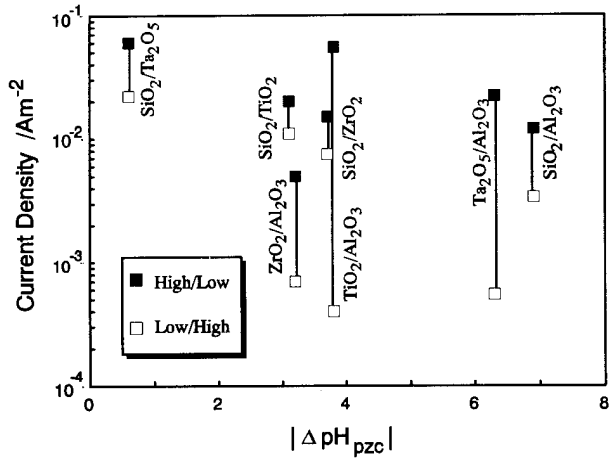

Fig. 7. Passive current densities of the double-layered oxide-coated steels; a pair of the coated oxides is compared by changing the sequence of the coating.

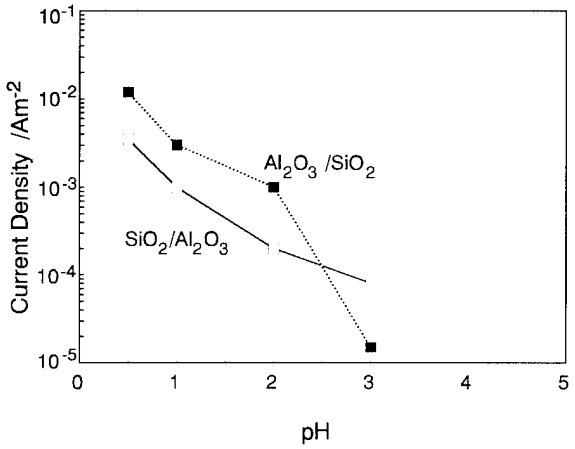

Fig. 8. Change of the passive current densities of steel coated with the double-layered oxides Al_2O_3 and Si_2O, with the change of the solution pH.

significant meaning for these oxide coatings. To decrease the defect probability an increase in the thickness of the film is effective. However, the defect distribution appears statistically, and it is difficult to produce a perfect film by r.f. sputtering.

The passive current, on the other hand, is low and is much influenced by the change of the environment inside the pinhole. The electrical charge on the inner wall of the pinhole varies with the change of the oxide and the solution pH. The cation and anion distribution in the solution inside the pinhole is modified by the nature of the oxide. On the inner wall of the pinhole of the oxide with a high pH of zero charge, a positive charge exists, and anions can easily penetrate into the pinhole. Since the solution does not contain halogen ions, the anodic current is not due to pitting by Cl^-. The passive film is formed inside the pinhole, and the rate of the passive film formation is limited by the transfer of OH^-. The supply of anions keeps the passivation current a little high,

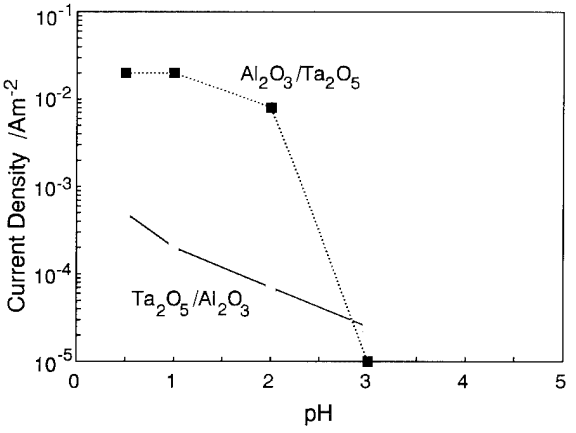

Fig. 9. Change of the passive current densities of steel coated with the double-layered oxides Al_2O_3 and Ta_2O_5, with the change of the solution pH.

which means that anion-selective films show higher passive currents. For the double-layered coating the nature of the outer coating may regulate the passivation current. The anion-selective film of the outer layer transports OH^- into the pinhole and keeps the passivation current higher. The details of the mechanism are not yet clear, but the change of passive current by the sequential order of the oxide coatings may be explained as an effect of the surface charge of the oxide. Multilayering is one of the ways to have high corrosion resistivity. For the design of a layering coating the pH of zero charge of the oxide is one factor to be taken into account.

5. Conclusion

Various oxides were coated on stainless steels by sputtering, and their effect on corrosion has been studied. Pinhole defects were inevitable in the oxide films. The defect probability is measured by an electrochemical method and by direct observation using a liquid crystal. Both results showed a good correlation. The passive current densities measured during the anodic polarization had some correlation with the values of pH of zero charge of the oxides. This effect was more clearly shown for the double-layered oxide coatings. Specimens coated with an oxide with a larger value of pH of zero charge as an inner coating showed a lower passive current density. This effect was observed for all pairs of the oxides studied. The passivation of the steel occurs at the bottom of the pinhole, and the passivation current is influenced by the excess electrical charge on the inner wall of the pinhole in the oxide.

References

[1] S. Ito, *J. Surf. Finish. Soc. Jpn.*, *41* (1990) 249.
[2] S.R. Morrison, *Electrochemistry at Semiconductor and Oxidized Metal Electrodes*, Plenum, New York, 1980, p. 49.
[3] P.M. Natishan, E. McCafferty and G.K. Hubler, *J. Electrochem. Soc.*, *135* (1988) 321.
[4] N. Sato, *Boshoku Gijutsu*, *39* (1990) 495.
[5] K. Sugimoto, *Tetsu To Hagne*, *77* (1991) 258.
[6] J.M. Keen, *Electron. Lett.*, *7* (1971) 432.
[7] A.K. Zakzouk, R.A. Stuart and W. Eccleston, *J. Electrochem. Soc.*, *123* (1976) 1551.
[8] K. Sugimoto, *Proc. 95th Fushoku-boshoku Symp.*, Japan Soc. Corr. Eng., Tokyo, 1993, p. 1.
[9] G.A. Parks, *Chem. Rev.*, *65* (1965) 177.
[10] F.S. Mandel and H.G. Spencer, *J. Colloid Interface Sci.*, *77* (1980) 577.
[11] G.W. Smith and T. Salman, *Can. Met. Quart.*, *5* (1966) 93.
[12] J.A. Yopps and D.W. Fuerstenau, *J. Colloid Sci.*, *19* (1964) 61.
[13] H. Sadec, A.K. Helmy, V.M. Sabet and Th.F. Tadros, *J. Electroanal. Chem.*, *27* (1970) 257.
[14] M. Tschapek, C. Wasowski and R.M. Torres Sanchez, *J. Electroanal. Chem.*, *74* (1976) 167.
[15] Y. Aikawa, *Zairyo To Kankyo*, *41* (1992) 111.

ELSEVIER

Materials Science and Engineering A198 (1995) 75–83

MATERIALS SCIENCE & ENGINEERING A

Surface modification of stainless steel in plasma environments

M. Hashimoto[a], Y. Miyamoto[a], Y. Kubo[a], S. Tokumaru[a], N. Ono[b], T. Takahashi[b], I. Ito[c]

[a]*Advanced Materials and Technology Research Laboratories, Nippon Steel Corporation, 1618 Ida, Nakahara-ku, Kawasaki 211, Japan*
[b]*Hikari Works, Hikari R&D Laboratory, Nippon Steel Corporation, 3434 Shimata, Hikari City, Yamaguchi Pre. 743, Japan*
[c]*Metal Foil Products Division, New Materials Divisions Group, Nippon Steel Corporation, 6-3 Otemachi 2-chome, Chiyoda-ku, Tokyo 100, Japan*

Abstract

Stainless steels are widely used for architecture, vehicles, etc. because of their good corrosion resistance and surface aesthetics. In order to provide additional surface functions, such as decorative colors, we have developed a continuous dry coating process, which can provide stainless steel strip with a multilayer ceramic or metallic coating. In this paper, the role of the environment will be discussed from two different points of view. The first is the performance of these coated stainless steels in corrosive and mechanically stressed environments. The second is the influence of the plasma environment used to synthesize the coating materials on the quality of thin films.

Keywords: Surface modification; Plasma-assisted CVD; Sputtering; Ion plating; Stainless steel

1. Introduction

Stainless steels are used in architectural, automotive and chemical processing applications because of their good corrosion resistance, clean appearance and workability. Coating these metals with ceramics, other metals or alloys adds innovative surface functions, such as insulation or dielectric properties, aesthetic appeal and optical characteristics. In order to develop these additional surface functions, a combined process utilizing sputtering, ion plating and plasma-assisted chemical vapor deposition (PACVD) has been assessed.

Thin film processes that use ion and low-temperature plasmas are commonly applied to modify the surface characteristics of materials. Unfortunately, handling problems associated with many toxic coating materials and the severe process requirements, such as high vacuum or material purity, have limited the large-scale production use of ion and plasma deposition techniques. We have developed a dry coating process that combines ion plating, sputtering and PACVD in a tandem arrangement to coat continuously coils of material on a semi-production scale [1].

The above three processes have been selected since they generally give dense and adherent films. However, each coating process has its own limitations. For example, stainless steel coated with SiO_2 or Si_3N_4 by PACVD shows higher corrosion resistance than that coated by sputtering; in addition, the applicability of PACVD is limited by the availability of coating materials in the form of gases [2]. Therefore the combination of the above-mentioned three processes is particularly meaningful.

By eliminating exposure to external environments, the tandem arrangement allows improvements in conventional coating systems. It also creates a procedure for developing new composite materials by allowing different materials to be sequentially coated. Although our coating process is compatible with many materials, we have used it to coat stainless steel strip.

In this paper, the role of the environment will be discussed from two different points of view. The first is the performance of the coated stainless steels in corrosive and mechanically stressed environments. The second is the influence of the plasma environment used to synthesize the coating materials on the quality of thin films.

SSDI 0921-5093(94)04510-0

2. Experimental details

2.1. Substrate

The materials used in this study were commercially available cold-rolled type 304 and 430 stainless steels, which are the most versatile stainless steels, and YUS180 (19Cr–0.3Ni–0.4Cu–0.4Nb, low carbon and nitrogen), which is widely used in outdoor applications. These materials were received as bright annealed (BA) sheet.

2.2. Pretreatment

Before deposition, the specimens were pretreated by one or a combination of the following methods: (1) no treatment; (2) acetone ultrasonic cleaning; (3) ion bombardment; (4) sputter etching; (5) nitric acid pretreatment [3]. Ion bombardment and sputter etching eliminate the surface contamination and, as a result, improve the adhesion of deposited layers. The nitric acid pretreatment was employed to stabilize the pre-existing passive film on stainless steels [4] and thus to make the interface between the deposited layer and the stainless steel more resistant to corrosion. In this treatment, stainless steel was oxidized using 5% HNO_3 at 35 mA cm^{-2} for 40 s.

2.3. Coating processes and conditions

Three deposition processes, i.e. ion plating, sputtering and PACVD, were employed in this study. The first set of processes was performed in a batch coating apparatus for small sample fabrication. This was used to investigate the basic properties of metal- or ceramic-coated stainless steels. The details of these batch processes and typical operating conditions are listed in Table 1 [2].

Table 1
Batch coating processes and typical deposition conditions [2]

Process	Deposition conditions
Ion plating	HCD: $p = 1.06$ Pa (8 mTorr); maximum power, 16 kW Electron beam: maximum power, 1 kW D.c. bias: maximum, 2 kV Maximum temperature, 300 °C
Sputtering	R.f. or d.c. magnetron sputtering: $p = 0.67$ Pa (5 mTorr) maximum power, 3 kW; maximum temperature, 700 °C; target diameter, 15.2 cm
PACVD	Capacitively coupled plasma: $p = 13.3$ Pa (0.1 Torr); maximum power, 500 W; maximum temperature, 500 °C d.c. bias: maximum, 1.5 kV; electrode size, 10 cm × 10 cm

HCD: hollow cathode discharge.

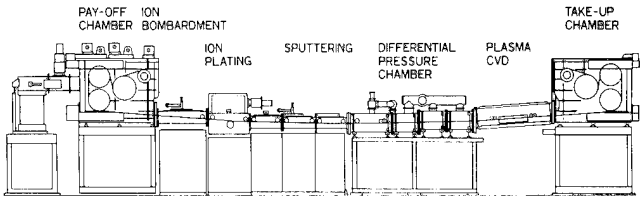

Fig. 1. Schematic diagram of the in-line dry coating process [1].

The second of the processes is a continuous dry coating process installed at Hikari Works on a semi-production scale. This process is illustrated schematically in Fig. 1. The three units are made continuous through extremely narrow slits, typically 5–15 mm. The substrate of stainless steel strip is passed along the line in contact with rolls on its top surface and is coated on its bottom surface. The ion plating and sputtering chambers are located adjacent to each other because they have very similar operating pressures. PACVD differs so much in operating pressure from the other two processes that a four-compartment differential pressure chamber is provided between the sputtering and PACVD chamber [5]. The substrate conditions are as follows; material, cold-rolled stainless steel in coil; thickness, 0.1–0.5 mm; width, 370 mm; coil length, 300 m. The substrate transfer conditions are as follows: substrate temperature, maximum of 300 °C for ion plating and sputtering, maximum of 420 °C for PACVD. The coating conditions for five different combinations of steel substrate and coating material are summarized in Table 2.

2.4. Evaluation

2.4.1. Measurement of coating thickness

The thickness of the coatings was measured by either a surface profilometer (DEKTAK) or ellipsometry in the case of transparent films.

2.4.2. Analysis of coating composition

The compositions of the films were analyzed by X-ray photoelectron spectroscopy (XPS) or glow discharge spectroscopy (GDS). The argon content coming from the processing gas was measured by Rutherford backscattering spectrometry (RBS).

2.4.3. Corrosion resistance

Specimens were tested by atmospheric exposure on a rack placed 5 m from the sea and 1 m above the ground for coatings. The modified salt spray test (MST, 5%NaCl + 0.2%H_2O_2, 35 °C, 24 h) was also utilized as an accelerated test to assess the saline environment corrosion resistance. The degree of corrosion degradation in the above methods was measured and rated by

Table 2
In-line dry coating process and deposition conditions for typical coating materials [1]

Coating species	Process	R.f. power of HCD current	Pressure (Pa)	Substrate	
				Temperature (°C)	Speed (m min^{-1})
General applications					
Al_2O_3	Sputtering	5 kW	0.133 (1×10^{-3} Torr)	200	0.1
Cr	Sputtering	5 kW	0.133 (1×10^{-3} Torr)	200	0.1
SiO_2	PACVD	35 kW	26.6 (2×10^{-1} Torr)	250	0.08
TiN	Ion plating	280 A ($\times 2$)	0.133 (1×10^{-3} Torr)	260	0.4
TiC	Ion plating	250 A ($\times 2$)	0.133 (1×10^{-3} Torr)	260	0.4
Insulation					
Al_2O_3	Sputtering	1.25–5 kW	0.133 (1×10^{-3} Torr)	200	0.01

visual inspection of the substrate after the corrosion test as described elsewhere [6]. The anodic polarization of the coating was measured with a potentiometer in 0.1 N NaCl solution.

2.4.4. Wear resistance

The wear resistance of each coating was tested by placing alumina paste between a piece of felt and the coated surface of a specimen and repeatedly rubbing the two together under a load of 200 gf cm^{-2}. The change in color before and after the test was measured using differential colorimetry.

2.4.5. Mechanical test

Adhesion was studied using a modified scratch test with a steadily increasing load. We have modified a conventional CSEM-Revetest unit to observe how the film is scratched in situ [7]. Using this equipment, we can observe the change in acoustic emission (AE) and the real-time image of the film detachment and detect accurately the critical load (L_c) value of the films. The scratch conditions employed in this study were as follows: radius of the diamond indenter tip, 0.8 mm; rate of increase in load, 100 N min^{-1}; rate of traversal of the table on which the specimens were mounted, 10 mm min^{-1}; AE sensitivity, 2.0.

The hardness was measured by a Vickers microindentation tester using a low indentation load of 5 gf.

The internal stresses were measured by the curvature of the bent substrate (a Pyrex glass disk 0.5 mm thick and 25 mm in diameter) caused by the internal stress of the film on it [8]. The curvature of the substrate was measured by a surface profilometer. The internal stress was calculated using Stoney's equation [9].

2.4.6. Electric insulation

Aluminum electrodes, 5 mm in diameter, were evaporated over the Al_2O_3 coatings and the electric resistance between the aluminum electrodes and the substrates was measured by an insulation resistance tester [10].

3. Results and discussion

3.1. General properties of the coatings

3.1.1. Coating composition

The XPS results are summarized in Table 3 for five typical coating materials produced by the continuous coating process. The [O]/[Al] ratio of the Al_2O_3 coating was around 1.5–1.6, which is roughly equal to the stoichiometric ratio of alumina. The [O]/[Si] ratio of the SiO_2 coating was slightly oxygen deficient. The chromium coating contained oxygen at the surface, although it was vapor deposited as metallic chromium. The composition of TiN was approximately equal to the stoichiometric ratio. However, TiC was intentionally deposited with a high carbon content to develop the decorative black color.

3.1.2. Corrosion resistance

Of the coating materials and processes investigated in this study, SiO_2 and Si_3N_4 coatings produced by PACVD were found to be the most suitable for corrosion resistance. Table 4 shows the corrosion resistance of SiO_2- and Si_3N_4-coated type 430 stainless steels evaluated by a modified salt spray test. From the table, it is clear that a thickness of 0.1 μm or more is enough to increase the corrosion resistance of these ceramic-coated type 430 stainless steels well above the level of

Table 3
Atomic ratios of coatings (XPS) [1]

Coating species	Atomic ratio	Depth (μm)		
		0.002	0.006	0.02
Al_2O_3	[O]/[Al]	1.54	1.53	1.55
Cr	[O]/[Cr]	12.76	6.66	1.50
SiO_2	[O]/[Si]	1.74	1.39	1.27
TiN	[N]/[Ti]	1.05	1.05	1.07
TiC	[C]/[Ti]	3.82	3.58	3.20

Table 4
Corrosion resistance of SiO_2- and Si_3N_4-coated type 430 stainless steel by batch process [2]

Material	Process	Pretreatment	Thickness (μm)	Corrosion resistance[a]
430BA	—	—	—	F
430BA	—	Nitric acid	—	D
SiO_2	PACVD	—	0.1	E–F
SiO_2	PACVD	Nitric acid	0.1	A–B
SiO_2	PACVD	Nitric acid	0.5	A–B
SiN_4	PACVD	—	0.1	D–E
Si_3N_4	PACVD	Nitric acid	0.1	A–B
Si_3N_4	Sputtering	—	0.1	F
304BA	—	—	—	C–D

[a] Rating of corrosion resistance (modified salt spray test): A, good (no rust); G, poor (severe red rust).

type 304. It should be emphasized here that the nitric acid pretreatment is the key step in making the high corrosion resistance possible. Thus a suitable surface pretreatment is a prerequisite for highly corrosion-resistant stainless steels.

The Si_3N_4 coating is also beneficial for improving the corrosion resistance as shown in Table 4. In this table, a comparison of Si_3N_4 coatings formed by PACVD and sputtering is presented. The results clearly show that the PACVD process is superior to the sputtering process in producing highly corrosion-resistant stainless steel. Detailed observation of the defect population by transmission electron microscopy indicates that the film deposited by sputtering tends to exhibit microcracks, whereas that deposited by PACVD has essentially no microcracks. In this sense, the PACVD technique is the best process examined in this study for depositing corrosion-resistant coatings, although the material selection in PACVD is limited by the availability of gases for the coatings.

As described above, certain ceramics are suitable for corrosion-resistant coatings. However, ceramics are generally brittle. Therefore when the coated stainless steels undergo deformation, the formation of microcracks is inevitable. In order to evaluate quantitatively the effect of deformation on the corrosion behavior, atmospheric corrosion tests were performed on bent specimens produced by the continuous coating process. Fig. 2 shows the results of a 1 year exposure test for five kinds of ceramic- or metal-coated stainless steels. The exposure site was a harsh environment where the specimens were exposed directly to seawater splashes on windy days. The SiO_2 coating showed the best corrosion resistance, followed by the Al_2O_3, Cr, TiN and TiC coatings. It should be noted in particular that the underside portion, labeled 4 in Fig. 2, of the convex part of the specimen is most severely corroded and the vertical portion 1 is least affected. A similar phenomenon was observed with uncoated stainless steel specimens. The effect of the coating in improving the corrosion resistance is most clearly demonstrated on the underside of the convex bent part of the specimen. The above experimental observation could be explained by the length of time taken for the underside portion to dry after the deposition and condensation of seawater splashes.

In addition to the corrosion resistance, a top coating of SiO_2 is a useful decorative color coating, since SiO_2 is essentially transparent in the visible range when its thickness is below a critical value; hence this top layer enables the undercoating color to be retained. An example is a stainless steel coated with SiO_2 as a transparent corrosion-resistant top coating and TiN as a decorative undercoating. TiN is a decorative gold color, but has poor corrosion resistance as shown in Fig. 2. Thus the top SiO_2 coating increases the corrosion resistance, and the TiN gold color remains unchanged.

The anodic polarization curves in 0.1 N NaCl solution of the two-layer film (TiN overcoated with SiO_2) are compared in Fig. 3 with those of a monolayer TiN coating and the substrate (type 304 stainless steel). The two-layer coating has a higher pitting potential than the other coatings. Thus the film overcoated with SiO_2 has an improved corrosion resistance without spoiling the decorativeness of the TiN coating. This example shows that the multiple, continuous coating system provides considerable freedom in the design of multilayer, i.e. multifunctional, coatings.

3.1.3. Wear resistance

Stainless steels are widely used for architecture, vehicles, etc. because of their good corrosion resistance and surface aesthetics. Thus a further improvement in corrosion resistance by ceramic coatings is beneficial for the development of excellent corrosion-resistant stainless steels. Ceramics can also add color to stainless steels for decorative applications. However, wear resistance is also required since the removal of surface stains by polishing is necessary to maintain a good surface appearance. It should be noted here that wear resistance in this case has to be evaluated in terms of the decorative appeal. In other words, it is necessary to keep the original decorative color even after polishing the surface. Thus the wear resistance in this case was evaluated from the change in color before and after the rubbing test using alumina paste. Fig. 4 shows the results of the wear resistance test of the various coatings. Each coating exhibited a wear resistance higher than that of the chemical conversion coating in aqueous solution. The Cr coating was found to have the best wear resistance, followed by the TiN, SiO_2, TiC and Al_2O_3 coatings. The best result for the Cr coating is mainly due to the fact that the metal is essentially colorless from the beginning. TiN keeps its good decorative golden color even after rubbing for 100 times.

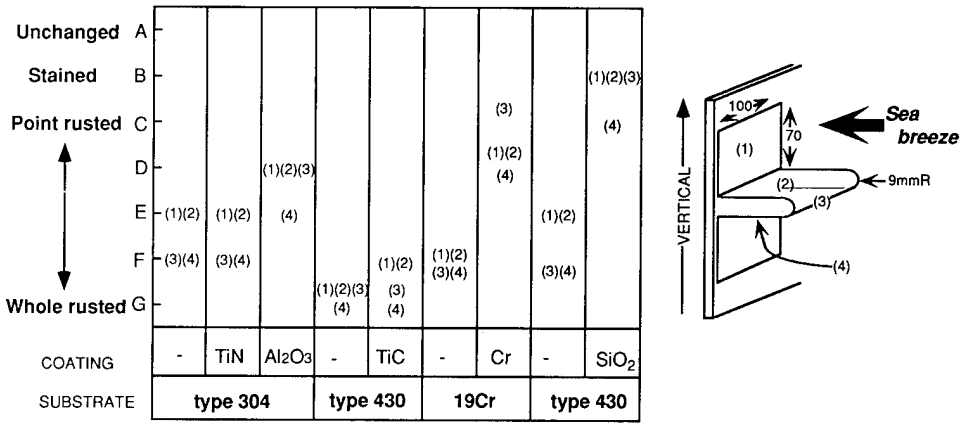

Fig. 2. Results of the atmospheric exposure test at the seashore after 1 year [1].

3.1.4. Mechanical properties of the coatings

TiN has been widely used as a decorative and wear-resistant coating because of its golden color and high hardness [11,12]. The experimental results clearly show that TiN has a high wear resistance and exhibits a decorative golden color. However, in general, the interface between the ceramic and metal is not well bonded. Therefore, in some cases, peeling off of the TiN films was observed especially when the coated stainless steels underwent deformation. Thus it is important to increase the adhesion of ceramic coatings on metallic substrates. In this section, the mechanical properties of TiN coatings applied by a batch sputtering process are investigated to reveal the basic relationship between the mechanical properties and the deposition parameters.

In this experiment, the substrates were ultrasonically cleaned in acetone and sputter cleaned at 500 W for 30 min. During sputtering, the substrate was ground and a substrate bias was not applied [7].

It was found that the operating pressure during sputtering was the most critical deposition parameter in terms of the mechanical properties of the coatings. The relationship between the internal stress and the pressure is shown in Fig. 5. It can be seen from the figure that the internal stress of the TiN film deposited at over 2.6 Pa (region 2) was slightly tensile, but compressive at less than 2.3 Pa (region 1). In region 1, the color was gold and the coating was dense. In this region, the compressive stress increased with a decrease in pressure, and at a pressure of 0.6 Pa it increased steeply from 3 to 8 GPa. In region 2, the color was dark brown and the coating had an open columnar structure.

The critical load L_c of TiN in region 1 is given in Fig. 6 as a function of pressure. The critical load, a measure of the adhesion of the films, increased with an increase in the deposition pressure, especially when the pressure was above 0.6–0.7 Pa. The hardness as a function of pressure is also given in Fig. 6. The hardness decreased with an increase in pressure. Such changes in adhesion and hardness correspond well with the change in the internal stress. As a result, TiN films have a high hardness but poor adhesion at low pressures.

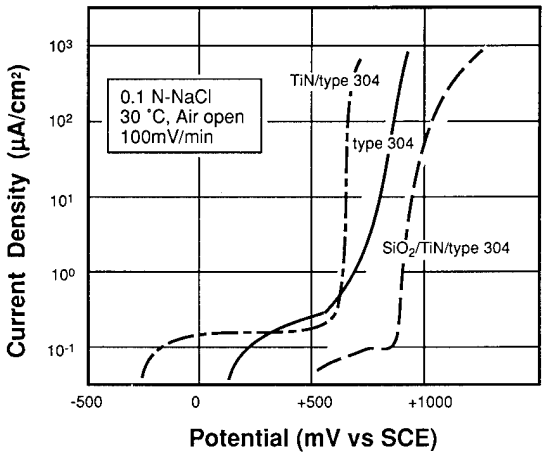

Fig. 3. Anodic polarization curves of type 430 substrate, monolayer TiN coating and TiN/SiO_2 two-layer coating [1].

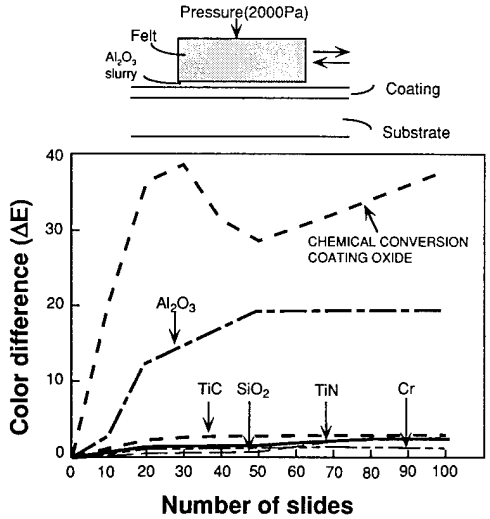

Fig. 4. Comparison of wear resistance [1].

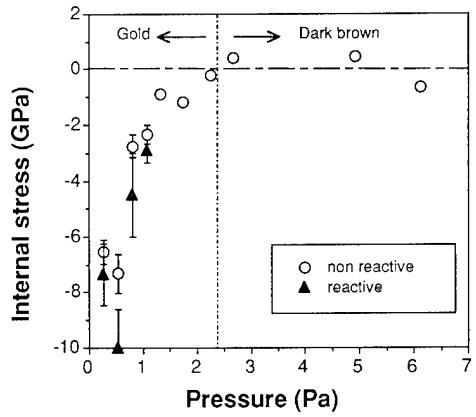

Fig. 5. Internal stress of TiN films as a function of the pressure during deposition [7].

The film adhesion to the substrate depends on the bonding energy and the internal stress. If the film stress is high, the film will easily be detached by a low external stress. In contrast, the hardness will increase when the film has a high compressive stress, because the stress resists the deformation by the loading indenter. Thus the pressure dependence of the adhesion and hardness can be explained by the change in internal stress. At a fixed pressure, we can make either good adherent films or hard films, but not both.

Although with a constant deposition pressure it is difficult to deposit a good adherent and hard film, it is possible by changing the pressure during deposition from high to low. The film with an underlayer deposited at high pressure had a higher critical load than that with an underlayer deposited at low pressure. This result shows that high-pressure deposition for the underlayer improves the adhesion. Even if the low-pressure overlayer is thick, the adhesion is good as long as the underlayer is deposited at high pressure. This indicates that the stress at the interface of the film is a key factor for obtaining good adhesion, although the total stress is also important. On the other hand, the hardness depends on the thickness of the layer deposited at

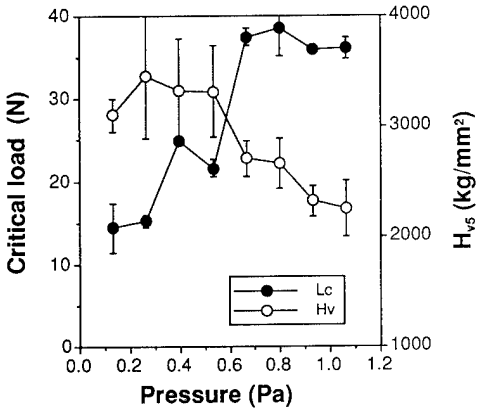

Fig. 6. Critical load and microhardness of TiN films (2 μm) on type 430 stainless steel as a function of the pressure during deposition [7].

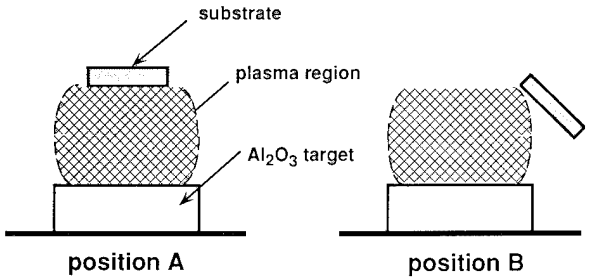

Fig. 7. Schematic drawing showing the position of the substrate for r.f. magnetron experiments [10].

low pressure. As a result, when the underlayer is deposited at high pressure, we can obtain both good adhesion and hard coatings by appropriate design of the thickness ratio.

3.1.5. Electric insulation

Electrically insulated stainless steels can be produced by depositing dielectric materials such as SiO_2 or Al_2O_3. An advantage of using these insulator-coated metals is that they not only insulate, but also possess good thermal conductivity and mechanical flexibility for microelectronic applications in contrast with conventional bulky ceramic substrates. Al_2O_3 films show good dielectric properties and a number of attempts have been made to deposit thin films with low leakage current and a high breakdown strength [13,14].

However, a major problem with the preparation of Al_2O_3 films on metals by sputtering is pinhole formation, which causes a short circuit or a deterioration of resistivity. Therefore a thicker deposit of at least a few micrometers is required to bury such pinholes [13]. In this section, we show that high-resistivity Al_2O_3 films can be prepared by a novel sputter deposition technique in which the first layer and the second layer are controlled independently, thus differentiating it from the usual one-step sputter deposition.

R.f. magnetron sputtering was used in this work [10]. Films of 500 nm total thickness were deposited on type 430BA stainless steel; 25 aluminum-sputtered top electrodes, 100 nm thick and 5 mm in diameter, were formed on insulators using a metal mask. In this experiment, the Al_2O_3 films were prepared at two different positions: the normal position (position A) and at an oblique angle off the normal (position B) as shown in Fig. 7.

Two-step processes were performed in which the first layer and second layer were controlled independently. The first layer was deposited at position B and the second layer at position A. The film properties were estimated by the insulation probability, which was defined as the percentage of the number of insulated electrodes over 20 MΩ at 1 V d.c. Fig. 8 shows the dependence of the insulation probability on the nominal thickness of the first layer deposited at position B.

It should be noted that the total thickness was 500 nm in all cases, and the second layer was deposited at position A. The experimental result clearly indicates that the insulation probability is sensitive to the first-layer thickness. Although no one-step process was able to give an insulating sample, 100% insulation probability was almost always attained by the two-step process, in which the first layer was deposited to a nominal thickness of approximately 20 nm at position B and the second layer, 480 nm thick, was deposited at position A.

We also attempted to form films by various one-step processes and other two-step processes, but the good insulation could not be achieved under any conditions except a position B–position A two-step process.

The above result suggests that the density of pinholes in insulating films is strongly affected by the substrate positions during deposition. In order to estimate the density of pinholes per unit area in a film, an aluminum-coated silicon wafer was used as a substrate. The silicon substrate was used to eliminate the effect of surface roughness. The density was estimated by electrocrystallization in an electrolyte solution ($CuSO_4 \cdot 5H_2O$) at an electrode potential of approximately -0.2 V vs. a saturated calomel electrode (SCE) by counting the number of Cu electroplated particles on the insulating film using an optical microscope. The pinhole density of the film deposited at position A was 460 cm^{-2} and that at position B was 800 cm^{-2}. However, the density of pinholes in the film deposited by a two-step process showed the lowest value, 140 cm^{-2}. Thus the novel two-step process creates fewer pinholes, and hence good insulator films.

3.2. Role of plasma in thin film growth

A number of interesting experimental observations have been made so far, in particular in terms of the relationship between the performance of the coatings and the deposition parameters.

(1) Corrosion-resistant coatings formed by PACVD are superior to those obtained by sputtering since the film deposited by sputtering tends to bear microcracks.

(2) The operating pressure during sputtering is the most critical deposition parameter in terms of the mechanical properties of the coatings. The compressive internal stress increases, and hence the hardness increases and the adhesion decreases, with a decrease in pressure.

(3) The density of pinholes in insulating films formed by sputtering is strongly affected by the substrate positions during deposition. High-resistivity Al_2O_3 films can be prepared by a novel sputter deposition technique in which the first layer and second layer are controlled independently, thus differentiating it from the usual one-step sputter deposition.

It is necessary to reveal the basic characteristics of the plasma itself in order to understand the above experimental observations. For example, in the sputtering process, the plasma is created between the sputtering target, called a cathode, and the substrate. In the plasma region, a number of species, such as neutral gases, ions and electrons, are generated by the externally supplied electricity. These species interact with the substrate and cause a variety of surface reactions, such as deposition, chemical reactions with other species, resputtering of the deposited films, surface mixing, enhancement of adatom diffusion and heating of the substrate. Although we can control the external parameters, such as the operating pressure, gas flow rate, power density, substrate position and so on, it is obvious that the environment near the growing film is the most critical factor determining the characteristics and performance of the film. In this sense, the concept used to describe electrochemical reactions may help in the understanding of the thin film growth mechanism in plasma environments, although there are a number of differences in both cases. In this sense, surface science, in particular the role of the environment in surface reactions, is the key issue in understanding, and hence controlling, the plasma-assisted coating process.

A plasma can be roughly defined as a gas consisting of ions and electrons both having approximately the same density over the Debye length. Thus electric neutralization is held over this characteristic length. In most cases, the energy necessary to generate the plasma is supplied by accelerated electrons. The accelerated electrons cause a variety of reactions, such as elastic collision, excitation, dissociation, ionization and so on. Since the excited species can react chemically with other species even at low temperatures, chemical vapor deposition can be assisted by a plasma. An external electric field is used for the ease of generation of accelerated

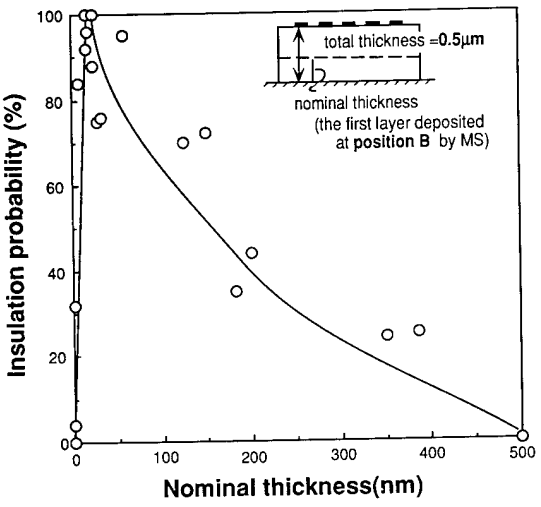

Fig. 8. Dependence of the insulation probability on the nominal thickness of the first layer deposited at position B [10].

ions for the sputtering process. Thus the plasma has unique characteristics in both physical and chemical reactions.

In the case of a low-pressure plasma, where the frequency of collisions is low, the temperature of the electrons is much higher than that of the ions since light electrons can be easily accelerated and gain high velocity without losing their energy. The typical temperature of electrons is about 10^4 K or higher, whereas that of ions stays around several hundred kelvin. Thus a low-pressure plasma is also called a low-temperature plasma.

However, the situation becomes quite different when a solid is placed in a low-pressure, low-temperature plasma. Since the velocity of electrons is much higher than that of ions, the flux of negative charge towards the solid surface is also initially higher than that of positive ions. Therefore the surface is negatively charged and develops an excess positive ion region called an ion sheath. When an external bias voltage, for example a negative bias, is applied to one of the two electrodes, an electric field is artificially generated near the cathode, and positive ions are accelerated towards this cathode and hit it. If the energy is high enough to sputter the cathode material, the material is deposited onto the anode. The depositing atoms sputtered from the cathode have an energy of several electronvolts. However, it should be noted that Ar ions, which are commonly used as the processing ions accelerated towards the cathode at several hundred electronvolts, are reflected at the cathode. Thus the neutralized and reflected Ar atoms hit the anode and hence affect the thin film growth at the anode. In other words, the growing film is always exposed to the high- energy processing gas as well as the flux of depositing atoms. This is a rough picture of the sputtering process. Thus the mobility of electrons and ions (the electrode potential), which is either unintentionally or intentionally generated, and the flux of various species having different energies are the key factors describing the sputter deposition. Fig. 9 summarizes the reactions and fundamental steps of radicals and ions in a reactive plasma.

The above picture of the sputtering process can be used to explain the dependence of the mechanical properties of TiN films on the operating pressure. In Section 3.1.4, it was found that the operating pressure during sputtering was the most critical deposition parameter in terms of the mechanical properties of the coatings, and the compressive internal stress increased (and hence the hardness increased and the adhesion decreased) with a decrease in the pressure. Scanning electron microscopy (SEM) observations also show that the density of TiN films increases with a decrease in pressure.

The above result suggests that a decrease in pressure has the same effect as a bias on the substrate. Kumer et al. [15] reported that a brown columnar film changed to

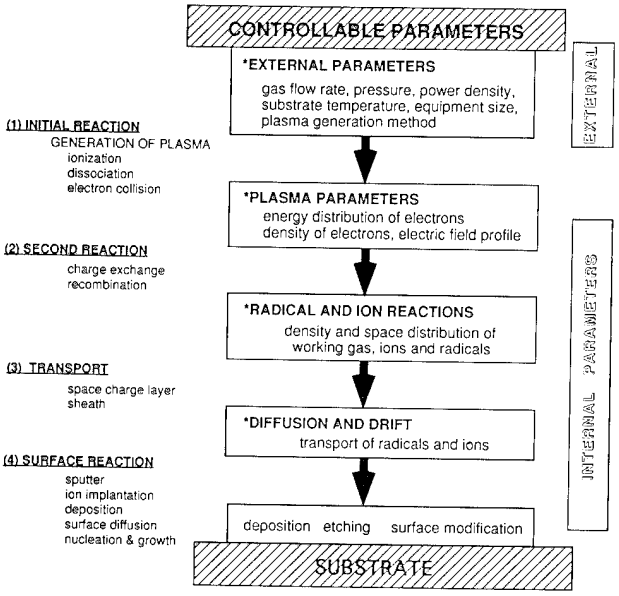

Fig. 9. Atomic and molecular reactions in reactive plasma.

a golden dense film when the substrate was negatively biased. They suggested that densification by a high-energy, argon-ion-peening effect could explain the dense structure. Hoffman and Thornton [16] investigated the stress of sputtered metal films, and explained the cause of the stresses by the argon-ion-peening effect.

On decreasing the deposition pressure, the argon-ion-peening effect becomes more evident. The energy delivered to the film surface depends on the discharge pressure. After high-pressure deposition without a substrate bias voltage, the deposited films exhibit a rough morphology and slight tensile stress because the working gas atoms or the sputtered atoms are thermalized by collision with working gas atoms, and the energy transferred to the film surface is small. On the other hand, during deposition at low pressure, energy is delivered to the film surface by the energetic gas atoms backscattered from the sputtering target or by the sputtered atoms, and a film with a smooth morphology and a large compressive stress is obtained.

The above picture is supported by the measurement of the concentration of Ar atoms in the films using proton backscattering spectroscopy [17]. It was found that the Ar content in the films is high at low operating pressure, typically 9 at.%, but low at high pressure, about 6 at.%. It is considered that the concentration of Ar atoms in the films depends on the energy of the Ar atoms impinging on the film surface.

Thus the operating pressure affects the energy of the processing gas atoms delivered to the growing films, and hence the density, morphology, internal stress and adhesion of the films.

The above picture can also be used to explain the experimental observation that the density of pinholes in

insulating films formed by sputtering is strongly affected by the substrate position during deposition. We showed that high-resistivity Al_2O_3 films could be prepared by a novel sputter deposition technique in which the first layer and second layer were controlled independently, thus differentiating it from the usual one-step sputter deposition. At the initial stage, strong bombardment at position A in the plasma leads to large adatom-depleted islands. These zones will cause pinhole-type defects. A thicker deposit over several micrometers is therefore required to bury such pinholes. In contrast, with weak bombardment, i.e. position B, large adatom-depleted zones are difficult to form. The energetic particle assistance at position A can lead to densification of the near-surface region and the burial of smaller defects. It is reasoned that the dependence of the insulation probability on the thickness of the first layer, typically 20 nm, is due to a necessary minimum thickness for the burial of defects. This thickness depends on how the defects arise in the initial stages, i.e. larger defects arising in a film at position A cannot be buried at position B, while smaller defects arising at position B can be covered with a second layer, 480 nm thick, at position A. We believe that it is necessary to optimize the deposition conditions for the formation of the first layer and the second layer independently in order to achieve high insulation probability.

This example clearly indicates that the initial stage of thin film growth should be carefully controlled to obtain the most desirable island structure for the latter stage. However, the optimum conditions for the latter stage are not necessarily the same as those for the initial stage. Thus, in general, the initial stage, in which the nucleation of the island structure is critical, and the latter stage, in which the coalescence of islands and morphology development are critical, should be separately optimized in order to obtain high-quality thin films.

The two-step process may also be applicable to the design of wear-resistant coatings. As shown in Section 3.1.4, a good adherent and hard film can be obtained by changing the pressure during deposition from high to low even when the same material is deposited. Thus the design of the plasma coating process should be performed by considering the basic aspects of the thin film growth mechanism in the environment, where the behavior of energetic particles is the crucial factor.

4. Conclusions

In this paper, the role of the environment on coated stainless steels was discussed from two different points of view. The first involved the performance of ceramic-coated stainless steels in corrosive and mechanically stressed environments. It was found that an SiO_2 coating deposited by PACVD led to the largest increase in the corrosion resistance of type 430 stainless steel to well above the level of type 304 stainless steel. It was also possible to coat stainless steel with TiN and other ceramics for decorative applications. The combination of the color of the TiN undercoating and the SiO_2 corrosion-resistant top coating provides the potential to develop multifunctional stainless steels. Other examples are wear-resistant coatings and insulating coatings.

The second viewpoint was the influence of the plasma environment used to synthesize the coated materials on the quality of thin films. Since the growing film is always exposed to the plasma during deposition, the flux and energy of various species, such as the processing gas, ions and depositing atoms, are the key factors in describing thin film growth. We believe that it is necessary to optimize the deposition conditions for the initial stage and latter stage independently in order to achieve high-quality thin films.

References

[1] T. Takahashi, Y. Oikawa, T. Komori, I. Ito and M. Hashimoto, *Surf. Coat. Technol., 51* (1992) 522.
[2] M. Hashimoto, S. Miyajima, W. Ito, S. Ito, T. Murata, T. Komori, I. Ito and M. Onoyama, *Surf. Coat. Technol., 36* (1988) 837.
[3] H. Omata, S. Ito and T. Murata, U.S. Patent 4,612,095, 1986.
[4] H. Omata, S. Ito, M. Yabumoto and T. Murata, *Proc. 4th Asian-Pacific Corrosion Control Conf., Tokyo, May 26–31, 1985*, Vol. 1, 1985, p. 475.
[5] Y. Hosoi, I. Ito, S. Saida, T. Murata, S. Ito and N. Okubo, Japanese Patent Application Publication, No. Sho 62-205272, September 9, 1987.
[6] U. Nakata, I. Ito, M. Onoyama and H. Inagaki, *Proc. 28th Joint Symp. on Corrosion Science and Technology*, Japan Society of Corrosion Engineering, 1981, p. 18.
[7] Y. Kubo and M. Hashimoto, *Surf. Coat. Technol., 49* (1991) 342.
[8] J.D. Finegan and R.W. Hoffman, *J. Appl. Phys., 30* (1950) 597.
[9] G. Stoney, *Proc. R. Soc. London, Ser. A, 32* (1909) 172.
[10] S. Tokumaru and M. Hashimoto, *Surf. Coat. Technol., 54/55* (1992) 303.
[11] K. Nakamura, K. Inagawa, K. Tsuruoka and S. Komiya, *Thin Solid Films, 40* (1977) 155.
[12] B. Zega, M. Kornmann and J. Amiguet, *Thin Solid Films, 45* (1977) 577.
[13] M.N. Khan, *Thin Solid Films, 124* (1985) 55.
[14] J. Saraie, S. Goto, Y. Kitao and Y. Yodogawa, *J. Electrochem. Soc., 134* (1987) 2805.
[15] N. Kumer, J.T. McGinn, K. Pourrezaei, B. Lee and E.C. Douglas, *J. Vac. Sci. Technol. A, 6* (3) (1988) 1602.
[16] D.W. Hoffman and J.A. Thornton, *Thin Solid Films, 40* (1976) 355.
[17] K. Tanaka, Y. Kubo, N.B. Chilton and M. Kumagai, *Nucl. Instrum. Methods B, 83* (1993) 525.

ELSEVIER

Materials Science and Engineering A198 (1995) 85–90

MATERIALS SCIENCE & ENGINEERING A

Oxidation resistance of TiAl significantly improved by combination of preoxidation and Hf addition

S. Taniguchi, T. Shibata, S. Sakon*

Department of Materials Science and Processing, Faculty of Engineering, Osaka University, 2-1 Yamadaoka, Suita, Osaka 565, Japan

Abstract

The cyclic-oxidation resistance of a TiAl coupon in a flow of purified oxygen at 1300 K has been significantly improved by preoxidation at 1200 K for 100 ks in a pack of a mixture of 70 mass% chromia and 30 mass% metallic chromium powders under an Ar atmosphere. The excellent oxidation resistance obtained is attributable to the formation of alumina scales by the preoxidation, where oxygen partial pressure was thought to be maintained very low. The addition of 0.24 mass% Hf to TiAl improved the oxidation resistance by forming scales rich in alumina. A combination of the preoxidation and the Hf addition further improved the oxidation resistance. After 10 cycles (200 h) of oxidation at 1300 K the scale thickness was still less than 1 μm.

Keywords: Oxidation resistance; TiAl; High temperature; Hf addition; Preoxidation; Cr_2O_3 powder

1. Introduction

The measures for improving high-temperature oxidation resistance of TiAl and TiAl-base alloys are receiving much attention, because they are expected to be high-temperature construction materials having high specific strengths. Further, mechanical properties of a range of such materials are being improved as a result of extensive research activity [1–3].

The measures for improving the oxidation resistance studied so far involve alloying additions [4–9] and surface treatments [10–16]. The present authors have shown [17,18] that the preoxidation of TiAl coupon specimens, packed with a mixture of chromia and metallic chromium powders, at 1200 K for 100 ks is very effective for forming alumina scales which are very protective during the subsequent oxidation at 1300 K for at least 10 cycles (200 h). The formation of the protective scales by the preoxidation was explained in terms of oxidation under a very low oxygen partial pressure, which enhanced preferential oxidation of Al. Further, the addition of 0.24 mass% Hf to TiAl was found [19] to be very effective in improving its oxidation resistance.

The present paper deals with the effect of a combination of preoxidation and Hf addition.

2. Experimental procedures

2.1. Specimen

Coupon specimens measuring about 15 × 10 × 1 mm^3 were machined from TiAl and TiAl–0.24 mass% Hf ingots, the chemical compositions of which are shown in Table 1. Metallographic examinations and X-ray diffraction (XRD) revealed that both specimens consisted predominantly of equiaxed γ-TiAl grains and a few γ-TiAl grains containing the Ti_3Al phase in parallel platelets. The coupon specimens were abraded with a series of SiC polishing papers of up to 1000 grit and then thoroughly washed with acetone in an ultrasonic bath.

2.2. Preoxidation

Three or four prepared specimens were packed with a mixture of 70 mass% chromia and 30 mass% metallic chromium powders in an alumina tube having an inner diameter of 30 mm and a length of 140 mm. The preoxidation was performed by heating the tube in a muffle furnace at 1200 K for 100 ks under an Ar atmosphere. These conditions were decided on the basis of the best oxidation resistance obtained in the previous study [17,18], where the mass ratio of chromia powder was varied as 30%, 70% and 100%, and the temperature

* Present address: Matsushita Electric Co. Ltd., Kadoma 1048, Kadoma-shi, Osaka 571, Japan.

SSDI 0921-5093(94)04511-9

Table 1
Chemical compositions of the TiAl and TiAl–Hf specimens (mass%)

	Al	Ti	Hf	Fe	C	H	O	N
TiAl	37.8	Balance		0.010	0.006	0.002	0.044	0.011
TiAl–Hf	36.2	Balance	0.24	0.040	0.005	0.005	0.012	0.004

as 1100, 1200 and 1300 K. Chemical reagent powders were used in the experiment. Then the specimens were taken out of the tube, washed ultrasonically in a bath of acetone, and dried in air.

2.3. Cyclic oxidation

The oxidation resistance was assessed by a cyclic oxidation test in flowing purified oxygen under 1 atm pressure. One cycle consisted of heating to 1300 K at a rate of about 0.3 K s^{-1} and holding at temperature for 72 ks (20 h), and then cooling to room temperature in about 5 ks. The exact temperature pattern was attained by using an infrared image furnace. Two specimens were placed in an alumina boat, which was then placed in a transparent quartz tube. The specimen temperature was monitored with a (Pt–13%Rh)/Pt thermocouple attached to a dummy specimen placed very close to the specimen. The atmosphere in the furnace was replaced with oxygen gas which was purified by flowing through towers of silica gel, phosphorus pentoxide and alkali asbestos in this order. The oxidation run was started by switching on the furnace. After each cycle the specimens were taken out of the furnace and subjected to mass measurement and visual inspection. Then they were returned to the furnace for the next run.

2.4. Metallographic examinations

The specimens after preoxidation and after cyclic oxidation were examined by XRD using Cu Kα radiation at 40 kV and 30 mA. The coupon specimens with scales were tested in XRD.

Outer surfaces and fractured sections of the specimens were observed by scanning electron microscopy (SEM). Elemental analyses were performed by energy-dispersive X-ray spectroscopy (EDS) or wavelength-dispersive X-ray spectroscopy (WDS) and X-ray photoelectron spectroscopy (XPS). Optical microscopy was also used in some cases.

3. Results

3.1. Kinetic test

The results of cyclic oxidation at 1300 K are summarized in Fig. 1, which includes the results for the non-treated specimens for comparison. The mass gain is about 25×10^{-3} kg m^{-2} after 1 cycle (20 h) for the non-treated TiAl specimen. Contrary to this, the non-treated TiAl–Hf specimen shows much smaller mass gain, indicating a remarkable effectiveness of Hf addition to TiAl.

The preoxidation treatment further decreases the mass gains for both the TiAl and TiAl–Hf specimens, and their small mass gains continue for up to 10 cycles. The combination of preoxidation and Hf addition results in extremely small mass changes, implying the formation of a very protective scale by the combination.

3.2. Metallographic examinations

The oxides identified by XRD and XPS after the preoxidation and the subsequent cyclic oxidation were α-Al_2O_3, rutile (TiO_2), and chromia which was thought to originate from the powder used for the preoxidation. No hafnium oxide was found, probably because of its very small amount.

An example of an XPS chart is shown in Fig. 2, which is for a TiAl specimen after the preoxidation. Both rutile and alumina were formed on the outer surface. As the sputtering toward the depth direction proceeds, the amount of alumina increases, implying the establishment of an alumina-rich layer beneath the thin outer layer. This view was supported by examinations of fractured sections with SEM and EDS, which will be shown later. A similar result was obtained for a TiAl–Hf specimen after the preoxidation. On the other hand, relatively thick outer rutile layers were formed in scales for the non-preoxidized specimens.

The results of XRD also showed the formation of scales very rich in alumina, except for the non-preoxidized TiAl specimen. The scale on the non-preoxidized TiAl specimen was thick and consisted of an outer rutile layer and an inner layer which is a porous mixture of rutile and alumina grains. This structure was similar to that often reported [20–22].

Fig. 3 shows outer surfaces (Figs. 3(a) and 3(b)) and fractured sections (Figs. 3(c) and 3(d)) of the TiAl specimens preoxidized (Figs. 3(a) and 3(c)) and subsequently oxidized for 10 cycles (Figs. 3(b) and 3(d)). Polishing marks (parallel lines) are recognizable in Figs. 3(a) and 3(b), implying that the scales are very thin. The particles remaining in Fig. 3(a) were powders used for the packing. Most of these particles seem to be

incorporated in the scales after 10-cycle oxidation as shown in Fig. 3(b).

The thickness of the scale after preoxidation is less than 1 μm as shown by the arrows in Fig. 3(c). The scale thickness increased very slightly by 10-cycle oxidation as similarly shown in Fig. 3(d). EDS analyses, summarized in Table 2 for areas 1 to 7 in Figs. 3 and 6 below, show the formation of thin layers where the Al content was decreased beneath the scale, in areas 1, 3 and 4. The Al present there was thought to be used for forming the alumina-rich scales.

Fig. 4 shows line profiles of Al and Ti across the scale (right-hand end) shown in Fig. 3(d). From the above results together with the results of XRD we can say that alumina scales were formed by the preoxidation or cyclic oxidation for a short period.

Fig. 5 shows outer surfaces (Figs. 5(a) and 5(b)) and fractured sections (Figs. 5(c) and 5(d)) of the TiAl–Hf specimens preoxidized (Figs. 5(a) and 5(c)) and subsequently oxidized for 10 cycles (Figs. 5(b) and 5(d)). Similar to the TiAl specimen shown in Fig. 3, polishing marks and particles remaining on the surfaces can be seen in Figs. 5(a) and 5(b). The fractured sections again show that the scales, shown by arrows, are very thin after the preoxidation (Fig. 5(c)) and the subsequent cyclic oxidation for 10 cycles (Fig. 5(d)).

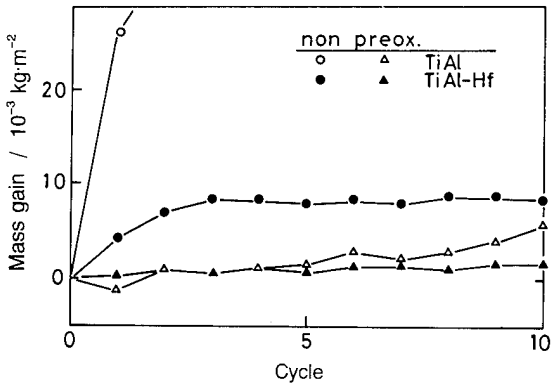

Fig. 1. Summary of the cyclic-oxidation curves of TiAl and TiAl–Hf specimens at 1300 K in a flow of purified oxygen under atmospheric pressure. The preoxidation is very effective for improving the oxidation resistance.

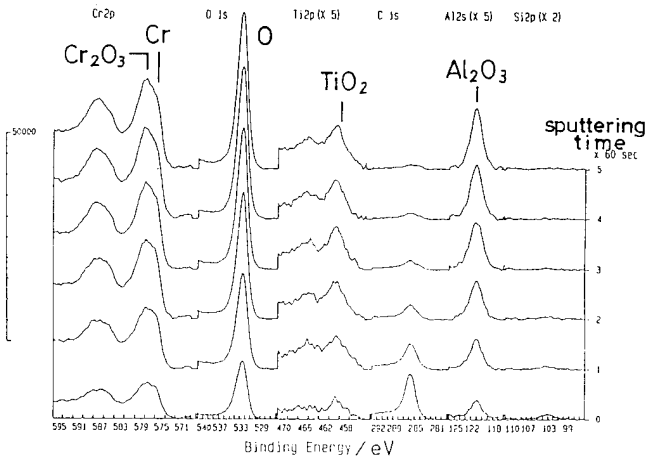

Fig. 2. An example of an XPS chart for the preoxidized TiAl specimen, showing the formation of a scale rich in alumina.

The EDS analyses revealed results very similar to those obtained for the TiAl specimen. In particular, the scales are very rich in Al and Al-impoverished layers are formed beneath them.

Fig. 6 shows outer surfaces (Figs. 6(a) and 6(b)) and fractured sections (Figs. 6(c) and 6(d)) of a TiAl specimen oxidized for 10 cycles (Figs. 6(a) and 6(c)) and a TiAl–Hf specimen oxidized for 5 cycles (Figs. 6(b) and 6(d)). Neither specimen was preoxidized.

The outer surfaces (Figs. 6(a) and 6(b)) show rutile grains. The TiAl specimen formed a very thick scale (upper half in Fig. 6(c)), the structure of which is similar to that found in previous studies [20–22]. On the other hand, the TiAl–Hf specimen formed a thin scale, shown by arrows in Fig. 6(d), rich in Al, even though rutile grains can be seen on the surface (Fig. 6(b)). An Al-impoverished layer, area 7, was again formed next to the alumina-rich scale.

4. Discussion

4.1. Influence of preoxidation

There is a general agreement [20–22] on the structure of a scale formed on TiAl in oxygen or air in the temperature range around 1100–1400 K. The general scale structure is similar to Fig. 6(c). The oxide scale consists mainly of two layers: an outer layer consisting mainly of rutile grains and a porous inner layer which is a mixture of rutile and alumina grains. The inner layer contains many small pores uniformly distributed. Alumina grains are enriched near the interface between the two layers. However, they cannot be sufficiently continuous to become a protective layer. In addition, there are several large voids near the interface between the two layers. Since the mass transport through rutile is much faster than through alumina, scales containing a large fraction of rutile cannot be protective. Therefore the formation of an alumina scale or at least a continuous alumina layer in the scale is prerequisite for attaining sufficient oxidation resistance for TiAl.

Contrary to the above, the preoxidation in the present study resulted in the formation of scales very rich in alumina or virtually alumina scales of thicknesses less than 1 μm. Their protectiveness during the subsequent cyclic oxidation at 1300 K is excellent as shown in Fig. 1.

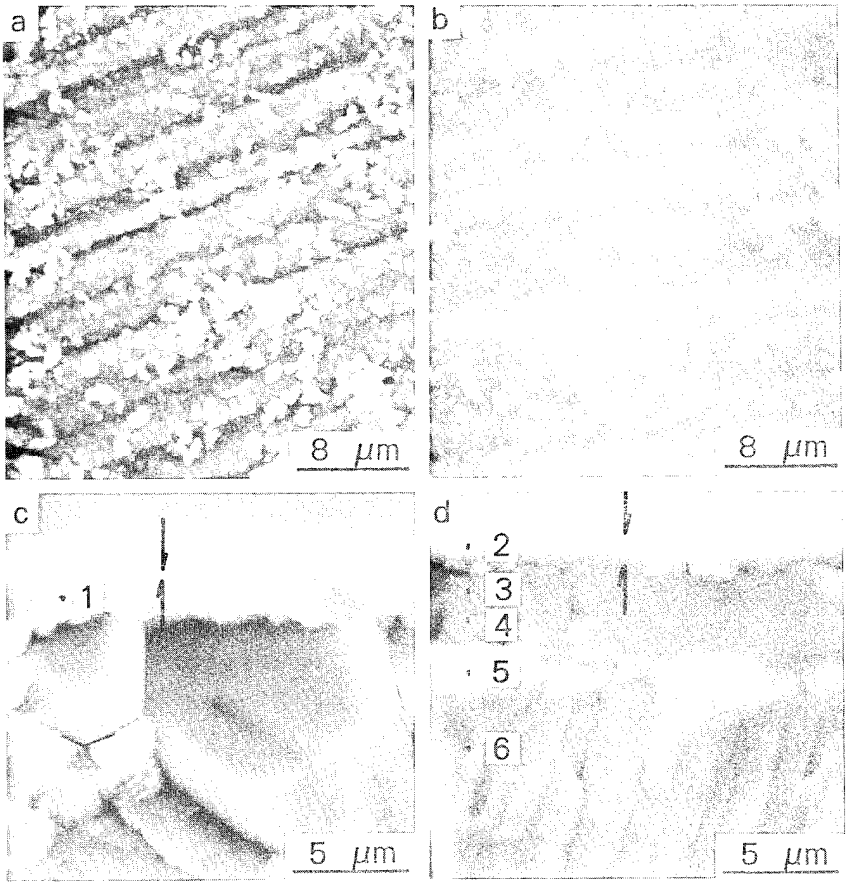

Fig. 3. (a), (b) Outer surfaces and (c), (d) fractured sections of TiAl specimens (a), (c) preoxidized and (b), (d) subsequently oxidized at 1300 K for 10 cycles. Scales, shown by arrows in (c) and (d), are very thin.

The formation of the alumina-rich scales is attributable to a low oxygen partial pressure which may cause preferential oxidation of aluminium. Even though the dissociation pressures of alumina and rutile are close to each other, and are lower than that of chromia, kinetic factors such as slow rate of oxygen supply to the specimen surface may have led to the good result.

4.2. Influence of Hf addition

The effect of Hf addition is clearly shown in Fig. 1, where the TiAl–Hf specimen shows much smaller mass gains than TiAl and the scales after preoxidation and the subsequent cyclic oxidation are very thin. In a previous study [19] a detailed structural examination was performed for TiAl and TiAl–Hf specimens. The addition of Hf resulted in the formation of two alumina-rich layers in the scale. One is beneath the outer rutile layer and the other is next to the substrate. The

Table 2
EDS analyses for areas 1–7 in Figs. 3 and 6 (mol.%)

Area	Al	Ti	Cr
1	45.9	52.6	1.5
2	81.6	4.2	14.2
3	39.1	60.9	–
4	37.1	62.9	–
5	45.0	55.0	–
6	46.9	53.1	–
7	36.2	63.8	–

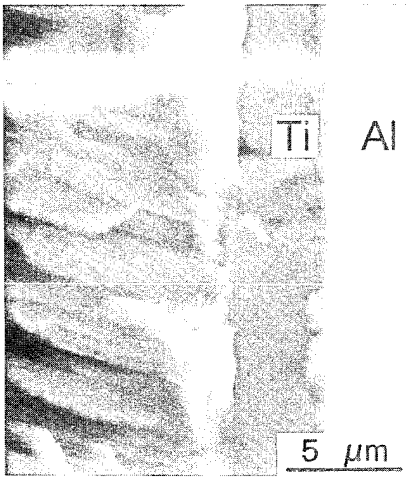

Fig. 4. EDS line profiles of Al and Ti across the scale (right-hand end) shown in Fig. 3(d), showing that the scale is virtually alumina.

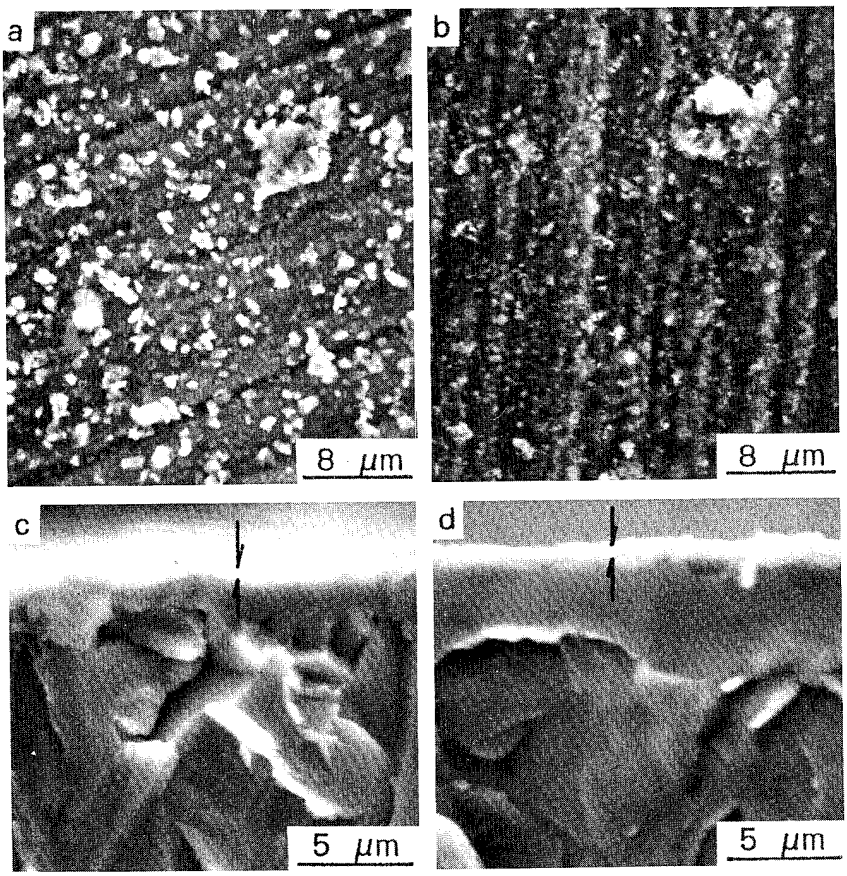

Fig. 5. (a), (b) Outer surfaces and (c), (d) fractured sections of TiAl–Hf specimens (a), (c) after preoxidation and (b), (d) subsequently oxidized at 1300 K for 10 cycles. Scales, shown by arrows in (c) and (d), are very thin.

effect of Hf addition was thus found to enhance alumina growth during the early oxidation period.

4.3. Influence of Cr

Since the preoxidation was performed using chromia and metallic chromium powders, and they remain on the specimen surface after the preoxidation, there might be some influence on the nature of the scale formed by the preoxidation. In particular, as the cyclic oxidation proceeds, these particles are incorporated in the scale and metallic chromium may be oxidized. However, alumina and chromia having the same crystal structure dissolve in each other. Therefore it is thought that they form a stable oxide. Since the effect of preoxidation appears at the beginning of the cyclic oxidation, the incorporation of chromia into the scale would have smaller influence, if any.

In addition, if a small amount of chromium is dissolved in rutile, this will enhance the oxidation according to the valence-control rule. It is known [4,8] that a small addition of Cr to TiAl enhances the oxidation. However, in the present study the scales formed by the preoxidation were very protective. Therefore it can be concluded that such an effect is not operative.

Further, a recent study [23] in which only rutile powder was used for preoxidation showed the formation of similarly alumina-rich scales. In this case there is no possibility of incorporation of foreign elements. Therefore the excellent oxidation resistance obtained by the preoxidation in this study is primarily attributable to the preoxidation under low oxygen partial pressure. Of course, chromium may have some influence, and this point should be studied further.

5. Conclusion

The preoxidation of TiAl, buried in a mixture of 70 mass% chromia and 30 mass% metallic chromium powders, at 1200 K for 100 ks under an Ar atmosphere resulted in the formation of very protective scales. They are sufficiently resistant to cyclic oxidation at temperatures between room temperature and 1300 K for at least 10 cycles (200 h). The addition of 0.24 mass% Hf to TiAl further improved the oxidation resistance.

Acknowledgements

The authors are grateful to Mr. S. Yamauchi of Sumitomo Sitix Ltd. for supplying the specimen ingots

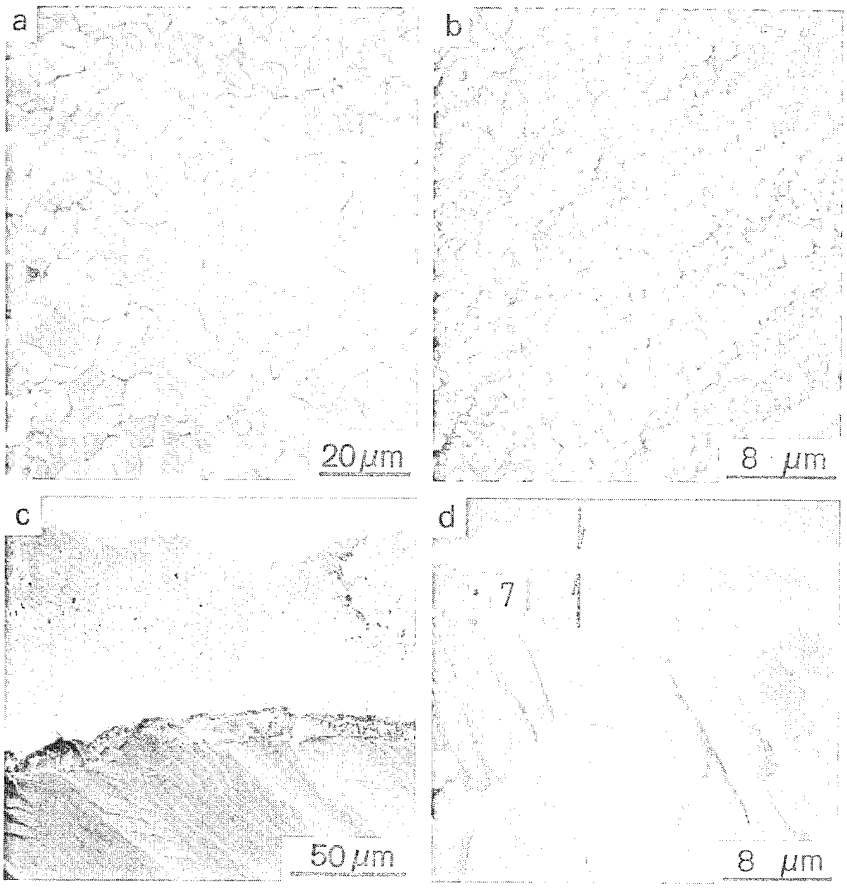

Fig. 6. (a), (b) Outer surfaces and (c), (d) fractured sections of (a), (c) a TiAl specimen oxidized at 1300 K for 10 cycles, and (b), (d) a TiAl–Hf specimen oxidized for 5 cycles.

and to Mr. J. Nakata of our laboratory for his partial assistance in the experimental work. A part of this work was supported by a Grant in Aid in the Scientific Research of the Ministry of Education, Science and Culture of Japan.

References

[1] O. Izumi (ed.), *Proc. Int. Symp. on Intermetallic Compounds (JIMIS-6)*, The Japan Institute of Metals, Sendai, 1991.
[2] H.A. Lipsitt, D. Shechtman and R.E. Schafrik, *Metall. Trans. A, 6* (1975) 1991.
[3] T. Kawabata, T. Kanai and O. Izumi, *Acta Metall., 33* (1985) 1355.
[4] K. Kasahara, K. Hashimoto, H. Doi and T. Tsujimoto, *J. Jpn. Inst. Met., 54* (1990) 948.
[5] Y. Ikematsu, T. Hanamura, H. Morikawa, M. Tanino and J. Takamura, in O. Izumi (ed.), *Proc. Int. Symp. on Intermetallic Compounds (JIMIS-6)*, The Japan Institute of Metals, Sendai, 1991, p. 191.
[6] H. Anada and Y. Shida, in O. Izumi (ed.), *Proc. Int. Symp. on Intermetallic Compounds (JIMIS-6)*, The Japan Institute of Metals, Sendai, 1991, p. 731.
[7] T.A. Wallace, R.K. Clark, S.N. Sankaran and K.E. Wiedemann, in R.H. Jones and R.E. Ricker (eds.), *TMS Proc. Conf. on Environmental Effects on Advanced Materials* (1991) 79.
[8] D.W. McKee and S.C. Huang, *Corros. Sci., 33* (1992) 1899.
[9] S. Becker, A. Rahmel, M. Schorr and M. Schutze, *Oxid. Met., 38* (1992) 425.
[10] J. Subrahmanyam and J. Annapurna, *Oxid. Met., 26* (1986) 275.
[11] A. Takei and A. Ishida, *Rep. 123rd Committee of The Japan Society for the Promotion of Science*, Vol. 31, JSPS, Tokyo, 1990, p. 327.
[12] M. Yoshihara, T. Suzuki and R. Tanaka, *Tetsu To Hagane, 77* (1991) 274.
[13] T. Shimizu, T. Iikubo and S. Isobe, *Mater. Sci. Eng. A, 153* (1992) 602.
[14] D.W. McKee and K.L. Luthra, *Surf. Coat. Technol., 56* (1993) 109.
[15] S. Taniguchi, T. Shibata, N. Aasanuma, H. Lou, F. Wang and W. Wu, *Oxid. Met., 39* (1993) 457.
[16] S. Taniguchi, T. Shibata, T. Yamada, X. Liu and S. Zou, *ISIJ Int., 33* (1993) 869.
[17] S. Taniguchi, T. Shibata and S. Sakon, in O. Izumi (ed.), *Proc. Int. Symp. on Intermetallic Compounds (JIMIS-6)*, The Japan Institute of Metals, Sendai, 1991, p. 719.
[18] S. Taniguchi, T. Shibata and S. Sakon, *Zairyo To Kankyo, 41* (1992) 453.
[19] S. Taniguchi, T. Shibata, H. Juso and N. Katoh, *Oxid. Met., 42* (1994) 205.
[20] K. Kasahara, K. Hashimoto, H. Doi and T. Tsujimoto, *J. Jpn. Inst. Met., 53* (1989) 58.
[21] Y. Umakoshi, M. Yamaguchi, T. Sakagami and T. Yamane, *J. Mater. Sci., 24* (1989) 1599.
[22] S. Taniguchi, T. Shibata and S. Itoh, *Mater. Trans. Jpn. Inst. Met., 32* (1991) 151.
[23] S. Taniguchi, T. Shibata, A. Murakami and K. Chihara, *Oxid. Met., 42* (1994) 17.

ELSEVIER

Materials Science and Engineering A198 (1995) 91–102

MATERIALS SCIENCE & ENGINEERING A

Role of transport properties in corrosion product growth

J.H. Payer, G. Ball, B.I. Rickett, H.S. Kim

Department of Materials Science and Engineering, The Case School of Engineering, Case Western Reserve University, Cleveland, OH 44106, USA

Abstract

The tendency for corrosion and the observed rate of corrosion are determined in large part by the transport properties of thin corrosion product layers. Both ionic and electronic transport are important. For continued corrosion, a corrosion product film capable of high ionic transport is required at the metal surface. The electronic transport properties will affect the spatial distribution of reduction reactions in the corroding system. In this paper, a generalized model for a corroding system is presented, and the relevant processes that control corrosion are identified. Four systems currently under study in our research group are diagnosed in relation to the generalized model: copper in sulfurous gases, metals in chloride solutions, bronze disease of ancient artifacts and silver in sulfurous gases.

Keywords: Corrosion; Bronze; Copper; Silver

1. Introduction

Atmospheric corrosion has recently received increased interest, and our understanding has benefited from the application of several new test methods for controlled exposures and the increased use of analytical techniques to determine the chemistry and structure of corrosion products. A major factor driving this renewed interest in the mature field of corrosion has been the ubiquitous usage of microelectronic devices for communication, computing and process control. The reliability of these devices depends upon the integrity of thin film structures, and nearly immeasurable amounts of corrosion can destroy the functionality of thin films or can result in high resistance faults from thin layers of corrosion products. The corrosion processes often occur in moist air that contains corrosive species at parts per billion concentrations. The electrolyte which supports the corrosion reactions may be as thin as several monolayers of water adsorbed on the surface.

The tendency for corrosion and the observed rate of corrosion are determined in large part by the transport properties of thin corrosion product layers. Both ionic and electronic transport are important. The reactive metal substrate is seldom, if ever, in direct contact with the electrolyte; instead, a corrosion product layer separates the metal and the aqueous phase. If the layer is a barrier to transport, the corrosion rate is low and the metal is categorized as passive under the exposure conditions. If the layer is not a barrier, corrosion proceeds. For continued corrosion, a corrosion product film capable of high ionic transport is required at the metal surface. The electronic transport properties will affect the spatial distribution of reduction reactions in the corroding system. With sufficient electronic conductivity, reduction reactions can proceed at the outer surface of the corrosion product layer, i.e. the corrosion product can act as an electrode for electrochemical reactions.

In this paper, a generalized model for a corroding system is presented, and the relevant processes that control corrosion are identified. Four systems currently under study in our research group are diagnosed in relation to the generalized model.

(1) Copper in sulfurous gases. Copper exposed to clean moist air develops a thin protective oxide layer, whereas copper exposed to moist air with parts per billion concentrations of sulfurous gases corrodes rapidly with the growth of thick tarnish films. The growth of the tarnish films is interpreted in terms of the transition from a protective oxide layer to a non-protective, mixed oxide/sulfide layer.

(2) Metals in chloride solutions. A layer of copper chloride develops on the copper surface and rapid

SSDI 0921-5093(94)04512-7

corrosion rates are supported by transport through this layer. Several other metal chloride systems are cited.

(3) Bronze disease of ancient artifacts. The eruption of voluminous, powdery, green corrosion products on apparently sound bronze artifacts when they are removed from anaerobic burial environments is interpreted in terms of the role of a thick layer of copper chloride that develops on the objects during burial.

(4) Silver in sulfurous gases. The corrosion rate of silver in single and mixtures of sulfurous gases is interpreted in terms of the transition from a protective oxide layer to non-protective sulfide layers. The effects of mixed gases on corrosion rates are interpreted in terms of the generalized model.

For each of the systems, current areas of focus and work in progress are described.

2. Model of corroding systems

Our general model of the atmospheric corrosion process is described in this section. The structure of corrosion product films on the metal and the processes that control the rate of corrosion are identified. The model is applied here for the diagnosis of corroding systems where a thin layer of electrolyte is present. This condition pertains to indoor and outdoor environments where relative humidities are sufficient to result in a thin adsorbed layer of moisture on the metal. Corrosion in thin layer electrolytes is also experienced when equipment and devices are operated under condensing conditions for moisture on surfaces. In all cases, the corrosion process is electrochemical, and the principles developed for corrosion in bulk electrolytes with complete immersion pertain, with consideration of the special constraints imposed by the thin electrolyte layer.

Four stages in the development of a corroding metal system are shown schematically in Fig. 1. In the absence of the corrosive gas species, a reactive metal exposed to air develops a thin (2–5 nm) protective film. This film is often a metal oxide or hydroxide which has

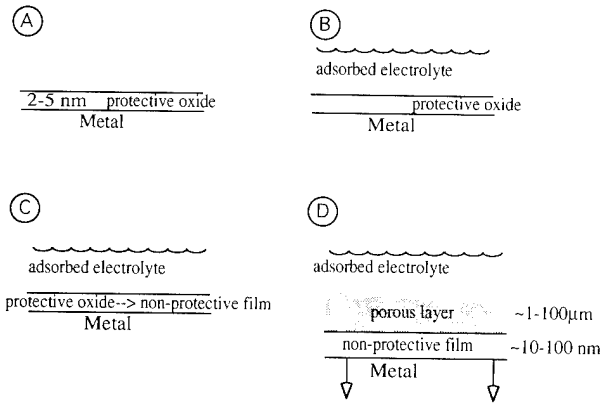

Fig. 1. Four stages in the development of a corroding metal system.

low ionic transport properties. This creates a barrier to further corrosion, and the metal is passive. On exposure to moist air above a critical relative humidity, a thin (several monolayers) adsorbed water layer forms on the surface. The absorption of atmospheric gases, dissolution of ionic species on the surface and deposition of airborne particulates into the water layer control the composition of the electrolyte. For corrosion to initiate, the protective layer on the metal must be changed to a non-protective layer that has substantial ionic transport. The non-protective layer with high ionic transport typically remains thin (several hundreds of nanometers) and becomes an inner layer of a duplex film of corrosion products. A thicker (several micrometers or greater) outer layer develops through the precipitation of soluble species and further reaction of the corrosion products with the atmosphere. The outer layer is porous or cracked and can permit the penetration of water and gases.

For all of the systems considered here, it is assumed that corrosion proceeds on metal that is covered by a non-protective film. Cations are produced by the oxidation of metal at the metal/inner layer interface. Cations and/or anions move through the non-protective film. The electrolyte is not in direct contact with the metal. The critical factors are therefore those that affect (a) the competition between the formation of protective and non-protective films on the metal, (b) the ionic and electronic transport properties through the inner layer and (c) the composition and structure of the outer layer. Conditions that promote protective film stability stifle the corrosion, and conditions that promote the stability of a non-protective inner layer are required for corrosion to proceed.

A schematic diagram of a cross-section through a bilayer corrosion product film on a corroding metal is shown in Fig. 2. A compact inner layer is adjacent to the metal surface, and a porous layer of corrosion products and deposits comprises the outer layer. There is an aqueous solution adsorbed on the outer layer which penetrates the layer through pores and cracks. A gaseous atmosphere is in contact with the thin electrolyte.

The inner layer is a non-protective film that has high ionic transport and may have significant electronic conductivity. This layer is represented in the figure as a metal chloride or sulfide. The inner layer is thin, i.e. on the order of 10–100 nm. The outer layer is porous, non-protective and thicker than the inner layer, i.e. on the order of 1–100 μm. This layer contains oxides, hydroxides, sulfates, oxychlorides, etc. These compounds result from precipitation from the aqueous solution, reaction of the inner layer with adsorbed moisture or interaction with the gaseous environment during dry periods. Particulate deposition from the atmosphere results in the appearance of a variety of

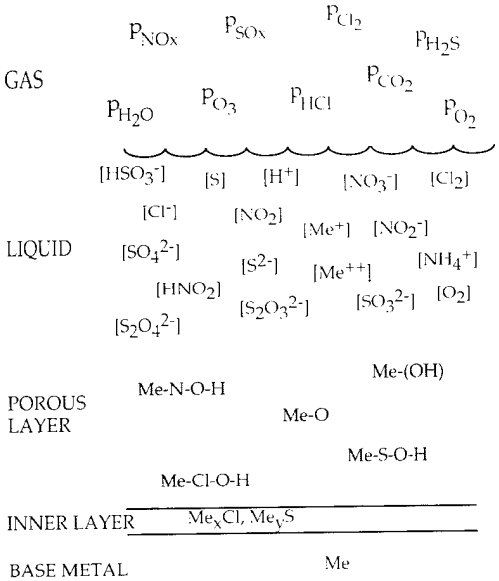

Fig. 2. Cross-section through a duplex corrosion product layer on a corroding metal.

compounds. Furthermore, these particulates can interact with adsorbed moisture and other species to form additional corrosion products.

The aqueous solution results from the adsorption of water from the atmosphere. The amount of water present depends on the relative humidity, mixed gas composition of the atmosphere and the adsorption properties of the surface. The composition of the liquid is determined in part by the solubility of gaseous species. The dissolution of solid corrosion products and deposits and their subsequent ionic dissociation will also affect the liquid composition and properties. The composition of the outer layer will be determined by the relative stability of the compounds for the conditions that exist. For example, precipitation will be controlled by solubility products and ionic concentrations in the liquid. Constituents can interact and react in the gas, liquid and solid states. Furthermore, the environment typically changes with time and there are dynamic changes in the gas and solution chemistry that affect the formation and stability of the corrosion product/deposit layers.

Transport through this complex system will control the tendency for corrosion and the resulting corrosion rate. Gaseous species are exchanged between the gas and liquid. Soluble gases and ionic species move through the bulk liquid and along tortuous paths through the outer corrosion product layer. Oxidizing species move to cathodic sites and are reduced, and the reduction products move from the cathodic sites. Oxidation of metal occurs at the metal/inner layer interface. Anodic and cathodic sites must be linked by paths for ionic and electronic transport.

Fig. 3 shows the non-protective inner layer denoted in Fig. 2 in more detail. The inner layer is shown on the

Fig. 3. The non-protective inner layer as a bulk film or as a continuous network of the non-protective constituent.

left as a homogenous bulk film covering the metal surface. A continuous network of the non-protective constituent along boundaries in a protective film is shown on the right of Fig. 3. Either of these will provide a "fast transport" path between the metal and the corrosive environment. The bulk film is representative of several metal–chloride systems, and the discontinuous network is representative of the copper–sulfide/oxide system.

Processes at the inner film interfaces are identified in Fig. 4. A bulk inner layer separates the reactive metal substrate from a porous outer layer and the corrosive environment. Transport through the inner layer is by ionic and electronic conduction, and transport through the outer layer occurs via liquid along pores and cracks in the layer. The inner layer is an ionic solid. At (i) the inner layer can dissolve in the aqueous phase. Hydration of the ionic solid occurs at (ii). Oxidation of the metal to metal ions occurs at the metal/inner layer interface (iii). The corrosion product layer grows by transport of cations away from the metal or transport of anions towards the metal surface. The transport of ions through the layer permits corrosion to proceed. Reducible species arriving at the metal interface can be reduced at cathodic sites (iv). This is represented by the reduction of water with the generation of hydrogen and hydroxyl ion. The reaction requires the transport of water across the inner layer and the transport of products away from the reaction sites. For ionic solids with appreciable electronic conductivity, reduction reactions can be supported at the solution/inner layer interface

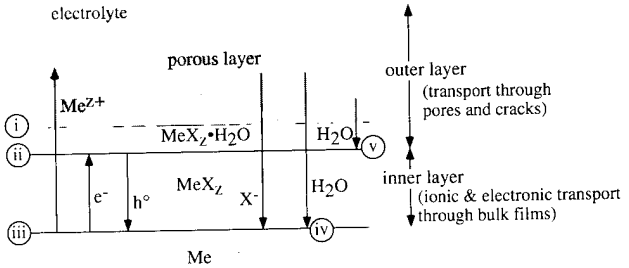

Fig. 4. Processes at the inner film interface.

(v). The overall oxidation of metal must be balanced by an equal amount of reduction. The reduction at (iv) and (v) can be supplemented by reduction at remote cathodic sites (vi). Ionic transport through the inner layer occurs by migration, e.g. high-field conduction and diffusion.

In the remainder of this paper, this general model is applied to the diagnosis of several corroding systems. This framework for the processes that control corrosion was useful in identifying common behavior and distinguishing features for each of the systems.

3. Copper in sulfurous gases

On exposure to air with no corrosive gas species, copper reacts to form a native oxide film of Cu_2O approximately 1.6 nm thick, covered by an adsorbed water/hydroxyl layer with adventitious hydrocarbon approximately 0.8 nm thick [1]. When relative humidity and sulfur-containing gases in the low parts per billion concentration range combine to form a corrosive electrolyte on the surface of copper, the protection afforded by the native oxide is lost. Corrosion products increase in thickness and, with time, a thick tarnish film develops. The transition from a protective to a non-protective layer and the subsequent growth processes in the thick corrosion product films on copper are the subject of current research in our group.

Observations of copper oxidation in dry air provide a suitable basis for discussion of the principles governing the conversion of a protective native copper oxide layer into a non-protective tarnish film. Transmission electron microscopy (TEM) analysis of cross-sections of thermal oxides formed on copper under dry conditions below 200 °C indicate that the oxides have a "mosaic" type of structure with some metal grains experiencing significantly more oxidation than others [2]. Rapidly oxidized metal grains are covered by a layer of small spherical oxide particles separated by high-angle boundaries. Although slow ionic transport occurs through the bulk oxide at room temperature, the diffusion of species along the grain boundaries, which is several orders of magnitude higher, will account for the growth of the oxide film [2]. In contrast, grains which experience only minor oxidation are covered by larger oxide plates that contact one another at low-angle boundaries. The low-angle boundaries restrict the transport of the species necessary for oxidation.

Overall, the oxide layer continues to grow by the transport of ionic species through the thickness of the film via the grain boundaries. More rapid growth and thicker oxides are observed where transport across the film is enhanced by a large number of high-angle, fast diffusion boundaries. Therefore the transport has been increased by the formation of "fast transport" channels through an otherwise "slow transport" bulk material. Similarly, a key premise of our interpretation of the corrosion of copper in moist air with sulfurous gases is the development of fast transport paths through the thickness of the initially protective oxide on copper between the film/electrolyte interface and the film/metal interface. These channels provide the transport necessary to support continued corrosion. In the absence of a corrosive electrolyte, the native copper oxide would continue to protect the metallic substrate from further corrosion.

The adsorption of moisture and sulfur dioxide from the surrounding environment is the essential first step in the tarnishing of copper. The relative humidity of the environment has been shown to have a large effect on the overall tarnishing rate reported [3], with the absence of atmospheric moisture having been shown to shut off completely the tarnishing process [4]. Thermodynamic solution chemistry indicates that the absorption of sulfur dioxide into the adsorbed water layer would initially create an electrolyte dominated by the bisulfite ion, HSO_3^-, at a pH of 4.5 for 100 ppb SO_2 [5].

Sulfur dioxide exposure has been shown to cause the growth of copper oxide, Cu_2O, with the incorporation of small amounts of copper sulfide [6–8]. The growth of oxide during exposure has also been reported by others [9,10]. Oxysulfur species, in the form of sulfite, have also been detected [6,7,9,10], with X- ray photoelectron spectroscopy (XPS) depth profiling indicating that this sulfite, HSO_3^-, and possibly an $S_2O_4^{2-}$ species exist as an outer layer to the oxide/trace sulfide structure mentioned above [6,7]. Samples examined after field exposures frequently exhibit another oxysulfur constituent, sulfate [11,12]. During laboratory exposure, higher sulfur dioxide gas concentrations and longer exposure times seem to correlate with the appearance of copper sulfate [4,13].

The addition of nitrogen dioxide to a moist flowing gas stream of sulfur dioxide can affect, synergistically, the tarnishing of copper [10]. XPS analysis has revealed that cupric species, CuO and $Cu(OH)_2$, are encouraged under these exposure conditions [7]. Cuprous oxide, Cu_2O, as well as a trace signal from copper sulfide are still detected. Traces of sulfite are found on the surface of the tarnish film and slightly into the bulk. At higher gas concentrations, sulfite and/or nitrate species have been reported to form [14]. When functioning alone, nitrogen dioxide has been shown to produce Cu_2O and CuO, although the reaction rates are more than an order of magnitude lower than those observed for a combined sulfur dioxide/nitrogen dioxide exposure [10]. Our findings for the tarnish film compositions and thicknesses in the Cu–O–S–H system, based on X-ray photoelectron spectroscopic analysis and coulometric reduction, are summarized in Table 1.

Table 1
Summary of film compositions and thicknesses produced on copper by sulfurous gases

Corrosive gas environment	Bulk tarnish film composition based on XPS analysis	Film thickness based on coulometric reduction[a]
75 ppb sulfur dioxide at 23 °C and 70% relative humidity	Predominantly Cu_2O with several per cent Cu_2S (sulfide peak became more distinct with longer exposure times)	10 h sample: Cu_2O, 5 nm 30 h sample: Cu_2O, 9 nm 60 h sample: Cu_2O, 5 nm
75 ppb sulfur dioxide and 120 ppb nitrogen dioxide at 23 °C and 70% relative humidity	Copper oxides, CuO and Cu_2O, with $Cu(OH)_2$ (cupric species formation was enhanced with longer exposure time)	10 h sample Cu_2O, 6 nm CuO, $Cu(OH)_2$[b], 4 nm 30 h sample: Cu_2O, 10 nm CuO, $Cu(OH)_2$[b], 7 nm 60 h sample: Cu_2O, 10 nm CuO, $Cu(OH)_2$[b], 13 nm

[a]Film thickness was adjusted to account for the surface roughness by assuming that the real surface area (15 μm roughness) was greater than the apparent geometric area by a factor of $\pi/2$.
[b]Film thickness was calculated as though $Cu(OH)_2$ was the only cupric species, although CuO was also present in the film.

The phenomenology observed for the tarnishing of copper to form products in the Cu–O–S–H system agrees well with the overall mechanistic viewpoint presented within this paper. The features presented in Fig. 2 are pertinent to the Cu–O–S–H system. In an environment lacking corrosive gases, the native oxide film on copper protects the substrate from further oxidation; therefore the oxide must undergo modification to allow the tarnishing processes to initiate. Once the transport properties of the original oxide have been altered to enhance species mobility, the concentration of copper ions in solution increases to the point at which the porous outer layer of the duplex structure begins to precipitate.

The synergy experienced for combined sulfur dioxide/nitrogen dioxide exposures can be interpreted with respect to our model. The role of sulfur dioxide is to create conditions for the formation of continuous channels of copper sulfide along the boundaries of copper oxide. This provides the necessary fast transport path through the oxide. The role of nitrogen dioxide is to increase the driving force for species transport across the non-protective film. The oxidizing power of the aqueous environment is greatly increased by nitrogen dioxide, thereby establishing a greater redox potential across the film thickness. The presence of a fast transport network and a greater driving force for corrosion and transport across the film combine to produce the synergy.

Sulfur dioxide has been shown to act as a cathodic depolarizer on copper [15], effectively undergoing reduction to sulfide [6,7]. This small amount of sulfide becomes incorporated into the growing oxide film. In particular, the sulfide constituent becomes localized along the oxide grain boundaries and extensive modifications of the transport properties of the native oxide film result. Copper sulfides are known to have significantly faster ionic transport than copper oxides.

Nitrogen dioxide serves as a highly oxidizing species, thereby establishing the activity or, alternatively, the potential gradient needed to drive the transport of species across the thickness of the film. As mentioned earlier, the oxidizing nature of nitrogen dioxide has been shown by the formation of cupric species, CuO and $Cu(OH)_2$ [7]. As nitrogen dioxide gas enters the layer of adsorbed moisture, a tarnishing reaction takes place which reduces N(+4) in N_2O_4 to N(+3) in HNO_2. This nitrous acid, HNO_2, is a gaseous product of the reaction and, on reaching its saturation level in solution, leaves the electrolyte to rejoin the flowing gas stream. Hence the absence of nitrogen-containing tarnish products under certain exposure conditions is understandable. The formation of HNO_2 as a product of the reaction of nitrogen dioxide with metals has been detected previously [10,16].

As this copper oxide/trace sulfide structure develops, copper ions are also going into solution at the adsorbed water electrolyte layer/tarnish film interface. The formation of hydroxide, sulfite or nitrate species depends on the solubility products of the various compounds. At higher concentrations of corrosive gas species, e.g. SO_2 and NO_2, and therefore lower pH, the sulfite and nitrate species may develop, with hydroxide constituents forming at lower corrosive gas species concen-

trations and higher pH values. The small volume of adsorbed moisture and the stagnant nature of the film will make the build up of ionic species prior to precipitation relatively easy.

This overall process ultimately produces a film consisting of two layers. The inner layer is the compact, solid-state-formed oxide/trace sulfide structure and the outer layer is a porous, precipitated structure of either hydroxide, sulfite or nitrate species. At longer reaction times, the diffusion and convection of the reacting electrolyte species through the tortuous paths within the precipitated layer can control the kinetics of tarnishing. Duplex layered films such as these have been reported in a variety of systems [17,18].

The copper sulfate observed on the surface of some samples could originate in several ways. The oxidation of the outer part of the precipitated sulfite layer to copper sulfate can occur either in the latter stages of tarnishing or during a dry period of relative humidity fluctuations. Direct deposition of sulfate- containing particulates could also explain the observation of sulfates in samples retrieved from field exposures [19,20].

Experimental work remains to be done to examine in more detail the substructure of the tarnish films formed on copper in sulfur- containing gases. The morphology of the products and the location of individual species, particularly sulfides, need to be determined. Such work is necessary in order to develop in more detail the processes which control the initiation and growth of tarnish films.

4. Metals in chloride solutions

Chloride-containing bilayer films are observed in a variety of systems, including the pitting and anodic dissolution of metals, aqueous corrosion of metals in seawater, patinas formed on copper in outdoor environments and the indoor corrosion of metals. In these systems, the corrosion product film structures are consistent with the general model proposed here: a thin, compact inner layer, covered by a thicker layer of corrosion products, has been observed in a variety of systems. Reactant transport through the inner layer has been cited as an important process in the growth of corrosion films in a number of systems.

4.1. Observations of chloride-containing films in corrosion environments

In studies of the localized corrosion of metals, the presence of a salt film at the base of active pits has been demonstrated. Beck has shown that chloride films are involved in the pitting of titanium [21,22], aluminum [23–25], magnesium [26] and silver [27]. In his studies on the pitting of titanium, Beck [21,22] presented a model in which the bottom of an active pit is covered with a salt film. Metal loss continues by dissolution of the metal halide or oxyhalide at the film/solution interface. The salt film grows by high-field conduction of ions through the salt film and, depending on the specific system, either the metal cation or halide anions will be the predominant mobile ionic species. Continued work on aluminum [23–25,28] showed the existence of a salt film in active aluminum pits. The salt film observed in artificial pit experiments appears to have a bilayer structure consisting of an inner anhydrous $AlCl_3$ layer, which grows by high-field conduction, covered by an outer hydrated layer which has ohmic characteristics [24].

Bilayer films have also been observed in studies of the anodic dissolution of metals in chloride solutions. Clerc and Landolt [29] have analyzed films formed on nickel in chloride solutions. In their a.c. impedance studies, they have modeled the anodic film as a duplex layer with a compact layer which forms by high- field conduction covered by a looser film of corrosion products. Similar studies by Grimm et al. [30] on the dissolution of iron in a chloride solution also used a bilayer film model.

The corrosion of metals in chloride-containing electrolytes, such as seawater, also yields corrosion films with bilayer structures. Copper and copper alloys have been studied in a variety of aqueous systems, with considerable emphasis on chloride- and sulfide-containing solutions, such as seawater and polluted seawater. Pickering and coworkers [18,31,32] have studied the mechanism of corrosion of Cu–9.4Ni–1.7Fe alloy in aerated aqueous NaCl solutions. A multilayer structure was indicated, with a thin (much less than 500 nm), strongly adherent inner layer in contact with the electrolyte through a much thicker (10–70 μm) porous outer layer. The composition of the protective surface layer was determined by XPS, scanning electron microscopy (SEM) and X-ray diffraction. The outer layer was mainly copper oxychlorides, and the inner thin layer contained appreciable chloride, oxygen, copper and some nickel. XPS analysis revealed chloride throughout the film, with a maximum concentration along a plane located within the inner layer near the inner layer/outer layer interface [31].

The behavior of metals in gaseous exposure conditions has not been investigated as thoroughly as the behavior during bulk aqueous exposure. Much of the present work in tarnishing involves the characterization of films grown by natural exposure, both indoors and outdoors. Analyses of copper patinas formed in the atmosphere include metallography [33,34], X-ray diffraction [34,35] and evolved gas analysis [35] as well as Auger electron spectroscopy (AES) [36,37] and XPS [37]. In these naturally formed copper patinas, oxides, sulfates, chlorides, carbonates and oxalates were found

[34–36]. These patinas were found to have a layered structure with numerous voids distributed throughout the film; patina thicknesses ranged from 4–6 μm for 1–2-year exposures (horizontal orientation) to 10–12 μm formed on 44-year-old copper exposed in a horizontal position [33]. Metallographic examination of a 100- year-old sample from the Statue of Liberty revealed copper oxide adjacent to the metal with a copper sulfate layer on top; chemical analyses (SEM, energy dispersive X-ray analysis (EDXA)) showed the presence of small amounts of Cl [33]. Opila [36] examined similar specimens by AES in conjunction with Ar^+ sputtering and found that chloride-containing species represent a significant fraction of the patina next to bulk Cu. The presence of a copper chloride layer adjacent to the metal may be indicated by this analysis, and this would be consistent with the general model proposed here.

In the case of indoor atmospheric corrosion, the films are thinner and lower in oxygen content than patina films formed during outdoor exposures. Schubert and D'Egidio [38] observed indoor tarnish film thicknesses from 41 nm for a 3-year exposure to 434 nm for a sample exposed for 49 years. They attribute these differences to moisture, citing several studies which demonstrate that the rates of tarnish reactions increase with relative humidity in the presence of pollutant gas species. Haque and Antler [39] observed chloride films on clad palladium and palladium–silver alloys exposed to indoor environments. While these materials were not noticeably affected by a typical air-conditioned office in the 40-month exposure, samples exposed to a non-air-conditioned indoor environment showed substantial particulate contamination and chloride films on the surface. In discussions on the development of mixed flowing gas test environments for atmospheric corrosion, Abbott [40] cites the presence of chloride in atmospheric corrosion product films, and the presence of chloride in copper samples exposed to Battelle Class II, III and IV test environments. Rice et al. [37] report the presence of chloride on nickel, copper and silver exposed to indoor environments. Neither the identity of the chloride-containing corrosion product, nor the distribution of chloride in the corrosion product film, is addressed in these investigations, but the presence of chloride in atmospheric corrosion product films is shown. Further studies on the corrosion products formed in these environments are needed to elucidate the structure of the corrosion product films and the exact role of chloride in the corrosion processes.

4.2. Corrosion product film formation processes and properties

Once a corrosion product film is formed, reactants for further corrosion (metal atoms and reducible species) are separated by that film. In order for the corrosion reaction to continue, ionic and/or electronic transport through the formed layer must occur. The formation processes and transport properties of the corrosion product films can play a crucial role in the rate of corrosion.

In many of the cases of corrosion discussed above, a thin compact layer was observed adjacent to the metal surface; this layer is no longer the thin native (2–5 nm) oxide that forms on exposure to air, but is an ionic solid consisting of metallic cations and various anions, including chloride and oxide. Ionic solids, such as metal chlorides, have considerably higher ionic conductivities than metal oxides, as pointed out by Beck [24] in the case of aluminum. The transformation from protective oxide to non-protective film is controlled by competition between protective species, such as oxides, and species that are non-protective, such as chlorides.

The relative stability of possible corrosion product species in the Cu–Cl–O–H system can be examined by use of a potential–pH diagram, calculated from thermodynamic data. The potential vs. pH diagram for the copper–chlorine–water system, shown in Fig. 5, illustrates that cuprous chloride is stable under acidic and slightly reducing conditions, as can be seen by considering the equilibrium between cuprite (Cu_2O) and nantokite (CuCl)

$$Cu_2O + 2H^+ + 2Cl^- \rightleftharpoons 2CuCl + H_2O \qquad \Delta G^\circ = -64.2\ \text{kJ mol}^{-1} \quad (1)$$

$$pH = 6.14 + \log[Cl^-]$$

As the chloride ion concentration increases, the pH boundary between cuprite and nantokite moves towards more alkaline conditions.

The equilibrium between CuCl and the cupric ion (Cu^{2+}) is as follows

$$Cu^{2+} + Cl^- + e^- \rightleftharpoons CuCl \quad \Delta G^\circ = -52.4\ \text{kJ mol}^{-1} \quad (2)$$

$$\mathscr{E}(V) = 0.54 - 0.059(pCl + pCu^{2+})$$

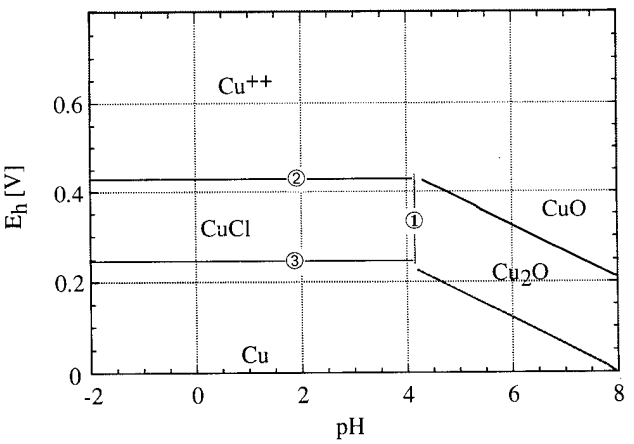

Fig. 5. E–pH diagram of the Cu–Cl–H_2O system at $[Cl^-] = 10^{-2}$ M.

Above this potential, the cupric ion is stable, and precipitation of basic cupric salts, such as carbonate, sulfate and chloride, will occur. This equilibrium potential will shift to higher potentials with increasing chloride concentration.

The equilibrium between copper and nantokite is expressed as

$$CuCl + e^- \rightleftharpoons Cu + Cl^- \quad \Delta G^\circ = -13.3 \text{ kJ mol}^{-1} \tag{3}$$

$$\mathcal{E}(V) = 0.138 + 0.059 pCl$$

The equilibrium potential decreases with increasing chloride concentration.

As shown by the equilibrium equations above, an increase in chloride concentration results in an increase in the size of the stability field for copper chloride on the E–pH diagram. The conditions required for chloride stability can be achieved near the corroding metal surface. Pollutant gases in moist air, such as SO_2 and HCl, will yield acidic electrolytes on the surface [5,24]. As shown by the E–pH diagram, cuprous chloride is stable with respect to cuprous oxide under low pH conditions. The formation of a cuprous chloride film could occur at the metal/film interface in the case of solid-state formation or at the inner/outer film interface in the case of precipitation.

In the discussion above, the conditions under which cuprous chloride is stable were outlined. In addition, the conditions that lead to the consumption of a cuprous chloride film are of interest. The thickness of an inner salt film, such as CuCl, is determined by the relative difference in the rates of film formation and consumption. Processes that can cause film loss include dissolution and chemical reaction. These processes will occur at the interface between the inner and outer layer. Dissolution of cuprous chloride into the adsorbed electrolyte will be limited, as the solubility of cuprous chloride is low, approximately 10^{-3} mol l^{-1}. Possible chemical reactions include the hydrolysis of cuprous chloride to form cuprous oxide and hydrochloric acid and the oxidation of cuprous ions to form cupric salts. As shown in the discussion of the definition of the stability field for CuCl, reaction (1) is the hydrolysis reaction and reaction (2) is the oxidation of cuprous ions to the cupric state. As dissolved cuprous ions are oxidized, the concentration of cuprous ions is maintained by further dissolution of the inner film. The oxidized ions, Cu^{2+}, form basic salts with anionic species in the adsorbed electrolyte, such as OH^-, Cl^-, CO_3^{2-} and oxysulfur species (e.g. SO_4^{2-}), as dictated by the K_{sp} values for these various salts. Depending on the rates of film formation and consumption reactions, a non-protective film will increase or decrease in thickness, or may disappear entirely when the consumption rate exceeds the formation rate.

The formation and dissolution reactions often occur at different interfaces, and the electrochemical and chemical conditions at these interfaces are different. The conditions at the metal surface promote oxidation (anodic sites) of copper to cuprous, and the conditions at the inner/outer layer interface promote reduction reactions (cathodic sites). The conditions result in film formation at the metal/inner layer interface, while encouraging film loss processes at the inner/outer layer interface. When in balance, the net result is the consumption of metal and a constant inner layer thickness, as the film appears to move into the metal substrate, with a thickening outer layer growing above the copper chloride film.

The transport properties of the thin inner layer are important as the conduction of ionic and electronic species through an established corrosion product film can limit the corrosion rate. The properties of inner films have been examined and several key observations are summarized below. In studies of localized corrosion, Beck [24,25] has developed a model of an active pit where the bottom of the pit is covered with a metal halide film. For aluminum pitting in chloride-containing solutions, the aluminum chloride film has a bilayer structure consisting of an anhydrous $AlCl_3$ layer adjacent to the metal surface and an outer layer of hydrated $AlCl_3 \cdot H_2O$. The inner layer was shown to form by high-field conduction, and the outer layer formed by water penetration and reaction with the anhydrous inner layer. Metal loss occurs by dissolution of the hydrated salt film at the film/electrolyte interface. Hydrogen evolution also occurs at the metal surface (oxide formed by the reduction of water is incorporated into the chloride film). These processes are equivalent to reactions (i) and (iv) in Fig. 4. From measurements of the peak current vs. stepped potential in an "artificial pit" shielded electrode, values for the conductivity of anhydrous aluminum chloride were determined [25]. The values calculated for $AlCl_3$ conductivity were on the order of 10 Ω cm^2, many orders of magnitude larger than the conductivity of anodic aluminum oxide, approximately 10^{-22} Ω cm^2.

Clerc and Landolt [29] modeled the anodic dissolution of nickel and Grimm et al. [30] modeled the anodic dissolution of iron in chloride solutions by a bilayer model that consists of a metal electrode covered by an inner compact layer with semiconducting properties and an outer porous film. Metal ions are transported through the inner layer by a high-field conduction mechanism; oxidation of the metal atoms occurs at the metal/inner film interface. These processes are consistent with the general model proposed here. Although Clerc and Landolt [29] assume that this inner layer is an oxide, they state that they do not know the oxide stoichiometry and that it is possible that the film is more like a chloride than an oxide. Their model does

not depend on the chemical composition of the inner film, only its electrical and ionic conduction properties. By measuring the influence of disk rotation speed and applied potential on the a.c. impedance, this bilayer film model was verified for the dissolution of iron in chloride solution, and transport parameters such as the thickness (approximately 10 nm) and donor density (17.9×10^{18} cm^{-3}) of the compact film were determined [30].

The corrosion behavior of copper–nickel alloys in seawater has been linked to the properties of an inner compact layer in a bilayer corrosion product structure. Popplewell et al. [41] studied the corrosion characteristics of a 90–10 cupro-nickel alloy and found that the addition of iron increased the corrosion resistance; they attributed this increased resistance to a modification of the defect structure of the compact inner film and an increase in the electronic resistance of the film. However, later studies by Hack and Pickering [42] suggested that the corrosion resistance of copper–nickel alloys is due to the limited oxygen reduction reaction rates. The inner layer provides a diffusion barrier to the cathodic reaction and exhibits poor kinetics for the oxygen reduction reaction. The outer porous corrosion product has less of an effect on the cathodic reaction rate for pure copper than fot the 90–10 and 70–30 copper–nickel alloys; the greater corrosion resistance of the alloys was attributed to the poor kinetics exhibited by the porous outer layer for oxygen reduction [42].

5. Chloride corrosion of bronze antiquities

In the case of the corrosion of bronze artifacts buried in chloride-containing environments, the formation of a layered corrosion product structure is evident. The bronzes are copper–tin alloys (usually 17%–25% Sn) with small amounts of lead (approximately 5%) added to improve casting properties [43]. A degradation phenomenon known as "bronze disease" is observed in some ancient bronzes. It is characterized by the rapid deterioration of an apparently sound bronze artifact when removed from an anaerobic burial environment to moist air. The eruption of voluminous powdery green corrosion products is a telltale sign of this corrosion in action. If left unchecked, the entire piece may be reduced to a pile of green powder [44]. The latent nature of bronze disease makes it particularly interesting. Under dry or anaerobic storage conditions the artifact is stable, and degradation occurs only with exposure to moisture (relative humidity above about 40%) and air.

The multilayer corrosion products observed on ancient bronzes are shown in Fig. 6. Closest to the bronze metal surface is a layer of bulk cuprous chloride (nantokite), and a layer of cuprous oxide (cuprite) is located

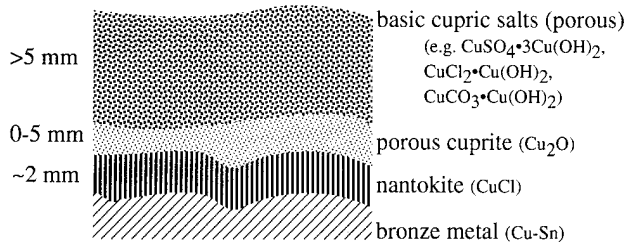

Fig. 6. Schematic diagram of the corrosion product layers resulting from bronze disease.

on top of the nantokite. While these films may be thick, on the order of millimeters, they are adherent and relatively compact. The cuprite layer is, in turn, covered with various cupric salts, such as basic chlorides and carbonates. Tin from the base alloy forms an oxide which does not yield a separate distinct layer, but is seen mainly within the cuprite layer as disconnected seams, tracing the original dendritic structure of the metal in places. Organ [45] has noted that the location of the cuprous chloride layer is the "epidermis" of the object or the original surface (the cuprous oxide and basic salts are formed from copper ions that have been conducted through the cuprous chloride film).

According to Garrels and Christ [46], the oxidation potential range of natural groundwater is coincident with the stability range for cuprous chloride, so that under slightly acidic burial conditions, the formation of cuprous chloride will be favored. The inner metal chloride layer is not protective under burial conditions, and the formation of cuprous chloride will proceed at a finite rate as copper ions are transported through the metal chloride layer. Over the thousands of years of burial, metal chloride films have attained thicknesses on the order of several millimeters. In fact, the complete mineralization of bronze artifacts has been observed [45].

After the object is recovered from the burial environment, the oxidizing power of the environment increases. This enhances metal chloride consumption reactions, such as the oxidation of cuprous ions and the dissolution of the CuCl film. On exposure to both moisture and air, the generation of basic cupric salts is accelerated, resulting in the disruption of the artifact surface and the consumption of the metal substrate.

The bronze disease phenomenon provides an opportunity to observe the development of corrosion product films over extended periods of time, on the order of thousands of years. The burial conditions yield an environment that is conducive to the continued growth of a CuCl film. Exposure to a more oxidizing environment demonstrates the role of oxidizing species in the corrosion process. While it is a somewhat unusual phenomenon, bronze disease fits well within the general model proposed in this paper. Oxidation of the metal occurs at the metal/film interface, the inner CuCl film is

Table 2
Reaction products formed on silver in hydrogen sulfide environments

Exposure conditions	Products	Exposure time (h)
No exposure	CO_3^{2-}, a small amount of H_2O(ad) on surface	
100 ppb H_2S with 75% RH N_2 gas	H_2O(ad), a small amount of CO_3^{2-} on surface, Ag_2S in bulk	72
100 ppb H_2S with dry air	CO_3^{2-}, SO_3^{2-}, a small amount of H_2O(ad) on surface, Ag_2S in bulk	92
100 ppb H_2S with dry air	CO_3^{2-}, a small amount of H_2O(ad) on surface, Ag_2S in bulk	24
100 ppb H_2S with 75% RH air	H_2O(ad), a small amount of CO_3^{2-} on surface, Ag_2S in bulk	62
100 ppb H_2S + 1.3 ppm NO_2 with dry air	CO_3^{2-}, a small amount of H_2O(ad) on surface, Ag_2S in bulk	92
100 ppb H_2S + 1.3 ppm NO_2 with 75% RH air	CO_3^{2-}, a small amount of H_2O(ad) on surface, Ag_2S in bulk	66

RH, relative humidity.

consumed at the inner film/outer film interface and a layer of copper minerals is observed on top of the inner layer.

6. Silver in sulfurous gases

Silver is commonly used for electronic materials and devices, and exposure to a humid environment containing sulfurous gases can cause the formation of a tarnish film. As compared with the complex compositions mentioned earlier for copper, corrosion of silver in sulfur-containing gases results in thick tarnish films comprised principally of silver sulfide (Ag_2S). Ag_2S is known to have high ionic and electronic conductivity with an electrical conductivity of $6 \times 10^{-4}\ \Omega^{-1}\ cm^{-1}$ at room temperature [47], as well as a much lower K_{sp} value, 1.6×10^{-49} [48], than many other compounds.

Here, the results of a series of mixed gas exposures of silver will be summarized, and the results of work in progress are interpreted in terms of the general model for atmospheric corrosion. Table 2 documents the results obtained for XPS analysis of silver exposed to a variety of gaseous environments that contained hydrogen sulfide. As can be seen, Ag_2S is the dominant tarnish product, with only small amounts of water and carbonate adsorbed on the outer surface. Importantly, silver oxide was not detected either prior to or following exposure to humidified hydrogen sulfide.

The kinetics of tarnish film growth were measured by a quartz crystal microbalance to reveal further details of the process of silver sulfide formation. Results of weight gain vs. exposure time in a series of gas environments are presented in Fig. 7. Curve 1 indicates that, without moisture and oxygen, little if any tarnishing occurs. The presence of oxygen with no water (dry air) produces only a slight mass gain with time as demonstrated by curve 2. Both oxygen and humidity are shown to be required for significant amounts of corrosion (curve 3). With longer exposure times, the tarnishing rate can be seen to slow significantly for this condition. The addition of nitrogen dioxide to a humidified gas stream containing hydrogen sulfide in air dramatically increases the rate of tarnishing. Curves 4 and 5 (dry air (approximately 10% relative humidity) and 75% relative humidity respectively) are essentially identical. The linear nature of the growth rate for both cases suggests that the mass transport of reactant gas species to the tarnishing metal surface controls the rapid growth under these conditions. Work by others has demonstrated the importance of gas phase mass transport in kinetic studies of tarnishing, particularly for silver in sulfidizing environments [16].

Furthermore, the identical weight gain vs. time for curves 4 and 5 in dry air and moist air suggest that conditions on the corroding metal are identical. Since it is known that a thin aqueous electrolyte exists on the corroding silver in moist air, it is assumed that a thin aqueous electrolyte develops on the specimens exposed in dry air. This is presumed to be the result of reaction between H_2S, NO_2 and O_2 to produce water that is adsorbed on the substrate. Experiments are under way to test this premise.

The phenomenology mentioned above for the tarnishing of silver in hydrogen sulfide can be evaluated in terms of the generalized model for atmospheric corrosion presented within this paper. Although the ionic and electronic transport properties for silver sulfide are

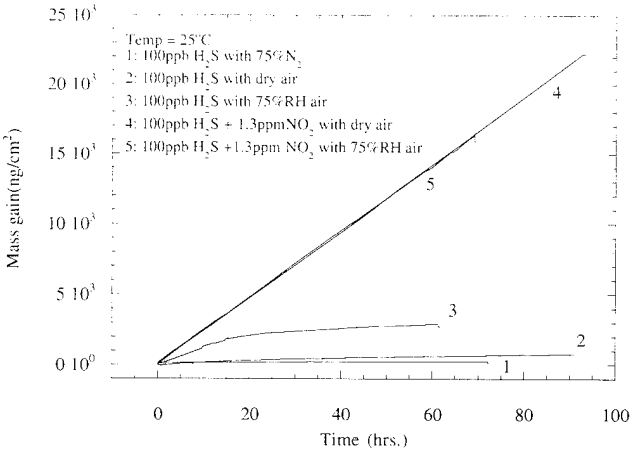

Fig. 7. Kinetics of silver tarnishing in hydrogen sulfide-containing environments as measured by quartz crystal microbalance.

favorable for considerable film growth, silver sulfide will not form unless an oxidizing agent is present within the environment. Oxygen or nitrogen dioxide in the environment provide the required oxidizing species. The hydrogen sulfide supplies the necessary sulfide ions, S^{2-}, but the formation of sulfide will not occur unless a species is available to form a redox couple with silver to produce silver ions Ag^{+}. As noted for the synergism of a sulfur dioxide/nitrogen dioxide environment on the tarnishing of copper, the highly oxidizing nitrogen dioxide gas imposes a greater driving force for species transport through the tarnish film than is established by oxygen acting alone. The formation of gaseous HNO_2 as a byproduct of the hydrogen sulfide/nitrogen dioxide reaction on silver has been documented by others [16].

Unlike the situation for copper, silver does not possess a protective native oxide film, relying instead on its own natural immunity from oxidation in benign environments. Thus the modification or breakdown of a native oxide to create fast transport channels is not a necessary precursor to the formation of a tarnish film structure on silver. Nitrogen dioxide acting alone produces little if any tarnishing, as the formation of silver compounds is not thermodynamically favored under these conditions. Thus the silver ions produced by the nitrogen dioxide/silver redox couple are not consumed, and only with the introduction of sulfide ions by hydrogen sulfide does the tarnishing process propagate, with the formation of a highly ionically and electronically conductive silver sulfide. A duplex layer did not develop for the tests reported here, as silver sulfide was the only thermodynamically favored product during the time period of the tarnishing process. Indeed, the formation of other products is highly unlikely, except perhaps by dry oxidation of the sulfide to give various oxysulfur species during dry periods of wet/dry relative humidity cycling.

7. Conclusions

The tendency for corrosion and the observed rate of corrosion are determined in large part by the transport properties of thin corrosion product layers. Both ionic and electronic transport are important. For continued corrosion, a corrosion product film capable of high ionic transport is required at the metal surface. The electronic transport properties will affect the spatial distribution of reduction reactions in the corroding system. A generalized model for a corroding system was presented, and the relevant processes that control corrosion were identified. Four systems currently under study in our research group were diagnosed in relation to the generalized model: copper in sulfurous gases, metals in chloride solutions, bronze disease of ancient artifacts and silver in sulfurous gases.

Acknowledgements

The authors acknowledge the support of Dr. Bruce A. MacDonald of the Division of Materials Research at the National Science Foundation (NSF Grant No. DMR-9015475). B.I. Rickett was supported by a National Science Foundation Graduate Fellowship. Portions of the work were supported by IBM through IBM/CWRU SUR Grant No. 1314.

References

[1] S.K. Chawla, B.I. Rickett, N. Sankarraman and J.H. Payer, *Corros. Sci., 33* (1992) 1617.
[2] K. Shimizu, K. Kobayashi, G.E. Thompson and G.C. Wood, *Corros. Sci., 36* (1994) 621.
[3] M. Seo, I. Sawamura and N. Sato, *Proc. Int. Symp. on Corrosion of Electronic Materials and Devices*, Vol. 91-2, The Electrochemical Society, Pennington, NJ, 1991, p. 165.
[4] W.H.J. Vernon, *Trans. Faraday Soc., 27* (1931) 255.
[5] S.K. Chawla and J.H. Payer, *Corrosion, 46* (1990) 860.
[6] S.K. Chawla, B.I. Rickett and J.H. Payer, *Corrosion of Electronic and Magnetic Materials, ASTM STP 1148*, American Society for Testing and Materials, Philadelphia, PA, 1992, p. 21.
[7] B.I. Rickett and J.H. Payer, *Proc. 2nd Int. Symp. on Corrosion and Reliability of Electronic Materials and Devices*, Vol. 93-1, The Electrochemical Society, Pennington, NJ, 1993, p. 437.
[8] T. Sydberger and N.-G. Vannerberg, *Corros. Sci., 12* (1972) 775.
[9] S. Zakipour and C. Leygraf, *J. Electrochem. Soc., 133* (1986) 21.
[10] P. Eriksson, L.-G. Johansson and H. Strandberg, *J. Electrochem. Soc., 140* (1993) 53.
[11] T.E. Graedel, *Corros. Sci., 27* (1987) 721.
[12] E. Mattsson, *Mater. Perform., 21* (1982) 15.
[13] R. Ericsson and T. Sydberger, *Werkst. Korros., 28* (1977) 755.
[14] D. Persson and C. Leygraf, *J. Electrochem. Soc., 137* (1990) 3163.
[15] I.L. Rosenfel'd, *Proc. 1st Int. Congr. on Metallic Corrosion*, National Association of Corrosion Engineers, Houston, TX, 1962, p. 243.
[16] L. Volpe and P.J. Peterson, *Corros. Sci., 29* (1989) 1179.
[17] H.D. Speckmann, M.M. Lohrengel and J.W. Schultze, *Ber. Bunsenges. Phys. Chem., 89* (1985) 392.
[18] C. Kato, H.W. Pickering and J.E. Castle, *J. Electrochem. Soc., 131* (1984) 1225.
[19] R.E. Lobnig, R.P. Frankenthal, D.J. Siconolfi and J.D. Sinclair, *J. Electrochem. Soc., 140* (1993) 1902.
[20] J.D. Sinclair, *J. Electrochem. Soc., 135* (1988) 89C.
[21] T.R. Beck, *J. Electrochem. Soc., 120* (1973) 1310.
[22] T.R. Beck, *J. Electrochem. Soc., 120* (1973) 1317.
[23] T.R. Beck, *Electrochim. Acta, 29* (1984) 485.
[24] T.R. Beck, *Electrochim. Acta, 30* (1985) 725.
[25] T.R. Beck and J.H. Mueller, *Electrochim. Acta, 33* (1988) 1327.
[26] T.R. Beck and S.G. Chan, *J. Electrochem. Soc., 130* (1983) 1289.
[27] T.R. Beck and D.E. Rice, *J. Electrochem. Soc., 131* (1984) 89.
[28] T.R. Beck, *Electrochim. Acta, 33* (1988) 1321.
[29] C. Clerc and D. Landolt, *Electrochim. Acta, 33* (1988) 859.
[30] R.D. Grimm, A.C. West and D. Landolt, *J. Electrochem. Soc., 139* (1992) 1622.
[31] C. Kato, J.E. Castle, B.G. Ateya and H.W. Pickering, *J. Electrochem. Soc., 127* (1980) 1897.
[32] C. Kato, B.G. Ateya, J.E. Castle and H.W. Pickering, *J. Electrochem. Soc., 127* (1980) 1890.

[33] J.P. Franey and M.E. Davis, *Corros. Sci., 27* (1987) 659–668.
[34] I.R. Scholes and W.R. Jacob, Atmospheric corrosion of copper and copper-base alloys during twenty years' exposure in a marine and an industrial environment, in *Copper and its Alloys*, Institute of Metals, 1970, p. 330.
[35] K. Nassau, P.K. Gallagher, A.E. Miller and T.E. Graedel, *Corros. Sci., 27* (1987) 669.
[36] R.L. Opila, *Corros. Sci., 27* (1987) 685.
[37] D.W. Rice, R.J. Cappell, W. Kinsolving and J.J. Laskowski, *J. Electrochem. Soc., 127* (1980) 891.
[38] R. Schubert and S.M. D'Egidio, *Corros. Sci., 30* (1990) 999.
[39] C.A. Haque and M. Antler, *Corros. Sci., 22* (1982) 939.
[40] W.H. Abbott, *IEEE Trans. Components, Hybrids Manufacturing Technol., 11* (1988) 22–35.
[41] J.M. Popplewell, R.J. Hart and J.A. Ford, *Corros. Sci., 13* (1973) 295.
[42] H. Hack and H.W. Pickering, The influence of corrosion product film formation on the corrosion of copper–nickel alloys in aqueous NaCl, in J.R. Scully, D.C. Silverman and M.W. Kendig (eds.), *Electrochemical Impedance: Analysis and Interpretation, ASTM STP 1188*, American Society for Testing and Materials, 1993, p. 220.
[43] R.J. Gettens, *J. Chem. Educ., 28* (1951) 69.
[44] Bangkok National Museum, Department of Fine Arts, *Bronze Disease and its Treatment, a Catalogue of Special Exhibit*, Bangkok, Thailand, 1975.
[45] R.M. Organ, The current status of the treatment of corroded metal artifacts, in B.F. Brown, H.C. Burnett, W.T. Chase, M. Goodway, J. Kruger and M. Pourbaix (eds.), *Corrosion and Metal Artifacts – a Dialogue Between Conservators and Archaeologists and Corrosion Scientists*, National Bureau of Standards, US Department of Commerce, 1977, p. 107.
[46] R.M. Garrels and C.L. Christ, *Solutions, Minerals and Equilibria*, Jones and Bartlett, 1990.
[47] Y.G. Vlasov and Y.E. Ermolenko, *Sov. Electrochem., 17* (1981) 1068.
[48] R.C. Weast (ed.), *CRC Handbook of Chemistry and Physics*, CRC Press, Boca Raton, FL, 1981, p. B-242.

ELSEVIER

Materials Science and Engineering A198 (1995) 103–112

MATERIALS SCIENCE & ENGINEERING A

High temperature corrosion and crack growth of SiC–SiC at variable oxygen partial pressures

R.H. Jones, C.H. Henager, Jr., C.F. Windisch, Jr.

Pacific Northwest Laboratory, Richland, WA 99352, USA

Abstract

Thermal gravimetric analysis (TGA) and subcritical crack growth measurements of chemical-vapor-infiltrated SiC matrix reinforced with Nicalon fibres and with a 1 μm thick C fiber–matrix interface have been conducted at 1100 °C over O_2–Ar mixtures ranging from 0.25% to 20.0% O_2. The TGA and interface recession measurements both gave linear reaction kinetics for O_2 concentrations of 2.0% or less and a reaction order of unity. Subcritical crack growth measurements demonstrated that the crack velocity, in the stress-intensity-independent stage II regime, increases with increasing O_2/Ar ratio. Also, the transition from stage II to the stress-intensity-dependent stage III regime is shifted to lower stress intensities with increasing O_2/Ar ratio. A time-dependent crack growth model that incorporates creep of the bridging SiC fibers and the removal of the C interfacial layer by oxidation successfully explains the subcritical crack growth characteristics.

Keywords: Silicon carbide; Crack growth; Carbon interface; Oxidation

1. Introduction

Continuous-fiber-reinforced ceramic matrix composites (CMCs) are being developed for high temperature applications such as turbine combustors, heat exchangers, fusion reactor first wall and blanket, and boilers. Composite materials with SiC, Si_3N_4 and Al_2O_3 as either the matrix or fiber reinforcement are under development. These materials have been chosen for their high-temperature strength and corrosion resistance; however, the desired fracture toughness is imparted by a thin interface layer between the matrix and fiber. This interface layer provides load transfer to the fiber combined with an interface fracture strength that provides pseudoductility to these ceramic–ceramic composite materials. The pseudoductility results from the energy absorbed during interface fracture and fiber pull-out at stresses exceeding the fiber interface fracture strength.

A 200–1000 nm thick fiber–matrix interfacial layer of C or BN has been used successfully in many of these composite materials; however, the stability of these materials in oxidizing environments is a concern for their long-term durability. Therefore, although SiC and Si_3N_4 form a protective SiO_2 layer in oxidizing environments, loss of the fiber–matrix interfacial layer will seriously degrade the structural properties of these composites. The objective of this paper is to report on the effects of oxygen partial pressure on the weight loss and time-dependent subcritical crack growth of SiC–SiC composites with C as the fiber–matrix interfacial layer.

2. Experimental technique

2.1. Material

The CMC material tested in this work was fabricated by Refractory Composites Inc. of Whitter, CA, and consisted of 4 mm thick pieces of eight-ply Nicalon fiber cloth (0°/90°) and chemical-vapor-infiltrated β-SiC. The C interfaces were deposited on the Nicalon fibers before the β-SiC chemical vapor infiltration (CVI) fabrication step. The photomicrograph of the material in Fig. 1 shows a region with the fibers in cross-section. The fiber diameter was measured to be 15 ± 2 μm and the C interface was approximately 1.0 ± 0.2 μm thick.

Elsevier Science S.A.
SSDI 0921-5093(94)04513-5

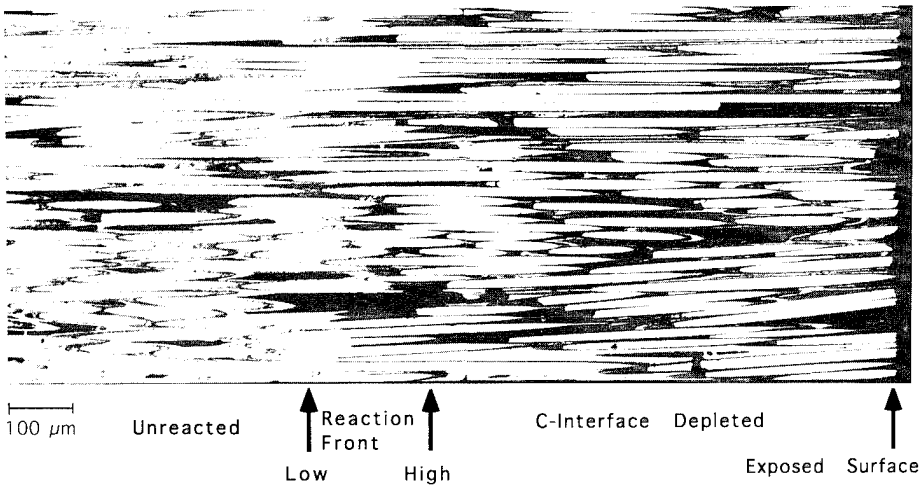

Fig. 1. Cross-section of the C interface in a CMC showing the depth of interface removal (1100 °C; 0.5% O_2; 6 h).

2.2. Thermal gravimetric analysis

Samples with dimensions of about 4 mm × 4 mm × 8 mm were tested at 1100 °C using thermal gravimetric analysis (TGA). One face of the 4 mm × 8 mm side of the samples was cut so that it was free of the SiC coating applied to the surface of the material during the last phase of fabrication. All other faces of the samples had a thin, approximately 5 μm thick, SiC coating. Analysis of specimens after testing revealed that only the uncoated surfaces had reacted. Consequently, all rates were normalized with respect to the cut, uncoated surface. Samples tested at 800, 900 and 1000 °C were cut so that their dimensions were about 4 mm × 4 mm × 4 mm. Unlike the larger samples, they had two uncoated surfaces, so all rates for these samples were normalized with respect to the sum of these two surfaces. Comparison of data for the two size samples revealed consistent behavior. Coincidentally, the total area of the uncoated surfaces was also similar for the two geometries: ranging from a low of about 0.30 cm^2 for the larger specimens to a high of about 0.40 cm^2 for the smaller ones.

TGA studies were performed using a Netzsch STA409 thermogravimetric analyzer. Gas flow was maintained at about 1 SCFH through the instrument furnace and composition was controlled using an MKS 147 multigas controller with O_2 content displayed on a Thermox meter. Mixtures of O_2 with Ar were used in these experiments. In each test, a sample was placed in an alumina cup in the analyzer furnace, the furnace was sealed, gas flow was adjusted, and the balance was allowed to equilibrate for about 2 h before heat-up. This approach minimized the effect of experimental drift that was most noticeable during the first hour. The temperature was then controlled according to the following program: (1) a ramped heat-up to the temperature of interest within 0.5 h, (2) a hold at the temperature of interest for 3–12 h, and (3) a cool-down to ambient temperature that took about 2 h or more. Throughout the test, mass change was recorded using a Netzsch analog recorder with an accuracy of about 0.1 mg. Traces showed some irreproducibility within the first few minutes after attaining the set temperature, which was attributed to both mass loss and experimental drift during heat-up. The latter was determined to be equivalent to about a 1 mg increment, by performing the same experiment on dry Al_2O_3 powder. Treatment of the SiC–SiC material in Ar at 1100 °C revealed no significant mass change so all the results reported here were attributed to reactions involving O_2.

2.3. Subcritical crack growth

The subcritical crack growth (SCG) studies were performed using constant-load tests for times up to 1×10^5 s, giving long-term crack velocity data, and using stepped load tests with load-holding times of 1000 s carried out at 1100 °C in Ar and Ar plus varying O_2 levels. Single-edge-notched bend bar (SENB) specimens with dimensions of 4 mm × 5.5 mm × 50 mm were tested. The SENB specimens were tested in four point bending using a fully articulated SiC bend fixture [1–3]. The specimens were typically loaded at an applied stress intensity of 7–8 MPa $m^{1/2}$ to begin the test. The test continued until a load drop was observed. Specimens that were tested in Ar plus O_2 were brought up to temperature in pure Ar.

The displacement–time curves for the 1000 s exposures at constant load in Ar indicate that the specimen displacement (and thus the crack-opening displacement) undergoes a transient period of displacement that is logarithmic in time over the 1000 s hold time. The slope of the displacement–curve over the final 600 s of the load step was taken as proportional to the crack velocity for each 1000 s period. The longer term hold dis-

placement–time data were fit to polynomial functions and differentiated to give $\partial\delta/\partial t$.

Writing $\delta = PC(\alpha)$, where δ is the displacement, P is the load, C is the specimen midpoint compliance, and α is equal to a/W (normalized crack length), gives

$$\frac{\partial\delta}{\partial t} = \frac{\partial}{\partial t}[PC(\alpha) = P\frac{\partial C}{\partial \alpha}\frac{\partial \alpha}{\partial t} = \frac{P}{W}\frac{\partial C}{\partial \alpha}\frac{\mathrm{d}a}{\mathrm{d}t} \quad (1)$$

which is used to derive an expression for $\mathrm{d}a/\mathrm{d}t$ $(= V_c)$:

$$\frac{\mathrm{d}a}{\mathrm{d}t} = V_c = \frac{(\partial\delta/\partial t)W}{PC'(\alpha)} \quad (2)$$

where V_c is the crack velocity and W is the specimen thickness. An expression was determined for the midpoint compliance of an SENB specimen in four-point bending and was used to calculate crack length and $C'(a)$ [2]. The slope of the displacement–time curve at a given load is $\partial\delta/\partial t$.

The instantaneous specimen compliance at any point along the corrected load–deflection curve was calculated as the slope of the line from the origin to any point on the load–deflection curve. Bridging zone contributions to the specimen compliance were not included; i.e. the cracks, for the purposes of the compliance calculations, were idealized as unbridged elastic cracks obeying linear-elastic fracture mechanics. It is recognized that this assumption is not true and causes errors in crack length calculations (see the discussion below) [4]. However, visual observations of crack length during the test were not possible and, without detailed knowledge of the bridging zone, the specimen compliance cannot be corrected for bridging fiber contributions. Therefore, all references to crack length, velocity, and stress intensity are made with the understanding that the reference is to an effect elastic crack [4]. Data are presented in the discussion comparing calculated and measured crack lengths (from sacrificial specimens) that revealed the crack lengths are overpredicted by about 35%.

3. Experimental results

3.1. TGA

TGA mass losses as a function of time for CMC materials at 1100 °C are shown in Fig. 2 for four O_2 partial pressures. The data are nearly linear at 0.5%, 1.0% and 2.0% O_2, within the first 3–6 h. At 20% O_2 (approximately air), the data are non-linear, showing a very rapid mass loss within the first 2 h and then apparently "saturating" with no additional significant mass change thereafter. As shown in Fig. 3, the mass losses varied parabolically with time when the O_2 was 0.25% (compare to 0.5%), especially at longer times. For the purpose of this analysis, however, the variation

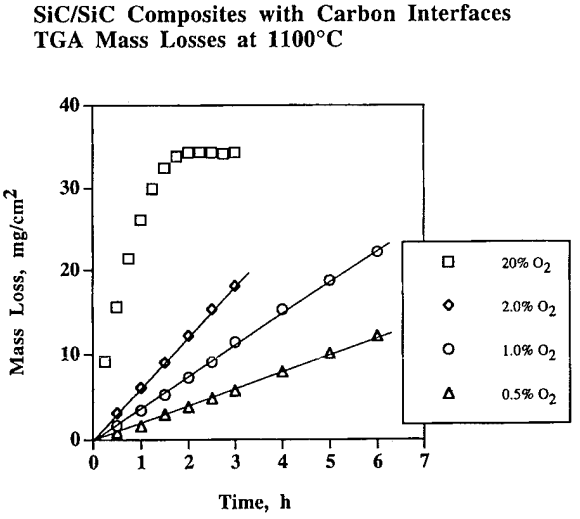

Fig. 2. TGA mass losses, at 1100 °C, of SiC–SiC composites with carbon interfaces.

at 0.25% and 1100 °C was considered nearly linear under 3 h.

After the TGA tests, samples were cut and polished for microscopic examination. Similar to previous studies by Henager and Jones [3], the samples showed evidence of C interface removal as a result of exposure to O_2-containing environments. In the present study, this interface removal proceeded along a surprisingly uniform reaction front at a rate that depended on the O_2 partial pressure. Fig. 1 shows a photomicrograph of the cross-section of one of the CMC samples after exposure to 0.5% O_2 for 6 h at 1100 °C. A clearly defined reaction front can be seen between 600 and 900 μm, which define the "high" and "low" positions, from the exposed surfaces in this sample. Between this front and the surface, almost all of the C interface was removed, while below this front the C interface appears largely intact.

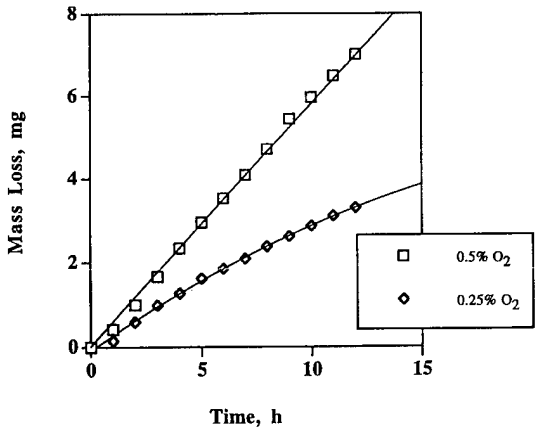

Fig. 3. Non-linear behavior, at low p_{O_2}, of SiC–SiC composites with carbon interfaces.

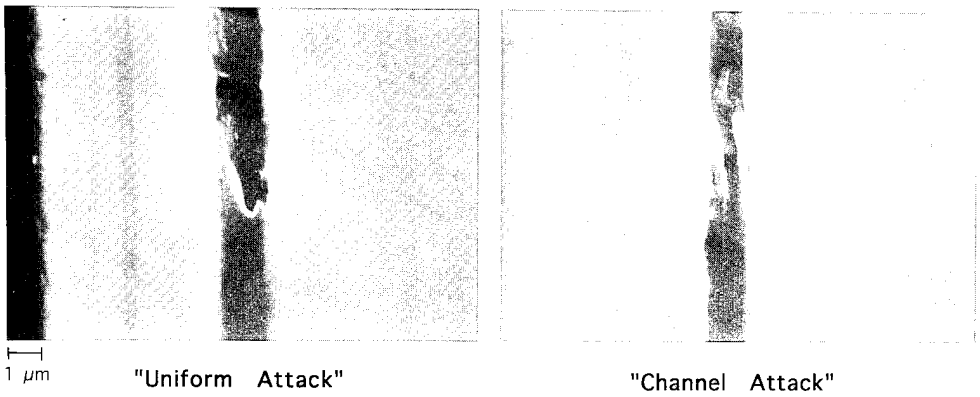

Fig. 4. Scanning electron photomicrographs showing different morphologies at the reaction front (1100 °C; 0.5% O_2; 6 h): (a) uniform attack; (b) channel attack.

The morphology of the C interface right at the reaction front varies somewhat within a sample as shown in Fig. 4. In some cases (Fig. 4(a)) the C interface appears more uniformly attacked across the interface width, while in other cases (Fig. 4(b)) the reaction is slower at the fiber–carbon and carbon–matrix interfaces. In the latter case, a channel appears to form near the center of the interface material, suggesting the C attached to the matrix and fiber may be less reactive.

Similar C interface recession morphologies were observed for samples treated at other O_2 partial pressures at 1100 °C, although the depth of recession for samples treated for the same time increased with increasing O_2 partial pressure. Average recession rates were determined by dividing the average recession depth (average of high and low positions of the reaction front) by the time of exposure for samples tested at 0.25%, 0.5%, 1.0%, and 2.0% O_2 and these are plotted against the O_2 partial pressure in a log–log format in Fig. 5. The error bars for these data reflect both the uncertainties in the position of the reaction front in a given sample determined from the difference between the high vs. low positions (giving $\pm 7 \times 10^{-7}$ cm s^{-1}) and the variations of results for different samples tested under the same conditions ($\pm 1.2 \times 10^{-6}$ cm s^{-1}).

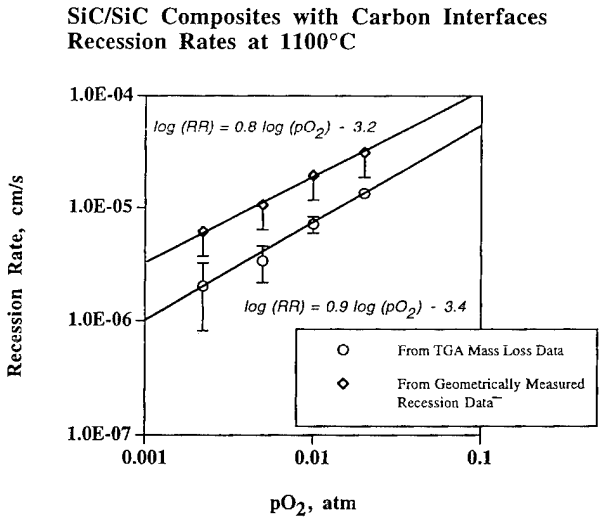

Fig. 5. Recession rates, at 1100 °C, of SiC–SiC composites with carbon interfaces.

As shown in Fig. 5, the relationship between the measured recession rates and O_2 partial pressure is nearly linear. The slope calculated by linear regression indicates a reaction order with respect to O_2 of 0.9 ± 0.2 or about unity. The intercept of the regression gives the rate of 1 atm O_2 $k_{1\,atm}$ equal to $4(\pm 2) \times 10^{-4}$ cm s^{-1} at 1100 °C.

The TGA mass loss data were also used to determine the recession rates for the various O_2 partial pressures. A number of assumptions were used in this analysis. Most importantly, it was assumed that all of the mass loss was associated with C interface removal. This assumption may not be completely accurate since other sources of oxidizable C are present including the SiC matrix, the Nicalon fibers, and the exposed sample surface. Xu and Zangvil [5] recently reported up to 14% excess C in SiC fibers and even more within 200 nm of the surface including a 30 nm surface region containing mainly C.

The recession rates RR were calculated from the TGA data for experiments at 0.25%, 0.5%, 1.0% and 2.0% O_2 at 1100 °C using the following relationship:

$$RR = \frac{ML}{t}\frac{1}{r}\frac{1}{A_1} \quad (3)$$

where ML is the mass loss at time t; ML/t is the rate of mass loss or the slope of the time vs. mass loss curves in grams per second (Fig. 2). Duplicate experiments gave slopes that agreed to within 5% of each other. The density of the C interface r is taken as 2 g cm^{-3}, and A_1, the total area of the C interface for the whole exposed surface, was determined by image analysis of the surface and found to be $8.6(\pm 0.5) \times 10^{-3}$ cm^2.

The recession rates calculated from the mass loss rates using Eq. (3) are plotted in Fig. 5 for comparison with the geometrically measured values. Again, the data are quite linear with a slope of 0.8 ± 0.1, which agrees

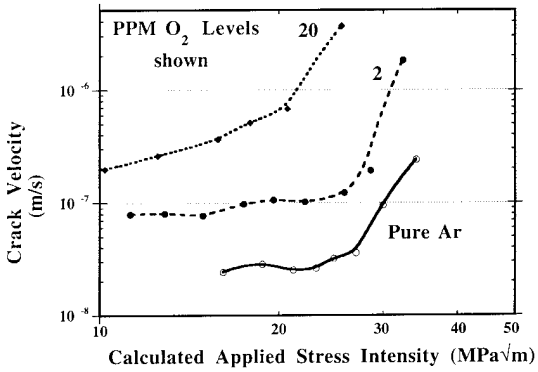

Fig. 6. Crack velocity as a function of effective applied stress intensity for pure Ar and two oxygen levels for C interface removal.

with the value for the reaction order obtained from the TGA mass loss data.

3.2. SCG

The data for the C interface materials, when plotted as crack velocity vs. applied stress intensity (V–K curves), reveal a stage II region where the crack velocity is essentially independent of the applied stress intenstiy (Fig. 6) followed by a stage III, or power-law, crack growth region at high stress intensities.

The power-law region exhibits a strong dependence, but the stage II region exhibits a weak dependence, on the applied stress intensity. The data reveal a measurable increase in stage II crack velocity because of O_2 in the gas. The crack velocity increases with increasing O_2 content for the C interface material (Figs. 6 and 7). Also, the stress intensity required for the onset of stage III is shifted to a lower value of the applied stress intensity.

4. Model of oxygen effects on crack growth

A discrete, two-dimensional (2D), micromechanics model was developed to understand the effects of the fiber-bridging zone on crack-tip stress intensities and to

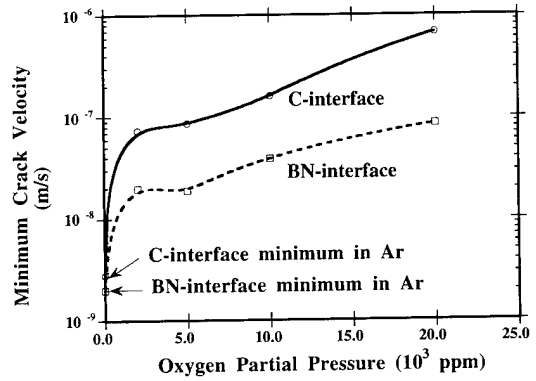

Fig. 7. Minimum or limiting crack velocity in C and BN interface materials as a function of oxygen partial pressure at 1100 °C.

predict crack velocities for an idealized composite under conditions of fiber creep and interface removal. Although other models [6–12] have been developed to describe crack-wake bridging in continuous-fiber composites, it is desirable to have a discrete model that allows numerical calculations of cracks closure forces and is amenable to time-dependent calculations. The model developed here places a semi-infinite crack in a linear-elastic body and simulates the bridging fibers by crack-closure forces placed along the crack face. The forces applied by the fibers to the crack face are calculated using an explicit frictional bridging model [9] that describes the fiber load transfer as a function of distance from the crack tip. The modeling performed here is similar in many respects to that performed by Davidson [13] and has been presented by the present authors elsewhere [2].

The details of the bridging zone calculation require knowledge of the interfacial shear strength and fiber fracture strength. The value of the interface strength determines the stress on a given fiber in the bridging zone. The fiber fracture strength then determines the length of the bridging zone based on the last unfailed fiber and, together, these determine the amount of crack-tip screening for an equilibrium bridging zone. An independent estimate of the interfacial shear strength gives a nominal value for the interface strength equal to or less than about 35 MPa. It would be expected that this shear strength will be less than 35 MPa at 1100 °C because of the thermal expansion mismatch of the Nicalon fibers and the β-SiC matrix. Data [14] for strengths of Nicalon fibers at elevated temperatures in air indicate that 1.5 GPa at 1100 °C is an average strength value. Therefore, values for the interfacial shear strength τ ranging from 10 to 50 MPa and a fiber fracture stength σ_f^c equal to or less than 1.5 GPa are chosen for the calculations performed later. Additionally, $E_m = 400$ GPa and $E_f = 200$ GPa are chosen as representative elastic moduli for matrix and fiber, respectively. A nominal fiber radius of 5 μm is used for r_f. The fiber failure stress σ_f^c is used to define the bridging zone length for frictional bridging. The length of the bridging zone is defined as the distance from the crack tip to the last unfailed fiber.

A comprehensive model of SCG in continuous-fiber-reinforced composite (CFC) materials must take into account all possible time-dependent behaviors in the crack-wake bridging zone. These include fiber creep, fiber–matrix interface creep, possible viscoelastic effects at the interface, and time-dependent interface removal due to oxidation. The net effect of any time-dependent deformation in the crack-wake region is to relax the crack closure forces. Fiber creep undoubtedly plays a role since the bridging fibers are highly stressed in the crack-wake region and are being held at those loads for long times. Interface removal must also be important

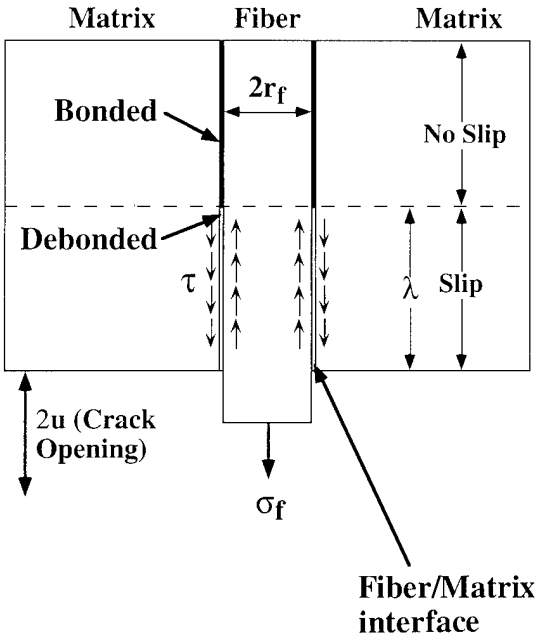

Fig. 8. Schematic diagram of the fiber debond model showing λ, τ, u, and σ_f. Oxygen ingress occurs along the fiber–matrix interface and increases λ. Thus, λ and τ become time dependent in this model.

based on the TGA and optical microscopy results. It is unlikely that viscous or glassy phases are being formed because the SCG experiments are performed in argon or argon plus small amounts of oxygen.

Available creep data for Nicalon fibers at 1100 °C in pure Ar [15] were used to construct a constitutive equation for the stress and time dependences of creep in Nicalon fibers at 1100 °C. A stress relaxation calculation for Nicalon fibers undergoing creep was performed by partitioning the total fiber strain into elastic and plastic (creep) components and by requiring that the total strain rate be zero such that the fiber elastic strain is replaced by plastic strain.

The mechanics of frictional bridging is typically given in terms of an interface debond length λ, interfacial shear strength τ, crack-opening displacement u and fiber stress σ_f (Fig. 8). The fiber–matrix debond crack length is determined by the interfacial shear strength and crack-opening displacement. The effect of oxygen, and subsequent interface removal, in the bridging mechanics is simulated by allowing this debond crack length λ to become time dependent. As λ increases due to interface removal, the fiber is gradually decoupled from the matrix and, therefore, σ_f must decrease with time due to interface removal. In terms of existing mechanics models the debond crack length can be related to the interfacial shear strength as

$$\lambda^2 = \frac{u r_f E_f}{\tau(1+\eta)} \qquad \eta = \frac{E_f V_f}{E_m V_m} \tag{4}$$

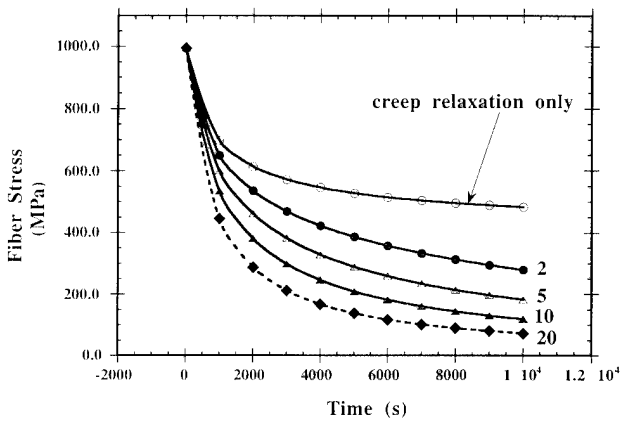

Fig. 9. Stress in a bridging fiber as a function of time for pure Ar (fiber creep only) and in varying p_{O_2} levels. The fiber is initially at a stress of 1 GPa and relaxes according to the model described in the text.

and the fiber stress is then related to λ through the following relation to the interfacial shear strength τ as

$$\sigma_f = 2\left[\frac{u E_f \tau(1+\eta)}{r_f}\right]^{1/2} \tag{5}$$

The TGA and optical microscopy data can be used to calculate the time dependence of λ and, therefore, τ and σ_f. Model results for fiber stress as a function of time in the crack wake due to fiber creep only and, additionally, due to interface removal are shown in Fig. 9. It can be seen that the model predicts faster relaxation due to fiber creep plus interface removal compared to fiber creep only.

The discrete micromechanics model can be used to calculate the crack velocity using a quasi-static approach given these time-dependent quantities. A quasi-static approximation to the crack velocity assumes that bridging zone is in equilibrium by virtue of a balance between crack advances and relaxation of bridging zone stresses. As the crack advances, it bridges additional fibres, which retards its growth. As the stresses in the bridging zone relax, the crack-tip screening is reduced and the crack tends to advance. This assumption does not require detailed information about the physical mechanism of crack advance due to matrix cracking.

The quasi-static approximation assumes that the stress intensity at the crack tip is a constant such that

$$K_{tip}(a, t) = C \Rightarrow dK_{tip} = 0 \tag{6}$$

Therefore, one can write the total differential of K_{tip} as

$$dK_{tip} = \frac{\partial K_{tip}}{\partial a} da + \frac{\partial K_{tip}}{\partial t} dt \tag{7}$$

which can be used to derive an expression for crack velocity V_c as

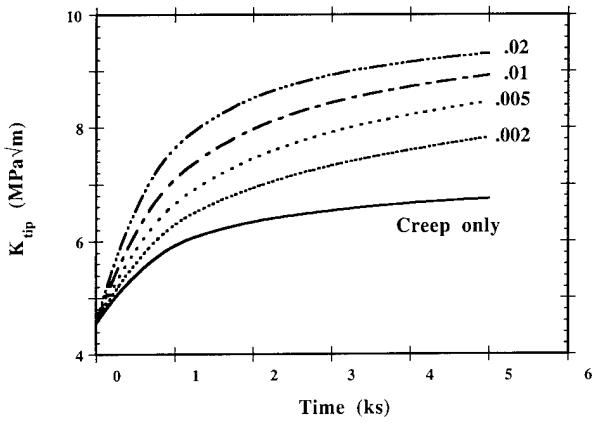

Fig. 10. K_{tip} as a function of time using the 2D model to account for fiber creep and interface removal relaxation events. Addition of oxygen can be seen to increase the relaxation rate compared to fiber creep only.

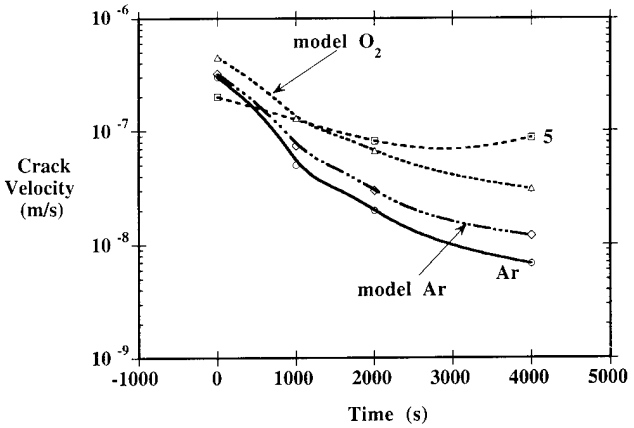

Fig. 11. Calculated crack velocities for pure Ar (fiber creep only) and p_{O_2} equal to 0.005 (5000 ppm) showing the increase in velocity associated with interface removal in addition to fiber creep relaxation.

$$V_c = \frac{da}{dt} = -\left(\frac{\partial K_{tip}/\partial t}{\partial K_{tip}/\partial a}\right) \quad (8)$$

where the crack velocity is expressed as the ratio between the time dependence of K_{tip} due to stress relaxation of bridging forces $\partial K_{tip}/\partial t$, and the change in K_{tip} due to crack advance $\partial K_{tip}/\partial a$.

Values for $\partial K_{tip}\partial t$ can be calculated from differentiating a polynomial fit to K_{tip} data calculated as a function of time due to fiber creep and interface removal (Fig. 10) for varying p_{O_2}. For this case, the fiber volume fraction V_f was set to 0.3, τ was set to 10 MPa, and K_A was set to 10 MPa $m^{1/2}$. The bridging zone was 300 μm in length and contained 19 intact bridging fibers. The rate of change of K_{tip} with respect to a is readily calculated from the bridging model by computing K_{tip} for incremental changes in crack length. For a given choice of model parameters, of material constants, this quantity is constant.

The quasi-static approximation gives a range of crack velocities depending on the rate of stress relaxation of the fiber bridging stresses given that $\partial K_{tip}/\partial a$ is a constant (Fig. 11). The model results clearly show that the additional stress relaxation in the bridging fibers caused by interface removal acts to increase the crack velocity compared to pure Ar where fiber creep only is occurring.

5. Discussion

The data presented here are given in terms of the length and velocity of an effective elastic crack, with the applied stress intensity representing the K field of such a crack. Although this has been adopted by others [4], it is recognized that the actual crack lengths and velocities will differ from this idealized situation. The presence of large-scale bridging zones in these materials suggests that the use of indirect crack length measurements, such as specimen compliance measurements, will not accurately determine the actual crack length. These materials and testing conditions do not allow direct crack length measurements, however.

As a first step in determining actual crack lengths for these CFC materials, several specimens were cracked under identical SCG conditions (1100 °C in pure Ar), sectioned, and polished to reveal crack lengths and crack morphologies. A comparison between measured and calculated crack lengths was made. The experimentally measured instantaneous compliance was used to calculate effective crack lengths using the procedure discussed in Section 2 and this calculated crack length was compared to the crack length measured optically from sectioned and polished specimens. The optical photomicrography revealed that the specimens were multiply cracked, with up to nine separate and equally spaced cracks, at the notch root. The width of this cracked, or damaged, region was approximately equal to 1 mm, or about twice the notch width. Each subcritical crack was fully bridged from the notch root to the crack tip and all the bridging fibres appeared to be intact. The measured crack length was determined from the length of the longest visible crack. The calculated crack lengths are, perhaps fortuitously, within 36%, on average, of the measured crack lengths. More importantly, the slope of the two $C(a/W)$ curves are nearly equal resulting in equal values of dC/da used to compute crack velocities. Therefore, calculated effective crack velocities should accurately reflect the velocity of cracks in the damage zone. Since large-scale bridging of a single crack in an SENB specimen should result in under predicting the crack length, contrary to what is observed here, the effect of the multiple cracking must be to increase the specimen compliance enough to over predict actual crack lengths.

Comparison of typical SCG V–K data for monolithic ceramics with the data presented here reveals this

distinguishing feature, namely the appearance of a K-independent regime (stage II) in the V–K diagram for the CFC material. The power-law dependence of crack velocity observed in monolithic ceramics is replaced by a K-independent, or weakly K-dependent, regime (stage II) that corresponds to the material's R curve. The interpretation of this behavior is that the extent of the stage II regime for CFCs corresponds to the formation of the equilibrium bridging zone as the cracks extends. Stage II behavior is observed under certain conditions in monolithic materials and in glasses [16–19] when the transport of a critical species to the crack tip is rate controlling. This is analogous to the situation here as the stress relaxation of the crack-wake region is rate controlling. A major distinction is the very weak K dependence observed here. The exponent of K in stage II is less than unity for the CFC materials, but is typically larger than this for monolithic ceramics [18,19].

The transition to stage III, or power-law growth, corresponds to saturation of the bridging zone and the inability of the material to further shield the crack tip from the far-field K_A. It would be reasonable to expect that the crack velocities would revert to a power-law growth rate in stage III. Indeed, this appears to be the case (Fig. 6); however, only a limited range of data are available for determining the power-law exponent in the stage III regime because the specimen fails soon after making the transition. Nevertheless, power-law exponents in the range of 8–20 are obtained for the limited data in this study. Exponents in this range are typical in SCG exponents measured for glasses and monolithic ceramics at elevated temperatures [16,20–28]. This behaviour is interpreted as power-law crack growth dominated by matrix cracking in the regime where the bridging zone is unable to effectively shield the crack tip from K_A. The model described here is, therefore, not valid for this regime since the quasi-static approximation is not expected to hold. It is worth noting that there are no models available that accurately describe SCG of ceramic materials in the power-law regime, although attempts have been made [19].

The nature of the agreement of the model with experiment when fiber creep is simulated is encouraging (Fig. 11). Not only is the absolute magnitude of the crack velocity predicted, but the observed time dependence of V_C is also rationalized. There are no adjustable parameters in the model and typical values for material constants were assumed.

The model developed here predicts similar results to those obtained by Thouless [7], Nair et al. [6], and Jakus et al. [29]. Crack advance is controlled by the time-dependent behavior of the crack-bridging ligaments, whether the relaxation is due to viscoelasticity or thermal creep. The crack-opening displacement and, therefore, the crack-tip stress intensity are shown to obey similar time-dependent relationships.

High temperature SCG of CFCs is expected to be influenced by the following environment-induced effects (other than thermal effects) where crack bridging controls the local stress intensity: (1) fiber stability and strength, (2) fiber–matrix interface stability, and (3) effects on the viscosity of the grain boundary phase at the crack tip. Therefore, a study on the corrosion and crack growth behavior of CFCs should evaluate the contribution of these processes to time-dependent composite properties. While a more comprehensive study is in preparation, several important points can be made from the data presented here. The experiment was designed (1100 °C and low p_{O_2}) to have negligible effects on fiber stability and strength [30], and to have little or no effect due to oxidation of the SiC matrix material [31]. However, the experimental conditions were such that the C interfaces would be attacked by the O_2 atmosphere used in this study. Indeed, the only discernible effect of the O_2 was to partially remove these reactive interfaces during the high temperature exposure.

The addition of O_2 to the 1100 °C Ar environment increases the crack velocity in the stage II regime and shifts the stage-II-to-stage-III transition to lower K values (Fig. 6). The shift to lower K values for the transition to stage III crack growth is consistent with a reduction in the closure forces imparted on the crack faces by the bridging fibers. Optical and scanning electron micrographs of the specimens exposed to the O_2 plus Ar reveal the partial removal of the C interfaces due to oxidation. The TGA data substantiate that this material is removed by relating the specimen mass loss to the interface removal. The removal of this interface material reduces to ability of the matrix to transfer load to the fibers, and, in turn, reduces the bridging zone effectiveness. Since the oxygen exposure, and hence the interface removal, began when the SCG test was initiated and is cumulative, the interface removal of the crack-bridging fibers should be progressive during the SCG test, being small at the beginning (small K_A) and larger at the end of the test (large K_A). The principle effects of this gradual interface removal appear to be an increase in crack velocity compared to pure Ar and a shift in the stage-II-to-stage-III transition to lower applied stress intensities.

Therefore, in addition to fiber creep causing relaxation of bridging zone stresses, there will be a time-dependent decrease in the fiber–matrix mechanical coupling as the interface is removed. In turn, this acts to decrease the fiber bridging stress, in accord with Eq. (5), and will increase $\partial K_{tip}/\partial t$, as was shown by the model (Fig. 10). Since significant oxidation of interfaces ahead of the crack is not expected, nor observed, $\partial K_{tip}/\partial a$ is expected to remain constant. The net result is an increase in crack velocity, and, since the bridging zone as a whole is less effective in screening the crack

tip from the applied stress intensity, a shift in the stage-II-to-stage-III transition is also expected.

These calculations reveal that relaxation of bridging zone stresses, by any of the mechanisms discussed above, will delay fiber fracture and result in increased available strain energy for crack-tip screening. Therefore, CFCs can actually become tougher and absorb more strain energy in SCG compared to fast fracture. In other words, the amount of crack-wake bridging depends on the temperature, the loading rate, and the constitutive laws obeyed by the bridging ligaments. This is much like the results found by Knehans and coworkers [32,33] and Fett and Munz [34] for monolithic ceramics and it was concluded that the toughness of materials exhibiting R curve behavior was dependent on specimen history [33]. However, although increases in bridging zone stress relaxation rates can increase apparent toughness, these same increases will increase $\partial K_{tip}/\partial t$ and SCG velocities, and mechanical instabilities will be achieved at lower stress intensity values. Experimentally, the stage-II-to-stage-III transitions occur at K_A values that are much larger than K_Q (Fig. 6) and processes that are known to increase bridging zone relaxation rates, such as oxidation-induced interface removal, result in increased SCG velocities and lower stage-II-to-stage-III transitions.

6. Summarizing remarks

TGA of CMC material consisting of a CVI SiC matrix reinforced with Nicalon fibers and with C with 1 μm thick C interfaces revealed linear kinetics for mass loss within the first 3–6 h at temperatures at 1100 °C and in 0.25%, 0.5%, 1.0% and 2.0% O_2. Mass loss at 20% O_2 was very rapid and non-linear. The TGA results, when converted to recession rates involving the C interfaces, compared very well with the recession rates measured geometrically on tested samples that were cross-sectioned for microscopic analysis. The oxidation of the C interface appeared to follow first-orders kinetics and the order of the reaction with respect to oxygen appeared to be closs to unity.

The velocity of subcritical cracks in CMCs with continuous fibers has been related to the rate of relaxation of fiber-bridging forces in the crack-wake bridging zone. It is proposed that the crack velocity is controlled by the rate of relaxation of the bridging zone stresses by Nicalon fiber creep and a time-dependent change in the fiber–matrix mechanical coupling. A 2D, discrete micromechanics model using a simple constitutive law for creep of Nicalon fibers at 1100 °C was able to rationalize measured SCG rates and the time dependence of V_C in continuous-fiber-reinforced β-SiC materials tested in O_2-containing environments. Extension of $p(u)$ functions to the modeling of SCG indicate that knowledge of $p(u,t)$ is required to compute $K_{tip}(t)$ and that such computations are useful in understanding SCG processes for materials with bridged cracks.

Acknowledgements

The assistance of J.L. Humason in performing the TGA and SCG measurements is gratefully acknowledged. This research was supported by the Office of Basic Energy Sciences of the US Department of Energy (DOE) under Contract DE-AC06-76RLO 1830 with Pacific Northwest Laboratory, which is operated for DOE by Battelle Memorial Institute.

References

[1] C.H. Henager, Jr., and R.H. Jones, The effects of an aggressive environment on the subcritical crack growth of a continuous-fiber ceramic composite, *Ceram. Eng. Sci. Proc.*, *13* (7–8) (1992) 411–419.

[2] C.H. Henager, Jr., and R.H. Jones, High-temperature plasticity effects in bridged cracks and subcritical crack growth in ceramic composites, *Mater. Sci. Eng. A*, *166* (1993) 211–220.

[3] C.H. Henager, Jr., and R.H. Jones, Effects of varying p_{O_2} on subcritical crack growth in continuous-fiber reinforced ceramic composites, *Ceram. Eng. Sci. Proc.*, *14* (7–8) (1993).

[4] A. Bornhauser, K. Kromp and R.F. Pabst, R-curve evaluation with ceramic materials at elevated temperatures by an energy approach using direct observation and compliance calculation of the crack length, *J. Mater. Sci.*, *20* (1985) 2586–2596.

[5] Y. Xu and A. Zangvil, *J. Am. Ceram. Soc.*, *76* (1993) 3034.

[6] S.V. Nair, K. Jakus and T.J. Lardner, The mechanics of matrix cracking in fiber reinforced ceramic composites containing a viscous interface, *Mech. Mater.*, *12* (3–4) (1991) 229–244.

[7] M.D. Thouless, Bridging and damage zones in crack growth, *J. Am. Ceram. Soc.*, *71* (1988) 408–413.

[8] S.V. Nair and T.-J. Gwo, Role of crack wake toughening of elevated temperature crack growth in a fiber reinforced ceramic composite, *J. Eng. Mater. Technol.*, 115 (1993) 273–280.

[9] A.G. Evans and R.M. McMeeking, On the toughening of ceramics by strong reinforcements, *Acta Metall.*, *34* (1986) 2435–2441.

[10] D.B. Marshall, B.N. Cox and A.G. Evans, The mechanics of matrix cracking in brittle-matrix fiber composites, *Acta Metall.*, *33* (1985) 2013–2021.

[11] B. Budiansky, J.M. Hutchinson and A.G. Evans, Matrix fracture in fiber-reinforced ceramics, *J. Mech. Phys. Solids*, *34* (1986) 167–189.

[12] B.N. Cox and C.S. Lo, Simple approximations for bridged cracks in fibrous composites, *J. Am. Ceram. Soc.*, *40* (1992) 1487–1496.

[13] D.L. Davidson, The micromechanics of fatigue crack growth at 25 °C in Ti–6Al–4V reinforced with SCS-6 fibers, *Metall. Trans. A*, *23* (1992) 865–879.

[14] D.J. Pysher, K.C. Goretta, R.S. Hodder, Jr., and R.E. Tressler, Stengths of ceramic fibers at elevated temperatures, *J. Am. Ceram. Soc.*, *72* (1989) 284–288.

[15] G. Simon and A.R. Bunsell, Creep behavior and structural characterization of high temperature of Nicalon SiC fibres, *J. Mater. Sci.*, *19* (1984) 3658–3670.

[16] S.M. Weiderhorn, S.W. Freiman, E.R. Fuller and C.J. Simmons, Effects of water and other dielectrices on crack growth, *J. Mater. Sci.*, *17* (1982) 3460–3478.

[17] B.J. Pletka and S.M. Wiederhorn, Subcritical crack growth in glass-ceramics in R.C. Bradt et al. (eds.), *Fracture Mechanics of Ceramics*, Vol. 4, Plenum, New York, 1978, pp. 745–759.
[18] K.D. McHenry and R.E. Tressler, Subcritical crack growth in silicon carbide, *J. Mater. Sci., 12* (1977) 1272–1278.
[19] H. Cao, B.J. Dalgleish, C. Hsueh and A.G. Evans, High temperature stress corrosion cracking in ceramics, *J. Am. Ceram. Soc., 70* (4) (1987) 257–264.
[20] S.M. Wiederhorn and L.H. Bolz, Stress corrosion and static fatigue of glass, *J. Am. Ceram. Soc., 53* (10) (1970) 543–548.
[21] A.G. Evans, A method for evaluating the time dependent failure characteristics of brittle materials—and its application to polycrystalline alumina, *J. Mater. Sci., 7* (1972) 1137–1146.
[22] A.G. Evans, L.R. Russell and D.W. Richerson, Slow crack growth in ceramic materials at evaluated temperatures, *Metall. Trans. A, 6* (1975) 707–716.
[23] A.G. Evans and F.F. Lange, Crack propagation and fracture in silicon carbide, *J. Mater. Sci., 10* (1975) 1659–1664.
[24] K.D. McHenry and R.E. Tressler, Subcritial crack growth in silicon carbide, *J. Mater. Sci., 12* (1977) 1272–1278.
[25] J.L. Henshall, D.J. Rowcliffe and J.W. Edington, KIC and delayed fracture measurements on hot-pressed SiC, *J. Am. Ceram. Soc., 62* (1–2) (1979) 36–41.
[26] J.L. Henshall, High temperature slow crack growth in hot pressed silicon carbide, *Res Mech., 1* (1980) 229–248.
[27] J.L. Henshall, The mechanism and mechanics of subcritial crack propagation in hot-pressed SiC above 1000C, in D. Francois (ed.), *Advances in Fracture Research (Fracture 81)*, Pergamon, New York, 1981, pp. 1541–1549.
[28] P.F. Becher and M.K. Ferber, Grain-size dependence of the slow-crack growth behavior in noncubic ceramics, *Acta Metall., 33* (7) (1985) 1217–1221.
[29] K. Jakus, J.E. Ritter and R.H. Schwillinski, Viscous glass crack bridging forces in a sintered glassy alumina at elevated temperatures, *J. Am. Ceram. Soc., 76* (1) (1993) 33–38.
[30] T. Mah, N.L. Hect, D.E. McCullum, J.R. Hoenigman, H.M. Kim, A.P. Katz and H.A. Lipsitt, Thermal stability of SiC fibers (Nicalon), *J. Mater. Sci., 19* (1984) 1191–1201.
[31] E.A. Gulbransen and S.A. Jansson, The high temperature oxidation, reduction, and volatilization reactions of silicon and silicon carbide, *Oxid. Met., 4* (1972) 181–201.
[32] R. Knehans and R. Steinbrech, Memory effect of crack resistance during slow crack growth in notched Al_2O_3 bend specimens, *J. Mater. Sci. Lett., 1* (1982) 327–329.
[33] R. Steinbrech, R. Knehans and W. Schaarwächter, Increase of crack resistance during slow crack growth in Al_2O_3 bend specimens, *J. Mater. Sci., 18* (1983) 265–270.
[34] T. Fett and D. Munz, Determination of fracture toughness at high temperatures after subcritical crack extension, *J. Am. Ceram. Soc., 75* (11) (1992) 3133–3136.

ELSEVIER

Materials Science and Engineering A198 (1995) 113–118

MATERIALS SCIENCE & ENGINEERING A

Corrosion resistance of Al-based metal matrix composites

Yoshiaki Shimizu, Toshiyasu Nishimura, Iwao Matsushima*

Materials and Processing Research Center, NKK Corporation, Minamiwatarida-cho, Kawasaki-ku, Kawasaki 210, Japan

Abstract

Corrosion characteristics of Al 6061-based metal matrix composites (MMCs) containing carbon fibres, alumina fibres or silicon carbide whiskers (SiC_w) and the effects of ageing heat treatment on the stress corrosion cracking resistance of SiC_w–Al 7075 MMC were studied in chloride solutions. MMCs were prepared by the squeeze casting method in the laboratory. The pitting potentials for Al 6061 and the three Al 6061-based MMCs were similar. The resistance of SiC_w–Al 6061 MMC to pit initiation is the same as that of the monolithic alloy. Once pits initiate, damage by pitting corrosion would be greater owing to the formation of crevices between the reinforcement and the matrix by the dissolution of the latter in the pits. The cathodic current of the SiC_w–Al 6061 is slightly larger than that of the matrix alloy, possibly owing to an interfacial layer observed by transmission electron microscopy. Ageing of SiC_w–Al 7075 MMC at 170 °C for more than 1 h following ageing at 110 °C makes the MMC resistant to stress corrosion cracking in 3.5% NaCl and increases the pitting potential.

Keywords: Al-based metal matrix composites; Silicon carbide whiskers; Pitting potential; Stress corrosion cracking

1. Introduction

Among various useful aluminium alloys, Al 6061 and 7075 are two typical examples characterized by reasonable corrosion resistance and high strength, respectively. Further, these are alloys often used as the base metal for metal matrix composites (MMCs) reinforced by various non-metallic fibres, particles and whiskers.

The corrosion resistance of a metal tends to be adversely affected by the presence of a second phase. The only exception may be ferritic–austenitic stainless steel. The literature [1–9] on the corrosion behaviour of MMCs has shown that the presence of a reinforcing material may or may not increase the corrosion susceptibility, depending not only on the metal–reinforcement combination but also on manufacturing process parameters.

In this work, corrosion characteristics were examined and compared for three Al 6061-based MMCs prepared in the laboratory using the same procedure with carbon fibres (C), alumina fibres (Al_2O_3) and silicon carbide whiskers (SiC_w). The effect of heat treatment of SiC_w–Al 7075 MMC on the resistance to stress corrosion cracking (SCC) was also studied.

2. Experimental

The same heats of Al 6061 and 7075 were used to prepare metal plates and MMCs in the laboratory. The chemical analyses are shown in Table 1. The materials were heat treated following the specifications listed in Table 2. The properties of the reinforcing materials are given in Table 3.

MMCs were prepared using the squeeze casting method, which was considered to give most stable physical properties of MMC. The fibres and the whiskers were supplied by Tokai Carbon in the form of preforms. The casting was performed at 800 °C under

Table 1
Chemical analyses of matrix metal (%)

Alloy	Zn	Mg	Cu	Cr	Si	Fe	Al
Al 6061	0.00	1.13	0.33	0.11	0.46	0.18	Balance
Al 7075	5.62	2.52	1.63	0.22	0.06	0.18	Balance

* Corresponding author.

SSDI 0921-5093(94)04514-3

Table 2
Heat treatment of the specimens used

Specimen	Annealing	Ageing	
		1st step	2nd step
Al 6061-based MMC	540 °C for 1 h	170 °C for 8 h (T6)	
Al 7075-based MMC	470 °C for 1 h	110 °C for 6 h	170 °C for 1–6 h (T7)

Table 3
Properties of reinforcing materials

Material	Diameter (μm)	Length (μm)	Density (g cm^{-3})	Tensile strength (kgf mm^{-2})	Young's modulus (kfg mm^{-2})	Crystal phase	Surface finish
SiC_w	0.1–1.0	30–100	3.19	$(3–14) \times 10^2$	$(4–7) \times 10^4$	β-SiC	–
Al_2O_3	3	500	3.30	2×10^2	3×10^4	β-Al_2O_3	
C	7	1000	2.40	3.5×10^2	2.3×10^4	–	Cu coat

an argon atmosphere at 10 kgf cm^{-2}. An examination under the microscope confirmed randomly distributed networks of the reinforcing materials. The tensile properties were isotropic.

Polarization curves were obtained potentiodynamically in deaerated 3.5% NaCl at 25 °C. The potential was swept at 20 mV min^{-1} from a potential 500 mV negative to the rest potential in the noble direction until the critical pitting potential (V'_c) was exceeded. The specimens for electrochemical study, measuring $10 \times 10 \times 3$ mm^3, were abraded with wet emery paper to a #600 finish and degreased.

The resistance to SCC was examined by the slow strain rate test (SSRT) in aerated 3.5% NaCl solution at room temperature at a strain rate of 6×10^{-6} s^{-1}. The specimens used were 6 mm diameter × 80 mm long rods with a gauge section 2 mm diameter × 14 mm long. The resistance was determined by comparing the elongation to fracture or fracture strength with those in air. Some tests were conducted using the constant-load technique.

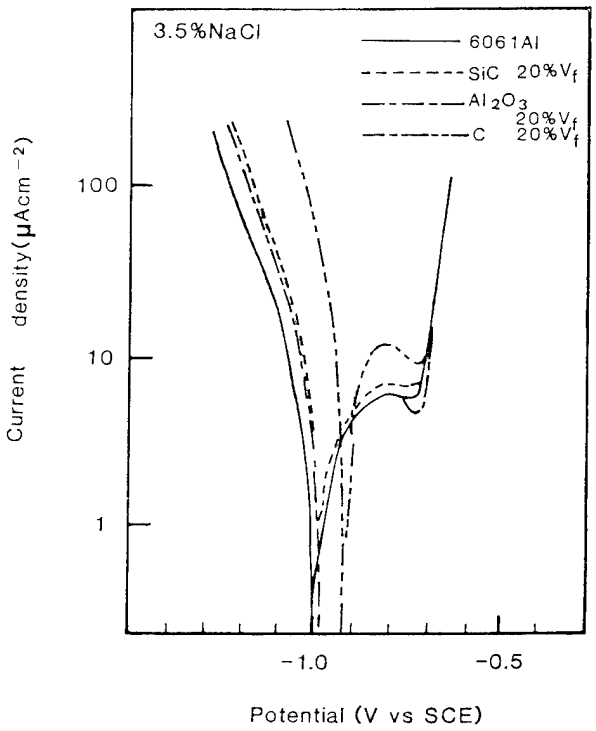

Fig. 1. Potentiodynamic polarization curves for Al 6061 and Al 6061-based MMCs in deaerated 3.5% NaCl solution at 25 °C.

3. Results and discussion

3.1. Corrosion behaviour of Al 6061-based MMCs

Typical polarization curves for Al 6061 and three Al 6061-based MMCs containing 20 vol% (v/o) C, Al_2O_3 and SiC_w in deaerated 3.5% NaCl solution at 25 °C are shown in Fig. 1. The pitting potentials for the unreinforced alloy and the three MMCs are identical. The surface after the measurements showed that the sites of pit initiation were not limited to the metal/reinforcement interface, but were distributed randomly throughout the surface of the metal matrix.

Polarization curves for SiC_w–Al 6061 MMCs containing 10 and 20 v/o SiC_w are compared in Fig. 2. These curves show that the pitting potential is independent of the amount of SiC_w.

When the MMCs and the base metal were left in deaerated 3.5% NaCl solution at room temperature, small pits initiated after about 1 week on all specimens. On further immersion, pit growth was faster on all the MMCs compared with the unreinforced alloy. This is presumably due to the detrimental effect of crevices generated by the dissolution of the matrix at pits. The formation of crevices is readily suggested by the appearance of the pit shown in the scanning electron

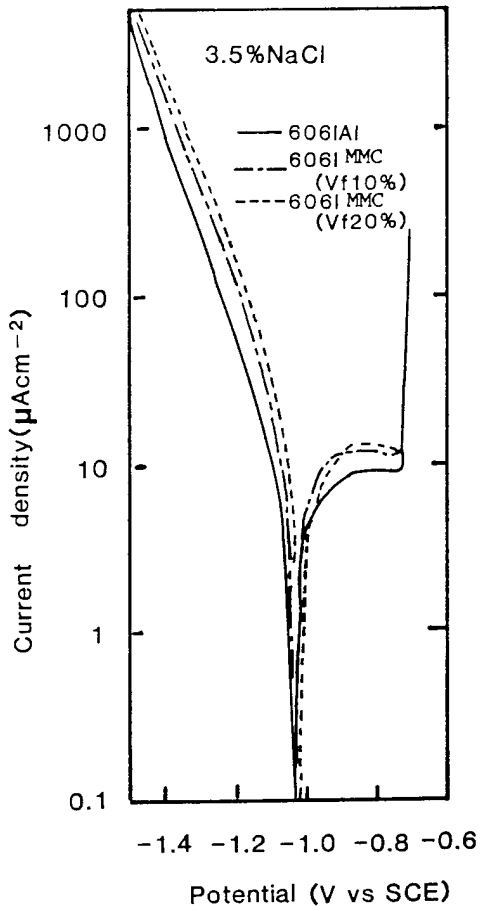

Fig. 2. Potentiodynamic polarization curves for 10 and 20 v/o SiC_w–Al 6061 MMCs in deaerated 3.5% NaCl solution at 25 °C.

micrograph in Fig. 3, which was taken for a pit generated on 20 v/o SiC_w–Al 6061 held at a potential slightly more noble than the pitting potential for 1 h in 3.5% NaCl solution. Along the same lines, Aylor and Moran [1] observed that pitting corrosion was concentrated around SiC_w on an SiC_w–Al 6061 panel which had been immersed in filtered seawater for 60 days.

Fig. 3. Scanning electron micrograph of a pit on 20 v/o SiC_w–Al 6061 MMC held for 1 h in 3.5% NaCl solution at a potential slightly more noble than the pitting potential.

The present result that the pitting potential of SiC_w–Al 6061 is not affected by the presence of SiC_w is in agreement with those of Trzaskoma et al. [2], Aylor and Moran [1] and Noda et al. [3] for the same MMC systems and some other Al-based MMCs. Sun et al. [4] did not find a significant difference in the pitting potential for Al 6061 reinforced by 15–40 v/o SiC particles (SiC_p). Buarzaiga and Thorpe [5] reported that Al 356-based MMCs containing 10 and 15 v/o SiC_p, but not that with 20 v/o SiC_p, showed less noble pitting potentials than the base metal. It is reasonable to assume that the presence of SiC_w in the Al 6061-based composite does not increase the susceptibility to pit initiation or surface film breakdown.

In contrast, some investigators [1,2,6] found that pit morphology was changed by the presence of SiC; pits on the MMCs were significantly more numerous, shallow and widespread than those on the corresponding unreinforced alloys. Also, once pits initiate, the growth and the resulting damage would be greater than for the base metal. In practice, it should be borne in mind that an aluminium-based material, whether it is an alloy or an MMC, must be used under conditions where pitting corrosion does not initiate. Because the SiC_w–Al 6061 MMC has the same resistance as the Al 6061 alloy as far as pit initiation is concerned, the limits of safe use would be the same.

The present results also show that the pitting potential of the C–Al 6061 is the same as that of the unreinforced matrix alloy. However, unlike the case of the SiC_w–Al 6061 MMC, the susceptibility of the MMC to pit initiation would be greater than the matrix alloy owing to the galvanic coupling of carbon fibres and aluminium. The well documented noble potential and effective cathodic nature of C cause localized corrosion at the interfacial area to form crevices that accelerate pit initiation. The poor corrosion resistance of C–Al composites in chloride environments has been reported by various authors [7,8]. In view of the unaffected pitting potential and the non-conductive nature of Al_2O_3, the resistance of Al_2O_3–Al 6061 MMC would presumably be the same as that of the matrix alloy.

The cathodic current for C–Al 6061 is much greater than the unreinforced alloy (Fig. 1), reflecting the effective cathodic nature of carbon fibres. In view of the non-conductive nature of SiC_w and Al_2O_3, it is puzzling that the cathodic currents for SiC_w and Al_2O_3 composites are slightly, but definitely, larger than that for the monolithic matrix alloy. Such an increase in cathodic current may explain the reported higher corrosion rates in SiC–Al MMCs in comparison with their matrix alloys [7,8]. The cathodic current density for a solid SiC electrode in deaerated 3.15% NaCl solution

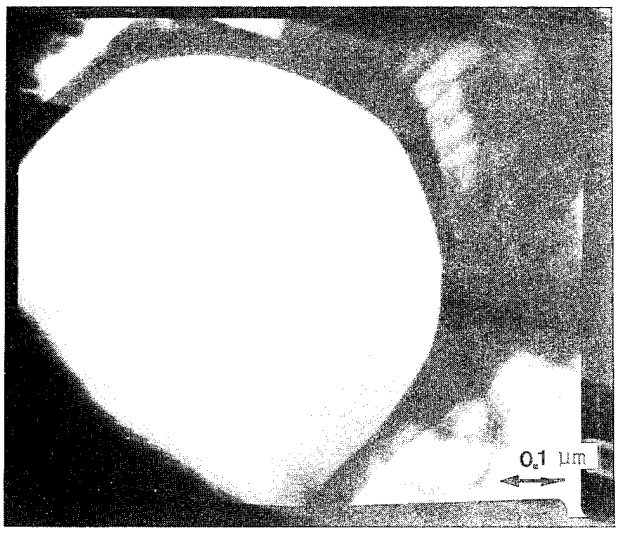

Fig. 4. Transmission electron micrograph of the interface between SiC_w and the metal matrix in SiC_w–Al 6061 MMC.

reported by Hihara and Latanision [9] was much lower, e.g. 0.1 μA cm^{-2} SiC at −1.2 V (vs. SCE) than the increment of current density for the SiC_w–Al 6061 MMC observed in this work.

The presence of some interfacial material that contributes to the current increase was suspected. With much effort to prepare samples suitable for transmission electron microscope (TEM) studies without disturbing the reinforcement, the TEM result shown in Fig. 4 was obtained. Obviously, an interfacial layer (dark) exists at the interface between SiC_w and the metal matrix. Its thickness was much less than 0.1 μm and energy-dispersive X-ray analysis failed to identify the material. Possibly it is a reaction product of SiO_2 that might have formed on SiC_w with magnesium in the molten Al 6061 to form MgO and Si. Possible causes of the increased cathodic current for the Al_2O_3–Al 6061 MMC were not found.

3.2. *Effect of heat treatment on SCC resistance of SiC_w–Al 7075*

The SiC_w–Al 7075 MMC was annealed at 470 °C for 1 h, aged at 110 °C for 6 h (1st-step ageing) and then further aged at 170 °C for 0–6 h (2nd-step ageing). The latter ageing is used to impart SCC resistance to aluminium alloys of the 7000 series.

Typical SSRT curves in air and in 3.5% NaCl solution for the MMC with and without the 2nd-step ageing for 6 h are shown in Fig. 5. The 2nd-step ageing gives SCC resistance to the MMC which is otherwise susceptible. Similar curves for the MMC aged at 170 °C for different periods of time indicated that immunity was obtained by ageing for more than 1 h.

In view of the possible initiation of SCC at the bottom of a pit, the pitting potentials for the composite with different ageing treatments were measured in deaerated 3.5% NaCl solutions. As shown in Fig. 6, the pitting potential shifts in the noble direction with the 1st-step ageing (110 °C for 6 h) and shifts further with the subsequent 2nd-step ageing at 170 °C. A peak that appeared in the anodic branch of each curve may seem unusual. Presumably, this corresponds to the active–passive transition made apparent by complete removal of the surface film during cathodic polarization that preceded anodic polarization.

The pitting potentials in 0.3, 3.5 and 15% NaCl solution are plotted in Fig. 7 as a function of the ageing time. The beneficial effect of the 2nd-step ageing on the pitting potential saturates after about 1 h of ageing.

Hence the 2nd-step ageing for more than 1 h is effective in reducing the susceptibility to both SCC and pit initiation. To substantiate these results, constant-load SCC tests were conducted. The results are shown in Table 4. The specimens heat treated for the 2nd-step ageing for 1 and 6 h, which did not show SCC susceptibility in SSRT, did not fail for the maximum test period of 500 h under an applied stress level of 90% yield strength.

The TEM results shown in Fig. 8 compare the microstructures of the 20 v/o SiC_w–Al 7075 MMC with and without the 2nd-step ageing for 6 h. It is seen that some precipitates have grown in the metal matrix adjacent to the SiC_w/metal interface by ageing. The beneficial effect of the 2nd-step ageing on monolithic 7000

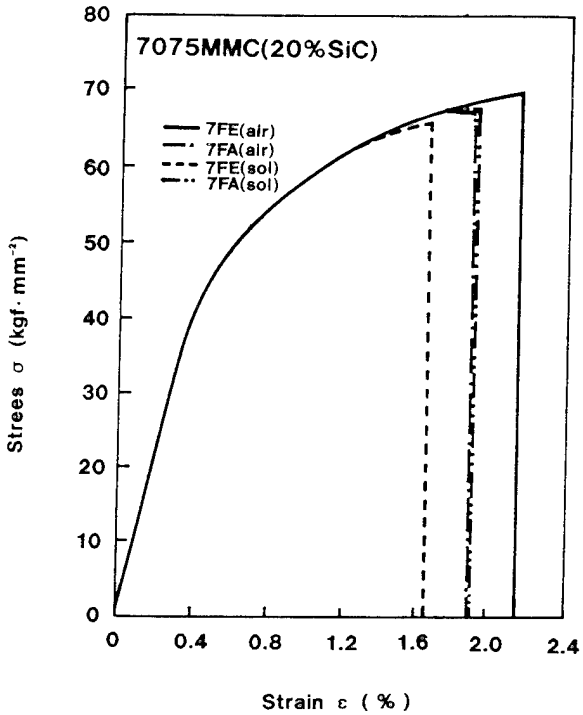

Fig. 5. SSRT curves for 20 v/o SiC_w–Al 7075 MMC in air and in aerated 3.5% NaCl solution at rest potential and room temperature. 7FE, aged at 110 °C for 6 h; 7FA, aged at 170 °C for 6 h after ageing at 110 °C for 6 h.

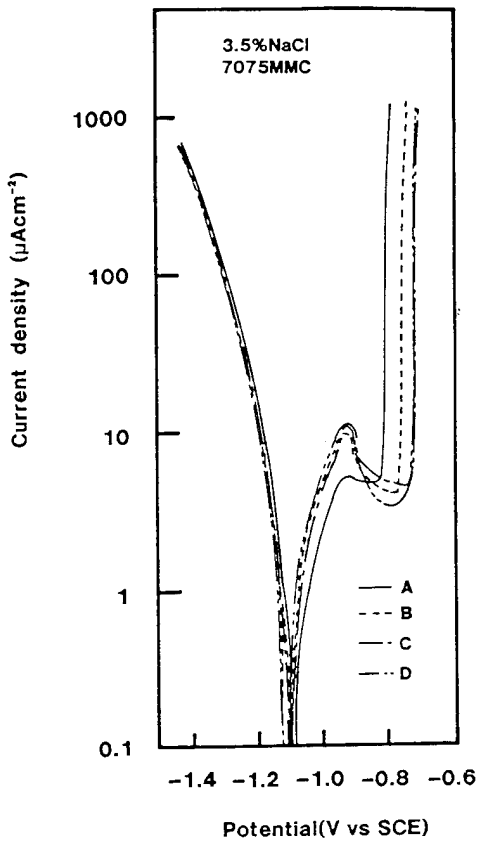

Fig. 6. Potentiodynamic polarization curves in deaerated 3.5% solution at 25 °C for 20 v/o SiC_w–Al 7075 MMC after various ageing treatments. (A) As cast; (B) 110 °C for 6 h; (C) 110 °C for 6 h + 170 °C for 1 h; (D) 110 °C for 6 h + 170 °C for 6 h.

series alloys has been attributed to the coagulation of detrimental grain boundary precipitates. While the SiC_w composite not aged sufficiently shows stress corrosion cracks intergranularly and not along the SiC_w/metal interface, the interfacial growth of the precipitates may contribute to the SCC resistance of an aged composite that does not fail by SCC intergranularly.

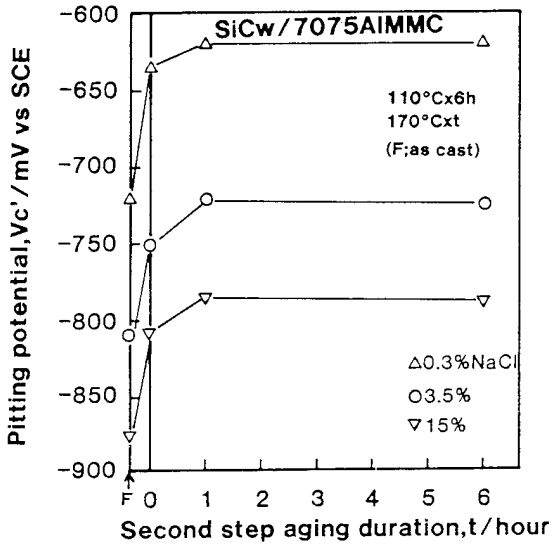

Fig. 7. Pitting potentials for 20 v/o SiC_w–Al 7075 MMC in deaerated (△) 0.3, (○) 3.5 and (▽) 15% NaCl solution at 25 °C as a function of ageing time at 170 °C.

4. Conclusions

Pitting potential for Al 6061-based MMCs containing 20 v/o carbon fibres, Al_2O_3 fibres and SiC whiskers and 10 v/o SiC whiskers are the same as that for monolithic Al 6061.

The resistance of SiC_w–Al 6061 MMC to pit initiation is as good as that of monolithic Al 6061. However, once pits initiate, the corrosion damage of the composite may be greater owing to the formation of crevices between the reinforcement and the matrix by the dissolution of the latter in the pits. The composite must be used under conditions where pitting does not initiate in the matrix alloy.

In spite of the fact that the pitting potential of C–Al 6061 is not affected by the presence of carbon fibres, the MMC is more susceptible to pit initiation because of

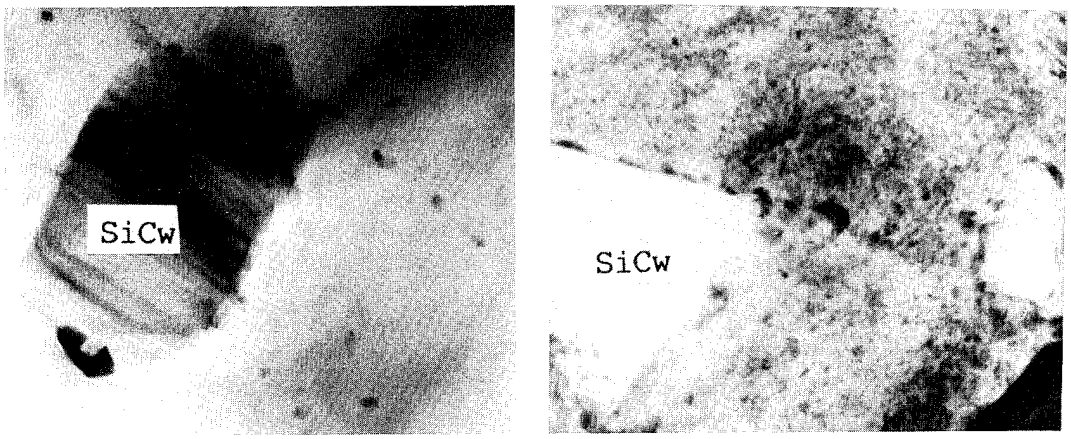

Fig. 8. Transmission electron micrograph of microstructure in 20 v/o SiC_w–Al 7075 MMC. (left panel) Aged at 110 °C for 6 h; (right panel) aged at 110 °C for 6 h and then at 170 °C for 6 h.

Table 4
Constant-load SCC test results for 20 v/o SiC_w–Al 7075 MMC in 3.5% NaCl solution at room temperature

Heat treatment	Applied load[a]		
	90% yield strength	80% yield strength	60% yield strength
As cast	–	F (3)	F (105)
110 °C for 6 h	F (5)	F (220)	F (204)
110 °C for 6 h + 170 °C for 1 h	NF	NF	–
110 °C for 6 h + 170 °C for 6 h	NF	NF	–

[a] F = failure after the number of hours given in parentheses; NF = no failure after 500 h.

the galvanic coupling of the matrix metal and the carbon fibres, the latter being effective cathodes.

A possible cause of the increased cathodic current on the SiC_w–Al 6061 is the formation of an interfacial layer between the matrix metal and SiC whiskers.

Ageing of SiC_w–Al 7075 at 170 °C for more than 1 h following ageing at 110 °C makes the composite resistant to SCC in 3.5% NaCl solution. The pitting potential becomes more noble.

Precipitates are formed in the metal matrix adjacent to the SiC_w–Al 7075 interface by the ageing at 170 °C. The significance of the precipitates on the SCC resistance needs further study.

References

[1] D.M. Aylor and P.J. Moran, *J. Electrochem. Soc.*, *132* (1985) 1277.
[2] P.P. Trzaskoma, E. McCafferty and C.R. Crowe, *J. Electrochem. Soc.*, *130* (1983) 1804.
[3] K. Noda, H. Ono, H. Tsuru, H. Tezuka and A. Kamio, *J. Jpn. Inst. Met.* *56* (1992) 641.
[4] H. Sun, E.Y. Koo and H.G. Wheat, *Corrosion*, *47* (1991) 741.
[5] M.M. Buarzaiga and S.J. Thorpe, *Corrosion*, *50* (1994) 176.
[6] P.P. Trzaskoma, *Corrosion*, *46* (1990) 402.
[7] W.F. Czyrklis, presented at *CORROSION/85*, *1985*, paper No. 196.
[8] D.M. Aylor and R.M. Kain, *ASTM STP*, *864* (1983) 632.
[9] L.H. Hihara and R.M. Latanision, *Corrosion*, *48* (1992) 546.

ELSEVIER

Materials Science and Engineering A198 (1995) 119–125

MATERIALS SCIENCE & ENGINEERING A

Corrosion of SiC monofilament/Ti-15-3-3-3 metal-matrix composites in 3.15 wt.% NaCl

L.H. Hihara, C. Tamirisa

Department of Mechanical Engineering, University of Hawaii at Manoa, 2540 Dole St., Honolulu, HI 96822, USA

Abstract

The corrosion behavior of silicon carbide monofilament/Ti-15-3-3-3 (SiC MF/Ti-15-3) metal-matrix composites (MMCs) were examined in 3.15 wt.% NaCl solutions at 30 °C. Electrochemical experiments were conducted on monolithic ultrapure Ti, Ti-15-3 alloy, hot-pressed SiC, SiC monofilament and the SiC/Ti-15-3 MMC to identify the degradation mechanisms that operate in the SiC/Ti-15-3 MMC. At oxidizing potentials, the Ti-15-3 matrix passivated, whereas the carbon cores and carbon-rich surfaces of the SiC MFs were severely damaged. The anodic polarization curve of the actual MMC and a curve generated using the mixed-potential theory were compared. The curves were very similar, indicating that MMC processing did not significantly affect the electrochemical dissolution behavior of the MMC constituents. Galvanic corrosion between the SiC monofilament and Ti-15-3 matrix metal was negligible. The MMC had excellent corrosion resistance in the open-circuit condition.

Keywords: Corrosion; Galvanic; Titanium; Silicon carbide; Metal-matrix composites

1. Introduction

Silicon carbide monofilament/titanium (SiC MF/Ti) metal-matrix composites (MMCs) have utility in high-temperature applications requiring strong, lightweight materials. The SiC MF/Ti MMCs can be used up to approximately 815 °C [1], owing to the high-temperature strength imparted by the SiC monofilament (MF) reinforcement. The SiC MF/Ti MMCs are significantly lighter than nickel-based superalloys, and have densities approximately equal to 3.9 g cm^{-3} (about 13% less than Ti) [1]. These composites have been used in prototype drive shafts, turbine-engine discs, compressor discs and hollow fan blades, and are also candidate materials for the skin of the National Aerospace Plane [1]. These materials may also find use in room-temperature applications owing to excellent room-temperature properties. Textron Specialty Materials (Lowell, MA) produces SiC MF/Ti MMCs having either Ti-6Al-4V or Ti-15V-3Cr-3Sn-3Al (Ti-15-3) matrices [2]. The Ti-15-3 MMCs were studied in this investigation. The SiC MF/Ti-15-3 MMC has an ultimate tensile strength of approximately 1950 MPa (283×10^3 lbf in^{-2}) and an elastic modulus of approximately 213 GPa (31×10^6 lbf in^{-2}) [2].

The SiC MF/Ti MMCs have an inherent advantage over aluminum and magnesium MMCs when corrosion resistance is considered. The Ti matrix is more resistant to corrosion than Al and Mg. The SiC MF/Ti MMC, however, could become less resistant to corrosion than monolithic Ti owing to the presence of the SiC MFs, contaminants introduced into the MMC microstructure during processing, or the formation of interphases at the filament–matrix interface.

This study was conducted to determine the mechanisms by which the SiC MF/Ti-15-3 MMC corrodes while subjected to oxidizing and open-circuit conditions in 3.15 wt.% NaCl at 30 °C. Electrochemical experiments were conducted on monolithic ultrapure Ti, Ti-15-3 alloy, hot-pressed SiC, SiC MF, and the SiC/Ti-15-3 MMC. The data from the above constituents and the MMC were used to identify the degradation mechanisms that operate in the SiC/Ti-15-3 MMC. The anodic polarization curve of the actual MMC and a curve generated using the mixed-potential theory were compared. No significant discrepancies were found between the curves, indicating that the processing of the MMC did not affect electrochemical corrosion behavior of the MMC constituents. Galvanic-corrosion rates between SiC MF and Ti-15-3 were determined using galvanic

SSDI 0921-5093(94)04515-1

couples and polarization data. Galvanic corrosion was negligible.

2. Materials

2.1. Ultrapure Ti and Ti-15-3 electrodes

Ultrapure (i.e. 99.99% metallic purity) Ti rods of 1.25 cm diameter and Ti 15-3 bars with cross-sections of either 1 cm^2 or 0.035 cm^2 were cut into wafers to make planar electrodes. The larger electrodes were used for polarization experiments, and the 0.035-cm^2 electrode was used for galvanic-couple experiments. The 0.035-cm^2 electrode size was necessary to maintain a 0.6 area fraction of Ti-15-3 in galvanic couples with SiC MF (cross-section) electrodes, which are discussed below. The Ti-15-3 alloy was solution-heated to 790 °C for 30 min and aged at 510 °C for 8 h [3]. One surface of the wafers was coated with silver paint to make electrical contact with a copper wire lead. The sides and silver-painted surface of the wafers were then sealed with an epoxy adhesive (EPOXY-PATCH of Dexter Corp., Seabrook, NH). The front planar surface was left bare and served as the electrode surface.

2.2. Hot-pressed SiC electrodes

Planar electrodes were fabricated from bars of SiC that were hot-pressed to near theoretical densities (over 98%) without sintering aids or binders. Special precautions were taken in making the SiC electrodes owing to the high electrical resistivity of SiC. The SiC bars were cut into 9 mm × 9 mm square wafers about 1 mm thick. The entire back side of the SiC wafers was silver-painted to make electrical contact with a copper wire lead. This procedure was followed to ensure that the ohmic drop through the SiC wafer was uniform over the electrode face during polarization experiments. The sides and silver-painted surface of the SiC wafer were sealed in the epoxy adhesive. Only the front surface was left bare and served as the electrode surface. The resistance through the thickness of the SiC wafers was about 1 kΩ.

2.3. Silicon carbide MF electrodes

Planar SiC MF electrodes were fabricated from Textron SCS-6 SiC MFs of 140 μm diameter. The MF consists of a pitch-based, carbon-fiber core of 33 μm diameter that is surrounded by chemical-vapor-deposited SiC and a carbon-rich outermost layer (Fig. 1). A total of 147 SiC MFs were bundled and then aligned unidirectionally and infiltrated with an epoxy resin (EPON 828 RESIN of Miller–Stephenson Chemical Co. Inc., Danbury, CT). The resulting product, an

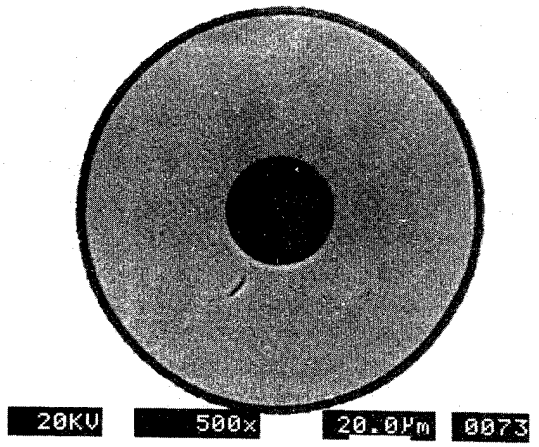

Fig. 1. SEM image of SiC MF. Notice carbon core (dark), SiC layer (light) and carbon-rich outer surface (dark).

SiC MF/epoxy composite rod, was cut into disks by sectioning the rod perpendicularly to the axis of the MFs. The disks were then made into electrodes by silver-painting the back side to make electrical contact with a copper wire lead. The sides of the disk and the silver-painted surface were then sealed with the epoxy adhesive. The total cross-sectional surface area of the SiC MFs was about 0.023 cm^2. Note that, in these planar electrodes, only the cross-sectional filament surface is exposed.

To study the electrochemical properties of the carbon-rich surface of the SiC MFs, electrodes exposing only the carbon-rich circumferential surface (Fig. 2) were prepared. Silicon carbide MFs were cut into lengths of about 3 cm. Only the circumferential surface near each end of the MFs was silver-painted onto a copper wire lead to make electrical contact. The electri-

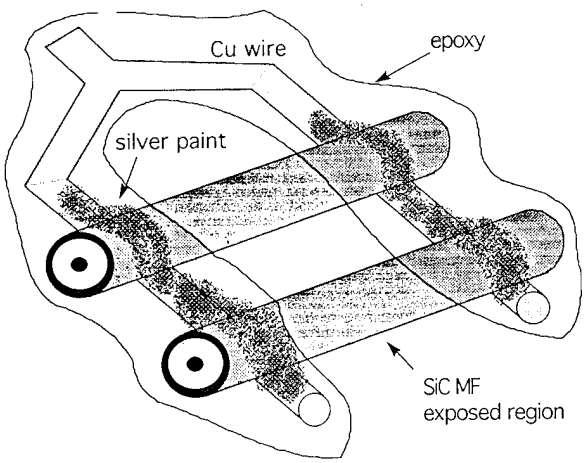

Fig. 2. Schematic drawing of SiC MF (carbon-rich surface) electrode. Notice that only the carbon-rich surface is exposed, and that electrical contact is made to the carbon-rich surface with conductive silver paint.

cal-contact area and the copper wire lead were then sealed with the epoxy adhesive so that only the circumferential surface of the MF was exposed. The total circumferential surface area was about 0.79 cm^2.

2.4. SiC/Ti-15-3 MMC electrodes

The SiC/Ti-15-3 MMC was a product of Textron Specialty Materials. The MMC was nine plies thick, and unidirectionally reinforced with SCS-6 SiC MFs. The MMC was solution-heated to 790 °C for 30 min and aged at 510 °C for 8 h. The volume fraction of SiC MF was approximately 40%. To make planar electrodes, the MMC was cut to expose the cross-sections of the MFs. The axes of the MFs were perpendicular to the planar electrode surface. Electrical contact was made by silver-painting a copper wire lead to the back side of the specimen. The sides and silver-painted surface of the specimen were sealed in the epoxy adhesive.

2.5. Aqueous solutions

Near-neutral 3.15 wt.% NaCl solutions were prepared from 18 MΩ cm water and analytical-grade NaCl. The solutions were kept at 30 ± 0.1 °C, and de-aerated with pre-purified nitrogen (99.99%) or aerated with compressed air. Gas pressure was 1 atm.

3. Instrumentation and procedures

The surface of all planar electrodes was polished to a 0.05 μm finish with γ-alumina powder, and rinsed with 18 MΩ cm water prior to each experiment. The SiC MF (carbon-rich surface) electrodes were rinsed with 18 MΩ cm water prior to each experiment.

Potentiodynamic polarization experiments were conducted with a Model 273 PAR potentiostat/galvanostat (EG&G, Princeton, NJ). The electrodes were stabilized at their corrosion potential prior to polarization. Potentials were measured against a saturated calomel electrode (SCE). All electrodes were polarized at a rate of 0.1 mV s^{-1}. Each polarization experiment was performed at least three times to verify reproducibility. To generate polarization diagrams, the logarithm of the current density was averaged over at least three experiments and plotted as a function of potential.

Galvanostatic experiments were conducted with the PAR potentiostat/galvanostat. Potentials were measured against a SCE. The real potential was obtained by subtracting the electrode ohmic loss from the measured potential. The ohmic loss was measured with an oscilloscope using the current-interrupt method [4]. Measured and real potentials were plotted as a function of time. Each curve represents one experiment.

Galvanic currents were measured between a Ti-15-3 electrode (0.035 cm^2) and a SiC MF (cross-section, 0.023 cm^2) electrode with a ZA 100 zero-shunt ammeter (Intertech Systems, Inc., San Jose, CA). The 0.40 area fraction of SiC MF in the couple was used so that the results could be applied to the actual MMC, which had approximately 0.40 area fraction of exposed SiC MF. The galvanic current was normalized with respect to the Ti-15-3 area to obtain the galvanic-corrosion current density (i_{galv}). The value of i_{galv} was plotted as a function of time for each experiment.

Scanning electron microscopy (SEM) was used to characterize degradation of the SiC MFs and the Ti-15-3 matrix. To obtain micrographs, samples were carbon-coated to avoid charging that could distort the SEM image. Energy-dispersive X-ray analysis (EDXA) was used to identify oxidation products on SiC MFs. EDXA was conducted on samples without carbon coating to avoid carbon contamination.

4. Results and discussion

Polarization and zero-resistance ammeter (ZRA) experiments were conducted to determine the mechanisms by which the SiC MF/Ti-15-3 MMC corrodes at oxidizing and open-circuit potentials. Anodic dissolution behavior of the MMC constituents was studied to determine the inherent degradation properties of the constituents. An anodic polarization curve of the MMC was generated using the mixed-potential theory and polarization data of the MMC constituents. The mixed-potential curve was compared to an actual anodic polarization curve of the SiC MF/Ti 15-3 MMC to determine if MMC processing affected electrochemical dissolution behavior. Galvanic corrosion between the SiC MF and the Ti-15-3 matrix was studied using polarization diagrams and the ZRA technique. The discussion is sectioned into the three primary topics discussed above: (a) degradation behavior of the MMC constituents, (b) mixed-potential theory and effect of MMC processing, and (c) galvanic corrosion.

4.1. Degradation behavior of constituents

Ultra-pure Ti and Ti-15-3 behave very similarly during anodic polarization in de-aerated 3.15 wt.% NaCl at 30 °C (Fig. 3), indicating that the approximately 24% of alloying elements in Ti-15-3 have negligible effect on dissolution rates. The passive current density was approximately 5×10^{-7} A cm^{-2}.

Hot-pressed SiC had lower anodic dissolution rates in de-aerated 3.15 wt.% NaCl (Fig. 4) as compared to SiC MF (cross-section) and SiC MF (carbon-rich surface). Data from P100 graphite [5] was included in Fig. 4 for comparative purposes. The anodic polarization curve of SiC MF (carbon-rich surface) almost traces

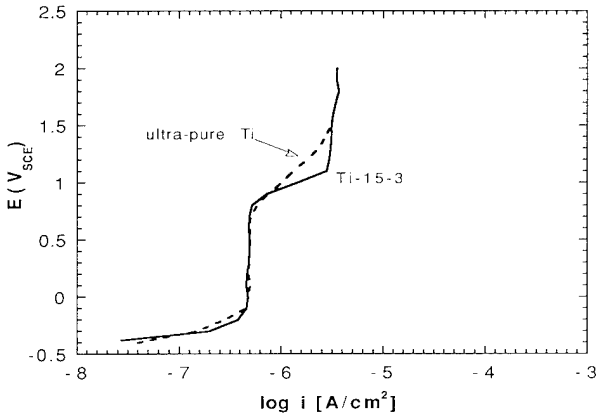

Fig. 3. Anodic polarization diagrams of ultra-pure Ti and Ti-15-3 alloy exposed to de-aerated 3.15 wt.% NaCl at 30 °C. Scan rate = 0.1 mV s^{-1}.

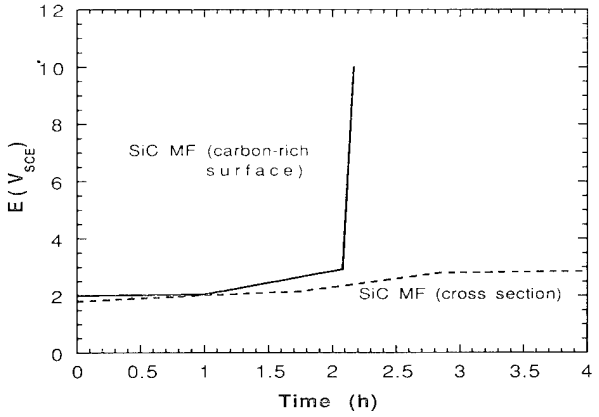

Fig. 5. Potential (measured)-vs.-time diagrams of SiC MF (cross-section) and SiC MF (carbon-rich surface) exposed to de-aerated 3.15 wt.% NaCl at 30 °C. The current density was galvanostatically held at 10^{-2} A cm^{-2}.

that of the P100 graphite, while that of the SiC MF (cross-section) has higher current densities at potentials near open-circuit, but converge with that of P100 graphite at about 1.5 V (SCE). The SiC MF in the cross-section and carbon-rich-surface exposed conditions behave more like graphite than hot-pressed SiC, which is most likely due to the carbon core and carbon-rich surface of the MFs.

To study the oxidation behavior of SiC MF in greater detail, galvanostatic experiments were conducted in de-aerated 3.15 wt.% NaCl at 30 °C at a current density of 10^{-2} A cm^{-2}. The measured potential (Fig. 5) for SiC MF (carbon-rich surface) increased precipitously after approximately 2 h, whereas the potential variation for SiC MF (cross-section) was slight in comparison. Carbon cores were oxidized and consumed in the SiC MF (cross-section) electrodes (Fig. 6). Consumption of the carbon core was attributed to oxidation of carbon into primarily CO_2, which has been observed in graphite fibers [6]. The surface layers of the SiC MF (carbon-rich surface) electrodes flaked and peeled severely (Fig. 7), as compared to new SiC MF (Fig. 8). Comparison of the EDXA spectra of the outer, carbon-rich layer before (Fig. 9) and after (Fig. 10) galvanostatic testing shows that oxygen was incorporated into the oxidized layer. It was theorized that the precipitous increase in measured potential (Fig. 5) was caused by ohmic loss due to an increase in the electrode resistance, either by loss of the conducting carbon-rich layer and or by formation of a non-conducting oxidized layer. Subtracting the ohmic loss from the measured potential and plotting the resulting real potential (Fig. 11) showed that the real potential remained constant at approximately 1.5 V (SCE), indicating that the sharp increase in measured potential was caused by ohmic losses.

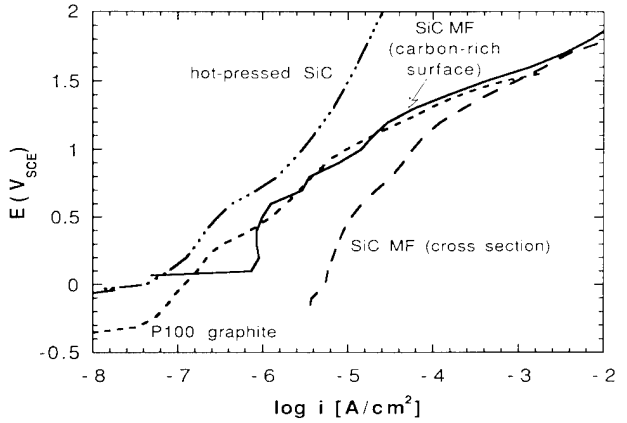

Fig. 4. Collection of anodic polarization diagrams of hot-pressed SiC, SiC MF (cross-section), SiC MF (carbon-rich surface), and P100 graphite [5] exposed to de-aerated 3.15 wt.% NaCl at 30 °C. Scan rate = 0.1 mV s^{-1}.

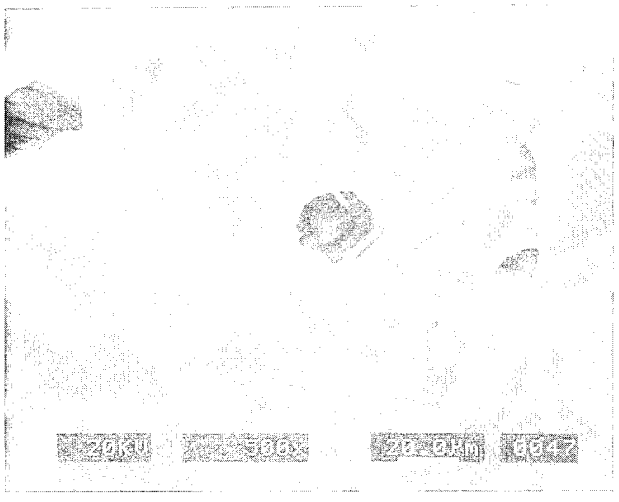

Fig. 6. SEM image of one SiC MF (cross-section) after current density was held galvanostatically at 10^{-2} A cm^{-2} for 6 h in deaerated 3.15 wt.% NaCl at 30 °C. Notice that the carbon core has been consumed.

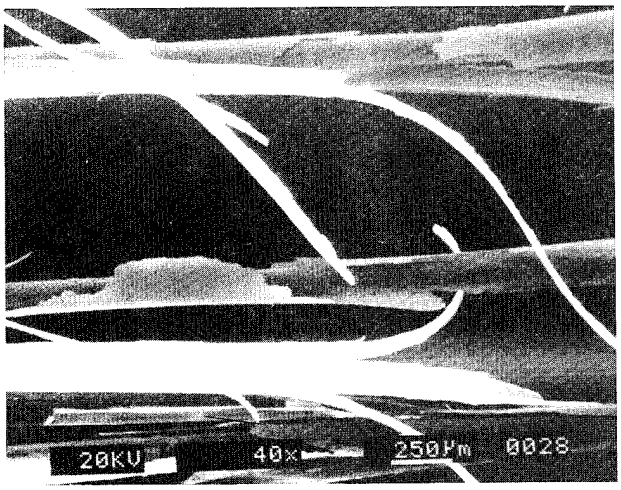

Fig. 7. SEM image of SiC MFs (carbon-rich surface) after current density was held galvanostatically at 10^{-2} A cm^{-2} for 2 h in deaerated 3.15 wt.% NaCl at 30 °C. Notice flaking and peeling of the outermost layer.

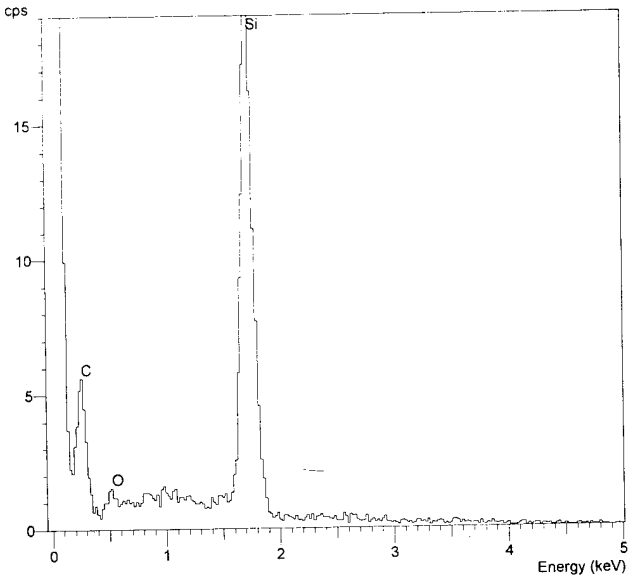

Fig. 9. EDXA spectrum of the carbon-rich surface of a new SiC MF. Beam voltage = 5 kV.

4.2. Mixed-potential theory

A polarization diagram of the MMC was constructed using the mixed-potential theory and the polarization data of the individual MMC constituents. In Fig. 12, the mixed-potential diagram and the actual diagram of the MMC are compared. The area fraction of exposed SiC MF cross-sections for the actual MMC and that corresponding to the mixed-potential diagram is approximately 40%. There is very good correlation between the two diagrams, indicating that the MMC processing did not affect anodic dissolution behavior of the constituents. The shapes of the mixed-potential and actual diagrams are strongly dominated by that of SiC MF (cross-section). The Ti-15-3 remains passive throughout the anodic scan. An SEM image of an MMC electrode after anodic oxidation verifies that damage is concentrated over the SiC MF (Fig. 13).

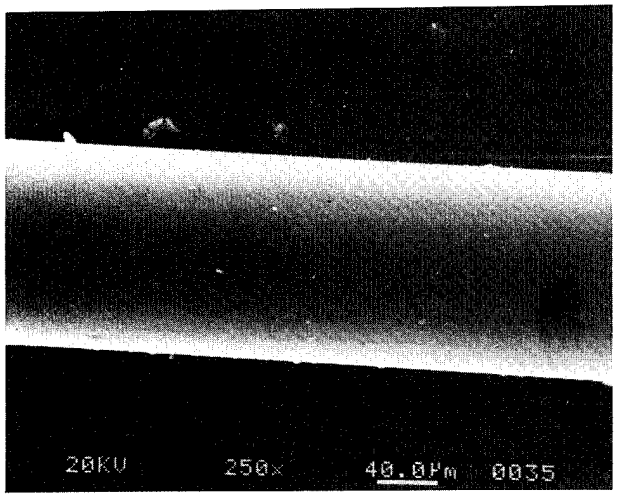

Fig. 8. SEM image of a new SiC MF (carbon-rich surface).

4.3. Galvanic corrosion

The extent of galvanic corrosion between the SiC MF (cross-section) and the Ti-15-3 matrix was assessed using the mixed-potential theory and the ZRA technique. The mixed-potential theory gives the galvanic-corrosion current corresponding to the conditions used in obtaining the polarization diagrams. The advantage of the ZRA technique is that the galvanic-corrosion current can be monitored over time.

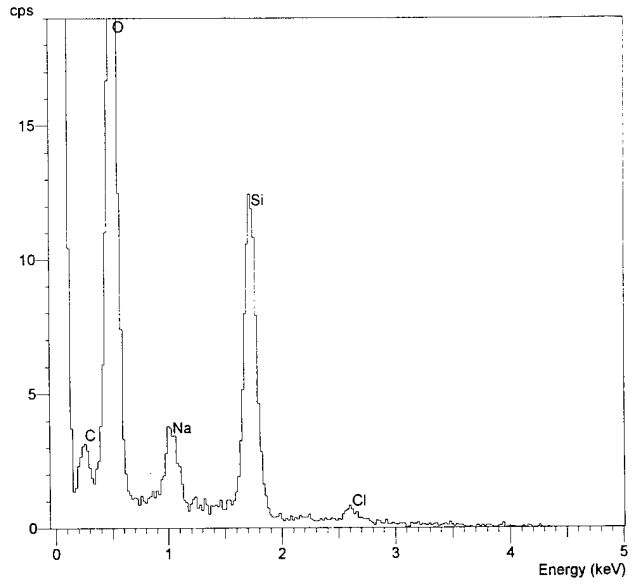

Fig. 10. EDXA spectrum of a flake from an oxidized SiC MF (carbon-rich surface). Beam voltage = 5 kV.

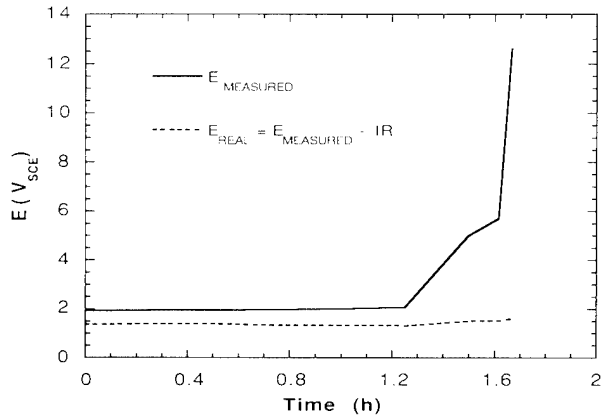

Fig. 11. Potential-vs.-time diagrams of SiC MF (carbon-rich surface) exposed to deaerated 3.15 wt.% NaCl at 30 °C. Current was galvanostatically held at 10^{-2} A cm^{-2}. The real potential was obtained by subtracting the ohmic loss from the measured potential.

Using the mixed-potential theory, the galvanic-corrosion current can be obtained from the intersection of the anodic polarization diagram of Ti-15-3 (de-aerated solution) and a cathodic polarization diagram of SiC MF (cross-section, aerated solution). The galvanic-corrosion current was predicted for aerated 3.15 wt.% NaCl at 30 °C (Fig. 14). The galvanic current was normalized with respect to the Ti-15-3 area and was approximately equal to 5×10^{-7} A cm^{-2}. The ZRA technique was used to study the fluctuation of the galvanic current over time. The galvanic current density (Fig. 15) initially ranged from approximately 4 to 6×10^{-7} A cm^{-2} and decayed significantly within approximately 10 h. In one of the experiments, the current density decayed to zero and then switched signs. The potentials of the galvanic couples also became more negative, indicating that the decrease in galvanic current was due to the cathodic curve of the SiC MF (cross-section) shifting to lower current densities. These

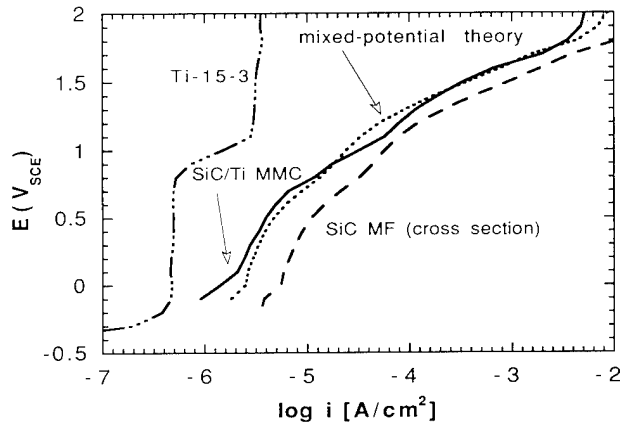

Fig. 12. Collection of anodic polarization diagrams of Ti-15-3, SiC MF (cross-section), SiC MF/Ti-15-3 MMC, and mixed-potential model of the MMC. The environment is de-aerated 3.15 wt.% NaCl at 30 °C. Scan rate = 0.1 mV s^{-1}.

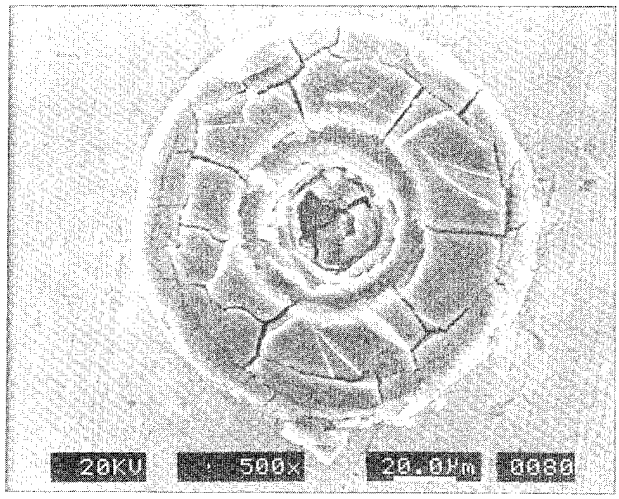

Fig. 13. SEM image of an SiC MF and surrounding Ti-15-3 matrix from an electrode that was used for the generation of an anodic polarization diagram of SiC MF/Ti-15-3 MMC (Fig. 12). Notice that degradation is concentrated on the SiC MF.

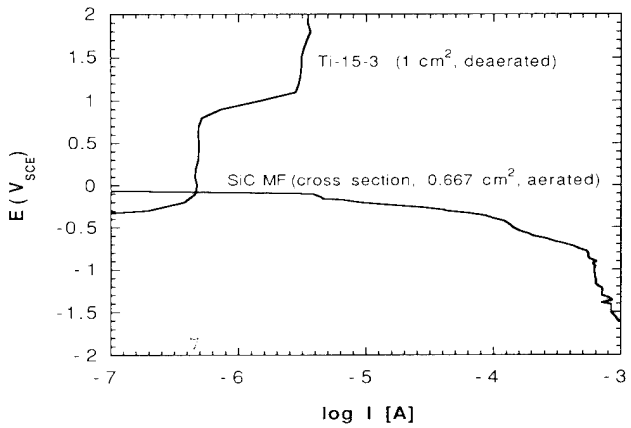

Fig. 14. Polarization diagrams of Ti-15-3 alloy and SiC MF (cross-section) used to predict galvanic-corrosion rates in aerated 3.15 wt.% NaCl at 30 °C. The SiC MF (cross-section) area fraction is 0.4. Scan rate = 0.1 mV s^{-1}.

results indicate that galvanic corrosion is insignificant in the SiC MF/Ti-15-3 MMCs.

5. Conclusions

The SiC MFs are susceptible to degradation at oxidizing potentials in de-aerated 3.15 wt.% NaCl at 30 °C. The carbon cores of the SiC MFs were consumed, which was primarily attributed to CO_2 formation. Flaking and peeling was observed in the outer, carbon-rich surface of the SiC MFs. The oxidized flakes and outer layer of the SiC MFs were enriched with oxygen. The Ti-15-3 matrix alloy passivated at the oxidizing potentials. An anodic polarization diagram of the MMC was generated using the polarization data of the MMC constituents in concert with the mixed-poten-

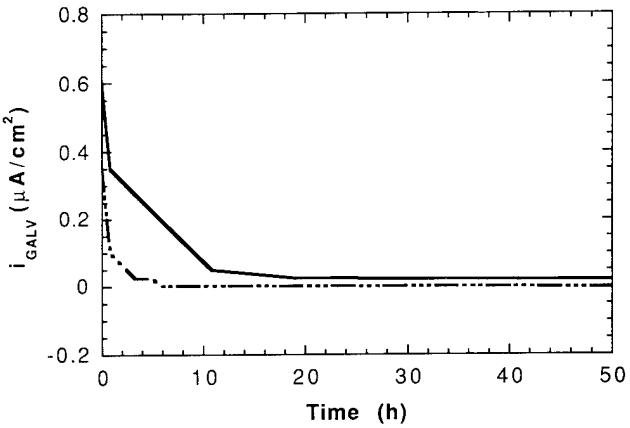

Fig. 15. Galvanic-corrosion current density vs. time for galvanic couples of Ti-15-3 alloy and SiC MF (cross-section) exposed to aerated 3.15 wt.% NaCl at 30 °C. The SiC MF area fraction is 0.4.

tial theory. The mixed-potential diagram was compared to an actual diagram of the SiC MF/Ti-15-3 MMC. The excellent correlation between the two diagrams indicated that MMC processing did not have any significant effects on the electrochemical dissolution behavior of the MMC constituents. Galvanic corrosion between the Ti-15-3 alloy and the exposed cross-section of the SiC MFs was negligible in aerated 3.15 wt.% NaCl at 30 °C. Near the open-circuit potential of the MMC, the SiC MF/Ti-15-3 MMC had excellent resistance to corrosion.

Acknowledgements

The financial support of the National Science Foundation (NSF) (grant no. DMR-9057264) is gratefully acknowledged. The authors are particularly grateful to Dr. B. A. MacDonald of NSF. The contributions of MMC materials from Mr. M. A. Mittnick of Textron Specialty Materials, and Ti-15-3 samples from Mr. J. S. Grauman of TIMET are gratefully acknowledged.

References

[1] D. Hughes, *Aviat. Week Space Technol.* (Nov. 28, 1988) 91.
[2] Continuous Silicon Carbide Metal Matrix Composites, *Company Report* (Textron Specialty Materials, Lowell, MA).
[3] W.A. Reinsch and H.W. Rosenberg, *Met. Prog., 117(4)* (1980) 64.
[4] M. Hayes, in A.T. Kuhn (ed.), *Techniques in Electrochemistry, Corrosion and Metal Finishing — A Handbook*, Wiley, New York, 1987, p. 43.
[5] L.H. Hihara, *Ph.D. Dissertation*, Massachusetts Institute of Technology, Cambridge, MA, 1989.
[6] L.H. Hihara and R.M. Latanision, *Corrosion, 47(5)* (1991) 335.

ELSEVIER

Materials Science and Engineering A198 (1995) 127–134

MATERIALS SCIENCE & ENGINEERING A

Corrosion resistance of zirconium and zirconium–titanium alloy in hot nitric acid

Hiroo Nagano[a], Haruhiko Kajimura[a], Kazuo Yamanaka[b]

[a]*Research and Development Center, Sumitomo Metal Industries Ltd., 1-8, Fusoh-cho, Amagasaki 600, Japan*
[b]*Sumitomo Metal Technology, Inc., 1-8, Fusoh-cho, Amagasaki 600, Japan*

Abstract

Since zirconium (Zr) has superior corrosion resistance to concentrated nitric acid (HNO_3) at elevated temperature, it has been successfully used as a material for chemical plants to produce HNO_3 or spent nuclear fuel reprocessing plants. However, the occurrence of stress corrosion cracking (SCC) has recently been reported in hot nitric acid conditions. The necessary conditions for SCC in Zr, and the preventive method against SCC by alloying were investigated. The slow strain rate technique test, electrochemical measurements, strain electrode tests, and analysis of corrosion products were carried out in this work. SCC does not occur in Zr in boiling HNO_3 at concentrations less than 70%, whereas SCC is initiated in 6–94% HNO_3 when a potential is applied above the critical potential for SCC. A new invention of Zr-15%Ti alloy is immune to SCC under applied potential conditions in hot HNO_3: this alloy forms a stable passive film composed of ZrO_2 and TiO_2.

Keywords: Zirconium; Zirconium–titanium alloy; Passivity; Stress corrosion cracking; Spent nuclear fuel; Nitric acid

1. Introduction

Reprocessing of spent nuclear fuels has been carried out usually in HNO_3 by the Purex method in plants made of stainless steels or zirconium. Stainless steels are now indispensable constructional materials for dealing with HNO_3, because they have good corrosion resistance against nitric acid solutions as well as appropriate practical properties such as working, welding properties, etc. [1,2]. However, they have a drawback: they are susceptible to general and intergranular corrosion in highly oxidizing nitric acid media which contain oxidizing reagents such as Cr^{6+}, Ce^{4+}, etc., with high oxidation–reduction potentials [1–4].

On the other hand, Zr generally has higher corrosion resistance than stainless steel [5–8]. For example, it shows excellent corrosion resistance to hot HNO_3 both with and without oxidizing species [3,7,9]. It is used these days as an important constructional material for dissolver tanks of spent nuclear fuels [10]. However, recent studies have shown that even Zr is susceptible to stress corrosion cracking (SCC) under specific conditions in HNO_3 [11–14]. Beavers [11] describes that Zircaloy-4 (UNS R60804, Zr-1.5%Sn alloy) is susceptible to SCC in HNO_3 with concentrations greater than 20% by the slow strain rate technique (SSRT). Yau [12] investigated SCC for commercially pure Zr, Zr-1.5%Sn alloy and Zr-2.5%Nb alloy in HNO_3 by the U-bend and C-ring tests, and reports that although all of them have high SCC resistance in 70% HNO_3 up to the boiling

Table 1
Chemical composition of Zr used (mass%)

Hf	Fe	Cr	H	N	O
0.009	0.083	0.012	0.0009	0.0012	0.106

SSDI 0921-5093(94)04517-8

Table 2
Tensile properties of Zr

	Tensile stress (MPa)	0.2% proof stress (MPa)	Elongation (%)
Longitudinal at R.T.	426	249	28.9
Transverse at R.T.	415	328	26.3
Longitudinal at 373 K	333	188	35.4
Transverse at 373 K	319	244	36.5

point, they become susceptible to SCC in HNO_3 above 80%.

It is an interesting and important research topic to make sure the mechanism of SCC in Zr in extremely oxidizing nitric acid solutions although it has generally excellent corrosion resistance to hot pure HNO_3. The susceptibility of Zr to SCC is featured in terms of concentration of HNO_3, concentration of oxidizing species, and temperature as well as such factors as potential, applied stress, extension rate on the metal, etc.

Therefore, first, this paper is aimed at clarifying the relationship between occurrence of SCC in Zr and its electrochemical behavior in hot oxidizing HNO_3 by considering a transition of the passive film formed on Zr from a stable to an unstable state. Second, it deals with a countermeasure against SCC. Zr has excellent general corrosion resistance to high temperature pure HNO_3 even though it is not immune to SCC. On the other hand, titanium (Ti) has good general corrosion and SCC resistance in hot oxidizing HNO_3 although it is severely attacked in pure HNO_3 at elevated temperatures. Alloying Ti to Zr is expected to exhibit synergistic effects on improving both the general corrosion and SCC resistance [15]. Consequently, optimization of corrosion resistance has been studied in Zr–Ti alloys.

2. Experimental procedure

2.1. Material

Tables 1 and 2 show the chemical composition and tensile properties of commercially pure Zr used for SCC tests. Table 3 is the chemical composition of Zr and Zr–Ti alloys, of which Ti content was changed up to 25 mass%. Synergistic effects of Zr and Ti on the corrosion resistance of Zr–Ti alloys were evaluated by using these materials. Commercially pure Zr and Zr–Ti alloys were melted in vacuum, forged, rolled to plate, and finally annealed at 923 K for 5 h.

2.2. Corrosion test

General corrosion and SSRT tests were conducted in 6–94% HNO_3. The solutions were kept under boiling conditions or isothermal conditions during the tests. The specimens for the SSRT tests were strained to failure at a strain rate of 4.17×10^{-6} s^{-1}. The SSRT specimens were kept at open-circuit potentials or under applied potentials. The SCC susceptibility of Zr and Zr–Ti alloys was evaluated by the fracture strain. Constant-load SCC tests were also carried out under constant-potential conditions in 40% HNO_3 for 500 h. A load of 196 MPa, equal to the 0.2% proof stress at 373 K, was applied to the specimens.

2.3. Measurement of electrochemical polarization curves

Anodic polarization curves for Zr and Zr–Ti alloys were measured in 6–94% HNO_3 at boiling temperatures, and also in 40% HNO_3 at 373 K. The potential sweep rate was 0.33 mV s^{-1}. The potentials of specimens were measured vs. the saturated calomel electrode (SCE).

2.4. Measurement of strain electrode behavior

The strain electrode test method [16,17] was used to investigate the speed of film regeneration on Zr or Zr–Ti alloys. The parallel part of the strain electrode is 1 mm in diameter and 10 mm in length. The electrode was rapidly extended to 3% strain at a rate of 3.8 s^{-1}, and then current decay responding to new film formation on metal surfaces was measured.

2.5. Analysis of corrosion films on post-test metal surfaces

The corrosion films formed on specimen surfaces were analyzed by X-ray diffraction or X-ray photoelectron spectroscopy (XPS).

3. Experimental results

3.1. Effects of nitric acid concentration and electrode potential on SCC in Zr

SSRT tests for Zr were carried out in 6–94% HNO_3 over a wide potential range. Fig. 1 shows the relation-

Table 3
Chemical compositions of Zr-Ti alloys (mass%)

Alloy	Ti	C	Fe	Cr
Zr	<0.01	0.004	0.130	0.021
Zr-2.5Ti	2.44	0.003	0.077	0.017
Zr-5Ti	4.94	0.005	0.069	0.015
Zr-10Ti	9.94	0.003	0.079	0.018
Zr-15Ti	14.88	0.002	0.059	0.015
Zr-20Ti	19.78	0.003	0.096	0.017
Zr-25Ti	24.82	0.004	0.080	0.013

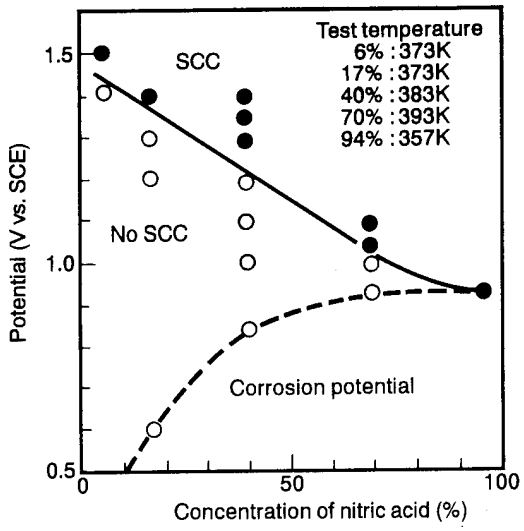

Fig. 1. Relationship between potential and concentration of HNO_3 on the SCC susceptibility of Zr by the SSRT test.

ship between boiling HNO_3 concentration and potential on SCC susceptibility. The dashed line shows the change in the corrosion potential of Zr with HNO_3 concentration, and the solid line the initiation potential for SCC, respectively. The potential allowance to SCC from the corrosion potential is 0.8 V in 17% HNO_3, but only 0.1 V in 70% HNO_3. In 94% HNO_3, there is no potential allowance to SCC. SCC occurs in Zr at an open-circuit potential in 94% HNO_3.

Fig. 2 shows the fracture surfaces due to dimple fracture at 1.2 V, and SCC at 1.3 V by constant-potential SCC tests, respectively. The cleavage-type fracture surface is characteristic in the SCC of Zr and Zr–Ti alloys.

Anodic polarization curves for Zr in different concentrations of HNO_3 are depicted in Fig. 3. The polarization curve in boiling 6% HNO_3 is of a generic pattern for passivation metals, i.e. consisting of three major potential regions of the primary passivity below 1.3 V, the transition between 1.3 V and 1.7 V, and the secondary passivity above 1.7 V. SCC occurs in the transition region. Sharp current increase in the transition region probably responds to weakening of a passive film on Zr during tests. This transition region becomes narrower and less noble as the concentration of HNO_3 is increased. Whereas the initiation potential for the transition region becomes more noble with decrease in temperature, e.g. 1.3 V at 383 K and 2.0 V at 323 K in 40% HNO_3, respectively.

3.2. Improvement of SCC resistance with addition of Ti to Zr

Zr and Ti are completely soluble at every mixing ratio, as shown in Fig. 4 [18]. Since Zr is extremely resistant to pure HNO_3 at high temperatures, and Ti,

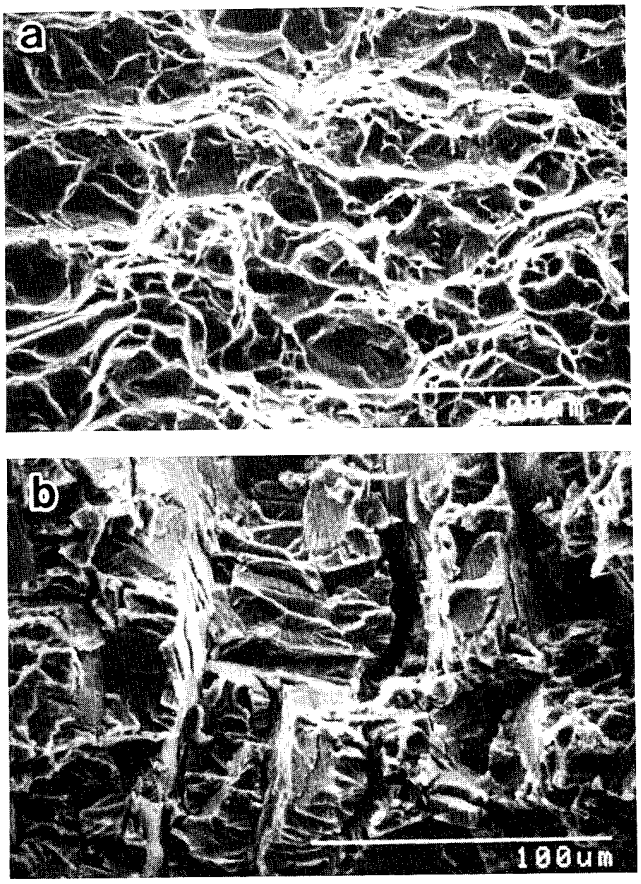

Fig. 2. Scanning electron micrographs of the fracture surfaces after the constant-potential SSRT tests in 40% HNO_3 at boiling temperature: (a) $E = 1.2$ V(SCE); (b) $E = 1.3$ V(SCE).

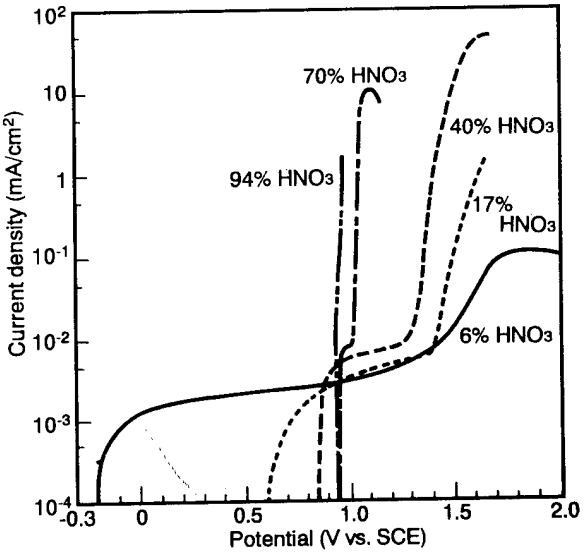

Fig. 3. Anodic polarization curves for Zr in (6–94)% HNO_3 at boiling temperature.

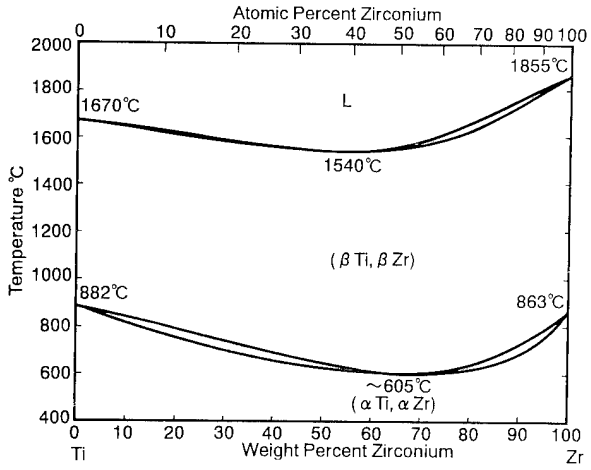

Fig. 4. Zr–Ti phase diagram.

on the other hand, has good corrosion resistance to highly oxidizing HNO_3 except pure HNO_3. A synergistic effect by both of them could possibly lead to the birth of a new Zr–Ti alloy with high corrosion resistance, free from SCC in nitric acid environments.

The target of the research to invent a new alloy is shown in Table 4: an extremely low general corrosion rate in boiling 40% HNO_3 like pure Zr, no SCC up to 2000 mV in concentrated HNO_3 at the boiling point, and appropriate mechanical properties.

Ti has a disadvantage of being attacked in pure HNO_3. However, Zr–Ti alloy below 15% Ti addition shows almost the same corrosion rate as pure Zr, as shown in Fig. 5. Fig. 6 shows that both Zr-2.5%Ti and Zr-15%Ti alloys have higher critical potentials for SCC occurrence compared with Zr. In particular, Zr-15%Ti alloy is immune to SCC up to 2000 mV in HNO_3 with concentrations up to 70% at the boiling point.

Fig. 7 illustrates the effect of annealing temperature on the mechanical properties of cold-rolled Zr-15% Ti alloy: complete recrystallization is achieved around 873 K.

3.3. Relationship between strain electrode behavior and SCC susceptibility for Zr and Zr-15%Ti alloy

It has generally been known in stainless steel that SCC is initiated and propagates only under specific conditions where localized corrosion takes place: there is no SCC under general corrosion either at active dissolution potentials or transpassive dissolution potentials. Therefore, an alloy having rapid film regeneration ability after the film breakdown is expected to have good SCC resistance.

Specimens of Zr, Ti, and Zr-15%Ti alloy were rapidly strained in 17% HNO_3 at the specific potentials shown by arrows in Fig. 8. Only Zr showed SCC at the potentials of 1.4 and 1.7 V in SSRT and constant-load SCC tests. Current–time decay curves for Zr and Zr–Ti alloy are depicted in Figs. 9 and 10, respectively. For Zr, the curves at 1.4 and 1.7 V (SCC occurs at both potentials) are located at higher current-density positions than that at 1.2 V (no SCC). On the other hand, Zr-15%Ti alloy was immune to SCC. No distinct difference is observed in the decay curves at the potentials between 1.7 and 2.0 V.

4. Discussion

4.1. Mechanism of SCC in Zr in HNO_3

SCC occurs in Zr in hot HNO_3 above the critical potential in the transition potential region between the primary passive and the secondary passive regions.

Two types of mechanisms are considered for SCC in HNO_3. One is embrittlement by the presence of hydrides, and the other is the model of passive film rupture by stress in the corrosive environment. The thermodynamic hydrogen evolution potential (less than 0 V vs. SHE) in HNO_3 is considerably less noble than the corrosion potential of Zr in HNO_3. Furthermore, no SCC cracks were observed at potentials lower than the corrosion potentials in this study. The model of embrittlement by hydrides, therefore, cannot be considered in HNO_3.

In general, SCC is likely to occur in three potential regions of a polarization curve for a stainless steel: the active dissolution region, the region between the active and primary passive states, and the region between the primary and secondary passive states. Film weakening proceeds on metal surfaces at these potential regions, leading to localized corrosion, which could form the sites for SCC under stress.

The model of passive film rupture was also examined on the SCC of Zr. ZrO_2 film is formed on Zr in HNO_3 at potentials in the passive state and also at potentials above the critical potential for SCC in the transition state. Fig. 11 shows X-ray diffraction patterns of corrosion products after the immersion test in HNO_3 at 1.4 V, which exceeds the critical potential for SCC.

Film weakening or roughening was observed on Zr surfaces at potentials above the critical potential. Fig. 12 consists of transmission electron micrographs of Zr surfaces after the constant-potential corrosion test in the transition potential region in 17% HNO_3 at boiling temperature. There are many corrosion traces with shallow hollows in the photographs. The traces formed at 1.5 V are bigger and more in number than those at 1.4 V.

The passive film of ZrO_2 partially breaks down at potentials in the transition region in HNO_3 according to the following chemical reactions [15,19]

Table 4
Goal of improvement in Zr–Ti alloys

	Item	Goal to be achieved in Zr–Ti alloys	Value for pure Zr
General corrosion rate	40% HNO_3	<0.15 mm $year^{-1}$	0.001 mm $year^{-1}$
Critical potential for SCC	17% HNO_3	No SCC up to 2000 mV(SCE)	1400 mV
	40% HNO_3	2000 mV(SCE)	1300 mV
	70% HNO_3	2000 mV(SCE)	1050 mV
Mechanical property	0.2% proof strength	Higher strength than pure Zr	RT: 343 MPa (≥207)[a]
			273 K:274
	Tensile strength		RT: 421 (≥379)[a]
			273 K: 343
	Elongation		RT: 24% (≥16)[a]
			273 K: 30

[a]( ): ASTM designation for R60702

$$ZrO_2 + 4H^+ = Zr^{4+} + 2H_2O \quad (1)$$

or

$$ZrO_2 + 2H^+ = ZrO^{2+} + H_2O \quad (2)$$

A schematic illustration is given in Fig. 13 on the degradation of passive films in the transition region. Plenty of defects formed in the films result in weakening or roughening of the film.

Consequently, it is concluded that SCC is triggered under stress above the specific potential in the transitional potential region in HNO_3 where weakening or roughening of corrosion films occurs on Zr surfaces.

4.2. Synergism of Zr and Ti on improving corrosion resistance of Zr–Ti alloys

A current–time decay behavior represents the tendency for newly born metal surfaces to regenerate a passive film. A schematic illustration of a typical current decay curve is given in Fig. 14. Two stages appear on the curve: the first stage, for only a few milliseconds, is for the formation of monolayer oxide films, and the subsequent second stage is for the growth of oxide films.

The synergistic effect of adding Ti to Zr has made it possible to produce an alloy resistant to SCC as well as to general corrosion in HNO_3. The excellent corrosion resistance of Zr-15%Ti alloy comes from the formation of a mixture of ZrO_2 and TiO_2 on metal surfaces, shown in Fig. 15.

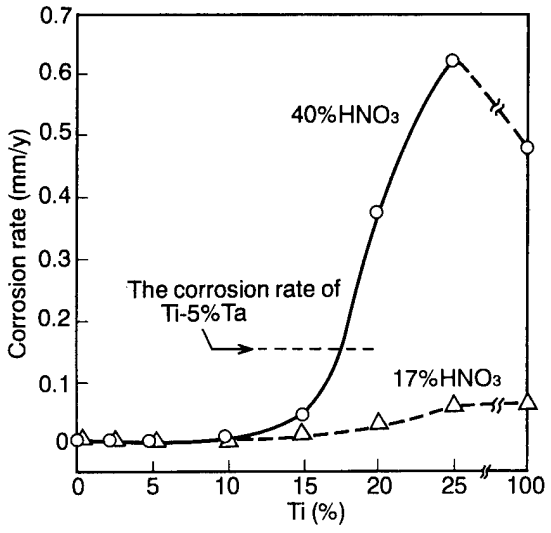

Fig. 5. Effect of Ti on the corrosion rates of Zr–Ti alloys in HNO_3 at boiling temperature.

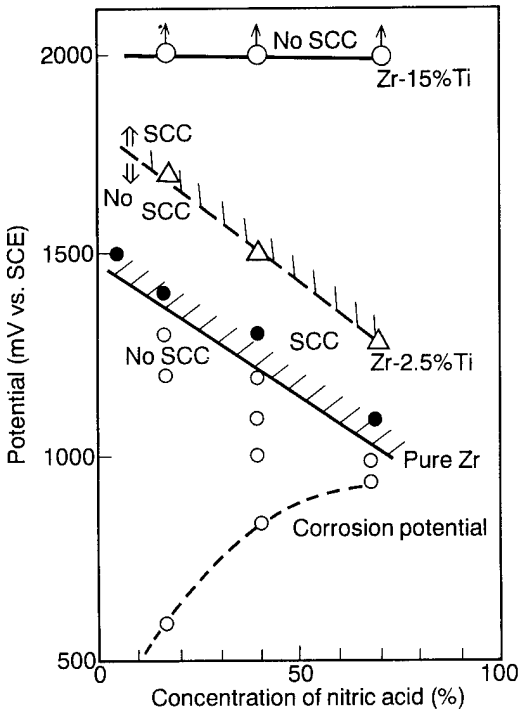

Fig. 6. Effect of HNO_3 concentration at boiling temperature on the critical potential for SCC in pure Zr and Zr–Ti alloys.

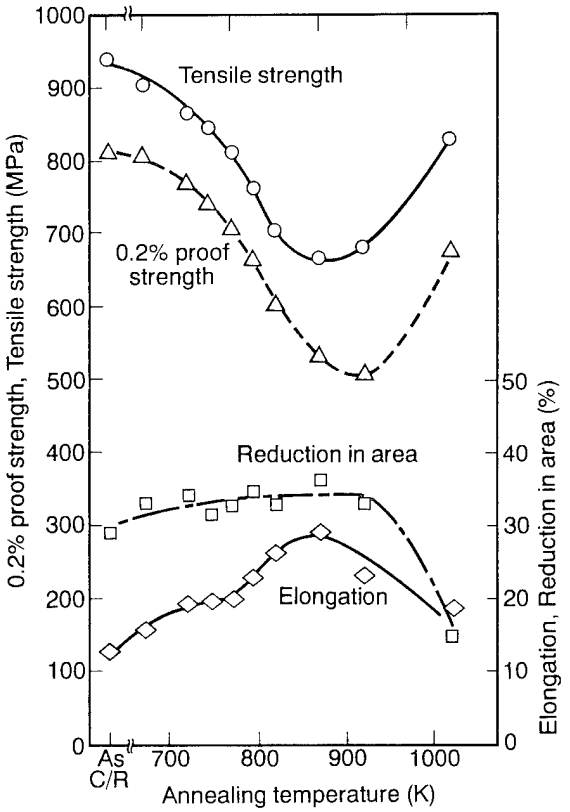

Fig. 7. Effect of annealing temperature on room-temperature mechanical properties of Zr-15%Ti alloy with 80% cold-rolling.

Fig. 16 shows the charge for growth of a passive film on Zr at transpassive potentials. Zr-15% Ti alloy has a lower charge in the second stage than Zr, because Zr-15%Ti alloy maintains a more stable and compact passive film. This is the reason for the immunity of this alloy to SCC in hot oxidizing nitric acid environments.

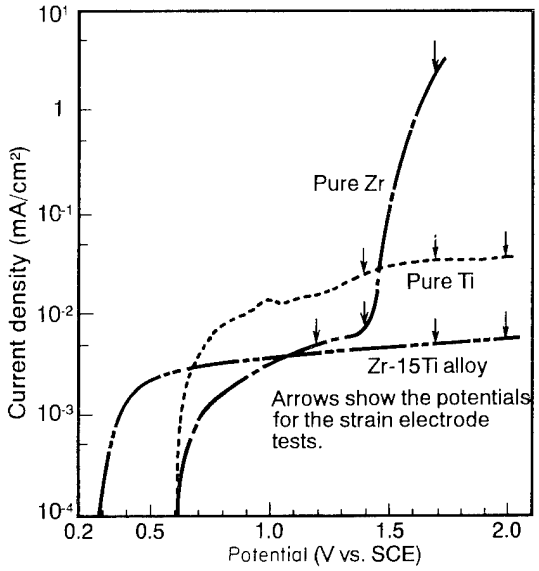

Fig. 8. Anodic polarization curves for pure Zr, Zr-15%Ti alloy, and pure Ti in 17% HNO_3 at 373 K.

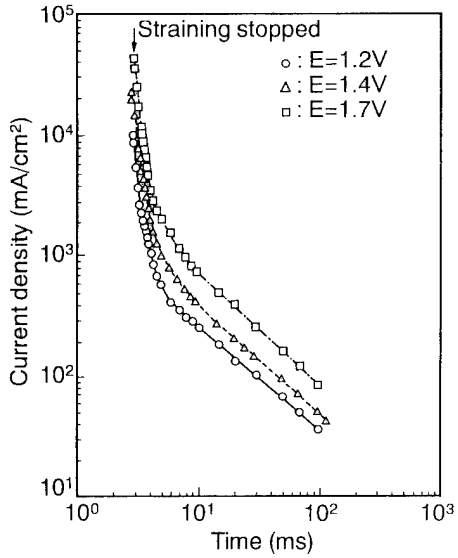

Fig. 9. Current–time decay curves for pure Zr in 17% HNO_3 at 373 K at the potentials of 1.2, 1.4 and 1.7 V(SCE).

5. Conclusion

The SCC susceptibility of Zr and its SCC mechanism were studied by SSRT and constant-load tests in HNO_3 with and without applied potentials. Then, the effect of adding Ti to Zr was investigated from the viewpoint of the prevention of Zr SCC. The results are summarized as follows:

(1) Zr does not have any SCC attack at open-circuit potentials in hot HNO_3 with concentrations less than 70%.
(2) SCC occurs in Zr in boiling (6–94%) HNO_3 at potentials higher than the critical potential at which SCC is initiated.

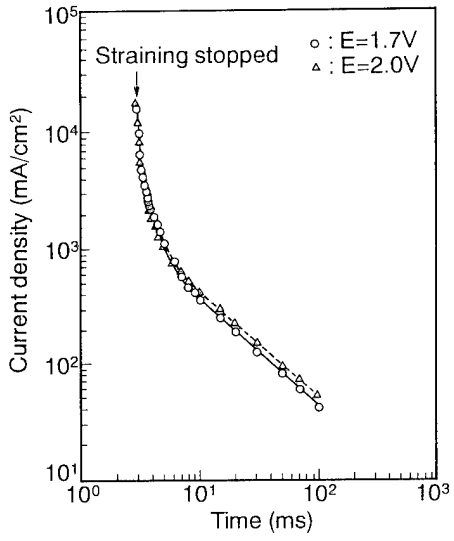

Fig. 10. Current–time decay curves for Zr-15%Ti alloy in 17% HNO_3 at 373 K at the potentials of 1.7 and 2.0 V(SCE).

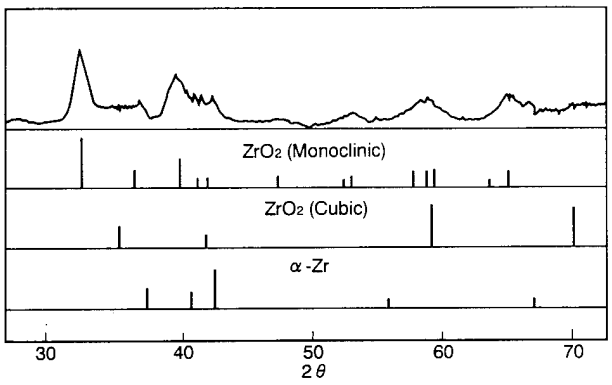

Fig. 11. X-Ray diffraction patterns of pure Zr after immersion tests in HNO_3 at boiling temperature at 1.4 V for 1 h.

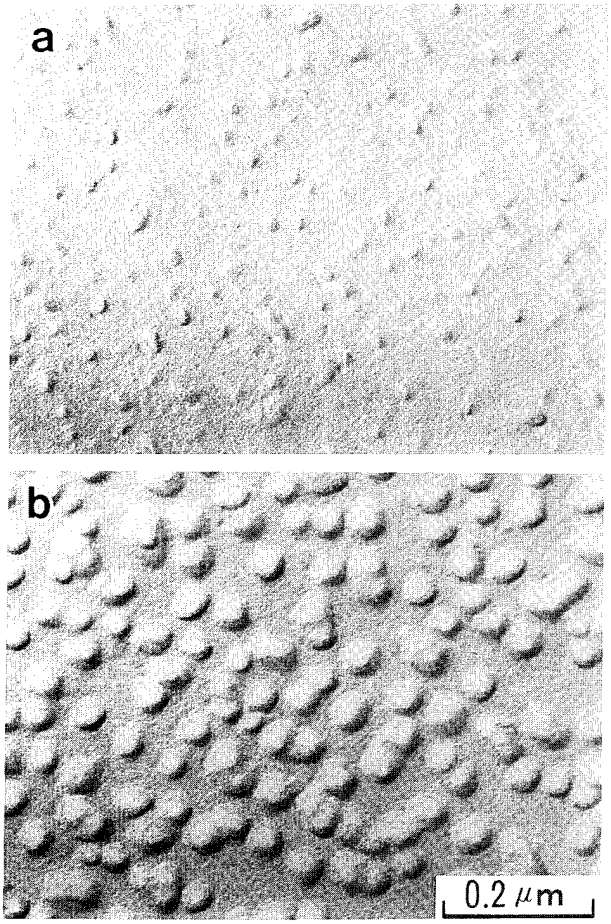

Fig. 12. Electron micrographs of the Zr surface by the replica method after the constant-potential corrosion tests in 17% HNO_3 at 373 K for 1200 s: (a) E = 1.4 V(SCE); (b) E = 1.5 V(SCE).

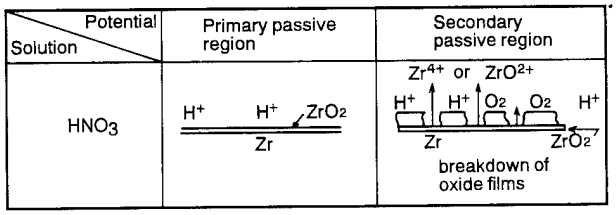

Fig. 13. Schematic illustration of the surface films formed on zirconium in the characteristic potential regions.

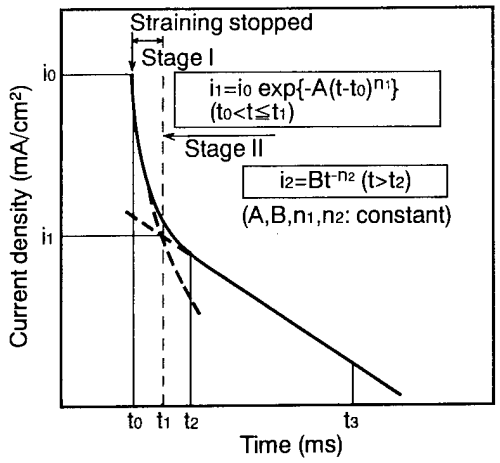

Fig. 14. Schematic illustration of a current–time decay curve.

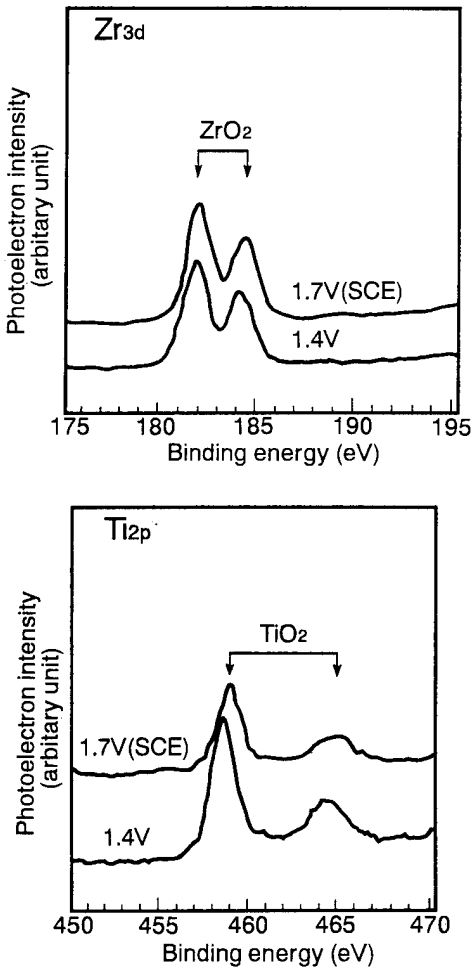

Fig. 15. XPS spectra of Zr-15%Ti alloy after the constant-potential corrosion tests at the potentials of 1.4 and 1.7 V in 17% NHO_3 at 373 K for 24 h.

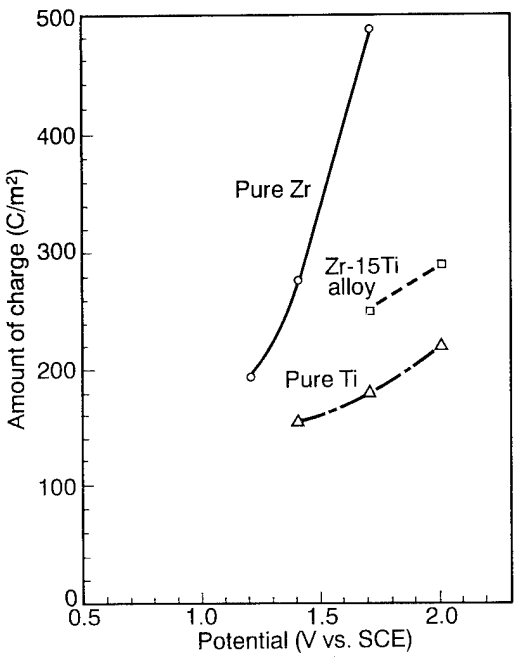

Fig. 16. Effect of potential on the amount of charge for the growth of films.

(3) The critical potential for SCC exists in the transition region between the primary and secondary passive states. Zr oxide film formed in the transition region becomes unstable with increasing shallow hollows in the film.

(4) The addition of Ti to Zr improves the SCC resistance of Zr to hot HNO_3. Zr-15%Ti alloy is im mune to SCC at applied potentials up to 2000 mV(SCE). A mixture of ZrO_2 and TiO_2 film formed on the alloy in hot HNO_3 is thought to contribute to the SCC resistance.

References

[1] H. Nagano, *Boshoku Gijutu*, *37* (1988) 301.
[2] H. Kajimura and H. Nagano, *Bull. Jpn. Inst. Met.*, *31* (1992) 725.
[3] C.R. Bishop, *Corrosion*, *19* (1963) 308t.
[4] J.S. Armijo, *Corrosion*, *21* (1965) 235.
[5] R.T. Webster, *Met. Prog.*, *113* (February 1978) 62.
[6] D.R. Knittel, *Chem. Eng.*, *87* (June 1980) 95.
[7] D.R. Knittel and R.T. Webster, *Industrial Application of Titanium and Zirconium, ASTM Special Technical Publication 728*, ASTM, Philadelphia, PA, 1979, p. 191.
[8] C.A. Hampel, *Corrosion*, *17* (1961) 9.
[9] P.J. Gegner and W.L. Willson, *Corrosion*, *15* (1959) 341t.
[10] P. Auchapt, L. Patarin and M. Tarnero, *Meeting on Fuel Reprocessing and Waste Management, American Nuclear Society, La Grange Park, 1984*, ASM, La Grange Park, IL, 1984, p. 2.
[11] J.A. Beavers, J.C. Griess and W.K. Boyd, *Corrosion*, *36* (1981) 292.
[12] T.L. Yau, *Corrosion*, *39* (1983) 167.
[13] T.L. Yau, *Corrosion/87*, NACE, Houston, TX, 1987, Paper No. 170.
[14] H. Kajimura and H. Nagano, *Corros. Sci.*, *31* (1990) 261.
[15] H. Kajimura, T. Kodama and H. Nagano, *J. Atomic Energy Soc. Jpn.*, *30* (1988) 1107.
[16] T. Shibata and R.W. Staehle, *Proc. 5th Int. Congr. on Metallic Corrosion*, NACE, Houston, TX, 1975, p. 487.
[17] S. Hujimoto and T. Shibata, Bulletin of the Japan Institute of Matals, 29 (1990) 132.
[18] M. Pourbaix, Atlas of Electrochemical Equilibria, Pergamon Press, Oxford, 1966, p. 223.
[19] T.B. Massalski, J.L. Murray and H. Baker, Binary Alloy Phase Diagrams, vol. 2, ASM, Metals park, OH, p. 2142.

ELSEVIER

Materials Science and Engineering A198 (1995) 135–144

MATERIALS SCIENCE & ENGINEERING A

Passivity of high-nitrogen stainless alloys: the role of metal oxyanions and salt films

Clive R. Clayton[a], Gary P. Halada[a], Jeffery R. Kearns[b]

[a]*Department of Materials Science and Engineering, State University of New York at Stony Brook, Stony Brook, NY 11794-2275, USA*
[b]*Allegheny Ludlum Steel, Steel and Alloy Research and Development Group, Technical Center, Alabama and Pacific Avenue, Brackenridge, PA 15014-1597, USA*

Abstract

Surface-analytical studies of high-nitrogen austenitic stainless steels exposed to de-aerated 0.1 M HCl have revealed that nitrogen alloying additions influence the composition of salt layers and the passive film/alloy interface. It was shown that nitrogen, nickel and molybdenum additions stimulate selective dissolution of iron, resulting in a significant enrichment of chromium beneath the passive film. The build-up of a protective ferrous molybdate layer was seen to be most strongly enhanced with additions of nickel and, to a lesser extent, nitrogen. While the primary kinetic barrier to anodic dissolution of high-nitrogen stainless steels is a chromium-oxide-based passive film, it appears that a mixed nitride surface layer and an ultra-thin layer of ferrous molybdate act as secondary kinetic barriers.

Keywords: Molybdate; Nitrogen; Passivity; Stainless steels; XPS

1. Introduction

High nitrogen stainless steels represent a relatively new group of the commercially available austenitic stainless alloys. Nitrogen represents an economically and environmentally attractive and versatile alloying element, which has been shown for some time to be a powerful austenite stabilizer as well as a strengthener. Of particular importance is the well-known, but poorly understood, improvement to corrosion resistance, especially pitting resistance, attributable to N alloying of Mo-bearing austenitic stainless steels. Many of the beneficial effects of N alloying on the corrosion resistance of stainless steels have been reported [1–5].

In this paper we draw particular attention to the formation of pre-passive ultra-thin salt films formed on N-bearing ferritic and austenitic stainless alloys and their possible role in improving corrosion resistance. While, for brevity, the discussion will relate to the "18-8" group of stainless steels, many of the observations are relevant to more highly alloyed stainless alloys. In this study we compare the influence on corrosion behavior of Ni and Mo additions to an Fe-19Cr base alloy. Specifically, this study will consider two ferritic alloys; Fe-19Cr and Fe-19Cr-2.5Mo, and two austenitic alloys; Fe-19Cr-9Ni and Fe-19Cr-9Ni-2.5Mo. To determine what influence N may have as an alloying addition to each of the above alloys, we have chosen to employ a previously developed electrochemical surface nitriding treatment which simulates N alloying [6].

2. Background

2.1. The role of metal oxyanions and salt layers in passivity

Passivation of metals is most commonly associated with the rapid formation of several monolayers of an insoluble oxide barrier film on exposure of the metal or alloy to an aqueous environment. The speed of the repassivation process precludes easy observation of the metal surface during repassivation to determine the sequence of events, but the result is usually the same: an oxide film forms directly on the metal or alloy

SSDI 0921-5093(94)04518-6

surface, and then one or several monolayers of a salt film form on the surface of the oxide layer.

Salt layers provide excellent passivation under certain conditions in which oxide films cannot be established. In one recent case, surface studies of the passivity of amorphous alloys containing phosphorous have shown effective passivation due to phosphorous oxyanions of various types [7]. In another case, several authors have speculated that Mo additions to stainless steel result in improvements to pitting resistance owing to the formation of an insoluble chloride complex of Mo in the highly acidified chloride solution inside a pit [8–9]. Indeed, it has been shown recently that Mo passivates in 4 M HCl not by formation of an oxide film such as MoO_2, which is formed in 0.1 M HCl [10], but rather by formation of several layers of a molybdenum oxyhydroxychloride complex [11]. This salt layer formed on Mo facilitated a wider passive range of potential in 4 M HCl media than in 0.1 M HCl.

Metal oxyanions such as chromates, molybdates and tungstates are well known to act as powerful corrosion inhibitors. Surface analytical studies have shown [7,12–14] that alloys, under suitable conditions, often develop salt layers in the outer regions of the passive film by dissolution of metals as oxyanions and by subsequent redeposition with an egressing cation [10,15].

Some controversy exists about claims of observing various metal oxyanions on passive film surfaces, based on the nature of the spectral evidence or on the prediction of anion stability for a given pH potential as indicated by the theoretical data. Chromates are particularly difficult to observe by X-ray photoelectron spectroscopy (XPS) owing to reduction resulting from the atomic relaxation process associated with photoelectron emission [16]. However, molybdate is readily and precisely observable by XPS and has been observed to be generated on Mo-bearing FeCrNi alloys and stainless steels in conditions of potential and pH where the theoretical data indicate instability [10].

Experiments have recently been reported in which a bipotentiostat has been employed to study the dissolution of molybdenum in the passive state in de-aerated hydrochloric acid solutions [15]. Closely separated electrodes of Fe and Mo, Ni and Mo, and Mo and Cr were polarized at the same potential: the potential was one at which Mo and Cr are passive and Fe and Ni are active. XPS analysis of the electrodes was performed after the electrochemical exposure. The Fe/Mo couple revealed evidence of $FeMoO_4$ on the surface of the Mo, on top of an MoO_2-based passive film. A similar result was found for the Ni and Mo couple: XPS spectra indicated the presence of $NiMoO_4$ on the Mo surface. In the case of the Mo/Cr couple, the molybdenum surface revealed only the MoO_2-based passive film, while the passive film formed on Cr had a layer of molybdate on its surface. The lack of molybdate on the Mo surface resulted from the greater stability of the passive film formed on Cr.

Through this work it has been established that Mo, under acidic conditions, can form either insoluble chloride complexes, in conditions associated with pitting, or molybdate salts in milder conditions, along with MoO_2, MoO_3 and a pentavalent salt of unknown properties.

Salt films of metal oxyanions have been shown to have cation-selective properties [17]. When a molybdate salt, for instance, is deposited on an anion-selective oxide layer, typically formed in acidic media, the salt provides a vital component of an ionic rectifier which influences passivation in two important ways. The first is to prevent ingress of aggressive anions, and the second effect is to promote deprotonation of underlying hydroxyl groups. It has been proposed that the combined influence of the positive surface excess charge on the metal and the negative fixed charge on the molybdate provide an electric field which induces O–H bond stretching and sometimes failure. This oxylation process ultimately results in the growth of the inner oxide layer, resulting in a more efficient diffusion barrier.

2.2. The role of anodic segregation in passivity

Stainless alloys are commonly found to exhibit anodic segregation in the surface alloy layers of one or several alloy constituents. Most notably in austenitic stainless steels, Ni has been found to segregate to the alloy–passive film interface, while it is barely detected in the passive film [18]. This raises several questions as to the role of Ni in improving pitting resistance and reducing active dissolution.

In a series of experiments with pure metals, it has been demonstrated that Ni, unlike Mo, does not passivate in 4 M HCl, and therefore there is no insoluble chloride complex which is likely to aid the repassivation of pits [19]. Hence the relatively sluggish dissolution of Ni, leading to Ni build-up at the alloy surface, would suggest a mechanism by which pit repassivation may be assisted by Ni. However, since pure Ni is so readily dissolved in chloride solutions of higher pH than expected in a pit, this simple model does not hold, unless anodically segregated Ni is more strongly bound to the metal surface lattice. One method by which Ni may be more strongly bound to the alloy lattice, following anodic segregation, would be the formation of an intermetallic bond. The Engle–Brewer valence bond theory [20] of metallic bonding predicts intermetallic bonding between "hyper" and "hypo" d-electron transition metals, such as between Ni and Cr or Mo [6]. According to the model, the strength of the bond increases from 3d to 4d valence shell elements. This leads to the prediction of stronger bonding between Ni and Mo as compared to Ni and Cr. It has been shown that, in Mo-bearing austenitic stainless steel alloys, both Ni and

Mo are susceptible to anodic segregation, but as yet no direct evidence for Ni–Mo intermetallic bonding resulting from anodic segregation has been found [21].

It has been shown by non-destructive variable-angle XPS and destructive Auger electron spectroscopy (AES) depth profiling that N is anodically segregated during the dissolution of N-bearing austenitic stainless steels [22–24]. XPS-derived electron binding-energy data indicate that nitrogen is retained in the surface of the alloy as a mixed nitride rather than as a single nitride (say with Cr) [6]. Based on XPS measurements of the oxide phase [12], nitrogen appears to be present as an ammonia ligand to trivalent Cr. In sulfuric acid an additional form of N is observed, bound to Fe and sulphate as an ammonium cation. The protective properties of this salt against chloride ion attack have been discussed elsewhere [13].

The surface nitride formed by the anodic dissolution of a N-bearing austenitic stainless steel in acidic media appears to be strongly associated with Ni and Mo retention and less so with Cr [25]. This implies that a mixed nitride of Cr, Ni and Mo may be formed by anodic dissolution. The importance of Ni and Mo is implied by a comparison of the thermodynamic stability of Ni_2Mo_3N with Ni_3N and Mo_2N (see Fig. 1) [26]. It is apparent from Fig. 1 that the mixed nitride is much more stable than the single nitrides. The source

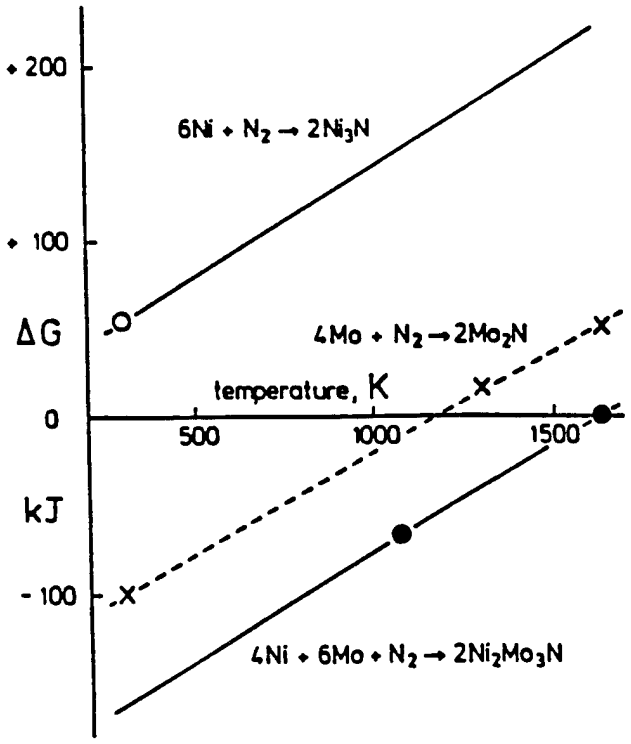

Fig. 1. A comparison of the thermodynamic stability of Ni_2Mo_3N with Ni_3N and Mo_2N (from Ref. [26]).

Table 1
Alloy compositions (wt.%)

Alloy	Fe	Cr	Ni	Mo	N	C	S
Fe19Cr	bal.	18.7	—	—	0.002	0.05	0.025
Fe19Cr9Ni	bal.	18.9	8.9	—	0.002	0.0025	0.004
Fe19Cr2.5Mo	bal.	19.0	—	2.5	0.002	0.05	0.025
Fe19Cr9Ni2.5Mo	bal.	18.8	8.8	2.2	0.002	0.025	0.004

of the stronger lattice binding has not been established, but a strong intermetallic interaction may explain the high-temperature stability. In the context of the anodic segregation of N in austenitic stainless steels, we might expect that the mixed Ni and Mo surface nitride will provide a kinetic barrier to metal egress owing to similarly enhanced lattice binding.

3. Experimental details

3.1. Materials

Table 1 gives the composition of the alloys used in this study. The samples (7 mm × 10 mm × 1 mm) were sealed in a pre-evacuated quartz tube and annealed at 1100 °C for 3 h followed by a water quench. Samples were then polished up the grades to a 0.25 μm diamond polishing compound finish. Before electrochemical treatment, all samples were ultrasonically cleaned in acetone, followed by isopropanol and doubly distilled water, to remove any contamination from the polishing process.

3.2. Electrochemical polarization

Polarization was performed using a Princeton Applied Research Corporation (PARC) Potentiostat Model 173 with a Model 276 computer interface, controlled by a PARC Model 352 data acquisition and analysis system. A modified Greene's cell was used in which the platinum counter-electrodes were placed in two separate compartments on opposite sides of the cell to minimize contamination. A porous frit was placed between each compartment and the main cell. All of the solutions used were de-aerated with high-purity argon for at least 2 h prior to analysis. Potentials were measured against a saturated calomel electrode (SCE). Cathodic pretreatments were performed in order to remove the air-formed oxide film. Samples were allowed to reach equilibrium at open-circuit potential (OCP) and then were either immediately polarized to form a passive film or potentiodynamically polarized in the anodic direction at a rate of 1 mV s^{-1}. Certain samples were immediately electrochemically surface-

nitrided following the cathodic pretreatment, as described in the next section. Samples to be analyzed by XPS were removed from the cell, washed with de-aerated doubly distilled water, dried in Ar, mounted onto an XPS sample holder, and transferred to the spectrometer under Ar. The entire drying procedure was carried out in an Ar-purged glove box to reduce the possibility of surface modification during transfer.

3.3. Surface nitriding

Recent work has shown the effects of electrochemical surface nitriding to be analogous to those created through the use of N as an alloying element in stainless steels [6]. The process of electrochemical surface nitriding involves contact adsorption of NO_3^-, followed by reduction of N to form an intermediate surface nitride product. When exposed continuously to nascent hydrogen formed by cathodic polarization, the surface nitride eventually reacts to form NH_3. In the absence of nitrate ions in the solution, the surface nitride is readily removed during cathodic polarization.

It has been proposed that a metal surface undergoing cathodic polarization undergoes the following reaction in a nitrate-bearing solution:

$$M + NO_3^- \rightarrow NO_{3ads}^- M \quad (1)$$

(where $NO_{3ads}^- M$ represents nitrate contact adsorbed on the bare metal surface) followed by:

$$NO_{3ads}^- M + 6H^+ + 8e^- \rightarrow NM + 3H_2O \quad (2)$$

This does not rule out the parallel proton consuming reaction proposed by Galvele [27]:

$$NO_3^- + 10H^+ + 8e^- \rightarrow 3H_2O + NH_4^+ \quad (3)$$

Surface nitriding was conducted following cathodic pretreatment in de-aerated 0.1 M HCl solution. The electrolyte was then replenished under Ar with the sample maintained at OCP with de-aerated 0.1 M HCl + 0.5 M $NaNO_3$. Samples were then immediately polarized to − 700 mV(SCE) and the current carefully monitored until 750 mC of charge had passed. The cell was then flushed twice with de-aerated 0.1 M HCl with the sample held at OCP, followed immediately by either potentiodynamic or potentiostatic polarization as described above. Potentiodynamic polarization of the nitrided samples was conducted from OCP to avoid any loss of surface nitrogen through the formation of ammonia or ammonium during H_2 evolution.

3.4. XPS

All XPS measurements were performed with either a modified VG Scientific ESCA 3 Mk. II spectrometer or a customized system equipped with a VG CLAM 100 analyzer, with lensing controlled by a VGX900 data acquisition system. The entrance and exit slit widths for both hemispherical analyzers were 4 mm, resulting in a half-angle for photoelectron emission of 0.095 radians. Photoelectron take-off angles reported for variable-angle XPS were measured with respect to the sample surface. An Al $K\alpha_{1,2}$ (1486.6 eV) X-ray source and a 20 eV pass energy were used for all analyses, providing a full width at half-maximum (FWHM) of 1.35 eV for the Au $4f_{7/2}$ singlet. For reference, the binding energy of the Au $4f_{7/2}$ singlet was found to be 83.8 eV and that of the Cu $2p_{3/2}$ singlet was found to be 932.4 eV. All binding energies were corrected for charge-shifting by referencing to the C 1s line from the adventitious carbon at 284.6 eV. Base pressures during analysis were about 1×10^{-9} Torr. Detailed information on the methodology used for data analysis and peak fitting, as well as peak-fitting parameters and sensitivity factors derived from standards, have been published elsewhere [28].

4. Results and discussion

4.1. Effects of N surface alloying on electrochemical behavior in 0.1 M HCl

The polarization data of Fig. 2 show a steady progression in electrochemical behavior as a function of alloy additions. The Fe-19Cr alloy exhibits a sizeable active nose followed by a passive region which terminates by breakdown at 120 mV(SCE). Surface nitriding of this alloy results in the removal of the active–passive transition, and the passive state is only maintained over a relatively narrow range of potential. Addition of 9 wt.% Ni to Fe-19Cr shifts the OCP in the noble direction and reduces the critical current density. Surface nitriding is seen to further reduce the critical current density and to reduce the passive current density. The passive range of potential for nitrided and untreated Fe-19Cr-9Ni remains narrow (Figs. 2B and 2C, respectively). Surface nitriding in all cases appears to raise the OCP. The combined addition of 9 wt.% Ni and 2.5 wt.% Mo (Fig. 2D) reduce the critical current density, but no more so than separate additions of Ni or Mo to the Fe-19Cr base alloy (Figs. 2B and 2C, respectively). The greatest effect of the combined additions of Ni and Mo is the significant increase in the passive range of potentials (Fig. 2D). Surface nitriding appears only to contribute a further reduction in the critical current density for passivation. From these data there appears to be a synergy between N and each of the alloying elements, with the most beneficial synergy being between N and Ni + Mo. Elucidation of any such synergy requires surface chemical analysis.

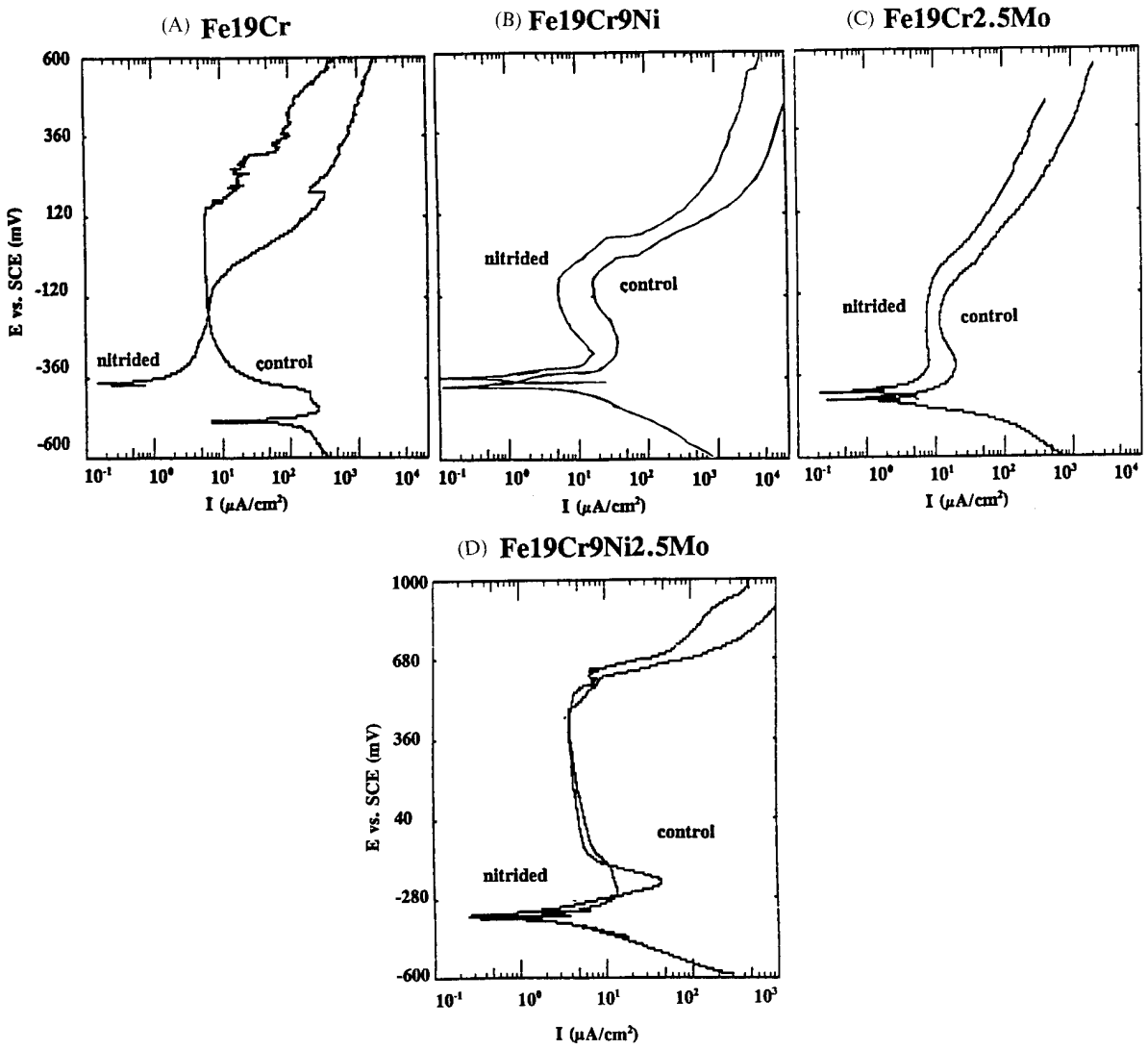

Fig. 2. Electrochemical data for alloys (A–D) polarized in de-aerated 0.1 M HCl with and without prior surface nitriding (as indicated).

4.2. Effects of N surface alloying on the passive film composition

It was generally found by XPS that Ni was absent from the passive films formed on the Ni-bearing stainless alloys, in agreement with previous work [9]. The spectra of Ni derived from the Fe-19Cr-9Ni alloy in Fig. 3 quite clearly show no evidence of a chemical shift indicative of oxidized species. Each of the surface-nitrided alloys exhibited surface nitride N 1s signals having a binding energy previously found to be associated with a mixed nitride [6]. Fig. 4 presents spectra derived from the analysis of the passive film formed on Fe-19Cr-9Ni-2.5Mo following electrochemical surface nitriding. The spectrum is an overlapping multiplet of the Mo $3p_{3/2}$ and N 1s energy levels. The N 1s photoelectron spectra are quite typical of the N 1s spectra for each of the alloys, in that the nitride contribution is strongest for the 50° take-off angle spectrum, representative of the signal derived from the metal/film interface. The contribution from NH_3 is probably from a ligand around Cr^{3+} and is not considered a major contributor to the anodic film. The spectrum of Mo from the metal surface is clearly observed at the 50° take-off angle. A poorly defined peak, labeled "N", appears from numerous peak fits to relate probably to Mo bound as a nitride or as part of a mixed nitride compound. The products MoO_2, Mo^{5+} (probably $Mo(OH)_5$), MoO_4^{2-} and MoO_3 are typically observed in the anodic films formed on Mo-bearing stainless steels, and have been extensively characterized in the past.

In this and other studies, the molybdate signal tends to be most enhanced in spectra derived from the outer layer, while the MoO_2 appears to grow from the metal surface layer. At present we cannot comment on the properties of the pentavalent Mo species, except to say that it is often observed in the presence of Mo(IV) and

Mo(VI). The Fe $2p_{3/2}$ spectra shown in Fig. 5 are typical of those found for each of the alloys studied, except that the ratios of ferrous to ferric components were found to vary with composition, as will be further discussed below.

In Fig. 6 we have presented the Cr concentration in the alloy layer just beneath the passive film for each of the alloys studied. The data indicate that the retention of Cr was strongly influenced by alloy additions. The deleterious effect of N on the passivity of the Fe-19Cr alloy is reflected in the significant reduction in the Cr concentration in the alloy layers beneath the film. This behavior indicates that N has stimulated selective dissolution of Fe to the point of possibly undercutting the passive film. By contrast, addition of Ni or Mo (or both) results in a significant enrichment of Cr in the alloy surface layer, thus providing sufficient Cr to repair localized film failure. However, N is seen to reduce slightly the Cr enrichment effect of separate Ni and Mo additions. Only in the case of Fe-19Cr-9Ni-2.5Mo, the most stable alloy, does the addition of N have no significant effect on the Cr content of the alloy surface layer.

In Fig. 7 we present the ratios of the Cr_2O_3 to $Cr(OH)_3$ concentration as a function of alloying addition. It can be seen that both Ni and N additions tend to raise the $Cr(OH)_3$ content of the passive films formed on the alloys. It is interesting to note that the most

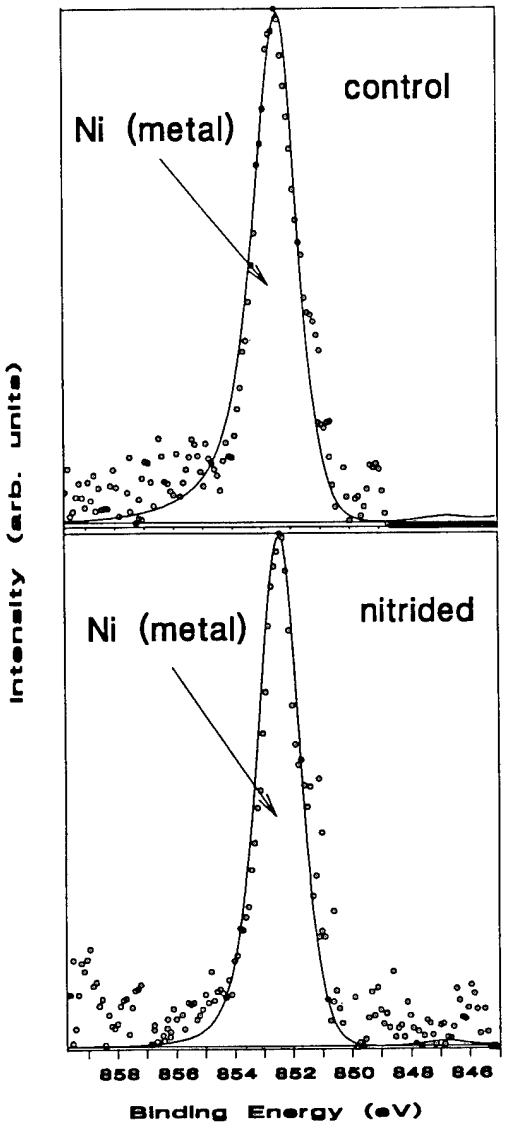

Fig. 3. Ni $2p_{3/2}$ photoelectron spectra from passive film formed in de-aerated 0.1 M HCl on Fe-19Cr-9Ni alloy in 1 h at −180 mV(SCE). Take-off angle, measured with respect to sample surface, was 20°.

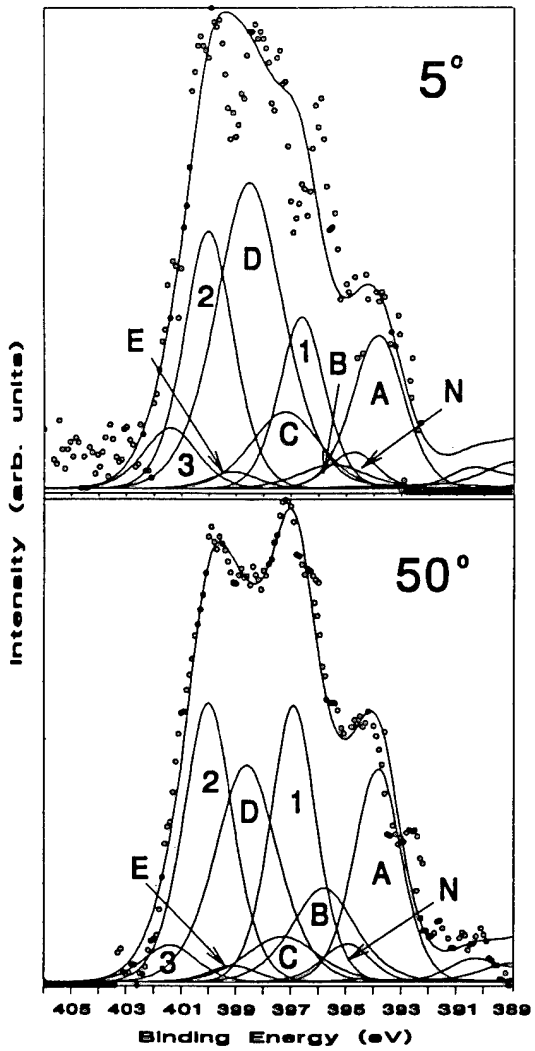

Fig. 4. N 1s/Mo $3p_{3/2}$ photoelectron spectra from passive film formed in de-aerated 0.1 M HCl on nitrided Fe-19Cr-9Ni-2.5Mo alloy in 1 h at 180 mV(SCE). Take-off angles, measured with respect to the sample surface, are as noted on the diagram. Peak indentification: (A) Mo $3p_{3/2}$ from Mo (metal); (N) Mo $3p_{3/2}$, possibly from mixed nitride; (B) Mo $3p_{3/2}$ from Mo^{4+} (MoO_2); (C) Mo $3p_{3/2}$ from Mo^{5+}; (D) Mo $3p_{3/2}$ from Mo^{6+} (MoO_4^{2-}); (E) Mo $3p_{3/2}$ from Mo^{6+} (MoO_3); (1) N 1s from nitride; (2) N 1s from NH_3; (3) N 1s from NH^{4+}.

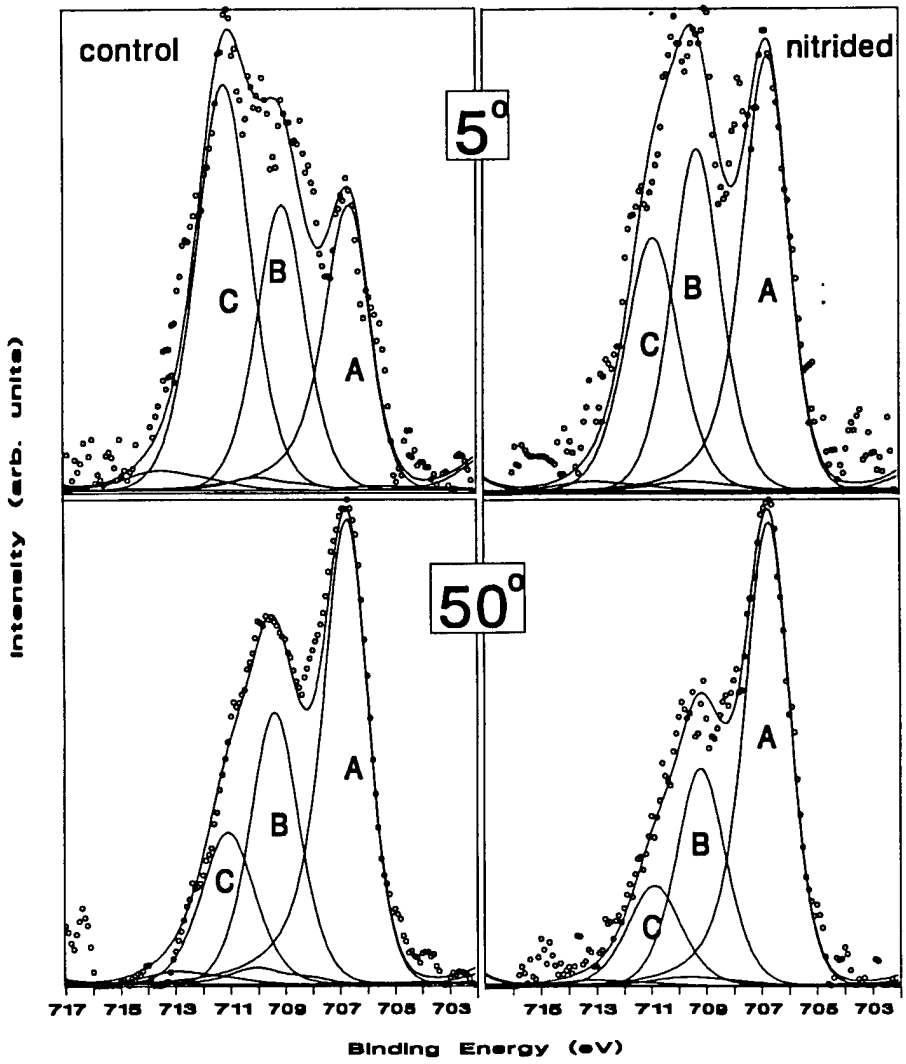

Fig. 5. Fe $2p_{3/2}$ photoelectron spectra from passive film formed in de-aerated 0.1 M HCl on nitrided and non-nitrided Fe-19Cr-9Ni-2.5Mo alloy in 1 h at 180 mV(SCE). Take-off angles, measured with respect to the sample surface, are as noted on the diagram. Peak identification: (A) Fe (metal); (B)Fe^{2+}; (C) Fe^{3+}.

corrosion-resistant alloy, Fe-19Cr-9Ni-2.5Mo, has a chromium oxide/hydroxide ratio which is independent of N addition. From Fig. 8 it can be seen that the proportions of molybdate to other Mo constituents in the passive film are generally much higher for the Fe-19Cr-9Ni-2.5Mo alloy compared to the Fe-19Cr-2.5Mo alloy, and that surface nitriding contributes further to the formation of the molybdate salt. It is apparent from Fig. 9 that the ferrous-to-ferric ion content ratio for anodic films is highest following nitriding for all alloys. This correlates with a general increase in molybdate with surface alloying. This may give support to the proposed pH shift to higher values at the metal/solution interface during the active stage of dissolution due to ammonium formation [4]. In addition, it is possible that the general increase in the $Cr(OH)_3$ content of the films formed following nitriding, except for the nitrided Fe-19Cr-9Ni-2.5Mo alloy, may also support this proposed pH effect.

The Fe-19Cr-9Ni-2.5Mo alloy is seen to exhibit a similar ferrous-to-ferric ratio in its anodic film as compared to the other nitrided alloys. Indeed, because the passive layer on this alloy has a higher ferrous-to-ferric ion content ratio than that formed on the Fe-19Cr-9Ni and Fe-19Cr-2.5Mo alloys, it would seem likely that Ni and Mo together are responsible for the higher proportions of ferrous ions in the anodic film formed on Fe-19Cr-9Ni-2.5Mo. It seems reasonable to attribute the higher ferrous ion content of anodic films as being due to the activation of Fe in the alloy surface. This activation by N appears to be similar to that stimulated by Ni and Mo. One probable cause of activation of Fe by the combination of Ni and Mo would be a by-product of surface clustering or preferential surface

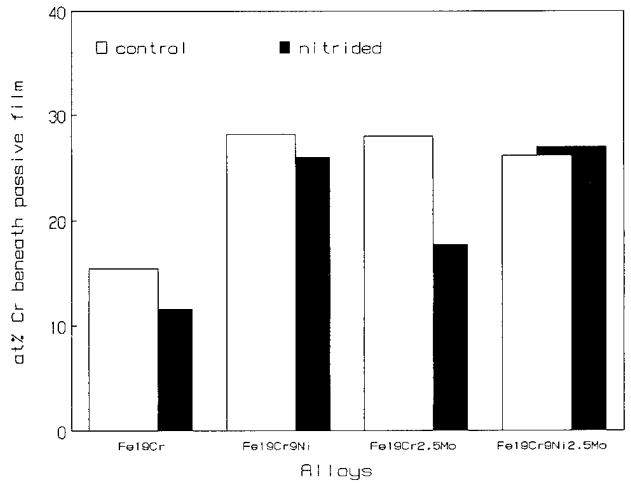

Fig. 6. Chromium concentrations in the alloy layer beneath the passive film formed in de-aerated 0.1 M HCl, derived from 20° photoelectron take-off angle XPS analysis.

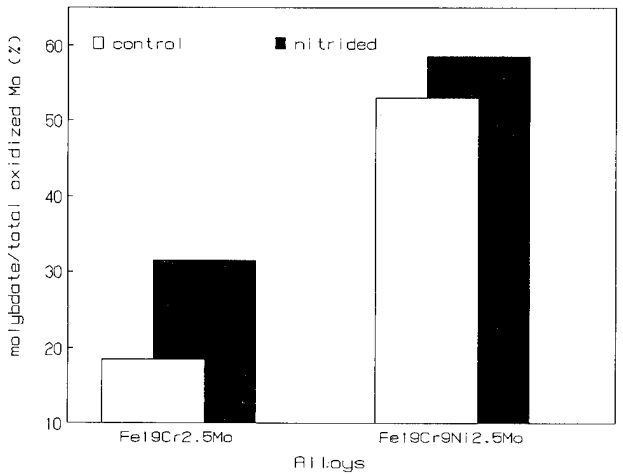

Fig. 8. Molybdate as a percentage of all oxidized molybdenum species in the passive films formed in de-aerated 0.1 M HCl, derived from 50° photoelectron take-off angle XPS analysis.

bonding of Ni with Mo. This bonding would serve to localize valence electrons within the cluster, thereby weakening bonding between Fe and the cluster constituents. This would in turn reduce the atomic coordination of surface Fe atoms and lower the activation energy for release of Fe from the alloy surface.

In a similar fashion, N would tend to surface-cluster with Cr in Fe-19Cr and Fe-19Cr-9Ni alloys, with Cr and Mo in the Fe-19Cr-2.5Mo alloy, and with Cr, Mo and Ni in the Fe-19Cr-9Ni-2.5Mo alloy. The atomic bonding energies of the cluster components, which may be mixed nitrides or intermetallics, must be significantly increased. Therefore, the activation energy for dissolution for each of the constituents of the cluster must also be increased. This may explain the cause of anodic segregation. Anodic segregation may in turn significantly reduce active dissolution during repassivation and, consequently, may lead to improvement in pit repassivation and active–passive transition characteristics when the segregated phases form a continuous single phase.

In summary, it would appear that N-bearing steels exhibit the greatest corrosion resistance when Ni, Mo and N are present. Under these conditions it would appear that, in addition to the formation of a passive film containing Cr_2O_3 and MoO_2 as the main components of the primary kinetic barrier to cation egress and anion ingress, the formation of two further kinetic barriers is achieved; namely, a metallic nitride phase at the metal/film interface and a ferrous molybdate salt layer in the outer region of the anodic film.

4.3. Commercial alloys

In Table 2 we briefly summarize some of the salient results obtained by electrochemical polarization and surface-analytical studies of five recently studied alloys [13,20,29]. The beneficial effects of N alloying of

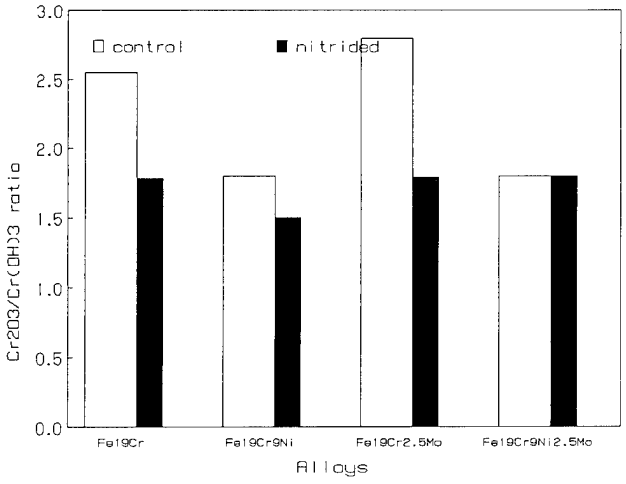

Fig. 7. Ratios of Cr_2O_3 to $Cr(OH)_3$ for passive films formed in de-aerated 0.1 M HCl, derived from 50° photoelectron take-off angle XPS analysis.

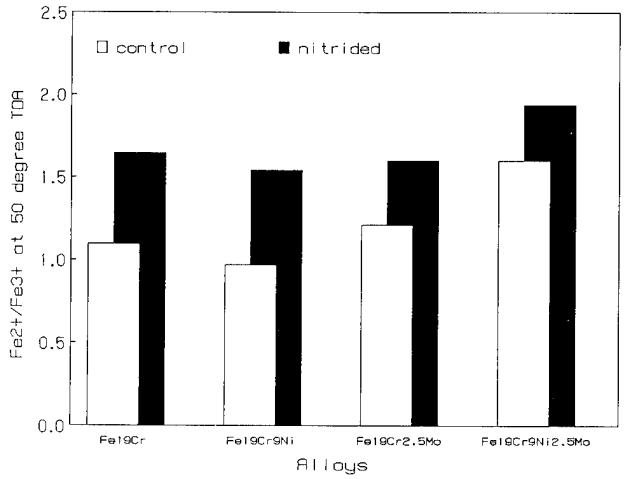

Fig. 9. Ferrous-to-ferric ion content ratios for passive films formed in de-aerated 0.1 M HCl, derived from 50° photoelectron take-off angle XPS analysis.

Table 2
Effects of surface nitrogen alloying on electrochemical behavior and passive film formation on a series of laboratory heats of commercial grades

Alloy in test environment[a]	Observations due to cited change in alloy N content
Type 304 (Fe18Cr8Ni) in 0.1 M HCl	0.24 vs. 0.04 wt.% N ● decrease in active/passive transition dissolution kinetics, ● decrease in corrosion current density, ● increase in pitting potential ● decrease in passive current density, ● Cr, Ni and N enriched beneath the passive film, and ● mixed nitride observed at metal/film interface
317LX™ alloy[b] (Fe18Cr13Ni3.3Mo) in 0.5 M HCl	0.19 vs. 0.06 wt.% N ● decrease in active/passive transition dissolution kinetics, ● decrease in corrosion current density, ● increase in pitting potential, and ● decrease in passive current density
Al 904L™ alloy (Fe20Cr24Ni4.5Mo) in 0.1 M HCl + 2.0 M NaCl	0.20 vs 0.005 wt.% N ● decrease in active/passive transition dissolution kinetics, ● decrease in passive current density, ● enrichment of Mo beneath the passive film, ● enrichment of Cr_2O_3 in the passive film relative to $Cr(OH)_3$, and ● mixed nitride observed at metal/film interface
Al-6XN® alloy (Fe20Cr25Ni6.3Mo) in 0.1 M HCl + 0.2 M NaCl	0.19 vs. 0.04 wt.% N ● decrease in active/passive transition dissolution kinteics, ● decrease in passive current density in 0.1 M HCl, ● enhanced deprotonation in the outer region of the passive film, ● enrichment of Cr_2O_3 in the passive film relative to $Cr(OH)_3$, ● enrichment of Cr and Mo beneath the passive film, and ● mixed nitride observed at metal/film interface

[a]317LX, AL 904L, and AL-6XN are trademarks of Allegheny Ludlum Corporation.
[b]No XPS analysis.

austenitic stainless steels are clearly in evidence. However, for studies of the interaction of N with various alloying elements, a broader range of alloys is required in order to understand the more complex commercial alloys. Recently it has been shown that the anodically segregated nitride phase can be successfully simulated by plating N out of a nitrate solution and onto a metal or alloy [6]. The technique has been performed on low-nitrogen base compositions of Type 304, 317LX™ alloy, AL 904L™ alloy, and AL-6XN® alloy[1], and their electrochemical properties and surface composition compared with their high-nitrogen base-composition counterparts. The agreement between the high-nitrogen alloys and the surface-nitrided alloys suggests that the surface-nitriding technique is a useful tool for understanding the role of N in improving the corrosion behavior of austenitic stainless steels.

5. Conclusions

(1) Ni and N exhibit the following behavior in stainless steels passivated in 0.1 M HCl:

(i) anodic segregation during dissolution,
(ii) are not major constituents of the passive film,
(iii) lower the overall anodic kinetics,
(iv) selectively activate iron dissolution, though Ni requires the presence of Mo, and
(v) enhance the surface deposition of iron molybdate.

(2) The primary kinetic barrier to anodic dissolution of high-nitrogen stainless steels is a chromium-oxide-based passive film.

(3) The following appear to be important secondary kinetic barriers:

(i) a mixed nitride surface layer formed at the metal/anodic film interface, and
(ii) an ultra-thin layer of ferrous molybdate situated in the outer region of the anodic film.

(4) Nitrogen alloying is most beneficial to corrosion properties of stainless steels when added with Ni and Mo.

Acknowledgement

This work was supported by the Office of Naval Research (Dr. A. J. Sedriks, contract officer) under contract number N0001485K0437.

[1] 317LX, AL 904L and AL-6XN are trademarks of Allegheny Ludlum Corporation.

References

[1] A.J. Sedriks, *Corrosion, 42(7)* (1986) 376.

[2] J.E. Truman, M.J. Coleman and K.R. Pirt, *Br. J., 12* (1977) 236.

[3] J.E. Truman, in J. Foct and A. Hendry (eds.), *High Nitrogen Steels*, Institute of Metals, London, 1989, p. 225.

[4] K. Osozawa and N. Kato, *Passivity and its Breakdown on Iron and Iron-Base Alloys*, NACE, Houston, TX, 1976, p. 135.

[5] J.J. Eckenrod and C.W. Kovack, *ASTM Special Technical Publication 679*, Philadelphia, PA, 1977, p. 17.

[6] R.D. Willenbruch, C.R. Clayton, M. Oversluizen, D. Kim and Y.C. Lu, *6th Int. Symp. on Passivity, Hokkaido, Japan, 1989; Corros. Sci., 31* (1990) 179.

[7] R.B. Diegle, N.R. Sorensen, C.R. Clayton, M.A. Helfand and Y.C. Lu, *J. Electrochem. Soc., 135* (1988) 1085.

[8] D.J. Duquette, personal communication 1986.

[9] B. Brox and I. Olefjord, in M. Froment (ed.), *Passivity of Metals and Semiconductors*, Elsevier, New York, 1983, p. 561.

[10] Y.C. Lu, C.R. Clayton and A.R. Brooks, *Corros. Sci., 29* (1989) 863.

[11] G.P. Halada, C.R. Clayton, H. Herman, S. Sampath and R. Tiwari, in C.R. Clayton and K. Hashimoto (eds.), *Corrosion, Electrochemistry and Catalysis of Metastable Metals and Intermetallics*, The Electrochemical Society, Pennington, NJ, 1993, p. 263.

[12] G.P. Halada and C.R. Clayton, *J. Vac. Sci. Technol. A, 11(4)* (1993) 2342.

[13] C.R. Clayton, L. Rosenzwieg, M. Oversluizen and Y.C. Lu, in E. McCafferty and R.J. Brodd (eds.), *Surfaces, Inhibitors and Passivation*, The Electrochemical Society, Pennington, NJ, 1986, p. 323.

[14] K. Doss, A.R. Brooks and C.R. Clayton, *Proc. Int. Cong. on Metallic Corrosion, Toronto, Vol. 1*, National Research Council, Ottawa, 1984, p. 138.

[15] C.R. Clayton and Y.C. Lu, *Corros. Sci., 29* (1989) 881.

[16] G.P. Halada and C.R. Clayton, *J. Electrochem. Soc., 138* (1991) 2921.

[17] M. Sakashita and N. Sato, *Corrosion, 35* (1979) 351.

[18] J.E. Castle and C.R. Clayton, *Corros. Sci., 17* (1977) 7.

[19] G.P. Halada, 1992 unpublished work.

[20] I. Olefjord and C.R. Clayton, *ISIJ Int., 31* (1991) 134.

[21] L. Brewer, *Science, 161* (1968) 115.

[22] Y.C. Lu, R. Bandy, C.R. Clayton and R.C. Newman, *J. Electrochem. Soc., 130* (1983) 1774.

[23] R.C. Newman, Y.C. Lu, R. Bandy and C.R. Clayton, Ref. [13], Vol. 3, p. 394.

[24] R. Bandy, Y.C. Lu, R.C. Newman and C.R. Clayton, in R.P. Frankenthal and J. Kruger (eds.), *Equilibrium Diagrams and Localized Corrosion*, The Electrochemical Society, Pennington, NJ, 1984, p. 369.

[25] C.R. Clayton and K. Martin, Ref. [3], p. 256.

[26] K.H. Jack, Ref. [3], p. 117.

[27] J.R. Galvele, in R.P. Frankenthal and J. Kruger (eds.), *Passivity of Metals*, The Electrochemical Society, Pennington, NJ, 1978, p. 285.

[28] A.R. Brooks, C.R. Clayton, K. Doss and Y.C. Lu, *J. Electrochem. Soc., 133* (1986) 2459.

[29] D. Kim, *Ph.D. Thesis*, Department of Materials Science and Engineering, State University of New York at Stony Brook, NY, 1992.

ELSEVIER

Materials Science and Engineering A198 (1995) 145–152

MATERIALS SCIENCE & ENGINEERING A

Corrosion-resistant Ni–Cr–Mo alloys in hot concentrated sulphuric acid with active carbon

Yoshio Takizawa, Katsuo Sugahara

Central Research Institute, Mitsubishi Materials Corporation, 1-297 Kitabukuro-Cho, Omiya, Saitama 330, Japan

Abstract

Dewpoint corrosion by sulphuric acid has often been observed in the heat exchangers of coal-burning plants. If ashes contain active carbon, corrosion becomes particularly serious. Various nickel-base alloys with high corrosion resistance in such environments have been designed. The corrosion behaviour of these alloys was examined in hot concentrated sulphuric acid with and without active carbon. The corrosion resistance of ternary Ni–Ci–Mo alloys in the acids without active carbon increases with increasing alloy molybdenum content. When active carbon is added to the acids, the corrosion rate increases significantly. This is due to acceleration of transpassive dissolution of molybdenum as a result of enhancement of cathodic activity with the addition of active carbon. The corrosion resistance in the acids with active carbon is enhanced by an increase in alloy chromium content, which improves the passivity in the acids.

Keywords: Dewpoint corrosion; Sulphuric acid; Active carbon; Passivity; Ni–Cr–Mo alloy

1. Introduction

Flue gas environments in heavy oil-fired or coal-fired boilers are composed of gaseous components, such as N_2, O_2, H_2O, CO_2, SO_2, SO_3, NO_x and HCl, unburned carbon and fly ashes. For given partial pressures of H_2O and SO_3, the maximum temperature at which aqueous H_2SO_4 can exist is defined as the "acid dewpoint" [1–5]. Basically, dewpoint corrosion occurs when a gas is cooled below the saturation temperature. In power generation plants, the dewpoint temperature is in the range 100–140 °C. A typical system of coal-burning plants is shown in Fig. 1. A hot exhaust flue gas from the boiler is cooled to a temperature 20–30 °C higher than the dewpoint temperature, and accordingly dewpoint corrosion is avoidable. It is important, however, to recover the huge waste heat for energy cost saving. In fact, if the energy is used by applying a further 20 °C decrease in the waste gas temperature in the final heat recovery plant, one can gain an additional 0.32% in generation efficiency [6]. Consequently, we need materials resistant to sulphur dewpoint corrosion.

It is known that corrosion in strong acids is particularly accelerated by the presence of active carbon. Laboratory corrosion tests with mixtures of sulphuric acid and active carbon powder were performed by Nagano and co-workers [7–9] in view of the catalytic oxidizing action of unburned carbon, that is, active carbon. Their results for carbon steels were very well correlated with those of field tests. Chang [10] also carried out the same laboratory corrosion tests on austenitic stainless steel and the results were very well correlated with those of field tests.

In order to improve the sulphur dewpoint corrosion resistance at high temperatures, alloys with concentrations of chromium and molybdenum are required. However, the roles of chromium and molybdenum in enhancing the corrosion resistance are not always the same, since molybdenum is effective in less oxidizing environments whereas chromium is effective in oxidizing environments.

The purpose of this work was to obtain a better understanding of the specific roles of chromium and molybdenum in enhancing the corrosion resistance of nickel-base alloys to withstand sulphur dewpoint corrosion. Particular attention was paid to the effect of the presence of active carbon.

SSDI 0921-5093(95)04519-4

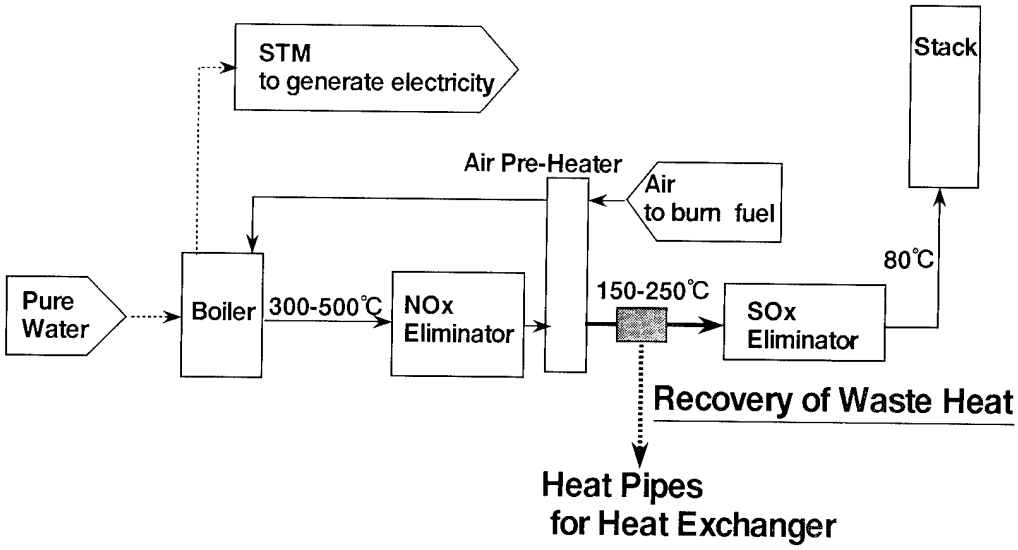

Fig. 1. Schematic diagram of coal-burning plant.

2. Experimental procedure

2.1. Samples

The chemical compositions of the Ni–Cr–Mo alloys used are given in Table 1. There are two chromium levels, 16 and 20%. Alloys were produced by argon-arc melting with high-purity metals. After hot rolling, all alloy sheets were annealed at a solid solution temperature of 1250 °C for 4 h and then water quenched.

2.2. Immersion corrosion tests and electrochemical measurements

Immersion corrosion tests and electrochemical measurements were made in four different testing environments, 60% and 80% H_2SO_4 with and without active carbon. The mixtures of sulphuric acid and active carbon powder were made with a ratio of 1 g of active carbon to 3.3 cm^3 of sulphuric acid. The test temperature was kept at 120 °C. Immersion corrosion tests were carried out for 24 h. For a better understanding of the corrosion behaviour, potentiodynamic polarization measurements were conducted after immersion for 10 min. After the immersed specimen had been polarized at −500 mV vs. SCE for 1 min, potentiodynamic polarization was performed at a potential sweep rate of 200 mV min^{-1} up to 1500 mV. The corrosion potential after immersion for 10 min was also recorded.

Table 1
Chemical compositions of alloys

Alloy	Cr (wt.%)	Mo (wt.%)	Ni (wt.%)
1620	15.8	19.8	Balance
1625	16.0	24.7	Balance
2017	19.9	16.9	Balance
2020	19.8	19.8	Balance
2024	19.9	23.9	Balance

Table 2
Impurities and gaseous components adsorbed on active carbon

Element	Concentration (wt.%)	Element	Concentration (wt.%)
O	16.0	Mg	0.005
N	0.6	Al	0.005
H	0.3	Cu	0.002
S	0.02	Ca	0.002
Si	0.02	C	Balance
Fe	0.005		

2.3. Characterization of active carbon

Impurities of the active carbon analysed and gaseous components adsorbed on the active carbon are shown in Table 2. It is noteworthy that 16% oxygen is adsorbed on the active carbon. Fig. 2 shows a scanning electron micrograph of the active carbon. The active carbon particle size is about 10 μm.

3. Results and discussion

3.1. Pure molybdenum

Potentiodynamic polarization curves of pure molybdenum measured in different solutions are shown in Fig. 3. Increasing acid concentration results in an increase in cathodic current density and a decrease in

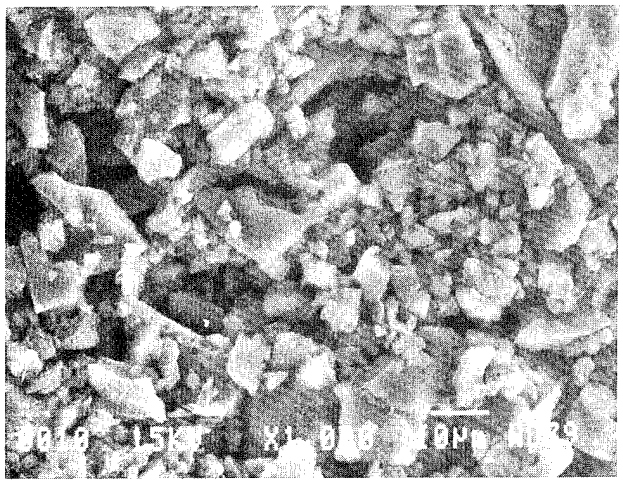

Fig. 2. SEM image of active carbon.

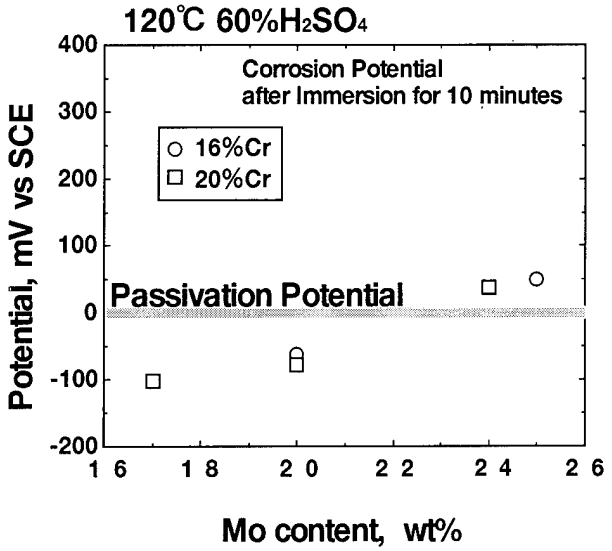

Fig. 4. Corrosion potential after immersion for 10 min in 60% H_2SO_4 at 120 °C as a function of alloy molybdenum content. The passivation potential where the anodic peak current density is observed by potentiodynamic polarization is shown as a grey line.

anodic current density. The addition of active carbon significantly increases the cathodic current density, whereas it does not affect the anodic current density, for transpassive dissolution of molybdenum.

3.2. 60% H_2SO_4 with and without active carbon

Corrosion potentials after immersion for 10 min in 60% H_2SO_4 are shown as a function of alloy molybdenum content in Fig. 4. An increasing molybdenum content results in an increase in the corrosion potential. Corrosion potentials are classified into two groups, in the active region and in the passive state. Low-molybdenum alloys are in the active state whereas high-molybdenum alloys are in the passive state. Fig. 5 shows potentiodynamic polarization curves for Ni–Cr–Mo ternary alloys measured in 60% H_2SO_4. The potentials where the current changes from negative to positive for all alloys are located in the active region. After immersion for 10 min, the open-circuit potential of alloys with high molbdenum contents, such as 2024 and 1625, shifts to the passive region showing spontaneous passivation. There are two stages in the passive region. Alloys are passive at low potentials in the passive region. However, transpassive dissolution of molybdenum occurs at a potential of about +100 mV

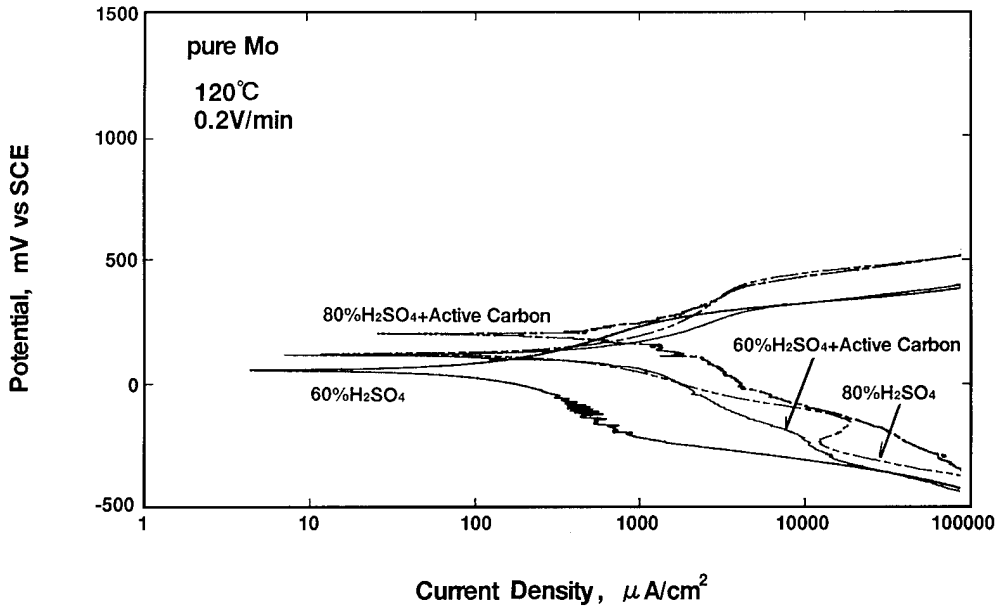

Fig. 3. Potentiodynamic polarization curves of pure molybdenum measured in four different solutions at 120 °C, i.e. 60% and 80% H_2SO_4 with the without active carbon.

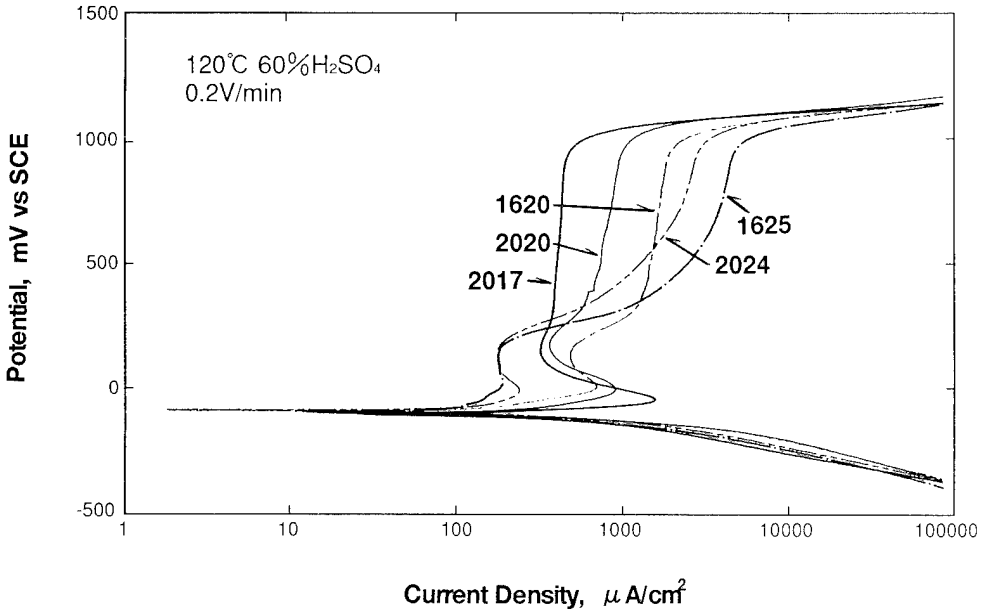

Fig. 5. Potentiodynamic polarization curves of Ni–Cr–Mo ternary alloys measured in 60% H_2SO_4 at 120 °C.

vs. SCE. Changes in peak current density and the passive current density are plotted in Fig. 6. Increasing the molybdenum content decreases the active dissolution current and the current density at low potentials in the passive region. The current density in the passive region where transpassive dissolution of molybdenum occurs is lower when the alloy contains higher chromium and lower molybdenum levels.

Corrosion potentials in 60% H_2SO_4 with active carbon are shown as a function of alloy molybdenum content in Fig. 7. The corrosion potentials of high-molybdenum alloys are significantly ennobled by the active carbon addition. By contrast, the corrosion potentials of low-molybdenum alloys remain in the active region. Fig. 8 shows the polarization curves of alloys 2017 and 2024 which are typical of active and spontaneously passive alloys, respectively. The spontaneously passive high-molybdenum alloy is depassivated by cathodic polarization for 1 min before potentiodynamic polarization in the acid without carbon. However, when carbon is added, spontaneous passivation of the high-molybdenum alloy can be seen by potentiodynamic polarization, since the carbon addition enhances the

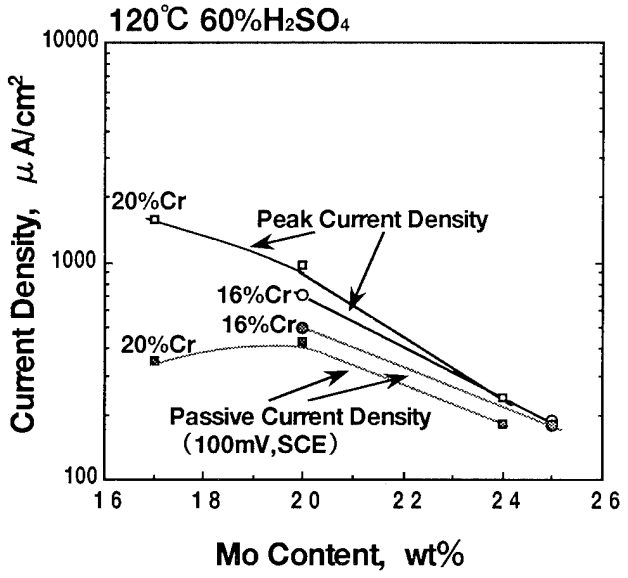

Fig. 6. Effects of chromium and molybdenum on the critical current density for passivation and the passive current density at 100 mV vs. SCE.

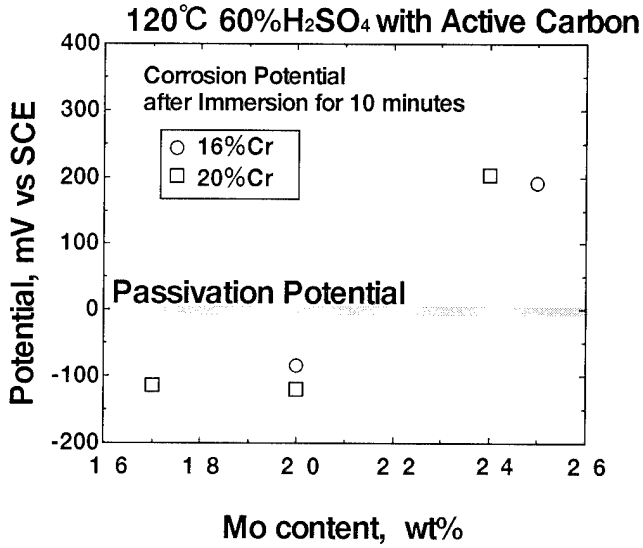

Fig. 7. Corrosion potential after immersion for 10 min in 60% H_2SO_4 with active carbon at 120 °C as a function of alloy molybdenum content. The passivation potential where the anodic peak current density is observed by potentiodynamic polarization is shown as a grey line.

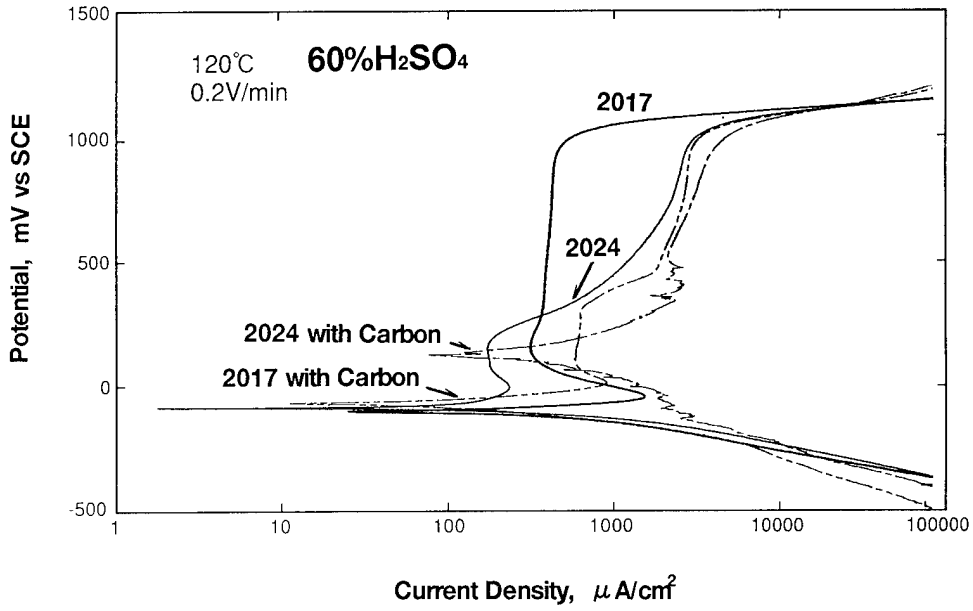

Fig. 8. Potentiodynamic polarization curves of alloys 2017 and 2024 measured in 60% H_2SO_4 with and without active carbon at 120 °C.

cathodic activity exceeding the anodic dissolution current. For the low-molybdenum alloy the carbon addition does not produce a large change in the corrosion potential but significantly increases the passive current density in the transpassive region of molybdenum.

Fig. 9 shows corrosion rates of alloys with two chromium levels in 60% H_2SO_4 with and without active carbon as a function of alloy molybdenum content. In the carbon-free acid, the corrosion rate decreases almost exponentially with increasing alloy molybdenum content. This is in agreement with the fact that the low-molybdenum alloys are in the active state, whereas the high-molybdenum alloys are in the passive state. Obviously, the corrosion rate is strongly dependent on the molybdenum content and almost independent of chromium content. The active carbon addition gives rise to a considerable increase in the corrosion rate for every alloy. For the high-molybdenum alloys, the active addition increases the corrosion rate because of an increase in the current density in the passive state, whereas for the low-molybdenum alloys, the corrosion rate in the active state increases because of enhancement of the cathodic reaction.

3.3. 80% H_2SO_4 with and without active carbon

The corrosion rates in 60 and 80% sulphuric acid are compared in Fig. 10. The corrosion rates in both

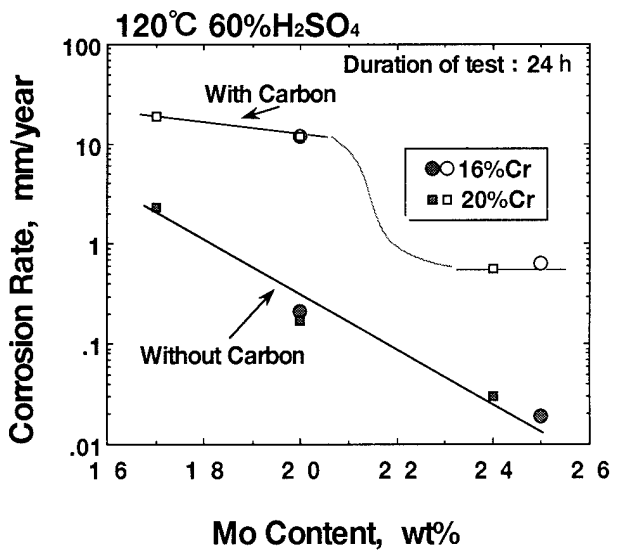

Fig. 9. Corrosion rates of Ni–Cr–Mo ternary alloys in 60% H_2SO_4 with and without active carbon at 120 °C.

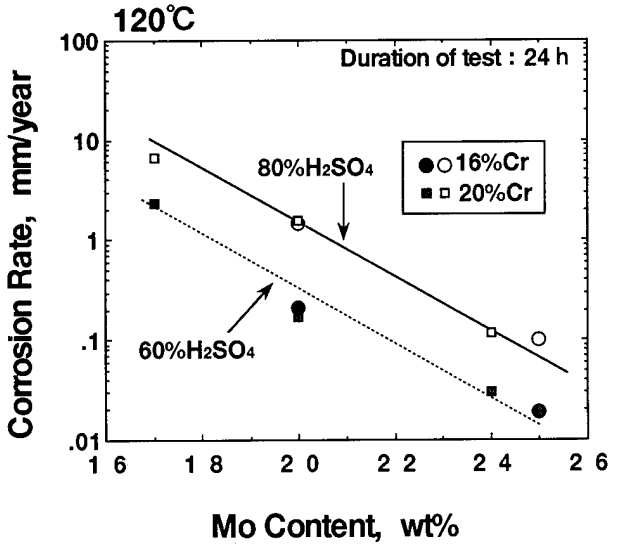

Fig. 10. Corrosion rates of Ni–Cr–Mo ternary alloys in 60% and 80% H_2SO_4 at 120 °C.

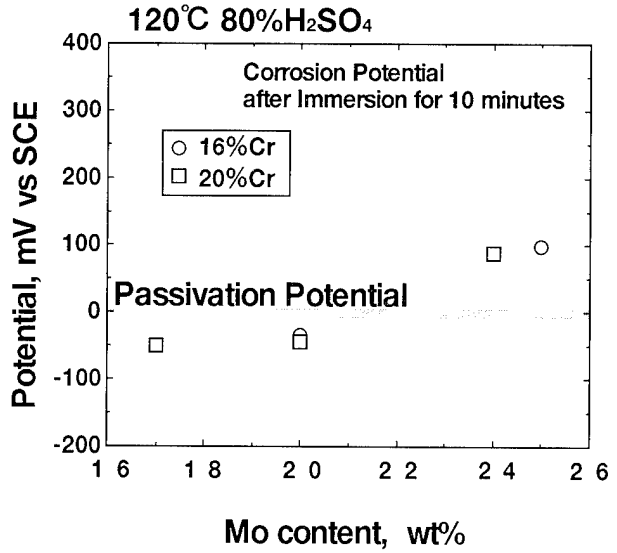

Fig. 11. Corrosion potential after immersion for 10 min in 80% H_2SO_4 at 120 °C as a function of alloy molybdenum content. The passivation potential where the anodic peak current density is observed by potentiodynamic polarization is shown as a grey line.

solutions decrease exponentially with increasing alloy molybdenum content, but are independent of chromium content. The corrosion rate in 80% H_2SO_4 is just shifted upwards compared with that in 60% H_2SO_4. Fig. 11 shows corrosion potentials measured after immersion for 10 min in 80% H_2SO_4 without active carbon. The corrosion potentials are classified into two groups, in the active and passive regions. The low-molybdenum alloys are in the active state and the high-molybdenum alloys are in the passive state. This phenomenon is the same as that observed in 60% H_2SO_4 without active carbon.

Fig. 12 shows potentiodynamic polarization curves measured in 80% H_2SO_4 without active carbon. Potentials where the current changes from negative to positive are shifted about 20 mV in the noble direction in comparison with those measured in 60% H_2SO_4. Similarly to the passive region observed in 60% H_2SO_4, there are two stages in the passive region. When the molybdenum content is high, the current density at low potentials in the passive region is low but that at high potentials in the passive region is high. These two passive regions are hereafter called the first and second passive regions, respectively. Low-chromium alloys such as alloys 1620 and 1625 exhibit high current densities in the second passive region.

Current densities at the first and the second passive regions are compared in Fig. 13. The current densities at +300 mV vs. SCE in the first passive region and at +800 mV vs. SCE in the second passive region are plotted as a function of molybdenum content. When the molybdenum content increases, the first passive current density gradually decreases, whereas the second passive current density increases. Accordingly, molybdenum is effective in enhancing the passivity in the low-potential region, but is detrimental at high potentials owing to transpassive dissolution. It is clear that the higher the chromium content, the lower is the passive current density.

Fig. 14 shows the change in corrosion potential in 80% H_2SO_4 with active carbon as a function of alloy molybdenum content. The corrosion potentials of all alloys are in the passive state. An increase in molybde-

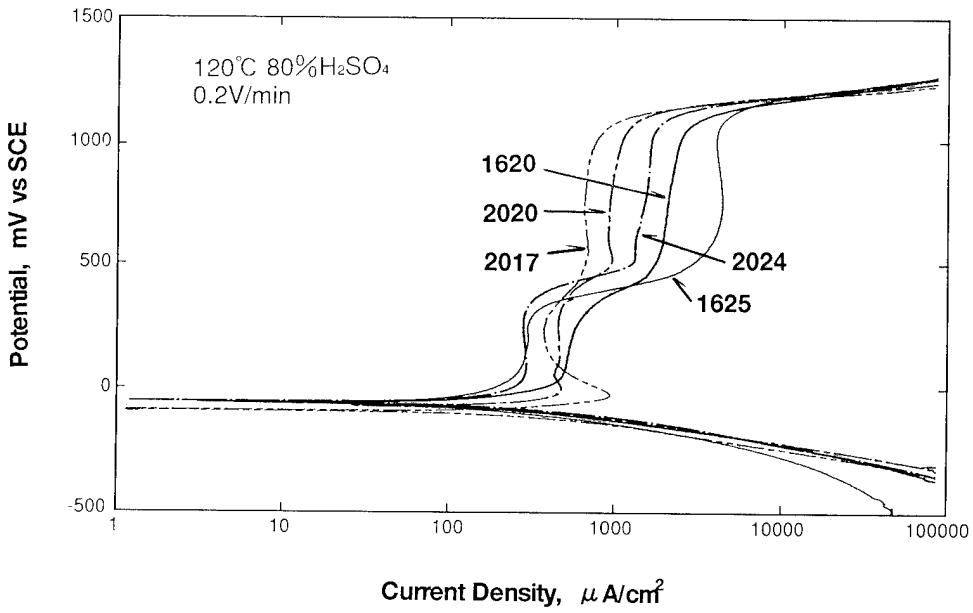

Fig. 12. Potentiodynamic polarization curves of Ni–Cr–Mo ternary alloys measured in 80% H_2SO_4 at 120 °C.

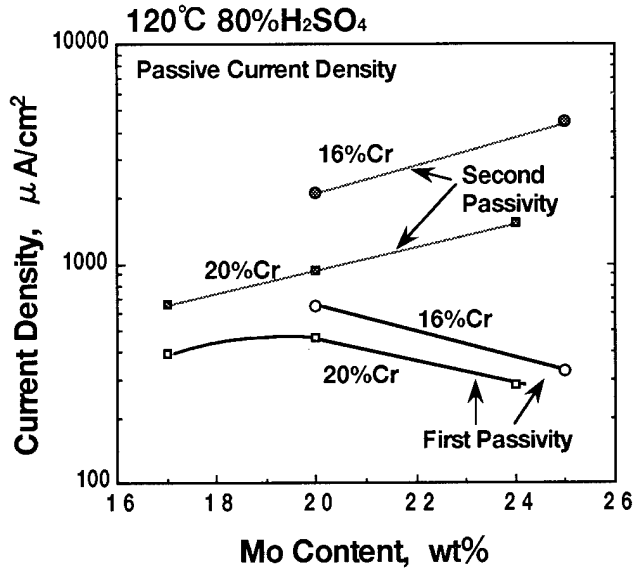

Fig. 13. Effects of chromium and molybdenum on the current densities at 300 mV vs. SCE in the first passive region and 800 mV vs. SCE in the second passive region.

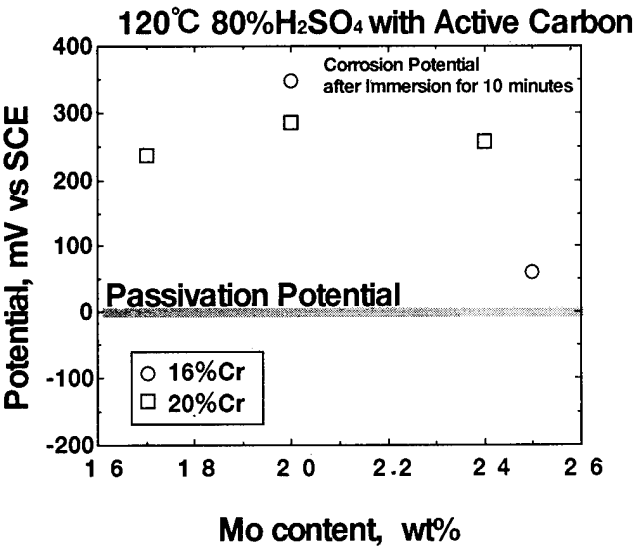

Fig. 14. Corrosion potential after immersion for 10 min in 80% H_2SO_4 with active carbon at 120 °C as a function of alloy molybdenum content. The passivation potential where the anodic peak current density is observed by potentiodynamic polarization is shown as a grey line.

num content decreases the corrosion potential for the 16% chromium alloys but does not affect the corrosion potential for the 20% chromium alloys. Fig. 15 shows a comparison of the polarization curves of alloys 2017 and 2024 in 80% H_2SO_4 with and without active carbon. When the active carbon is added, the corrosion potential shifts to the first passive region and the current density in the second passive region increases. It is obvious that the open-circuit corrosion rate depends on the first passive current density. When the molybdenum content is high, the current density in the first passivity is low and the current density in the second passivity is high.

The relationships between the corrosion rate and molybdenum content in 80% H_2SO_4 with and without active carbon are shown in Fig. 16. In the acid without carbon, the low-molybdenum alloys dissolve in the active state but the high-molybdenum alloys are in the passive state. When the active carbon is added, all the alloys become passive and the corrosion rate of the low-molybdenum alloys decreases. However, for the spontaneously passive high-molybdenum alloys, the current density in the passive state increases and hence the corrosion rate increases. Accordingly, the corrosion rate in the carbon-containing acid is not greatly dependent on the molybdenum content, but is dependent on the chromium content.

Corrosion through the passive film is very rapid in the carbon-containing acids. Consequently, there are no alloys that withstand severe corrosion attack, unless the alloys contain high concentrations of chromium.

4. Conclusion

The resistance of Ni–Cr–Mo alloys against sulphur dewpoint corrosion has been investigated in 60% and 80% H_2SO_4 at 120 °C.

The corrosion rate for alloys with 16% and 20% chromium decreases with increasing molybdenum content but is independent of the chromium content. When active carbon is added to the acids, the corrosion rates increase significantly, except those for 20% chromium alloys with 17% and 20% molybdenum. The presence of active carbon results in ennoblement of the corrosion potential because of promotion of the catalytic action for cathodic reactions [7–9]. In 60% H_2SO_4, when the molybdenum content is less than about 20%, the potential ennoblement is insufficient for the alloys to passivate spontaneously, and hence the carbon addition increases the corrosion rate. The alloys with 24% or more molybdenum are spontaneously passive and the active carbon addition, enhancing the cathodic reaction, increases the corrosion rate because of transpassive dissolution of molybdenum. In 80% H_2SO_4, the active carbon addition ennobles the corrosion potential of actively dissolving alloys to the passive state with a consequent decrease in the corrosion rate. However, for the alloys with a molybdenum content of 24% or more, the enhancement of cathodic activity leads to transpassive dissolution of molybdenum, and accordingly, to an increase in the corrosion rate.

Consequently, the corrosion behavior of Ni–Cr–Mo ternary alloys in sulphuric acid with and without active carbon is strongly related to passivation and stability of the passivation film.

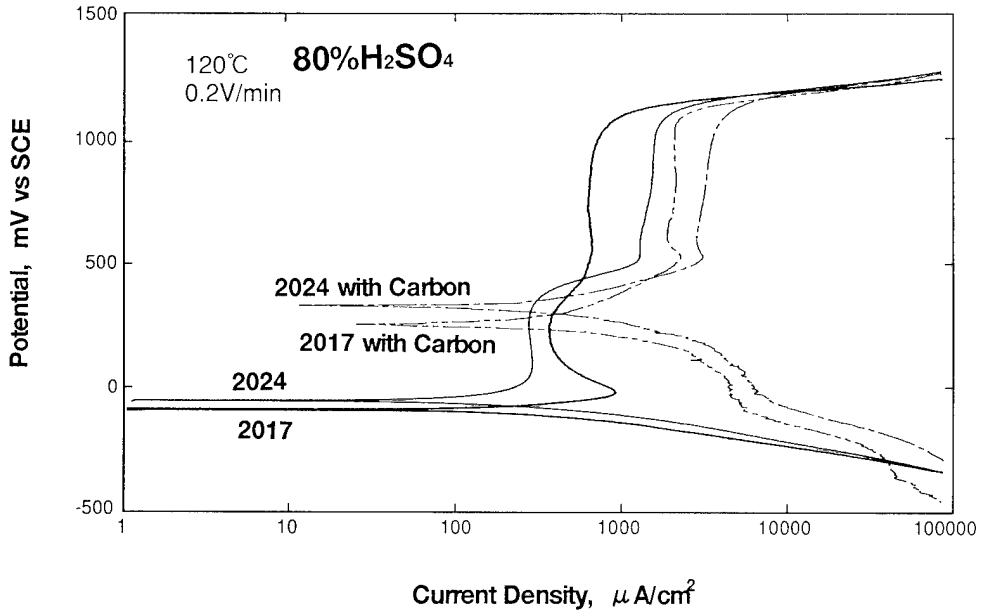

Fig. 15. Potentiodynamic polarization curves of alloys 2017 and 2024 measured in 80% H_2SO_4 with and without active carbon at 120 °C.

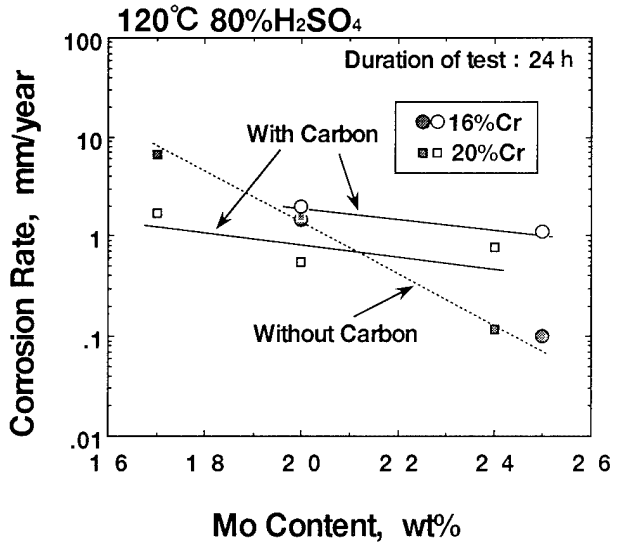

Fig. 16. Corrosion rates of Ni–Cr–Mo ternary alloys in 80% H_2SO_4 with and without active carbon at 120 °C.

Increasing the molybdenum content from 17 to 25% for alloys with 16–20% chromium gives rise to a decrease in the critical current density for passivation owing to suppression of active dissolution and to a decrease in the current density in the passive region of molybdenum, but to an increase in the current density in the transpassive region of molybdenum. Increasing the chromium content of Ni–Cr–Mo alloys suppresses the corrosion rate in hot concentrated sulphuric acid that contains active carbon.

References

[1] Y. Sakae and Y. Harada, *Kagaku Kogaku*, *31* (1967) 217.
[2] G. Whittengham, *J. Appl. Chem.*, *1* (1951) 383.
[3] E.S. Lisle and J. D. Sensenbaugh, *Combustion*, January (1965) 12.
[4] W. Grimm, *Combustion*, September (1963) 38.
[5] D.B. Meadowcroft, in D.R. Holmes (ed.), *Dewpoint Corrosion*, Ellis Horwood, Chichester, 1985, p. 17.
[6] J.A. Bernie, in D.R. Holmes (ed.), *Dewpoint Corrosion*, Ellis Horwood, Chichester, 1985, p. 11.
[7] M. Kowaka, D. Moroishi and H. Nagano, *Bull. Jpn. Inst. Met.*, *34* (1970) 23.
[8] M. Kowaka, D. Moroishi and H. Nagano, *Bull. Jpn. Inst. Met.*, *34* (1970) 32.
[9] H. Nagano, *Boshoku Gijutsu*, *26* (1977) 731.
[10] Y.-N. Chang, *Anti-corrosion*, August (1986) 4.

ELSEVIER

Materials Science and Engineering A198 (1995) 153–160

MATERIALS SCIENCE & ENGINEERING A

Electrochemical aspects of corrosion resistance and etching of metallizations for microelectronics

R.B. Comizzoli[a], R.P. Frankenthal[a], K.J. Hanson[a], K. Konstadinidis[a], R.L. Opila[a], J. Sapjeta[a], J.D. Sinclair[a], K.M. Takahashi[a], A.L. Frank[b], A.O. Ibidunni[b]

[a]*AT&T Bell Laboratories, Murray Hill, NJ 07974, USA*
[b]*AT&T Microelectronics, North Andover, MA 01845, USA*

Abstract

The electrochemical aspects of metal etching to form patterned conductors and of corrosion of conductors in the field are closely related. Both need to be considered in designing metallization structures for microelectronic devices. The evolution of a manufacturing process for a multi-level interconnect structure is discussed from an electrochemical perspective. A galvanic corrosion problem during manufacture and its solution for the interconnect metallization on a silicon integrated circuit are also discussed. Following the discussion on etching processes and corrosion during manufacture, a discussion of electrochemical and electrolytic failure mechanisms for electronic equipment in field environments and some steps that can be taken to prevent harmful environmental effects are presented. Recent research on the adhesion of various protective coatings and interlevel polymeric dielectrics is presented in the context of failure prevention.

Keywords: Etching; Microelectronics; Undercutting; Galvanic corrosion; Covercoats; Ionic contamination

1. Introduction

As the circuit density of electric equipment steadily increases, the patterned metallizations used to interconnect transistors on integrated circuit chips and to interconnect the chips become increasingly important to overall performance. For advanced integrated circuits, as are found in personal and mainframe computers, personal communication devices and even microprocessor-controlled appliances, as many as four levels of interconnect metallization will be required on the chip itself. Off-chip interconnect frequently has more than 10 levels of patterned metallization in currently manufactured products. This increasing circuit density requires that linewidths for both on-chip and off-chip metallizations continuously decrease. If these linewidths are not reduced, the time delay associated with signal transmission on chips and between chips will limit, at least indirectly, the performance of advanced computers and communication devices. Manufacturing technologies must be continually improved to achieve the linewidth reductions required to realize the functional objectives and yields required for success in the marketplace.

Without improvements in hardening against environmental effects, advancing generations of interconnection technology are also more susceptible to field failure resulting from electrochemical and electrolytic degradation processes [1–3]. These failure mechanisms must be understood so that required design improvements can be made.

The electrochemical aspects of metal etching to form patterned conductors and of corrosion of conductors in the field are closely related. Both need to be considered in designing a metallization structure. In this paper, the evolution of manufacturing process for multichip modules is discussed from an electrochemical perspective. A galvanic corrosion problem with interconnect metallization on a silicon integrated circuit is also discussed and its solution is described.

Following the discussion on etching processes and corrosion during manufacturing, a discussion of electrochemical and electrolytic failure mechanisms for electronic equipment in field environments and some steps that can be taken to prevent harmful environmental effects [2,3] are presented. Coatings play an important role in preventing failures. Recent research on the adhesion of various protective coatings and interlevel polymeric dielectrics is presented in the context of failure prevention.

Elsevier Science S.A.
SSDI 0921-5093(94)04520-8

2. Evolution of a multichip module manufacturing technology

Alumina is commonly used as a substrate material for the assembly of integrated circuits and other components into a functional unit. These earliest hybrid integrated circuits (HICs) were constructed with a single layer of metallization on the top surface. The HICs were typically mounted on a printed wiring board along with other discrete components. In more advanced HICs, greater interconnect density was achieved by patterning metal on both sides. Holes connected the two levels of metal. As requirements for interconnect density have increased, additional layers of patterned metal have been added by interleaving each layer with a polymeric dielectric material. Typicaly, photodefineable polymers are used as the dielectric material to facilitate formation of via holes between metallization levels.

A typcial metallization used for HICs is the stacked structure depicted in Fig. 1. Copper, with its very low specific resistivity (1.68×10^{-6} ohm cm), is the primary conductor. Copper does not adhere well to alumina so titanium is used as a glue layer. Gold is used as the top layer to provide a suitable surface for connecting integrated circuits and other components by soldering or wire bonding. Copper readily diffuses through small pores that are always present in gold films of practical thickness, so nickel is deposited between the copper and gold to prevent copper migration to the gold surface. During the early 1970s this structure was typically formed in the following way. First, blanket layers of titanium and copper were sputter deposited. This was followed by a blanket layer of electrodeposited copper. A patterned resist layer was then formed and nickel and gold were electrodeposited in the trenches of the resist. The resist was then stripped and the copper and titanium were etched with the gold/nickel layer serving as the etch mask. Until recently, etching was accomplished by the following two-step process:

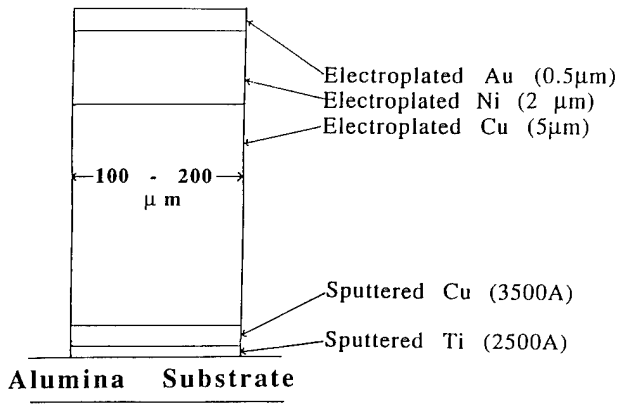

Fig. 1. Schematic illustration of a metallization structure used for the earliest hybrid integrated circuits.

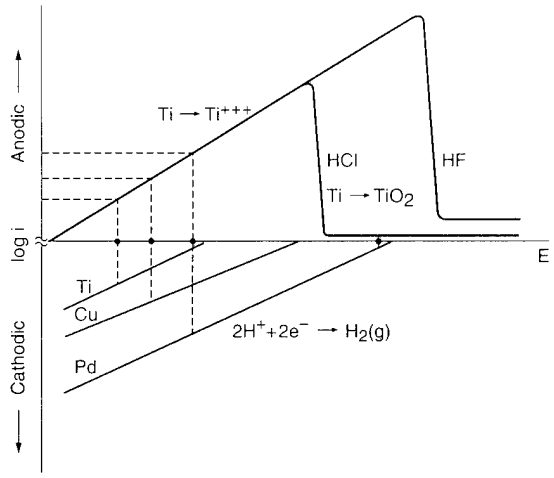

Fig. 2. Conceptual illustration of the current–voltage curves relevant to corrosion and anodic passivation of the titanium in the metallization structure in Fig. 1.

Step 1:

$$Cu + Cu(NH_3)_4^{2+} \rightarrow 2Cu(NH_3)_{2+}$$

$$Cu(NH_3)_2^{+} + 1/4O_2 + H^{+} \xrightarrow{NH_3} Cu(NH_3)_4^{2+} + 1/2H_2O$$

Step 2:

$$TiO_2 + 4H^{+} + 6F^{-} \rightarrow TiF_6^{2-} + 2H_2O$$

$$Ti + 6F^{-} \rightarrow TiF_6^{2-} + 4e^{-}\ [4,5]$$

$$2H^{-} + 2e^{-} \rightarrow H_2$$

Early experience with this metallization showed that the titanium layer corroded in chlorine-containing environments [6]. Fig. 2 illustrates schematically the mechanism for this corrosion process and a mechanism for titanium passivation. The copper–titanium galvanic couple increases the rate of titanium corrosion due to the lower hydrogen overpotential on copper. However, the deposition of a layer of palladium between the copper and titanium passivates the latter in chloride media by shifting the corrosion potential into the passive region [7]. Since titanium is not passivated by palladium in hydrofluoric acid solutions (the passivation potential in HF is too positive), the titanium etch is successful even in the presence of palladium. Besides accelerating the corrosion of titanium, the copper–titanium galvanic couple in hydrofluoric acid solution may also contribute to the undercutting of the titanium metallization during etching. The linewidths required through the late 1980s ($<100\,\mu m$) were sufficiently large to insure good adhesion in spite of the undercutting.

By the late 1980s, as requirements for interconnect density increased to the point that multiple levels of interconnection and linewidths of $<50\,\mu m$ were required, two new issues emerged: (1) palladium metal residues from the etch process causes device failures

during temperature/humidity/bias testing and (2) titanium undercut became a yield concern.

The palladium metal residues were associated with the etch process described above. Neither step dissolves palladium. It is "rejection etched", that is, it floats off as the underlying titanium dissolves during step 2. Since palladium passivates titanium in chloride media either when the two metals are coupled to each other or when a small amount of palladium is alloyed with the titanium [7], the solution to the first problem was clear: replace the sputtered titanium and palladium layers of the metallization by a thin layer of sputtered titanium followed by a thick sputtered layer of a titanium–palladium alloy having a palladium content sufficiently high to passivate the titanium in chloride environments but not high enough to make etching the alloy in HF difficult. Titanium–palladium alloys containing from 1 to 15% palladium were found to behave satisfactorily, as illustrated by the following example: a Ti–3% Pd/Cu metallization exhibited a corrosion potential (−0.20 V vs. SCE) in the passive potential region of titanium in boiling 10% HCl and was not corroded after more than 5 min. On the other hand, a Ti/Cu metallization had a corrosion potential (−0.74 V vs. SCE) in the active potential region and was completely corroded in less than 1 min. The higher corrosion current expected for the alloy in hydrochloric acid solution compared with titanium metal (see Fig. 2) should lead to a more rapid etch rate and lower manufacturing cost.

Solving the undercutting problem proved to be a greater challenge. Laboratory-scale experiments showed that the finest linewidths that could be reproducibly made without experiencing adhesion problems were typically 30–40 μm. Cross-sections of metallizations showed the undercut of titanium on each side of the metallization was frequently 5–10 μm. Finding a solution to the undercutting problem required a detailed unraveling of the etch chemistry. The galvanic effect described above was found to be of minor importance. It was shown that the etching of the titanium in HF only begins following an induction period, after which etching is very rapid (Fig. 3). Further studies showed that (1) the copper etch and subsequent rinse process produced an etch inhibiting film on the titanium and (2) the etch rate and induction time were sharply dependent on pH and F^- concentration.

The undercutting of the titanium was caused by the uncontrollability of the induction time. To insure that all circuits were adequately etched, most circuits were being severly overetched. Linewidths in the 10–15 μm range would clearly not be possible unless an etch chemistry could be found that would terminate etching in a controllable way or eliminate the etch inhibiting film. Both types of etch chemistries were found.

Initially it was speculated that, if the solubility of the etch products could be sufficiently reduced, conditions might be found that would cause an etch inhibiting film to form after a fixed thickness of titanium had been removed. To test this hypothesis, buffered HF solutions in water were mixed in various proportions with ethylene glycol. Fig. 4 shows that the induction period still exists but, since the etch shuts down in a controllable way, overetch can be prevented. Fig. 5 shows that the amount of titanium removed is a smooth function of the fraction of ethylene glycol. X-ray photelectron spectroscopic (XPS) analysis of the inhibiting film shows that it contains nitrogen, fluorine, oxygen and titanium. Further work is rquired to characterize fully this "salt film".

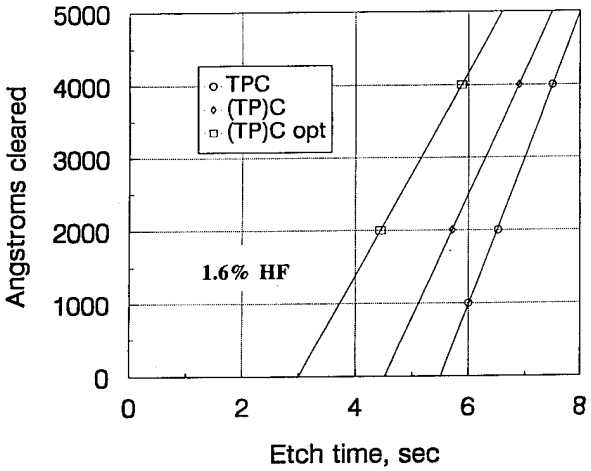

Fig. 3. Etch behavior of Ti or Ti–3% Pd in HF, all under standard manufacturing conditions; except where noted, TPC is the Ti–Pd/Cu metallization structure; (TP) C is the Ti–3% Pd/Cu metallization structure; (TP) C opt is Ti–3% Pd/Cu metallization structure under standard manufacturing conditions except that the times in the Cu etch and following water rinse were shortened.

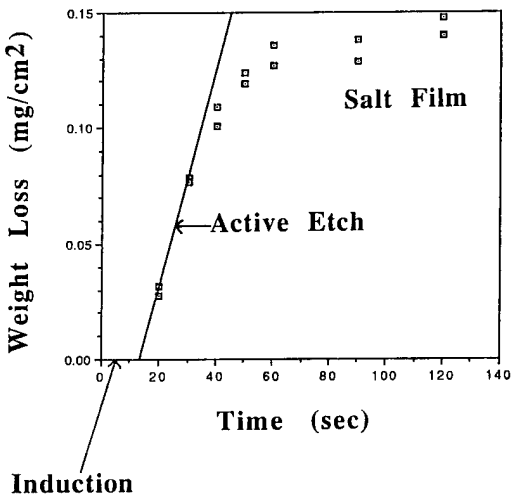

Fig. 4. Etching behavior of titanium in HF–NH_4F with 20% ethylene glycol added, showing that the induction time still exists but that etching essentially stops after formation of the salt film.

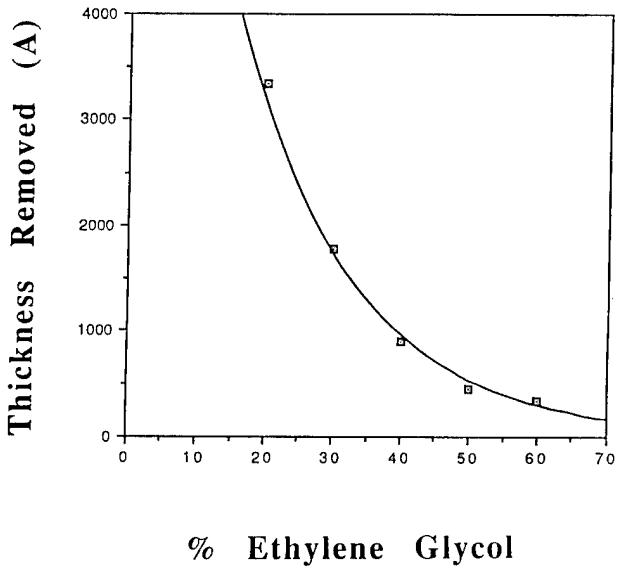

Fig. 5. Effect of ethylene glycol concentration on the amount of titanium etched in $HF-NH_4F$ solution.

The second approach was to seek an aqueous chemistry that would etch copper and titanium at the same rate. From the start it was decided that HF would be required for etching titanium, which dictates that the copper must be etched in an acid solution. The commercial etch used in step 1 of the original two-step etch process is basic. Laboratory experimentation showed that a solution containing 1 M $CuCl_2$, 1 M KCl and 4% HF [8] etched the Ti–3% Pd/Cu layers at equal rates and completely eliminated the undercutting. The Cu etch process is mass transport limited whereas the Ti etch process is not, so that the proper concentrations depend on the design of the etch process. The pertinent chemistry is as follows:

Copper dissolution:

$$\left.\begin{array}{l} Cu + Cu^{2+} \rightarrow 2Cu^{+} \\ Cu^{+} \xrightarrow{O_2} Cu^{2+} \end{array}\right\} \; Cu^{+} \text{ and } Cu^{2+} \text{ present as chloride complexes}$$

Titanium dissolution [4,5]:

$$Ti + 4H^{+} + 6F^{-} \rightarrow TiF_6^{2-} + 2H_2$$

$$Ti + 4Cu^{2+} + 6F^{-} \rightarrow TiF_6^{2-} + 4Cu^{+}$$

Titanium etches more slowly in this solution than in simple HF solutions, allowing the amount of Ti removed to be easily controlled. Titanium polarization curves show why the Ti etch is suppressed (Fig. 6). For the 4% HF solution, the corrosion potential is about −1 V vs. SCE, with the etch rate increasing with increase in potential up to a peak near −0.3 V. At higher potentials the titanium passivates, although the corrosion current is still about 20% of the peak current. When 1 M KCl is added, the corrosion potential is unchanged, but the passivation peak is shifted to more negative potentials, and the current decays with increasing potential within the passive region, becoming much lower than in the absence of KCl. The presence of KCl appears to affect the passivation process. Finally, the addition of 1 M $CuCl_2$ shifts the corrosion potential by nearly 900 mV, indicating that the slow hydrogen evolution reaction has been replaced by reduction of Cu(II) ion, probably to the Cu(I) complex. The corrosion potential is in the passive region for the 4% HF^-–1 M KCl curve, meaning that $CuCl_2$ passivates the titanium surface.

The composition of the passive film was characterized by XPS. Within the XPS sample depth, the only elements observed were potassium, titanium and fluorine, with copper and chlorine notably absent. All of the Ti was oxidized and had a chemical shift consistent with a fluoride complex rather than the more common TiO_2. The $CuCl_2$ does not appear to play a role in passive film formation. Rather, it poises the potential of the Ti metal within the passive region, allowing the etch to proceed at a controllable rate.

3. Corrosion of metallization for silicon integrated circuits

Aluminum is currently the metal of choice for interconnecting transistors on silicon integrated circuits (ICs). The most advanced ICs require three or four levels of metallization to achieve the desired signaling rates within and between ICs. In some applications, TiN is used as a diffusion barrier between the titanium glue layer and the aluminum, and as an antireflection film over the aluminum (see Fig. 7). The metallization is patterned in several steps. First a resist is applied, patterned and developed to produce a positive image of

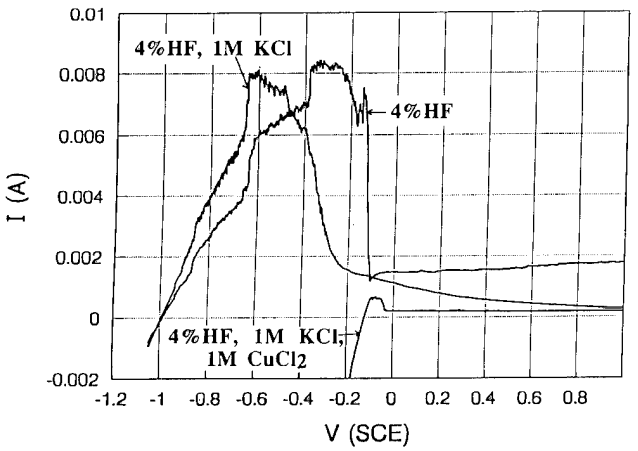

Fig. 6. Titanium polarization curves in various solutions, showing that KCl shifts only the passivation potential, whereas $CuCl_2$ shifts the corrosion potential by changing the cathodic reaction from hydrogen evolution to Cu^{2+} reduction.

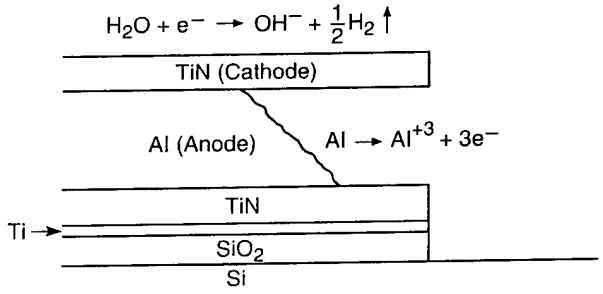

Fig. 7. Schematic illustration of the metallization structure and corrosion mechanism. The TiN–Al galvanic couple accelerates corrosion of aluminum when the TiN–Al area ratio is too large.

the described conductor pattern. The unprotected metal is then reactive ion etched, typically in a plasma produced from a mixture of BCl_3, Cl_2 and N_2. The etch process is followed by a water rinse to remove any residual chloride that could pose a later corrosion problem [9]. In the course of developing a new manufacturing process, it was found that the aluminum in the Ti/TiN/Al/TiN sandwich was severly corroded after the water rinse step. It was suspected that TiN and Al were a galvanic couple in an aqueous chloride environment. The metallization structure and proposed corrosion mechanism are shown in Fig. 7.

Several experiments were conducted. Fig. 8 shows a current–potential plot for an Al(Cu, Si) alloy in 10^{-3} M HCl. (Aluminum metallizations for integrated circuits are usually alloyed with approximately 1% Cu

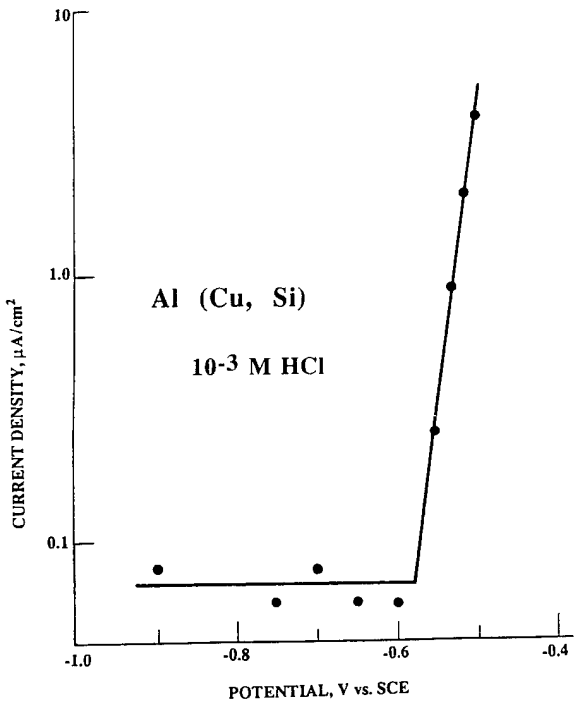

Fig. 8. Polarization curve for an Al(Cu, Si) alloy in 10^{-3} M HCl solution, showing that pitting initiates at about −0.6 V vs. SCE.

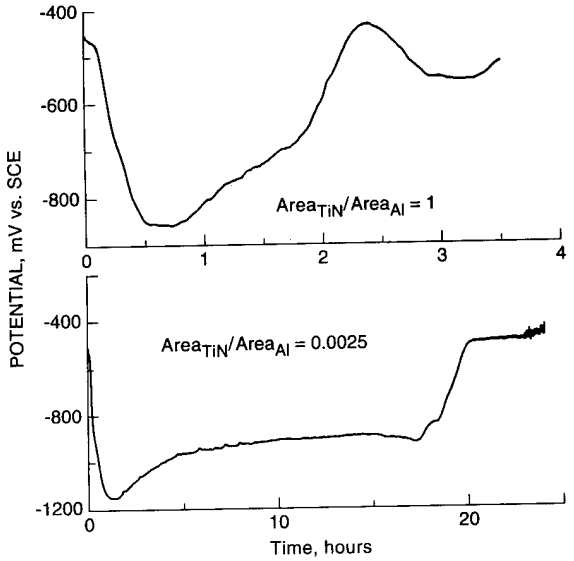

Fig. 9. Polarization curves for the TiN–Al galvanic couple for two cathode/anode area ratios, showing that pitting occurs more rapidly for a large cathode/anode area ratio.

and Si.) Not surprisingly, rapid pitting initiates at roughly −0.6 V vs SCE. Fig. 9 shows potential–time curves for the Al alloy electrically coupled to TiN in 10^{-3} M HCl for two cathode/anode area ratios. For $Area_{TiN}/Area_{Al} = 1$, the cathodic reaction is rate controlling. At potentials more positive than −600 mV ($T < 2$ h), pitting occurs. On the device manufacturing line, local fluctuations in Cl^- concentrations may rise to $\gg 10^{-3}$ M, resulting in much shorter pit initiation times. For $Area_{TiN}/Area_{Al} = 0.0025$, the anodic reaction is rate controlling, and the pit initiation time (18 h) is the same as in the absence of any TiN. Even at much higher Cl^- concentrations, the pit initiation time will be longer than the etch–rinse process. These data confirm that the metallization failures were caused by galvanic corrosion. Once the corrosion mechanism was understood, the solution to the corrosion process was obvious. If the water rinse is conducted before the photoresist is removed, the cathode/anode area is greatly reduced and galvanic corrosion is prevented.

4. Corrosion prevention

4.1. Electrical leakage and corrosion failures

Most environment-related failures in electronics are a result of electrical leakage between conducting pathways or electrolytic corrosion of the pathways [1–3]. Both are enhanced by the presence of ionic contamination. The degradation process can be described by

$$V = E_{anode} + IR + E_{cathode}$$

where V is the potential difference between two conducting pathways, E_{anode} and $E_{cathode}$ are the potentials of the anodic and cathodic electron transfer processes, respectively, I is the current flow between conductors and R is the resistance. IR depends on the amount and composition of contamination, the presence and effectiveness of protective coatings and the relative humidity (RH). At low humidity, charge transport through the bulk of the substrate may be comparable to surface current. However, for RH > 30%, the surface ionic current is much greater than the bulk currents in most cases. Fig. 10 shows the current–RH curves for a variety of different contaminants on an interdigitated test structure. The clean surface shows much lower current at high humidity than any of the contaminated surfaces. Most of the samples show an exponential dependence on RH. A phenomenological model described by Comizzoli [10] explains this exponential dependence. All of the samples exhibiting the exponential dependence were substantially ionic. The samples that did not exhibit the exponential dependence had very low ionic content. The Kuwait sample was collected during the oil fires following the Gulf War and is largely carbonaceous. The Mt. Pinatubo sample is volcanic ash from the recent eruption.

The similarity between field degradation of metallizations and the etch processes used to form them during manufacture is shown in Fig. 11. In this illustration, the anodic reaction leading to corrosion of the metal conductor is comparable to the copper and titanium etch reactions described above, whereas the cathodic reaction is reduction of water or H^+, depending on the local pH. The limited amount of water present in field corrosion leads to precipitation of metal hydroxides, whereas with etch processes, the large amount of water, coupled with solution agitation, prevents most of the ions formed by the anodic and cathodic reactions from precipitating.

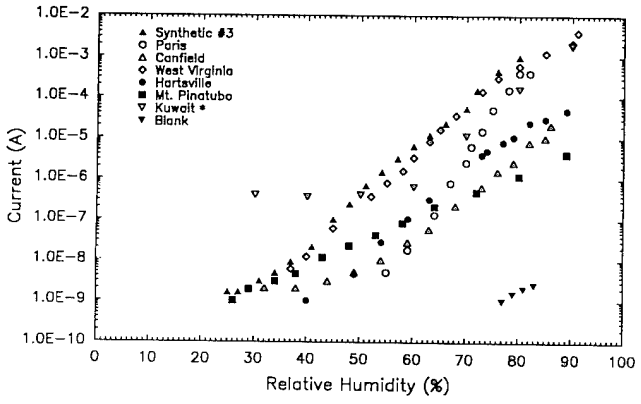

Fig. 10. Leakage current at various relative humidity levels for the indicated contaminants deposited on an interdigitated test structure. The voltage between conductors was 400 V.

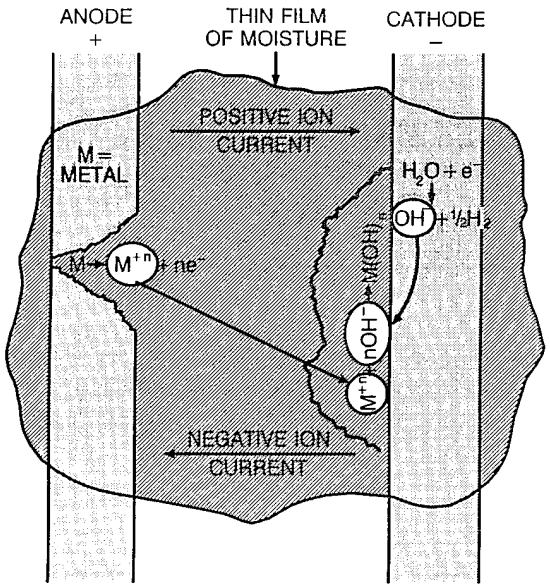

Fig. 11. Schematic illustration of the typical reactions associated with electrolytic corrosion of adjacent conductors of opposite electrical polarity.

4.2. Defect-free covercoats

To prevent corrosion of electronics in field environment, either the voltage between conductors must be reduced to levels below the reaction potential of the anodic and cathodic corrosion processes, or the conducting pathways need to be protected by a coating that keeps contamination and moisture from coming in contact with surfaces. At present, all but a few integrated circuits are powered at 5 V or more. Much higher voltages are found in mainframe computers and telecommunications equipment. Environmental concerns and heat dissipation issues are pushing integrated circuit designers to use lower voltages. In the next 10 years it is likely that many integrated circuits will operate at less than 1–2 V. Whereas the electric fields between conductors may not change significantly, since the line spacings will also be descreasing, electrochemical reactions will be prevented. Even so, electrical leakage issues will remain important and there will still be many circuit designs that require much higher voltages. Fig. 12 illustrates a known failure mechanism when closely spaced conductors are powered with a differential of a few hundred volts. In the absence of a cover coat, the failure process described in Fig. 11 would have been operative, and the anodic conductor would have corroded until an open circuit occurred. With contamination and moisture present on top of the covercoat, the potential drop between the component lead and the interconnect trace on the circuit board is concentrated across the covercoat. An arc will occur when the breakdown voltage of the covercoat is exceeded. This breakdown usually occurs at weak points (pinholes or thin spots) in the film. For this and other

reasons, the electronics industry has made a substantial investment in the development of effective covercoats.

Conformal coatings applied to a circuit board after all components and integrated circuits have been attached are very effective in preventing corrosion. Silicones and polyimides are among the materials that make effective conformal coatings. Unfortunately, these coatings add too much cost to the manufacturing process to be used in most applications. More commonly, the "resist" material used to pattern solder on bonding pads (for subsequent component attachment) is left in place after solder deposition to serve as a covercoat. As shown in Fig. 12, most of the conductors on the circuit board are covered with this resist coating but the bond pads are not. Thus, in addition to the failure process described in Fig. 12, the type of process shown in Fig. 11 can occur between leads. While these "solar mask" coatings are not as effective as conformal coatings, reliability is nevertheless substantially enhanced by their presence.

Several types of solder masks are available. The most reliable are photodefineable laminated polymer films, but these are expensive and rarely used. More common are materials that can be applied using a screening process. These are inexpensive but tend to have pinhole defects that result from bubble formation during application and cure. In recent years many companies have started using photodefineable polymers similar to those used as interlevel dielectrics for multichip modules. One of the critical reliability requirements with respect to polymeric coatings and interlevel dielectrics is good adhesion.

4.3. Polymer/metal adhesion

Improving the adhesion of coatings and interlevel dielectrics requires an understanding of the chemical or physical bonding mechanisms. Polyimide, a material used throughout the industry, and a proprietary triazine-based polymer were studied. Photodefineable polyimides are known for their excellent adhesion and

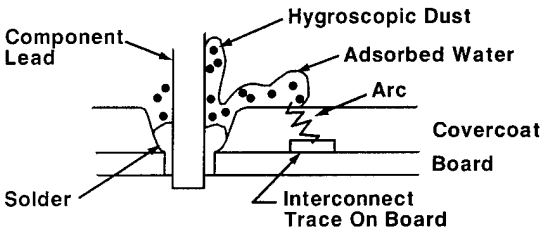

Fig. 12. Schematic illustration of a failure mechanism that is manifested as an electrical arc between a component lead and a metal interconnect trace of different polarity on a printed wiring board. Initially, water is adsorbed on the contaminated surface at elevated relative humidity. The potential drop is concentrated across the covercoat. An arc occurs if the covercoat breakdown voltage is exceeded.

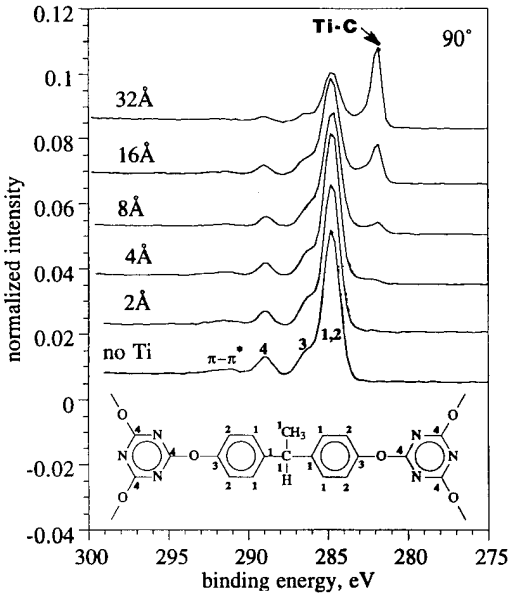

Fig. 13. C 1 s core level XPS for various thicknesses of titanium deposited on 100 Ångstrom of a triazine-based polymer, showing formation of the Ti–C bond with increasing titanium thickness. Spectra were taken at a 90° takeoff angle.

thermal stability, but can exhibit hydrolytic instability. Photodefineable triazine polymers are hydrolytically stable and have good adhesion properties when the polymer is Ar^+ sputtered prior to metal deposition, which suggests that mechanical bonding may be important. In practice, chromium is almost always used as the glue layer on polyimide, whereas titanium is used as the glue layer on triazine polymers. Several different experiments were conducted to evaluate the mechanism of titanium and chromium adhesion to these polymers.

The results of an experiment in which thin layers of titanium were evaporated, in situ, on triazine in an XPS chamber are shown in Fig. 13 [11]. The evolution of the C 1 s core-level XPS spectra as the thickness of the titanium layer increases shows that the polymer and titanium react to form Ti–C bonds. The attenuation in the intensities of the signals for carbon types 1–4 is due at least in part to the presence of the Ti, so it cannot be determined which carbons may be reacting with Ti from these data. Regardless, the Ti–C bonds are short lived. Fig. 14 shows that aging the sample for 60 days in room air causes most of the Ti–C bonds to be replaced by C–O and C=O bonds, suggesting that oxygen has inserted in the Ti–C bonds.

Although the XPS data are informative with respect to the types of chemical bonding, they do not give a clear picture of the metal–polymer structure. Using the synchrotron facility at Brookhaven, extended X-ray absorption fine structure (EXAFS) studies were undertaken [12]. The data show that Cr forms a π complex with the aromatic ring in polyimide and with the triazine ring in the triazine-based polymer. In contrast, the

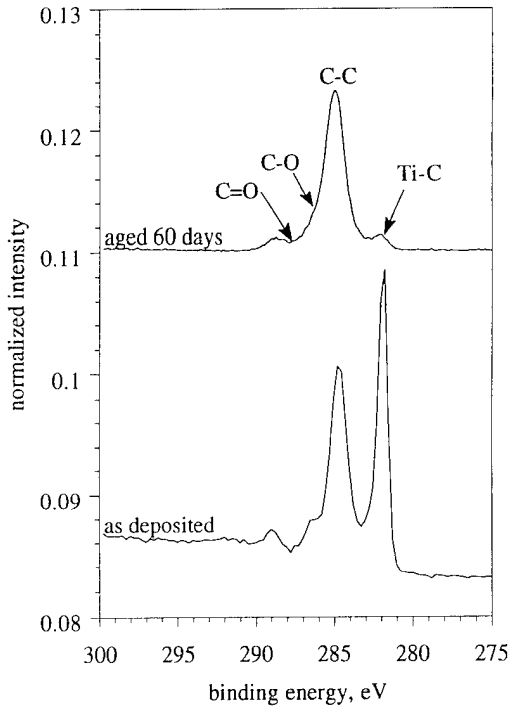

Fig. 14. C 1 s core level XPS of aged in air and non-aged titanium deposited on 100 Ångstrom of a triazine-based polymer, showing that aging causes the conversion of the Ti–C bond to C–O and C=O bonds. Spectra were taken at a 90° takeoff angle.

results for Ti support the conclusion that Ti interactions with either polymer are through Ti–O–C bonding.

Ar^+ sputtering was found to improve dramatically the adhesion of Ti to the triazine-based polymer. To understand that effect of Ar^+ sputtering, atomic force microscopy was used to evaluate untreated and sputtered triazine. The untreated surface shows large hills and valleys with an rms roughness of 66 nm. The typical width of the hills was 1.5 μm. In contrast, the sputtered polymer showed the same hills and valleys with a much finer level of roughness on top of the original, untreated topography. The rms of the fine features was 30 nm and the typical width was 100–200 nm.

These and other results [11,12] taken together show that the adhesion of Cr to polyimide and Ti to triazine-based polymers is both chemical and mechanical when the polymer is Ar^+ sputtered.

5. Future considerations

As the widths of metal conductors and bond pads continue to decrease and functional density increases, the uniformity of line profiles will become increasingly important. Etch processes used to pattern the metallizations must produce nearly vertical side-walls, undercut must be essentially non-existent and corrosion reactions that would consume metal or lead to electrical shorts must be controlled to currently unmeasureable levels. Continued research aimed at a mechanistic understanding of etch processes and corrosion phenomena is needed. Improvements in the adhesion of metals to silicon, ceramics and polymers and of polymers to silicon, ceramics and metals are also required to improve the robustness of manufacturing processes and the immunity of electronic devices and equipment to environmental effects. Use of analytical techniques such as XPS, EXAFS and AFM will be a key to meeting these requirements.

References

[1] R.B. Comizzoli, R.P. Frankenthal, P.C. Milner and J.D. Sinclair, *Science, 234* (1986) 340.
[2] R.P. Frankenthal, D.J. Siconolfi and J.D. Sinclair, *J. Electrochem. Soc., 140* (1993) 3129.
[3] R.B. Comizzoli and J.D. Sinclair, *Encyclopedia of Applied Physics, 6*, UCH, 1993, p. 21.
[4] M.E. Straumanis and C.B. Gill, *J. Electrochem. Soc., 101* (1954) 10.
[5] I.I. Baram, *Zh. Prikl. Khim., 46* (1973) 834.
[6] A.T. English and P.A. Turner, *J. Electron. Mater., 1* (1972) 1.
[7] M. Stern and H. Wissenberg, J. Electrochem. Soc., *106* (1959) 759.
[8] K.J. Hanson, B. Miller, B.J. Sapjeta, A.V. Shah and K.M. Takahashi, US Patent 5 298 117, 1994.
[9] J.R. Scully, R.P. Frankenthal, K.J. Hanson, D.J. Siconolfi and J.D. Sinclair, *J. Electrochem. Soc., 137* (1990) 1365, 1373.
[10] R.B. Comizzoli, *Materials Developments in Microelectric Packaging, Conference Proceedings, Montreal, August 19–22, 1991*, ASM International, 1991, p. 311.
[11] K. Konstadinidis, R.L. Opila, J.A. Taylor and A.C. Miller, *J. Adhesion, 46* (1994) 197.
[12] K. Konstadinidis, R.L. Opila, M.A. Marcus, K. Short, A.E. White, A.O. Ibidunni, A.J. Davenport and H.S. Isaacs, *Materials Research Society Symposium Proceedings, Vol. 323, Electronic Packaging Materials Science VII*, Materials Research Society, Pittsburgh, PA, 1994, p. 345.

ELSEVIER

Materials Science and Engineering A198 (1995) 161–168

MATERIALS SCIENCE & ENGINEERING A

Electrochemical studies on corrosion under a water film

Tooru Tsuru, Atsushi Nishikata, Jia Wang[1]

Department of Metallurgical Engineering, Tokyo Institute of Technology, 2-12-1, O-okayama, Meguro-ku, Tokyo 152, Japan

Abstract

The corrosion mechanism and corrosion rate were studied as a function of the water film thickness using Kelvin probe (non-contacting reference electrode) and impedance methods. Cathodic polarization curves were measured at different film thicknesses on copper, platinum, iron and gold electrodes. The diffusion-limiting current of oxygen increased with decreasing thickness to around 20–30 μm, and then decreased with decreasing thickness. The corrosion rate of copper as a function of the water film thickness was measured by the impedance method. It was confirmed that the rate is constant for a thick film, increases with decreasing thickness to give a maximum and then decreases, as reported by Tomashov. The water film thickness was measured by the solution resistance of the water film. Using the impedance method, the corrosion rates of steels were monitored during wet and dry cycles. The importance of monitoring the corrosion rate, during evaluation or conventional corrosion tests, is illustrated by the results.

Keywords: Kelvin probe; Limiting current; Water film; Wet and dry cycle; Corrosion monitoring

1. Introduction

The atmospheric corrosion of metals and alloys has been investigated for many years; the importance of this type of corrosion, indoors and outdoors, is now increasing. The major problems with this corrosion are that the corrosion reaction occurs under a thin water film and the concentration of electrolytes in the water film changes significantly with wet and dry cycles.

In the 1960s, Tomashov [1] reported that the rate of corrosion is influenced by the thickness of the water film. He concluded that the corrosion rate is controlled by the diffusion-limiting current of oxygen when the water film thickness is greater than the diffusion layer thickness (Fig. 1). Therefore the rate is not affected by the water film thickness for very thick films, e.g. region IV in Fig. 1. When the water film thickness is less than that of the diffusion layers, the oxygen diffusion rate, which is equal to the corrosion rate, increases with a decrease in the water film thickness, as shown in region III. On the other hand, the anodic reaction rate decreases with decreasing water film thickness in region II, because the solubility of the reaction products decreases with the decreasing amount of water which exists near the electrode surface. Therefore Tomashov [1] reported that a maximum corrosion rate appears around several micrometres.

Since the interpretation of Tomashov's results [1] is reasonable, it has been widely accepted as the corrosion

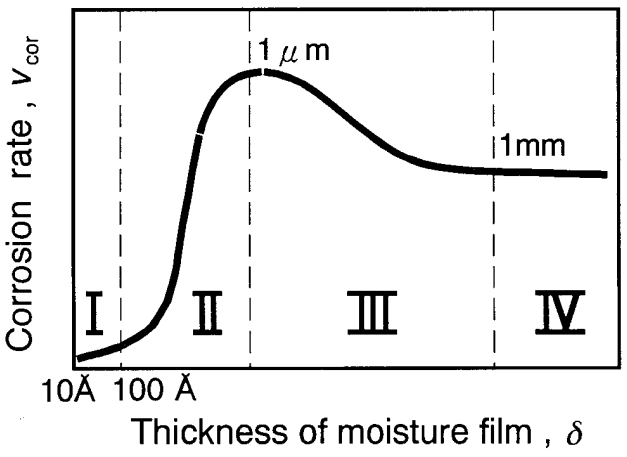

Fig. 1. Dependence of the corrosion rate on the water layer thickness (schematic, after Tomashov [1]).

[1] Present address: Institute of Oceanology, Academia Sinica, Quingdao, People's Republic of China.

SSDI 0921-5093(94)04521-6

mechanism. However, few data are available on the kinetics of oxygen reduction and the corrosion reactions in very thin water films covering a metal surface.

In this paper, the mechanism and interpretation mentioned above are examined quantitatively using a Kelvin probe [2–4] as a non-contacting reference electrode and an impedance method for monitoring the corrosion rate under a thin water layer.

2. Diffusion-limiting current of oxygen in the water film [5,6]

Stratmann et al. [7] applied the Kelvin probe method to the measurement of the corrosion potentials of steels and other metals. They developed several measurement systems and reported the relationship between the corrosion potential and the corrosion rate. They reported polarization curves showing the diffusion-limiting current of oxygen at thin water films; however, no systematic reports of the oxygen transport kinetics were given. In this study, polarization curve measurements for different water film thicknesses and electrode materials are made to examine the oxygen transport kinetics under thin water films.

2.1. Kelvin probe for reference electrode

The Kelvin probe has been used to measure the contact potential difference in the field of semiconductor physics and the absolute potential of an electrode. The main feature of this method is that it can measure the contact potential difference between a reference electrode in air and an electrolyte solution on a working electrode which is placed parallel to the reference electrode.

The Kelvin probe, used as a non-contacting reference electrode, has been described elsewhere [5]. In this method, the potential is determined as a bias potential; the induced current via probe vibration is minimal, and it takes several minutes to measure the potential manually.

2.2. Experimental apparatus and conditions

2.2.1. Kelvin probe

A gold electrode (0.5 mm × 8 mm) was attached to the top of a piezo-ceramics actuator which enables the tip to be vibrated up to 100 μm. This electrode was placed just above the working electrode which was covered by a thin electrolyte solution layer. The vibration frequency was selected in the range 50–200 Hz.

2.2.2. Electrochemical cell

A cross-sectional view of the cell is shown in Fig. 2, where the width of the working electrode is 0.2–1 mm and the length is 8–10 mm. The cell had two solution pools which served to minimize the change in thickness and electrolyte concentration of the solution by evaporation of water during the measurements. The counterelectrodes of platinum wire were immersed into the solution pools. Whole electrode configurations were placed in a closed chamber in which the relative humidity and temperature were controlled. For correction of the potential measured by the Kelvin probe, a Luggin capillary from a silver/silver chloride reference electrode (SSE) was immersed into the solution pool. Polarization curves were measured with galvanostatic conditions. The relationship between the potentials measured by the Kelvin probe and the Ag/AgCl electrode showed a good linear relation for a wide potential range. The potential measured by the Kelvin probe can be converted to that measured by the Ag/AgCl electrode by the following equation

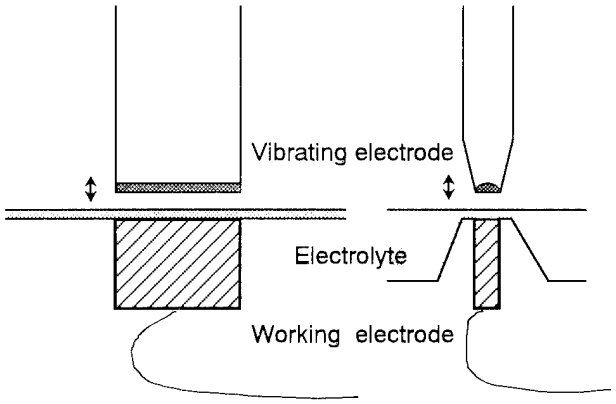

Fig. 2. Cross-sectional view of the cell, indicating the working and counterelectrodes and pools for the electrolyte solution.

$$E_{SSE} = -0.484 + 1.028E_{Kelvin} \quad (1)$$

Copper, iron, platinum and gold were used as working electrodes. Sodium sulphate solutions of 0.05–1.0 kmol m^{-3} were used as electrolyte.

2.3. Cathodic polarization curves under a thin water film

The cathodic polarization curves of copper, iron, platinum and gold in a solution of 0.2 kmol m^{-3} Na_2SO_4 (thickness, 50 mm) are shown in Fig. 3. It can be seen that all curves exhibit a region of diffusion-limiting oxygen current as well as a region of hydrogen evolution.

The potential of hydrogen evolution on gold and platinum is about 0.5 V more positive than that on copper and iron because of the lower overpotential for hydrogen evolution. These results are consistent with those measured in bulk solution.

Fig. 4 shows the polarization curves of platinum in 0.2 kmol m^{-3} Na_2SO_4 solution as the thickness is

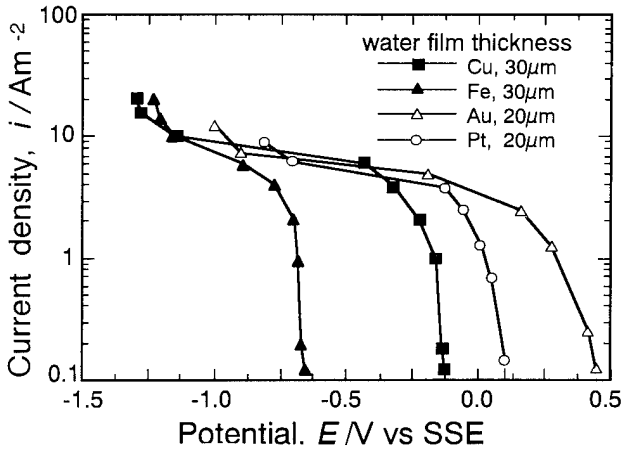

Fig. 3. Cathodic polarization curves of platinum, copper, iron and gold in a solution of 0.2 kmol m^{-3} Na_2SO_4 (solution thickness, 50 μm).

changed from 300 to 5 μm. For thicknesses greater than 5 μm, the polarization curves exhibit the same features as those in bulk solution, except for the different values of the diffusion-limiting current at different thicknesses. However, for thicknesses less than 2 μm, the polarization curve is totally different. This may arise from the high solution resistance which will lead to an inhomogeneous current distribution.

2.4. Diffusion-limiting current density and water film thickness

The diffusion-limiting current density of oxygen, determined from the polarization curve, is plotted against the water film thickness in Fig. 5 for a platinum electrode. The limiting current increases gradually with decreasing water film thickness. With a further decrease in thickness, the current reaches a maximum and then decreases. It is well known that the limiting current, i_{lim}, controlled by diffusion depends on the diffusion layer thickness δ

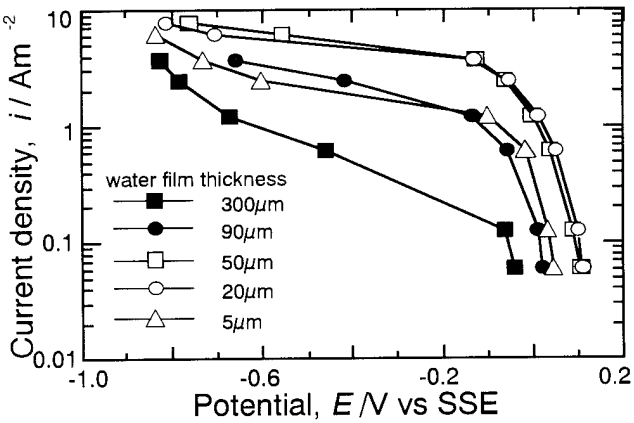

Fig. 4. Cathodic polarization curves of platinum in 0.2 kmol m^{-3} Na_2SO_4 at different water film thicknesses.

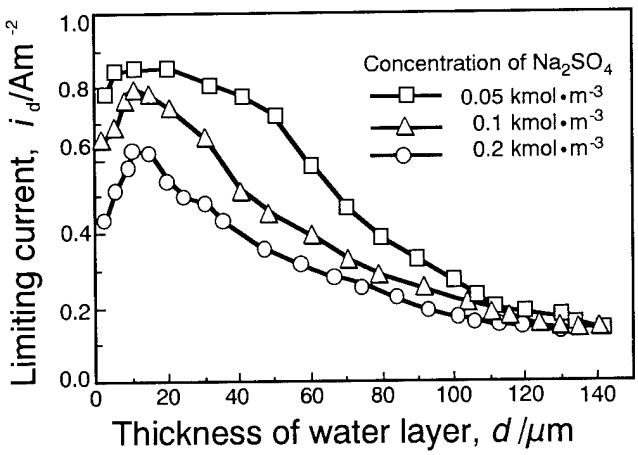

Fig. 5. Diffusion-limiting current density of oxygen on a platinum electrode vs. the water film thickness.

$$i_{lim} = nFD_{ox}C_{ox}^{b}/\delta \quad (2)$$

where D_{ox} is the diffusivity and C_{ox}^{b} is the bulk concentration of the oxidant.

When the thickness of the water film d_w is less than that of the diffusion layer in the bulk solution, the limiting current should be proportional to $1/d_w$. As shown in Fig. 6, this relation is observed in thick regions; however, it deviates from a linear relation and decreases after the peak. Assuming that oxygen at the water film surface is in a saturated condition, the diffusivity of oxygen is calculated to be 2.9×10^{-5}, 3.5×10^{-5} and 4.4×10^{-5} cm^2 s^{-1} for a platinum electrode in 0.2, 0.1 and 0.05 kmol m^{-3} Na_2SO_4 solutions respectively. The calculated diffusivity should be corrected, because of the different saturated concentrations of oxygen in solutions of different salt concentration.

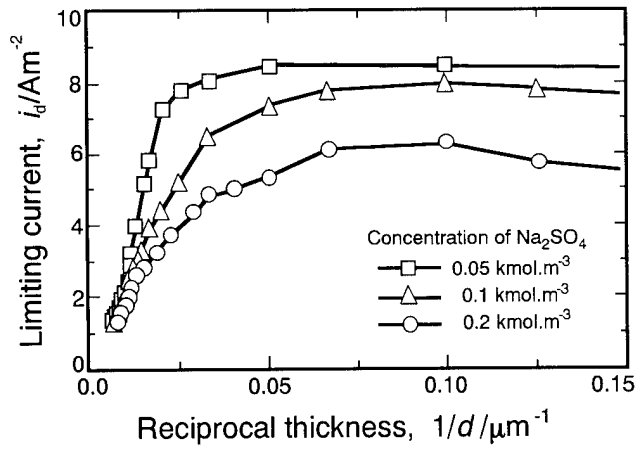

Fig. 6. Diffusion-limiting current of oxygen reduction on a platinum electrode vs. the reciprocal thickness of the water film.

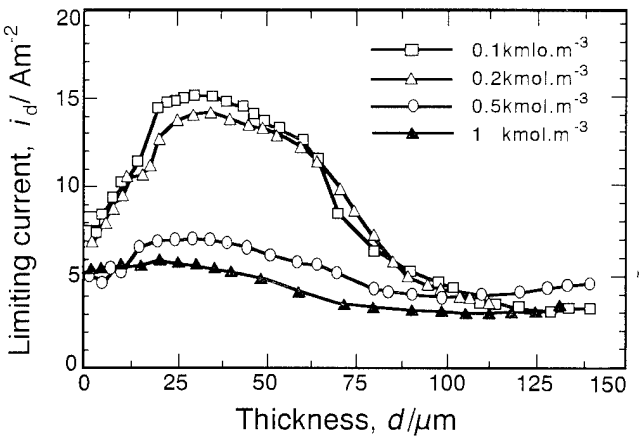

Fig. 7. Limiting current of oxygen reduction on a copper electrode vs. the water film thickness.

2.5. Effect of salt concentration and cathode material

If the limiting current is controlled by transport processes in the water, the value of the limiting current should not be affected by the cathode material or the type and concentration of the salt in the electrolyte. Fig. 7 shows the limiting current of a copper electrode vs. the water film thickness at different salt concentrations. In this case, the maximum appears at a slightly greater thickness compared with that on platinum. A similar behaviour, showing the current maximum, was observed on iron and gold electrodes, and confirmed in a KNO_3 solution.

From Figs. 5 and 7, it is worth noting that the maximum current increases with a decrease in the concentration of the salt, and in spite of the different concentrations, the limiting current remains almost constant when the thickness exceeds about 150 μm. This suggests that the stagnant diffusion layer thickness is about 150 μm.

2.6. Limiting current during dry and wet processes

The limiting current was measured during dry and wet processes by evaporation and addition of water. In the usual case, the salt concentration of the surface water changes from an initial concentration to saturation, as described later. However, in this experiment, the water pools, which are located beside the electrode, act as a buffer for the change in salt concentration of the solution at the surface. The change in the limiting current is shown in Fig. 8, where the open symbols denote the dry process and the filled symbols denote the addition of water. It can be seen that a current maximum is not observed on drying, but is observed on addition of water.

A maximum in the cathodic limiting current is found for the four kinds of metals in solutions with various pH values and different salt concentrations. In all circumstances, the thickness at which i_{lim} reaches a maximum is about 20 μm, and the thickness corresponding to a sudden decrease in the limiting current is about 10 μm.

Stratmann et al. [7] have reported a similar result using the Kelvin probe method. They suggested that the occurrence of a maximum in the diffusion-limiting oxygen current can be attributed to the decrease in oxygen solubility due to the enrichment of solutes during drying, the so-called salting out effect.

However, in our results, the thickness corresponding to the maximum limiting current was almost the same for salt concentrations from 0.05 to 1 kmol m^{-3}, and no shift of the current maximum was observed. In addition, the two pools located on both sides of the electrode must be greatly reduced in size in order to concentrate the salt at the surface. As expected, even under dry conditions, no salt deposits were observed on the electrode, although the limiting current showed a considerable decrease. Moreover, the appearance of a sudden decrease in i_{lim} at a thickness of 10 μm cannot be explained by the salting out effect. The results shown in Fig. 8 do not support the salting out effect.

The results obtained can be summarized as follows.
(1) When the water film thickness exceeds a certain value, around 150 μm, the limiting current is not affected so strongly by the salt concentration.
(2) The electrode materials do not affect the limiting current.
(3) The limiting current increases linearly with the reciprocal thickness as it decreases to 10–30 μm. The slope of this linear relation increases with a decrease in the salt concentration.
(4) Below a thickness of around 10–30 μm, the limiting current decreases with decreasing thickness.
(5) The maximum of the limiting current depends on the salt concentration and increases with a lower salt concentration.

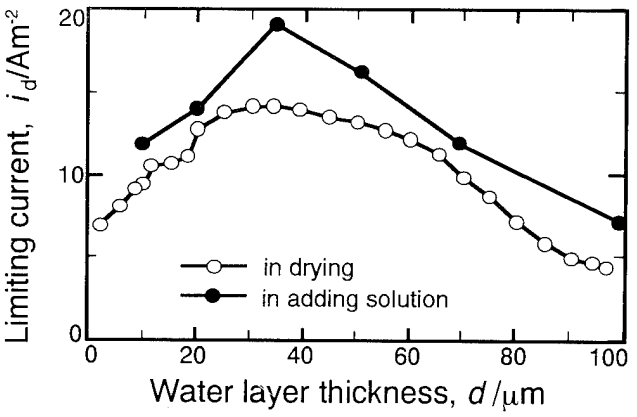

Fig. 8. Cathodic limiting current on a copper electrode vs. the water film thickness.

Results (1), (2) and the first part of (3) can be interpreted by a simple diffusion-controlled oxygen rate. The second part of (3) can be explained by the different saturated concentrations of oxygen in solutions of different salt concentrations; however, this conflicts with result (1). Moreover, results (4) and (5) cannot be explained by a simple diffusion-limited oxygen phenomenon. Possible interpretations include: (a) a change in the reaction mechanism of oxygen reduction with the pH at the surface; (b) a change in the dissolution reaction rate at the gas–water interface with the salt concentration; (c) an inhomogeneous current distribution on the electrode surface because of a very high solution resistance.

The experimental results described above support the explanation proposed by Tomashov [1] in a general sense; however, this explanation is not sufficient to interpret in detail our results, such as the maximum and decrease in the limiting current with a decrease in the thickness.

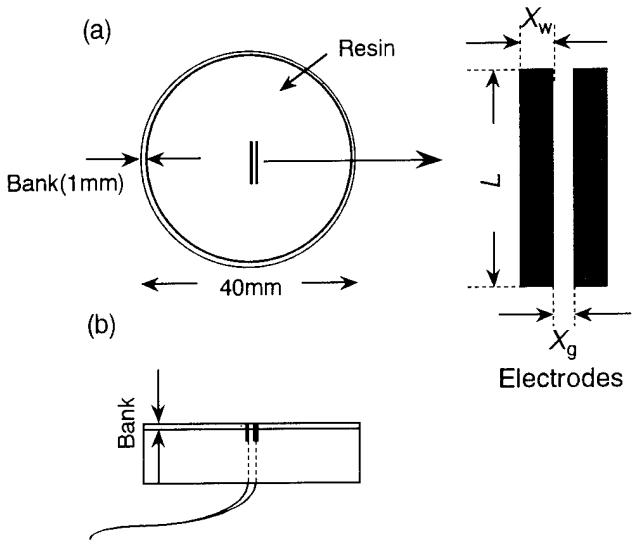

Fig. 9. Electrochemical cell for measurement of the impedance and corrosion potential during water film corrosion: (a) top view; (b) side view ($w = 10$ mm; $l = 0.1–1.0$ mm; $d = 0.1–1.0$ mm; height of bank, 0.5–1.0 mm).

3. Impedance method for the determination of the corrosion rate under the water film [8,9]

The use of the impedance method to measure and monitor the corrosion rate has been applied and reported for various corrosion systems by many workers. We have also attempted to measure the corrosion rate of copper under a thin water film. The impedance data contain information about the corrosion rate, double layer capacitance, solution resistance and other kinetic information. Since the solution resistance reflects the thickness of the water layer in the data analysis, the corrosion rate, which corresponds to the reciprocal of the corrosion resistance, and the solution resistance should be analysed carefully. Here, the change in the corrosion rate with decreasing water layer thickness was measured during drying of the solution.

3.1. Experimental apparatus and procedure

3.1.1. Electrochemical cell and electrodes

A pair of copper electrodes (width, 10 mm; thickness, 0.1–1 mm) were mounted in epoxy resin a distance of 0.1–1 mm apart. Around the surface of the epoxy resin (diameter, 40 mm), a bank (height, 1 or 0.5 mm) was attached to maintain a constant thickness of the solution at the start of drying. A schematic diagram of the cell is shown in Fig. 9. The electrolyte solution was 0.001–1.0 kmol m^{-3} Na_2SO_4.

3.1.2. Experimental procedure

The impedance was measured between two electrodes at 10 kHz and 10 mHz, where that at 10 kHz is considered to be the solution resistance and that at 10 mHz corresponds to the corrosion resistance. The cell was dipped into the solution and the water was drained to complete dryness. In this case, the water layer thickness at the beginning of the drying process was always constant in spite of the surface tension of the water. The time for drying was controlled by the relative humidity of the chamber which contains the cell assembly. In some experiments, the impedance over the whole frequency range was measured.

3.2. Effect of water layer thickness on impedance characteristics

When the water layer thickness becomes very thin, the current is distributed inhomogeneously. The current is localized in the region close to the other electrode because of the very high solution resistance of the thin layer. This effect and the theoretical analysis have been reported elsewhere [10]. For the experimental conditions of a small electrode thickness (less than 1.0 mm) and a relatively high corrosion resistance (10 kΩ cm^2), the corrosion resistance measured at 10 mHz will involve an error of less than 0.1% as long as the thickness is greater than 0.1 μm. Therefore the impedances measured at 10 kHz and 10 mHz are considered as the corrosion resistance and the solution resistance respectively assuming a simple electrode equivalent circuit.

3.3. Change in impedance during drying

Fig. 10 shows a typical result when the relative humidity was 95%. The corrosion rate is plotted as a reciprocal of the corrosion resistance R_{cor} and the solution resistance is normalized to that at the beginning of

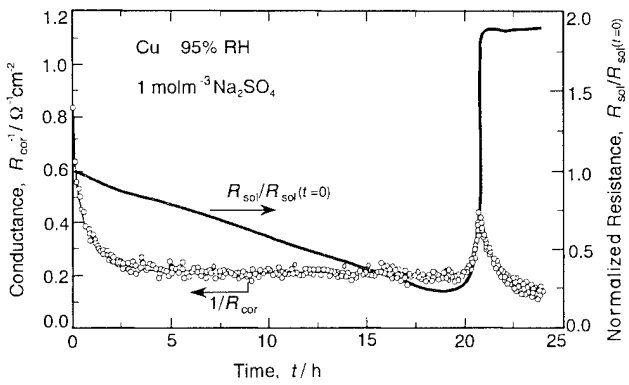

Fig. 10. Change in the reciprocal corrosion resistance (corresponds to the corrosion rate) and normalized solution resistance during the drying process in 95% relative humidity (copper electrode; initial concentration, 1.0 mol m^{-3} Na_2SO_4 solution).

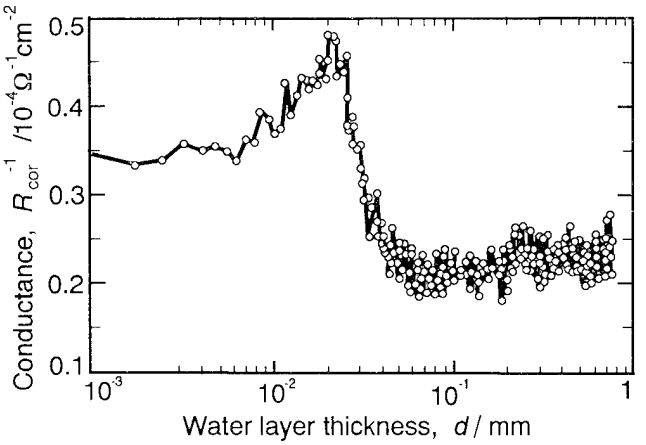

Fig. 12. Corrosion rate vs. the water film thickness calculated from the solution resistance. Same conditions as in Fig. 10.

drying. The corrosion rate decreases at the initial stage due to the fresh surface exposed to the solution; it then remains at a constant rate for several hours. Just before complete dryness, the corrosion rate increases rapidly and then decreases. On the other hand, the solution resistance decreases almost linearly due to an increase in the concentration of the solute. Before complete dryness, it also increases abruptly. After this rapid change in resistance, the solution resistance measurement becomes unstable, since the water film becomes discontinuous and the electrical connection between the electrodes becomes very narrow and unstable.

The change in solution resistance can be calculated by assuming a constant evaporation rate of water. Calculated and measured solution resistances are shown in Fig. 11 for 95% relative humidity. The simulation coincides very well, and so we can calculate the water film thickness during the course of drying. In Fig. 12, the corrosion rate shown in Fig. 10 is plotted against the water layer thickness estimated from the solution resistance. From the figure, the corrosion rate is constant between 1 mm and 100 μm; it increases with a further decrease in thickness, reaches a maximum and then decreases. The maximum of the corrosion rate appears around 20 μm. This value is the same as that reported by Tomashov [1].

The result mentioned above is very similar to that described in Section 2; however, it should be noted that Fig. 12 shows the corrosion rate, whereas in Section 2 the cathodic reaction rate is described. In spite of the different kinds of rates plotted, it is very interesting that a similar behaviour is observed.

In summary, impedance analysis for corrosion rate measurements was applied successfully. The corrosion rate depends strongly on the water film thickness when it is less than 100 μm. It exhibits a maximum at a thickness of around 20 μm and decreases with a further decrease in thickness.

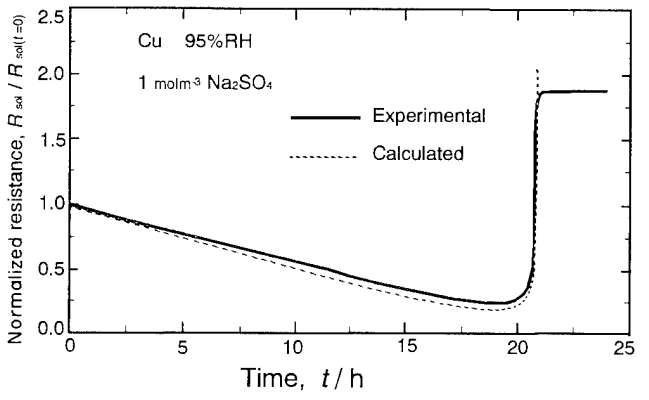

Fig. 11. Calculated and measured normalized solution resistances during drying. Same conditions as in Fig. 10.

4. Monitoring the corrosion rate under a thin water film [11]

For atmospheric corrosion and indoor corrosion, the corrosion reaction occurs under a thin water film or layer. The thickness of the layer varies with the relative humidity, temperature, raindrops or sunshine. These factors which influence the corrosion resistance are usually evaluated by an exposure test. Moreover, corrosion tests for coated metals and surface-finished steels are conducted with wet and dry cycles to accelerate the corrosion damage. An evaluation of the results is made by weight loss, appearance or some other factor.

We have attempted to develop a technique to monitor the corrosion rate during testing using the impedance method. A monitoring method based on impedance has been developed by Haruyama and Tsuru [12]; we have extended this method to corrosion during wet and dry cycles and under thin water films.

4.1. Experimental apparatus and procedure

4.1.1. Electrochemical cell and procedure

The cell is similar to that shown in Fig. 9, and copper, pure iron and mild steel (SS41) are used as electrodes. To repeat the wet and dry cycle, the solution was pumped to and drained from the immersion chamber and a constant water layer thickness was maintained. Usually, for ambient temperature and humidity, it takes 4–5 h to dry completely, so that the cycle consists of 1 h immersion in the solution and 5 h for drying. The impedance of the cell was measured at 10 kHz and 10 mHz and recorded on a computer.

4.2. Change in corrosion rate during wet/dry cycles

The monitoring of the corrosion rate of mild steel in 3% NaCl solution is shown in Fig. 13. The corrosion rate increases with an increase in the number of cycles. Fig. 13(b) shows some of the cycles, where the wet (immersion) cycle starts at 60 and 66 h and total dryness is achieved at 63.5 and 69.5 h. It is interesting that the corrosion rate shows two sharp peaks in one wet/dry cycle. One peak, at the point of complete dryness, should be the same as that observed in Fig. 10 for copper, so that the diffusion of oxygen controls the corrosion rate. The other peak is observed for mild steels, but not for marine steel which contains a small amount of Cu and P.

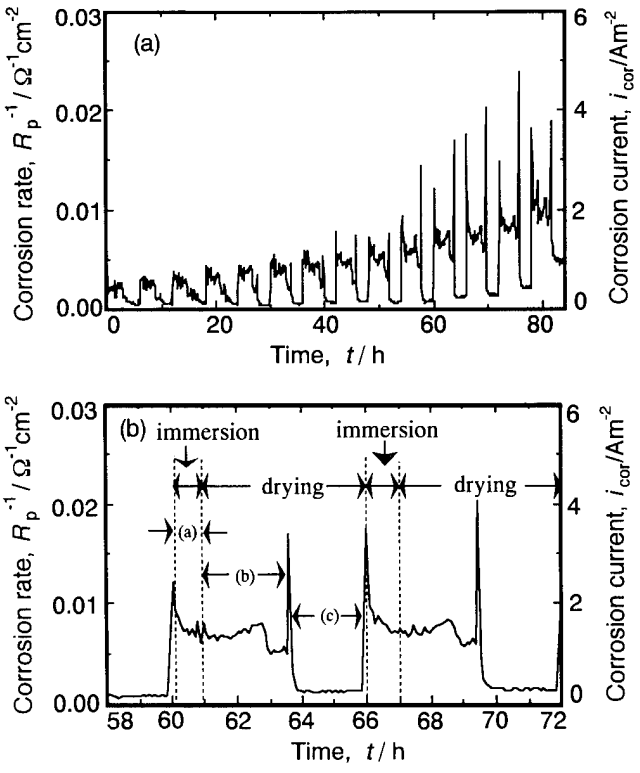

Fig. 13. (a) Change in the corrosion rate during wet (1 h immersion) and dry (5 h) cycle corrosion test; (b) 11th and 12th cycles of the test. Mild steel (SS41) and 3% NaCl solution.

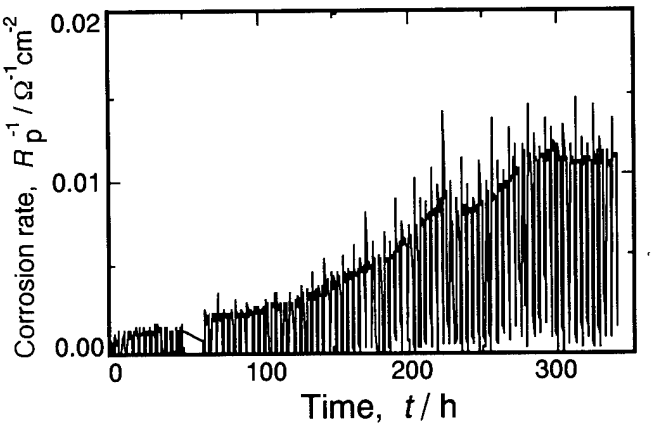

Fig. 14. Change in the corrosion rate monitored by the impedance method for long-term wet and dry test of pure iron using 3% NaCl solution.

The rust formed during polarization experiments, which has completely dried out, is oxidized to higher oxidation states and activates the cathodic reduction reaction, in contrast with rust kept in the wet condition. Therefore we can conclude that dried rust promotes the cathodic reduction itself; it then works as an oxidizer for the steel beneath the rust to increase the corrosion rate when the rusted steel becomes wet again. A similar discussion can be applied to the peak of the corrosion current at the beginning of immersion, i.e. the corrosion products formed on the steel surface, when dried, act as an oxidizing agent for steel corrosion when the surface becomes wet again. Further experiments and discussion are required on this topic.

4.3. Corrosion rate monitoring for corrosion test

According to the results described in the preceding section, this method is applicable to the evaluation of the corrosion rate and for monitoring the corrosion rate during corrosion cycle tests even if a dry period is used. Fig. 14 shows the result of a cyclic corrosion test of pure iron for 340 h using 3% NaCl solution. In this case, the rate increases gradually and becomes constant after 300 h. It should be noted that the electrode surface is covered by thick corrosion products for non-corrosion-resistant materials, so that the time required for complete dryness increases gradually. When seawater is used as the test solution, it takes a very long time to dry. Furthermore, very thick corrosion products cover not only the electrode surface, but also the insulating gap between the two electrodes. Even for these cases, the impedance can be measured and reflects the corrosion rate. Theoretical and practical analysis is required to interpret the impedance in detail.

Similar experiments have been performed on some plated steels, such as electroplated/non-electroplated zinc and zinc–aluminium alloy plating, to simulate and evaluate the resistance against atmospheric corrosion. The compositions of the solution and gas atmosphere were changed to simulate environmental conditions.

For the indoor corrosion of metals, the important factors are the water condensed from air, the gas dissolved in the water and the dust particles on the surface. This situation can be simulated using very thin electrodes and an insulating gap. Using vacuum evaporation, an electrode assembly can be fabricated.

The monitoring of the corrosion rate during the evaluation test is very important for the investigation of the corrosion mechanism and for the evaluation of the testing method. A combination of this method with conventional evaluation and test techniques will provide a powerful tool for the interpretation of results.

In summary, the impedance method, using a cell with wet and dry cycles, reveals a change in the corrosion rate during cycling. The dried rust formed on the steel promotes the cathodic reduction itself; it then works as an oxidizer for the steel beneath the rust to increase the corrosion rate when the rusted steel becomes wet again. It is suggested that monitoring the corrosion rate by the impedance method will lead to considerable information when combined with conventional corrosion cycle tests and exposure tests in the field.

5. Conclusions

Focusing on the corrosion reaction under a thin water film, three sets of experiments and results are described. The mechanism and rate-determining steps for this type of corrosion can be explained in a general sense according to Tomashov [1]. However, our results reveal some conflicting observations. In this connection, we wish to stress that electrochemical approaches provide a powerful tool for the investigation of the corrosion mechanism. If we use the polarization curves and impedance analysis appropriately, we can obtain useful information from these data.

References

[1] N.D. Tomashov, *Corrosion, 20* (1964) 7t.
[2] L. Kelvin, *Philos. Mag., 46* (1898) 82.
[3] W.A. Zisman, *Rev. Sci. Instrum., 3* (1932) 367.
[4] R. Gomer and G. Tryson, *J. Chem. Phys., 66* (1977) 4431.
[5] T. Tsuru, J. Wang and A. Nishikata, *Extended Abstracts USA–Japan Joint Meeting of Electrochemical Societies, 1993, Hawaii*, Electrochemical Society, 1993, p. 298.
[6] J. Wang and T. Tsuru, *Proc. JSCE Corrosion '93*, A306, Japan Society of Corrosion Engineering, 1993, p. 93.
[7] M. Stratmann, *Corros. Sci., 27* (1987) 869. M. Stratmann and H. Streckel, *Ber. Bunsenges. Phys. Chem., 92* (1988) 1244; *Corros. Sci., 30* (1990) 681, 697. M. Stratmann, H. Streckel, K.T. Kim and S. Crockett, *Corros. Sci., 30* (1990) 715.
[8] A. Nishikata and T. Tsuru, *Extended Abstracts 2nd Int. Symp. Electrochemical Impedance Spectroscopy, Santa Barbara, 1992*, Electrochemical Society, 1992, p. 350.
[9] A. Nishikata and T. Tsuru, in R. Zhu (ed.), *Corrosion Control, Proc. 7th APCCC, 1991, Beijing*, International Academic Publishers, 1991, p. 1312.
[10] A. Nishikata, S. Kumagai and T. Tsuru, *Zairyo to Kankyo, 43* (1994) 82.
[11] A. Nishikata, T. Takahashi, B.R. Hou and T. Tsuru, *Zairyo to Kankyo, 43* (1994) 188.
[12] S. Haruyama and T. Tsuru, in F. Mansfeld and U. Bertocci (eds.), *Electrochemical Corrosion Testing, ASTM STP 727*, ASTM, 1981, p. 167. T. Tsuru, S. Sudoh and S. Haruyama, *Proc. Symp. Computer Aided Acquisition and Analysis of Corrosion Data*, Electrochemical Society, 1984, p. 45.

ELSEVIER

Materials Science and Engineering A198 (1995) 169–175

MATERIALS SCIENCE & ENGINEERING A

Growth of a passive film on iron in a neutral borate solution by three-parameter ellipsometry

Toshiaki Ohtsuka, Atsushi Ohta

Nagoya Institute of Technology, Gokiso-cho, Showa-ku, Nagoya 466, Japan

Abstract

The growth of passive film on iron has been traced during potential sweep at various sweep rates in a neutral borate solution at pH 8.4. The transient thickness increase from a stationary state at 0.0 V (vs. Ag–AgCl) was measured by automated ellipsometry by which the ellipsometric parameters Ψ and Δ, and the reflectivity change $\Delta R/R$, are simultaneously obtained. The transient thickness change and the complex refractive index, $N = n - jk$, of the film were calculated by the three parameters. The complex refractive index of the film during the transient growth is estimated to be $N = 2.18 - 0.352j$ for light of 632.8 nm wave length. The linear potential increase initially causes an increase of the potential difference at the film/solution interface, where the film thickness remains constant and the observed current increases gradually. In the latter stage, where the interfacial potential difference reaches a constant value, steady growth of the film thickness takes place and the current reveals an almost constant value. The interfacial potential difference is a function of the potential sweep rate, and accordingly the current at the steady film growth stage is also a function of the sweep rate. From the transient change of the film thickness and current during the potential sweep at various sweep rates, the interfacial ionic transfer reactions and the mechanism of the film growth are discussed.

Keywords: Passive film; Iron; Ellipsometry; Growth

1. Introduction

The growth of a passive film on iron under the non-stationary condition has already been investigated by several authors [1–3]. Since the investigation by Sato and Cohen [1], two mechanisms have been proposed for the growth of a film; the ion-migration mechanism and the place-exchange mechanism. In both mechanisms, the ionic flow is assisted by a high electric field or a large potential difference in the film. The interfacial reactions at the film–solution interface under the non-stationary condition were experimentally and theoretically investigated by Vetter and Gorn [3] and Heusler [4]. They proposed two ionic-transfer reactions of film formation and film dissolution, reaction rates of which strongly depend on the interfacial potential difference. Furthermore, Kirchheim [5] performed a computer simulation of non-stationary film growth according to Vetter's model [3]. The simulation result indicated that the model combining field-assisted ionic migration through the passive film with the transfer reactions at the film–solution interface can quantitatively explain experimental results on current, potential, and film thickness obtained in neutral solution by Sato

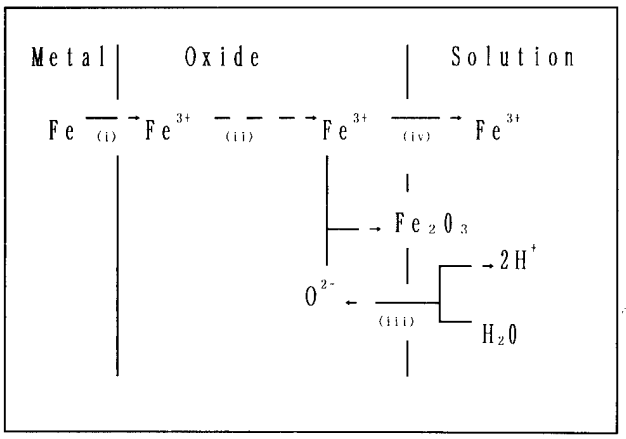

Fig. 1. Schematic representation of reactions of the iron electrode covered with passive oxide film.

SSDI 0921-5093(94)04522-4

and Cohen [1] and in acidic solution by Vetter and Gorn [3].

Since the ellipsometry technique is sensitive to changes of thickness and optical properties of the surface films, it has been applied to passive film on iron by several authors [6–14]. On the growth mechanism of passive films, most of the authors discussed it from ellipsometric measurements during the potentiostatic oxidation started from the film-free surface. Since initial oxidation of the film-free surface takes place with a relatively high reaction rate and a complicated behavior, the discussion on the film growth cannot be made in detail from these results. Sato and Noda [6], on the other hand, measured thickness of the stationary films that were obtained by long-time oxidation at various potentials in acidic phosphate solution at various pH values. They explained the potential and pH dependences of the film thickness by field-assisted ionic migration connected with the ionic transfer interfacial reactions.

In this paper we measure the growth of passive film on iron with linear potential increase in a borate solution at pH 8.4 by an automated three-parameter ellipsometer [15]. The non-stationary film growth starts with a thin stationary oxide film which was obtained by long-time oxidation at 0.0 V. From the transient growth of the thickness, we discuss the potential distribution and the growth mechanism.

2. Film growth model

The film growth under the non-stationary condition was described in the ionic transfer model by Vetter and Gorn [3] and Sato and Noda [6]. When we assume Fe_2O_3 for the passive film on iron, the ionic transfer in the passive oxide film can be illustrated in Fig. 1. At the iron metal/film interface a charge transfer reaction takes place:

$$Fe_{[M]} \rightarrow Fe^{3+}_{[ox]} + 3e \quad (1)$$

The Fe^{3+} ion then migrates to the film/solution interface owing to a large potential difference or a high electric field in the film.

$$Fe^{3+}_{[M/ox]} \rightarrow Fe^{3+}_{[ox/soln]} \quad (2)$$

The migration rate under the large potential difference is followed by the high field-assisted ionic migration mechanism [3,6]

$$i_{2m} = i_{2m(0)} \exp\left(\frac{zaF}{RT}\frac{\Delta E_{ox}}{d}\right) \quad (3)$$

or by the place-exchange mechanism [1]

$$i_{2p} = i_{2p(0)} \exp\left(\frac{\Delta E_{ox}}{\beta_f} - dB\right) \quad (4)$$

In Eqs. (3) and (4), ΔE_{ox} is a potential difference in the film, d is the film thickness, and $i_{2m(0)}$ and $i_{2p(0)}$ are exchange currents. In Eq. (3), z and a, respectively, are the ionic valency of migration and the jumping distance for ion migration. In Eq. (4), B is an activation energy at unit thickness and β_f is a acceleration coefficient related to the potential difference in the film.

At the film/solution interface the following two reactions take place and their rates depend on the interfacial potential difference according to the Tafel law. The first one is a film formation reaction, where an anionic species transfers from solution to oxide film at the interface with the thickness growth and vice versa with the thickness decrease;

$$H_2O_{[soln]} \rightleftharpoons 2H^+_{[soln]} + O^{2-}_{[ox]} \quad (5)$$

The second is a Fe^{3+} dissolution reaction, where a cationic species transfers from oxide film to solution;

$$Fe^{3+}_{[ox]} \rightarrow Fe^{3+}_{[soln]} \quad (6)$$

Under the stationary state, since the thickness remains constant, reaction (5) is in equilibrium, and the observed current is thus in agreement with the rate of reaction (6). Under the non-stationary condition, the ionic species flowing through the film is consumed by both reactions, with the reaction currents depending on the potential difference at the film/solution interface.

$$i = i_f + i_{diss} \quad (7)$$

$$i_f = i_{f,0}[\exp(\Delta E_{[ox/soln]}/\beta_3) - \exp(-\Delta E_{[ox/soln]}/\beta_{-3})] \quad (8)$$

$$i_{diss} = i_{diss,0}\exp(\Delta E_{[ox/soln]}/\beta_4) \quad (9)$$

where i_f and i_{diss} are, respectively, the currents of the reactions (5) and (6), $i_{f,0}$ is an exchange current of reaction (5) at a potential difference under the stationary state, $i_{diss,0}$ is a current of reaction (6) under the stationary state where the reaction (6) is not in equilibrium, so that the reverse reaction of the reaction (6) may be ignored, and $\Delta E_{[ox/soln]}$ is an over-potential for the interfacial reaction (5), which corresponds to a potential difference between the stationary and non-stationary states.

From mass balance of the flowing ions, the current measured, i, is considered to be related to the rates of the reactions (1), (2), (5), (6).

$$i = i_1 = i_{2m} \text{ (or } i_{2p}) = i_f + i_{diss} \quad (10)$$

Since the thickness growth of the film takes place according to reaction (5), the growth rate, dd/dt, can be related with the current i_f

$$i_f = K\,d(d)/dt \quad (11)$$

where d is film thickness and K a conversion factor from the thickness to charge accumulated in the film.

Under the stationary condition, since the thickness remains constant, the following equations are established.

$$i_f = 0 \quad (12)$$

and

$$i = i_{2m} \text{ (or } i_{2p}) = i_{diss} \quad (13)$$

Under the non-stationary condition, the measurable variables are d, i and E. The Fe^{3+} dissolution current is calculated in the following way.

$$i_{diss} = i - K\mathrm{d}(d)/\mathrm{d}t \quad (14)$$

The distribution to ΔE_{ox} and ΔE[ox/soln] of the applied potential can be estimated from the transient change of film thickness, as will be discussed later. In the later section, from rearrangement of the relations among i_{2m} (or i_{2p}), i_f, i_{diss}, ΔE_{ox} and $\Delta E_{[ox/soln]}$ under the linear potential sweep at various sweep rates, the growth mechanism of the passive film will be discussed.

3. Experimental details

The electrode used was polycrystalline iron of 99.99% purity in sheet form purchased from Johnson–Matthey. The electrode was cut in a rectangular form of $1 \times 1 \times 0.1$ cm^3 with a small tab for the electrical connection. The specimen was mechanically polished with alumina abrasive of 0.05 μm diameter.

The ellipsometer and the cell for the in-situ measurement have been described in previous work [15]. It is a rotating-analyzer type of apparatus in which the ellipsometric parameters Ψ and Δ and the reflectivity R are monitored simultaneously every 1 s. From three parameters, the three unknowns of the refractive index, extinction index and thickness of the surface film on electrodes are determined without any assumptions. The measurement was made at an incidence angle of 60.15° with light of 632.8 nm wavelength from a He–Ne laser.

The electrolyte solution was a 1:1 mixture of 0.30 mol dm^{-3} boric acid and 0.075 mol dm^{-3} sodium borate at pH 8.4, which was prepared from analytical reagents and pure water obtained by deionization and subsequent distillation in a glass vessel. The electrolyte solution was purged by pure nitrogen gas for 3 h or longer before experiments.

The experiment started with initial cathodic reduction at −0.85 V vs. Ag–AgCl electrode at saturated KCl solution for 1800 s to obtain the film-free surface. The anodic oxidation was then performed at 0.00 V for 1000 s. After the oxidation the potential was raised from 0.00 V to 0.90 V by potential sweep at sweep rates from 0.001 to 0.1 V s^{-1}. The stationary film at 0.00 V

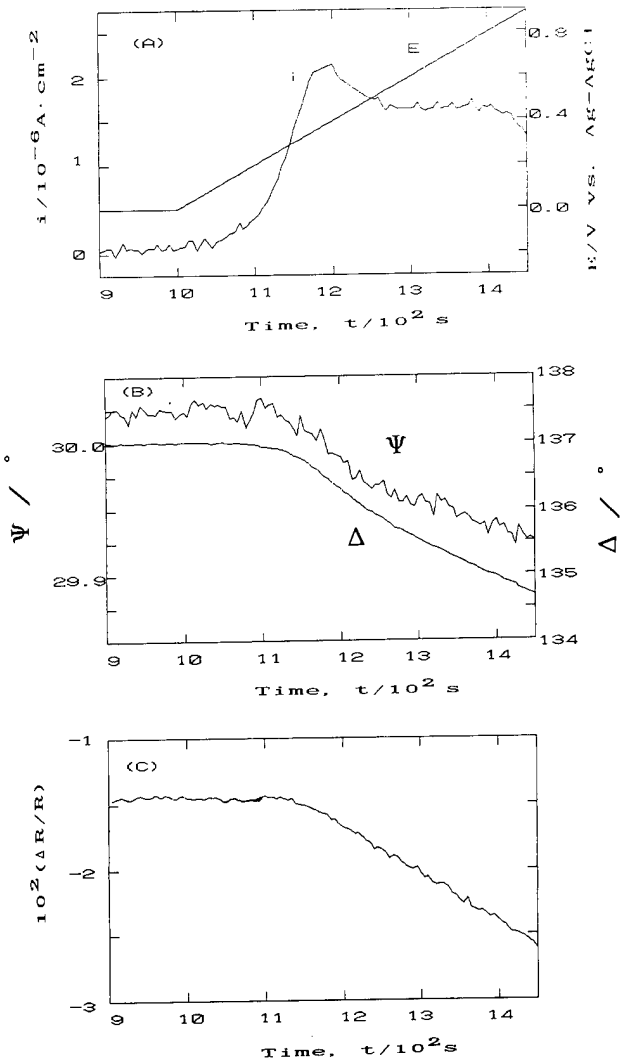

Fig. 2. Change of (A) potential E and current i, and ellipsometric parameters (B) Ψ and Δ, and (C) $\Delta R/R$ during the potential sweep from 0.00 V (vs. Ag–AgCl) to 0.90 V at a sweep rate of 0.002 V s^{-1}. The passive film was formed at 0.00 V for 1000 s before the potential sweep.

and the non-stationary film growth during the potential sweep was traced by the ellipsometer.

4. Results

4.1. Ellipsometry

Fig. 2 shows an example of the changes of current i and ellipsometric parameters (Ψ, Δ and $\Delta R/R$) during the potential sweep from 0.00 V to 0.90 V at a sweep rate of 0.002 V s^{-1}, where $\Delta R/R$ was the reflectivity change with respect to the reflectivity of the film-free surface obtained by the cathodic reduction at −0.85 V. The current, as shown in Fig. 2(A), remains a small value at the initial stage of the potential sweep and then increases gradually with increase of potential. After reaching a maximum, the current then becomes an

almost constant value. The transient change of current is interpreted by a gradual change of the potential difference at the film/solution interface, which will be discussed later. The change of the ellipsometric parameters, as shown in Figs. 2(B) and 2(C), corresponds to the film growth during the potential increase. These changes are small in the initial stage and increase in the latter stage of the high-potential region.

From the changes of the parameters, the complex refractive index, $N = n - jk$ (n, refractive index; k, extinction index), of the surface film was estimated from the growing film model. Fig. 3 shows a comparison between the experimental results and the theoretical curves calculated from the model in which the flat and homogeneous layer is assumed to form as an interfacial phase between the substrate and the solution. In Fig. 3 the experimental relations between Ψ and Δ, and between $\Delta R/R$ and Δ, are plotted as well as the theoretical relations calculated as a parameter of thickness with complex refractive indices of $N = 2.11 - 0.330j$, $N = 2.18 - 0.352j$, and $N = 2.27 - 0.359j$. For the calculation, a complex refractive index of the substrate, $N = 3.122 - 3.255j$, was assumed, which corresponded to the value of $\Psi = 30.08°$ and $\Delta = 140.30°$ measured for the film-free iron surface from the cathodic reduction at -0.85 V. The calculation was made numerically with a computer program from Fresnel's and Drude's equations for light reflection. The agreement between the experimental loci and the theoretical curve for the Ψ–Δ and $\Delta R/R$–Δ relations indicates that the value of complex refractive index of the film corresponds to a unique theoretical solution. Thereafter we estimate the thickness of the film from the average value of the complex refractive index, $N = 2.18 - 0.352j$, of the film.

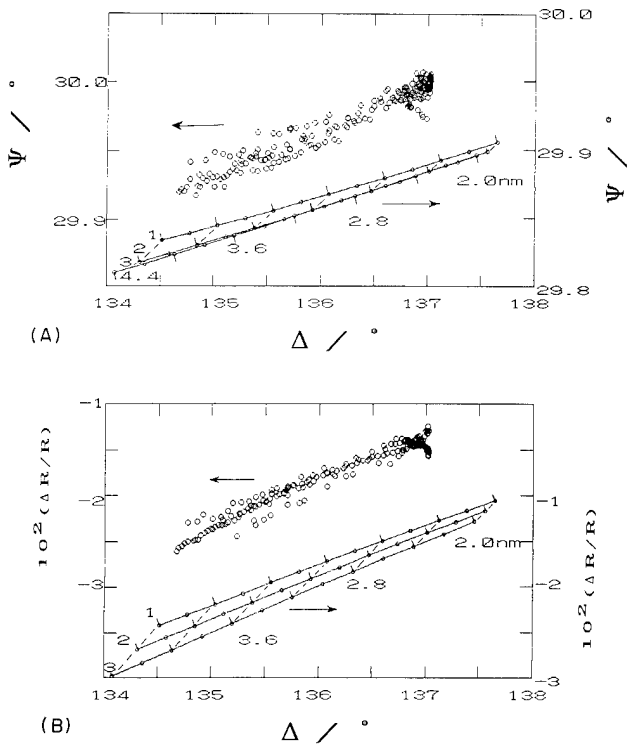

Fig. 3. Comparison between experimental loci and theoretical curves of (A) Ψ–Δ and (B) $\Delta R/R$–Δ relations for growing film with complex refractive indices: curve (1), $N = 2.11 - 0.330j$; curve (2), $N = 2.18 - 0.352j$; curve (3), $N = 2.27 - 0.359j$.

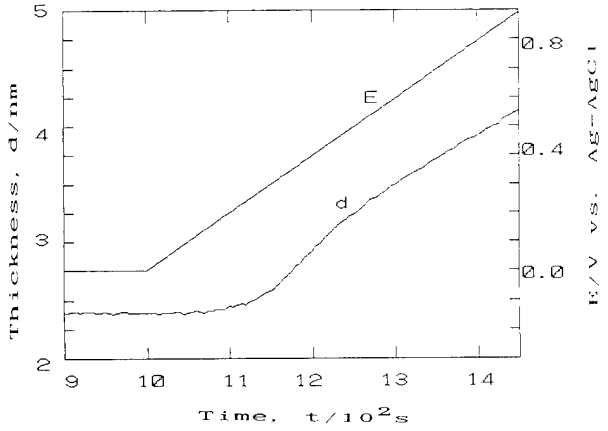

Fig. 4. Change of film thickness d and potential E with time during a potential sweep from 0.00 V to 0.90 V at a sweep rate of 0.002 V s^{-1}.

4.2. Thickness–potential relation

Fig. 4 shows an example for the thickness calculation during potential sweep. In Fig. 4 the sweep rate is 0.002 V s^{-1}. In the initial stage, the thickness of the film remains constant at 2.4 nm, which is same as the stationary thickness at 0.00 V. After 140 s from the beginning of the potential sweep, the film starts to grow. The time at which the thickness starts to increase corresponds to the time at which the current starts to increase gradually in Fig. 2.

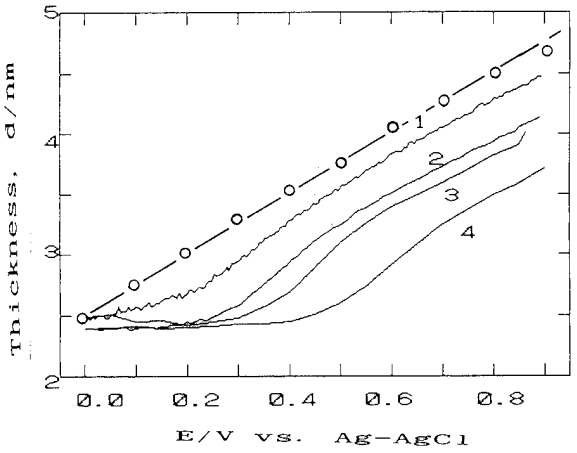

Fig. 5. Change of film thickness d with potential E during potential sweep at various sweep rates: curve (1), 0.001; curve (2), 0.002; curve (3), 0.01; curve (4), 0.05 V s^{-1}. The circles indicate thickness obtained by stepwise oxidation from 0.00 V to 0.90 V.

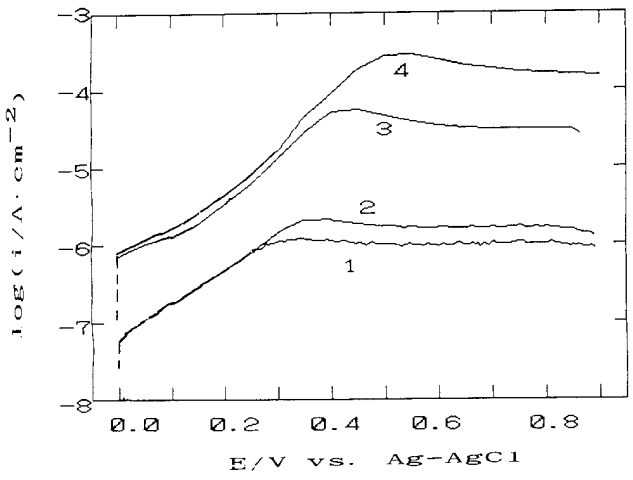

Fig. 6. Change of current i with potential E during potential sweep at various sweep rates: curve (1), 0.001; curve (2), 0.002; curve (3), 0.01; curve (4), 0.05 V s^{-1}.

Fig. 5 shows the thickness increase as a function of potential during the potential sweep at various sweep rates. In Fig. 5 the stationary thickness is also plotted, which was calculated from an ellipsometric measurement by a stepwise oxidation from 0.00 to 0.90 V. In the stepwise oxidation the electrode was kept at each potential for 1000 s. The thickness during potential sweep strongly depends on the sweep rates. If being compared at constant potential, the thickness decreases with increasing sweep rate. Fig. 6 shows the current measured during the potential sweep, where the current changes in logarithmic scale with the sweep rates. From comparison of the thickness data in Fig. 5 with the current data in Fig. 6, it is seen that the thickness does not increase in the initial period where the current gradually increases with potential; it increases linearly with potential after the current maximum. The potential width of the initial region, in which the thickness remains constant, increases with increasing sweep rate.

5. Discussion

5.1. Potential distribution

The changes of thickness of the passive film and current during the potential sweep starting from the stationary film at 0.00 V are schematically illustrated as Fig. 7. The initial increase of potential does not bring about the thickness growth. In this potential region, denoted as region (B), the thickness remains same as the stationary thickness at 0.0 V, and the current gradually increases. The thickness growth starts at higher applied potentials. In the potential region denoted as region (C), the thickness grows linearly with potential, while the current reveals an almost constant value.

The above transient change can be interpreted from the model illustrated in Fig. 8 for the distribution of applied potential. In the initial potential increase, the increasing applied potential appears at the film/solution interface. The increase of the potential difference at the interface mainly causes an increase of the ionic transfer of Fe^{3+} ion from the film to the solution (reaction (6)) and consequently results in the gradual increase of current. At the latter stage the potential difference at the interface remains constant, while the increasing applied potential appears in the film; the growing potential difference in the film brings about the thickness increase.

5.2. Relation between the potential difference and the reaction rate at the interface

As illustrated in Fig. 8(B), the over-potential of the interfacial potential difference $\Delta E_{[ox/soln]}$ during the steady growth of the passive film can be estimated from the potential region (B) in Fig. 7 for various sweep rates; i.e. the applied potential is placed at the interface until the steady growth of the film starts. This over-potential at the interface is seen to increase with increase of the sweep rate in Figs. 5 and 6.

The partial interfacial currents for reactions (5) and (6) were estimated from the comparison between the thickness increase and the charge passed during potential sweep. The rate of thickness increase is proportional to the current of reaction (5), i_f (Eq. (11)), and the current experimentally obtained is equal to the total

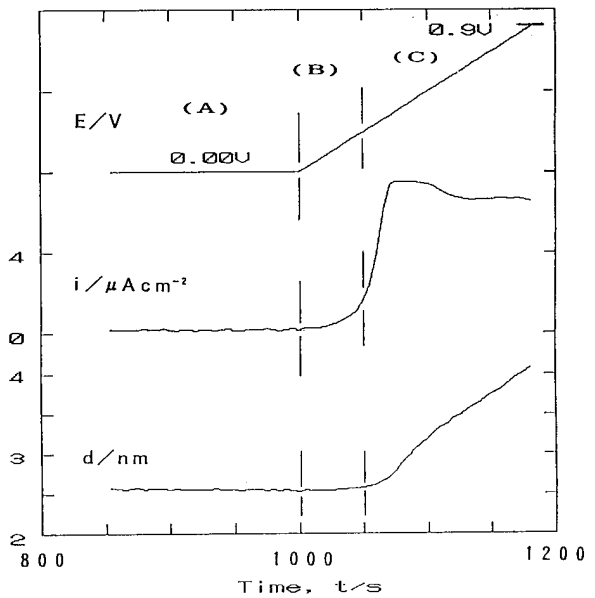

Fig. 7. Scheme of change of potential E, thickness d and current i during potential sweep: region (A), stationary state at 0.00 V; region (B), initial non-stationary state; region (C), non-stationary state in which a steady growth of the film takes place. The data correspond to those obtained at a sweep rate of 0.005 V s^{-1}.

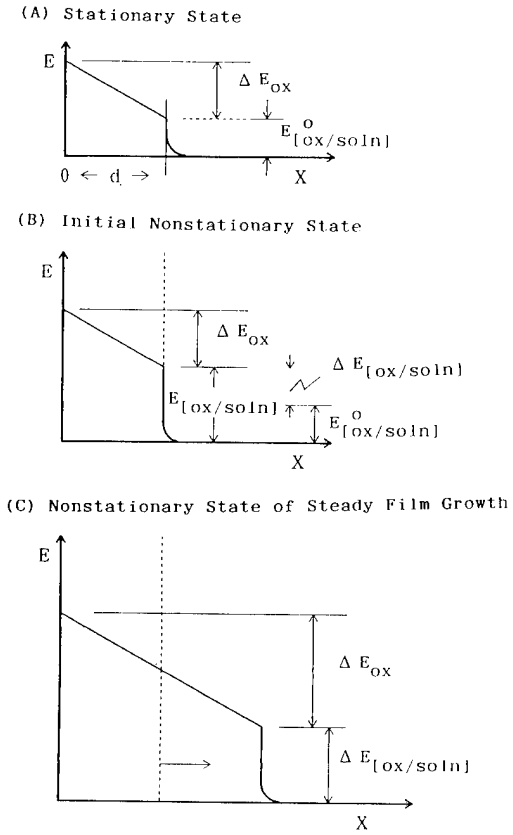

Fig. 8. Schematic representation of potential distribution under non-stationary state during potential sweep: (A) stationary state; (B) initial non-stationary state; (C) non-stationary state of steady film growth.

current $i_f + i_{diss}$ (Eq. (10)). Fig. 9 shows the relation between the thickness increase and the amount of charge passed with the sweep rate as a parameter. The lower value of dd/dQ corresponds to the lower

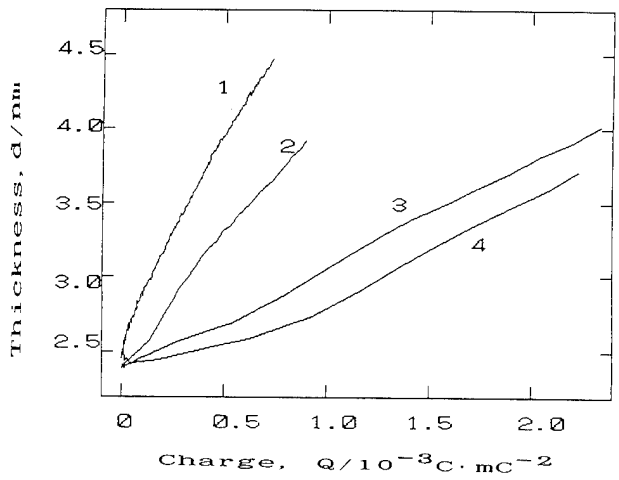

Fig. 9. Comparison between charge passed and thickness increase during potential sweep at various sweep rates; curve (1), 0.001; curve (2), 0.005; curve (3), 0.01; curve (4), 0.05 V s^{-1}.

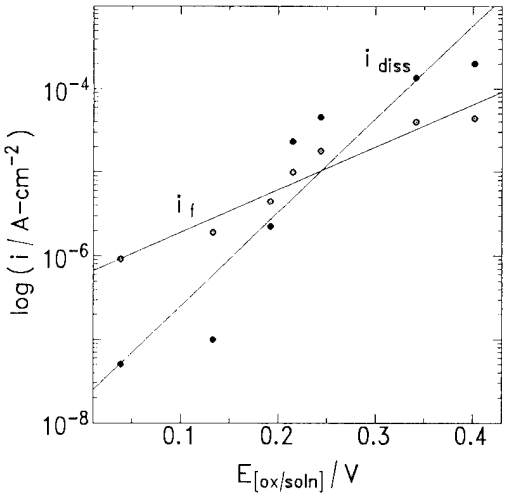

Fig. 10. Film formation current i_f and Fe^{3+} dissolution current i_{diss} vs. non-stationary potential difference $E_{[ox/soln]}$, at the film/solution interface at the steady film-growth stage during potential sweep.

efficiency of the film growth. It means that the ratio of $i_f/(i_f + i_{diss})$ becomes smaller with the higher sweep rate. Since at the sweep rate of 0.001 V s^{-1} the i_{diss} is considered to be much smaller than i_f, the film growth may take place at 100% efficiency; $i_f/(i_f + i_{diss}) = 1$. The ratio $i_f/(i_f + i_{diss})$ for the other sweep rates can be estimated from the comparison of dd/dQ obtained at various sweep rates with that at the sweep rate of 0.001 V s^{-1}. The value of i_f and i_{diss} can thus be derived from the ratio and the total current.

In Fig. 10 the calculated partial currents i_f and i_{diss} are plotted against the interfacial over-potential obtained at various sweep rates. The plots do not reveal a good linear relation: a tendency is, however, observed that both the partial currents increase with increase of the interfacial potential difference. When a linear relation is assumed in Fig. 10 for both the partial currents, the Tafel coefficients are calculated to be 0.20 V per decade for reaction (5) and 0.11 V per decade for reaction (6). If we assume that the transfer ion across the film/solution interface is univalent, the charge transfer coefficients are $\alpha_f = 0.33$ for reaction (5) and $\alpha_d = 0.54$ for reaction (6). The possible reaction schemes may be described as follows for the film formation of reaction (5),

$$H_2O_{[soln]} \rightarrow OH^-_{[ox]} + H^+_{[soln]} \quad (5a)$$

$$OH^-_{[ox]} \rightleftharpoons O^{2-}_{[ox]} + H^+_{[soln]} \quad (5b)$$

and for the Fe^{3+} dissolution of reaction (6):

$$Fe^{3+}_{[ox]} + 2H_2O \rightleftharpoons Fe(OH)^+_{2[ox]} + 2H^+_{[soln]} \quad (6a)$$

$$Fe(OH)^+_{2[ox]} \rightarrow Fe(OH)^+_{2[soln]} \quad (6b)$$

5.3. Electric field in the passive film

In the latter stage of the sweep measurement, a steady growth of the film is observed with the increase of potential. In this region the potential difference at the film/solution interface is assumed to be constant, and an additional applied potential is placed on the film. The linear thickness-to-potential relation in Fig. 5, therefore, reflects an electric field strength in the film during the steady growth in thickness under the constant current. The electric fields estimated from dE/dd for various sweep rates are given on the abscissa in Fig. 11, where the current during the steady growth in thickness is plotted against the field strength in the film. The current i corresponds to the ionic migration current, i_{2m} or i_{2p}, through the film according to Eq. (10). The plot indicates that the logarithm of the migration current increases with the electric field in the current region below 10^{-4} A cm^{-2}. At currents above 10^{-4} A cm^{-2}, the film composition and the growth mechanism may be changed, probably because the growth rate is too high to form a distinct oxide film. The relation between $\log(i)$ and dE/dd can be described by the following equation at currents below 10^{-4} A cm^{-2}.

$$\ln(i) = \ln(i_0) + D(dE/d(d)) \quad (15)$$

where $i_0 = 5.8 \times 10^{-23}$ A cm^{-2} and $D = 88$ nm V^{-1}.

The relation corresponds to Eq. (3) for the field-assisted ion migration mechanism, where i_0 is an exchange current under the zero field and D is a constant given by $D = zaF/RT$. The jumping distance calculated from $z = 3$ is $a = 2.2$ nm, which seems to be too large for the lattice of Fe_2O_3. Other mechanisms like place exchange may be included partially. In the place-exchange mechanism the electric field in the film is expected to be constant, not depending on the migration current.

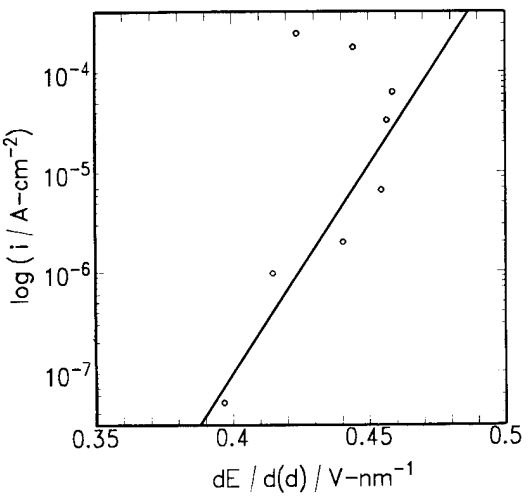

Fig. 11. Relationship between the electric field strength and the ionic current in the passive film at the steady film-growth stage during potential sweep.

6. Conclusion

The non-stationary growth of passive film on iron was investigated in a neutral borate solution by automated ellipsometry. The following conclusions may be drawn.

(1) The complex refractive index of the passive film under non-stationary condition is $N = 2.18 - 0.352j$ at 632.8 nm wavelength of light.

(2) The non-stationary film growth during a potential sweep from the stationary state at 0.0 V (vs. Ag–AgCl) to the higher potentials can be divided into two stages. In the initial stage the current increases gradually with increase of potential, while the film thickness remains constant. In the latter stage the current remains almost constant, whereas the film thickness increases linearly with increase of potential. This behavior can be explained from the distribution of increasing applied potential; the increasing applied potential is initially placed at the film/solution interface and in the latter stage appears in the film.

(3) The thickness increase and current variation during the potential sweep strongly depend on the potential sweep rate. From estimation of the non-stationary potential differences in the film and at the film/solution interface, the growth mechanism of the film and the interfacial reactions were discussed.

References

[1] N. Sato and M. Cohen, *J. Electrochem. Soc.*, *111* (1964) 512.
[2] R.V. Mostev, *Ber. Bunsenges. Phys. Chem.*, *71* (1967) 1079.
[3] K.J. Vetter and F. Gorn, *Electrochim. Acta*, *18* (1973) 321; *Werkst. u. Korrosion*, *21* (1973) 703.
[4] K.E. Heusler, *Ber. Bunsenges. Phys. Chem.*, *72* (1968) 1197.
[5] R. Kirchheim, *Electrochim. Acta*, *32* (1987) 1619.
[6] N. Sato and T. Noda, *Z. Phys. Chem., N.F.*, *98* (1975) 271; *Electrochim. Acta*, *22* (1977) 839.
[7] C.-T. Chen and B.D. Cahan, *J. Electrochem. Soc.*, *129* (1982) 17.
[8] Y.-T. Chin and B.D. Cahan, *J. Electrochem. Soc.*, *139* (1992) 2432.
[9] Z. Scklarska-Smialowska and W. Kozolowski, *J. Electrochem. Soc.*, *131* (1984) 234.
[10] F.C. Ho and J.L. Ord, *J. Electrochem. Soc.*, *119* (1972) 139.
[11] J.L. Ord and D.J. DeSmet, *J. Electrochem. Soc.*, *123* (1976) 1876.
[12] J.L. Ord, in M. Froment (ed.), *Passivity of Metals and Semiconductors*, Elsevier, Amsterdam, 1983, p. 95.
[13] T. Ohtsuka, K. Azumi and N. Sato, in M. Froment (ed.), *Passivity of Metals and Semiconductors*, Elsevier, Amsterdam, 1983, p. 79.
[14] K. Azumi, T. Ohtsuka and N. Sato, *Denki Kagaku* (J. Electrochem. Soc. Jpn.), *53* (1985) 306.
[15] T. Ohtsuka, *Denki Kagaku* (J. Electrochem. Soc. Jpn.), *60* (1992) 1123.

ELSEVIER

Materials Science and Engineering A198 (1995) 177–196

MATERIALS SCIENCE & ENGINEERING A

Microvisualization of corrosion

J.P.H. Sukamto, W.H. Smyrl, N. Casillas, M. Al-Odan, P. James, W. Jin, L. Douglas

Corrosion Research Center, Department of Chemical Engineering and Materials Science, University of Minnesota, Minneapolis, MN 55455, USA

Abstract

Localized corrosion continues to be a major cause of degradation failure in a wide variety of technological applications. The propagation stage of failure is no longer a fundamentally difficult job to characterize for pits and stress corrosion cracks, for example. It is the initiation stage that remains difficult to characterize, arising in part because of the difficulty in being able to predict where and when localized attack will occur. Recent developments in scanned probe techniques have created renewed interest in this problem. The present paper will describe some of the recent advances in optical, electrochemical and photoelectrochemical techniques that are directed at providing local information on precursor sites and vulnerable areas on metal and semiconductor surfaces.

Keywords: Corrosion; Degradation failure; Pitting precursor sites

1. Introduction

Corrosion processes have a major financial impact on many industries. Because of this, the detection of corrosion for preventive purposes and new methods for studying the corrosion process are of great practical interest. While corrosion can be a problem for any material, the major focus here is on the corrosion of metals. It is the degradation in physical properties, such as strength and brittleness, that makes corrosion such an important problem.

Here we will discuss experimental techniques that have been used in our laboratory (1) to measure the corrosion rate, (2) to locate breakdown sites and (3) to study the fundamental properties of passive films and how they are related to the stability of the films in aggressive environments. The last is of particular interest since it will allow us to predict vulnerable spots in passive films. It should be noted that this review does not include discussion of all experimental techniques that have been used in the study of corrosion processes, such as thermal wave microscopy [1,2], microellipsometry [3–6], fluorescence microscopy [7,8], differential reflectometry [9], photoacoustic spectroscopy [10] and others.

Corrosion usually occurs locally and non-uniformly as illustrated in Fig. 1. Hence experimental methods that can measure local corrosion rates accurately are just as important as those that can locate the corroding sites. In locating corrosion sites, an entire region of the corroding surface is imaged simultaneously (Fig. 2(a)) or point by point using a scanned probe or beam (Fig. 2(b)). Both classes of experimental techniques will be discussed below. In particular, the following will be described: (1) the quartz crystal microbalance (QCM), (2) optical fiber micromirrors, (3) the phase detection interferometric microscope (PDIM), (4) the confocal laser-scanning microscope (CLSM), (5) the photoelectrochemical microscope (PEM) and surface PEM (s-PEM), (6) the scanning electrochemical microscope (SECM) and (7) the scanning photoelectrochemical and electrochemical microscope (SPECM). The QCM and optical fiber micromirrors have been used to measure

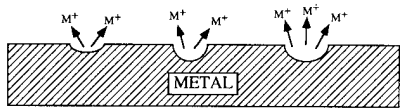

Corrosion is Often Distributed NonUniformly

- Rate is determined by
  - — Nature of aggressive environment
  - — Nature of metal
  - — Geometry
  - — Concentration effects (convection, diffusion, and mass transfer)
- Location is controlled by
  - — Flaws in oxide films
  - — Electronic defects in oxide films
  - — Crystallographic orientation of the substrate surface
  - — Adsorption of solution species

CHARACTERIZATION OF THE LOCAL RATE AND SIZE OF THE REGION OF ATTACK IS DESIRED

Fig. 1. Schematic of a corroding surface showing the localized nature of corrosion processes.

SSDI 0921-5093(94)04523-2

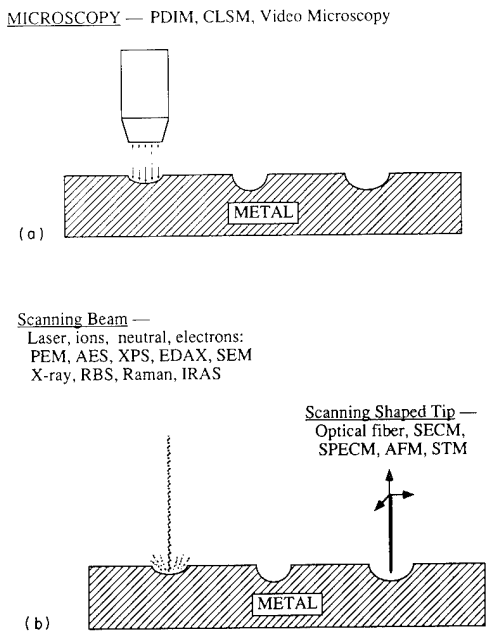

Fig. 2. General schematics of experimental methods useful in the study of localized corrosion: (a) conventional microscopy where an entire region is imaged simultaneously; (b) point-by-point imaging using a scanning probe or beam.

corrosion rates, while the PDIM has been used to measure local corrosion rates as well as to locate corrosion sites. Similarly to the PDIM, the CLSM can be used to locate and measure the corrosion at local sites, but in addition the CLSM can be used to obtain fundamental properties of the protective passive film. The PEM and s-PEM differ from the CLSM only in the data collection rate. Both the PEM and s-PEM are much slower than the CLSM but are simpler to implement, especially in systems where the photoresponse is very low. The SECM has been used to locate precursor sites *prior* to actual breakdown. The experimental set-up for each of the techniques listed above will be described below along with examples.

2. Quartz crystal microbalance

One of the oldest techniques used in corrosion studies is that of mass measurement of the corroding material. However, a modern version features the continuous measurement of very small changes in mass in situ using the QCM. Quartz and other piezoelectric materials may be used as mass sensors. Several different devices have been developed for the studies, including the quartz crystal microbalance (QCM), surface acoustic wave (SAW) devices, plate mode sensors and Lamb wave oscillators. In each case an increase in mass loading on the crystal leads to a decrease in the characteristic frequency of vibration of the crystal oscillator or a change in propagation velocity of surface elastic

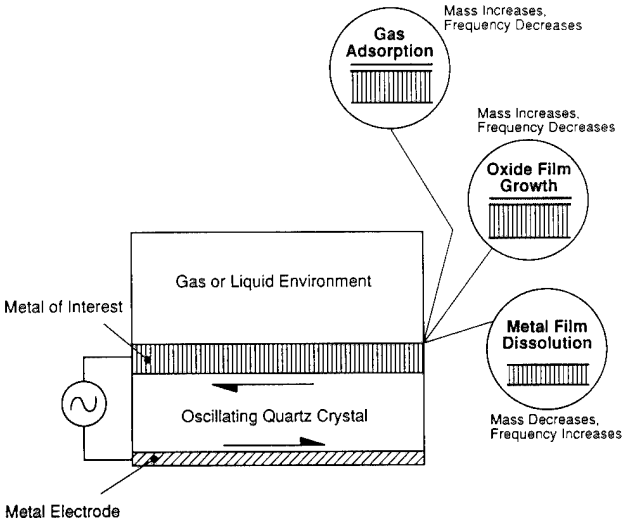

Fig. 3. Schematic of the QCM. Metal films deposited on both sides of the quartz crystal make it ready for use as an oscillator and mass sensor. The piezoelectric area is in the center where the two metal films overlap and face each other across the thin quartz membrane. Exposure of one (or both) of the metal films to an aggressive environment leads to chemical interactions and mass changes, which change the resonant frequency of the quartz.

waves on the piezoelectric substrate material. The relationship between the change in mass and the associated change in frequency (or velocity of propagation) is linear over a fairly wide range of operation. This, coupled with the low cost and high mass sensitivity, makes the gravimetric sensors quite attractive for a wide range of applications in corrosion sensing. The operational simplicity of the QCM is illustrated in Fig. 3. The sensitivity of a QCM operating at 6 MHz, for example, is $1.221 \times 10^{-8}\,g\,cm^{-2}\,Hz^{-1}$. The frequency can be determined to at least 0.1 Hz and thus the sensitivity corresponds to changes of less than one atomic layer on the surface. In addition to the advantages offered by the sensitivity, one may make direct and continuous mass change measurements in stagnant or flowing gas and liquid streams. The latter measurements demonstrate that the monitors are potentially useful for practical applications as well as for basic studies. Even though the QCM was first proposed for corrosion studies in 1966, the application was not widely used for that purpose until recently. QCM, SAW and plate mode devices have all been used in these studies and the first has been used for liquid phase corrosion studies especially [11]. Experimental results obtained using the QCM will be discussed below in conjunction with data taken using the phase detection interferometric microscope.

3. Optical fiber micromirror sensors

Optical fibers offer a number of advantages for chemical sensing: long-distance telemetry, freedom from elec-

tromagnetic interference and small size (approximately that of a human hair). Furthermore, the basic components necessary for sensor applications are being developed by the optical communications industry. Optical communications systems and optical sensors have the same functional design. Both need a light source, a detector and a method of transmitting the light from the source to the detector (the optical fiber). For optical communications a modulator is used to impose the information to be transmitted on the light beam. For optical sensing the sensing element replaces the modulator and again imposes information on the light beam. The similarity between these two functions means that the components developed at great cost for optical communications can be used for optical sensing applications. One of these applications is in localized corrosion.

A requirement for the study of localized corrosion is a sensor small enough to access the microenvironment in which the corrosion process occurs. Optical fibers with small diameter (typically 50 μm core and 125 μm cladding diameters) offer the opportunity to study sample volumes as small as 1000 μm^3. Thus they offer access to crevices and cracks that cannot be examined using conventional sensors. One simple method of optical fiber sensing is the "micromirror" sensor, which measures changes in the reflectivity of chemically sensitive coatings at the end of the optical fiber [12–14]. Interactions between various chemical species and optically thin metal films produce reflectivity changes large enough that detection of a submonolayer change in the thickness of a metal film is possible. In this case there is a small perturbation in the metal film thickness as a corrosion product is formed on the other surface. Alternatively, one may follow the total removal of the metal film in (liquid) environments where the corrosion products are soluble. Both kinds of studies have been discussed in the literature [12–15].

4. Phase detection interferometric microscope

The phase detection interferometric microscope (ZYGO MAXIM 3D Laser Interferometric Microscope) measures vertical heights over a moderately large surface area using the technique of optical measurement interferometry. This technique is similar to but considerably more accurate, rapid and powerful than traditional visual detection of the curvature of interference fringes resulting from light reflected from a textured surface. The vertical resolution of the microscope is limited primarily by stray vibrations and specified by the manufacturer to be 0.6 nm. In our laboratory we routinely measure calibrated vertical steps on metal films as small as 4 nm. A major drawback of the PDIM is its inability to image features with height differences exceeding $\lambda/4$, or approximately 150 nm if the 632.8 nm line of an He–Ne laser is used.

A schematic diagram of the key components of the instrument is shown in Fig. 4 [73]. Essentially, the PDIM consists of a Fizeau interferometer attached beneath the objective of an optical microscope. Light emitted by a 1 mW He–Ne laser passes through a rotating disk diffuser, reflects off a polarizing beam splitter and is recollimated by the microscope objective. The light passes through a quarter-wavelength retardation plate and illuminates the test surface. The bottom of the retardation plate is coated with a partially reflecting film that acts as the reference surface and the beam splitter for the interferometric analysis. Reflected light from the electrode and reference surface interferes and the resulting spatially resolved intensities are recorded on a 244 × 388 pixel charge injection device (CID) array camera. The digitized output from the CID camera is analyzed to produce a phase map representing the relative differences in height between the reference and test surfaces. A video monitor connected to the array camera provides a direct optical image of the sample.

Several types of data can be extracted from the images provided by the PDIM software. Figs. 5(a) and 5(b) show typical images taken by the PDIM of a copper polycrystalline sample. Fig. 5(a) gives a three-dimensional image of the surface profile of the sample in the area of view. The image is shown as a grey scale map that represents the relative heights of the surface. Fig. 5(b) shows a single line of the surface profile between two points on the surface (for the same area viewed in Fig. 5(a)). The latter optical profilometer mode provides a local map of the topography between the two points. The images were analyzed to provide the RMS surface roughness, which is the RMS deviation from the average or mean plane of the actual surface. The difference between the maximum peak and the minimum valley in the image is identified as P–V. Because of the short time required to obtain an image (on the order of 1–2 s per image), it is possible to study surface evolution by taking "snapshots" at consecutive time intervals.

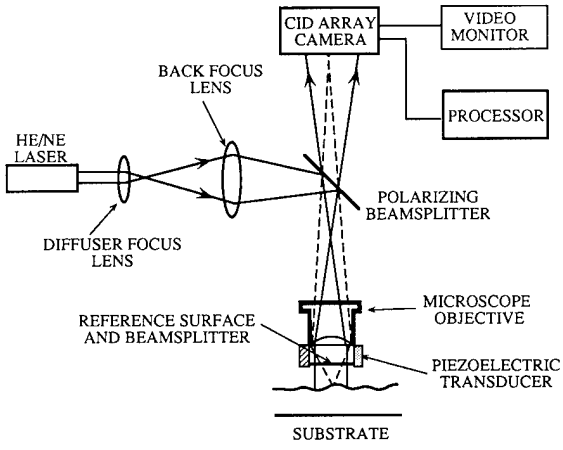

Fig. 4. Simplified description of the PDIM.

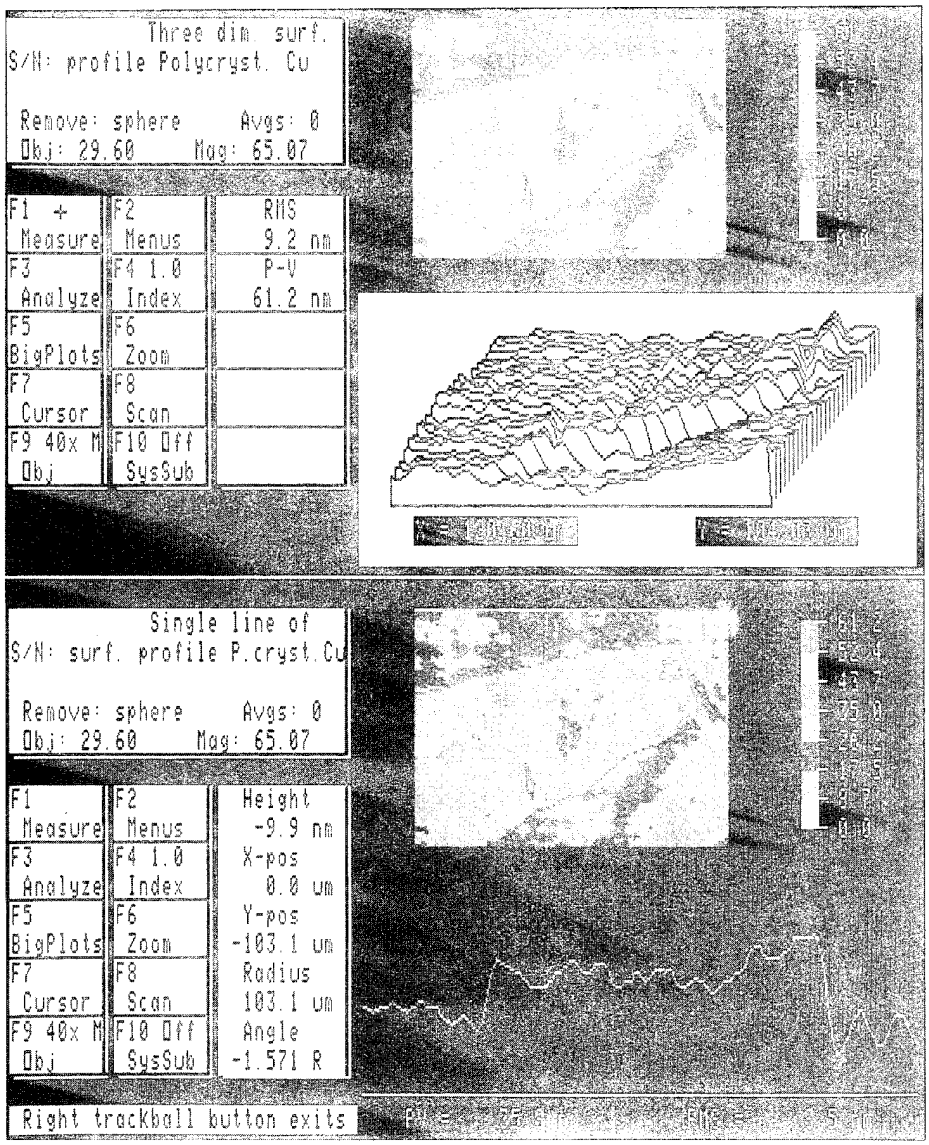

Fig. 5. PDIM images of a polycrystalline Cu surface: (a) 3D rendered image; (b) profile of a line within the same area shown in (a).

The PDIM has been used in situ simultaneously with electrochemical measurements to reveal surface roughness changes upon dissolution of a copper film deposited on quartz. The experiments were carried out using a custom-built flow cell (see Fig. 6) that allowed various solutions to be used without moving the sample. Faceting during the dissolution of polycrystalline Cu substrates has been studied. Copper samples with grain sizes of about 50 μm were used. The samples were etched by two different solutions: (1) 5 mM H_2O_2 and 0.1 N HCl (solution A) and (2) 10 mM H_2O_2 and 0.1 N H_2SO_4 (solution B). Solution A was circulated first through the cell then followed by solution B to separate the effects of the different kinds of acids and H_2O_2 on the corrosion rates of different grains. Fig. 7(a) shows the Cu surface prior to the introduction of any etching solution. The surface is relatively smooth, with a 4.1 nm RMS and a 43.3 nm P–V. The surface profile of the same area after 316 s of etching solution A is shown in Fig. 7(b). It can be seen that certain grains were attacked faster than others. Solution A was then flushed out and replaced by solution B. After 250 s in solution B another image was taken and the result is shown in Fig. 7(c). Comparison of Figs. 7(b) and 7(c) shows that solutions A and B attack the Cu in the same way, i.e. the grains that corroded faster in solution A also corroded faster in solution B. Since the only difference between solutions A and B was the type of acid used, one may conclude that it was H_2O_2 that was responsible for the preferential etching of Cu. The profile at the middle of the three grains shown in Fig. 7(c) is shown in Fig. 7(d). The profile indicates the relative heights of the different grain orientations; that is, it represents the difference in the corrosion rates of the different grain orientations. In order to determine the absolute difference in heights of the different grains, the Cu surface

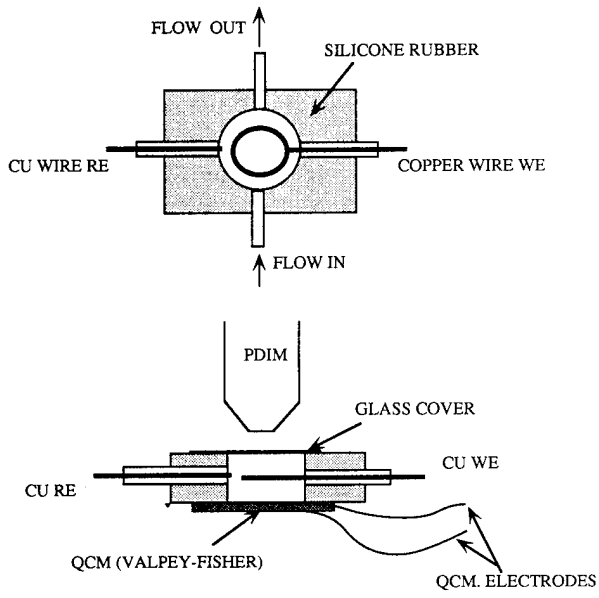

Fig. 6. Schematic of the flow cell used for the Cu corrosion studies.

was half masked and immersed in solution B for 20 min. The result is shown in Fig. 8. It can be seen that the difference in the height of the masked (i.e. unexposed) and the exposed (but non-corroded) grain is small, at least during the time scale of the experiment. It should be noted that the same result was found when solution A was used. Hence the P–V (and RMS) data can be used as a qualitative indication of the corrosion rate of the attacked grains. In Fig. 9 the RMS and P–V changes with time are shown over the whole area as viewed by the PDIM. The Cu was etched in solution A for 400 s, followed by solution B. The slopes of the two lines in Fig. 9 indicate the rates of corrosion. It can be seen that the corrosion rate of Cu is more rapid in the HCl solution than in the H_2SO_4 solution. The corrosion rates can be calculated from Fig. 9 by noting that the P–V values represent the decrease in thickness of the faster-corroding grain. In solution B the corrosion rate is 0.13 nm s^{-1} and in solution A it is 0.213 nm s^{-1}; these data agree well with previously reported results [16,17].

In order to monitor both the instantaneous mass decrease and morphological changes of Cu due to corrosion, the QCM was used in conjunction with the PDIM. A relatively thick copper film (1000 nm) was deposited on a Valpey Fisher quartz crystal, which was then corroded in solution B. The increase in the crystal frequency due to dissolution of the Cu film is shown in Fig. 10. The corrosion rate can be calculated from the slope of the line in Fig. 10. An image of the corroding Cu surface was taken every 3 min by the PDIM and some of the results are shown in Figs. 11(a) and 11(b). An image of the Cu surface prior to exposure to the corroding solution is given in Fig. 11(a), which shows a 1.7 nm RMS roughness and a 52.5 nm P–V. After 824 s the Cu became rougher as shown in Fig. 11(b). The RMS roughness and P–V data were collected with each image taken. The RMS and P–V values as a function of time are shown in Fig. 12. As discussed above, the corrosion rate can be obtained from either the slope of the line in Fig. 10 or from the slope of the lines in Fig. 12. From Fig. 10 the corrosion rate is found to be 0.13 nm s^{-1}, while from Fig. 12 it is found to be 0.096 nm s^{-1}. The corrosion rates determined by the two independent methods agree well.

5. Confocal laser-scanning microscope

The application of the CLSM in corrosion studies spans all three topics mentioned in Section 1. It can be used (1) to measure the rate of corrosion, (2) to locate the breakdown sites and (3) to study the fundamental properties of passive films (such as the optical and electronic properties) and their relationship to the stability of the films. A schematic diagram of a CLSM is shown in Fig. 13 [74]. In contrast with a conventional microscope where all parts of an object within the field of view are imaged simultaneously, the same image is obtained sequentially using a CLSM. In a CLSM an image is obtained point by point, whereby only a small part of the object is illuminated. There are a number of significant advantages in using a CLSM, e.g. the image is stored digitally and thus can be readily subjected to image processing and image enhancement. More importantly, the use of a focused light source in conjunction with a pinhole aperture in front of the detector (see Fig. 13) allows for a higher lateral and depth resolution than with a conventional optical microscope. The improved lateral resolution results from elimination of the interference of light originating from different points on the object. The main advantage of a CLSM, however, is not in the increased lateral resolution, but rather in its ability to perform "optical slicing". Fig. 14 shows that light originating from planes other than the focal plane is blocked by the pinhole aperture placed in front of the detector. Typical lateral and depth resolutions for a 60 × objective lens with a numerical aperture of 1.4 are 0.17 and 0.54 μm respectively [18,19]. The requirement of the CLSM that one must scan either the sample or light source can be a serious disadvantage. For instance, the time required to obtain an image using a CLSM is longer than that required when using a conventional microscope. Scanning the stage, where the sample is placed, has the advantage of simplifying the optical system; however, this method is inherently slow. The other option of scanning the beam over a stationary sample is much faster, but it also complicates the required optical system. There are a number of scanning beam set-ups: (1) vibrating galvanometer-type mirrors, (2) rotating mirror wheels and (3) acousto-optic beam deflectors [18]. We

will discuss data collected using a CLSM equipped with galvanometer-type mirrors.

To demonstrate the optical slicing capability of a CLSM, we have imaged a polycrystalline Cu substrate which has been etched preferentially with a solution of a deaerated 0.1 M H_2SO_4 and 0.1 M H_2O_2 for 30 min. A series of optical slices was obtained where an individual slice (section scan) represents a plane of focus and the series of section scans was combined to form a 3D image. A section scan of an etched polycrystalline Cu sample is shown in Fig. 15. The 514.5 nm line of an Ar^+ ion laser was used with a 60×/oil objective lens. The brighter regions represent reflective areas within the plane of focus, i.e. surfaces. It should be noted that in imaging some samples within a volume, it is possible for apparent "surfaces" to be seen owing to changes in the optical properties within the volume. This is not true for Cu, since the penetration depth of 514.5 nm light is 15.7 nm, which is much smaller than the depth resolution of the CLSM. The combined section scan, from which a 3D image was obtained, is shown in Fig. 16 as a fish-net plot of the etched Cu surface. This figure was obtained by depth coding the section series; that is, the maximum intensity along the Z axis for each point in the $X-Y$ plane was determined and the Z position was then converted to intensity. Another way to view the data is shown in Fig. 17, where a section scan is shown along with an $X-Z$ slice and a $Y-Z$ slice which show the surface profile viewed from two perpendicular directions. In the latter mode the CLSM becomes a non-contact optical

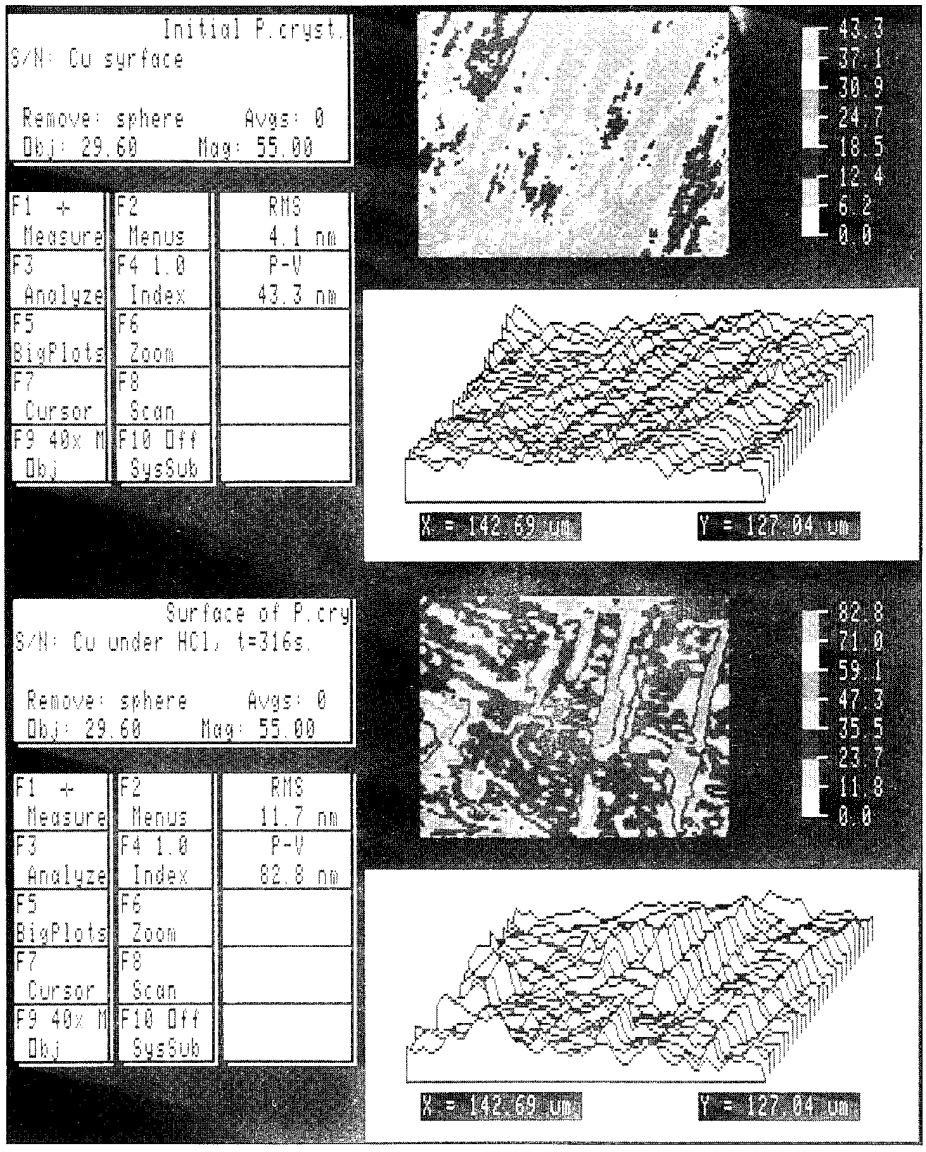

Fig. 7(a–b).

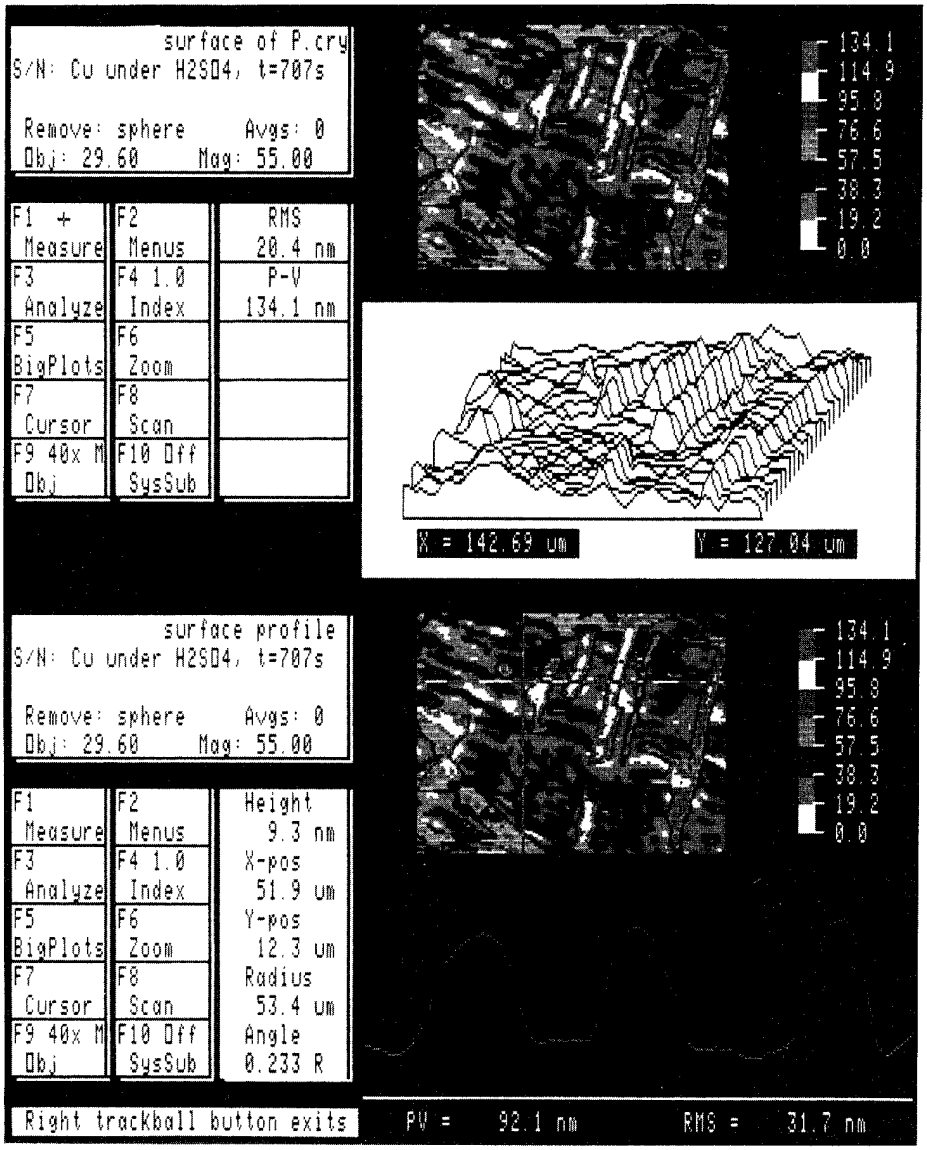

Fig. 7(c–d).

Fig. 7. (a) Phase map of the initial Cu surface. (b) Same surface as in (a) after 316 s under 4 mM H_2O_2 and 0.1 N HCl. (c) Same as (a) and (b) after an additional 250 s in 10 mM H_2O_2 and 0.1 N H_2SO_4. (d) Line profile (cross-section of (c)).

profilometer. In addition to the images shown above, the CLSM software can also provide 3D projections of the series of sections. This allows visualization of the inside of objects, e.g. the pores of porous materials. Since the reflected light intensity is dependent on the optical properties of the medium(s) traversed by the incident beam, it also contains information regarding the composition of the medium(s) which directly affects the optical properties. This can be used to image reactant–product layers on corroding surfaces, which is similar to the use of the PDIM for refractive index mapping of concentration profiles [20]. There are, however, some differences. As mentioned earlier, the height–depth resolution of the PDIM is better than for the CLSM. An advantage of the CLSM is that the measured intensity can be correlated directly with the vertical position. It is still necessary, however, to deconvolute the data to account for non-uniformity in the composition of the corrosion layers. Finally, there are a host of 3D data-filtering routines that are usually included in the CLSM software or that can be obtained from other vendors.

The optical technique described above examines and/or monitors the corrosion rate by measuring topographical changes of the top surface, i.e. the surface in contact with the environment; in particular, topographical changes are determined from changes in the light

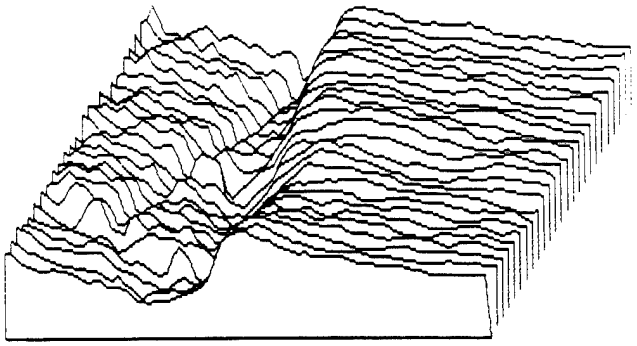

Fig. 8. Phase map of a half-masked (the right side) Cu surface showing the absolute difference between grains.

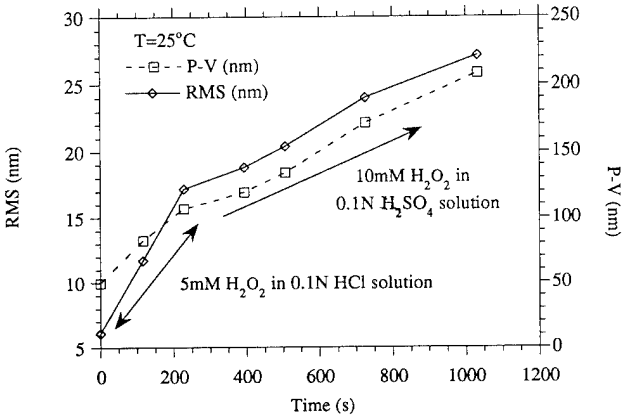

Fig. 9. RMS and P–V changes during the corrosion of a polycrystalline Cu substrate in 5 mM H_2O_2 and 0.1 N HCl. A solution of 10 mM H_2O_2 and 0.1 N H_2SO_4 was introduced after 400 s.

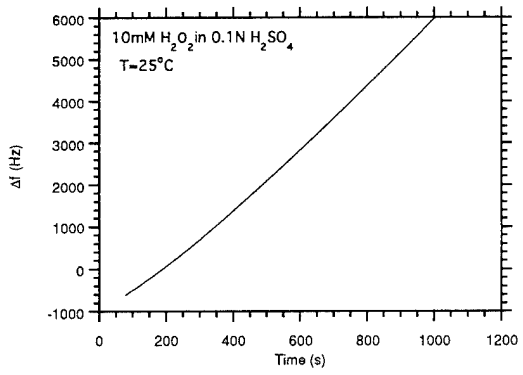

Fig. 10. Resonant frequency changes (Δf) of the QCM plated with Cu during the corrosion of the Cu electrode in a solution of 10 mM H_2O_2 and 0.1 N H_2SO_4.

reflected from an incident light coming from the top. Relative etching or corrosion rates are obtained directly; these can be converted to absolute rates if one part of the surface is masked off.

6. Photoelectrochemical microscopy (PEM) and surface PEM

Thus far, with the exception of the CLSM, we have only discussed techniques that are used (1) to monitor and/or measure the corrosion rate and (2) to locate the corroding sites. Of greater or equal importance are techniques that can be used to locate sites that are susceptible to localized corrosion *prior* to breakdown. The susceptibility of metals to localized corrosion invariably depends on the local properties of the protective passive films in addition to the local environment. Of particular interest are the structural, electronic and optical properties. Structural defects such as dislocations or surface steps are important since they are very susceptible breakdown sites, but a full discussion of their importance is outside the scope of the present paper. Here discussion will be limited to the optical and electronic properties of passive films. From the various experimental techniques available for the study of the electronic and optical properties of passive films, e.g. ellipsometry [3–6,21], differential reflectometry [9] and electroreflectance [22], we will focus on photoelectrochemical techniques.

Photoelectrochemical techniques were used to study the bulk optical and electronic properties of semiconductor materials, including oxides [23–29], as well as to investigate processes at interfaces with electrolytes and metals. Such studies have led to the development of several general principles for predicting the stability of metal oxides against corrosion and photocorrosion, which involve correlations with the location of the band edges with respect to the redox levels for decomposition and levels of competing redox reaction, especially the solvent [30–32]. For example, if the position of the conduction band edge lies above the energy of the redox level for reductive decomposition, the metal oxide is unstable with respect to reduction. Said another way, the reductive decomposition and dissolution (in the dark) of metal oxides are highest in electrolytes whose redox energy level is near and below the energy of the condution band (cf. the decomposition of manganese oxide materials [33]). Likewise, the stability of the metal oxide with respect to oxidative degradation is determined by the relative positions of the valence band edge and oxidative decomposition reactions. One can cite in the latter case the corrosion of etching of low band gap materials such as Si and GaAs in aqueous solution. For a wide band gap metal oxide such as TiO_2, single crystals of the material are stable in aqueous solutions both in the dark and under illumination, except under extreme pH conditions and in halide solution. Nevertheless, even for such stable metal oxides, photoelectrochemical methods are useful for determining barrier heights, flat-band potentials and band gaps, as well as properties that are influenced by surface

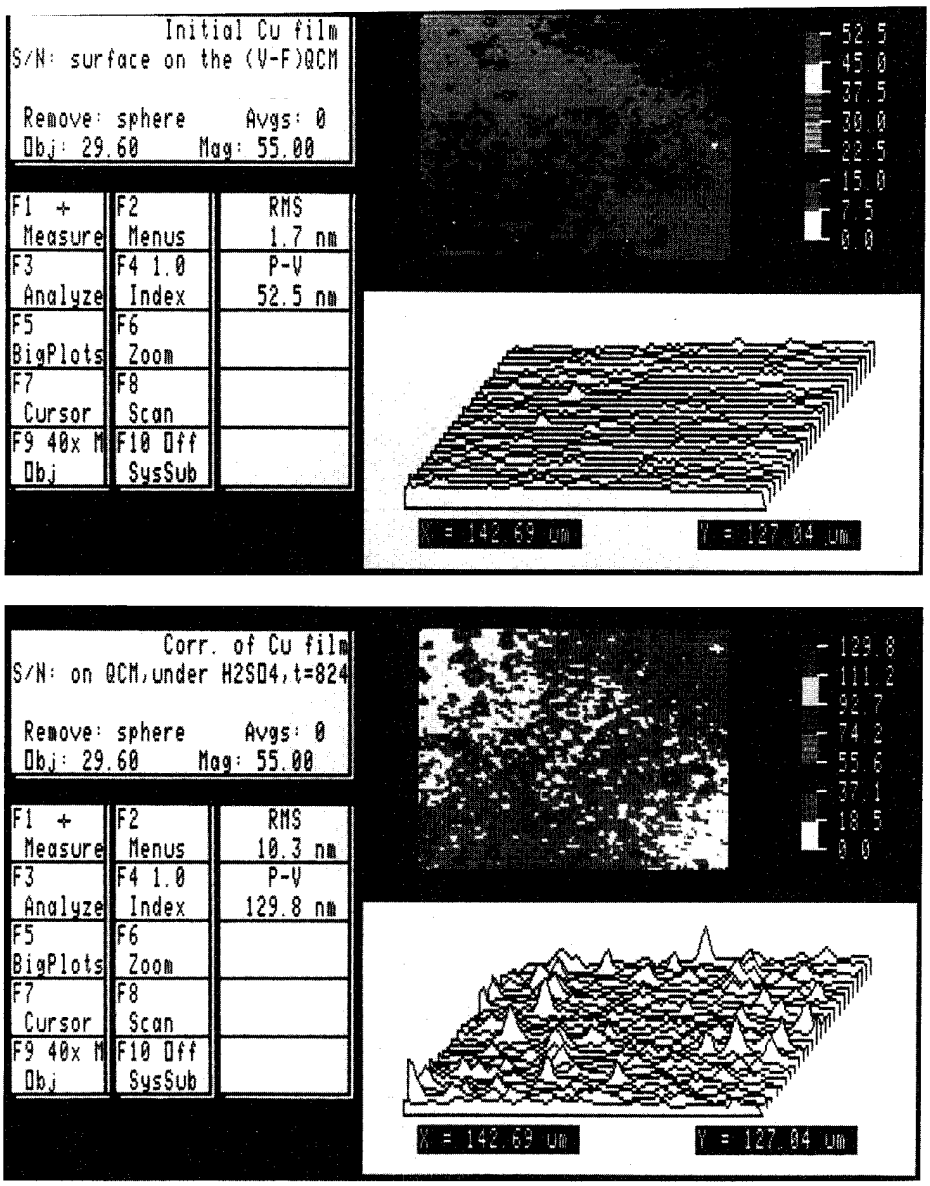

Fig. 11. (a) Phase map of the evaporated Cu film on the quartz crystal of the QCM prior to any corrosion. (b) Phase map of the same area as in (a) after corrosion in a solution of 10 mM H_2O_2 and 0.1 N H_2SO_4 for 824 s.

orientation, crystal imperfections and surface states on heterogeneous surfaces. In addition to the space charge effect at the surface of TiO_2 films (n type) which gives rise to anodic photocurrent when light above the band gap is absorbed, we are interested in surface recombination effects that may map crystal imperfections and structural defects at the surface.

Point defects in the bulk crystal lattice of metal oxides, specifically oxygen vacancies, have been found to serve as donor species and to provide sites for chemisorption and surface states at the interface with aqueous solutions or humid environments [26]. Bulk impurities or defects in semiconductors may give rise to electronic states in the band gap which will interact with light in several ways. For large band gap metal oxides such as TiO_2, recombination of electron–hole pairs in the bulk occurs predominantly through energy levels within the band gap. The extent or rate of recombination increases as (i) the depletion layer electric field decreases, (ii) the density of recombination states increases and (iii) the energy levels of the states approach the center of the band gap. When recombination effects are small, the photocurrent increases with decreasing donor density.

Defects in the bulk may also act as traps for charge carriers. This will alter the charge distribution in the depletion layer and will affect the electric field strength and the depletion layer width. Mechanically formed defects in ZnO, for example, have been shown to act as hole traps and recombination centers [34]. In some

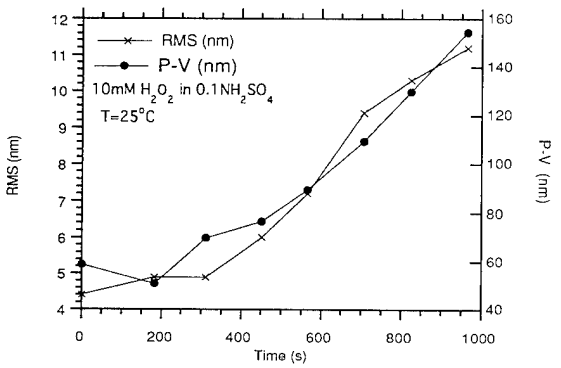

Fig. 12. RMS and P–V changes during the corrosion of a Cu film deposited on a quartz crystal for the QCM exposed to a solution of 10 mM H_2O_2 and 0.1 N H_2SO_4.

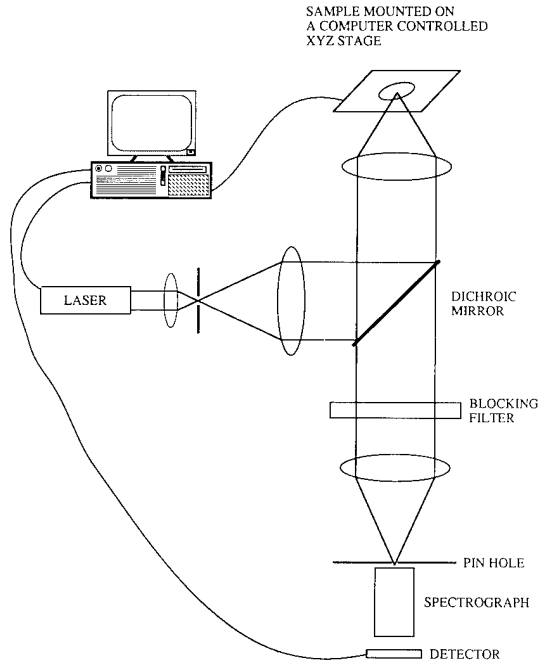

Fig. 13. Simplified description of the CLSM showing the essential parts.

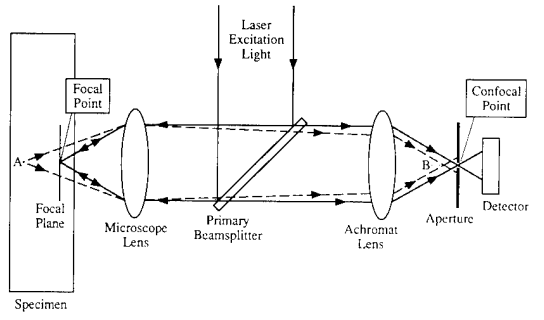

Fig. 14. Schematic showing the depth discrimination capability of the CLSM. Light not originating from the focal plane, e.g. point A within the sample, will come to a focus away from the aperture, e.g. point B, and thus will be blocked by the aperture.

Fig. 15. Section scan of an etched polycrystalline substrate. The brighter regions are regions that are relatively closer to the focal plane.

cases the presence of defect states in the band gap can be detected by measuring the photocurrent produced by subband gap illumination. For TiO_2 and $SrTiO_3$, for example, Butler et al. [35] observed a subband gap response which was related to bulk defect states.

The qualitative description of the photocurrent generated on polycrystalline and single-crystal samples is similar. For example, high fields may be applied across

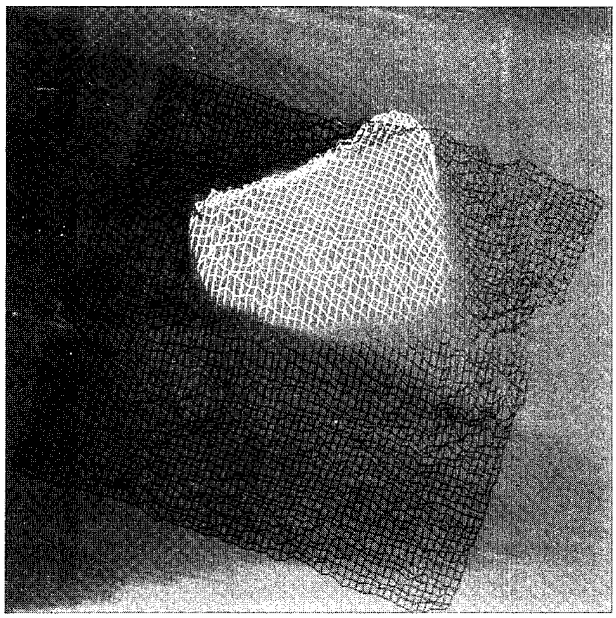

Fig. 16. A fish-net plot showing the topography of an etched polycrystalline Cu substrate generated from a 3D data set. Color representation significantly enhances the fish-net image, shown here in grey scale only.

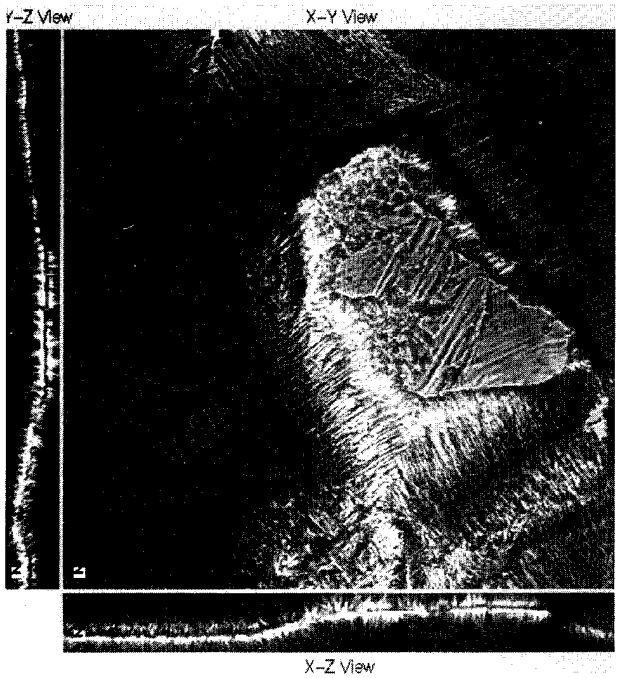

Fig. 17. Section scan of an etched polycrystalline Cu substrate along with two profile slices.

a relatively narrow region just inside the surface of an n-type semiconductor at the semiconductor–electrolyte junction, producing a depletion layer devoid of carriers of either sign. Optical excitation with light of energy larger than the band gap leads to the formation of electrons and holes that are separated by the high field, with holes migrating to the surface where they may react with solution species to give a photocurrent. Additional contributions to the photocurrent may come from diffusive transport of holes from the quasi-neutral region beyond the depletion layer and back diffusion of electrons generated within the depletion layer. Optical excitation of a sample by a rastered, focused laser beam across the surface will cause the resulting photocurrent to be a function only of the properties that are local to the irradiating light. Hence variation in the local photoresponse strongly suggests heterogeneity in the sample under study. Hereafter this technique will be referred to as photoelectrochemical microscopy (PEM).

In the study of thin metal oxide films, in situ photoelectrochemical techniques are particularly convenient, because the films may be studied in the presence of an aggressive environment. In the general case the interface between a metal oxide film and an electrolyte will behave as a Schottky junction. The photoresponse of semiconducting and insulating thin metal oxide films is very similar to that of bulk materials. However, surface effects such as surface recombination processes are more pronounced in thin films than in bulk materials, because the former are more defective. Effects of multiple internal reflections also become more significant in thin films and the resulting interference will cause the photoresponse to depend on the film thickness [36–38].

In the present section, discussion will be restricted to thin n-type metal oxide films where surface effects at the metal oxide–electrolyte interface dominate the photocurrent and this will be illustrated by the behavior of thin TiO_2 films grown on Ti. The importance of the metal oxide–electrolyte interface is revealed by separating the photoresponse of the surface from that of the bulk. This is accomplished by a technique complementary to PEM which sensitizes the surface to subband gap illumination so that the surface characteristics of the oxide may be probed laterally; this technique is termed surface PEM (s-PEM) [39,40]. Polycrystalline Ti has been used as the substrate for this technique to afford a range of film properties on each substrate, since the grain orientation (of Ti) has been found to influence the photoresponse. We seek to reveal the influence of the substrate metal on the oxide surface for thin films which are formed in a slow growth mode (SGM) to emphasize epitaxial effects. These SGM films, when grown on polycrystalline Ti substrates, have a non-uniform photoresponse which is caused by heterogeneity at the metal oxide–electrolyte interface.

In previous studies of SGM anodic TiO_2 films we have found the photocurrent to be uniform for films on single-crystal Ti substrates and uniform over single grains of polycrystalline substrate. However, in the latter case the photocurrent varies in the film from Ti grain to Ti grain, which are much larger than the grain size of the oxide film. The mapping of the substrate implies an influence of substrate factors (e.g. grain orientation, disorder, defect density and pretreatment) on the growth of the metal oxide film. Furthermore, the metal oxide is crystalline and partially ordered over some orientations of Ti [41,42]. The metal oxide grown in the transition zone over substrate metal grain boundaries is highly disordered and does not change properties smoothly from one grain to another.

The onset of anodic photocurrent on such film occurs nearly at the same potential, but the onset of the photocurrent on grains showing higher photocurrent is more negative than the onset on grains showing lower photocurrent. The latter opposes the argument that the photocurrent differrence can be ascribed to changes in depletion layer thickness brought about by changes in the doping density. Furthermore, the onset potentials are nearly the same on different titanium grains, which suggests that the flat-band potential is nearly the same [38]. A constant flat-band potential will cause the band bending at a given applied potential to be the same on those grains. This is especially true far away from flat band. Taken together, these arguments suggest that surface effects are responsible for the grain-to-grain photoresponse of the films.

Wilson [23] has argued that surface electronic states are needed in TiO_2 in order to account for the highly efficient

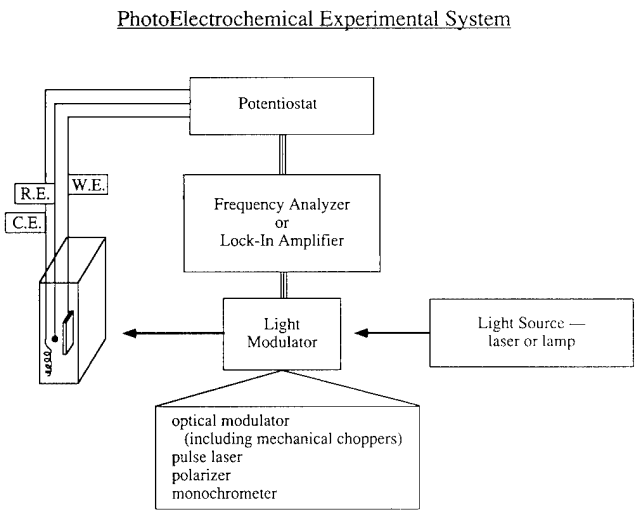

Fig. 18. General photoelectrochemical experimental set-up showing (i) light sources, (ii) a light modulator, (iii) an electrochemical cell and (iv) electrochemical components.

charge transfer in O_2 solution, in spite of the lack of overlap between electronic states in the electrolyte and the valence band. It was also found that these surface electronic states in TiO_2 can function as charge transfer and/or recombination sites [43] and that the recombination rates are increased for mechanically polished samples [44]. Frank and Bard [45] also explored the distribution of surface states on TiO_2 (single-crystal and polycrystalline films), while Tomkiewicz [46] and Siripala and Tomkiewicz [47] have assigned populations and energy levels of surface states on treated surfaces.

Below we will describe experimental results where the photocurrent is dominated by surface effects when the surface is sensitized. However, we will first describe a general photoelectrochemical experimental set-up (see Fig. 18). The light probe illuminating the sample first passes through a modulator. For example, if the photoelectrochemical signal is large relative to the dark current, then the modulator can simply be a focusing lens. However, if the dark current is the larger of the two, an optical modulator (e.g. a mechanical chopper or a variable-intensity modulator) is used in addition to the focusing lens. The reference frequency from the modulation is then used in either a frequency analyzer or a lock-in amplifier to isolate the small photoelectrochemical signal.

The apparatus for PEM and photoelectrochemical spectroscopy have been described in detail elsewhere [39,41,42]. Illumination is provided by either an Ar^+ ion laser or a xenon lamp and monochromator. The photoelectrochemical cell is mounted on a computer-controlled *XYZ* stage and is controlled by a potentiostat. A lock-in amplifier is used to discriminate between photocurrent and background currents. PEM images were obtained using a video printer and an IBM-compatible computer fitted with a video card.

TiO_2 films, nominally 180 Å thick, were prepared anodically by ramping the applied potential of the Ti working electrode at 0.1 mV s^{-1} from the open-circuit voltage (about −0.25 V vs. saturated calomel electrode (SCE)) to a final growth potential of 6 V(SCE). The electrolyte for metal oxide growth and photoelectrochemical studies was 0.05 M H_2SO_4. The electrolyte for s-PEM imaging and spectroscopic studies was 0.05 M H_2SO_4 and 0.1 M $K_4Fe(CN)_6$. Buffered pH solutions of the electrolyte for sensitization studies were prepared using 0.1 M $K_4Fe(CN)_6$ and phosphate buffer solutions.

PEM studies of SGM TiO_2 have been reported previously [41,42]. A typical PEM image is shown in Fig. 19(a), where the higher photocurrents are represented by brighter regions. The variation of photoresponse of the metal oxide film over different substrate grains was attributed to changes in the density of electronically active defects in the oxide films. The substrate influence on the outer surface (metal oxide–media) and the relative impact of surface effects on the photoelectrochemical behavior were the focal point of our study. The surface effects include electronic states that can influence the corrosion resistance of the oxide, as well as the optical response.

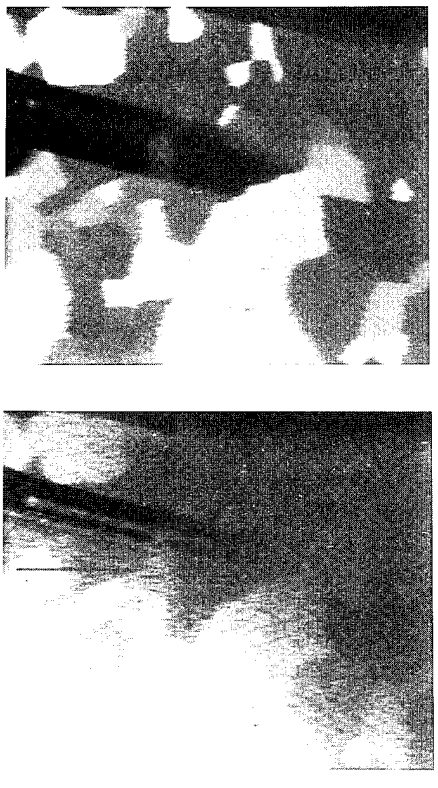

Fig. 19. (a) PEM image obtained from an SGM anodic TiO_2 film under illumination at 351 nm (above band gap energy) at an applied potential of 1 V(SCE). (b) s-PEM image obtained from the same film as in (a) under illumination at 528 nm (subband gap energy) at an applied potential of 0.5 V(SCE).

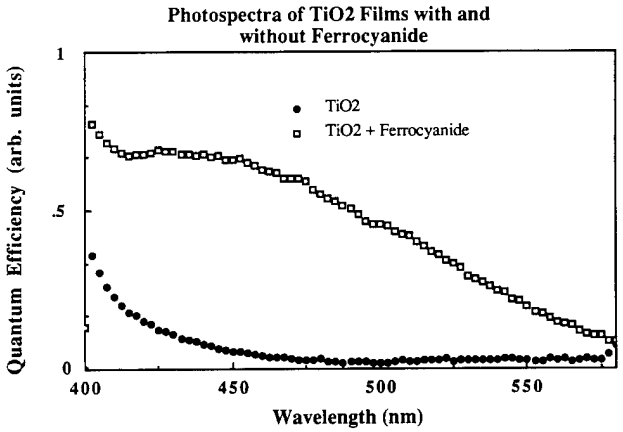

Fig. 20. Long wavelength photocurrent response of an SGM anodic TiO_2 film in the presence and absence of 0.1 M $K_4Fe(CN)_6$.

To examine the photoresponse further, the surface was modified so that a photocurrent image under subband gap illumination (Fig. 19(b)) could be obtained, i.e. an s-PEM image. Subband gap illumination was not substantially absorbed by the bulk oxide film and so provided a means to isolate the surface response from that of the oxide film as a whole. The metal oxide surface was made sensitive to subband gap illumination by ferrocyanide, whose use in dye sensitization for solar energy conversion has been discussed in the literature [48]. The effect of subband gap illumination on the oxide film in the presence of ferrocyanide in aqueous solution was a photoresponse whose spectrum is shown in Fig. 20 in comparison with the response of the oxide film in the absence of any sensitizer. The extension of the response to longer wavelengths (lower energy) was sufficient to allow an Ar^+ ion laser tuned to 528 nm to produce a photocurrent. *At this wavelength no photocurrent was produced in the absence of a dye sensitizer.* The photocurrent map or image produced in the presence of ferrocyanide ions using 528 nm illumination is referred to as an s-PEM image. The surface origin of

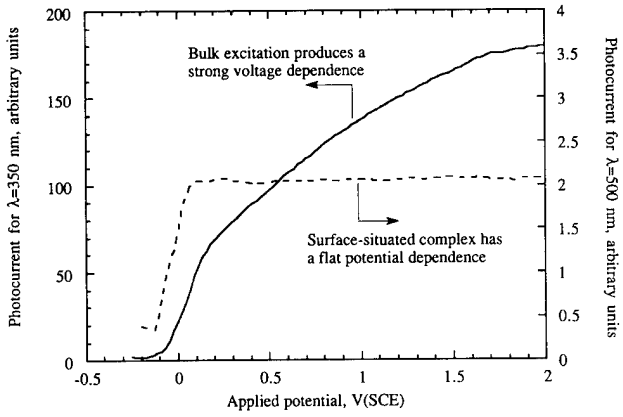

Fig. 21. Response of an SGM anodic TiO_2 film as a function of applied potential under illumination at 350 and 500 nm.

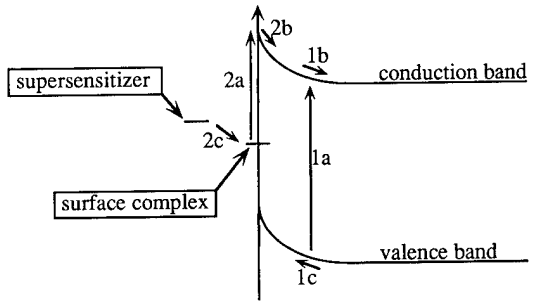

Fig. 22. Scheme of recombination paths mediated by surface electronic states: 1a, direct band gap generation of electron–hole pairs; 1b, motion of electrons generated by process 1a; 1c, motion of holes generated by process 1a; 2a, electrons generated at the surface by subband gap illumination; 2b, motion of electrons generated at the surface; 2c, electron replenishment of surface states.

the subband gap photocurrent from the ferrocyanide-exposed TiO_2 is indicated by the flat photocurrent–bias voltage response as compared with the typical square root potential dependence of the photocurrent under above-band gap illumination (Fig. 21). Very little band bending is required to separate the surface-generated electron–hole pairs as compared with pairs generated deeper in the oxide bulk.

The similarity of the PEM and s-PEM images implies a common influence on the photocurrent. Since the photocurrent generation mechanisms are different, the common loss mechanisms bear examination. Electronic surface states located within the energy range between the conduction band and the level of the oxidized surface complex are able to mediate surface recombination between conduction band electrons and valence band holes or between conduction band electrons and the oxidized form of the adsorbed surface–dye complex (Fig. 22). Surface recombination at surface states will cause lower charge transfer efficiency when these states are present in high concentrations. The fact that the PEM and s-PEM images both reflect the substrate grain arrangement suggests that the substrate metal grains influence the density of defects within the oxide film and at the surface. More detailed discussion of these results can be found in Ref. [40].

We should also note that photoelectrochemical spectroscopy, where the photocurrent is measured at various incident light wavelength, has been used to determine the absorption coefficient of passive films, from which the phase of the passive film under study was determined [49,50]. The photoelectrochemical technique used in conjunction with a lock-in amplifier is very sensitive and thus can be used to study very thin films. However, use of photoelectrochemical techniques to infer structural information should be discouraged and, whenever possible, structure should be determined more directly, e.g. using X-ray diffraction [51] or electron diffraction [41,52,53] methods.

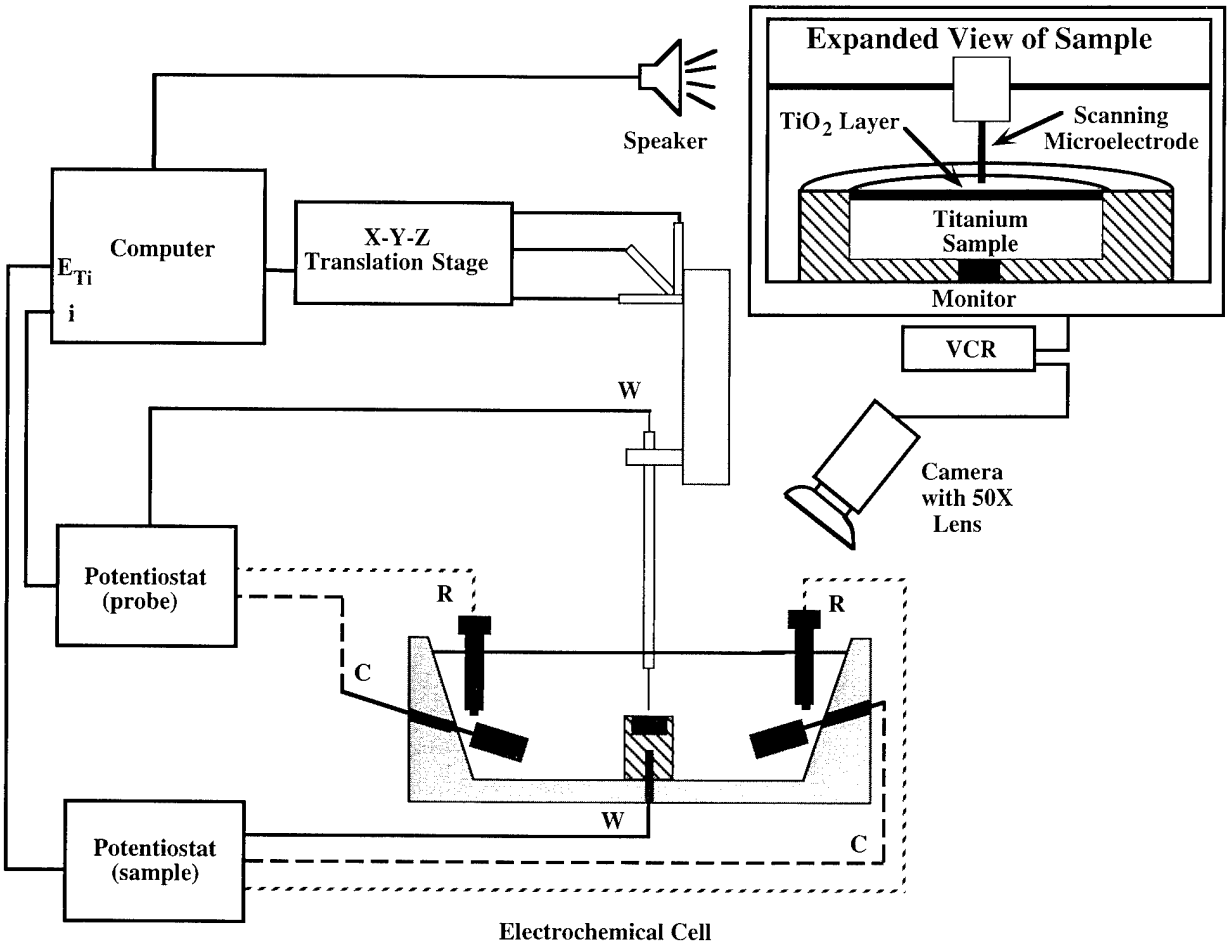

Fig. 23. Schematic of experimental set-up for the SECM showing the major components.

A disadvantage of PEM (or s-PEM) as described above is in its data acquisition rate. For example, a 2×2 mm^2 image taken at a scan rate of 40 μm s^{-1} and 10 μm resolution required approximately 3.5 h. We would like to emphasize, however, that if PEM (or s-PEM) is used to locate precursor sites to localized corrosion, then the data acquisition rate is not very critical provided that the samples do not change significantly during the experiments (see e.g. Ref. [54]). The long time required to obtain a PEM image is caused by the slow scan rate of the *XYZ* stage. A faster way to scan with the laser beam uses galvanometer-type mirrors such as found in a CLSM. Photoelectrochemical imaging of passive films (and corrosion) using a confocal microscope has been reported in the literature (see e.g. Refs. [55–57]). Of particular interest is Ref. [55], where sulfide inclusions in stainless steel were studied.

7. Scanning electrochemical microscopy

Recently the breakdown of 50 Å oxide films on Ti electrodes immersed in aqueous solutions containing Br^- was shown to occur at randomly positioned, microscopic surface sites that were identified by scanning electrochemical microscopy (SECM) prior to pitting corrosion [58,59]. A key finding to this investigation was that the site of oxide breakdown coincided with a highly localized surface activity for Br^- oxidation. The studies suggested that the electrical conductivity of the TiO_2 film is highly non-uniform and that this spatial heterogeneity is associated with the mechanism of oxide film breakdown. Electron-tunneling spectroscopy of the electrodes, employing a scanning tunneling microscope, more directly demonstrated local variations in the conductivity of the oxide, albeit for reasons that are not understood but which are probably related to variations in the structure (e.g. defect density) or stoichiometry of the film [60].

Fig. 23 shows a schematic diagram of the scanning electrochemical miroscope. The potentials of the Ti electrode and SECM scanning tip are controlled independently using two potentiostats, both operating in a conventional three-electrode configuration. A typical image is obtained by scanning the tip at a rate of 40 μm s^{-1} with the tip placed approximately 30 μm above the Ti sample. The Ti electrode and the scanning tip are monitored during imaging using a video camera

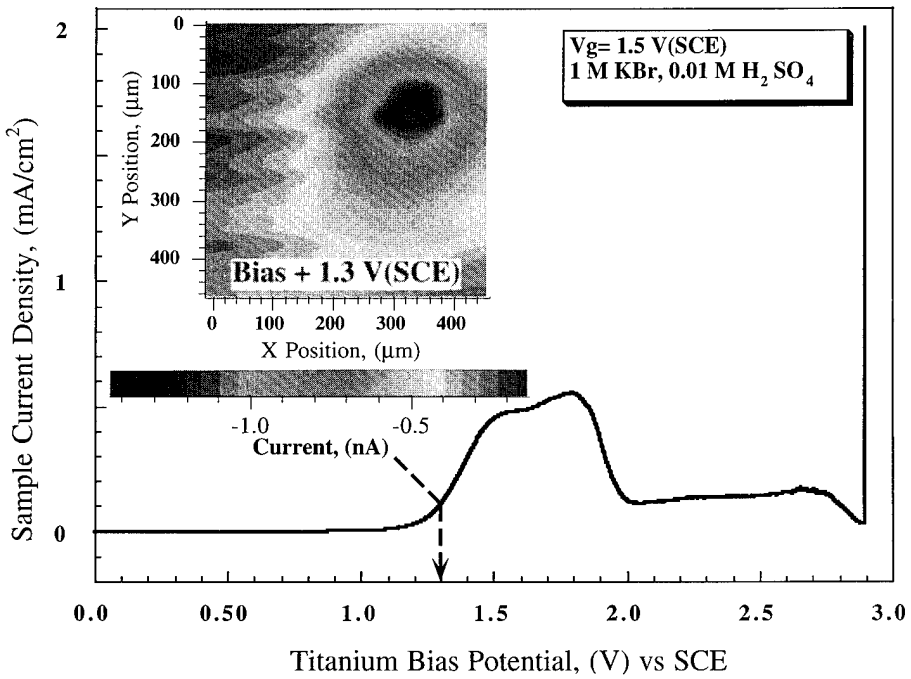

Fig. 24. Voltammetric response of a Ti–TiO_2 electrode in 1 M KBr and 0.05 M H_2SO_4 at 1 mV s^{-1}. Inset: SECM image of a 400 × 400 μm^2 region of the Ti–TiO_2 surface at 1.3 V(SCE). The SECM tip was held at 0.6 V(SCE).

equipped with a 50× magnification zoom lens; video images were recorded using a VHS video recorder [61–66].

Fig. 24 shows the voltammetric response of a Ti–TiO_2 (50 Å oxide) electrode immersed in a 1 M KBr and 0.05 M H_2SO_4 solution open to the ambient atmosphere. The i–V response of this sytems is characterized by a broad oxidation wave centered at about 1.6 V(SCE). The sudden and large increase in current at 3.0 V(SCE) is due to the onset of pitting corrosion, as readily verified by visual inspection of the electrode surface. The broad wave between 1.1 and 2.0 V(SCE) corresponds to Br^- oxidation.

When the Ti–TiO_2 surface was poised at potentials below about 1.0 V(SCE), images of the surface were essentially featureless and the tip current was approximately 0.1 nA. At potentials between 1.0 and 2.0 V (SCE) images revealed a few microscopic sites, such as the one shown in the inset of Fig. 24, where intense Br_2 generation occurred. The maximum current measured at the tip above an electroactive site was typically between 0.2 and 2 nA, well above the background current. At slightly more positive potentials the current at the tip decayed to background levels over a period of a few minutes as a result of the passivation of the active sites.

After determining the position of the active sites on the Ti–TiO_2 surface at potentials between 1.0 and 1.5 V (SCE), Casillas et al. [58,59] increased the potential of the Ti–TiO_2 electrode to a value sufficiently positive to initiate pitting. Pits rapidly grew to microscopic dimensions (about 1 mm) within a few minutes, so that their positions were easily determined by visual inspection. Comparison of images and video images revealed a close correspondence between the locations of the surface-active sites for Br_2 generation and the location of pit formation, i.e. pits nucleated at the same position where the electron transfer rate for Br^- oxidation was largest. A more complete analysis of the results presented here has been published elsewhere [58,59].

It is clear that SECM is very useful for identifying precursor sites. However, any information regarding the passive film can only be obtained indirectly, since the data measured reflect only product species produced at the working electrode. For example, the higher electrochemical activity at the precursor sites is consistent with a number of possible passive film properties, such as (1) the passive film at the precursor sites is thinner and/or (2) the passive film at the precursor sites is highly defective and more metallic. On the other hand, PEM (and/or s-PEM) probes the passive film bulk and film–electrolyte interface directly. Thus the combination of PEM and SECM may prove very advantageous [67].

8. Scanning photoelectrochemical and electrochemical microscopy

In this section we will describe a technique that combines the characteristics of the SECM and the PEM [67–69]. Hereafter this technique will be referred to as scanning photoelectrochemical and electrochemical microscopy (SPECM). To combine the SECM and the PEM, one needs a probe capable of serving both as an electrochemical sensor and a local illuminator. It was found that an optical fiber coated with a gold film and encased in an outer polymer film would serve this purpose. Cleaving the coated fiber exposed a gold ring electrode a few microns thick concentric with the optical fiber core (see Fig. 25). The gold ring served as the microelectrode for SECM, while the core of the optical fiber was used as the illuminator for PEM.

The advantages of SPECM are best described in terms of the possible modes of operation, which in turn are determined by the specific system under study and the type of information sought. First is the coupled mode, where SECM and PEM are carried out simultaneously. This is particularly useful for studying systems where there is virtually no electrochemical activity in the dark. With negligible dark probe currents (current measured at the gold probe without sample illumination), all probe currents measured while the sample is illuminated are due to photoelectrochemically generated products. Hence measurements of probe current at various probe potentials can assist in determining the products produced at the sample. In this respect SPECM is similar to the rotating ring–disk electrode (RRDE), where species generated at the central disk

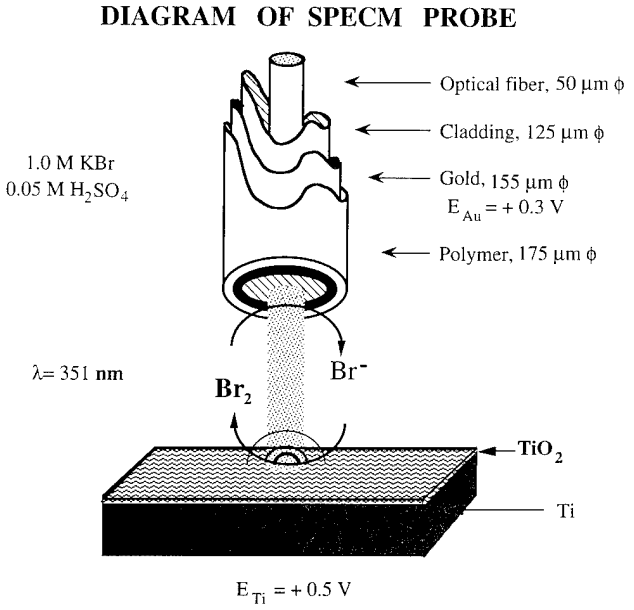

Fig. 25. Schematic representation of the optical tip used in the SPECM over the surface of a TiO_2–Ti disk 500 μm in diameter.

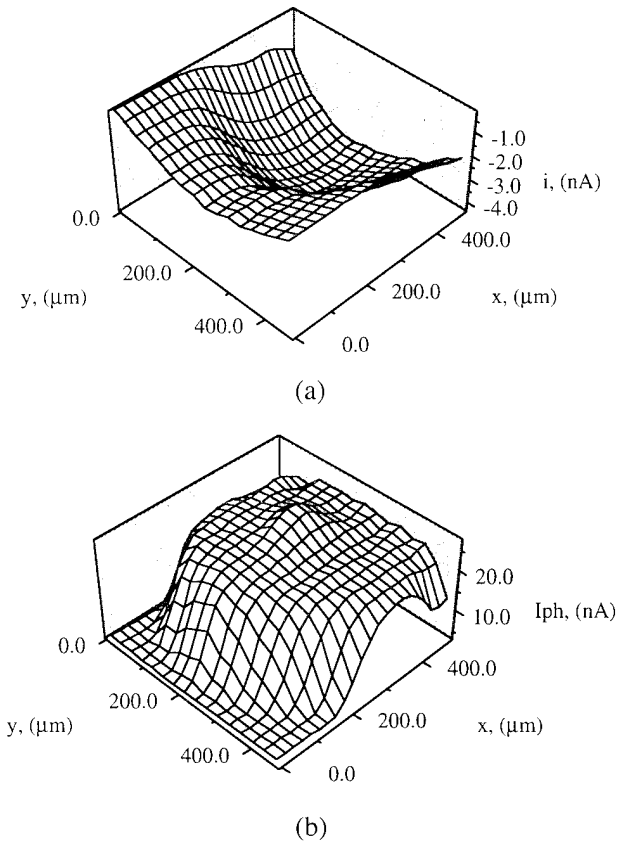

Fig. 26. (a) Electrochemical map of electroreduction current Br_2 molecules produced by electro-oxidation and photo-assisted oxidation of Br^- ions over the surface of a Ti disk 500 μm in diameter with a TiO_2 film 5.0 nm thick. (b) Photoelectrochemical current map obtained concurrently over the same area of a Ti 500 μm disk. The solution was 1 M KBr and 0.05 M H_2SO_4. Illumination was provided by an Ar^+ laser beam, wavelength 351 nm. The potentials for the gold ring electrode and the Ti sample were 0.3 V and 1.3 V(SCE) respectively.

electrode are swept by convection to the outer ring electrode which detects these species electrochemically. There is, however, one very important difference. In SPECM the product species are detected locally, whereas the RRDE yields only averaged information. To distinguish systems where there are considerable probe currents when the sample is not illuminated, the term partially coupled mode has been used [67]. Clearly the analysis of data in the latter is more complicated. Finally there is the decoupled mode, where SECM and PEM are used sequentially. In this mode the advantage of the SPECM set-up in comparison with an SECM set-up or a PEM set-up alone is only logistical.

Below we will only discuss SPECM results obtained in the coupled mode. For the initial test a model sample was used. The sample investigated was Ti disk 500 μm in diameter (Johnson–Matthey Electronics) with an anodically grown TiO_2 film 50 Å thick. The Ti surface was prepared by successive mechanical polishing with alumina (Buehler) slurries down to 0.05 μm grit, followed by a short chemical etch with a 2:4:94 volume

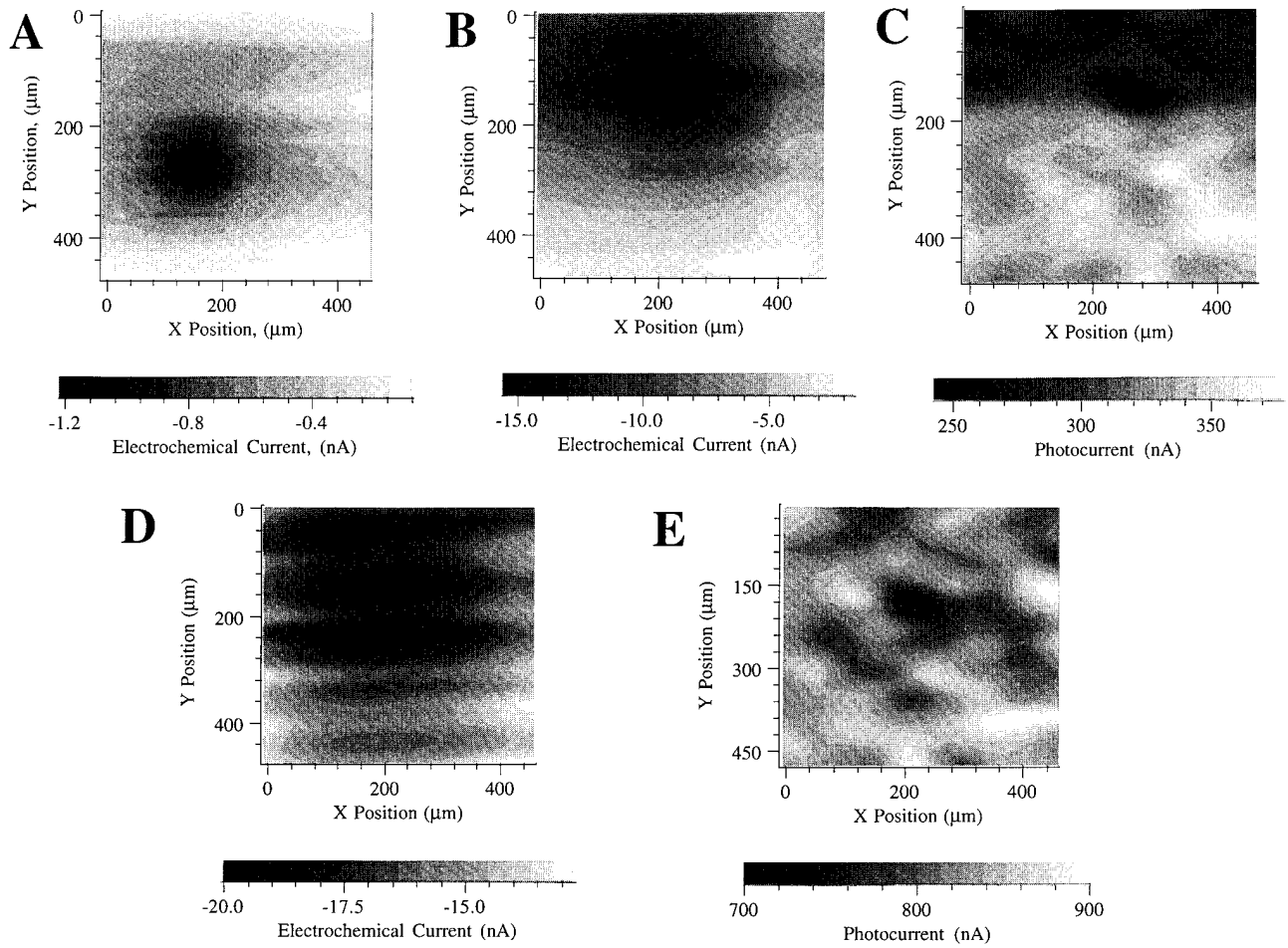

Fig. 27. Images generated by scanning over a pitting precursor site in 1 M KBr and 0.05 M H_2SO_4. Probe-to-substrate over a pitting percursor site in 1 M KBr and 0.05 M H_2SO_4. Probe-to-substrate separation was about 30 μm. (A) SECM image with substrate biased at 1.0 V(SCE), using a carbon fiber probe (8 μm). (B) SECM image at the same bias, using an Au-coated optical fiber probe as shown in Fig. 25. Note that the location was shifted slightly when the carbon fiber probe was switched to the Au probe. (C) PEM image with substrate biased at 0.5 V(SCE), $\lambda = 351$ nm, using an Au-coated optical fiber. (D), (E) SPECM images with substrate biased at 1.0 V(SCE), $\lambda = 351$ nm, using an Au-coated optical fiber. Probe-to-substrate separation was roughly 250 μm. (D) SECM image. (E) Concurrent PEM image.

per cent solution of $HF:HNO_3:H_2O$. Following an anodic oxidation in 0.05 M H_2SO_4, the sample and the probe were immersed in a solution of 1 M KBr and 0.05 M H_2SO_4. The probe was held at a potential of 0.3 V(SCE) and the applied potential at the Ti disk was fixed at either 0.5 or 1.3 V(SCE) as noted. Illumination at 351 and 364 nm was provided by an Ar^+ laser and the light was modulated at 17 Hz using a mechanical chopper. The photocurrent at the reference modulation frequency was measured using a lock-in amplifier as described previously. The experimental set-up for SPECM is similar to the one depicted in Fig. 23 with the addition of a lock-in amplifier.

Fig. 26 show SPECM results obtained with the probe placed about 40 μm above the sample and rastered at 40 μm s^{-1}. Fig. 26(a) shows the positional dependence of the electrochemical current on the gold ring of the probe with the TiO_2–Ti sample illuminated and held at a potential of 0.5 V(SCE), while Fig. 26(b) shows the corresponding photocurrent measured concurrently. The measured photocurrent was due mainly to the oxidation of Br^- to Br_2, which is more efficient than the oxidation of water to O_2 [70]. Correspondingly, the probe current was due mainly to the electroreduction of Br_2. The onset of the probe current is seen to coincide with the rise in photocurrent, which emphasizes the coupled nature of the reactions. Such coupling was found when the Ti–TiO_2 substrate was biased either at 0.5 V(SEC) (which is below the redox potential of the Br^-/Br_2 couple) or at 1.3 V(SCE). In the former case no Br_2 could be *electrochemically* produced at the substrate. More detailed discussion can be found in Ref. [67].

Preliminary SPECM studies to identify precursor sites for pitting on samples similar to those discussed in the previous section have been carried out. Fig. 27 shows the SPECM images of a sample similar to the one shown in Fig. 24. As can be seen, the precursor site which has a *high* electrochemical activity also has a *low*

photocurrent relative to the surrounding area. Tests performed by spiking the electrolyte with high concentrations of Br_2 (maximum absorbance 268 nm) indicate that the effect is much larger than could be accounted for by absorption of incident light. While SECM alone cannot distinguish whether the electrochemically active area is (1) thinner or (2) more highly doped (defective) than its surroundings, the SPECM results suggest that the electrochemically active area is thinner. A thinner film is consistent with a lower photocurrent [37,38], whereas a more highly doped region should have a higher photocurrent [71,72]. Surface analysis (scanning electron microscopy–energy-dispersive X-ray analysis and Auger) of the scanned region shown in Fig. 27 did not reveal any inclusions or other impurities which might indicate a chemical cause of the reduction in photocurrent. The results are preliminary and a more complete study is under way. Our results indicate that one may be able to use purely optical techniques to locate precursor sites, an approach that would be extremely valuable for corrosion prevention and surface treatment methods.

9. Summary

We have described a number of experimental techniques that have been used in our laboratory for fundamental studies of corrosion. The methods described included those that are used to measure corrosion rates (QCM, optical fiber microsensors, PDIM and CLSM), to locate corrosion sites (PDIM, CLSM, PEM and SECM) and to locate precursor sites that are susceptible to localized corrosion (CLSM, PEM, s-PEM, SECM and SPECM). We have shown that the above-mentioned methods have been successful in all three tasks of (1) measuring corrosion rates, (2) locating corroding sites and (3) locating precursor sites. However, much work still needs to be done to understand the fundamental causes of local oxide breakdown, and the experimental methods described in this paper should provide the means to verify the theoretical work.

Acknowledgments

Financial support for this work was provided by Smith and Nephew Richards (Casillas) and by NSF/DMR-9122044. Instrumentation grants from NSF for the PDIM and the CSLM are gratefully acknowledged. DOE/OBES supported some of the work on photoelectrochemical microscopy and quartz crystal gravimetry. One of the investigators (W.J.) received partial support from an IBM-SURP grant.

References

[1] T. Nguyen and A. Rosencwaig, Thermal-wave microscopy and its application to imaging the microstructure and corrosion of cold-rolled steel, *Appl. Surf. Sci.*, *24* (1985) 57.
[2] T. Nguyen and A. Rosencwaig, Thermal-wave microscopy in corrosion studies, *Mater. Charact.*, *28* (1992) 291.
[3] C.C. Streinz, J. Kruger and P.J. Moran, A microellipsometric study of the passive film formation on Al–Ta alloys. I. Solid solution alloys, *J. Electrochem. Soc.*, *141* (1994) 1126.
[4] C.C. Streinz, P.J. Moran, J.W. Wagner and J. Kruger, A microellipsometric study of the passive film formation on Al–Ta alloys. II. The role of A_3Ta precipitates in breakdown, *J. Electrochem. Soc.*, *141* (1994) 1132.
[5] K. Sugimoto and S. Matsuda, Analysis of passive films on austeno–ferritic stainless steel by microscopic ellipsometry, *J. Electrochem. Soc.*, *130* (1983) 2323.
[6] K. Sugimoto, S. Matsuda, Y. Ogiwara and K. Kitamura, Microscopic ellipsometric observation of the change in passive film on 18Cr–8Ni stainless steel with the initiation and growth of pit, *J. Electrochem. Soc.*, *132* (1985) 1791.
[7] N.E. Cipollini, Visual detection of hydrated aluminium oxide by staining with fluorescing and nonfluorescing dyes, *J. Electrochem. Soc.*, *129* (1982) 1517.
[8] R.C. Engstrom, S. Ghaffari and H. Qu, Fluorescence imaging of electrode–solution interfacial processes, *Anal. Chem.*, *64* (1992) 2525.
[9] R.E. Hummel and R.J. Smith, The passivation of nickel in aqueous solutions—IV. The optical and electrochemical investigations of the anodic behavior of nickel in chloride-containing solutions, *Corros. Sci.*, *30* (1990) 849.
[10] M. Seo, Z.C. Jiang and N. Sato, Photoacoustics study on cathodic reduction of anodic oxide films formed on copper in borate solution, *Werkstoffe Korros.*, *39* (1988) 583.
[11] W.H. Smyrl and M.M. Lien, The electrochemical QCM (quartz crystal microbalance) method, in N. Masuko, T. Osaka and Y. Fukunaka (eds.), *New Methods and Approaches in Electrochemical Technology*, VCH and Kodansha, Tokyo, 1993, p. 77.
[12] R.C. Hughes, A.J. Ricco, M.A. Butler and S.J. Martin, Chemical microsensors, *Science*, *254* (1991) 74.
[13] M.A. Butler, A.J. Ricco and R.J. Ricco, Reflectivity changes of optically-thin nickel films exposed to oxygen, *Sens. Actuat.*, *19* (1989) 249.
[14] M.A. Butler, A.J. Ricco and R.J. Baghman, Hg adsorption on optically thin Au films, *J. Appl. Phys.*, *67* (1990) 4320.
[15] W.H. Smyrl and M.A. Butler, Corrosion sensors, *Interface*, *2* (4) (1993) 35.
[16] L.J. Douglas and W.H. Smyrl, unpublished results, 1988.
[17] W. Jin and W.H. Smyrl, unpublished results, 1991.
[18] T. Wilson, Confocal microscopy, in T. Wilson (ed.), *Photocatalysis: Fundamentals and Applications*, Academic, London, 1990, p. 1.
[19] *Molecular Dynamics*, Vol. 2, *SetUp and Scanning the Confocal Microscope*, Molecular Dynamics, Sunnyvale, CA, 1994.
[20] H.J. Kragt, C.P. Smith and H.S. White, Refractive index mapping of concentration profiles, *J. Electroanal. Chem. Interfacial Electrochem.*, *278* (1990) 403.
[21] C.-T. Chen and B.D. Cahan, The nature of the passive film on iron. I. Automatic ellipsometric spectroscopy studies, *J. Electrochem. Soc.*, *129* (1982) 17.
[22] W. Paatsch, Investigation of passive metal electrodes using modulation spectroscopy, *Surf. Sci.*, *37* (1973) 59.
[23] R.H. Wilson, A model for the current–voltage curve of photoexcited semiconductor electrodes, *J. Appl. Phys.*, *48* (1977) 4292.
[24] J. Reichman, The current–voltage characteristics of semiconductor–electrolyte junction photovoltaic cells, *Appl. Phys. Lett.*, *36* (1980) 574.

[25] H. Reiss, Photocharacteristics for electrolyte–semiconductor junctions, *J. Electrochem. Soc.*, *125* (1978) 937.
[26] Yu.V. Pleskov and Yu.Ya. Gurevich, *Semiconductor Photoelectrochemistry*, Consultants Bureau, New York, 1986.
[27] S.R. Morrison, *Electrochemistry at Semiconductor and Oxidized Metal Electrodes*, Plenum, New York, 1980.
[28] S.R. Morrison, *The Chemical Physics of Surfaces*, Plenum, New York, 2nd edn., 1990.
[29] V.A. Myamlin and Y.V. Pleskov, *Electrochemistry of Semiconductors*, Plenum, New York, 1967.
[30] S.E. LeBlanc and H.S. Fogler, The role of conduction/valence bands and redox potential in accelerated mineral dissolution, *AIChE J.*, *32* (1986) 1702.
[31] H. Gerischer, Electrolytic decomposition and photodecomposition of compound semiconductors in contact with electrolytes, *J. Vac. Sci. Technol.*, *15* (1978) 1422.
[32] A.J. Bard and M.S. Wrighton, Thermodynamic potential for the anodic dissolution of n-type semiconductors: a crucial factor controlling durability and efficiency in photoelectrochemical cells and an important criterion in the selection of new electrode/electrolyte systems, in A. Heller (ed.), *Semiconductor Liquid-Junction Solar Cells: Proc. Conf. on the Electrochemistry and Physics of Semiconductor Liquid Interfaces under Illumination*, Proc. Vol. 77-3, Electrochemical Society, Pennington, NJ, 1977, p. 195.
[33] L.A. Harris and R.H. Wilson, Semiconductors for photoelectrolysis, *Ann. Rev. Mater. Sci.*, *8* (1978) 99.
[34] H. Gerischer, F. Hein, M. Lubke, E. Meyer, B. Pettinger and H.R. Schoppel, Der Einfluss von mechanisch erzeugten Gitterdefekten auf das Ranschichtverhalten des Kontaktes ZnO/Elektrolyt, *Ber. Bunsenges. Phys. Chem.*, *77* (1973) 284.
[35] M.A. Butler, M. Abramovich, F. Decker and J.F. Juliao, Subband gap response of TiO_2 and $SrTiO_3$ photoelectrodes, *J. Electrochem. Soc.*, *128* (1981) 200.
[36] J.P.H. Sukamto, W.H. Smyrl, C.S. McMillan and M.R. Kozlowski, Spatially resolved photoelectrochemical measurements of thin oxide films, in D.R. Baer, C.R. Clayton and G.D. Davis (eds.), *Proc. Symp. on the Application of Surface Anlaysis Methods to Environmental/Material Interactions*, Proc. Vol. 91-7, Electrochemical Society, Pennington, NJ, 1991, p. 302.
[37] J.P.H. Sukamto, W.H. Smyrl, C.S. McMillan and M.R. Kozlowski, Photoelectrochemical measurements of thin oxide films—multiple internal reflection effects, *J. Electrochem. Soc.*, *139* (1992) 1033.
[38] J.P.H. Sukamto, C.S. McMillan and W.H. Smyrl, Photoelectrochemical investigations of thin metal-oxide films: TiO_2, Al_2O_3, and HfO_2 on the parent metals, *Electrochim. Acta*, *38* (1993) 15.
[39] C.S. McMillan and W.H. Smyrl, Surface sensitive photoelectrochemical imaging of the derivatized surface of TiO_2 on Ti, *J. Electrochem. Soc.*, *139* (1992) L5.
[40] C.S. McMillan, J.P.H. Sukamto and W.H. Smyrl, Surface-controlled photoelectrochemical microscopy of thin metal oxide films, *Faraday Discuss. Chem. Soc.*, *94* (1992) 63.
[41] M.R. Kozlowski, P.S. Tyler, W.H. Smyrl and R.T. Atanasoski, Photoelectrochemical microscopy of oxide films on metals: Ti/TiO_2 interface, *Surf. Sci.*, *194* (1988) 505.
[42] P.S. Tyler, M.R. Kozlowski, W.H. Smyrl and R.T. Atanasoski, Photoelectrochemical microscopy as a probe of localized properties of thin TiO_2 films, *J. Electroanal. Chem. Interfacial Electrochem.*, *237* (1987) 295.
[43] R.H. Wilson, L.A. Harris and M.E. Gerstner, Characterized semiconductor electrodes—I. Effects of processing variables on the photoelectrochemical properties of single crystal TiO_2 (rutile), *J. Electrochem. Soc.*, *126* (1979) 844.
[44] R.H. Wilson, Observation and analysis of surface states on TiO_2 electrodes in aqueous electrolytes, *J. Electrochem. Soc.*, *127* (1980) 228.
[45] S.N. Frank and A.J. Bard, Semiconductor electrodes. II. Electrochemistry at n-type TiO_2 electrodes in acetonitrile solutions, *J. Am. Chem. Soc.*, *97* (1975) 7427.
[46] M. Tomkiewicz, The nature of surface states on chemically modified TiO_2 electrodes, *J. Electrochem. Soc.*, *127* (1980) 1518.
[47] W. Siripala and M. Tomkiewicz, Surface recombination at n-TiO_2 electrodes in photoelectrolytic solar cells, *J. Electrochem. Soc.*, *130* (1983) 1062.
[48] E. Vrachnou, M. Gratzel and A.J. McEvoy, Efficient visible light photoresponse following surface complexation of titanium dioxide with transition metal cyanides, *J. Electroanal. Chem. Interfacial Electrochem.*, *258* (1989) 193.
[49] J.S. Buchanan, N.P. Freestone and L.M. Peter, A photoelectrochemical study of the anodic oxidation of lead in alkaline solution, *J. Electroanal. Chem. Interfacial Electrochem.*, *182* (1985) 383.
[50] L.M. Peter, Photocurrent spectroscopy of anodic films on metal electrodes, *Ber. Bunsenges Phys. Chem.*, *91* (1987) 419.
[51] D.G. Wiesler, M.F. Toney, W.G. Samant, O.B. Melroy, C.S. McMillan and W.H. Smyrl, Structure and epitaxy of anodic $TiO_2/Ti(1\bar{1}0)$, *Surf. Sci.*, *268* (1992) 57.
[52] M.R. Kozlowski, Photoelectrochemical investigation of anodic oxide films on titanium, *Ph.D. Thesis*, University of Minnesota, Minneapolis, MN, 1989.
[53] P. Tyler, Structural and photoelectrochemical study of anodic oxide films on titanium, *Master's Thesis*, University of Minnesota, Minneapolis, MN, 1987.
[54] M.A. Butler, Aging effects in defect-doped semiconducting electrodes, *J. Electrochem. Soc.*, *126* (1979) 338.
[55] D.E. Williams, A.R.J. Kucernak and R. Peat, Photoelectrochemical imaging. Part I. Background and Theory, *Electrochim. Acta*, *38* (1993) 57.
[56] A.R.J. Kucernak, R. Peat and D.E. Williams, Photoelectrochemical imaging. Part II. The passivating oxide film on iron, *Electrochim. Acta*, *38* (1993) 71.
[57] A.R.J. Kucernak, R. Peat and D.E. Williams, Dissolution and reaction of sulfide inclusions in stainless steel imaged using scanning laser photoelectrochemical microscopy, *J. Electrochem. Soc.*, *139* (1992) 2337.
[58] N. Casillas, S.J. Charlebois, W.H. Smyrl and H.S. White, Pitting corrosion of titanium, *J. Electrochem. Soc.*, *140* (1993) L142.
[59] N. Casillas, S.J. Charlebois, W.H. Smyrl and H.S. White, Pitting corrosion of titanium, *J. Electrochem. Soc.*, *141* (1994) 636.
[60] N. Casillas, S.R. Snyder, W.H. Smyrl and H.S. White, Correlation of electron-transfer rates with the surface density of native and anodically grown oxide films on titanium, *J. Phys. Chem.*, *95* (1991) 7002.
[61] E.R. Scott, H.S. White and J.B. Phipps, Direct imaging of ionic pathways in stratum corneum using scanning electrochemical microscopy, *Solid State Ionics*, *53–56* (1992) 176.
[62] E.R. Scott, H.S. White and J.B. Phipps, Scanning electrochemical microscopy of a porous membrane, *J. Membr. Sci.*, *58* (1991) 71.
[63] E.R. Scott, H.S. White and J.B. Phipps, Measurements of iontophoretic transport through porous membranes using scanning electrochemical microscopy: application to in vitro studies of ion fluxes through skin, *Anal. Chem.*, *65* (1993) 1537.
[64] E.R. Scott, A. Laplaza, H.S. White and J.B. Phipps, Transport of ionic species in skin. Contribution of pores to the overall skin conductance, *Pharmaceut. Res.*, *10* (1993) 1699.
[65] E.R. Scott, H.S. White and J.B. Phipps, *J. Invest. Dermatol.*, *104* (1995) 142–145.
[66] K. Potje-Kamloth, J. Janata and M. Josowicz, Electrochemically prepared insulation for carbon fiber microelectrodes, *Ber. Bunsenges. Phys. Chem.*, *93* (1989) 1480.
[67] N. Casillas, P. James and W.H. Smyrl, submitted to the *J. Electrochem. Soc.*, *142* (1995) L16.

[68] L.S. Kuhn, A. Weber and S.G. Weber, Microring electrode/optical waveguide: electrochemical characterization and application to electrogenerated chemiluminescence, *Anal. Chem.*, *62* (1990) 1631.

[69] C.B. Cohen and S.G. Weber, Photoelectrochemical sensor for catalase activity based on the in situ generation of substrate, *Anal. Chem.*, *65* (1993) 169.

[70] S.J.N. Frank and A.J. Bard, Semiconductor electrodes. 12. Photoassisted oxidations and photoelectrosynthesis at polycrystalline TiO_2 electrodes, *J. Am. Chem. Soc.*, *99* (1977) 4667.

[71] K.H. Yoon and K.B. Park, Dependence of photoelectric behavior of TiO_2 electrodes on processing variables, *J. Appl. Phys.*, *64* (1988) 2189.

[72] K.H. Yoon and J.S. Kim, Photoelectric behavior of sintered TiO_2 electrodes, *J. Phys. Chem.*, *90* (1986) 6488.

[73] H.J. Kragt, D.J. Earl, J.D. Norton and H.S. White, Phase detection interferometric microscopy of electrode surfaces—measurements of localized dissolution of iron microelectrodes, *J. Electrochem. Soc.*, *136* (1989) 1752.

[74] *Molecular Dynamics*, Vol. 1, *The CLSM System*, Molecular Dynamics, Sunnyvale, CA, 1994.

ELSEVIER

Materials Science and Engineering A198 (1995) 197–203

MATERIALS SCIENCE & ENGINEERING A

A quartz crystal microbalance study of the corrosion of iron thin films in neutral aqueous solutions

Masahiro Seo, Kengo Yoshida, Kazuhiko Noda

Faculty of Engineering, Hokkaido University, Kita-13 Jo, Nishi-8 Chome, Kita-ku, Sapporo 060, Japan

Abstract

The quartz crystal microbalance (QCM) technique is capable of detecting small mass changes in the region of nanograms per square centimetre from resonant frequency changes of the quartz crystal. In this study, the QCM technique, combined with electrochemical measurements, was applied to the minute corrosion of iron thin films in deaerated neutral solutions.

An iron thin film with a thickness of 200 nm was electroplated on the gold electrode of a quartz crystal. The mass changes of the iron thin film during natural immersion or galvanostatic polarization in deaerated pH 6.48 borate solution, pH 6.42 borate solution with 10^{-2} M chloride ions, pH 6.0 borate solution with 0.5 M chloride ions and pH 6.48 phosphate solution were measured as a function of time or potential to evaluate the iron dissolution rate or iron dissolution current. The corrosion rate of the iron thin film on natural immersion increased in the order pH 6.48 phosphate > pH 6.0 borate with 0.5 M chloride ions > pH 6.42 borate with 10^{-2} M chloride ions > pH 6.48 borate solution.

The net current flowing through the external circuit during galvanostatic polarization near the corrosion potential was successfully separated into the iron dissolution current and hydrogen evolution current. Tafel plots of the iron dissolution current and hydrogen evolution current were made to evaluate the corrosion mechanism of the iron thin film. The Tafel slopes of iron dissolution and hydrogen evolution thus obtained depend on the electrolyte solutions, from which conclusions can be drawn on the corrosion mechanism.

Keywords: Quartz crystal microbalance; Iron thin film; Corrosion rate; Corrosion mechanism; Neutral aqueous solution

1. Introduction

The quartz crystal microbalance (QCM) technique [1] is capable of detecting small mass changes in the region of nanograms per square centimetre from resonant frequency changes of the quartz crystal. Recent application of the QCM technique to aqueous systems [2–8] has enabled in situ gravimetry under controlled electrochemical conditions to be performed. The simultaneous measurement of the mass change and electric charge would provide a better understanding of corrosion processes of metals in aqueous systems.

There have been many studies on the dissolution kinetics of iron in acidic solutions [9,10]. The mechanism of iron dissolution has been deduced from the Tafel slopes of the anodic current measured during polarization in various acidic solutions. Heusler [11] explained the Tafel slope of 30 mV per decade in terms of a catalytic mechanism in which an adsorbed intermediate species, $FeOH_{ad}$, acts as a catalyst for iron dissolution. Bockris et al. [12] proposed that iron dissolution proceeds stepwise, with two consecutive one-electron exchange reactions, to explain the Tafel slope of 40 mV per decade. The addition of halogen ions, such as chloride ions, to acidic solutions probably retards iron dissolution and provides a Tafel slope of 60 mV per decade or higher [13–17]. The influence of chloride ions on the Tafel slope was explained by taking into consideration the participation of chloride ions in the dissolution mechanism as an adsorbed intermediate [13–17].

The knowledge of iron dissolution in deaerated neutral solutions (as compared with acidic solutions) is insufficient to determine the corrosion kinetics and mechanism, because of difficulties in measuring the low corrosion rate and the limitations of anodic polarization in the narrow potential region. The precipitation of corrosion products, such as $Fe(OH)_2$, on the iron surface due to the low solubility will take place during anodic polarization in neutral solutions and will influence the dissolution kinetics. In some cases, the Tafel slopes near the potential of the active dissolution current peak have unexpectedly high values above 120 mV per decade [18]. Anodic polarization near the corrosion

SSDI 0921-5093(94)04524-0

potential avoids the influence of corrosion products on the dissolution kinetics, but the separation of the net current into the iron dissolution current and hydrogen evolution current, which are partially coupled near the corrosion potential, is necessary to evaluate the Tafel slope.

Recently, it has been recognized that the measurement of the low corrosion rate is important to predict the lifetime of overpack materials for the long-term storage (more than 1000 years) of nuclear waste under reducing environments [19]. Carbon steel [20] is one of the candidates for overpack materials; due to its uniform corrosion rate, it is easy to predict the lifetime in spite of the corrosion allowance material in a deaerated environment.

Moreover, the utilization of metal thin films in electronic materials and devices has increased with the increasing demand for data processing of high density and high speed. The corrosion of thin films, even if minute, will produce severe damage of the equipment because of the very small and limited size. A study of the minute corrosion of metal thin films [21–23] is also necessary to protect these materials from the environment.

In this study, the corrosion behaviour of iron thin films in deaerated neutral solutions was investigated using the QCM technique combined with electrochemical measurements. A special attempt was made to separate the net current into the iron dissolution current and hydrogen evolution current in order to evaluate the Tafel slopes for the iron thin films polarized near the corrosion potential.

2. Experimental details

A QCM sensor head (5 MHz, AT-cut quartz crystal) with an oscillator circuit (TPS 500, Maxtek, Inc.) was used in this experiment. Gold electrodes were evaporated onto both sides of the quartz crystal in the sensor head. The geometrical surface area of the electrode was 0.50 cm^2. The iron thin films, with a thickness of about 200 nm, were electroplated onto one side of the gold electrodes on the quartz crystal. The electroplating was performed in 0.9 M $FeSO_4(NH_4)_2SO_4 \cdot 6H_2O$ at pH 2.0 at 20 °C under a constant cathodic current density of 4×10^{-2} A cm^{-2} for 90 s.

The following relation between the mass change Δm and the change in the resonant frequency of the quartz crystal Δf holds [24]

$$\Delta m/\Delta f = -(\mu_q \rho_q)^{1/2}/(2f_0^2) \quad (1)$$

where f_0 is the resonant frequency, ρ_q is the density and μ_q is the shear modulus of the quartz crystal. For 5 MHz, AT-cut quartz crystal, the value of $\Delta m/\Delta f = -1.77 \times 10^{-8}$ g cm^{-2} Hz^{-1} is obtained as the mass sensitivity by substituting $f_0 = 5 \times 10^6$ Hz, $\rho_q = 2.648$ g cm^{-3} and $\mu_q = 2.947 \times 10^{11}$ g cm^{-1} s^{-2} into Eq. (1).

In liquid application of the QCM technique, the resonant frequency depends on the viscosity and density of the liquid in contact with the quartz crystal [25,26] according to Eq. (2)

$$\Delta f = -f_0^{3/2}(\eta_l \rho_l/\pi \mu_q \rho_q)^{1/2} \quad (2)$$

where η_l and ρ_l are the viscosity and density of the liquid in contact with the quartz crystal. However, it was confirmed [4,27] that Eq. (1) is still valid if the viscosity and density of the liquid do not change during the QCM experiment in the liquid.

Fig. 1 shows a block diagram of the electrochemical QCM system. The sensor head was mounted in an electrochemical cell, using an acryl resin holder. The gold electrode covered with the iron thin film on one side of the crystal was ground and used as the working electrode. The electrolyte solution of about 100 cm^3 introduced into the cell was circulated at a rate of 150 cm^3 min^{-1} with a pump to avoid apparent mass changes which may result from changes in the viscosity and density of the solution due to the enrichment of dissolved species near the surface [8]. The electrolyte solutions employed for this study were as follows: (a) pH 6.48 borate solution (0.292 M $H_3BO_3 + 2 \times 10^{-3}$ M $Na_2B_4O_7$); (b) pH 6.48 phosphate solution (0.192 M $NaH_2PO_4 + 0.108$ M Na_2HPO_4); (c) pH 6.42 borate solution with 10^{-2} M chloride ions (0.292 M $H_3BO_3 + 2 \times 10^{-3}$ M $Na_2B_4O_7 + 10^{-2}$ M NaCl); (d) pH 6.0 borate solution with 0.5 M chloride ions (0.292 M $H_3BO_3 + 2 \times 10^{-3}$ M $Na_2B_4O_7 + 0.5$ M NaCl).

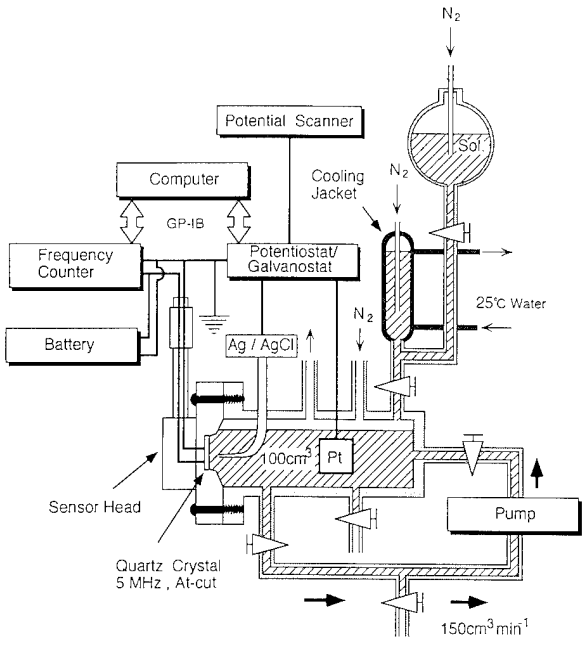

Fig. 1. Block diagram of electrochemical QCM system.

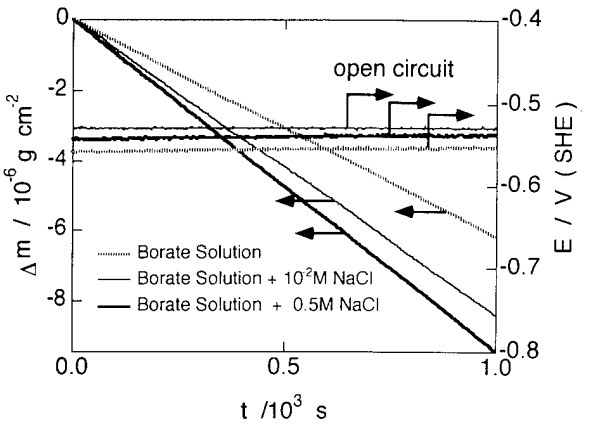

Fig. 2. Mass change Δm vs. time t and electrode potential E vs. time t curves for iron thin films on natural immersion in pH 6.48 borate solution, pH 6.42 borate solution with 10^{-2} M chloride ions and pH 6.0 borate solution with 0.5 M chloride ions.

These solutions were deaerated with ultrapure nitrogen gas before and during the experiments. The temperature of the solution introduced into the cell was kept at 25 ± 0.1 °C during the experiments. The iron thin film immersed in pH 6.48 borate or phosphate solution without chloride ions was cathodically reduced at a constant current density of $i_c = 5 \times 10^{-6}$ A cm^{-2} for 10^3 s to remove the air-formed oxide film [8]. After cathodic reduction, the solution was renewed or changed and the iron thin film was galvanostatically polarized in the anodic or cathodic direction near the corrosion potential. The changes in the resonant frequency of the quartz crystal due to the mass changes during polarization were monitored with a frequency counter and recorded on a personal computer. An Ag/AgCl electrode was used as the reference electrode and the electrode potential was referred to a standard hydrogen electrode (SHE).

3. Results and discussion

3.1. Corrosion rates of iron thin films on natural immersion in various solutions

Fig. 2 shows the mass change Δm vs. time t and the electrode potential E vs. time t curves for iron thin films on natural immersion in pH 6.48 borate solution, pH 6.42 borate solution with 10^{-2} M chloride ions and pH 6.0 borate solution with 0.5 M chloride ions which were circulated at a rate of 150 cm^3 min^{-1} in the cell. The mass decreases linearly with time, whereas the electrode potential remains almost constant. The linear relation between Δm and t holds irrespective of the concentration of chloride ions. The corrosion rate on natural immersion can be obtained from the slope of the straight line. The corrosion rate obtained from the linear relation increases with increasing concentration of chloride ions. The difference in corrosion behaviour between pH 6.48 borate and phosphate solutions is shown in Fig. 3. It can be seen that the corrosion rate in phosphate solution is 2.6 times that in borate solution in spite of the same pH value. The corrosion rates of iron thin films on natural immersion in various solutions are listed in Table 1. The values of i_{corr} were converted from the values of $d(\Delta m)/dt$ by assuming that the iron dissolves as ferrous ions with a current efficiency of 100%.

3.2. Galvanostatic polarization of iron thin films near the corrosion potential in various solutions

Fig. 4 shows the Δm vs. t and E vs. t curves for iron thin films galvanostatically polarized near the corrosion potential in pH 6.48 borate solution. The linear relation between Δm and t holds in both anodic and cathodic polarization. The linear slope increases with increasing anodic current density, whereas it decreases with increasing cathodic current density. Figs. 5 and 6 show the Δm vs. t and E vs. t curves for iron thin films galvanostatically polarized near the corrosion potential in circulated pH 6.0 borate solution with 0.5 M chloride ions and pH 6.48 phosphate solution respectively. The same tendency is observed in Figs. 5 and 6 as in Fig. 4.

3.3. Separation of net galvanostatic current density into iron dissolution current density and hydrogen evolution current density

At the corrosion potential of iron thin films, the iron dissolution reaction ($Fe \rightarrow Fe^{2+} + 2e^-$) is coupled with the hydrogen evolution reaction ($2H_2O + 2e^- \rightarrow H_2 + 2OH^-$), i.e. the iron dissolution current density i_a is equal to the hydrogen evolution current density i_c

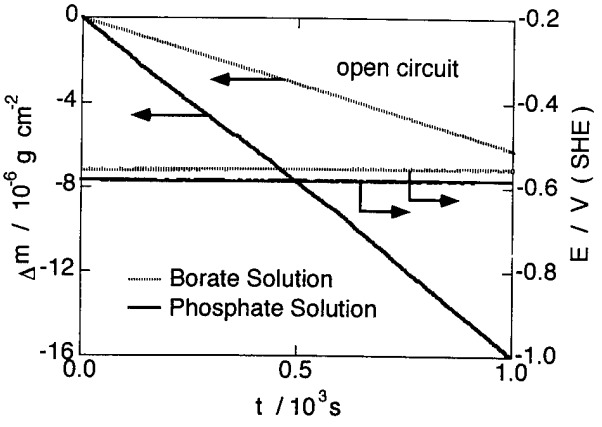

Fig. 3. Mass change Δm vs. time t and electrode potential E vs. time t curves for iron thin films on natural immersion in pH 6.48 borate and phosphate solutions.

Table 1
Corrosion rates of iron thin films on natural immersion in deaerated solutions

Solution	E_{corr}(V vs. SHE)	$d(\Delta m)/dt$(g cm^{-2} s^{-1})	i_{corr} (A cm^{-2})
pH 6.48 borate	−0.55	6.2×10^{-9}	2.1×10^{-5}
pH 6.42 borate with 10^{-2} M Cl^-	−0.53	8.4×10^{-9}	2.8×10^{-5}
pH 6.0 borate with 0.5 M Cl^-	−0.54	9.4×10^{-9}	3.2×10^{-5}
pH 6.48 phosphate	−0.58	1.6×10^{-8}	5.4×10^{-5}

and hence no net current flows through the external circuit. If the iron thin films are polarized in the anodic and cathodic directions slightly away from the corrosion potential, the net current which balances the difference between the iron dissolution current and the hydrogen evolution current flows through the external circuit. The following relation holds

$$i_g = i_a + i_c \quad (3)$$

where i_g is the net current density. The signs of i_a and i_c in Eq. (3) are defined as plus and minus respectively. The iron dissolution current density i_a can be obtained from the mass loss rate $d(\Delta m)/dt$ using Eq. (4)

$$i_a = (2F/M) \times d(\Delta m)/dt \quad (4)$$

where M is the atomic weight of iron and F is the Faraday constant. The hydrogen evolution current density i_c can be obtained by subtracting i_a from i_g.

The values of i_a and i_c thus separated for the iron thin films in various solutions are shown as a function of the electrode potential in Figs. 7 and 8. The correction for iR drop by a current interruption method was made for pH 6.48 borate solution because of the low conductivity (2.52×10^{-4} S cm^{-1}) of the solution. It appears from Fig. 7 that the addition of chloride ions to the borate solution promotes both the iron dissolution and hydrogen evolution. However, the promotion of hydrogen evolution may result from the decrease in the pH of the solution due to the addition of chloride ions.

As shown in Fig. 8, phosphate ions also promote both iron dissolution and hydrogen evolution relative to borate ions. The concentration of phosphate ions is significantly higher than that of borate ions at pH 6.48. The promotion of iron dissolution may be attributed to the high concentration of phosphate ions compared with borate ions. However, it seems difficult to explain the promotion of hydrogen evolution in terms of the difference in the concentration of electrolyte anions.

3.4. *Tafel plots of i_a and i_c for iron thin films polarized near the corrosion potential*

Figs. 9 and 10 show the Tafel plots of i_a and i_c for the iron thin films polarized near the corrosion potential in various solutions. The Tafel plots of i_a and i_c are almost

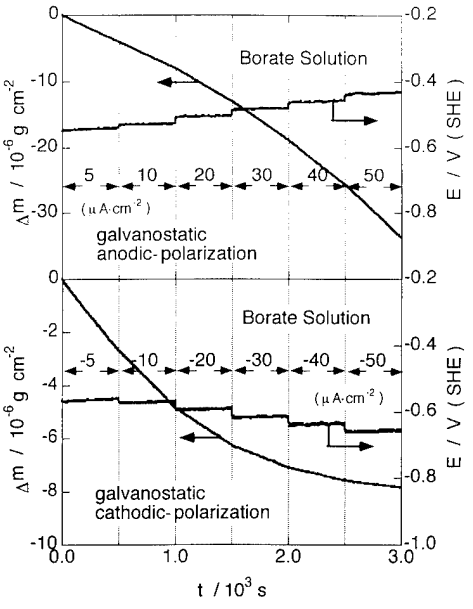

Fig. 4. Δm vs. t and E vs. t curves for iron thin films galvanostatically polarized near the corrosion potential in pH 6.48 borate solution.

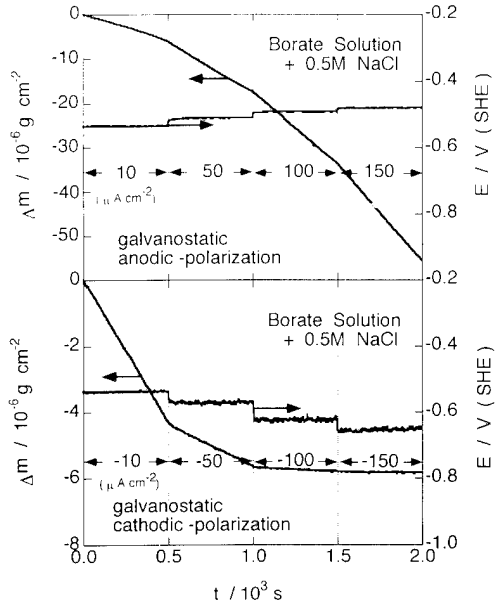

Fig. 5. Δm vs. t and E vs. t curves for iron thin films galvanostatically polarized near the corrosion potential in pH 6.0 borate solution with 0.5 M chloride ions.

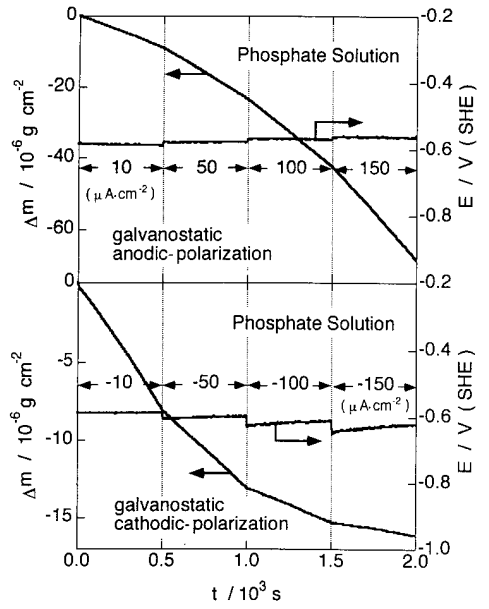

Fig. 6. Δm vs. t and E vs. t curves for iron thin films galvanostatically polarized near the corrosion potential in pH 6.48 phosphate solution.

linear in pH 6.48 phosphate solution. On the other hand, the Tafel plots in pH 6.48 borate solution consist of two linear parts. In pH 6.0 borate solution with 0.5 M chloride ions, the Tafel plot of i_c deviates abruptly

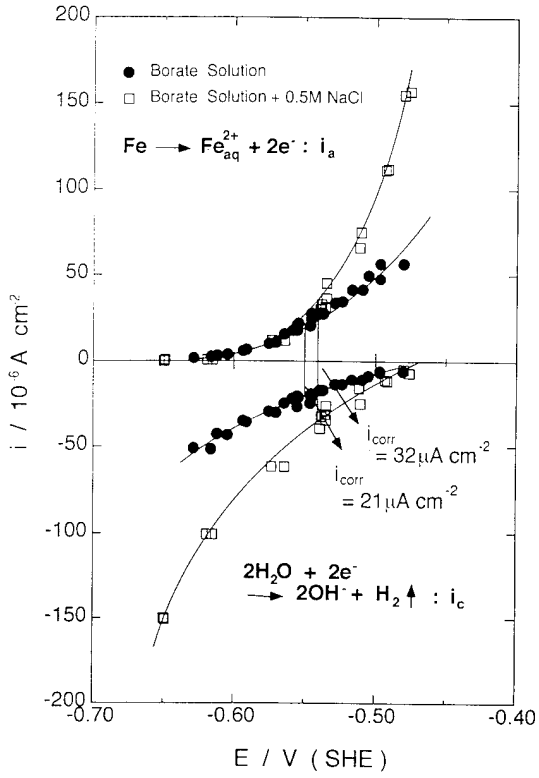

Fig. 7. i_a and i_c separated as a function of the electrode potential for iron thin films in pH 6.48 borate solution and pH 6.0 borate solution with 0.5 M chloride ions.

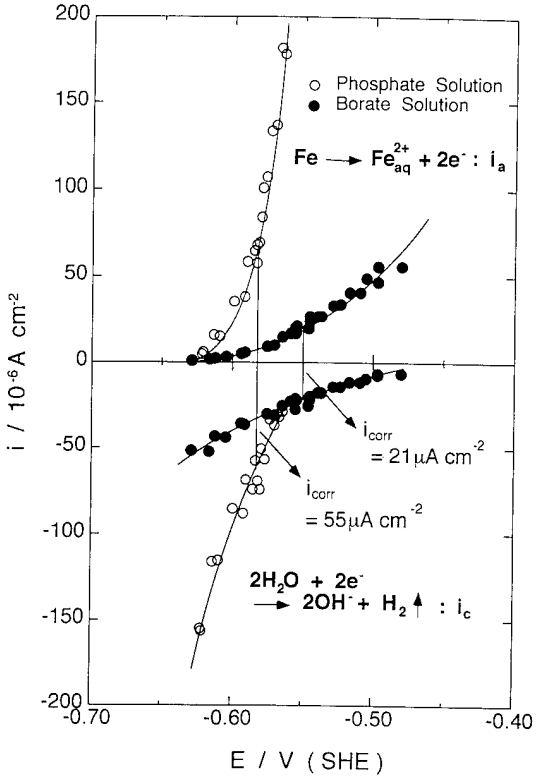

Fig. 8. i_a and i_c separated as a function of the electrode potential for iron thin films in pH 6.48 borate and phosphate solutions.

from linearity at potentials higher than -0.5 V, although the Tafel plot of i_a is linear. The Tafel slopes, b_a and b_c, obtained from the linear parts of these plots for i_a and i_c are summarized in Table 2.

A Tafel slope of $b_a = 40$ mV per decade is theoretically derived if the following mechanism, proposed by Bockris et al. [12], is operative in iron dissolution

$$Fe + H_2O = FeOH_{ad} + H^+ + e^- \quad (5)$$

$$FeOH_{ad} \rightarrow FeOH^+ + e^- \quad (6)$$

$$FeOH^+ + H^+ = Fe^{2+} + H_2O \quad (7)$$

where $FeOH_{ad}$ is the adsorbed intermediate and the reaction of Eq. (6) is the rate-determining step. The Tafel slope of $b_a = 44$ mV per decade obtained in pH 6.48 phosphate solution is close to 40 mV per decade, suggesting that iron dissolution obeys the Bockris mechanism. Two Tafel slopes of $b_a = 64$ mV per decade and $b_a = 154$ mV per decade are obtained in pH 6.48 borate solution. The lower value at log i_a (A cm^{-2}) < -4.5 is almost equal to the Tafel slope ($b_a = 60$ mV per decade) obtained in pH 6.0 borate solution with 0.5 M chloride ions. A Tafel slope of $b_a = 60$ mV per decade may be derived if an adsorbed intermediate, such as an iron borate complex, participates in the iron dissolution as follows

$$Fe + H_3BO_3 + H_2O = FeB(OH)_{4,ad}^- + H^+ \quad (8)$$

$$FeB(OH)_{4,ad}^- + H_2O \rightarrow FeOH{\cdot}B(OH)_4 + H^+ + 2e^- \quad (9)$$

$$FeOH{\cdot}B(OH)_4 = Fe^{2+} + B(OH)_4^- + OH^- \quad (10)$$

where $FeB(OH)_{4,ad}^-$ is the adsorbed intermediate and the reaction of Eq. (9) is the rate-determining step. The presence of boron on the iron surface subjected to active dissolution in pH 8.42 borate solution was confirmed by Auger electron spectroscopy [28]. The chloride ions may also participate in the iron dissolution

$$FeB(OH)_{4,ad}^- + Cl^- \rightarrow FeCl{\cdot}B(OH)_4 + 2e^- \quad (11)$$

$$FeCl{\cdot}B(OH)_4 = Fe^{2+} + B(OH)_4^- + Cl^- \quad (12)$$

where the reaction of Eq. (11) is the rate-determining step. The high Tafel slope of $b_a = 154$ mV per decade at log i_a (A cm^{-2}) > -4.5 in pH 6.48 borate solution is associated with the insufficient correction for the iR drop in the solution or the enrichment of ferrous borate complex ions near the surface [8].

Many studies of hydrogen evolution on various metals have been performed [29]. The Tafel slope of $b_c = 120$ mV per decade obtained in pH 6.48 phosphate solution means that the following mechansim is operative

$$H_2O + e \rightarrow H_{ad} + OH^- \quad (13)$$

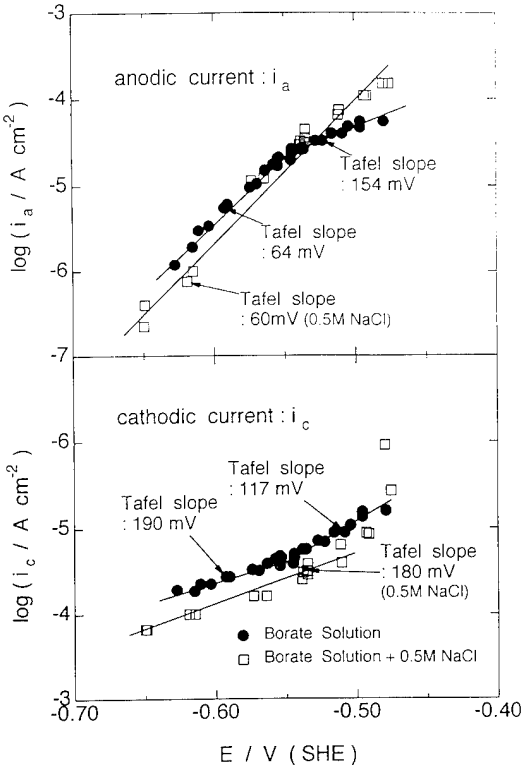

Fig. 9. Tafel plots of i_a and i_c for iron thin films polarized near the corrosion potential in pH 6.48 borate solution and pH 6.0 borate solution with 0.5 M chloride ions.

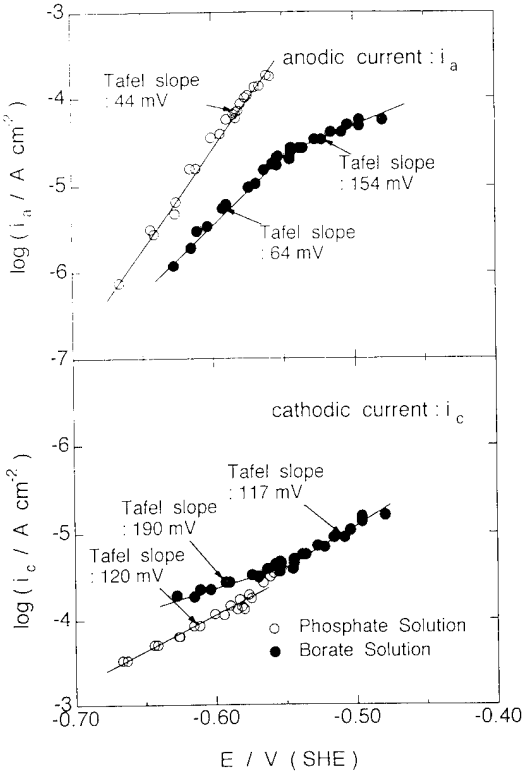

Fig. 10. Tafel plots of i_a and i_c for iron thin films polarized near the corrosion potential in pH 6.48 borate and phosphate solutions.

$$H_{ad} + H_{ad} = H_2 \quad (14)$$

where the reaction of Eq. (13) is the rate-determining step. It is known that the hydrogen evolution reaction on iron during cathodic polarization in acidic solutions has a Tafel slope of 120 mV per decade. At present, it seems difficult to explain the high Tafel slopes of $b_c = 190$ mV per decade and 180 mV per decade obtained in pH 6.48 borate solution and pH 6.0 borate solution containing 0.5 M chloride ions. The symmetry factor β for the charge transfer reaction is usually regarded as 0.5. An adsorbed intermediate, such as $FeB(OH)_{4,ad}^-$, may influence the potential energy–distance curve for the charge transfer reaction of Eq. (13) to give a symmetry factor β of 0.32, i.e. less than 0.5.

It seems that the measurement of i_c is not as accurate as that of i_a. The accuracy of the measurement of i_c becomes poor as i_g approaches i_a. The abrupt deviation of the Tafel plot of i_c from linearity at potentials higher than -0.5 V in pH 6.0 borate solution with 0.5 M chloride ions may result from errors in the measurement of i_c because i_g is comparable with i_a at -0.5 V.

Further conclusions on the mechanisms of iron dissolution and hydrogen evolution from the Tafel slopes will require improvements in the accuracy and reproducibility of electrochemical QCM measurements. Moreover, a wide range of electrochemical QCM exper-

Table 2
Tafel slopes of iron dissolution b_a and hydrogen evolution b_c for the iron thin films during galvanostatic polarization near the corrosion potential

Solution	b_a (mV per decade)	b_c (mV per decade)
ph 6.48 borate	64/153	190/117
pH 6.0 borate with 0.5 M Cl^-	60	180
pH 6.48 phosphate	44	120

iments in deaerated neutral solutions containing different concentrations of electrolyte anions (not only borate, phosphate and chloride, but also sulphate, perchlorate and carbonate) must be conducted to obtain a comprehensive understanding of the corrosion mechanism of iron thin films.

4. Conclusions

The following conclusions can be drawn from the electrochemical QCM results of the minute corrosion of iron thin films in deaerated neutral solutions containing various electrolyte anions.

(1) The corrosion rates of iron thin films on natural immersion were obtained from the mass change vs. time curves, and depend on the electrolyte solutions in the order pH 6.48 phosphate solution > pH 6.0 borate solution with 0.5 M chloride ions > pH 6.42 borate solution with 10^{-2} M chloride ions > pH 6.48 borate solution.

(2) The measurement of the mass change during the galvanostatic polarization of iron thin films near the corrosion potential has succeeded in separating the net current density i_g into the iron dissolution current density i_a and the hydrogen evolution current density i_c as a function of the electrode potential.

(3) A Tafel slope of $b_a = 44$ mV per decade was obtained for iron dissolution in pH 6.48 phosphate solution, indicating that the Bockris mechanism is operative here. On the other hand, Tafel slopes of $b_a = 64$ mV per decade and 60 mV per decade were obtained in pH 6.48 borate solution and in pH 6.0 borate solution with 0.5 M chloride ions, suggesting that an adsorbed intermediate, such as $FeB(OH)_{4,ad}^-$, participates in the rate-determining step of iron dissolution with the charge transfer of two electrons.

(4) A Tafel slope of $b_c = 120$ mV per decade was obtained for hydrogen evolution in pH 6.48 phosphate solution, which is consistent with that usually observed for hydrogen evolution on iron in acidic solutions, and indicates that the formation of adsorbed hydrogen atoms with the charge transfer of one electron from water molecules is the rate- determining step. The Tafel slopes of b_c in pH 6.48 borate solution and pH 6.0 borate solution with 0.5 M chloride ions were higher than 120 mV per decade, which may be attributed to the symmetry factor for the charge transfer reaction ($\beta < 0.5$).

References

[1] C. Lu and A.W. Czanderna (eds.), *Applications of Piezoelectric Quartz Crystal Microbalances*, Vol. 7, Elsevier, New York, 1984.
[2] O. Melroy, K. Kanazawa, J.G. Gordon II and D. Buttry, *Langmuir*, *2* (1986) 697.
[3] A. Grzegorzewski and K.E. Heusler, *J. Electroanal. Chem.*, *228* (1987) 455.
[4] L. Grasjo, M. Seo and N. Sato, *Corros. Sci.*, *31* (1990) 299.
[5] L. Grasjo and M. Seo, *J. Electroanal. Chem.*, *296* (1990) 233.
[6] M. Seo and K. Yoshida, *Proc. 12th Scandinavian Corrosion Congress and Eurocorr'92, Espoo, Finland, May 31–June 4, 1992*, Vol. II, Corrosion Society of Finland, 1992, p. 367.
[7] M. Seo, K. Yoshida, H. Takahashi and I. Sawamura, *J. Electrochem. Soc.*, *139* (1992) 3108.
[8] M. Seo and K. Yoshida, *Proc. 12th Int. Corrosion Congress, Houston, Texas, USA, September 19–24, 1993*, Vol. 5B, NACE International, Houston, TX, 1993, p. 3878.
[9] K.E. Heusler, in A.J. Bard (ed.), *Encyclopedia of Electrochemistry of the Elements*, Vol. IXA, Marcel Dekker, New York, 1982, p. 311.
[10] D.M. Drazic, in B.E. Conway, J.O'M. Bockris and R.E. White (eds.), *Modern Aspects of Electrochemistry*, No. 19, Plenum, New York, 1989, p. 120.
[11] K.E. Heusler, *Z. Elektrochem.*, *62* (1958) 582.
[12] J. O'M. Bockris, D.M. Drazic and A.R. Despic, *Electrochim. Acta.* *4* (1961) 325.
[13] R.T. Foley, *Corrosion*, *26* (1970) 58.
[14] K.E. Heusler and G.H. Cartledge, *J. Electrochem. Soc.*, *108* (1961) 732.
[15] K. Schwabe and C. Voigt, *Electrochim. Acta*, *14* (1969) 853.
[16] N.A. Darwish, F. Hilbert, W. Lorenz and H. Roswag, *Electrochim. Acta*, *18* (1973) 421.
[17] H.C. Kuo and K. Nobe, *J. Electrochem. Soc.*, *125* (1973) 853.
[18] L.I. Freiman and Ya.M. Kolotyrkin, *Zashch. Met.*, *1* (1965) 161.
[19] G.P. Marsh and K.J. Taylor, *Corros. Sci.*, *28* (1988) 289.
[20] Power Reactor and Nuclear Fuel Development Co. Japan (ed.), *Rep. PNC TN 1410 92-081*, Tokyo, 1992, p. 4–63.
[21] M. Seo, I. Sawamura, L. Grasjo, Y. Haga and N. Sato, *J. Soc. Mater. Sci. Jpn.*, *39* (1990) 357.
[22] J.D. Sinclair (ed.), *Proc. 1st Int. Symp. on Corrosion and Electronic Materials Development, Seattle, WA, October 14–19, 1990*, Electrochemical Society Inc., Pennington, NJ, 1991.
[23] P.J. Peterson (ed.), *Corrosion of Electronic and Magnetic Materials (STP 1148)*, ASTM, Philadelphia, PA, 1992.
[24] G. Sauerbrey, *Z. Phys.*, *155* (1959) 206.
[25] T. Nomura and T. Nagamune, *Anal. Chim. Acta*, *155* (1983) 231.
[26] K. Kanazawa and J.G. Gordon II, *Anal. Chem.*, *57* (1985) 1771.
[27] S. Bruckenstein and M. Shay, *Electrochim. Acta*, *30* (1985) 1295.
[28] M. Seo, N. Sato, J.B. Lumsden and R.W. Staehle, *Corros. Sci.*, *17* (1977) 209.
[29] H. Kita, in A.J. Bard (ed.), *Encyclopedia of Electrochemistry of the Elements*, Vol. IXA, Marcel Dekker, New York, 1982, p. 413.

ELSEVIER

Materials Science and Engineering A198 (1995) 205–211

MATERIALS SCIENCE & ENGINEERING A

Environmental resistance of intermetallic compounds and composite materials

D.J. Duquette

Rensselaer Polytechnic Institute, Troy, NY 12180-3590, USA

Abstract

Intermetallic compounds and composites based on them are candidate materials for high temperature structural applications. However, both elevated temperature and ambient temperature resistance to the environment pose potential problems. For example, minor alloying elements have been shown to have a significant influence on the static and cyclic oxidation resistance. In addition, at ambient temperatures, virtually all of the alloys that have been examined show considerable susceptibility to hydrogen embrittlement. A brief overview of these phenomena is presented.

Keywords: Intermetallic compounds; Composites; Oxidation; Hydrogen embrittlement; Alloying

1. Introduction

Intermetallic compounds, alloys based on them and composite materials using intermetallic compounds or alloys as matrix materials have been identified as potential high technology materials for structural applications. However, most intermetallics lack inherent ductility, often exhibit poor creep resistance and, since many are line or near line compounds, do not lend themselves to alloying without the precipitation of second phases which are usually deleterious. Nevertheless, several promising intermetallics are currently being developed either for use as monolithic materials or as components of composite materials. In the latter case, the inherent lack of ductility and the associated lack of significant toughness are overcome by controlled interfacial bonding between the matrix and the reinforcing phases. From an environmental point of view, those intermetallics which are line or near line compounds, in some instances, exhibit phase transformations when one of the elements in the compound is selectively oxidized at elevated temperatures. In addition, they are often sensitive to hydrogen embrittlement and/or oxygen-induced embrittlement, and many oxidize catastrophically at intermediate temperatures. While these disadvantages are certainly substantial, the development of a number of interesting systems is currently underway, with potential applications for both ambient and elevated temperatures.

2. Alloy systems

Although a large number of interesting alloy systems have been explored, only those systems which appear to be close to commercial application will be discussed here. These alloys include the nickel aluminides (Ni_3Al and NiAl), the iron aluminides (Fe_3Al and FeAl), the titanium aluminides (Ti_3Al, TiAl and $TiAl_3$), niobium aluminide ($NbAl_3$) and molybdenum disilicide ($MoSi_2$). Some of the known properties of these materials are shown in Table 1.

The discovery that small amounts of boron (approximately 0.1%) added to Ni_3Al resulted in a significant increase in the room temperature ductility has initiated a significant amount of research into other alloying elements [1] which might enhance the ductility in other alloy systems. However, with the exception of a very few specific alloying additions, it is generally conceded that the boron effect is rather selective. Boron has been shown to enhance the ductility of other $L1_2$ compounds including Ni_3Si [2] and Ni_3Ga [2], although neither of these alloys is currently being extensively developed. Ni_3Al also shows some enhanced ductility when alloyed

SSDI 0921-5093(94)04525-9

Table 1
Properties of selected intermetallic compounds

Compound	Crystal structure	Melting point (°C)	Density (g cm^{-3})	Modulus (GPa)	Specific modulus (GPA g cm^{-3})
Ni_3Al	$L1_2$	1390	7.50	178	23.7
NiAl	B2	1640	5.86	200	34.1
TiAl	$L1_0$	1460	3.91	175	44.8
$NbAl_3$	DO_{22}	1600	4.54	—	—
$MoSi_2$	C11	2030	6.3	359	57.0
Al_3Ti	DO_{22}	1325	3.40	—	—
Fe_3Al	DO_3	[a]	6.72	141	21.1

[a]Disorders at approximately 550 °C.

with manganese, chromium, iron, beryllium or palladium [3–6]. However, except for the palladium and beryllium effects, ductility is achieved with the other alloying additions due to the formation of ductile second phases. Fe_3Al and FeAl show a significant amount of ductility in dry air, but moisture is sufficient to induce embrittlement. This phenomenon will be addressed in a later section of this paper. No significant room temperature ductility has been achieved for other intermetallic alloys of interest for advanced technological applications, except for TiAl, which has been alloyed with chromium and vanadium to yield room temperature ductilities of approximately 3% [7]. These alloys are two-phase materials ($\gamma + \alpha$-2) [8], and the alloying additions generally decrease the melting temperatures of the alloys as well as increase their density; both effects reduce the advantages of the intermetallic alloys when compared with conventional high technology alloys. It should be noted that the alloys of most interest to technological applications contain significant amounts of aluminum or, in the case of $MoSi_2$, silicon. Since these alloys are generally intended for elevated temperature use, it is imperative that they form protective oxide scales. An exception to the use of these alloys for intermediate to high temperature applications is the development of the iron aluminides which are currently being studied as potential replacements for stainless steels.

3. Elevated temperature resistance

The intermetallic compound NiAl has already been widely utilized as a coating material for conventional nickel-based alloys in aerospace applications. In conventional oxidizing atmospheres, it forms a continuous aluminum oxide film which resists further oxidation by inhibiting cationic diffusion through the film. It is somewhat susceptible to spalling due to cyclic oxidation. This drawback has been addressed by the addition of rare earth elements to the aluminide, which has been shown to improve the adherence of the oxide film. As a monolithic material it undergoes a ductile to brittle transition at approximately 400 °C [9]. This transition results in inferior creep properties, and it is unlikely that the compound can be used at elevated temperatures without composite reinforcing. Single crystals of the compound have been developed [10], and in order to improve the low temperature toughness of the alloy, iron or cobalt has been added to provide crack-blunting second phases [11]. Other alloying additions have resulted in an improvement in the elevated temperature strength of the compounds to a level where they compete successfully with conventional nickel-based superalloys, with a density reduction of some 40% [12].

Even Ni_3Al shows a significant amount of oxidation resistance through the formation of alumina; the oxidation resistance is even better than that of pure silicon and considerably better than that of nickel or of the nickel–chromium alloys (Fig. 1) [13]. Unfortunately, the relatively low melting temperature of the compound, combined with its relatively high density, will probably inhibit its use for aerospace applications. On the other hand, it is currently being developed as a possible candidate for land-based turbines, for internal combustion engine applications and for incinerator components, etc.

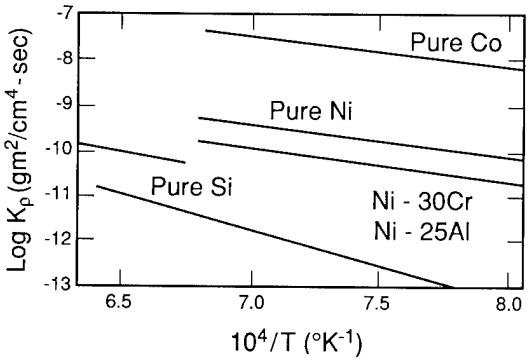

Fig. 1. Parabolic oxidation rate constants for aluminides and conventional alloys [13].

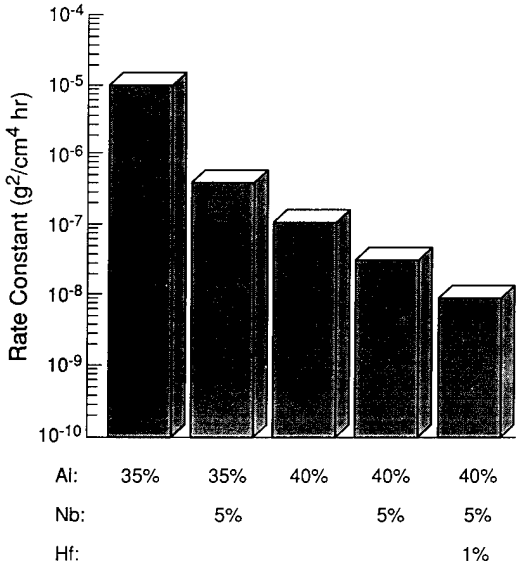

Fig. 2. Effect of niobium on the parabolic rate constant of TiAl [14].

The titanium aluminides show increasing oxidation resistance with increasing aluminum content. $TiAl_3$ shows the best oxidation resistance, but has the lowest melting temperature of the Ti–Al alloys, which may limit its elevated temperature use. However, its high ductility and outstanding oxidation resistance may make it a suitable coating material for titanium and its alloys for intermediate temperature applications. TiAl is considerably less oxidation resistant than $TiAl_3$, even with 50% aluminum in the compound. The inferior oxidation resistance arises because rutile (TiO_2) is a significant component of the oxidation products produced at temperatures in the vicinity of 1000 °C [14]. The cationic diffusivity is considerably higher in rutile than in alumina. Recent results indicate that the addition of niobium to TiAl can result in significantly improved oxidation resistance. The oxidation rate constant is reduced by at least two orders of magnitude with the addition of 5 wt.% niobium to a 40 wt.% aluminum alloy. Further addition of a small amount of hafnium results in a further decrease in the static oxidation rates of TiAl-based alloys (Fig. 2) [14]. Ti_3Al has undergone a considerable amount of development, with significant additions of niobium reported to improve the ductility and small amounts of vanadium and molybdenum imparting strength without sacrificing ductility [15]. However, the relatively low melting temperature limits the useful operating temperature to approximately 800 °C and the alloy shows a marked tendency towards hydrogen embrittlement (see following section). In any event, the alloy is not resistant to oxidation, due to the formation of rutile as its primary reaction product, and would probably only be successfully utilized in a coated condition.

The niobium aluminide of perhaps the most technological interest, $NbAl_3$, exhibits an interesting high temperature oxidation phenomenon [16]. Although this alloy contains a considerable amount of aluminum, an abnormally high rate of oxidation is observed. This behavior can be ascribed to the fact that this material is a line compound, allowing virtually no variation in either the niobium or aluminum content. Depletion of aluminum from the original aluminide due to oxidation results in a phase transformation from $NbAl_3$ to Nb_2Al. This compound exhibits significantly lower oxidation resistance and indeed oxidizes so rapidly that it is virtually consumed by the oxidative process. This, in turn, results in exposure of the original compound to oxidation, to form alumina, which is depleted in aluminum and undergoes a subsequent phase transformation. The final result is a banded reaction product zone consisting of alternate layers of alumina and niobium aluminate and, in some instances, niobia.

$MoSi_2$ is one of the most oxidation resistant compounds being considered for elevated temperature applications. The reaction product on this compound is silica (SiO_2), and the "pest" phenomenon described below does not occur in fully dense, crack-free material [17].

In addition to static oxidation considerations, thermal cycling also affects the elevated temperature environmental resistance of intermetallic compounds and alloys. The differences between the coefficients of thermal expansion of the oxides and the base materials can result in significant tensile or compressive stresses in the oxides with the result that the oxide film will fail in tension or by buckling. For superalloys and superalloy coatings this phenomenon can be alleviated by alloying with trace amounts of zirconium, hafnium or, more commonly, yttrium. A similar alloying scheme has also been successful for niobium aluminides as well as nickel aluminides. Fig. 3 shows the cyclic oxidation results for these alloys containing either yttrium or zirconium and,

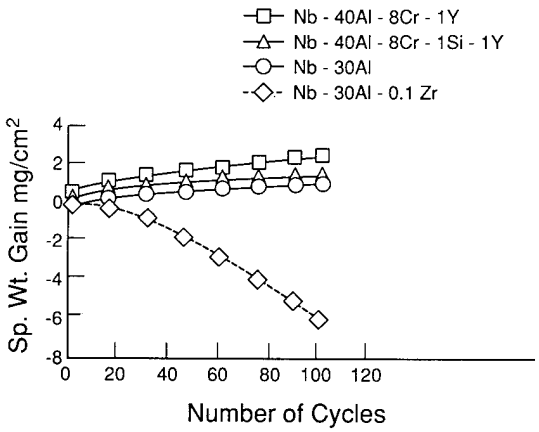

Fig. 3. Cyclic oxidation behavior of intermetallics alloyed with minor element additions [18].

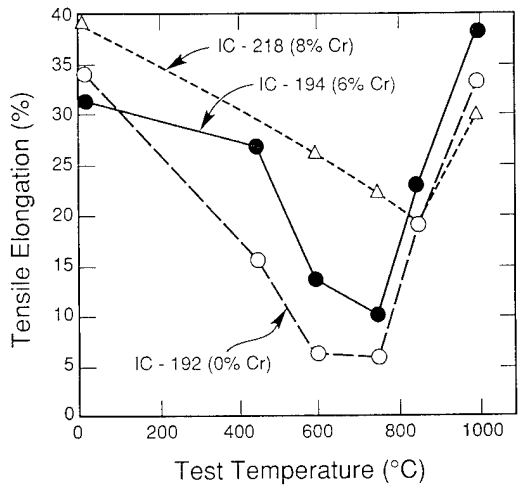

Fig. 4. Intermediate temperature embrittlement of Ni_3Al alloys in air showing the beneficial effect of Cr additions [20].

in one case, silicon [18]. Similar results have been reported for TiAl and for monolithic NiAl where such additions have been traditionally applied to coating materials [14,19].

At intermediate temperatures intermetallics suffer from two rather distinct phenomena which are not usually observed in conventional alloys. These are the so-called "pest" phenomenon and oxygen-induced embrittlement. The "pest" phenomenon results from rapid internal oxidation of the intermetallics, generally along grain boundaries. These internal oxidative processes generally generate large internal volumetric expansions, virtually always resulting in the serious degradation of mechanical properties and, in some cases, total destruction of the material in an almost explosive manner. While the specific mechanisms of this phenomenon have not been quantitatively established, it appears that surface oxide films, which are formed at intermediate temperatures, are not sufficient diffusion barriers to oxygen ingress. Grain boundaries, with their inherent defect structures, act as short circuit diffusion paths in preference to the usually ordered matrix. This phenomenon has been reported for virtually all of the aluminides with the possible exception of TiAl.

Oxygen-induced embrittlement, which has been reported in cases where internal oxidation has not had sufficient time to occur, is another recently observed phenomenon in some intermetallic compounds at intermediate temperatures. It has been observed in polycrystals and single crystals of Ni_3Al and in polycrystals of Ni_3Si [20,21]. The phenomenon is generally not observed in vacuum and, while it has generally been associated with oxygen, some recent results suggest that it may also be related to water vapor, and accordingly to hydrogen embrittlement. For Ni_3Al, this intermediate temperature embrittlement may be somewhat alleviated by alloying with chromium, as shown in Fig. 4 [20].

The effect of compositing on any of the phenomena described above has not been extensively studied. However, in a series of experiments conducted on TiAl as well as on NiAl, it has been shown that the chemistry of the reinforcing phase appears to play a significant role in the static and cyclic oxidation behavior. For example, the introduction of a zirconia-stabilized alumina reinforcing phase in TiAl results in a significant increase in the static oxidation rate and in otherwise unobserved internal oxidation processes. Substitution of the zirconium-stabilized reinforcing phase with pure alumina results in only slightly increased oxidation rates, the increase being associated with a rapid diffusion path along the interface between the reinforcing phase and the matrix material. The presence of reinforcing phase in TiAl virtually always results in enhanced oxide adherence on this compound during cyclic oxidation, although the exact cause of the enhanced adherence is still not well understood [14]. For NiAl, reinforcing phases of either HfB_2 or TiB_2 result in abnormally high static oxidation rates [16]. In this case, the enhanced oxidation is associated with the inclusion of boron oxide in the alumina film, which results in a non-protective barrier film, and may even result in the fluxing of the otherwise protective alumina. The inclusion of alumina reinforcing phases in NiAl has no effect on the intrinsic oxidation resistance of the compound.

Thus although research into the oxidation of composites based on intermetallic compounds is still in its infancy, it is apparent that the nature of the reinforcing phase can exert a profound effect on the oxidation resistance.

4. Ambient temperature resistance

In addition to elevated temperature considerations, many intermetallic compounds suffer from room temperature degradation, particularly by solid state dissolved hydrogen. Table 2 gives a brief summation of some of the intermetallic compounds and alloys which have been shown to be affected by this phenomenon.

The $L1_2$ compounds appear to be exceptionally susceptible, although perhaps only because they generally exhibit more inherent ductility than other crystal struc-

Table 2
Alloys embrittled by hydrogen

B2	L_{2_0}	DO_{19}	$L1_2$	Orthorhombic	DO_3
FeCo–V FeAl	TiAl	Ti_3Al	$Ni_3Al + B$ Ni_3Fe $(Fe,Ni)_3V$ Co_3Ti $Ni_3Al_{0.4}Mn_{0.6}$	Ni_2Cr	Fe_3Al

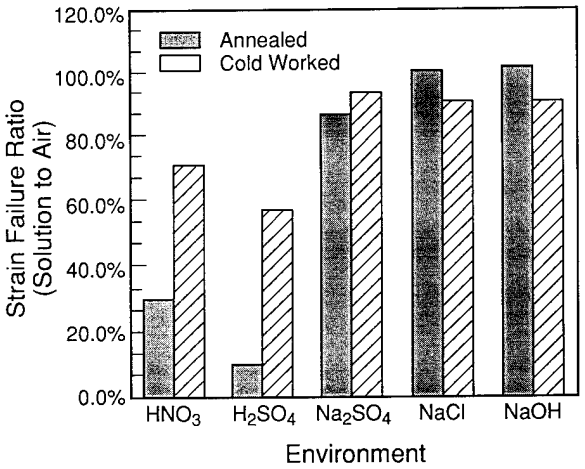

Fig. 5. Effect of environment on the ductility of Ni_3Al [27].

tures [22–26]. For example, Fig. 5 shows the results of slow strain rate tests for annealed and cold-worked Ni_3Al in several environments [27].

These data show that only acidic environments have any appreciable effect on the ductility of this compound, and that annealed samples show a larger reduction in ductility than cold- worked samples. The implications of these experiments are that hydrogen, produced by electrochemical reaction with the compound, is responsible for the marked reduction in ductility. Furthermore, sulfuric acid has a more damaging effect than nitric acid. This result is reasonable if it is assumed that sulfuric acid, being a reducing acid, can be expected to generate more hydrogen under freely corroding conditions than nitric acid, which is an oxidizing acid. The beneficial role of cold working is presumably to provide trapping sites for electrochemically generated hydrogen.

Fig. 6 shows the effects of the application of electrochemical potentials on the ultimate tensile strength ratios for an Ni_3Al alloy containing boron [27]. It is clear that only when hydrogen is actively generated

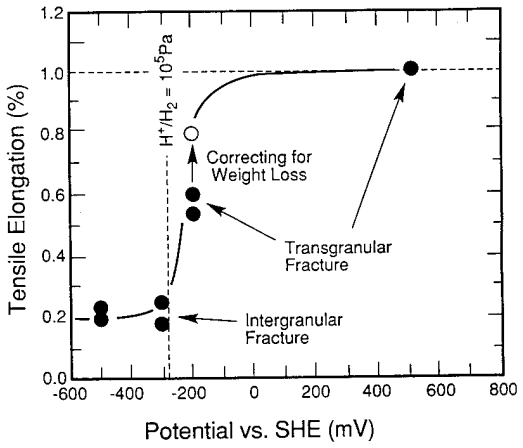

Fig. 6. Effect of potential on the ductility of Ni_3Al [27].

Table 3
Effects of environment on the room temperature tensile properties of Fe_3Al [25]

Test environment	Elongation (%)	Yield strength (MPa)	Tensile strength (MPa)
B2			
Air	4.1	387	559
Vacuum	12.8	387	851
Ar + 4% H_2	8.4	385	731
Oxygen	12.0	392	867
H_2O vapor	2.1	387	475
DO_3			
Air	3.7	279	514
Vacuum	12.4	316	813
Oxygen	11.7	298	888
H_2O vapor	2.1	322	439

does embrittlement occur. It has also been shown that cathodic precharging of a similar alloy results in large losses of ductility, while simultaneous charging of the alloy with cathodic hydrogen results in virtually no ductility, indicating that dynamic hydrogen effects are more damaging than simply introducing hydrogen into the alloy matrix [23]. Similar effects have been observed for Ni_3Fe compounds except that, for this compound, which can be ordered or disordered at room temperature, the ordered compound shows considerably more embrittlement when tensile testing and cathodic charging are applied simultaneously [23]. In both Ni_3Al and Ni_3Fe, the presence of hydrogen results in grain boundary separation.

Iron aluminides are also susceptible to hydrogen embrittlement. In fact, for these alloys it appears that laboratory air is a sufficient embrittlement medium for either Fe_3Al or FeAl [28,29]. For example, Table 3 shows the results of exposure of Fe_3Al to a variety of environments including air, vacuum, dry oxygen, dry hydrogen and water vapor. These data indicate that air and water vapor are extremely damaging to the ductility and strength of this material, but that hydrogen per se is only slightly damaging. Vacuum and dry oxygen have virtually no effect on the mechanical properties of the compound. These data also show that the embrittling effect is not a function of the crystal structure of the compound, the B2 and DO_3 structures (controlled by heat treatment) yielding essentially the same dependence on the environment. Similar results have been observed for FeAl, except that a vacuum of less than 10^{-4} Pa and argon + 4% hydrogen were apparently not sufficiently inert to inhibit at least some degree of embrittlement. The role of dry oxygen in virtually completely inhibiting hydrogen embrittlement is not totally understood, but it has been suggested that, since it appears to be more effective in the case of the higher

aluminum alloy, the formation of alumina may prevent the ingress of hydrogen.

It is perhaps interesting to note that, in the case of the iron aluminides, Fe_3Al exhibits cleavage cracking when it is hydrogen embrittled, while FeAl exhibits intergranular separation. This observation suggests that there is nothing intrinsic about hydrogen-induced intergranular failure, but that hydrogen embrittlement simply follows the line of least resistance with respect to the fracture path. Some recent results regarding the Fe_3Al alloy indicate that the hydrogen embrittlement phenomenon is similar to that for more conventional alloy systems. For example, decreasing strain rates result in decreased ductilities in environments containing air or water vapor, but have no effect on the ductility in dry oxygen [30]. The addition of 5% chromium to the Fe_3Al compound has been reported to inhibit cracking under conditions of cathodic charging when samples are statically loaded (U-bend tests) [31]. However, when dynamically tensile tested in air or after precharging with hydrogen, severe embrittlement is observed, the ductility being reduced to less than 2% compared with a value of 13% in vacuum [32]. Compositing of chromium-alloyed Fe_3Al with Al_2O_3 fibers has no significant effect on the susceptibility to hydrogen embrittlement of the alloy [30].

Hydrogen embrittlement has also been reported for titanium aluminides, including some relatively highly alloyed materials. In contrast with most of the intermetallics studied, these materials have been shown to precipitate hydrides when they contain more than 50 at.% titanium [33]. Embrittlement due to hydrogen gas has been reported for Ti–24Al–11Nb [34] and for Ti–25Al–10Nb–3V–1Mo [35]. For the former alloy, the ductility was reduced from 3% to 0% when it was annealed in hydrogen. For the latter alloy, the ductility was 1.7% for a test performed in hydrogen compared to a ductility of 2.8% for a test performed in helium. Interestingly, a loss of ductility was also observed for this alloy when the tests were performed at 204 °C, in contrast with many other hydrogen-embrittled alloys which show susceptibility only near room temperature. This can be interpreted as evidence that hydrides are associated with embrittlement in these alloys since the hydrides have been shown to be stable to relatively high temperatures (depending on the hydrogen content of the alloys). TiAl also appears to be susceptible to hydrogen embrittlement. A reduction in tensile strength has been reported for a Ti–48Al–2.5Nb–0.3Ta alloy after pre-exposure to hydrogen gas at 815 °C for 30 min [36,37].

With the exception of the titanium compounds and alloys, where the distinct possibility of hydride formation may provide an explanation for the observed ductility losses, the mechanisms for the hydrogen embrittlement of the intermetallic compounds and alloys appear to be similar to those suggested for other alloy systems. These include hydrogen-enhanced plasticity and/or decohesion of either cleavage planes or grain boundaries. Direct experimental evidence for either of these mechanisms (with the possible exception of a few experiments performed in situ in an electron microscope) has yet to be obtained.

5. Conclusions

Although considerable effort is being devoted to the development of intermetallic compounds and their alloys for structural applications, it is probable that most of these materials will be used for elevated temperature applications under conditions where conventional structural materials cannot be employed. In addition, it is probable that, given the intrinsic lack of ductility exhibited by most of the intermetallics, they will have to be composited in order to provide sufficient toughness for structural applications. However, independent of the attractive elevated temperature capabilities shown by these materials, considerations of static and cyclic oxidation will have to be addressed, particularly since it has been shown that reinforcements may have significant effects on elevated temperature environmental resistance. Finally, it has been shown that virtually every intermetallic compound or alloy examined is embrittled by hydrogen. Although it is unlikely that this phenomenon will be of direct importance for elevated temperature applications (with the possible exception of titanium compounds), each of the systems considered must resist hydrogen embrittlement at ambient temperatures. As a minimum, if resistance to hydrogen embrittlement cannot be realized, sufficient engineering data, related to the properties of the alloys in the presence of hydrogen, must be generated to ensure the successful utilization of these materials.

Acknowledgements

The author is grateful to the Advanced Projects Research Agency and Office of Naval Research for financial support through a University Research Initiative, under contract N00014-92-J-1779.

References

[1] K. Aoki and O. Izumi, *Nippon Kinzaku Gakkaishi, 43* (1979) 1190.
[2] A.I. Taub and C.L. Briant, in S.H. Whang, C.T. Liu, D.P. Pope and J.O. Steigler (eds.), *High Temperature Aluminides and Intermetallics*, TMS-AIME, Warrendale, PA, 1990, p. 183.
[3] T. Takasugi, O. Izumi and N. Masahashi, *Acta Metall., 33* (1985) 1259.
[4] G.E. Fuchs and N.S. Stoloff, *Acta Metall., 36* (1988) 138.

[5] A. Chiba, S. Hanada and S. Watanabe, in O. Izumi (ed.), *Proc. Int. Symp. on Intermetallic Compounds (JIMIS-6)*, Japan Institute of Metals, Sendai, 1991, p. 445.
[6] T. Takasugi, N. Masahashi and O. Izumi, *Scr. Metall., 20* (1986) 1317.
[7] Y.-W. Kim, in L. Johnson, D.P. Pope and J.O. Steigler (eds.), *High Temperature Ordered Intermetallic Alloys IV, MRS Symposia, 213*, MRS, Pittsburgh, PA, 1991, p. 777.
[8] J.M. Larsen, K.A. Williams, S.J. Balsone and S.M.A. Stuckie, in S.H. Whang, C.T. Liu, D.P. Pope and J.O. Steigler (eds.), *High Temperature Aluminides and Intermetallics*, TMS-AIME, Warrendale, PA, 1990, p. 521.
[9] R.N. Noebe, R.R. Bowman, C.L. Cullers and S.V. Raj, in L. Johnson, D.P. Pope and J.O. Steigler (eds.), *High Temperature Ordered Intermetallic Alloys IV, MRS Symposia, 213*, MRS, Pittsburgh, PA, 1991, p. 589.
[10] R. Darolia, *J. Met., 43* (3) (1991) 44.
[11] K. Ishida, R. Kainuma, N. Ueno and T. Nishizawa, *Metall. Trans. A, 22* (1991) 441.
[12] R. Darolia, C.T. Liu, R.W. Cahn and G. Southoff (eds.), *Ordered Intermetallics—Physical Metallurgy and Mechanical Behavior, NATO Workshop on Advanced Intermetallics*, Kluwer Academic, Dordrecht, Netherlands, 1992, p. 679.
[13] F.S. Pettit and G.W. Goward, *Metallurgical Treatises*, TMS-AIME, Warrendale, PA, 1981, p. 603.
[14] J. Fish and D.J. Duquette, Rensselaer Polytechnic Institute, Troy, New York, unpublished work, 1992.
[15] M.J. Blackburn and M.P. Smith, Titanium alloys of the Ti_3Al type, U.S. Patent 4,292,077, September 29, 1981.
[16] P. Korinko and D.J. Duquette, Rensselaer Polytechnic Institute, Troy, New York, unpublished work, 1992.
[17] J. Petrovic, Los Alamos National Laboratory, personal communication, 1991.
[18] M.G. Hebsur, J.R. Stevens, J.L. Smialek, C.A. Barrett and D.S. Fox, in T. Grobstein and J. Dychak (eds.), *Oxidation of High Temperature Intermetallics*, TMS-AIME, Warrendale, PA, 1989, p. 171.
[19] S. Mrowec and J. Jeddinski, in T. Grobstein and J. Doychak (eds.), *Oxidation of High Temperature Intermetallics*, TMS-AIME, Warrendale, PA, 1989, p. 57.
[20] C.T. Liu, C.L. White and E.H. Lee, *Scr. Metall., 19* (1985) 1247.
[21] W.C. Oliver and C.L. White, *High Temperature Ordered Intermetallic Alloys II, MRS Symposia, 81*, MRS, Pittsburgh, PA, 1987.
[22] A.K. Kuruvilla and N.S. Stoloff, *Scr. Metall., 19* (1985) 83.
[23] G.M. Camus, N.S. Stoloff and D.J. Duquette, *Acta Metall., 37* (1989) 7.
[24] T. Takasugi and O. Izumi, *Acta Metall., 34* (1986) 607.
[25] Y. Liu, T. Takasugi, O. Izumi and T. Yamada, *Acta Metall., 37* (1989) 507.
[26] A.K. Kuruvilla, S. Ashok and N.S. Stoloff, *Proc. 3rd Int. Congress on Hydrogen and Materials*, Vol. 2, Pergamon, Oxford, 1982, p. 629.
[27] R.E. Ricker, D.E. Hall and J.L. Fink, *Scr. Metall., 24* (1990) 291.
[28] C.T. Liu, C.G. McKamey and E.H. Lee, *Scr. Metall., 24* (1990) 385.
[29] C.T. Liu, E.H. Lee and C.G. McKamey, *Scr. Metall., 23* (1989) 875.
[30] J. Scott, N.S. Stoloff and D.J. Duquette, Rensselaer Polytechnic Institute, Troy, New York, unpublished research, 1992.
[31] R.A. Buchanan and J.G. Kim, *Proc. 4th Annual Conf. on Fossil Energy Materials, Oak Ridge, TN, May, 1990, Rep. ORNL/FMP-90/1*, p. 383.
[32] M. Shea, A. Castagna and N.S. Stoloff, *High Temperature Ordered Intermetallics IV, MRS Symposia, 213*, MRS, Pittsburgh, PA, 1991, p. 609.
[33] D.S. Shih, G.K. Scarr and G.E. Wasielewski, Abstract, *J. Met., 39* (7) (1987) 7.
[34] T. Fox, D.B. Knorr and N.S. Stoloff, Rensselaer Polytechnic Institute, Troy, NY, unpublished research, 1991.
[35] D.E. Matejczyk and P.R. Jewett, Summary, *Proc. 2nd Workshop on Hydrogen Materials Interactions, NASA Workshop Publ. 1004*, NASA, November, 1988, p. 137.
[36] J.H. Holbrook, H.J. Cialone and M.S. Majumdar, Abstract, *3rd NASA Workshop on Hydrogen Materials Interactions, Scottsdale, AZ, May, 1989*, NASA, 1989.
[37] L.G. Fritzemeier, M.A. Jacinto and G.D. Schnittgrund, Abstract, *3rd NASA Workshop on Hydrogen Materials Interactions, Scottsdale, AZ, May, 1989*, NASA, 1989.

ELSEVIER

Materials Science and Engineering A198 (1995) 213–223

MATERIALS SCIENCE & ENGINEERING A

The role of electrode potential distribution in corrosion processes

Howard W. Pickering

Department of Materials Science and Engineering, The Pennsylvania State University, University Park, PA 16802, USA

Abstract

The role of potential distribution inside cavities or recesses in a metal surface is discussed in the context of non-uniform corrosion rates where planar surfaces give way to pitted, cracked or porous surfaces or where planar surfaces contain crevices. The analysis uses the following concepts: (a) the aspect ratio (ratio of the depth to opening dimensions) of a cavity is an important factor in determining the electrode potential distribution into the cavity, and (b) since the aspect ratio is independent of the size of the cavity, large aspect ratios and hence large voltage differences (*IR* drops) can exist within the smallest of cavities. The consequences of a wide distribution of electrode potential on the internal cavity surface are discussed in the context of (i) crevice corrosion, (ii) hydrogen charging from inside cavities during anodic polarization of their external surface, (iii) the role of surface diffusion in dealloying corrosion and (iv) the transition from metastable to stable pitting corrosion.

Keywords: Potential distribution; Corrosion; Cavities; Pitting

1. Introduction

The non-uniform distribution of electrode potential within cavities or surface recesses is an important consideration in understanding the mechanisms of various forms of localized corrosion. The electrode potential varies significantly on planar surfaces and is considered a critical factor in various electrochemical processes, including those involved in corrosion prevention, specifically in the design of cathodic and anodic protection systems. The presence of cavities or recesses in the surface strongly accentuates the spatial non-uniformity of the potential distribution on the metal surface and within the depth of the cavity. Voltage drops of 10^2–10^3 mV and corresponding shifts of the local electrode potential from the cavity opening towards its bottom have been measured and/or calculated [1–8]. The voltage difference from the cavity opening to its bottom increases to a limiting value with increasing aspect ratio a of the cavity, where a is defined as the ratio of the depth to opening dimensions of the cavity [7–10]. Since the aspect ratio is independent of the actual size of the cavity, these large voltage differences can exist within the smallest of cavities [11]. The aspect ratio is a useful concept for discussing the potential distribution and can be described quantitatively so that one can define a critical aspect ratio needed for the initiation of localized corrosion for simple geometries (e.g. rectangular crevices or cylindrical pits) completely filled with the electrolyte[1], i.e. for a cavity of a given opening dimension the required depth for active dissolution at its bottom can be predicted; the results of some model calculations are described below.

These electrode potential differences exist on the internal cavity surface as a result of current flow within the cavity electrolyte, i.e. between the anodic reaction sites on the internal cavity surface and the cathodic reaction sites outside the cavity. Consequently, the difference $E(x) - E(x=0)$ must be matched by a similar difference of potential in the electrolyte phase, $\phi(x) - \phi(x=0)$. It follows that

$$E(x) = E(0) - \int_0^x I(x)R(x)\,\mathrm{d}x \tag{1}$$

where $E(x)$ is the electrode potential at a distance x into the cavity, $E(0)$ is the potential at the cavity

[1] The effective aspect ratio can be much larger than the geometrical value as a result of the formation of gaseous and/or solid corrosion products inside the cavity [6,12,13]. Though often a factor in localized corrosion, this complexity is not considered in detail in this paper.

SSDI 0921-5093(94)04526-7

opening, shown as $E(x=0)$ in Fig. 1, and $I(x)$ and $R(x)$ are the magnitudes respectively of the current flowing at a distance x through the cavity electroylte and of the resistance of the electrolytic path within the cavity, which might be constricted by (hydrogen) gas bubbles or solid corrosion products. Upon using Eq. (1), I is considered as positive for an anodic current and negative for a cathodic current. This IR is a complex function of the properties of the system and of the distance x [7–10].

Since the electrode potential varies with distance x into the cavity, the rate of metal dissolution also varies over the internal cavity surface in accord with the polarization behavior of the metal under the local electrochemical conditions. In fact, the current density may vary by orders of magnitude. In addition, other half-cell electrochemical reactions may occur at different depths on the cavity surface. Hence the internal cavity surface will be supporting one or more electrochemical reactions at various depths within the cavity. Furthermore, the rates of these reactions will also be dependent on the distance within the cavity.

The objective of this paper is to review the characteristics of potential distribution inside surface cavities for cases of cathodic and anodic polarizations. Treatments will be given of its role in localized and other forms of corrosion.

1.1. Cathodic polarization

Let us first consider a case of cathodic polarization of a metal surface with a recess or surface crack, as often happens under conditions of cathodic protection [7,14]. For such a system, the $i_c - E_c$ coordinates are located on the polarization curve of hydrogen evolution in Fig. 1, with the outer surface of the metal being at $E_c(x=0)$ and $i_c(x=0)$. From Eq. (1), $E(x)$ inside the cavity in Fig. 1 becomes more noble with increasing distance x into the cavity. Consequently, the current density i_c of the hydrogen evolution reaction (HER) decreases on the cavity surface with increasing distance x into the cavity. The exact current and potential distributions on the internal cavity surface and the ionic distributions within the cavity electrolyte will depend on the dimensions of the cavity and the electrochemical conditions prevailing at the external cavity surface. Solutions to the steady state diffusion–migration flux equations have been reported for the case of hydrogen charging of a metal surface containing a rectangular crack, along with measurements of potential and some ionic concentrations within artificial cracks in active (Fe and Ni) and noble (Cu) metals [7]. However, the actual distributions can be much more non-uniform than the calculated distributions as a result of hydrogen gas accumulation inside the cavity [7,12]; it was shown that owing to gas constriction the measured potential drop was much greater than that calculated [7].

For cavities of sufficiently large aspect ratio $E(x)$ increases with increasing x to the E_{lim} value at the $x = x_{lim}$ location on the internal cavity surface and $E(x)$ is also at the E_{lim} value at greater distances into the cavity, $x \geqslant x_{lim}$, i.e. the internal cavity surface at $x \geqslant x_{lim}$ is not under the influence of the polarization condition at the outer surface [8,14]. In the simplest case of cathodic polarization E_{lim} is the equilibrium potential of the HER, such as would be the case if the electrode were a noble or inert metal, e.g. Cu in Ref. [7]. For an active metal, e.g. Fe, E_{lim} is the mixed potential established (deep) inside the cavity by both the HER and the metal dissolution reaction occurring at the same rate and potential [7,14,15] as shown in Fig. 1. Consequently, at $x \geqslant x_{lim}$ the anodic and cathodic reactions occur together at the same location rather than being separated as is the case at $x < x_{lim}$ where the anodic reaction occurs in part or totally outside the cavity on the counterelectrode.

From the perspective typically encountered in both laboratory experiments and service experience, where electrochemical conditions can be monitored only at $x = 0$, one wishes to know the distribution of potential and current within the cavity. Knowing only the sign of the potential distribution is usually not enough, e.g. in

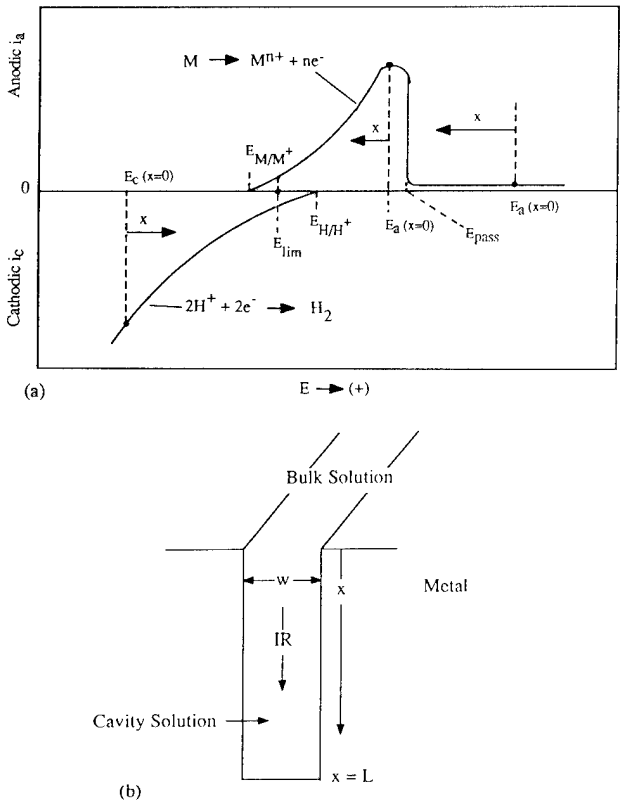

Fig. 1. Schematics that show (a) the directions of the shifts in the electrode potential on the cathodic and anodic polarization curves with increasing distance x into a cavity for cathodic, $E_c(x=0)$, and anodic $E_a(x=0)$, polarizations respectively and (b) a cavity with aspect ratio $a = w/L$.

designing cathodic protection systems or in analyzing the relative contributions of the HER and the metal dissolution reaction at the crack tip of a brittle-type crack propagation failure.

1.2. Anodic polarization in the active region

For anodic polarization of the external surface of a metal in the active region, i.e. $E_a(x=0) < E_{pass}$ in Fig. 1, $E(x)$ becomes less noble with increasing distance into a surface cavity. In accord with the decrease in overpotential, the rate of the metal dissolution reaction decreases with increasing distance x into the cavity. This current distribution follows the polarization curve in Fig. 1 from the higher current in the active region at $x=0$ to lower currents at $x>0$ and has the consequence that the aspect ratio of the cavity decreases with time. The presence of the cavity has the same effect on the overpotential and current distributions as in the case of cathodic polarization of the electrode: both the overpotential and the current density decrease with increasing distance into the cavity. Furthermore, as for cathodic polarization, a limiting electrode potential exists whose value is determined by the equilibrium potential of the metal dissolution reaction (for metals more noble than hydrogen) or by a mixed potential (as illustrated in Fig. 1) when both metal dissolution and hydrogen evolution occur beyond some distance into the cavity, as in the case of base metals.

1.2.1. Hydrogen embrittlement and stress corrosion cracking

In the context of crack propagation, beyond some stages of crack development, i.e. at greater than some aspect ratio, it follows that the E_{lim} condition also exists at the crack tip. Consequently, the crack propagation rate, to the extent that it depends on potential, responds to this E_{lim} value rather than to the potential at the metal's outer surface. With both metal dissolution and the HER occurring for the E_{lim} condition during either anodic or cathodic polarization, the conditions for hydrogen embrittlement and anodic stress corrosion cracking exist at the crack tip for either direction of polarization of the outer surface. For example, during free corrosion or anodic polarization of the sample the HER and its companion reaction, hydrogen absorption into the metal, can also occur at the crack tip (in addition to anodic dissolution) and can in principle lead to hydrogen embrittlement and subsequent failure of the structure.

1.3. Anodic polarization in the passive region

One often encounters a situation in which the external surface of the metal is under anodic polarization in the passive region, i.e. $E_a(x=0) > E_{pass}$ in Fig. 1 or E_{app} in the polarization curve of Fig. 2. This is a complicated situation which prevails in pitting and crevice corrosion. Consequently, its analysis is necessary for understanding the mechanism of these forms of localized corrosion. With the outer surface polarized into the passive region as shown in Figs. 1 and 2, $i(x=0)$ is the low current characteristic of the passive state. $E(x)$ decreases with increasing x and may decrease below E_{pass}. It is reported below that for active pits or crevices in iron $E(x)$ is below the passivation potential E_{pass} at some distance x_{pass} into the cavity. The situation $E(x) < E_{pass}$ occurs when the IR term in Eq. (1) exceeds the $\Delta\phi^*$ value defined in Fig. 2, i.e. $IR > \Delta\phi^*$. Hence, at $x > x_{pass}$, $E(x)$ is in the active region of the polarization curve where much higher metal dissolution rates can be supported. At greater distances the current decreases from the peak value in accord with the prevailing potential in the active region (Figs. 1 and 2). The local current flowing out of the cavity from these $x > x_{pass}$ locations decreases with increasing x (to zero at $x \geqslant x_{lim}$) and there is a region of the internal cavity surface (between $x_{H/H+}$ and x_{lim} corresponding to $E_{H/H+}$ and E_{lim}) where hydrogen gas evolution occurs.

These potential variations have been measured and the different potential regions at their specific distances into a cavity surface have been seen by in situ microscopy and photographically recorded [11,16,17], as shown in the photograph in Fig. 2. The region on the photograph between x_{pass} and x_{lim} labeled "active crevicing" develops the shape shown schematically in cross-section in the upper left diagram of Fig. 2. This shape reflects the kinetics in the active region of the polarization curve shown schematically at the top right of Fig. 2. The small round spots in the lower half of the photograph are hydrogen gas bubbles resulting from the HER in its potential region on the internal cavity surface. The bubbles grow while in place on the cavity surface.

For the case of iron in acidic solutions, e.g. the pH 4.6 buffered solution in Fig. 2, the measured potential inside cavities whose aspect ratios exceed the critical value for crevice corrosion decreases in a matter of seconds or minutes to the active loop region of the polarization curve. This decrease in $E(x)$ is matched by a steep increase in current to the 1–10 mA range. Since these synchronous $E(x)$ and I values have been found to be in accord with the polarization curve for the (bulk) electrolyte, the $IR > \Delta\phi^*$ condition is met virtually immediately and crevice corrosion begins simultaneously. Consequently, crevice corrosion begins without a need for prior changes in ionic concentration of the cavity electrolyte. This is in agreement with the constant measured pH in cavities formed in buffered acidic solutions (Fig. 2) [18,19].

On the other hand, this is not the situation in alkaline solutions, in the sense that considerable time (of the

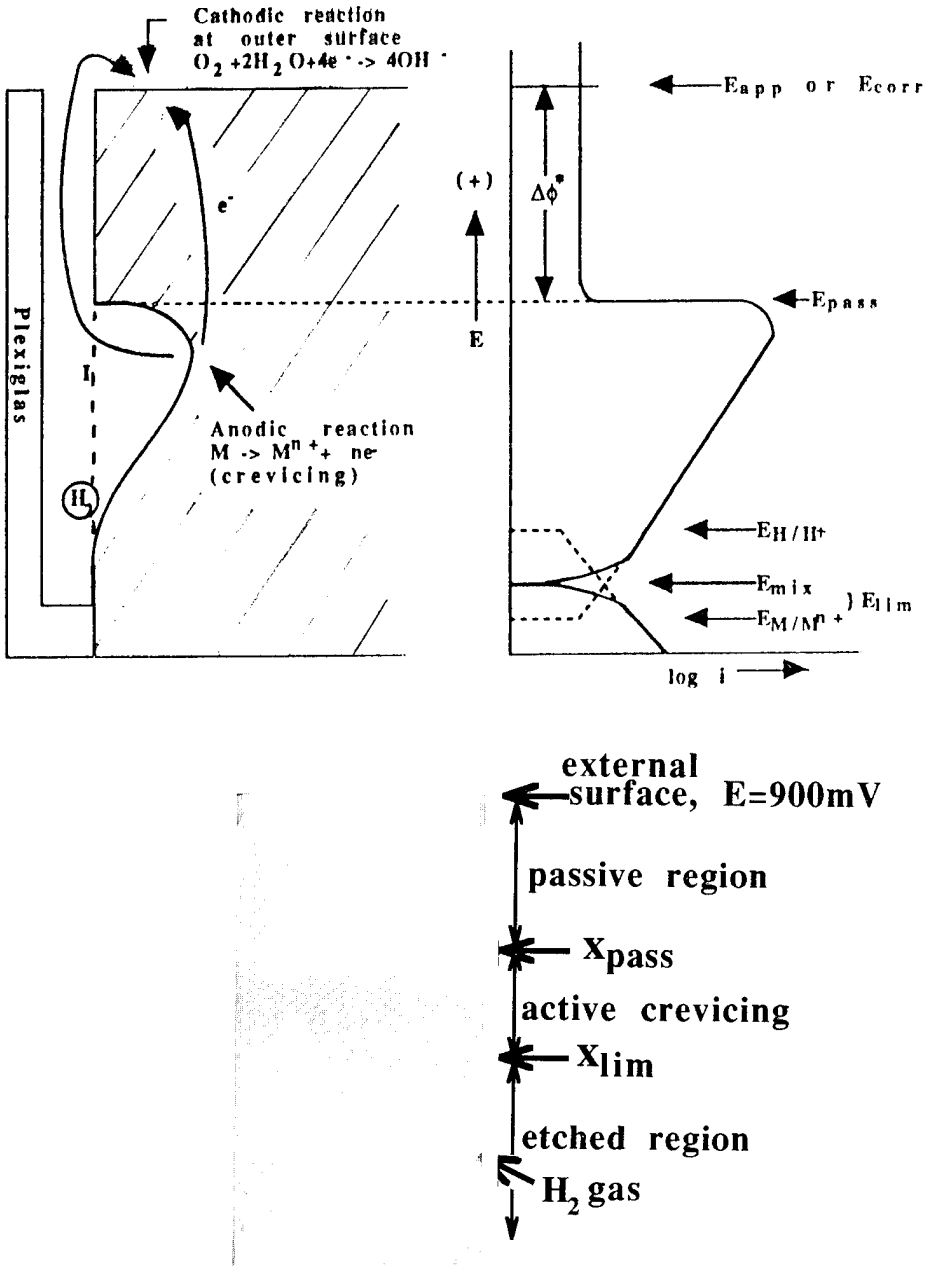

Fig. 2. Schematic illustrating metal dissolution and the HER on the internal cavity surface, with their locations corresponding to their respective polarization curves shown on the right, and in situ photograph of the corroding internal cavity surface taken through the Plexiglas (rebar steel in pH 4.7 acetic acid buffer solution [16]).

order of hours) is required before the measured potentials inside the cavity decrease significantly and crevice corrosion begins [19]. Thereafter the qualitative behavior is the same as for acid solutions. The $E(x)$ and I values change synchronously: during the induction period $E(x)$ decreases slightly from the $E(x=0)$ value and the low (passive) current increases slightly. Then much sharper and bigger changes in $E(x)$ and I occur synchronously during the transition to stable crevice corrosion [19]. Also, the same spatial regions are seen on the crevice surface as in the photograph of Fig. 2. One explanation for the induction period is that the $IR > \Delta\phi^*$ criterion is met only after acidification of the cavity electrolyte occurs during the induction period (12–15 h in Ref. [19]) as the original buffering capacity decreases because of the restricted cavity opening. In this case, since a lower pH increases the IR term and decreases the $\Delta\phi^*$ term [6,7,15], crevice corrosion begins when the pH has decreased to the value for which the condition $IR > \Delta\phi^*$ is met (for a given set of values for the other key parameters, i.e. aspect ratio, electrolyte conductivity and $E(x=0)$, as follows from the modeling results reported below).

1.4. Modeling of the potential and current distributions

The current distribution as a function of distance into a crevice can be calculated from the measured potential distribution [16]. The potential distribution can be readily measured for metal–electrolyte systems for which the required aspect ratio for susceptibility to crevice corrosion is relatively small. Then the cavity can be designed with a relatively large opening (e.g. 0.5 mm) so that the Luggin capillary probe can be moved in and out of the cavity [6,7,15–19]. Example systems with small critical aspect ratios for meeting the $IR > \Delta\phi^*$ condition are iron or nickel in acid solutions. The calculation method and its application to crevicing in steel are given elsewhere [16]. Modeling by Doig and Flewitt [8] also bears on this issue.

A first-generation computational model is now available for calculating the initial potential and current distributions and for predicting susceptibility to active dissolution (localized corrosion) within the cavity for a limiting situation [10]. The model is for the complex active–passive anodic polarization situation depicted in Figs. 1 and 2 where simultaneously both active and passive regions exist on the cavity surface. Because of this complexity, it is necessary to simplify other parameters. In particular, it was assumed that the concentrations of all species are uniform throughout the electrolyte, that linear geometry prevails and that the conductivity is uniform. These simplifications restrict the application of the model to a limited number of real systems. For example, metal–electrolyte systems for which the pH is constant include iron or nickel in buffered acidic sulfate solutions [17–20]. In this event the E_{pass} value of the polarization curve is relatively constant. Thus the flux equation is replaced with Ohm's law, current conservation and Laplace's equation for determining the potential and current distributions [10,11]. These systems, e.g. Fe–acidic SO_4^{2-}, also have small critical aspect ratios for IR-induced corrosion because of the large anodic currents in the active loops of their polarization curves. Consequently, a rather open cavity can be used which firstly facilitates the potential and ionic measurements inside the cavity, secondly reduces the extent to which gas bubbles from the HER (or solid corrosion products) modify the geometry of the cavity and thirdly enables effective pH control if a buffer is used. Solutions to the Laplace equation for regularly shaped cavities (rectangular crevice or cylindrical pit) and a non-linear boundary condition represented by the kinetics in the polarization curve were obtained using a finite element method [10,11,20].

The inputs needed in the model to calculate the potential and current distributions are the cavity aspect ratio, the electrolyte conductivity, the outer ($x = 0$) surface corrosion potential (or applied potential) and the metal–electrolyte polarization curve. The model predicts whether or not active dissolution in the cavity will occur for systems such as Fe–acidic SO_4^{2-} for which the polarization curve does not change appreciably during the induction period, i.e. susceptibility to crevice corrosion can be predicted for an existing cavity of given depth and opening dimensions. If the model predicts an active region in the cavity, crevice corrosion starts immediately upon exposure to the corrosive. If instead the model predicts that the entire cavity surface is in the passive state, active dissolution does not occur, at least not immediately. Crevice corrosion may still start eventually if the cavity electrolyte polarization curve changes appreciably with time in the direction of increasing the IR term or decreasing the $\Delta\phi^*$ term or both, e.g. if E_{pass} shifts in the noble direction, $\Delta\phi^*$ decreases, or if the peak current in the active region increases, IR increases. For iron, stainless steels and other alloys both these changes in the E–i curve occur when either the pH decreases or the Cl^- concentration increases in the cavity electrolyte [17–19]. These changes in solution composition also increase the magnitude of the passive current and, since the IR term increases, could be important for initiation of crevice corrosion when the entire surface is already in the passive state prior to or during exposure to the polarization condition at the outer ($x = 0$) surface.

Thus the size of the active loop, the active–passive transition potential and the passive current are strongly related to the solution composition, in particular pH or aggressive ion concentration in the cavity electrolyte[2]. In addition, passivating inhibitors also produce changes in the E–i curve but in the opposite direction to those produced by an increase in H^+ or Cl^- ion, so that the IR and $\Delta\phi^*$ terms shift in the opposite directions, making it more difficult to meet the $IR > \Delta\phi^*$ condition, as shown for the chromate ion [13,18,19]. This could explain the experimentally observed behavior of chromate as an inhibitor of crevice corrosion in iron.

The first test of the model was carried out for Fe in a buffered (pH 4.6) acidic solution [10]. The electrode potential at the outer ($x = 0$) surface was varied from 160 to 900 mV vs. a saturated calomel electrode (SCE), all being potentials in the passive region of the polarization curve. The model was then used to predict the depth into a crevice of given opening dimension (0.5 mm) below which active dissolution of the iron would occur, i.e. the x_{pass} value. The predicted x_{pass}

[2] Accumulation of aggressive anions in and/or acidification of the cavity solution are essential for meeting the $IR > \Delta\phi^*$ criterion when there is no active loop in the anodic polarization curve for the bulk electrolyte, e.g. as is the case for iron in some alkaline solutions and probably also for stainless steel in alkaline solution. In the case of stainless steel (or Al) an anodic loop, if present in the Cr (or Al) partial polarization curve at small overpotentials, may not be visible in the measured E–i curve because of domination of the measured current by the HER.

value increased from 0.15 to 0.60 cm for $E(x=0)$ increasing from 160 to 900 mV(SCE). Experiments were then performed using the buffered Fe–acidic sulfate solution and crevices of the same 0.5 mm opening dimension and a depth of 1 cm (which was greater than the largest predicted depth of $x_{pass} = 0.6$ cm). In all the experiments, active dissolution of the iron occurred as predicted and the measured x_{pass} location was nearly identical with the calculated value [10]. This good agreement between the calculated and predicted depth below which active crevicing occurs is a validation of the model and a strong quantitative support for the hypothesis that potential distribution is the fundamental factor affecting the localized corrosion process in this system. Note that the model is expected to be reasonably accurate for this system, since E_{pass} does not change appreciably with time, i.e. the pH was fixed by the buffer and by the fact that pH 4.6 is near the equilibrium pH for the hydrolysis reaction (pH 3–4); also, there were no aggressive ions such as Cl^- in the electrolyte.

The second test of the model was carried out for the same system using cylindrical cavities 1 mm in diameter. In this test the model was used to predict the x_{pass} value; the calculations give $x_{pass} = 0.27$–0.28 cm. Then, using a drill, cylindrical pits with depths less than and greater than this calculated x_{pass} value were drilled into the iron samples, one pit per sample. These samples were exposed to the buffered pH 4.6 solution with the outer surface held in the passive region at 300 mV(SCE). There was no active metal dissolution for the sample with the pit 0.25 cm deep, as predicted by the model; the test was run for 50 h. However, for the samples with the pits 0.30, 0.40 and 0.50 cm deep, active metal dissolution was noted without delay by the measured current, again as predicted. This occurrence of localized corrosion was subsequently confirmed by microscopic examination of the large corrosion-produced cavity viewed along its cross-section. This result is also a strong support for the validity of the model and the potential distribution premise upon which it is based. For the deeper pits, hydrogen gas bubbles evolved out of the pits, confirming that the active dissolution was caused by a potential shift to sufficiently negative values to allow for both hydrogen evolution and active metal dissolution within the pits.

1.5. The potential distribution in other forms of corrosion

The potential distribution is expected to be large and important in most if not all forms of non-uniform corrosion. These may include the transition from metastable to stable pitting [11], grain boundary corrosion once a grain boundary groove forms by any other process [21], dealloying and all forms of crack propagation. In addition, powder metallurgical structures of metals exhibiting active–passive behavior are potentially susceptible to the $IR > \Delta\phi^*$ form of localized corrosion, an example being sintered iron in ammoniacal solution [22]. Examples of the $IR > \Delta\phi^*$ and other IR-induced phenomena inside cavities are briefly discussed next in the context of the cathodic HER, the surface diffusion mechanism of dealloying corrosion and the transition from metastable to stable pitting corrosion.

2. Hydrogen charging inside cavities during anodic polarization

Whereas the above considerations show that the rates of the HER and therefore also hydrogen entry into the metal during cathodic polarization of the external metal surface decrease with increasing distance into a cavity, they show the opposite trend during anodic polarization. Thus, for anodic polarization of the external metal surface, the HER tendency increases with increasing distance into the cavity. At the outer surface ($x = 0$) the tendency for the HER is often zero, e.g. for anodic polarization of iron or stainless steel into the passive region, as depicted in Fig. 1, whereas deep inside a cavity a finite rate of the HER and hydrogen charging may occur.

Thus hydrogen charging of a ferrous alloy during anodic polarization can only occur if a cavity exists in the surface with a sufficiently large aspect ratio. A crevice formed by the contact of the alloy and another material could readily meet this requirement. Alternatively, the cavity may form during service. In a recent investigation of the grain boundary corrosion of a sensitized stainless steel it was found that anodic dissolution of the chromium-depleted zone produced grooves along the grain boundaries which eventually acquired an aspect ratio for which the $IR > \Delta\phi^*$ condition for dissolution of the non-sensitized alloy was met. Thereafter anodic dissolution of the bulk alloy of normal chromium content commenced inside the grooves accompanied by the HER [21]. The gas has now been identified as hydrogen and it has been established that some of the hydrogen enters the steel. These conclusions are based on the results of experiments utilizing the hydrogen permeation concept illustated in Fig. 3 [23]. Others have also observed hydrogen charging for anodic polarization conditions at the outer surface of the metal that are thermodynamically unfavorable for the HER [24–27].

Normal operation of the permeation experiment [28] is shown in Fig. 3(a), where the HER occurs on the surface of the metal membrane in cell 1 and some of the discharged protons enter the metal, diffuse to the other surface of the metal and are oxidized back to the proton in cell 2. The oxidation current in cell 2 is a measure of the hydrogen flux through the metal mem-

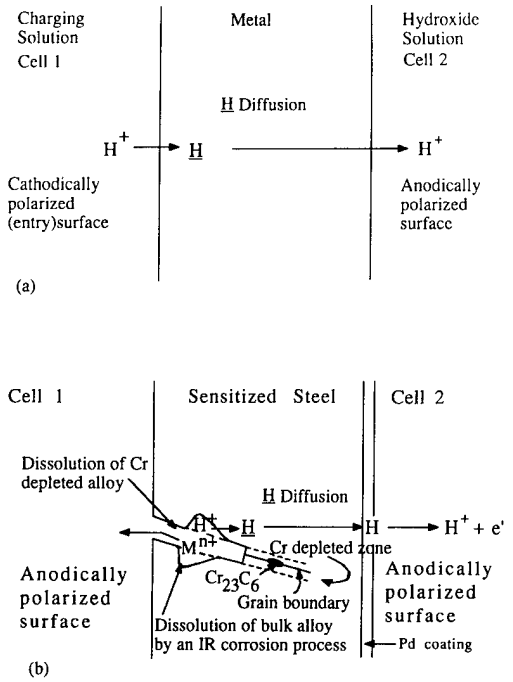

Fig. 3. Schematics of (a) the conventional arrangement for cathodic charging and permeation of hydrogen and (b) an arrangement where both surfaces are anodically polarized so the hydrogen charging can only occur deep inside cavities where $E(x)$ is much less noble.

brane. In this experiment the metal surface in cell 2 is anodically polarized so that the reaction

$$H_3O^+ + e^- = H_{ad} + H_2O \quad (2)$$

proceeds in the backward (right to left) direction, while the metal surface in cell 1 is cathodically polarized so that reaction (2) occurs in the forward direction followed by

$$H_{ad} + H_{ad} \longrightarrow H_2 \quad (3a)$$

or

$$H_{ad} + H_3O^+ + e^- \longrightarrow H_2 + H_2O \quad (3b)$$

and

$$H_{ad} \longrightarrow H_{ab} \quad (3c)$$

For steady state permeation of hydrogen through the metal membrane the rate of reaction (2) in cell 2 (backward direction) equals the rate of reaction (3c) in cell 1 (forward direction). Since hydrogen has a uniquely high solid state diffusivity in iron, the permeation current can be used to positively identify the diffusing species as hydrogen.

The experiment illustrated in Fig. 3(b), however, is radically different in that the metal surface in cell 1 is anodically polarized rather than cathodically polarized. Hence there is no tendency for the HER to occur at either of the metal surfaces. Rather, both surfaces are in a thermodynamic condition for which hydrogen atoms would be oxidized to the ionic state, H^+, in accordance with reaction (2) proceeding from right to left. Consequently, only if the electrode potential shifts significantly (10^2 mV) in the less noble direction on some internal cavity surface will reactions (2) and (3) proceed in the forward direction. The exact magnitude of the shift depends on the pH of the electrolyte—E_{H/H^+} shifts in the noble direction for increasing acidity of the electrolyte—and on the applied potential at the membrane surface. At pH values below the equilibrium pH for the hydrolysis reactions (e.g. below pH 2 for stainless steel) the pH of the cavity solution increases during anodic polarization with increasing distance into the cavity in accord with the migration of the positive H_3O^+ ions out of the cavity [6]. Hence the most noble equilibrium potential for the HER will exist for the bulk solution electrolyte and will decrease with increasing distance into the cavity when the bulk solution pH is less than the equilibrium pH for the hydrolysis reactions.

In the Kelly et al. [21] experiments on a sensitized type 430 ferritic stainless steel in 1 N H_2SO_4 (pH 0.36), anodic dissolution of the Cr-depleted alloy in the grain boundaries occurs during anodic polarization at 192 mV vs. a normal hydrogen electrode (NHE) to produce grain boundary grooves. The depth of these grooves, but not their width, which is set by the width of the chromium-depleted layer, increases with time. Hence the aspect ratio of the grooves and the magnitude of the *IR* drop inside the grooves also increase with time. At the time and depth which correspond to the $IR > \Delta\phi^*$ condition, $E(x)$ is less than E_{pass} for the bulk (normal Cr content) stainless steel in the cavity electrolyte and therefore active anodic dissolution of the bulk alloy is expected. From this time on, *IR*-induced corrosion of both the bulk and Cr-depleted alloy occurs at this and greater distances into the grooves. The transition from a Cr depletion to an *IR* mechanism of corrosion is consistent with the observation of subsurface grain boundary cavities which are much wider than the width of the Cr-depleted layer and with the observation of (hydrogen) gas bubble evolution from inside the grain boundary grooves.

The gas bubbles observed evolving from the grain boundary grooves [21] are hydrogen which forms by reactions (2) and (3a) or (3b) proceeding in the forward direction at locations deep inside the grooves where $E(x) < E_{H/H^+}$. In this event the occurrence of reaction (3c) in the forward direction is also expected and was recently confirmed in another experiment using the hydrogen permeation cell shown in Fig. 4 in the mode shown in Fig. 3(b) [23]. The surface of the stainless steel membrane in cell 1 (1 N H_2SO_4) was anodically polarized at 192 mV(NHE), causing the Cr-depleted alloy along the grain boundaries to dissolve. The other Pd-coated surface of the stainless steel membrane in cell 2

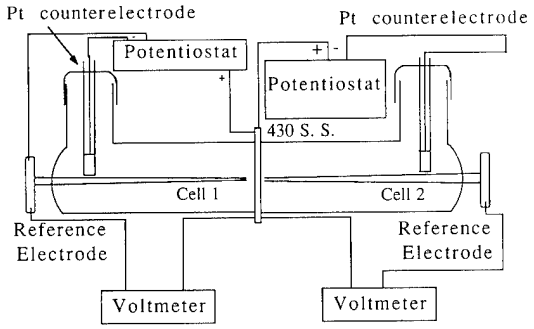

Fig. 4. Schematic of the permeation apparatus which can be used in either mode of operation (depicted in Fig. 3) by applying either cathodic or anodic polarization in cell 1.

(0.1 N NaOH, pH 13) was anodically polarized at 296 mV(NHE), for which potential in this alkaline solution both the bulk and Cr-depleted alloys are passivated and highly resistant to corrosive attack. At both stainless steel surfaces in cells 1 and 2 the imposed electrochemical conditions strongly favor reactions (2) and (3) to proceed in the backward direction, so there is no possibility for hydrogen charging to occur at the stainless steel membrane surfaces in cells 1 and 2. Thus the only possibility for hydrogen entry into the membrane is if the situation depicted in Fig. 3(b) develops, i.e. grooves form (along the grain boundaries) and achieve the critical aspect ratios for reactions (2) and (3) to occur in the forward direction deep inside the grooves where $E(x) < E_{H/H^+}$. Once reaction (3c) occurs (forward direction), the hydrogen entering the membrane will diffuse to the surface locations that are at potentials more positive than the E_{H/H^+} equilibrium potential and be oxidized back to the proton, i.e. reaction (3c) followed by reaction (2), both occurring in the backward direction. In the case of the Pd-coated membrane surface in cell 2, oxidation of the arriving hydrogen will be uniquely indicated by the current measured in cell 2 during the time preceding total penetration of the sample thickness by the grain boundary gooves. As such, the hydrogen permeation experiment can be used as a definitive test of hydrogen charging on the cavity surface for metal–electrolyte systems whose outer surfaces are otherwise under strongly oxidizing conditions unfavorable for reactions (2) and (3) to occur in the forward direction.

3. Role of potential distribution in dealloying and pitting corrosion

Since the aspect ratio of a regularly shaped cavity is the ratio of the cavity depth to its smallest opening dimension, e.g. depth to radius of a cylindrical pit, the critical aspect ratio corresponding to the $IR = \Delta\phi^*$ condition can in principle be achieved for cavities of any size. In both dealloying and pitting corrosion there is a critical anodic polarization above which a planar surface breaks down by the formation of stable pits, referred to as the critical potential E_c in dealloying and the pitting potential E_p in pitting corrosion. Both these forms of corrosion exhibit metastable behavior. Pits form and then might repassivate even above the E_p potential [6,29–35]. In dealloying corrosion, metastable pitting occurs below the E_c potential [36,37]. Above the E_c potential, catastrophic, global pitting immediately occurs in dealloying corrosion, in contrast with the random, stochastic pitting that occurs in pitting corrosion [32,38].

There is a major difference in the polarization behaviors of dealloying corrosion and pitting corrosion. In alloys susceptible to dealloying corrosion a protective layer of the more noble metal readily forms at low overpotentials, i.e. a passive state exists at $E < E_c$, whereas at higher overpotentials the alloy is in the active state, as shown in the classic dealloying polarization curve in Fig. 5 [39–42]. On the other hand, in metals susceptible to pitting corrosion the active region is at low overpotentials and the passive region is at higher overpotentials (Figs. 1 and 2). Thus non-uniform (pitting-type) corrosion in different metal–electrolyte systems can be characterized or distinguished in terms of the system's passivation–overpotential relationship. The difference in this relationship for dealloying corrosion and pitting corrosion is surely related to

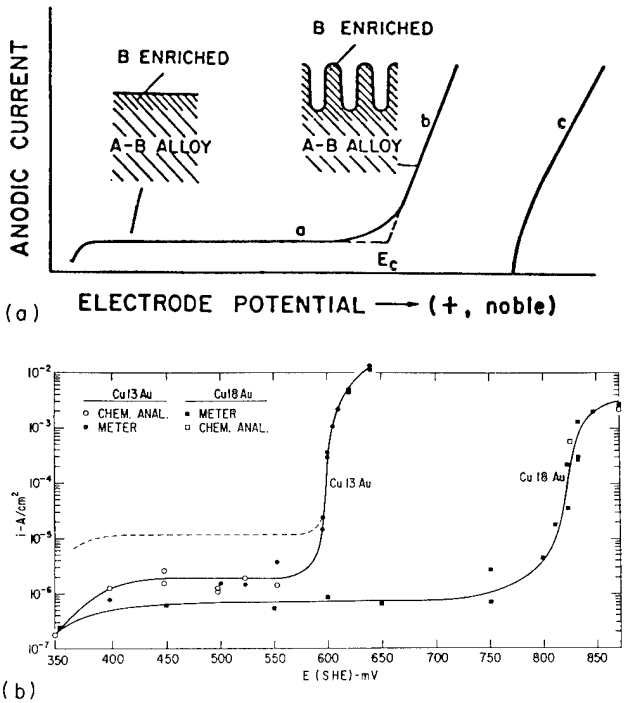

Fig. 5. The classic polarization behavior for systems susceptible to dealloying corrosion: (a) schematic [41]; (b) Cu–Au compositions in 1 N Na_2SO_4 and 0.01 N H_2SO_4 [42].

the fact that in dealloying corrosion the protective (passive) layer typically consists of the alloy constituents in the reduced form, e.g. an Au or Au–Cu alloy protective layer for the Cu–Au alloy system, whereas in pitting corrosion it consists of the alloy constituents in the oxidized form, e.g. iron oxides in the case of iron. One of the consequences of the active region being at higher rather than lower overpotentials in dealloying corrosion is that the $IR > \Delta\phi^*$ stability criterion of localized corrosion is not applicable. This follows from the fact that $\Delta\phi^*$ is undefinable in the absence of an anodic loop at low overpotentials in Fig. 5.

3.1. Surface diffusion and IR voltage in dealloying corrosion

Even though $\Delta\phi^*$ is undefinable in the polarization curve of Fig. 5, a significant potential distribution exists in principle within the porous structure that forms during corrosion at $E(x=0) > E_c$. Since E_c is 10^2–10^3 mV positive of $E_{Cu/Cu^{2+}}$ (Fig. 5(b)), the overpotential for anodic dissolution of the less noble metal is extraordinarily large, e.g. 0.5 V. Hence, at the start of dealloying of a planar alloy surface, all Cu atoms in direct contact with the electrolyte will be immediately oxidized, i.e. the activity of zero-valent Cu in contact with the electrolyte approaches zero. However, the potential distribution within the electrolyte of the porous structure that forms during dealloying corrosion soon becomes very steep in view of the pore structure's increasing aspect ratio with time of dealloying. The magnitude of the aspect ratio may be taken as the momentary thickness of the porous layer divided by the pore diameter, since the pore diameter is relatively independent of the thickness of the porous layer [43–46]. Thus the geometrical situation is a cylindrical cavity (pore) which increases in size only in the depth direction. Therefore the *IR* drop within the developing pore structure quickly becomes large so that $E(x)$ at the bulk alloy–pore electrolyte interface approximates the limiting potential E_{lim} beyond some critical thickness of the porous layer. For an all-noble-metal alloy such as Cu–Au, E_{lim} is the equilibrium potential of the Cu/Cu^{2+} reaction in non-complexing electrolytes [15]. Thus, except at the very early stages of the pore structure development, $E(x) \approx E_{Cu/Cu^{2+}}$ at the bulk alloy–pore electrolyte interface.

This low overpotential condition at the bulk alloy–pore electrolyte interface allows for a finite activity of Cu at the bottom of the pore. In principle, this could allow for the diffusion of Cu adatoms along the alloy–electrolyte interface and their incorporation with diffusing Au adatoms to form a solid solution Au–Cu alloy in the walls of the developing porous structure. For some experimental conditions the pore wall structure can contain significant amounts of the less noble metal, e.g. 10%–40% Cu is well documented by lattice parameter measurements using X-ray diffraction at advanced stages of the pore structure formation in Cu–Au alloys [44,47], while intermetallic phases form in the porous structure of Zn–Cu alloys [47]. Thus the formation of an alloy phase via a surface (or interface) transport process means that in addition to the interface diffusion of the more noble metal adatoms, some of the less noble metal adatoms simultaneousy diffuse via the interface to form the alloy walls of the porous structure.

In summary, at the beginning of a dealloying process that occurs via transport in the plane of the alloy–electrolyte interface, the residual Au pore wall structure that forms will contain little or no Cu. However, the situation changes as the porous layer thickens and the aspect ratio increases for the pores. Hence $E(x)$ at the base of the pores may be less noble than $E(x=0)$ by comparable *IR* drops of 10^2–10^3 mV according to Eq. (1). In this event the actual overpotential for Cu dissolution at the base of the pores will be quite small and Cu adatom lifetimes correspondingly long. In this way one can explain the later stage formation of an Au–Cu alloy porous structure via the surface diffusion of Cu and Au adatoms.

Alternatively, these alloy porous structures can be considered to form via transport normal to the alloy–electrolyte interface [44,47] as they do during dealloying of alloy-gas systems at elevated temperatures [43,46]. Several results indicate that a modified alloy of finite depth at the alloy–electrolyte interface, or selvedge, exists during dealloying corrosion [37,48–50]. It is not clear, however, if the selvedge thickness can be as large as the 5–10 nm wall thickness of the pore structure revealed by transmission electron microscopy [45]. The selvedge with a lower density would be more supportive of an interdiffusion process than the bulk alloy. The dynamic condition that exists during dealloying within the many atomic layers comprising the selvedge is indicated by the measured capacity, which changes significantly during and after dissolution [48,49], and by other measurements [37,50].

3.2. The metastable-to-stable transition in pitting corrosion

Following the initial passive film breakdown and repassivation event, a small micropit remains under the newly formed passive film. For various reasons a second breakdown could occur at this same site followed by a second repassivation; consequently, the micropit deepens and the aspect ratio increases. This breakdown–repassivation sequence may continue until the aspect ratio exceeds the critical value and the pitting process stabilizes in accord with the $IR > \Delta\phi^*$ criterion,

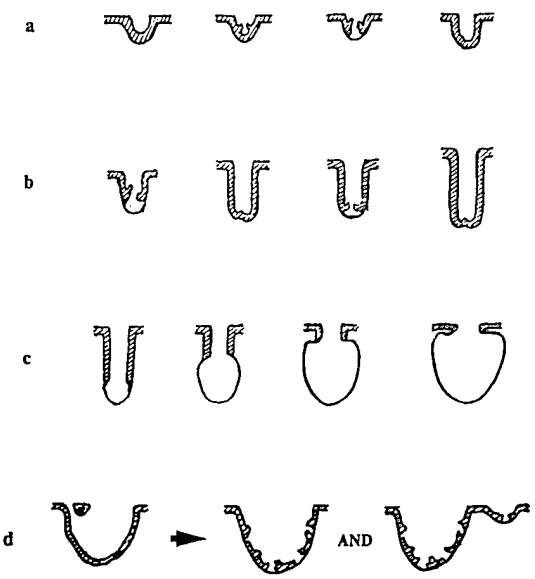

Fig. 6. Schematic of pit initiation and growth. (a) Local breakdown of the passive film and repassivation. (b) Breakdown and repassivation repeat, with the micropit deepening. (c) The micropit stabilizes when reaching the critical aspect ratio corresponding to the $IR \geq \Delta\phi^*$ condition and then grows. (d) The pit penetrates the outer surface from within, forming many holes in a repetitive fashion aroung its original opening, probably controlled by the $IR > \Delta\phi^*$ criterion [11,18], and eventually loses its cover to form the hemispherical shape [6,11].

i.e. the depth reaches the critical depth for the existing micropit diameter so that the micropit bottom is in the active region of the polarization curve of the metal in the micropit solution [11]. Under this condition, repassivation is no longer possible and the pitting process stabilizes. This transition from metastable to stable pitting at a critical aspect ratio for the $IR > \Delta\phi^*$ condition is schematically illustrated in Fig. 6.

4. Conclusions

Some consequences of steep potential gradients in cavities are as follows.

(1) Localized corrosion processes, e.g. crevice corrosion, occur when $IR > \Delta\phi^*$.

(2) The HER and hydrogen charging occur inside cavities during anodic polarization of their outer surfaces.

(3) The formation of an alloy porous structure during dealloying corrosion can be rationalized by a surface diffusion mass transport process.

(4) The transition from metastable to stable pitting corrosion can be rationalized by the $IR > \Delta\phi^*$ concept of localized corrosion.

Acknowledgments

B.G. Ateya and K.G. Weil provided valuable discussion, A. Sehgal assisted in the preparation of the figures, and some aspects of the work were sponsored by the Office of Naval Research, the National Science Foundaton and/or the International Copper Association.

References

[1] I.L. Rosenfeld and I.K. Marshakov, *Corrosion, 20* (1964) 115t.
[2] G. Herbsleb and J.H. Engell, *Z. Elektrochem., 65* (1961) 881; *Werkstoffe Korros., 17* (1966) 365.
[3] N.D. Greene, W.D. France Jr. and B.E. Wilde, *Corrosion, 21* (1965) 275.
[4] W.D. France Jr. and N.D. Greene Jr., *Corrosion, 24* (1968) 247.
[5] C.M. Chen, F.H. Beck and M.G. Fontana, *Corrosion, 27* (1971) 234.
[6] H.W. Pickering and R.P. Frankenthal, On the mechanism of localized corrosion of iron and stainless steel, *J. Electrochem. Soc., 119* (1972) 1297, 1304.
[7] B.G. Ateya and H.W. Pickering, On the nature of electrochemical reactions at a crack tip during hydrogen charging of a metal, *J. Electrochem. Soc., 122* (1975) 1018.
[8] P. Doig and P.E.J. Flewitt, *Metall. Trans. A, 9* (1978) 357.
[9] J.C. Walton, *Corros. Sci., 30* (1978) 357.
[10] Y. Xu and H.W. Pickering, The initial potential and current distributions of the crevice corrosion process, *J. Electrochem. Soc., 140* (1993) 658.
[11] Y. Xu, M. Wang and H.W. Pickering, On electric field induced breakdown of passive films and the mechanism of pitting corrosion, *J. Electrochem. Soc., 140* (1993) 3448.
[12] D. Harris and H.W. Pickering, On anodic cracking during cathodic hydrogen charging, in A.W. Thompson, I.M. Bernstein and A.J. West (eds.), *Effect of Hydrogen Behavior of Materials*, AIME, Warrendale, PA, 1976, p. 229.
[13] H.W. Pickering, The significance of the local electrode potential within pits, crevices and cracks, *Corros. Sci., 29* (1989) 325.
[14] B.G. Ateya and H.W. Pickering, Electrochemical processes within cavities and their relation to pitting and cracking, in A.W. Thompson and I.M. Bernstein (eds.), *Hydrogen in Metals*, American Society for Metals, Metals Park, OH, 1974, p. 206.
[15] H.W. Pickering, On the roles of corrosion products in local cell processes, *Corrosion, 42* (1986) 125.
[16] E.A. Nystrom, J.B. Lee, A.A. Sagues and H.W. Pickering, An approach for estimating anodic current distributions in crevice corrosion from potential measurements, *J. Electrochem. Soc., 141* (1994) 358.
[17] H.W. Pickering, K. Cho and E.A. Nystrom, Microscopic and local probe method for studying crevice corrosion and its application to iron and stainless steel, *Corros. Sci., 35* (1993) 775.
[18] A. Valdes and H.W. Pickering, *IR* drops in the absence of gas constrictions during crevicing of iron, in H. Isaacs, U. Bertocci, J. Kruger and S. Smialowska (eds.), *Advances in Localized Corrosion*, NACE 9, National Association of Corrosion Engineers, Houston, TX, 1990, p. 393; A. Valdes Moldon, *Ph.D. Thesis*, The Pennsylvania State University, University Park, PA, 1987.
[19] K. Cho and H.W. Pickering, The role of chloride ions in the $IR > IR^*$ criterion for crevice corrosion in iron, *J. Electrochem. Soc., 138* (1991) L56; Demonstration of crevice corrosion in alkaline solution without acidification, *J. Electrochem. Soc., 137* (1990) 3313; K. Cho, *Ph.D. Thesis*, The Pennsylvania State University, University Park, PA, 1992.

[20] M. Wang, H.W. Pickering and Y. Xu, Potential distribution, shape evolution and modeling of pit growth for Ni in sulfuric *J. Electrochem. Soc.*, in press.
[21] W.K. Kelly, R.N. Iyer and H.W. Pickering, Another grain boundary corrosion mechanism in sensitized stainless steel, *J. Electrochem. Soc.*, *140* (1993) 3134.
[22] H.S. Kim, Y.T. Kho, K. Osseo-Asare and H.W. Pickering, Active and passive behavior of sintered iron in ammoniacal ammonium carbonate solution, *Metall. Trans. B*, *22* (1991) 323.
[23] A. Sehgal, *Ph.D. Thesis*, The Pennsylvania State University, University Park, PA, 1995.
[24] J.H. Shively, R.F. Hehemann and A.R. Troiano, *Corrosion*, *23* (1967) 215.
[25] C.F. Barth, E.A. Steigerwald and A.R. Troiano, *Corrosion*, *25* (1969) 353.
[26] B.E. Wilde, *Corrosion*, *27* (1971) 326.
[27] I.H. Craig and R.N. Parkins, *Br. Corros. J.*, *19* (1984) 3.
[28] M.A.V. Devanathan and L. Stachurski, The mechanism of hydrogen evolution on iron in acid solutions by determination of permeation rates, *J. Electrochem. Soc.*, *111* (1964) 619.
[29] N. Stolica, *Corros. Sci.*, *9* (1969) 205.
[30] A.P. Bond and E.A. Lizłovs, *J. Electrochem. Soc.*, *115* (1968) 1130.
[31] P. Forchhemmer and H.J. Engell, *Werkstoffe Korros.*, *20* (1969) 1.
[32] D.E. Williams, C. Westcott and M. Fleischmann, *J. Electrochem. Soc.*, *132* (1985) 1804.
[33] G.S. Frankel, L. Stockert, F. Hunkeler and H. Böhni, *Corrosion*, *43* (1987) 429.
[34] H. Böhni and L. Stockert, *Werkstoffe Korros.*, *40* (1989) 63.
[35] P.C. Pistorius and G.T. Burstein, *Corros. Sci.*, *33* (1992) 1885.
[36] B. Kabius, H. Kaiser and H. Kaesche, in E. McCafferty and R.J. Brodd (eds.), *Surfaces, Inhibition, and Passivation*, Electrochemical Society, Pennington, NJ, 1986, pp. 562–573.
[37] J.D. Fritz and H.W. Pickering, Selective anodic dissolution of Cu–Au alloys: TEM and current transient study, *J. Electrochem. Soc.*, *138* (1991) 3209.
[38] T. Shibata and T. Takeyama, *Nature*, *260* (1976) 315.
[39] H. Gerischer and H. Rickert, *Z. Metallkd.*, *46* (1955) 681.
[40] L. Graf and J. Budke, *Z. Metallkd.*, *46* (1955) 378.
[41] H.W. Pickering, Characteristic features of alloy polarization curves, *Corros. Sci.*, *23* (1983) 1107.
[42] H.W. Pickering and P.J. Byrne, On preferential anodic dissolution of alloys in the low current region and nature of the critical potential, *J. Electrochem. Soc.*, *118* (1971) 209.
[43] H.W. Pickering and Y.S. Kim, De-alloying at elevated temperatures and at 298 K—similarities and differences, *Corros. Sci.*, *22* (1982) 621.
[44] H.W. Pickering and C. Wagner, Electrolytic dissolution of binary alloys containing a noble metal, *J. Electrochem. Soc.*, *114* (1967) 698.
[45] H.W. Pickering and P.R. Swann, Electron Metallography of chemical attack upon some alloys susceptible to stress corrosion cracking, *Corrosion*, *19* (1963) 373t.
[46] Y.S. Kim and H.W. Pickering, Kinetics of chlorination of Co and Co–10 a/o Pt alloy by reaction with HCl gas, *Metall. Trans. B*, *13* (1982) 349.
[47] H.W. Pickering, Formation of new phases during anodic dissolution of Zn-rich Cu–Zn alloys, *J. Electrochem. Soc.*, *117* (1970) 8; Volume diffusion during anodic dissolution of a binary alloy, *J. Electrochem. Soc.*, *115* (1968) 143.
[48] H.W. Pickering, The surface roughening of a Cu–Au alloy during electrolytic dissolution, *J. Electrochem. Soc.*, *115* (1968) 690.
[49] C. Wagner, *J. Electrochem. Soc.*, *116* (1969) 343.
[50] U. Pittermann, R. Reining and K.G. Weil, *J. Electrochem. Soc.*, *141* (1994) 3416.

ELSEVIER

Materials Science and Engineering A198 (1995) 225–230

MATERIALS SCIENCE & ENGINEERING A

Potential fluctuation during early stage of stress corrosion cracking of type-304 stainless steel in chloride solution

Hiroyuki Inoue, Hirohito Iwawaki, Koji Yamakawa

College of Engineering, University of Osaka Prefecture, 1-1 Gakuen-cho, Sakai, Osaka, Japan

Abstract

Potential fluctuation of type-304 stainless steel during stress corrosion cracking (SCC) was measured in 25 wt.% $MgCl_2$ solution. The power spectrum distribution of the observed fluctuation was computed by fast Fourier transform (FFT). During the early stage of SCC (the period when small cracks propagate from a pit), the frequency distribution of the power spectrum had a clear peak at the range from 8 to 10 mHz. The correlation between the number of microcracks and potential fluctuations was examined: both of the numbers showed a linear relation. From this result, it was speculated that the fluctuation was generated by the rapid formation of a bare metal surface and its repassivation with the connection of the microcracks. To confirm this speculation, the change in the power spectrum when the stress increased at an early stage of SCC was investigated, because the propagation rate of an advancing crack can be varied by the intensity of the tensile stress. While a peak at higher frequency appeared with an increase in the tensile stress, the peak at the range from 8 to 10 mHz remained.

Keywords: Stress corrosion cracking; Type-304 stainless steel; Corrosion potential fluctuation; Frequency analysis; Neutral chloride solution

1. Introduction

Fluctuation of the open-circuit potential (or of the current under potentiostatic control) during pitting or stress corrosion cracking (SCC) has been investigated to get information about the dynamic change in the locally corroding electrode. Many studies on fluctuation have been published for pitting, but few reports on SCC [1–8]. Less attention has been paid to the potential fluctuation during SCC, probably because the amplitude of the fluctuation is smaller than that during pitting. The smallness of the amplitude makes it difficult to obtain data, and to confirm the relationship between the signal and a physical phenomenon.

The first paper on the fluctuation of the electrochemical signals during SCC was written by Newman and Sieradzki in 1983 [1]. They observed oscillations of the current under potentiostatic control during SCC of α-brass. From the results of scratch tests and scanning electron microscope (SEM) images of the fracture surface, they speculated that the electrical charge passed during each current fluctuation was equal to that generated by each crack advance. Also, some studies about potential fluctuation during SCC have been published [2–5]. The time-series data of potential fluctuation were transformed to a frequency-domain representation — a power spectrum distribution — by use of the fast Fourier transform (FFT) or the maximum entropy method (MEM). The computed results were plotted on log–log scales. Then, the relation between physical changes in the specimen and the power spectrum at low frequencies was investigated. It was concluded that crack initiation and specimen rupture gave the highest power. On the power spectrum curves obtained by this method, there is a low frequency plateau. As Loto and Cottis stressed [5], this plateau is an experimental artifact, not the result of a physical phenomenon. Thus, analyses at low frequency are not reliable.

Yamakawa and Inoue [6] divided the observed potential fluctuation signals during SCC into two compo-

SSDI 0921-5093(94)04527-5

nents: a signal that shifts to a more noble potential and the one which shifts to a less noble potential. They then investigated the difference of the mean spectrum power for each type of signal, and found a good correlation with the elongation rate of the specimen. Wells et al. [7–8] investigated potential fluctuations and current pulse during the intergranular SCC of sensitized type-304 stainless steel. The frequency of the potential fluctuation was proportional to the degree of sensitization as indicated by the Electrochemical Potentiokinetie Reactivation (EPR) test. They assumed the fluctuation was caused by the initiation of cracks on the sensitized grain boundaries. Current transients were measured on a specimen coupled through a zero-resistance ammeter to a large cathode of annealed type-304 stainless steel. They confirmed that the number of current transients was roughly equal to the number of cracks found by SEM observation. They concluded that measured current pulses were associated with the nucleation of the microcracks.

SCC tests are generally carried out under more severe conditions than those actually employed, in order to finish the experiments within a reasonable time. However, in many cases, a material that has an excellent performance in accelerated tests ruptures in a shorter time upon actual usage. It was speculated that the morphology and the mechanism of SCC changed when the accelerated testing conditions were used, therefore giving rise to the above mismatch. If it were possible to get a result about SCC tests from the data at an earlier stage, the experimental time could be substantially shortened. In other words, tests could be done under milder conditions, which would be close to that of actual employment, which needs too long an experimental time with the method currently in general use. The observation of potential or current fluctuation makes it possible to detect the nucleation or propagation of a crack in the earlier stage of SCC. Now, it appears that the nucleation of a crack can be detected by the same methods as reviewed above. However, these methods are insufficient for the evaluation of SCC sensitivity. It is necessary not only to detect the nucleation of the cracks but also to assess the propagation rate directly, just after it has been nucleated.

We have measured the potential fluctuation of type-304 stainless steel during SCC in chloride solution and computed a power spectrum of observed data by the use of the FFT. During the early stage of SCC, the frequency distribution of the power spectrum had a clear peak. This suggests that the potential fluctuation occurs at regular intervals. It is expected that the potential fluctuation synchronizes with each step of the crack advance — a connection of a microcrack in the vicinity of the advancing crack tip — and there is a possibility that the propagation of a crack can be detected dynamically from an analysis of the potential fluctuation. So, we examine the correlation between the number of microcracks and potential fluctuation, and discuss the obtained results.

2. Experimental procedure

The material used in this study was type-304 stainless steel purchased from Japan Stainless Steel Association. This steel is a rolled sheet 2 mm thick and solution-annealed. The composition of the material was: 0.06C, 0.58Si, 0.82Mn, 0.29P, 0.002S, 8.75Ni, 18.29Cr, 0.14Mo, 0.14Cu in mass%. This was machined to a flat tensile specimen, with a 20 mm gage length and a 4×2 mm^2 cross-sectional area, and was finished with emery paper of 2000 grit. The specimen was annealed at 1373 K for 600 s to remove a residual strain induced by machining. It was sensitized at 923 K for 10.8 ks (3 h) in nitrogen gas and then cooled in air. After these heat treatments, the specimen was slightly etched in $HF + HNO_3$ solution to remove an oxide film, and then it was electropolished in $H_3PO_4 + CrO_3$ solution, followed by acid cleaning, and ultrasonic cleaning in acetone. 5 mm of the gage length was exposed to the test solution and the remainder was sealed with polysiloxane.

The testing environment was 25 mass% $MgCl_2$ solution. The solution was exposed to air throughout the testing and its temperature was kept at 353 ± 0.5 K. The solution was poured into the cell after the load was applied, and it was not agitated during the experiment. A constant tensile stress of 245 MPa was applied to the specimen with a spring-type tensile test apparatus. The fluctuation of the corrosion potential with respect to the saturated Ag/AgCl reference electrode was measured with an accurate digital voltmeter; the 1.2 V range was used and the least significant digit of this range was 1 μV. The sampling interval was 0.5 s, and the data were stored in a memory bank in the voltmeter successively. When the number of stored data reached 4096, these data, which were dealt with as one data block, were transferred to a desktop computer through an IEEE-488 bus, then saved on a floppy disk. This sequence of potential measurement was repeated every 2400 s.

The intensity of the inherent noise of the measurement system was assessed from the time record of potential difference between two reference electrodes inserted in one cell. A noise was observed synchronized with making or breaking of the heater circuit, which was inserted in a glass tube and placed inside the testing cell to control the solution temperature. The amplitude of the observed noise was 10 μV or below. The faradaic impedance of the Ag/AgCl electrode is higher than that of the specimen, therefore oscillation signals which exceeded 10 μV in amplitude were judged to be valid in this measurement system.

A power spectrum of corrosion potential was obtained to estimate the frequency of fluctuation using FFT. The Hanning window was employed for a window function. Calculation was done for every data block, including the 4096 points of potential data as mentioned above. For the data sampled every 0.5 s, the highest frequency of the computed power spectrum was 1 Hz and the frequency resolution of the spectrum was 1/2048 Hz. Before the execution of the FFT, d.c. and a drift component included in the original data were removed by use of the least-squares method; the deviation of each measured data value from the regression line is employed as data for the FFT computation.

3. Results and discussion

3.1. Macroscopic corrosion potential change throughout an SCC test

In this section, the focus is on the macroscopic change of corrosion potential throughout the SCC test. Fig. 1 shows the example of a typical corrosion potential change, from 7.2 ks after the solution was poured to 1.5 ks before the specimen ruptured. After the completion of the test, the ruptured surface was observed by SEM. The specimen was ruptured by one crack and any other macrocracks were not regarded on it. During period (A), potential rose to the peak, then oscillated a few times, and finally dropped to the lower potential. In other tests performed under the same experimental conditions, the potential reached a peak at 10 to 20 ks after the pouring of the solution. It is speculated that the formation of a stable pit brought about the potential drop. Throughout period (C), the corrosion potential gradually decreased as one macro crack was propagated further, which could be observed by the naked eye.

During period (B), the corrosion potential kept a steady value. This potential plateau was usually observed in the other experiments done under the same

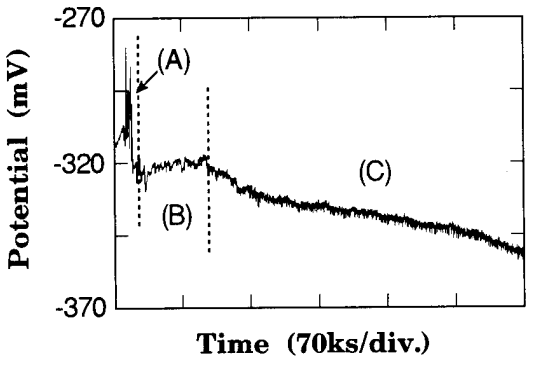

Fig. 1. Example of macroscopic corrosion potential change throughout an SCC test. (Periods (A)–(C): see text.)

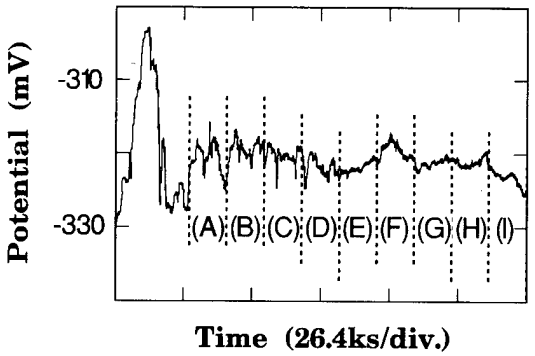

Fig. 2. Corrosion potential change during the initiation stage to the early stage of SCC.

experimental conditions. A few small cracks were observed by SEM on the surface of the specimen when the experiment terminated in this stage. These cracks generated from one pit and propagated almost perpendicular to the direction of the applied stress and were hardly visible any longer with the naked eye. We refer to this stage as the "early stage of SCC", and potential fluctuation observed in this period was analyzed and is discussed in this paper.

3.2. Frequency characteristics in the early stage of SCC

Fig. 2 shows the changes of corrosion potential during the initiation stage to the early stage of SCC. Potential measurements started from 3.6 ks after the pouring of the solution and terminated at the time corresponding to the right-hand end of this figure. Fig. 3 displays the power spectrum of the potential fluctuation shown in Fig. 2. These curves are calculated by averaging the six power spectra, which are computed from the sequentially saved six data blocks. Each section in Fig. 2, marked with letters (A) to (I), is con-

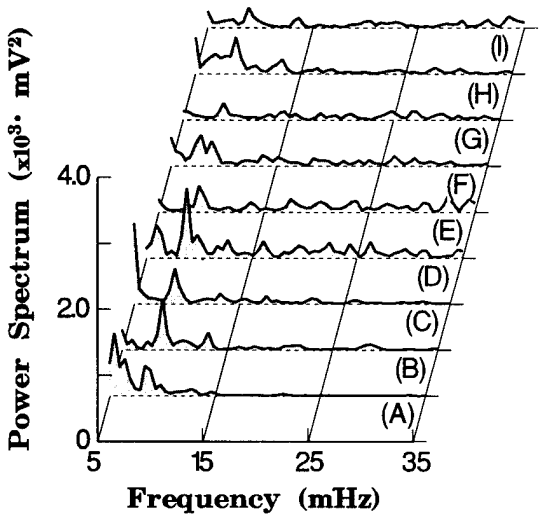

Fig. 3. Power spectrum of the potential fluctuation shown in Fig. 2.

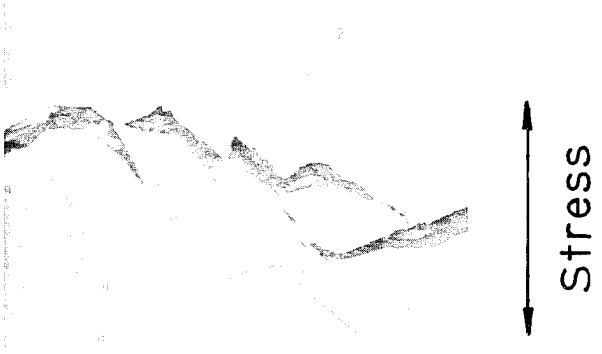

Fig. 4. Typical example of a SEM image of the surface area near a crack tip.

structed with six data blocks, so the power spectra are obtained in each section, and the letters written on the right side of each curve in Fig. 3 correspond to those of this figure. The frequency range represented in this figure is 5 to 35 mHz. The spectrum curves under 5 mHz are obviously affected by the drift components included in the data. In the frequency range over 35mHz to 1Hz, no peaks are detected and the intensity of the power spectrum decayed monotonically.

All power spectra shown in Fig. 3 have a clear peak frequency within 8 to 10 mHz. The same results were obtained in other experiments carried out under the same experimental conditions. However, when many cracks propagated from some pits simultaneously, the obtained power spectrum curves became complicated and a clear peak did not appear. The clear peak of the power spectrum indicates that the potential fluctuation occurs at a regular interval, and this type of potential fluctuation during SCC testing has not been reported before. In the following section, the origin of this signal will be discussed.

3.3. Surface morphology in the vicinity of the crack tip

The experiment terminated at an early stage, and then surface observation was carried out by SEM. The surface trace of the propagated crack was gradually corroded with time, but in the vicinity of the advancing crack tip, it was expected that some information about crack propagation was preserved. Fig. 4 shows a typical example of an SEM image of the surface area near a crack tip. The coarse slip lines were seen on the figure and were inclined at about 45° to the direction of the applied stress. From this micrograph, it can be supposed that a crack propagates on the surface of a specimen as follows. First, isolated microcracks are generated along coarse slip lines in front of the crack tip, where stress is concentrated. Then these micro-pits are coupled successively and the crack propagates further in this manner. It is estimated that the former process is controlled by corrosion along the coarse slip line and the latter is ruled by the mechanical crack advance. Therefore, the latter process induces a potential fluctuation, because a relatively large area of bare metal surface is generated rapidly and then repassivated. Also, it is speculated that when the process occurs at the inside of the specimen, a detectable potential fluctuation is not generated, because of the effect of the *IR* drop of the solution. If the above assumption is correct, it is speculated that the number of connected microcracks will be equal to the sum of the observed potential fluctuations.

3.4. The correlation between the number of microcracks and that of fluctuations

The average length of a microcrack was measured to estimate the number of microcracks included in the specimens. Nine experiments were terminated at an arbitrary time in the early stage of SCC and the surface of the tested specimens was observed by SEM. First, it was observed that the average microcrack length for each adequate area of SEM image where the trace of microcracks was well preserved was in the vicinity of the crack tip of the specimens. Four to twelve data values were taken for every specimen, which were sampled from different areas of the specimen. A histogram of the average microcrack length shown in Fig. 5. The average value of data displayed in this graph is 2.12 μm. The number of microcracks included in each specimen was computed by dividing the whole length of the surface crack-propagation trace by the average value of microcrack length. Also, the number of potential fluctuations, from the potential dropping to the experiment termination, was estimated from the peak frequency of the power spectrum of every data block: we multiplied the value of the each peak frequency by the total measurement time of each data block. The correlation between the number of microcracks and that of fluctuations is shown in Fig. 6. From this figure, it is judged that the number of microcracks is equal to the sum of the observed potential fluctuations. So it is speculated that the connection of microcracks is a signal source for the potential fluctuation in the early stage of SCC.

3.5. A shift of the peak frequency by the change of tensile stress in the middle of the SCC test

The propagation rate of the advancing crack increases with the intensity of the tensile stress. In the early stage of SCC, if the crack propagates with the connection of microcracks on the surface of a specimen and the potential fluctuation occurs when the microcracks connect each other, as speculated above, it is expected that increasing the stress will lead to the

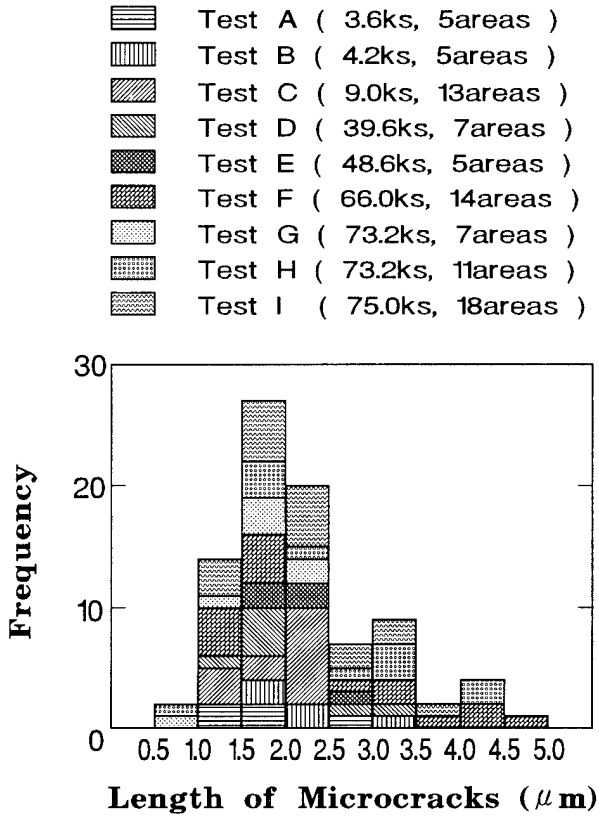

Fig. 5. Average microcrack length of each evaluated area. The termination time and the number of evaluated areas of each test are shown within the parentheses.

decreasing of the occurrence interval of the potential fluctuation. The interval can be evaluated from the peak frequency of its power spectrum, as shown in Fig. 3. So, to confirm the above speculation, the stress was increased at the early stage of SCC and the shift of the peak frequency of the power spectrum was investigated.

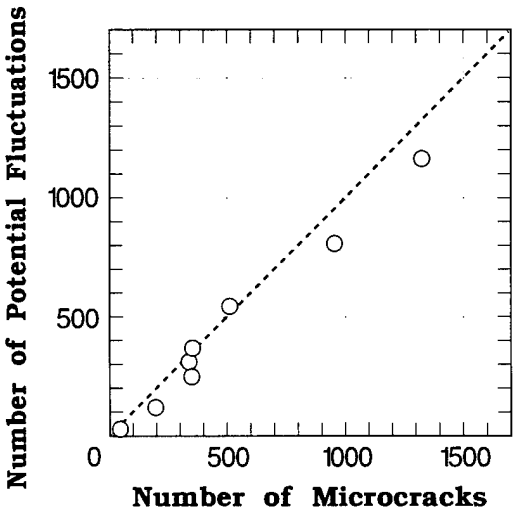

Fig. 6. Correlation between the number of microcracks and that of fluctuations.

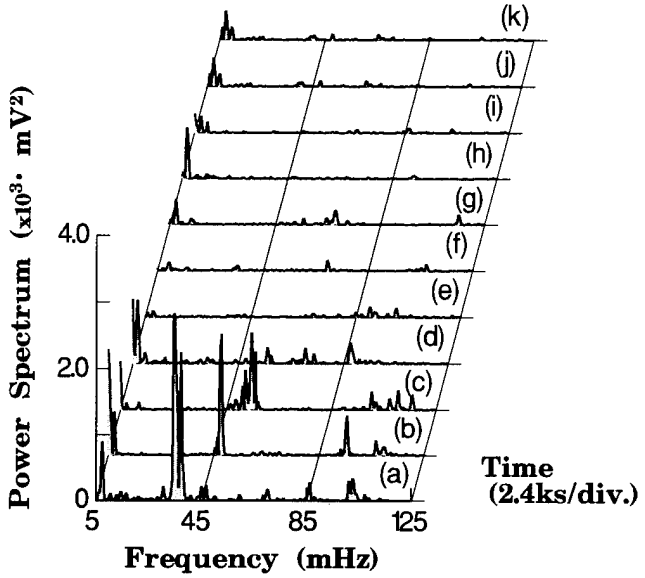

Fig. 7. Power spectrum of the potential fluctuation from 1.2 ks to 25.2 ks after the stress increase (245 to 294 MPa).

Figs. 7 and 8 show the change of the power spectrum from 1.2 ks to 25.2 ks after the increase in the stress intensity. The former is the result when the stress was increased from 245 to 294 MPa and the latter is that when the stress was changed from 245 to 343 MPa. These curves are computed from the sequentially saved

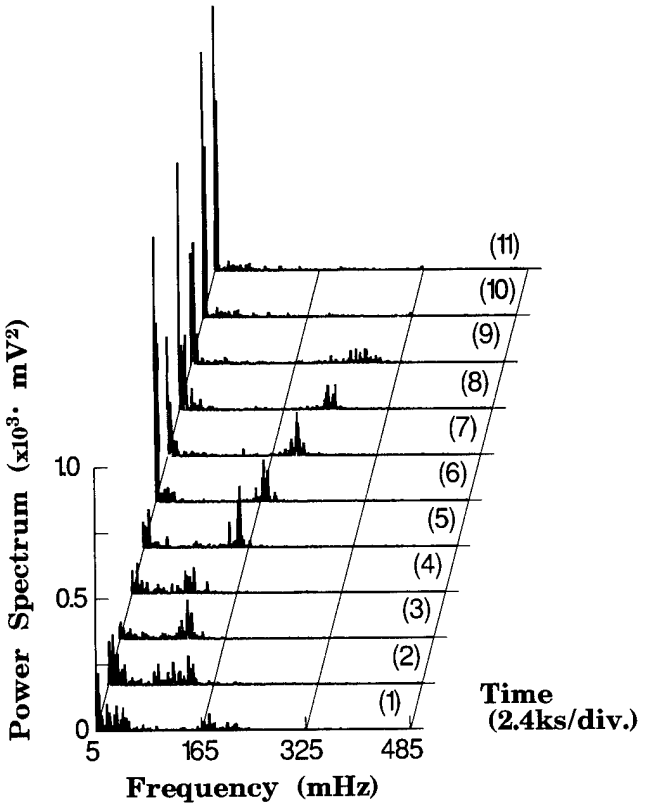

Fig. 8. Power spectrum of the potential fluctuation from 1.2 ks to 25.2 ks after the stress increase (245 to 343 MPa).

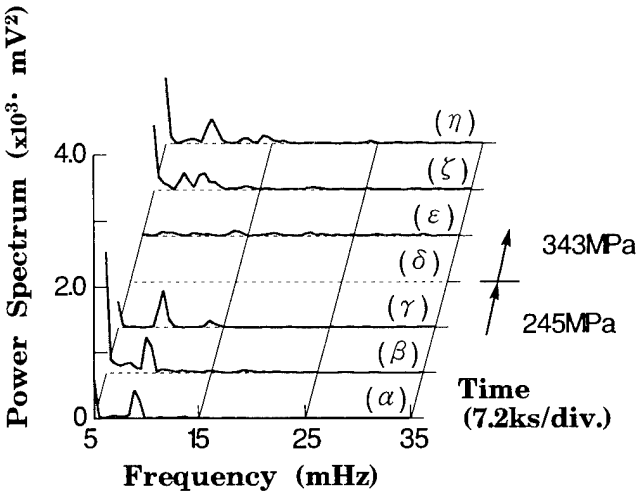

Fig. 9. Power spectrum of the potential fluctuation before and after the stress increase.

data block. In Fig. 7, a clear peak is shown around 45 mHz from 1.2 ks to 8.4 ks (the curves (a) to (c) in Fig. 7) after the increasing of the stress. This type of peak is also shown in Fig. 8. Its frequency is higher than that shown in Fig. 7 (curves (1) to (9) in Fig. 8), though the intensities of the spectrum peaks shown in Fig. 8 are lower than those shown in Fig. 7. When a constant stress of 245 MPa was applied to the specimen, as the result shown in Fig. 3, the frequency of the clear peak was within 8 to 10 mHz. It can be seen that the peak shifts to higher frequency with an increase of the stress, but the lower peak also remained as displayed in Figs. 7 and 8.

Fig. 9 is the change in the power spectrum at low frequency before and after the stress increase. The analyzed potential data are common with the data presented in Fig. 8. These curves are calculated by the averaging of the three power spectra, which are computed from the sequentially saved three data blocks. The averaged data of the curves (c),(d) and (e) in Fig. 8 are the curve (ϵ) in Fig. 9. The curves (ζ) and (η) in Fig. 9 correspond to the averages of the curves (f) to (h) and (i) to (k) in Fig. 8, respectively. A clear peak is seen before and after the increasing of the stress. The frequency of the peak is about 8 mHz and it does not change with the changing of the stress. As shown in Figs. 7 and 8, the higher-frequency peak disappeared after a while. It also cannot be explained if the higher peak is brought by increasing of the propagation rate. When the stress is increased, the strain rate of the specimen is also increased. So, there is a possibility that a peak which has a higher frequency is not generated by acceleration of the crack propagation, but it is induced by the increase in the strain rate.

4. Conclusion

Potential fluctuation of type-304 stainless steel during SCC was measured in 25 mass% $MgCl_2$ solution and its power spectrum was obtained by FFT. The power spectrum of the observed fluctuation had a clear peak, and its frequency was within the range from 8 to 10 mHz. Its source was speculated to be the rapid formation of a bare metal surface and its repassivation, with the connection of the microcracks which had been generated along coarse slip step lines in front of the crack tip on the surface of the specimen. To confirm this mechanism, the stress was increased in the middle of the SCC tests and the shift of the peak frequency of the power spectrum was investigated. A new peak appeared at a higher frequency, while a peak at the lower frequency also existed before and after the change of the tensile stress. These results were not explicable by the above-speculated mechanism, so it was concluded that the evidence about the correlation between the signal and the phenomenon could not be obtained within the extent of the results investigated in this paper.

References

1 R.C. Newman and K. Sieradzki, *Scr. Metall.*, *17* (1983) 621.
2 C.A. Loto and R.A. Cottis, *Corrosion*, *43* (1987) 499.
3 K. Yamakawa, N. Kajita, M. Murakami and T. Hirayama, *J. Soc. Mater. Sci. Jpn.*, *37* (1988) 43.
4 C.A. Loto and R.A. Cottis, *Corrosion*, *45* (1989) 136.
5 C.A. Loto and R.A. Cottis, *Corrosion*, *46* (1990) 12.
6 K. Yamakawa and H. Inoue, *Corros. Sci.*, *31* (1990) 503.
7 D.B. Wells, J. Stewart, P.M. Scott and D.E. Williams, *Corros. Sci.*, *33* (1992) 39.
8 D.B. Wells, J. Stewart, P.M. Scott and D.E. Williams, *Corros. Sci.*, *33* (1992) 73.

ELSEVIER

Materials Science and Engineering A198 (1995) 231–238

MATERIALS SCIENCE & ENGINEERING A

Origins of the aqueous corrosion and stress corrosion cracking behavior of ductile nickel aluminide

Richard E. Ricker

National Institute of Standards and Technology, Technology Administration, US Department of Commerce, Gaithersburg, MD 20899, USA

Abstract

The stress corrosion cracking resistance of ductile nickel aluminide, $Ni_3Al + B$, was evaluated by conducting experiments in solutions with varying pH and ionic concentration. The results demonstrate that the ductility of this material is greatly reduced and the fracture mode changes from ductile transgranular to brittle intergranular cracking when environmental conditions are favorable for hydrogen absorption during the steady state regardless of the solution composition and pH. The results also indicate that, in the absence of cathodic polarization, this material exhibits ductile behavior during free corrosion in solutions of neutral and alkaline pH. Thermodynamic calculations of the activity of aluminum in nickel aluminide indicate that there is sufficient thermodynamic driving force for hydrogen evolution in these environments. Although the presence of surface films and transport through these films prevent this from occurring during steady state free corrosion, the thermodynamic calculations indicate that hydrogen evolution should occur during the transients that follow film rupture in these environments. To evaluate if hydrogen evolution could occur during film rupture and repassivation, nickel aluminide samples were scratched and the resulting potential transient was monitored. The results indicate that the potential drop during the scratch repassivation event will not cause significant hydrogen evolution and absorption. It is postulated that this discrepancy between the thermodynamic calculations and kinetic behavior is due to the ordering of this A_3B compound into the $L1_2$ structure. To test this hypothesis, samples of Ni_3Fe, which can be easily ordered and disordered, were tested in the ordered and disordered conditions. The results indicate that ordering significantly alters the repassivation transient that follows scratching in A_3B-$L1_2$ compounds where the more active constituent is the B species.

Keywords: Aqueous corrosion; Stress corrosion cracking; Nickel aluminide; Ductility

1. Introduction

Nickel aluminide, Ni_3Al, is an intermetallic compound that forms as a result of the ordering of the nickel and aluminum atoms on the f.c.c. unit cell with the nickel atoms occupying the face center sites and the aluminum atoms occupying the corner sites (the $L1_2$ structure). Unfortunately, intrinsic polycrystalline nickel aluminide exhibits brittle behavior in laboratory air at ambient temperatures. This brittle fracture problem had prevented the development of high and low temperature applications for this material until it was found that it could be made ductile through microalloying additions of boron and by maintaining the aluminum concentration in the alloy slightly below the stoichiometric ratio [1,2]. The resulting intermetallicalloy offers high strength and ductility, making it a promising structural material for ambient temperature and high temperature applications.

Although interest in nickel aluminide is primarily due to its potential for high and intermediate temperature applications, it also possesses certain properties which make it a candidate for low temperature applications. Research has shown that the corrosion resistance of nickel aluminide in many ambient temperature aqueous environments is similar to that of nickel alloys [3–5]. However, it possesses other properties, such as a lower density and greater wear resistance, that may make it advantageous with respect to nickel alloys or stainless steels [6,7]. The low temperature aqueous corrosion behavior of this material is of concern for high temper-

Elsevier Science S.A.
SSDI 0921-5093(94)04528-3

ature applications because these materials will not always be at operating temperatures, and corrosion damage or crack initiation during fabrication or maintenance could lead to catastrophic failures during service. As a result, the corrosion, stress corrosion cracking and hydrogen embrittlement susceptibility of this material at ambient temperatures have been the subject of several studies [3,4,8–11].

Kuruvilla and Stoloff [10] demonstrated that the ductility of nickel aluminide is reduced by cathodic charging with hydrogen and that the fracture mode changes from transgranular to intergranular for simultaneous cathodic charging and straining. In earlier work, it was reported that exposure to low pH solutions resulted in a similar reduction in ductility and change in fracture mode [12]. Later, it was shown that low ductility and intergranular fracture can result in solutions of neutral and alkaline pH when the potential of the sample enters the range in which hydrogen absorption is expected [11,12], but Ni_3Al does not exhibit environmentally altered fracture behavior in neutral solutions in the absence of galvanic coupling [13]. The purpose of this paper is to summarize the earlier findings on the aqueous corrosion and environmentally induced fracture resistance of Ni_3Al, and to report on the results of follow-up studies conducted to obtain an understanding of the origins of the aqueous corrosion and environmentally induced fracture behavior of this material.

2. Experimental details

2.1. Materials

Samples of two ductile nickel aluminide alloys were provided by Oak Ridge National Laboratory for this study. The two alloys examined were IC-50 and IC 218 LZr, and the compositions of these alloys are given in Table 1. The alloys were tested in the as-received (cold worked, approximately 40%) and fully annealed conditions. The samples were annealed by placing them in a quartz tube which was evacuated, back filled with Ar and then sealed before annealing at 1100 °C for 1 h.

Table 1
Composition of the nickel aluminide alloys

Element	Weight per cent		Atomic per cent	
	IC 50	IC 218 LZr	IC 50	IC 218 LZr
Ni	86.83	83.01	77.0	74.62
Al	11.53	8.69	22.2	16.99
Cr	—	8.08	—	8.18
Zr	0.03	0.03	0.01	0.12
B	0.018	0.02	0.08	0.098

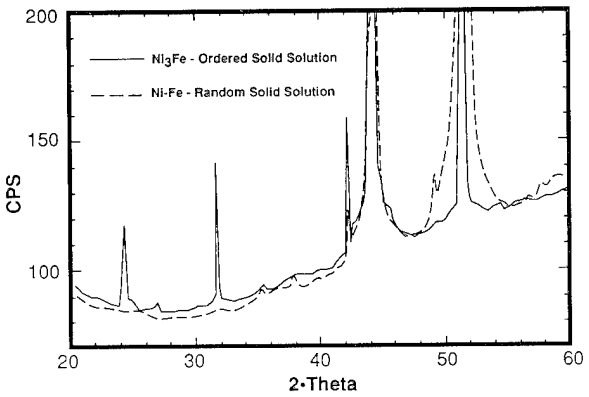

Fig. 1. X-Ray diffraction from Ni–Fe alloy heat treated to obtain a random solid solution and ordered Ni_3Fe.

To examine the influence of ordering on the electrochemical behavior of the alloys, two Fe–Ni alloys were prepared (Fe–77wt.%Ni and Fe–74wt.%Ni). These alloys were selected because of the ease of obtaining ordered (Ni_3Fe) and random (Ni–Fe) solid solutions with the same chemical composition from these alloys as compared with other A_3B-$L1_2$ compounds composed of nickel and a more active species as the minority or B component. These alloys were homogenized at 1100 °C for 16 h in vacuum followed by air cooling. To achieve a random solid solution, samples were heat treated at 1000 °C for 3 h followed by a decrease in the temperature of the samples to 580 °C for 3 h, which is above the ordering temperature (517 °C), before quenching to room temperature. To achieve a fully ordered condition, samples were heat treated at 470 °C for 19 days before quenching to room temperature. Ordering was confirmed by X-ray diffraction of the samples given the randomizing and ordering heat treatments (Fig. 1), and the relationship of Calvayrac and Fayard [14] indicates greater than 100% ordering for these samples.

2.2. Electrochemical measurements

Electrochemical experiments were conducted initially in four different solutions of varying pH: 0.5 mol l^{-1} H_2SO_4 (pH $\approx$ 0.7), 0.5 mol l^{-1} NaCl (pH $\approx$ 6.3), 0.5 mol l^{-1} Na_2SO_4 (pH $\approx$ 6.5) and 0.5 mol l^{-1} NaOH (pH $\approx$ 13.1). Additional experiments were conducted in other solutions and will be the subject of another paper. The electrochemical measurements consisted of steady state free corrosion potential measurements and potentiodynamic polarization measurements. For these measurements, samples of the alloys were embedded in epoxy resin with a wire attached to the back of the sample which was totally encased and isolated from the solution. The electrodes were polished to a 0.05 μm finish, and washed in ethanol and double distilled water immediately before use. For the potentiodynamic polarization tests, the samples were allowed to corrode freely

in the naturally aerated solution for 30 min before a potentiostat swept the potential of the sample with respect to a saturated calomel reference electrode between two predetermined potentials at a fixed rate. A wide variety of different sweep rates and potential limits were used.

2.3. Slow strain rate tensile tests

Slow strain rate tensile tests were conducted on samples of the nickel aluminide alloys under free corrosion and potentiostatic conditions at a constant crosshead speed of 2.54×10^{-8} m s^{-1} in the same solutions as used for the electrochemical measurements and in laboratory air for comparison. The samples used for these experiments were approximately 0.75 mm thick with a gage length of 25.4 mm. The samples were coated with a lacquer outside the gage section and the grips of the load frame were isolated from the solution. During the slow strain rate tensile tests, the load and stroke were monitored and recorded by computer and the resulting fracture surfaces were examined in a scanning electron microscope. To examine the ductility at pH values between 0.6 and 6.3, slow strain rate tensile tests were conducted at two concentrations of $AlCl_3$: 0.17 and 1.7 mol l^{-1}. The pH values of these solutions were measured and found to be 2.7 and 1.4 respectively. For the potentiostatic slow strain rate tensile tests, the potential difference between the sample and a reference electrode was kept constant with a commercial potentiostat and a Pt counterelectrode as shown in Fig. 2. Electrical contact was made to the sample in the grips outside the solution.

2.4. Scratch repassivation transient measurements

These experiments involved the artificial generation of a bare metal surface by scratching with a sapphire

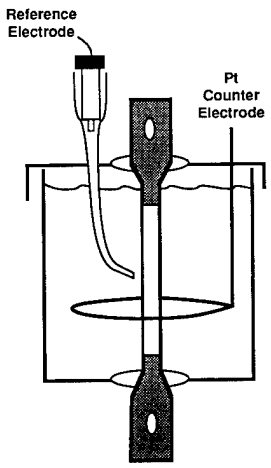

Fig. 2. Schematic diagram of the environmental chamber used for slow strain rate tensile tests.

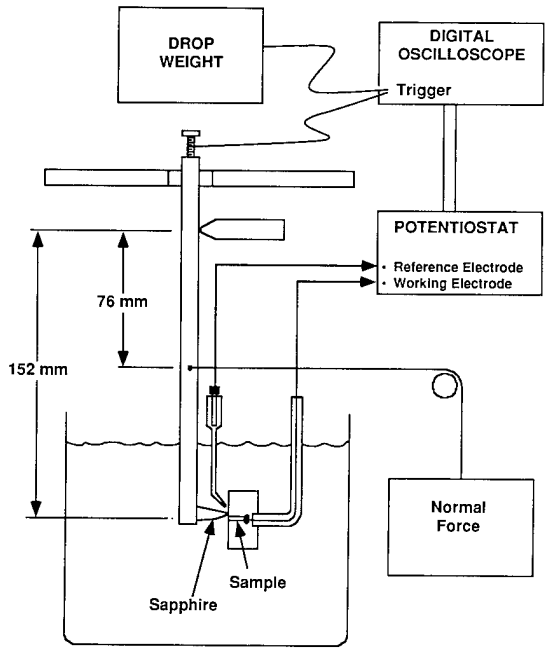

Fig. 3. Schematic diagram of the experimental equipment used for generating a bare surface by scratching for repassivation transient measurements.

scribe, and the recording of the potential transient that accompanies scratching and repassivation of the scratch. Fig. 3 shows a diagram of the apparatus used for these experiments. This same apparatus was used in a study of Al alloys and a more detailed description of the apparatus and the experimental technique can be found in Ref. [15]. Sheet samples of nickel, aluminum and nickel aluminide were mounted on edge in epoxy, polished and coated with lacquer in preparation for scratching. The scribe scratched through this lacquer coating and into the sample during the scratch process. Electrical contact was made to the sample with a wire, which was attached to the back of the sample and isolated from the solution. Three different solutions were used for these experiments: 0.5 mol l^{-1} NaCl (pH $\approx$ 6.3); and 0.5 mol l^{-1} Na_2SO_4 (pH $\approx$ 6.5) and 0.5 mol l^{-1} $NiCl_2$. The first two were used to represent typical neutral solutions with and without halide ions, and the third was used to determine the influence of nickel ions on the transient. Scratch tests were also conducted on ordered (Ni_3Fe) and disordered (Ni–Fe) samples of the nickel–iron alloys in 0.1 mol l^{-1} H_2SO_4.

3. Results and discussion

3.1. Electrochemical measurements

Potentiodynamic polarization curves were determined for each of the solutions. Initially, significant differences were observed between nickel and nickel

aluminide, but closer examination revealed that the main causes of these differences were the sample size and shape (edge effects). As a result, the measurements were repeated numerous times with samples that were as close to the same size and shape as reasonably possible. The electrochemical measurements will be the subject of another paper but, for this discussion, it is important to note that, in general, the electrochemical behavior of Ni_3Al was very close to, but not exactly the same as, pure nickel in all of the environments studied. Fig. 4 shows the relatively small differences between Ni_3Al and pure Ni for one of the environments: 0.5 mol l^{-1} H_2SO_4. Typically, the differences between Ni_3Al and pure nickel were so small that numerous repetitions were required to determine whether a difference was reproducible.

3.2. Slow strain rate tensile tests

Fig. 5(a) shows that the ductility and strain to failure are essentially unaffected by the environment in neutral and alkaline solutions, but in acidic solutions the ductility is greatly reduced. In Fig. 5(b), the free corrosion potentials of nickel aluminide in the solutions used for the slow strain rate tensile tests are plotted against the pH of the solutions, together with the hydrogen evolution potential calculated from the Nernst equation for fugacities of 10^3, 10^5 and 10^7 Pa. By comparing Figs. 5(a) and 5(b), it can be seen that the ductility and ultimate tensile strength (as percentages of the values observed in air) are essentially unchanged in the neutral and alkaline solutions when the hydrogen fugacity estimated from the steady state free corrosion potential is extremely low, but that the ductility, ultimate tensile strength and fracture mode change significantly when the steady state free corrosion potential is sufficiently low for the hydrogen fugacity to become appreciable.

Although this provides strong evidence that hydrogen embrittlement is the mechanism responsible for the observed environmentally induced fracture, it should be kept in mind that dissolution occurs during exposure to these acidic solutions, and other processes, such as film growth or dealloying, may also occur in these solutions. As a result, these possibilities must be eliminated before it can be concluded unambiguously that hydrogen embrittlement is the mechanism responsible. To achieve this objective, two different types of experiment were performed. First, slow strain rate tensile tests were conducted in sulfuric acid with the potential of the samples with respect to a reference electrode controlled with a potentiostat. Three potentials, besides the open-circuit free corrosion potential, were used for these experiments as shown in Fig. 6(a): (1) a potential below the free corrosion potential, which will reduce the rate of anodic processes and may increase the hydrogen fugacity; (2) an active potential above the free corrosion potential which will reduce the hydrogen fugacity but increase the rate of anodic dissolution; (3) a potential above the free corrosion potential and the active to passive transition such that the hydrogen fugacity will be essentially zero and the surface of nickel aluminide will be passivated. It should be noted that the steady state current densities may differ significantly from those observed on a potentiodynamic polarization curve, and the current density at the passive potential,

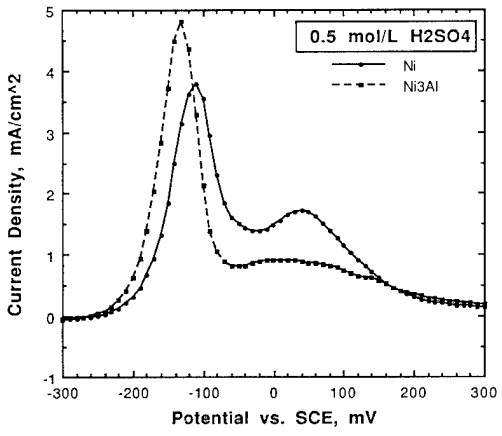

Fig. 4. Comparison of the potentiodynamic polarization curves obtained for pure Ni and Ni_3Fe in 0.5 mol l^{-1} H_2SO_4.

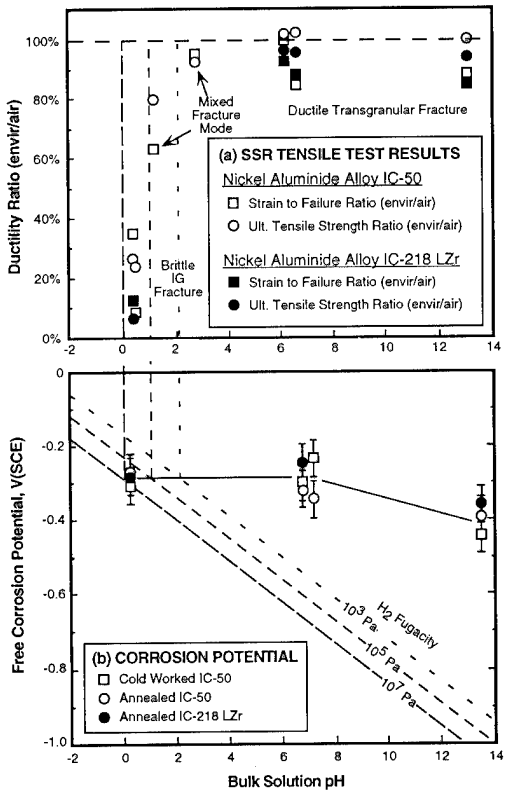

Fig. 5. Slow strain rate tensile tests in different environments: (a) strain to failure ratio and ultimate tensile strength ratio vs. pH; (b) steady state free corrosion potential vs. pH.

potential number (3), decreases to less than 10^{-1} A m^{-2} within 10 min. Fig. 6(b) shows the results of these experiments. It can be seen that polarization to a potential below the free corrosion potential does not significantly alter the fracture behavior, but polarization to more positive potentials, which reduces the hydrogen fugacity, increases the tensile strength. At the active potential, -200 mV_{SCE}, the rate of dissolution is significantly increased but intergranular fracture is not observed, and the tensile strength ratio increases although it is not as great as that observed in air. Since the tensile strength calculation is based on the cross-section of the sample measured before the initiation of the experiment, it is not surprising that the calculated tensile strength is lowered by the anodic attack because this attack will reduce the cross-section of the sample. As a result, the true tensile strength ratio for these samples was estimated by measuring the cross-section after completion of the test, estimating the cross-section from current density measurements and estimating a "reference" or air value for the ratio by corroding a sample in the solution for the same time as taken for the test and testing this sample in air. The open circle in Fig. 6 represents the value of these estimates, and it can be seen that the tensile strength, while considerably greater than that observed at open circuit, is not as great as that observed in air. This difference may be due

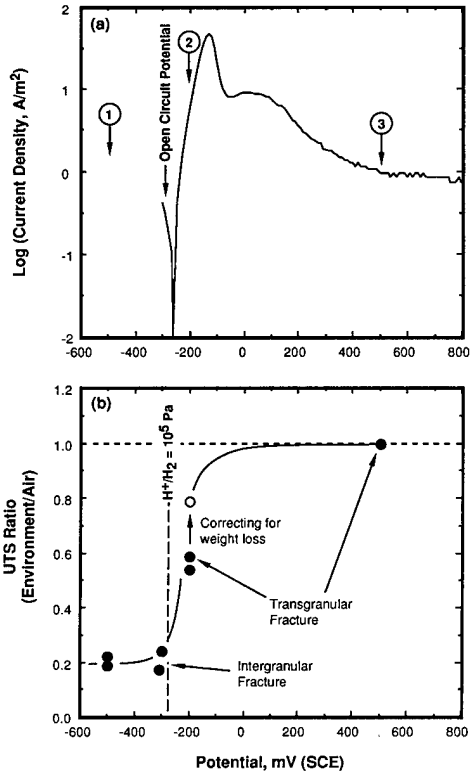

Fig. 6. Influence of potential on the strain to failure in 0.5 mol l^{-1} H_2SO_4: (a) polarization curve showing current densities; (b) ultimate tensile strength ratio.

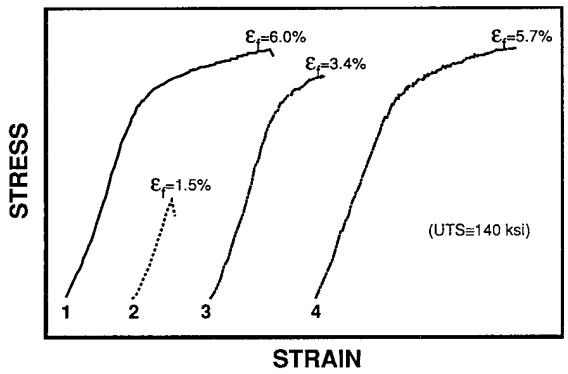

Fig. 7. Influence of pre-corrosion and hydrogen "bake-out" on the strain to failure of cold-worked nickel aluminide alloy IC 50.

to an environmental effect or our inability to account for the influence of surface roughening as a result of corrosion on the tensile properties. For the samples tested at the passive potential, 500 mV_{SCE}, fracture does not occur until the ultimate tensile strength is reached.

The second method used to evaluate whether hydrogen embrittlement is the mechanism responsible for the environmentally induced fracture in acidic solutions involved pre-exposure embrittlement experiments. The purpose of these experiments was to determine whether the charging of hydrogen into the sample by pre-exposure to sulfuric acid results in a reduction in the mechanical properties in a subsequent slow strain rate tensile test conducted in air before the absorbed hydrogen can diffuse out of the sample. Fig. 7 shows that pre-corrosion in sulfuric acid for 10 h reduces the strain to failure of cold-worked nickel aluminide to 57% of the value normally exhibited in air, but not as much as testing in sulfuric acid. Since the reduced ductility may be the result of surface damage during the pre-exposure as well as hydrogen embrittlement, a sample was given an identical pre-exposure to sulfuric acid, but was placed in a vacuum for over 100 h prior to testing in air; all of the ductility was restored in this sample (97%). Since hydrogen embrittlement is the only mechanism of environmentally induced fracture which is consistent with these observations, it was concluded that this is the mechanism responsible for environmentally induced fracture in acidic solutions.

3.3. Film rupture and scratch repassivation transients

When changing loads or creep result in the rupture of films on the surface or at the tip of a crack, bare metal will be exposed to the environment as shown in Fig. 8. When this occurs, the freshly exposed bare metal will immediately begin to react with the environment and attempt to bring the conditions towards equilibrium for the solution, alloy and surface film. When a bare surface is exposed, if the rate of the cathodic reactions

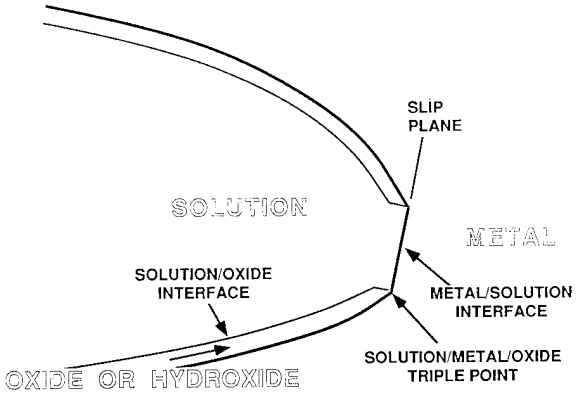

Fig. 8. Schematic diagram of film rupture at the tip of a crack.

does not increase as rapidly as the rate of the anodic reactions, the potential of the crack tip will decrease. If this difference is significant, the potential can approach that for equilibrium between the solution and the bare metal. Indeed, the generation of a fresh bare surface by scratching has been used to estimate the equilibrium potential for aluminum [16–18]. For pure aluminum metal, the minimum possible potential for a repassivation transient assuming minimum ionic concentration of 1×10^{-6} mol l^{-1} is illustrated by the line labeled "Al^{3+}/Al(s)" in Fig. 9. In this electrochemical equilibrium diagram for nickel and aluminum, it can be seen that the equilibrium potential for bare aluminum exposed to water at any pH is significantly active with respect to the potential required to cause hydrogen evolution at atmospheric pressure, as illustrated by the "$H^+/H_2 = 1$ atm" line in Fig. 9. As a result, high hydrogen fugacities should accompany film rupture and repassivation resulting in hydrogen absorption. Of course, the chemical

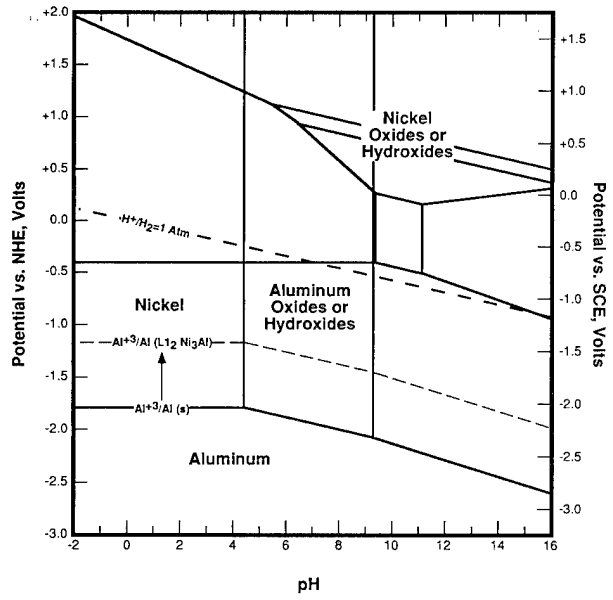

Fig. 9. Electrochemical equilibrium diagrams for nickel and aluminum in water superimposed. (Ionic concentration = 1×10^{-6} mol l^{-1}.)

potential of aluminum in nickel aluminide is not the same as for aluminum in the pure form. As a result, the chemical potential of aluminum in $L1_2$ Ni_3Al was calculated using the thermodynamic data available in the literature. It was found that the equilibrium potential for "Al^{3+}/Al($L1_2$ Ni_3Al)" is significantly increased, but still considerably active with respect to the potential required to cause hydrogen evolution at atmospheric pressure as shown by the broken lines in Fig. 9 [19,20]. Therefore thermodynamics predicts that film rupture in Ni_3Al should result in hydrogen evolution and absorption in any solution regardless of pH.

Since slow strain rate tensile tests showed no evidence of environmentally altered fracture in solutions of pH > 3, scratch repassivation experiments were conducted on samples of pure Ni, pure Al and Ni_3Al in 0.5 mol l^{-1} Na_2SO_4 and 0.5 mol l^{-1} NaCl. These experiments were designed to determine whether the repassivation transients following film rupture in nickel aluminide are influenced by the aluminum which may result in hydrogen absorption and embrittlement at pH values above pH 3. Fig. 10 shows the results of these experiments. It can be seen that, in both solutions, the scratch repassivation transient for Ni_3Al is similar to that of pure Ni in that it does not drop below the potential for hydrogen evolution at atmospheric pressure and does not approach the "Al^{3+}/Al($L1_2$ Ni_3Al)" potential shown in Fig. 9. This is significant as aluminum makes up almost 25% of this compound and yet has little influence on the potential transient that follows film rupture. Clearly, the surface activity for aluminum in this compound is significantly different from that calculated by thermodynamics for aluminum in the bulk compound. Understanding this phenomenon could enable intermetallic compounds to be used in situations in which one of the constituents should react with the environment.

Thermodynamic calculations form a useful basis for estimating behavior, but kinetics frequently influence the actual outcome. In A_3B-$L1_2$ compounds, the B atoms are surrounded by A atoms such that they have only A atoms for nearest neighbors. When a bare surface of a compound of this type is exposed to the environment, about 25% of the atoms exposed will be B atoms. After these have been ionized, the surface will be essentially 100% A atoms and no additional B atoms can be removed from the solid until some A atoms are removed. Another possibility is that the A_3B compound decomposes near the surface, A atoms diffuse on the surface to form A clusters and B atoms are exposed to the environment; however, this will also be a relatively slow process. Thus in an A_3B-$L1_2$ compound, where B is the more active component, ordering significantly reduces the surface reactivity of B atoms, because the $L1_2$ structure imposes physical barriers to the dissolution of B atoms, limiting it to that dictated by the

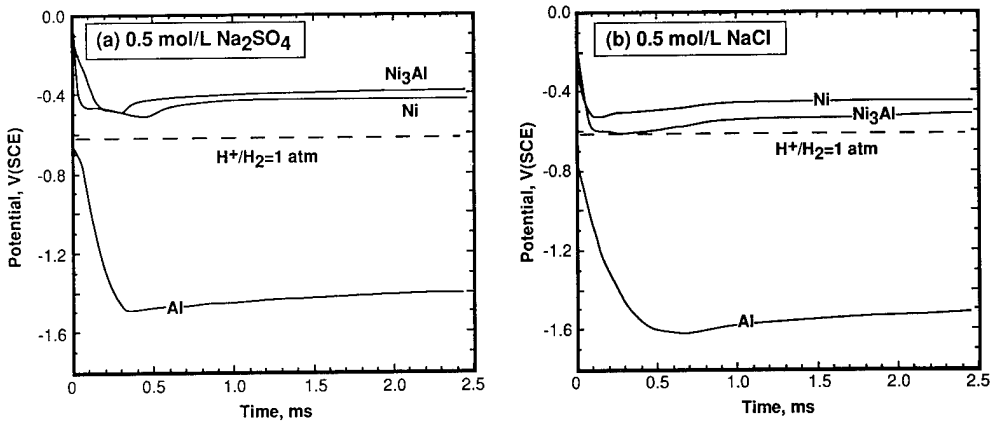

Fig. 10. Scratch repassivation transients for nickel aluminide alloy IC 50: (a) in 0.5 mol l^{-1} Na_2SO_4; (b) in 0.5 mol l^{-1} NaCl.

stoichiometry of the compound (stoichiometric dissolution).

To evaluate this hypothesis, samples of a nickel–iron alloy, which can be heat treated to obtain ordered and random solid solutions, were tested in 0.1 mol l^{-1} H_2SO_4. Fig. 11 shows a comparison of the potentiodynamic polarization curves for this alloy in the ordered and random solid solution conditions. It can be seen that the ordered condition has a lower critical current density and lower passive current density. Fig. 12 compares the scratch repassivation transients observed for the ordered and random solid solution conditions. It can be seen that ordering results in a minimum potential which is significantly greater than that observed for the ordered solid solution. On the other hand, the minimum potential observed for the ordered condition is very close to the calculated minimum potential for Ni in pure f.c.c. nickel (assuming an ionic concentration of 1×10^{-6} mol l^{-1}).

These results are in accordance with the hypothesis that ordering in A_3B-$L1_2$ compounds imposes a stoichiometric barrier to the dissolution of B. As a result, B cannot dissolve at rates in excess of those dictated by the dissolution rate of A and the stoichiometric ratio. This is interesting for a stoichiometric single crystal, but if one component is in excess or one component segregates preferentially to the grain boundaries, continuous dissolution at rates greater than those dictated by stoichiometry may be possible. Clearly, if the preferential dissolution of B is undesirable or could cause hydrogen absorption and embrittlement, it would be advantageous to keep the B composition slightly substoichiometric or to add something to the alloy that influences grain boundary segregation. Indeed, both of these factors have been found to result in improved room temperature ductility in nickel aluminide alloys [1,2].

4. Conclusions

Experiments were designed to evaluate the potential for environmentally induced fracture of ductile nickel

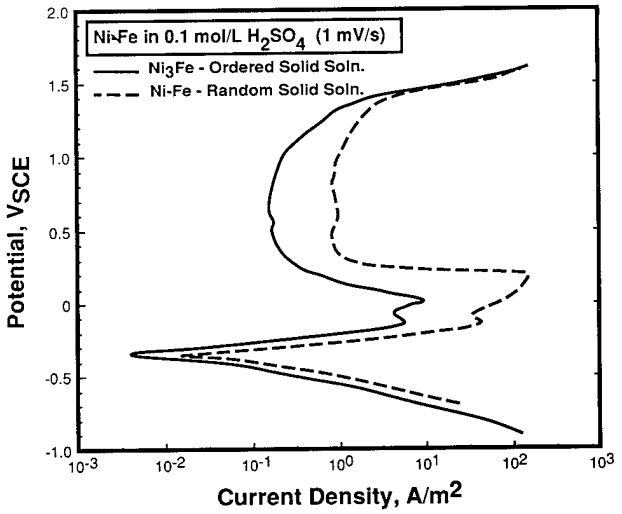

Fig. 11. Potentiodynamic polarization curves for ordered and random solid solutions of Ni–Fe.

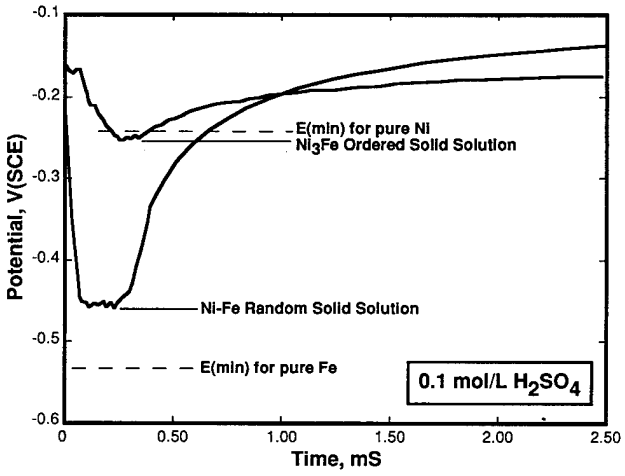

Fig. 12. Scratch repassivation transients for ordered and random solid solutions of Ni–Fe in 0.1 mol l^{-1} H_2SO_4.

aluminide alloys and to gain a fundamental understanding of the processes that dictate where these potentially catastrophic failures may occur. The results indicate that ductile nickel aluminide is susceptible to environmentally induced fracture in low pH solutions. This was found to be the result of hydrogen absorption and embrittlement of this material. No evidence of any other environmentally induced fracture mechanism was found. Because the chemical potential of aluminum in nickel aluminide is active with respect to the hydrogen evolution potential at atmospheric pressure, thermodynamics alone would predict that hydrogen absorption occurs during film rupture events in aqueous solution. However, scratch repassivation experiments revealed that the potential transient that accompanies scratch repassivation in nickel aluminide is very similar to that of pure nickel. This behavior was explained on the basis of the ordering of A_3B-$L1_2$ compounds such that B atoms have only A nearest neighbors and cannot dissolve at rates in excess of those dictated by the stoichiometric ratio. To test this hypothesis, experiments were conducted on nickel–iron samples which were heat treated to obtain either a completely random solid solution or a completely ordered compound (Ni_3Fe). These experiments revealed that ordering significantly reduces the activity of Fe in this alloy in accordance with this hypothesis.

Acknowledgements

The author would like to acknowledge the assistance of F. Biancaniello, J.L. Fink, D.E. Hall, M.R. Stout and U. Bertocci of National Institute of Standards and Technology, D. Gram, P. Madsen, J. Neilsen and J. Hansen of Danish Engineering Academy and V.K. Sikka, J.R. Weir and P. Angelini of Oak Ridge National Laboratory. This work was supported in part by the Department of Energy, Oak Ridge Operations under interagency agreement DE-AI05-900R21941.

References

[1] C.T. Liu and J.O. Stiegler, *Science, 226* (1984) 636.
[2] A.I. Taub and R.L. Fleischer, *Science, 243* (1989) 616.
[3] R.A. Buchanan and J.G. Kim, *Aqueous Corrosion Characteristics of Nickel Aluminides*, University of Tennessee, 1988.
[4] B.A. Dulmaine, *High-Temperature Ordered Intermetallic Alloys III*, Materials Research Society, Boston, MA, 1989, p. 597.
[5] U. Bertocci, R.E. Ricker, D.E. Hall, P.V. Madsen and J.L. Fink, *Corrosion Sci., 31* (1990) 471.
[6] P.J. Blau and C.E. DeVore, *J. of Tribol., 110* (1988) 646.
[7] P.J. Blau and C.E. CeDore, *Wear, 149* (1991) 27.
[8] R.A. Buchanan and J.G. Kim, *Aqueous Corrosion Characteristics of Nickel Aluminides, Six Month Progress Report*, University of Tennessee, 1987.
[9] R.D. Kane, *Environmental Cracking Tests of Iron and Nickel Aluminides, Final Report to Martin Marietta Energy Systems, Inc.*, Cortest Laboratories, Oak Ridge, TN, 1989.
[10] A.K. Kuruvilla and N.S. Stoloff, *Scr. Metall., 19* (1985) 83.
[11] R.E. Ricker, D.E. Hall and J.L. Fink, *Scr. Metall. Mater., 24* (1990) 291.
[12] R.E. Ricker, M.R. Stoudt and J.L. Fink, *Hydrogen Embrittlement of Ductile Nickel Aluminide During Corrosion in Aqueous Solutions*, TMS/AIME, Warrendale, PA, 1990.
[13] R.E. Ricker, U. Bertocci, J.L. Fink and M.R. Stoudt, in R.H. Jones and R.E. Ricker (eds.), *Environmental Effects on Advanced Materials*, TMS of AIME, Warrendale, PA, 1991, p. 213.
[14] Y. Calvayrac and M. Fayard, *Phys. Status Solidi, 17* (1973) 407.
[15] M.R. Stoudt, A.K. Vasudévan and R.E. Ricker, in V.S. Agarwala and G. Ugiansky (eds.), *Corrosion Testing of Aluminum Alloys*, ASTM, San Francisco, CA, 1990.
[16] T. Hagyard and J.R. Williams, *Trans. Faraday Soc., 57* (1961) 2288.
[17] T. Hagyard and M.J. Prior, *Trans. Faraday Soc., 57* (1961) 2295.
[18] T. Hagyard and W.B. Earl, *J. Electrochem. Soc., 114* (1967) 694.
[19] U. Kattner, unpublished calculations, 1992.
[20] I. Ansara, B. Sundman and P. Willemin, *Acta. Metall., 36* (1988) 977.

ELSEVIER

Materials Science and Engineering A198 (1995) 239–243

MATERIALS SCIENCE & ENGINEERING A

Corrosivity of Br^- and Cl^- on duplex stainless steel

Katsumi Yamamoto, Keizo Hosoya

Materials Engineering Department, Research and Development Division, JGC Corporation, 14-1, Bessho 1-chome, Minami-ku, Yokohama 232, Japan

Abstract

This report discusses the basis for material selection in chemical plants, especially focusing on the design of an actual plant based on laboratory corrosion test results. Both the chemical system created when chlorine gas and bromine gas were neutralized with alkaline solution, and material economics are considered when selecting duplex stainless steel as a construction material.

In addition, the corrosivity of Br^- and Cl^- with or without BrO^- and ClO^- on duplex stainless steel is discussed in terms of pitting and crevice corrosion. Br^- ions show a lower tendency to promote pitting and crevice corrosion on duplex stainless steel, compared with Cl^- ions. BrO^-, existing in a bromine gas neutralization system, acts as a strong oxidizer and easily shifts the corrosion potential of duplex stainless steel more noble, drastically promoting crevice corrosion.

Keywords: Material selection; Duplex stainless steel; Stress corrosion cracking; Pitting; Crevice corrosion; Bromide and chloride environments

1. Introduction

When selecting materials for chemical plants where halogen ions (1000 ppm or more), such as chloride ions, exist, the application of carbon steel is difficult owing to the corrosivity of process fluid and product contamination by corrosion. Austenitic stainless steel, such as 304 and 316, has been employed for major equipment and piping in terms of corrosion resistance, fabricability and weldability. This material's problems, however, are stress corrosion cracking (SCC), crevice corrosion and pitting, due to the influence of chloride ions and the like. Although many corrosion test results on Ni-base alloys have been reported in the environment previously mentioned, the application of Ni-base alloys to an actual plant is economically difficult. Thus, low-cost materials which have similar characteristics to 304 or 316 in corrosion resistance, and which are free from localized corrosion including SCC, have been wanted for years.

From this standpoint, low interstitial ferritic stainless steel such as type 444 has been adopted for chemical plants [1]. Type 444 has excellent advantages in SCC environments. However, it is sometimes difficult to apply as a structural material: i.e. crevice corrosion will occur where the halogen concentration exceeds 1000 ppm. Although some type-25Cr duplex stainless steels are not completely resistant to SCC, these steels are more resistant to crevice corrosion than type 444. This report covers the basis for material selection in chemical plants, especially forcusing on the design of an actual plant based on laboratory corrosion test results. Both the chemical system created when chlorine

Table 1
Corrosion failures in chemical plants

Corrosion forms		Sources	
		A (%)[a]	B (%)[b]
1	General corrosion (uniform attack)	13.1	34.4
2	Galvanic or two-metal corrosion	1.4	0.4
3	Crevice corrosion	4.8	6.0
4	Pitting	4.3	12.5
5	Intergranular corrosion	2.9	–
6	Selective leaching	1.0	–
7	Erosion corrosion	8.7	8.8
8	Stress corrosion cracking	41.1	17.1
–	Hydrogen damage	11.1	5.5
Others (including high-temperature corrosion)		11.6	15.3

[a]Reported by the laboratory.
[b]Reported by the inspectors.

SSDI 0921-5093(94)04529-1

gas and bromine gas were neutralized with alkaline solution, and material economics were considered when selecting duplex stainless steel as a construction material.

2. Basic concept in material selection

Basic factors when selecting materials in chemical plants are strength, corrosion resistance, fabricability, availability and cost, as proposed by Fontana and Green [2]. Allowable stress based on the design temperature/pressure is designated in standards such as ASME, JIS and DIN; thus, strength can be easily handled by plant engineers without difficulty. On the other hand, no standards provide requirements on corrosion resistance in actual usage; e.g. a carbon steel can be legally used as a pressure vessel material handling a 50% HCl solution at 50 °C. However, a fluid leakage accident deriving from a carbon steel adoption for such a vessel would be a major problem.

Although materials deemed to be suitable for actual usage have been adopted, many corrosion failures have been reported, unfortunately. Table 1 shows the corrosion failures which engineering firms have experienced to date in refineries and chemical plants.

This table shows that there is a slight difference between the failure analysis results reported by inspectors during plant shutdown maintenance and those conducted by research engineers in an engineering firm. It can be concluded that SCC and crevice corrosion occur frequently, as well as general corrosion in chemical plants.

Since considerable information [3,4] is available on corrosion resistance of many materials, general corrosion is controlled by the application of a corrosion allowance in the design stage. That is to say, the addition of a corrosion allowance to the necessary design wall thickness corresponding to a plant's life, and the prediction of equipment/piping life expectancy according to ultrasonic wall thickness measurement during maintenance or operation are available as countermeasures to general corrosion. However, both the position and time of occurrence of local corrosion, such as SCC and/or crevice corrosion, is difficult to predict. Therefore, reliable material selection is essentially needed in the designing stage.

Although details for preventing SCC are not described in this report, the basic requirement is that the materials which are not susceptible to SCC shall be selected in actual usage. For example, the following information is available for the design stage; the application of type 444 in the chloride-ion environments having caused SCC on 304 and 316 [1], the figure [3] showing available usage range of carbon steel in NaOH, and the relationship [5] between the maximum

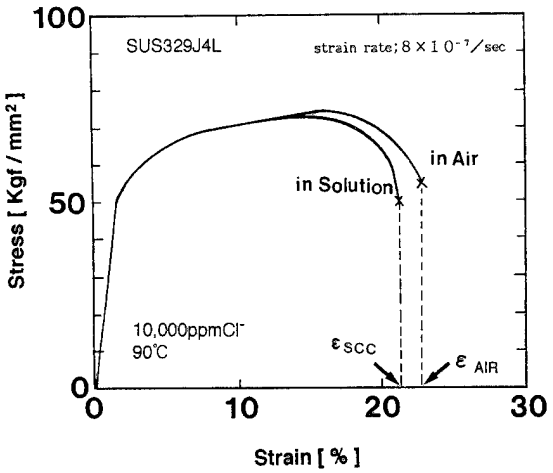

Fig. 1. SSRT result of SUS329J4L with 10 000 ppm of Cl^- at 90°C.

concentration of chloride ions and operating temperature in a cooling heat exchanger which employed austenitic stainless steel tubes. In addition, SCC evaluation methods based on laboratory test methods are also proposed; e.g. as an example, Fig. 1 shows the result of the SSRT (slow strain rate test) on 25Cr-type duplex stainless steel at 10 000 ppm of Cl^- at 90 °C. There is a slight difference in results between the evaluation above and data gained in air at 90 °C. However, when the formula below satisfies the n value, and neither the peculiar fractography of SCC nor secondary cracks are found at the ruptured surface, a material can be judged to have no SCC susceptibility from the engineering viewpoint.

$$\epsilon_{scc}/\epsilon_{air} \geqslant n \quad (1)$$

where, ϵ_{scc} is the fracture strain in SCC environment, ϵ_{air} is the fracture strain in air, and n is the minimum safety value for no SCC susceptibility.

Regarding the evaluation method for local corrosion other than SCC, the following section covers the different corrosivity of Br^- and Cl^- on duplex stainless steel.

3. Corrosivity of Br^- and Cl^- on duplex stainless steel

3.1. Test method

3.1.1. Specimen

The specimen tested was a commercially available plate of 25Cr-type duplex stainless steel (SUS329J4L), as shown in Table 2.

3.1.2. Test environments

When neutralizing bromine gas with an alkaline solution produces alkalinity, a solution including Br^- and

Table 2
Chemical composition of the duplex stainless steel (SUS329J4L) tested

	C	Si	Mn	P	S	Ni	Cr	Mo	N	Fe
SUS329J4L	0.012	0.44	0.87	0.025	0.001	7.19	24.96	3.13	0.13	Bal.

a small amount of BrO^- is formed. Thus, a NaBr solution and a NaBr solution including BrO^- were adopted as the corrosion test environments. In the case of neutralizing chlorine gas, it is hard to keep ClO^- in an alkaline solution. However, the solutions including NaCl and NaCl + ClO^- were also adopted as with the bromine gas system.

In both tests above, the halogen ion concentration was changed in the range of 1000 through 50 000 ppm and the pH of the solution was controlled at 12 by adding NaOH. Further, a sodium hypochlorite solution was used to adjust ClO^- in the solution, and BrO^- concentration was adjusted by generating BrO^-, keeping the pH of the bromine solution (commercially available) at 12 by adding NaOH and mixing the above-generated solution into NaBr solution. The BrO^- concentration was analyzed by the use of UV–VIS spectrophotometry.

3.1.3. Corrosion test

Corrosion behavior of a duplex stainless steel was studied at 90 °C by measuring the pitting potential (V'_c), threshold potential for crevice corrosion (E_{crev}) determined by the controlled potential test on a metal/metal crevice for 75 h, depassivation pH (pHd) and crevice corrosion resistance in immersion tests, respectively. On the E_{crev} test, the occurrence of corrosion is defined where a corrosion current density more than 10 μA cm^{-2} is measured and traces of corrosion are recognized after 75 h of testing.

3.2. Results and discussion

3.2.1. Corrosivity of Br^- and Cl^-

Fig. 2 shows the results of pitting potential tests on SUS329J4L in NaBr and NaCl solutions. When the Br^- and Cl^- concentration exceeds 10^{-1} mol l^{-1}, the pitting potential on SUS329J4L suddenly drops to a less noble value. The pitting potential in the NaBr solution was more noble than that in the NaCl solution in higher concentration regions (30 000 to 40 000 ppm or more) of the solution. Furthermore, E_{crev} in the Br^- solution, as shown in Figs. 3 and 4, was more noble than that in Cl^-, when the Cl^- ion concentration was the same as that of Br^- in the lower-concentration region; this was not similar to the dependency of Br^- and Cl^- concentration on V'_c. It can be said, however, that Cl^- showed higher localized corrosion activity than Br^-, based on the results of E_{crev} and V'_c.

In order to check the effect of Br^- and Cl^- on crevice corrosion and pitting, the depassivation pH was also measured in 1.7 M NaCl (10 wt.% NaCl) and 1.7M NaBr (17.5 wt.%) solution. As shown in Fig. 5, the depassivation pH on SUS329J4L in the Br^--ion environment was around −0.75, and in the Cl^--ion environment −0.25, which is similar to −0.20 reported by Okayama et al. [6]. These results show that the tendency for passivation of SUS329J4L in the Cl^- environment is no stronger than that in Br^-.

Based on the results above, it is clear that Cl^- ions produce a more corrosive environment than that in Br^-, when specifying pitting and crevice corrosion tendency on SUS329J4L.

3.2.2. Corrosivity of Br^-/Cl^- including BrO^-/ClO^-

As previously stated, the solution, after neutralization with bromine gas, includes BrO^- at a stabilized stage, when the solution is alkaline (ClO^- hardly exists in the neutralized solution of chlorine gas at pH 12); this has been confirmed by UV–VIS spectrophotometry.

Then, the effect of BrO^- on the corrosivity in Br^- solution and also ClO^- on the corrosivity in Cl^- solution were studied.

Fig. 6 shows the effect of BrO^- on the corrosion potential of SUS329J4L. When BrO^- exists in the solution, the corrosion potential easily rises up to +0.55 V (vs. SCE); this means that BrO^- acts as a

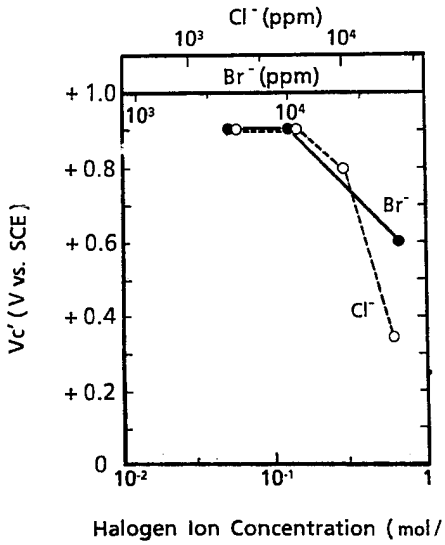

Fig. 2. Pitting potential in NaBr and NaCl solutions.

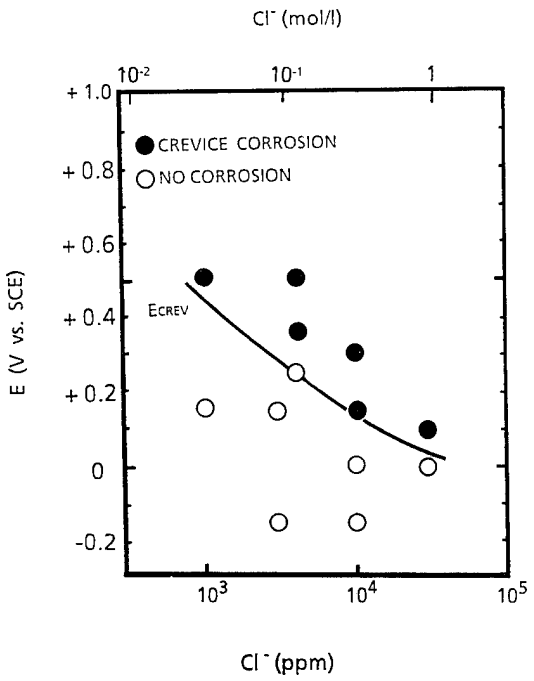

Fig. 3. Threshold potential for crevice corrosion in NaCl solution.

strong oxidizer. Fig. 7 shows the effect of ClO^- and BrO^- on corrosion potential when Cl^- and Br^- ion concentration is 10 000 ppm. That is, −0.2 V(SCE) of corrosion potential in only Cl^-/Br^- environment rises up to +0.6 V(SCE) when ClO^- and BrO^- co-exist with Cl^-/Br^-, respectively. BrO^- also shifted the corrosion potential noble even at a lower concentration such as several hundreds of ppm, as compared with ClO^-

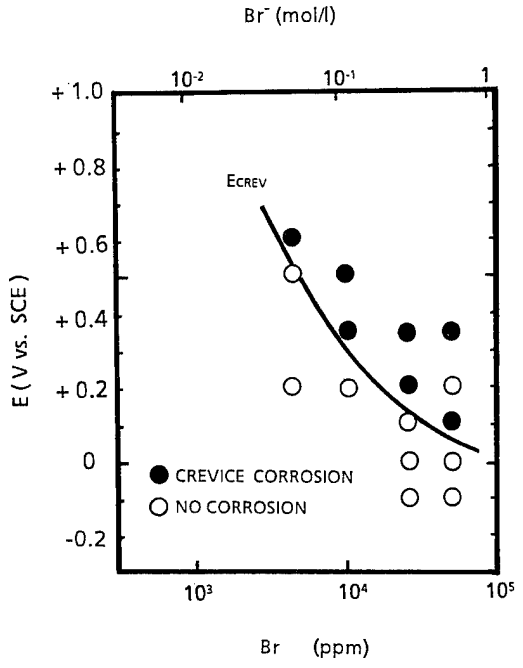

Fig. 4. Threshold potential for crevice corrosion in NaBr solution.

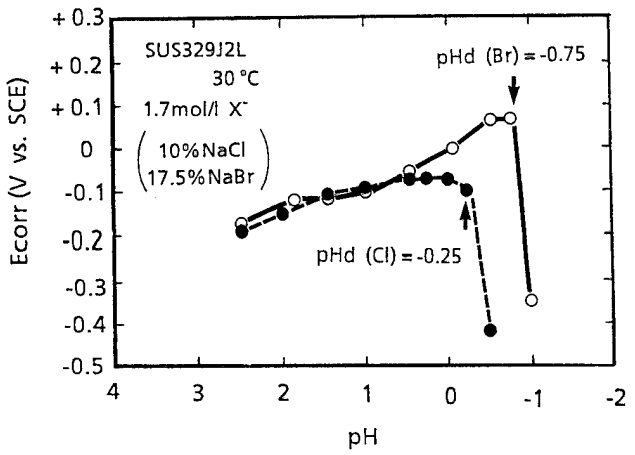

Fig. 5. Depassivation pH in Br^- and Cl^- solutions at 30°C.

Fig. 8 shows the effect of BrO^- on the corrosion potential and E_{crev} on SUS329J4L. When the Br^- concentration was about 3000 ppm, 600 ppm of BrO^- shifted the corrosion potential more noble than E_{crev}; that is, 3000 ppm of Br^- with 600 ppm of BrO^- will cause crevice corrosion. Then, the reliability of the E_{crev} test will be evaluated based on the immersion test.

As the concentration of Br^- is estimated to be 10 000 ppm for neutralizing bromine gas, the concentration of BrO^- necessary to cause crevice corrosion can be decided to be about 300 ppm, in both Figs. 6 and 8.

Table 3 shows crevice corrosion immersion test results in 10 000 ppm of Br^- with 300 ppm of BrO^- using SUS329J4L and Inconel 625 as reference material. Although no corrosion occurs in Cl^-/Br^- ions even continuing this test for 500 h at 10 000 ppm, it is clearly shown that only the addition of 300 ppm BrO^- generates a corrosive environment which would cause crevice corrosion even on Inconel 625, as well as in the duplex stainless steel. This means that the E_{crev} testing method can be used to predict the occurrence of crevice corrosion in an engineering sense.

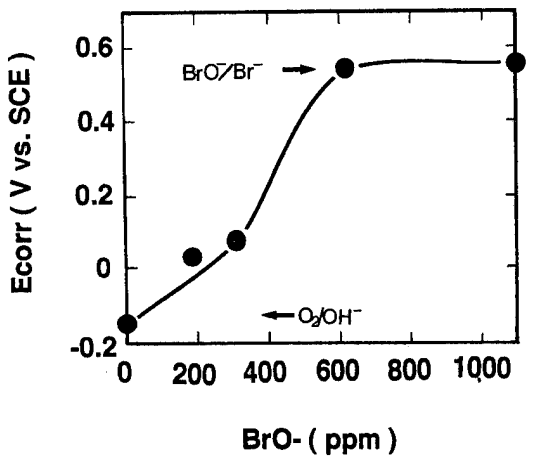

Fig. 6. Effect of BrO^- on corrosion potential in a 5000-ppm solution of Br^-.

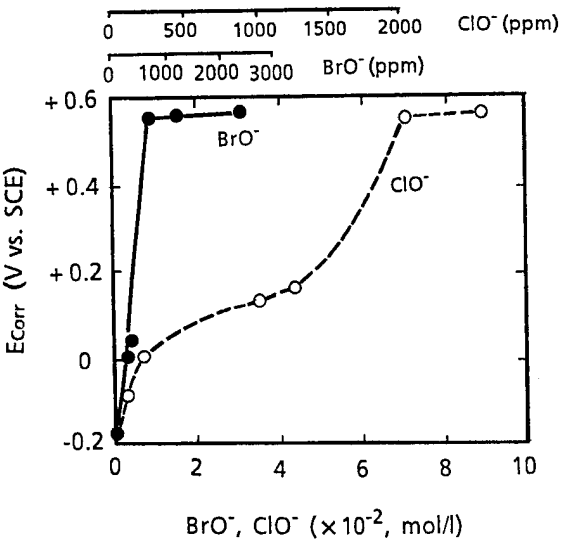

Fig. 7. Effect of BrO^-/ClO^- on corrosion potential in a 10000-ppm solution of Br^-/Cl^-.

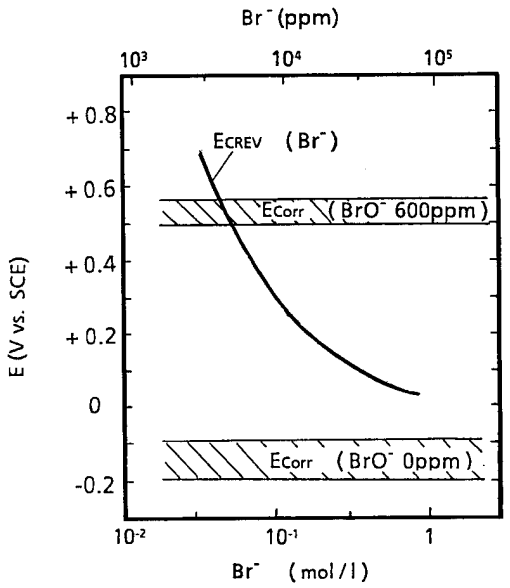

Fig. 8. Effect of BrO^- on threshold potential for crevice corrosion and corrosion potential in a Br^- solution.

Table 3
Immersion test results of SUS329J4L and Inconel625 in Br^- with BrO^- (90 °C, pH 12, 500 h; X, crevice corrosion; O, no corrosion)

		SUS329J4L	Inconel625
Br^-	10 000 ppm	○○	○○
BrO^-	300 ppm	× ×	× ×
Cl^-	10 000 ppm	○○	○○

4. Conclusions

In the chemical system produced by neutralizing chlorine gas and bromine gas by using alkaline solution, the evaluation of corrosivity and the applicability of a 25Cr-type duplex stainless steel can be concluded as follows;

(1) Br^- ions show lower corrosivity in pitting and crevice corrosion on SUS329J4L, compared with Cl^- ions; thus, the material selection can be made based on the corrosivity of the Cl^- environment rather than Br^-.
(2) BrO^-, existing in a bromine gas neutralization system, acts as a strong oxidizer and easily shifts the corrosion potential of SUS329J4L noble, which drastically promotes pitting and crevice corrosion. Thus, it will be concluded for the material selection that quantitative evaluation of BrO^- is needed under the actual operating conditions of the plant.
(3) The E_{crev} testing method clearly estimates the tendency for crevice corrosion on stainless steels.

References

[1] K. Yamamoto and N. Kagawa, *Mater. Perf., 20(6)* (1981) 32.
[2] M.G. Fontana and N.D. Green, *Corrosion Engineering*, McGraw-Hill, New York, 1978, p. 7.
[3] NACE, *Corrosion Data Survey*, Houston, 1985.
[4] P.A. Schweitzer, *Corrosion Resistance Tables*, Marcel Dekker, New York, 1976.
[5] S. Haruyama, *Mater. Perf., 21(3)* (1982) 3.
[6] S. Okayama, S. Tsujikawa and K. Kikuchi, *Boshoku-Gijutsu (Corrosion Engineering), 36* (1987) 702 (in Japanese).

ELSEVIER

Materials Science and Engineering A198 (1995) 245–256

MATERIALS SCIENCE & ENGINEERING A

Engineering with advanced and new materials

Roger W. Staehle

Department of Chemical Engineering and Materials Science, Corrosion Center, University of Minnesota, Minneapolis, MN, USA

Abstract

In engineering with advanced and new materials, it is necessary to recognize that they are, like older traditional materials, reactive chemicals which are prone to react and corrode in ambient environments. Engineering with these advanced and new materials to assure their satisfactory performance within their design life is approached by following the ten steps in the "corrosion based design approach." These steps include environmental definition, material definition, mode and submode definition, superposition, failure definition, statistical definition, accelerated testing, prediction, modification and optimization, and feedback and correction. When this approach is followed rigorously, maximum assurance of satisfactory performance is provided.

Keywords: Engineering; Advanced materials; New materials

1. Introduction

"Advanced" and "new" materials is a category which is broadly understood to include those with high strength–weight ratios, higher toughness, special electronic characteristics, special magnetic characteristics or special microstructures. Such materials include materials, ceramics, semiconductors, polymers, paper, wood, composite materials and special coatings. There is an extensive literature on the properties of such materials. Ashby, for example, has described in detail the strength–weight properties of all classes of materials [1].

Despite the improvements and special properties which are implicit in these materials, they are nonetheless still chemicals in solid form and will react with chemical environments according to well known thermodynamic predispositions. Metals even as nominally noble as platinum are reactive in certain environments, e.g. platinum reacts in hot chlorides to form chloroplatinate ions. In general, in view of their implicit reactivity, the surprise is not that materials fail, the surprise is that they work. In general, materials work or perform acceptably because they are designed to avoid aggressive conditions or because their corrosion resistance is increased to resist existing environments through alloying and through modifications of the environments.

In view of the inherent chemical reactivity of all engineering materials, including "new" materials, it is not reasonable to assume that the "newness" implies corrosion resistance, and predicting and assuring performance follow the same procedures as used for "old" materials. It should also be noted that some of the standard approaches to assessing corrosion resistance, such as polarization tests in acidic solutions, are not necessarily good predictors of corrosion behavior.

The intention of this paper is to describe in general how the performance of new materials may be predicted and assured. The approach used for the "new" materials is the same as that used for "old" materials, i.e. there is a set of steps which, when implemented, enables the corrosion performance of any material to be predicted. This approach is called the "corrosion-based design approach".

2. Corrosion-based design approach

A procedure has been described for predicting and assuring corrosion-resistant materials, regardless of their names and origins [2–4]. This procedure includes the following steps:

1. Environmental definition.
2. Material definition.
3. Mode and submode definition.
4. Superposition.
5. Failure definition.
6. Statistical definition.

SSDI 0921-5093(94)04530-5

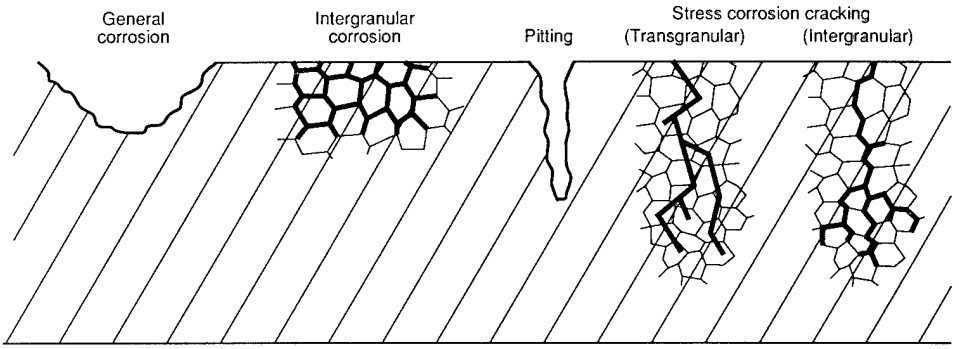

Fig. 1. Schematic views of four intrinsic modes of corrosion: general corrosion, intergranular corrosion, pitting and stress corrosion cracking. For stress corrosion cracking both intergranular and transgranular morphologies are shown. From Staehle [4].

7. Accelarated testing.
8. Prediction.
9. Modify and optimize: design, materials, environments, and operations.
10. Feedback and correction.

The significance of each of these is described in the references, and describing their significance for the many possible applications of new materials is not feasible here. However, since reliability and predictability for new materials are at least as important as for old materials, some discussion is useful. The approach here is to describe each of the ten steps with illustrations which may apply to several categories of advanced materials.

In considering corrosion for any material, there are essentially four morphologies or modes, as shown in Fig. 1. These modes occur regardless of the type of material. While these modes are not atomic "mechanisms", their morphologies are important in considering the velocity and implications of failure. In early texts on corrosion by Fontana [5] and Uhlig and Revie [6], more "forms" of corrosion than those in Fig. 1 were identified. Such additional forms included galvanic corrosion, crevice corrosion, erosion corrosion, microbiological corrosion and others. However, these are not really forms of corrosion; rather, they define different environments which affect the modes shown in Fig. 1. In this discussion, the morphologies of corrosion shown in Fig. 1 are referred to as "modes" of corrosion. When one of these modes, in a given material–environment combination, occurs according to several different dependences on stress, environment, temperature and material, these discretely different occurrences are described as different "sub-modes".

3. Environmental definition

Engineering environments have to be specifically defined in order to assess the extent of possible corrosion. In defining engineering environments specifically the following questions need to be asked:

1. How do the possible environments relate to the inherent reactivity of the material?
2. What is the full set of environments?
3. How do environments change over time?
4. How do stress environments relate to chemical environments?
5. How are design features incorporated into environmental considerations?
6. How is environmental control incorporated into environmental considerations?

In order to predict the possible occurences of various modes of corrosion, the relationship between the conditions in which the various modes of corrosion occur and the conditions which are produced by the environments needs to be determined. A simple approach to relating the conditions of the environment to the possible activity of corrosion modes is illustrated in Fig. 2. Fig. 2 shows the relationship between the conditions of the environment (Fig. 2(b)) and the conditions in which the mode of corrosion occurs (Fig. 2(a)). These conditions are shown in coordinates of potential and pH. Other coordinates could be used. Fig. 2(c) shows the superposition of these conditions; the overlap shows where failure by a specific mode in a specific environment is likely to occur without showing much, for the moment, about the rate of failure.

3.1. General relationship between materials and environments

The approach in Fig. 2 is similar to that developed by Pourbaix years ago, where he demonstrated the value of superimposing environmental and metallurgical equilibria on the same potential–pH diagrams. Fig. 3 shows the same principle of superposition utilized in Fig. 2 in the potential–pH diagrams. First, the modes of corrosion are defined in Fig. 3(a). These, of course, are the simpler ones of corrosion, nobility and passivity in contrast to the structure- and kinetic-related ones in Fig. 1. The environmental conditions are defined in Fig. 3(b); their superposition is shown in Fig. 3(c). Fig. 3(c) shows the conditions under which various

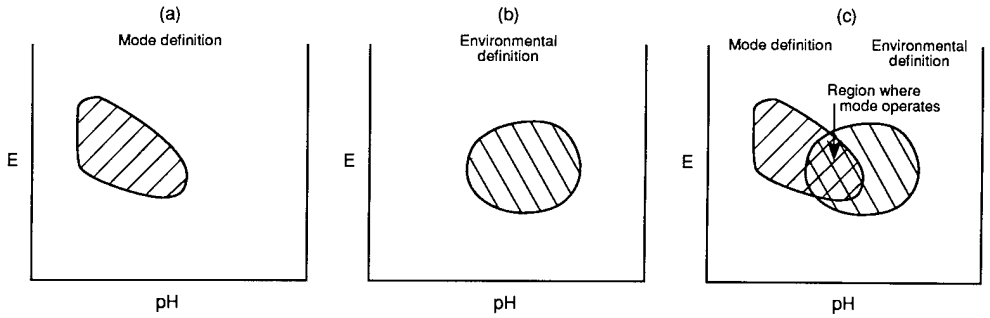

Fig. 2. Schematic view of (a) corrosion mode diagram, (b) an environmental definition diagram and (c) their superposition. From Staehle [4].

modes of corrosion can occur in the possible environments.

The main objective of the step of environmental definition is to define the environments which are directly adjacent to surfaces of materials of which components are fabricated. It is important to recognize that the bulk environments which surround the materials may not really be those which directly affect reactivity. Assuming that the bulk environments are the operative ones from a corrosion point of view has led to pervasively catastrophic corrosion in some applications.

3.2. Full set of environments

The environments which may occur adjacent to surfaces can be generally defined in four categories:

1. Major nominal.
2. Minor nominal.
3. Local nominal.
4. Accidental nominal.

These four environments are termed "nominal" to suggest that they are implicit parts of the design and need to be considered explicitly by designers. It is not necessary that designers understand the chemistry of these environments; it is important that they ask questions of those who do understand the chemistry as to the significance of each of these categories.

To give some examples which are relevant to new materials, the major nominal environment might be considered as moist air in the case of electronic materials. However, within the general category of moist air there are variations in corrosiveness, as shown in Fig. 4 relative to the amount of water. Below about 50% relative humidity (RH) there seems to be only several monolayers of water and this condition is generally not corrosive. However, above about 50% RH the surface is covered with progressively more water, and the corrosiveness is increased. Other examples of major nominal environments include sea water in the case of ships and pure deaerated water in the case of water-cooled power plants.

An example of minor nominal environments in the case of atmospheric corrosion would include CO_2 and, for more intense industrial environments, might include H_2S and other sulfur and nitrogen oxides. These would exist in minor but finite concentrations, and in atmospheric corrosion these species would be expected to accelerate corrosion because of their influence on acidity of the water layer. Examples of minor nominal environments in water-cooled power plants might include dissolved oxygen.

An example of local nominal environments in the case of atmospheric corrosion might include crevices or galvanic cells. For example, it is not uncommon in electronic circuits to use copper or aluminum as contacts or heat sinks. These might be juxtaposed with more active or more noble materials and produce accelerated corrosion. Similarly, a crevice produced by tightly fitting but non-bonded materials including insulations may accelerate corrosion especially in view of the ready availability of oxygen to act as a cathode on surrounding surfaces. Local nominal environments may also be produced by the actions of microbes.

Finally, an example of accidental nominals in atmospheric corrosion might include the fumes from a nearby industrial complex which blow in a normally unexpected direction. Another example in electronic components might involve chemicals leached from surrounding insulation. Accidental nominal for a power plant would include species which leak into a steam cycle from perforated condenser tubes.

Each of these nominals defines a set of questions which need to be answered to assure reliable performance. These four nominal conditions can be readily evaluated by experts and non-experts alike.

3.3. Change of environments over time

Environments change over time, and specific questions need to be asked for each time period concerning the chemical environments which may be immediately adjacent to component surfaces:

1. Manufacture.
2. Storage.
3. Shipment.
4. Installation.
5. Startup.
6. Operation.

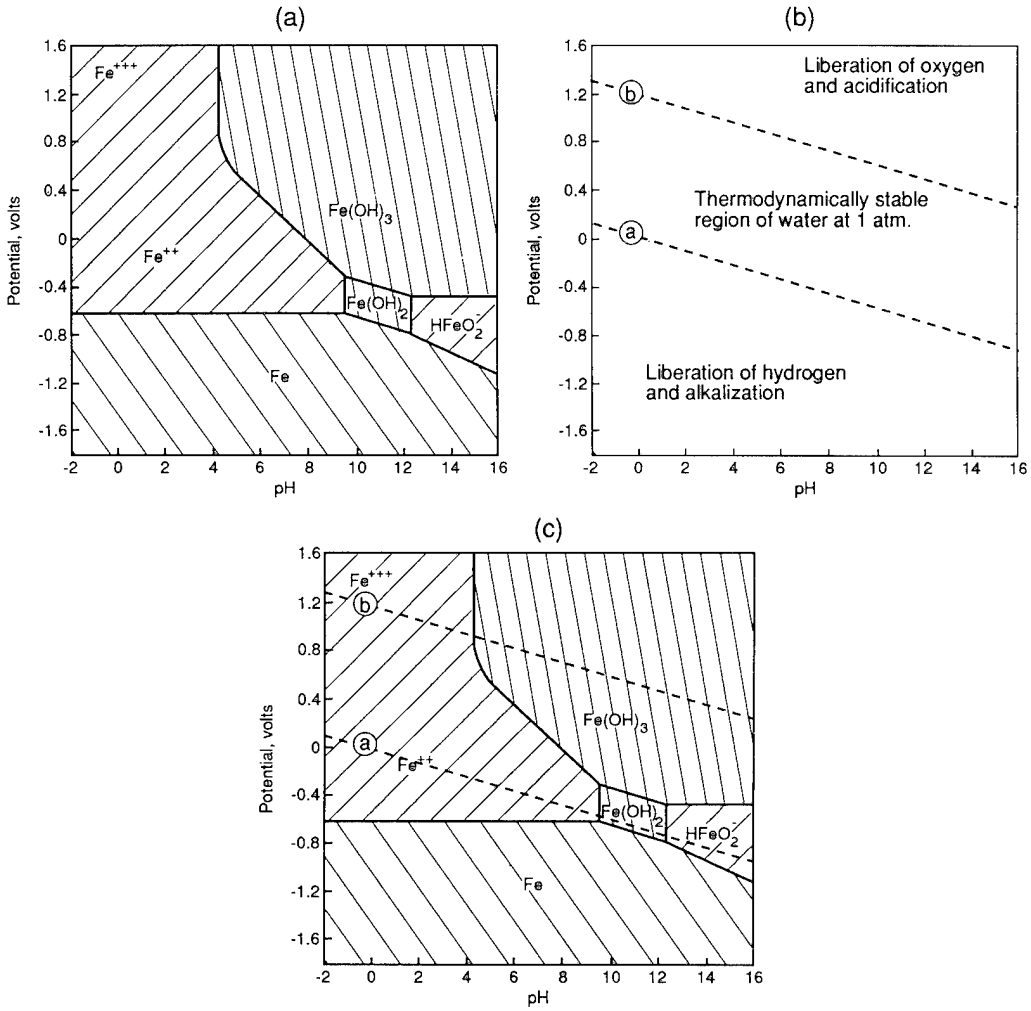

Fig. 3. Superposition of potential–pH diagrams for iron and water. (a) Potential–pH diagram for iron; (b) potential–pH diagram for water; (c) superposition of diagrams to give integrated view of relationship between metal and environment. Adapted from M.J.N. Pourbaix, *Atlas of Electrochemical Equilibria in Aqueous Solutions*, NACE, CEBELCOR, Houston, TX, 1974.

7. Shutdown.
8. Continued operation for long times.

Environments which are unique to each of these periods are best known to the designers and operators. Regardless, specific questions need to be asked concerning the environments at each of these time periods. From experience, corrosion failures can occur at each of these time periods. Once each of these periods is evaluated, appropriate preventative actions can be defined.

3.4. The stress environment

It has been well established that stress affects corrosion primarily through stress corrosion cracking (SCC). The effects of stress have been extensively discussed and need not be considered further here. Nonetheless, it is important to identify several features of stress which need to be considered in design of new materials.

In both "new" and "old" materials, residual stresses will continue to be the main contributer to stress corrosion cracking. Therefore, consideration needs to be given to the sources of such stresses and means to minimize them. Further, for many of the electrical materials, such as copper, thresholds for SCC are low.

Important stresses in small-dimensional structures are also produced by the expansion of corrosion products. Such stresses were first quantified in the early 1900s in connection with reinforcing bars in concrete, and numerous measurements of forces due to corrosion products have been made since, notably by Pickering et al. [8]. In thin electronic components, stresses are produced by the epitaxial formation of corrosion product films. These stresses have been measured and can be significant for stress corrosion cracking.

Finally, in the small dimensions of electronic components, stresses due to the differential expansion of dissimilar materials may contribute to stress corrosion cracking.

Thus, in components where there are no applied stresses which can be calculated, stresses leading to stress corosion cracking may still exist and their possible deleterious effects need to be accounted for.

3.5 *Effect of design features on corrosion*

Since all engineering materials are reactive chemicals, design contributes importantly to minimizing corrosion by utilizing materials in their optimally corrosion-resistant conditions or arrangements. Good design not only achieves the objectives of the resistant conditions or arrangements but also considers how long this component will function reliably from a corrosion point of view.

In considering the implicit relationship between design and corrosion, it is important to recognize that the component can fail by more than one process. Each of the processes by which corrosion can produce failure can be called a "mode-location" case of corrosion. Thus, a component can sustain the same submode of corrosion at different locations; it can also sustain failure by different submodes at the same location. In general, most components may sustain failure by several mode–location cases and each of these needs to be considered in assessing the total probability of failure. There is almost never a condition where a component will sustain only a single mode–location case of corrosion.

In addition to a component sustaining more than a single mode–location case of corrosion, it is important to consider corrosion occurring on both sides of a single piece of material. Often, corrosion is extensively considered as a material interacts with the process fluid, but effects of the exterior environment are not considered. Thus, failure may occur as impurities are leached from environments on the outside, e.g. from insulation, and deposited on the exterior surface.

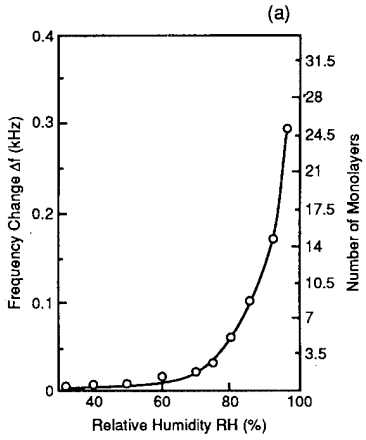

Fig. 4. Thickness of the water layer on iron as a function of relative humidity. The left ordinate refers to frequency change as measured by quartz crystal microbalance. Adapted from Y. Ishikawa, T. Yoshimura and T. Ozaki, *Zairyo-to-Kankyo (Materials and Environments), 40* (1991) 540.

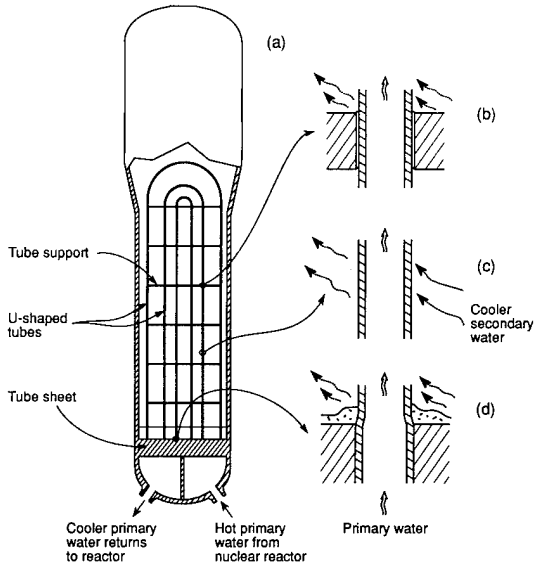

Fig. 5. Schematic view of a U-tube recirculating steam generator in a pressurized water nuclear reactor together with three specific locations which are characteristic of environmental conditions. (a) Overall view of the steam generator. Hot primary water flows inside the tubes and cooler feedwater flows over the outside of the tubes. Steam exists to the turbine. (b) Tube is held by tube support and creates a heat-transfer crevice. (c) Tube surface is washed by the environment inside and outside. (d) Tube is held in tube sheet. Layer of sludge is shown on top of tube sheet and creates a heat transfer crevice. From Staehle [4].

Other design features need to be considered as they exacerbate corrosion. One of these is heat transfer, which leads to superheat and concentration of impurities. Such superheat and subsequent concentration of impurities are important in steam generators of nuclear power plants, as shown in Fig. 5. Often, inpurities having a few parts per billion concentration in the bulk can be concentrated to 50% solutions or higher in heat-transfer crevices. This magnification is similar to that of the concentration of minimum concentrations of bulk impurities in grain boundaries.

Corrosion is also exacerbated when deposits form on surfaces. Such deposits occur when local conditions of low flow occur or when there is heat transfer on free surfaces. Deposits occur as temperatures increase and retrograde solubility produces insoluble products. Deposits also are produced with temperature gradient and activity gradient mass transfer.

Design may also produce unwanted galvanic couples. For example, graphite composites are much more efficient cathodes than aluminum. Thus, a graphite composite in intimate and non-insulated contact with aluminum can lead to extensive galvanic corrosion of

the aluminum. The same corrosion occurs when a relatively noble material such as copper, nickel or the platinum elements is juxtaposed with more active materials such as aluminum, zinc or iron base alloys.

Hence design is an important factor in corrosion. Intelligent design can minimize corrosion; on the other hand, corrosion may be exacerbated by design features such as heat-transfer crevices or low-flow-induced deposits.

3.6. *Effects of environmental control*

Corrosion may be minimized by controlling the environments. Such controls would be undertaken when it becomes clear that the naturally occurring conditions do not have the capacity to minimize corrosion adequately. Such steps in environmental control might include hermetic sealing, vapor-phase inhibitors, oxygen scavengers, pH adjustments using volatile or solid additions and specific anodic or cathodic inhibitors. These additions need to be carefully assessed from the point of view of their direct effects and from the point of view of unwanted side-effects.

A well known side-effect of pH-adjusting conditions is the use of caustics to raise pH. While additions such as phosphate, sodium hydroxide and lithium hydroxide can achieve their intended changes in pH, it is also possible that these species concentrate to produce caustic stress corrosion cracking.

4. Material definition

The following aspects of materials need to be defined with respect to corrosion:

1. Average composition.
2. Composition of multiple phases.
3. Impurity species and concentrations.
4. Grain boundary composition.
5. Anisotropy of grains.
6. Strength.
7. Toughness.
8. Cold work.
9. Surface conditions.

The importance of these conditions was discussed in detail in an earlier review [9]. Until these features have been defined, a material is not sufficiently well defined for predicting corrosion performance.

With respect to average compositions of metallic materials, it has been well established that the passive films relate to predictions from thermodynamic diagrams of the pure or component materials. Thus, in the case of iron in oxygenated environments, both Fe_3O_4 and Fe_2O_3 are observed, and the stability of these protective films depends directly on the pH with the optimum pH for corrosion resistance in room-temperature water being about 12.5. In alloys the passive film compositions on alloys relate directly to the pH dependence of the respective film stabilities. For example, in caustic solutions the passive films on iron–silicon alloys contain little silicon; similarly, the same occurs with iron–chromium alloys in caustic solutions. On the other hand, chromium is enriched in the films formed on iron–chromium alloys in acidic solutions. For iron–molybdenum alloys little Mo is seen in the films except in very acidic solutions.

Thus, in alloys where boron or phosphorus has been added, it is unlikely that these species would be present in the passive films since these species are broadly soluble in aqueous solutions. However, if boron and phosphorus form compounds with iron, then they may be expected to remain in the films and may affect the passivity according to effects on the defect structure or on the dissolution kinetics. Such effects have been identified by Sklarska-Smialowska and Staehle [10,11].

The importance of the compositon of second and third phases has been extensively documented in the literature. Such phases may be more corrosion resistant or less. They may also be more or less tough.

The progressive purification of materials in general seems to produce beneficial effects and especially on stress corrosion cracking parameters. Such trends have been summarized by Speidel and Atrens [12].

Defining the composition of grain boundaries is, perhaps, the most important feature of material definition since many of the modes of accelerated failure occur at grain boundaries. Understanding grain boundaries, including structure and composition, is important to predicting corrosion behavior in all types of solids, including wood. If the grain boundaries have compositions which are more prone to degradation than the bulk, corrosion will generally proceed at the boundaries. Fig. 6 shows possible profiles of compositions associated with adsorption of species at grain boundaries and with precipitation to form second phases. In the latter case the extent of the compositional change is relatively small, but the magnitude of the difference between the average impurity composition and the grain boundary composition may be five to six orders of magnitude. Where the precipitates form in Fig. 6(b), the extent of the compositional changes is larger and there are three regions of change: in the adjacent precipitate-free zone, in the composition of the precipitate and at the interface between the precipitate and precipitate free zone.

Fig. 7 shows that there are at least 11 avenues by which grain boundaries can lead to premature failure indicating that there is no unique avenue; this broad range of possibilities for the effects of grain boundaries on failure needs to be considered.

Effects of anisotropy, strength, toughness, cold work and surface conditions are similarly important and need

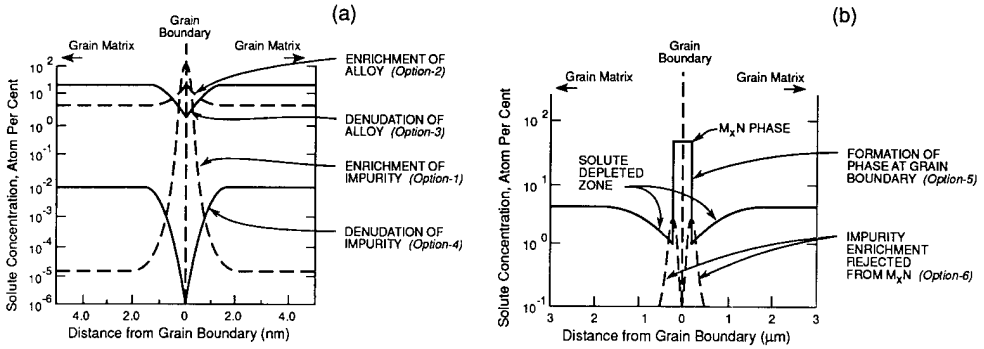

Fig. 6. Schematic view of concentration versus distance from grain boundaries for circumstances where precipitates are formed and where atomic species are adsorbed. (a) Four options for concentration versus distance where atoms are adsorbed or rejected at grain boundaries. (b) Principal features of composition versus distance for the case where precipitates are formed at grain boundaries. From Staehle [4].

to be defined with respect to possible corrosion processes. Until this full set of materials conditions, or their equivalent in the different types of materials, is defined, corrosion behavior cannot be predicted.

5. Mode and submode definition

Fig. 2 suggests that the occurrence of corrosion requires both the environments and the modes of corrosion be defined and compared over similar ranges of environmental parameters such as pH and potential. While the pH and potential are not necessarily the only set nor the total set of coordinates, they serve to illustrate an approach.

Fig. 2 suggests that the extent of any of the relevant modes and submodes of corrosion shown in Fig. 1 needs to be mapped according to the effects of several environmental variables such as pH and potential. Clearly, defining corrosion for a single environmental condition or for a not-well-defined condition would be inadequate.

The definition of modes and submodes of corrosion has been discussed in detail in several reviews and is considered specifically in Ref. [3]. In general, the definition of the simplest corrosion stability for metals is shown by the potential–pH diagram in Fig. 3. However, these plots do not provide information on the structure- and kinetic-related corrosion.

A more kinetically related plot of corrosion modes is provided by a mode diagram as shown for Inconel 600 in Fig. 8. This diagram applies to about 300 °C for Inconel 600 exposed to aqueous solutions and is based on the work of several investigators. The development of this diagram has been discussed in several reviews [2–4,13]. This diagram shows the domains of SCC,

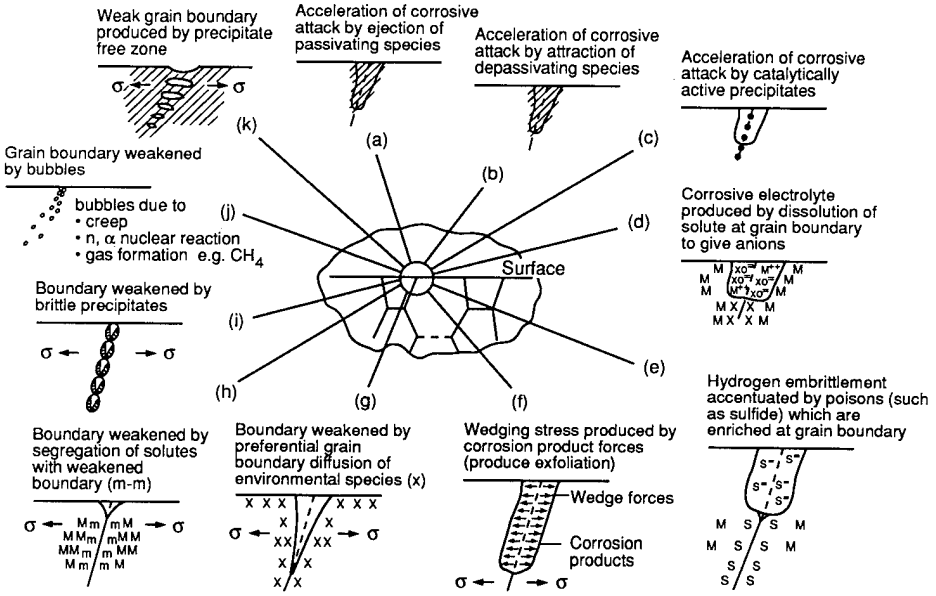

Fig. 7. Processes by which chemical and structural conditions at grain boundaries lead to SCC. Starting with (a) and going to (k) proceeds from mostly chemical to mostly mechanical processes. From Staehle [4].

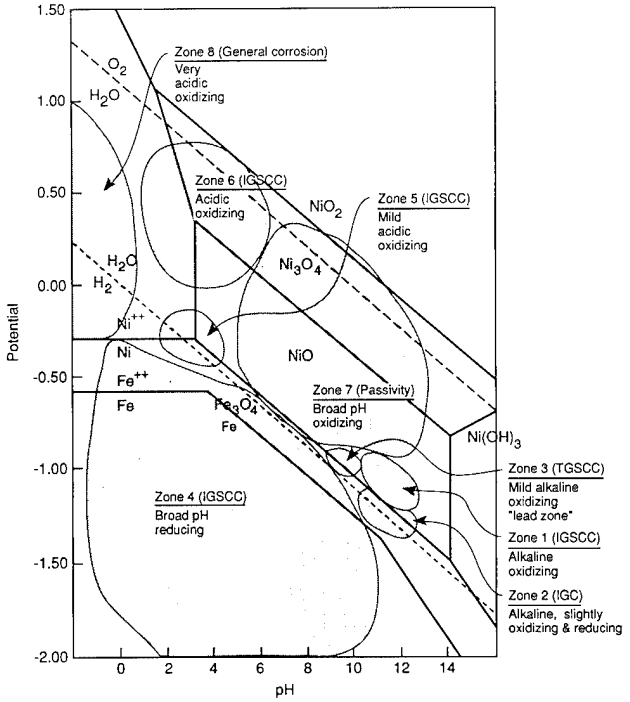

Fig. 8. Integrated view of SCC data for low-temperature mill-annealed Inconel 600 in high-temperature water generally in the range of 300–350 °C. Ranges of submodes based on judgment. Submodes of corrosion identified and are numbered starting from the right. From Staehle [4].

passivity and general corrosion for Inconel 600. Further, it shows domains for five separate submodes of stress corrosion cracking: the first occurs in the caustic region, the second in the low-potential region, the third in the acidic slightly oxidizing region, the fourth in the acidic highly oxidizing region and the fifth is associated with the existence of lead impurities. Slimilar arrays of submodes are found for stainless steels and low-alloy steels. This diagram in Fig. 8 can be converted to one which shows the effects of environmental parameters on the rate or threshold of corrosion, as shown in Fig. 9. Fig. 9 shows the effects of pH and potential on the $x-y$ axes on the threshold stress for SCC on the z axis.

Figs. 8 and 9 show that the modes and submodes of corrosion, which depend on structure and kinetics, occur according to regular patterns and can be correlated generally with thermodymanic boundaries related to the occurance of hydrogen or the instability of protective films. Such patterns are important for mechanistic understanding and also demonstrate that the occurrence of the modes and submodes can be predicted with some confidence. Figs. 8 and 9 also indicate that a certain amount of experimental work is necessary in order to define the domains of existence of the modes and submodes. Patterns similar to Figs. 8 and 9 can be expected for all materials.

6. Superposition

Figs. 2 and 3 show that the conditions for corrosion to occur can be defined by superimposing diagrams which define environments and those which define modes and submodes of corrosion. The approach to such superpositions and necessary conditions have been described in other reviews [2–4,9].

While Fig. 2 incicates that only one region of corrosion is found in superposition, this is schematic; in practice, several submodes of corrosion, stress corrosion cracking and the other modes identified in Fig. 1 might be identified.

Once the regions for corrosion have been identified by superposition in a specific application, it is necessary to determine how fast such corrosion occurs, and this is discussed in subsequent sections.

7. Definition of failure

Corrosion failures are often taken as complete perforation by some time which is less than the design life. However, in general, the definition of corrosion-related failure may be different for different materials and in different applications. Examples of failure definition may be the following:

1. Decrease in quality visual appearance.
2. Failure of some fraction of components (e.g. circuit boards).
3. Failure of some fraction of heat exchanger tubes.
4. Partial penetration by corrosion.
5. Release of product.

Once failure has been defined, it is possible to define experiments to evaluate it.

8. Statistical definition

It is not possible to predict exactly when failure will occur owing to the inherent variabilities in the many factors which contribute to failure. These variabilities are implicit in both the materials and the environments. Although it is interesting to speculate on the "deterministic" nature of failure, such determinism is not achievable and it is misleading to advise otherwise.

The statistical nature of failure is discussed extensively in textbooks, including that by Nelson [14], and is not discussed here. Regardless of whether and what type of statistical approach is used, some framework needs to be defined within which failure can be defined and predicted. Naturally, it is not necessary to use a statistical format and a simple failure depth versus time or a failure time versus $1/T$ may be used, as is often done. Such lesser methods are used when money is short of when failure times can be confidently known to

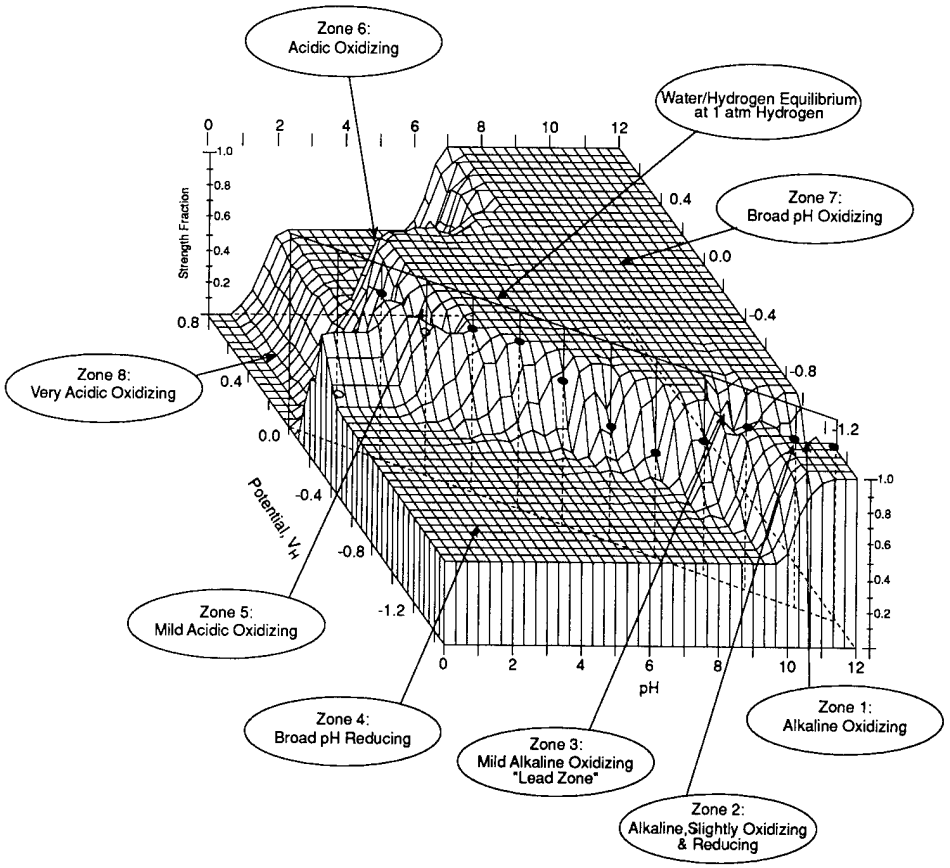

Fig. 9. Three-dimensional diagram for intensity of SCC and other modes of corrosion for Inconel 600 in the range of 300 °C for the low-temperature mill-annealed condition. Useful strength plotted versus environmental parameters of potential and pH. One atmosphere hydrogen equilibrium line shown as a vertical plane and indications are shown by dots where the hydrogen plane intersects surface topology. Submodes are designated. From Staehle [4].

be much greater than the design life. On the other hand, such approaches are risky and generally not adequate.

In developing a statistical format as a basis for quantitative model of failure, there are a number of well known approaches. The Weibull format is used here only because it is used so widely to describe failure phenomena. The probability density functions for describing time-to-failure is given in Eq. (1), and examples of such functions are shown in Fig. 10. The cumulative failure distribution is shown in Eq. (2) with the linear version in Eq. (3), and examples of such function are shown in Fig. 11. The curves in Fig. 11 show the fraction of items failed versus time.

$$f(t) = \left[\frac{b}{\theta}\left(\frac{t-t_0}{\theta}\right)^{b-1}\right]\exp\left[-\left(\frac{t-t_0}{\theta}\right)^{b}\right] \quad (1)$$

$$F(t) = 1 - \exp\left[\left(\frac{t-t_0}{\theta}\right)^{b}\right] \quad (2)$$

$$\log\left[\log\frac{1}{1-F(t)}\right] = A + b\log(t-t_0) \quad (3)$$

where

$f(t)$ = probability density function;
b = Weibull slope;
t = time;
t_0 = initiation time;
θ = Weibull characteristic time;
$F(t)$ = cumulative fraction failed.

The parameters of the above Weibull equations can be determined as a function of environmental variables, as suggested by the dependence of the Weibull parameters on stress shown in Fig. 12. This approach has been described in other reviews [4,9]. Once the Weibull parameters of Eqs. (1)–(3) are determined as a function of environmental variables, it is possible to utilize Eq. (3) to predict performance under other circumstances, as shown by Fig. 13. Once the Weibull parameters are determined as a function of environmental variables, it is also possible to predict the fraction failed as environmental variables change over time, as has been discussed in another review [4].

9. Accelerated testing

In order to obtain the necessary information to evaluate the statistical parameters of Eqs. (1)–(3), it is usually necessary to conduct experiments which are

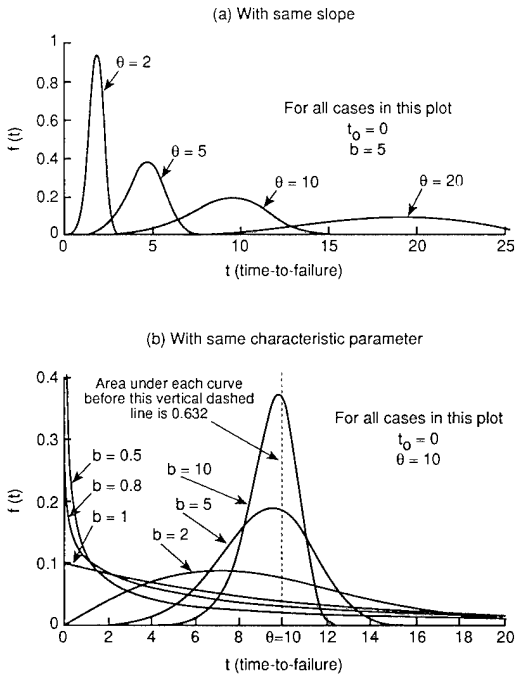

Fig. 10. Probability density function for Weibull distribution. (a) $b = 5$ with $\theta = 2, 5, 10, 20$; (b) $\theta = 10$ with $b = 0.5, 0.8, 1.0, 10$. The initiation time, t_0, is taken as zero in both cases. The time-to-failure is in arbitrary units. From Staehle [4].

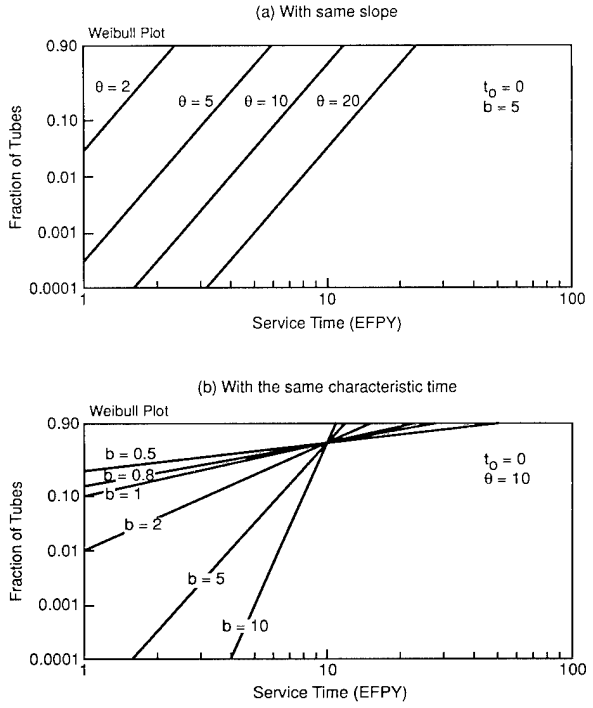

Fig. 11. Linearized cumulative Weibull distribution. (a) $b = 5$ with $\theta = 2, 5, 10, 20$; (b) $\theta = 10$ with $b = 0.5, 0.8, 1.0, 5, 10$. The initiation time, t_0, is taken as zero in both cases. The time-to-failure is in arbitrary units. From Staehle [4].

accelerated. In other words, it is necessary to conduct experiments for shorter times at more aggressive conditions, as indicated in Fig. 13. The results of such

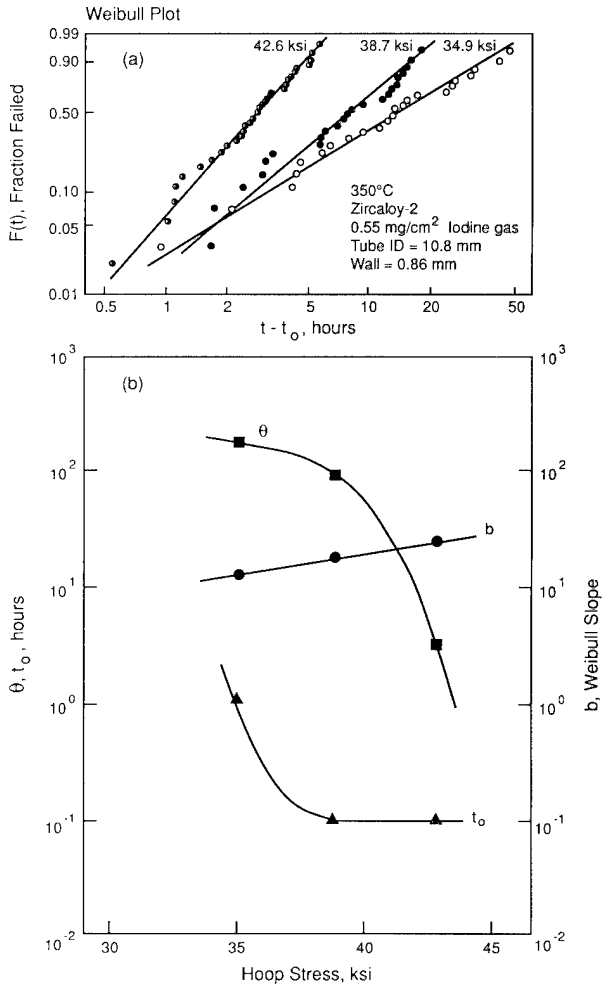

Fig. 12. Effect of stress on the cumulative failure rate of Zircaloy-2 in iodine gas. (a) Cumulative distributions for three stresses. (b) Effect of stress on characteristic time, slope and initiation time. Adapted from S. Shimada and M. Nagai, *Reliability Eng.*, *9* (1) (1984) 19.

experiments are conventionally extrapolated as in Fig. 13 to the conditions of operation.

In conducting accelerated tests, there are several critical considerations. The most important consideration is that the accelerated testing considers the modes and submodes which are expected at operating conditions. Other critical considerations in accelerated corrosion testing are discussed in a separate review [15].

It is important also to recognize that there are several avenues for achieving acceleration, such as via temperature, stress and environmental concentration. It is usually desirable to achieve acceleration by several of these avenues so as to maximize the confidence of prediction.

10. Prediction

In predicting performance, the data would appear much as they are in Fig. 11. However, it is likely that

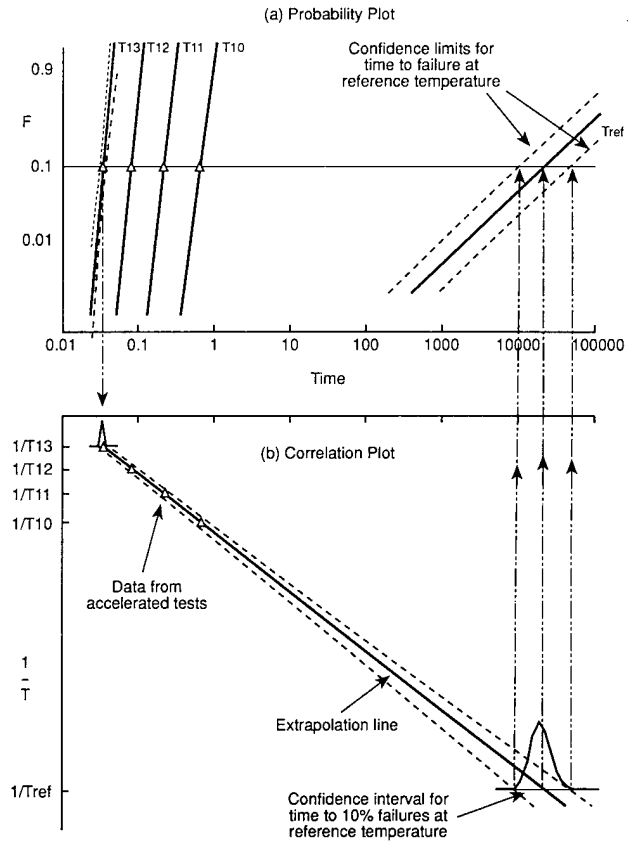

Fig. 13. (a) Schematic cumulative probability plot shoeoing curves for high temperatures and for a reference temperature. Confidence limits are also noted. (b) $1/T$ versus time plot showing probability density functions corresponding to cumulative probability plots. From R.W. Staehle and K.D. Stavropoulos, *Elements and Issues in Predicting the Life of Containers for Radioactive Waste*, Topical Report for Yucca Mountain Project, Department of Energy, University of Minnesota, Corrosion Center, November 7, 1991.

any given component could sustain more than one mode–location case of failure. Fig. 14 shows the situation where there are several mode–location cases of failure in tubes for nuclear steam generators. The total failure probability, F_T, is obtained from Eq. (4). Eq. (4) provides the means for aggregating the individual failure probabilities for the different mode–location cases on a single component. Thus, F_T gives the overall failure probability for the component.

$$F_T = (1 - F_1)(1 - F_2) \ldots (1 - F_n) \quad (4)$$

where F_T = total failure fraction and F_n = failure fraction for the nth submode.

There are many other avenues for predicting the preformance of components. Some of these were discussed in Ref. [4] and many were discussed by Nelson [14]. However, in general, prediction of failure from a corrosion point of view involves the steps in the corrosion-based design approach.

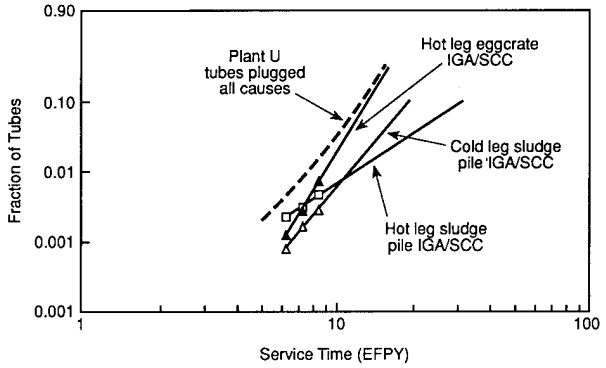

Fig. 14. Example of adding cumulative distributions from three separate model–location cases to produce a combined distribution for the failures of Inconel 600 tubes in a nuclear steam generator. Data taken from a hot leg sludge pile, cold leg sludge pile and tubes in the egg crate tube supports. From Staehle [4].

11. Modify and optimize: design, materials, environments and operations

The predictions which are developed will lead either to a demonstration that the design is satisfactory or that it is inadequate in some respects. These results will lead to modifications in the design, materials, environments and operations in order to avoid the predicted failures. Several iterations on this process may be required.

12. Feedback and correction

As equipment operates, certain unexpected problems occur. This information is used to modify the design, materials, environments and operations.

In order to provide useful feedback in addition to the failures themselves, it is usually desirable to provide instrumentation and periodic measurements of operating equipment. Such measurements for electronic equipment might include measurements of acidic gases in the environment and relative humidity. In other kinds of equipment, e.g. aircraft gases of power generation equipment, it is desirable to determine the existence and rate of growth of cracks using various NDE methods.

References

[1] M.F. Ashby, *Materials Selection in Mechanical Design*, Pergamon Press, Oxford, 1992.

[2] R.W. Staehle, Environmental definition, in R.W. Revie et al. (eds.), *Materials Performance Maintenance*, Pergamon Press, Ottawa, Ont., 1991.

[3] R.W. Staehle, Development and application of corrosion mode diagrams, in S.M. Bruemmer at al. (eds.), *Fundamental Aspects of Stress Corrosion Cracking*, TMS, Warrendale, PA, 1992.

[4] R.W. Staehle, Combining design and corrosion for predicting life, in *Life Prediction of Corrodible Structures, Proceedings of Meeting held in Kauai, Hawaii, November 1991*, NACE, Houston, TX, to be published.
[5] M.G. Fontana, *Corrosion Engineering*, McGraw-Hill, New York, 3rd edn., 1986.
[6] H.H. Uhlig and R.W. Revie, *Corrosion and Corrosion Control*, Wiley-Interscience, New York, 3rd edn., 1985.
[7] M.J.N. Pourbaix, *Thermodynamics of Dilute Aqueous Solutions*, Edward Arnold, London, 1949.
[8] H.W. Pickering, F.H. Beck and M.G. Fontana, *Corrosion, 18* (1962) 230t.
[9] R.W. Staehle, Understanding "situation-dependent strength": a fundamental objective in assessing the history of stress corrosion cracking, in R.P. Gangloff and R.P. Ives (eds.), *Environment-Induced Cracking of Metals*, NACE, Houston, TX, 1989.
[10] Z. Sklarska-Smialowska and R.W. Staehle, *J. Electrochem. Soc., 121* (1974) 1146.
[11] C. Lukac, J. Lumsden, Z. Szkarska-Smialowska and R.W. Staehle, *J. Electrochem. Soc., 122* (1975) 1571.
[12] M.O. Speidel and A. Atrens, *Corrosion in Power Generating Equipment*, Plenum Press, New York, 1984.
[13] R.W. Staehle and J.A. Gormon, *Corrosion Science and Engineering*, CEBELCOR, Brussels, Vol. 157–158, RT 297–298, 1989.
[14] W. Nelson, *Accelerated Testing*, Wiley-Interscience, New York, 1990.
[15] R.W. Staehle, in *Application of Accelerated Corrosion Tests to Service Life Prediction of Materials*, STP 1194, G. Cragnolino and N. Sridhar (eds.), ASTM, Philadelphia, PA, 1992.

ELSEVIER

Materials Science and Engineering A198 (1995) 257

MATERIALS SCIENCE & ENGINEERING A

Closing Comments

Development of the corrosion science community

We've learned many new things in these two-and-a-half days. When I come to the United States, I am always very pleased to learn that my old friends are still active in studying corrosion science and engineering and of the advances they have made.

When Professor Ron Latanision and I planned this seminar, we considered seriously the subject of these deliberations. Progress in science and engineering requires that we extend our perspectives to interdisciplinary fields. Otherwise, our science base will become narrower and narrower, and our community will become smaller and smaller.

To emphasize my concern, you may know that the Japan Society of Corrosion Engineering used to publish a monthly journal named *Corrosion Engineering*. However, we changed the name of the journal to *Materials and Environments* in 1991. We accept papers not only on corrosion but also on tailoring new materials and on various interactions of materials with environments.

In my own laboratory, about half of my colleagues are studying corrosion-resistant new materials and the other half are studying new materials for global conservation of the atmosphere and for providing an abundant energy supply, i.e. new electrodes, catalysts and corrosion-resistant materials for carbon dioxide recycling, direct decomposition of nitrogen oxides and hydrolytic decomposition of chlorofluorocarbons. Every autumn we hold a two-day seminar on these subjects at our Institute, inviting about 100 people from all over Japan including almost all Japanese delegates who are attending this seminar. Because I am Japanese, I feel that what's most important is the unity of our society or community, and this rather small informal meeting quite effectively unifies our society and encourages young people to follow us.

From the same point of view I wanted to organize this rather small seminar at Mt. Hood as an effective means of renewing and refreshing our friendship, of making new friends and, importantly, in encouraging us to study new areas of science. I suggest that the organizers of the next US–Japan Seminar look to subjects beyond pure corrosion science and engineering as we have done at Mt. Hood. I hope that all of us can meet again, accompanied by fresh perspectives and even more bright, young scientists and engineers with interdisciplinary interests which interface with corrosion science and engineering.

Finally I thank all of you for participating in this seminar and giving excellent papers and fruitful discussions.

K. Hashimoto
Guest Editor

ELSEVIER

Materials Science and Engineering A198 (1995) 259

MATERIALS SCIENCE & ENGINEERING A

Author Index of Volume 198

Elsevier Science S.A.

ELSEVIER

Materials Science and Engineering A198 (1995) 261–263

MATERIALS SCIENCE & ENGINEERING A

Subject Index of Volume 198

Elsevier Science S.A.

For:

Materials Scientists,

Solid-State Physicists and Chemists,

Semiconductor Physicists and Device Engineers,

Electronic Engineers,

Researchers in Superconductivity,

and

Computational Materials Scientists

MATERIALS SCIENCE & ENGINEERING

B Solid-State Materials for Advanced Technology

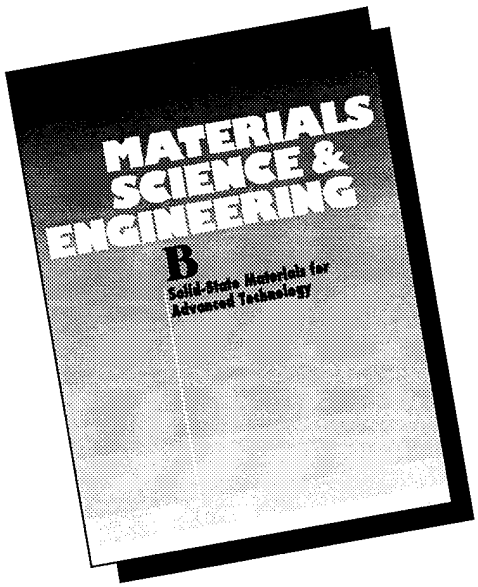

Editors:

M. Balkanski
Université Pierre & Marie Curie
Laboratoire des
Physiques des Solides
Tour 13, 2e Etage
4 Place Jussieu
75252 Paris Cedex 05, France

H. Kamimura
Science University of Tokyo
Faculty of Science
Department of Applied Physics
1-3 Kagurazaka, Shinjuku-ku
Tokyo 162, Japan

S. Mahajan
Carnegie Mellon University
Department of Materials
Science and Engineering
Pittsburgh, PA 15213-3890, USA

Commenced Publication 1988
Published in 21 issues in 1995
ISSN 0921-5107

AIMS AND SCOPE

Materials Science and Engineering B provides an international medium for the publication of theoretical and experimental studies and reviews related to the electronic, ionic, magnetic and optical properties of materials both in bulk and in thin films. Papers dealing with the processing, characterization, structure and physical properties and computational aspects of the crystalline, amorphous and glassy forms of metals, superconductors, semiconductors, insertion compounds, low-dimensional compounds and systems, fast-ion conductors, polymers and dielectrics are viewed as suitable for publication.

ELSEVIER SCIENCE S.A.
PO Box 564, 1001 Lausanne
Switzerland
tel. : +41 (21) 320 73 81
fax.: +41 (21) 323 54 44

For customers in the USA and Canada:

ELSEVIER SCIENCE INC.
Attn. Journal Information Center
PO Box 882
Madison Square Station, New York
NY 10159, USA
tel. : +1 (212) 633 3750
fax.: +1 (212) 633 3764

ELSEVIER

MATERIALS SCIENCE AND ENGINEERING: B

Please send:
- ❑ A free sample copy
- ❑ Instructions for authors
- ❑ Subscription information
- ❑ Advertising information

MSA95

Name: _____

Company/Institute: _____

Street: _____ City: _____

Country: _____ Postal Code: _____

Date: _____ Signature: _____

Current Japanese Materials Research, Volume 14

Cyclic Fatigue in Ceramics

Edited by **H. Kishimoto**, **T. Hoshide** and **N. Okabe**

Structural ceramics, such as silicon nitride, silicon carbide, alumina and zirconia have more potential than metallic materials for practical applications to various kinds of engineering components, especially for high temperature applications. For example, automotive engine parts, such as turbocharger rotors and swirl chambers, and ball bearing systems have been produced on a commercial basis using these materials for the last ten years. These industrial motivations have stimulated extensive progress in the research on evaluation of the strength properties of ceramics. In particular, cyclic fatigue has been investigated as one of the major concerns in the design of reliable ceramic components, and many researchers have been engaged in the field of cyclic fatigue in ceramics. As a result, new aspects such as crack bridging, *R*-curve behavior and fracture morphology have been clarified in the last decade. This book presents in three sections the most recent topics and experimental techniques in Japan, concerning ceramic fatigue under cyclic loading. The first two sections provide state-of-the-art references for a fundamental understanding of ceramic fatigue, while the third section presents more complicated analytical techniques for statistical treatment and engineering application.

Contents: Preface.

©1995 296 pages Hardbound
Price: Dfl. 270.00 (US$158.75)
ISBN 0-444-82154-6

ELSEVIER
An imprint of Elsevier Science

TO ORDER

Contact your regular supplier or:

ELSEVIER SCIENCE B.V.

P.O. Box 211
1000 AE Amsterdam
The Netherlands
Tel: +31 (20) 485 3642
Fax: +31 (20) 485 3598

Customers in the USA and Canada:

ELSEVIER SCIENCE B.V.

P.O. Box 945
New York, NY 10159-0945, USA
Tel: +1 (212) 633 3650
Fax: +1 (212) 633 3680

No postage will be added to prepaid book orders. Dutch Guilder price(s) quoted applies worldwide US Dollar price(s) quoted may be subject to exchange rate fluctuations. Customers in the European Union should add the appropriate VAT rate applicable in their country to the price(s). In New York State please add applicable sales tax. All prices are subject to change without prior notice.

415\b1707

Instructions for Authors

SUBMISSION OF PAPERS

Manuscripts for the main part of the journal should be submitted to the Editor-in-Chief, Professor H. Herman, or for authors in Japan to Professor M. Koiwa:

Professor Herbert Herman
Department of Materials Science and Engineering
State University of New York at Stony Brook
Long Island, NY 11794-2275, USA
Fax: +1 (516) 632 8052

Professor Masahiro Koiwa
Department of Metal Science and Technology
Faculty of Engineering
Kyoto University
Yoshida-Honmachi, Sakyo-ku
Kyoto 606-01, Japan
Fax: +81 (75) 751 7844

Manuscripts for the Letters Section should be submitted as follows:

For authors in Europe

Professor G. Kostorz
ETH Zurich
Institut für Angewandte Physik
CH-8093 Zurich, Switzerland
Fax: +41 (1633) 1105

For authors in Japan

Professor Masahiro Koiwa
Japan

For authors in North and South America and the rest of the world

Professor Herbert Herman
USA

Manuscripts

Three copies should be submitted to the Editor, in double-spaced typing on pages of A4 size and with wide margins (Letters should not exceed 2000 words and a maximum of 5 figures). All tables and illustrations should bear a title or legend.

An *abstract* should accompany reviews, original papers and Letters. It should present (preferably in 100–150 words; 50 words or less for Letters) a brief and factual account of the contents and conclusions of the paper, and an indication of the relevance of new material.

References should be indicated by numerals in square brackets, introduced consecutively and appropriately in the text.

References must be listed on separate sheet(s) at the end of the paper. Every reference appearing in the text should be quoted in the reference list, and *vice versa*. When reference is made to a publication written by more than two authors it is preferable to give only the first author's name in the text followed by "*et al.*" However, in the list of references the names and initials of all authors must be given.

Three sets of figures should be submitted. One set of line drawings should be in a form suitable for reproduction, drawn in Indian ink on drawing or tracing paper (letter height, 3–5 mm). Alternatively, such illustrations may be supplied as high contrast, black-and-white glossy prints. Duplicate original micrographs should be provided wherever possible to facilitate the refereeing process. Magnifications should be indicated by a ruled scale bar on the micrograph. Captions to illustrations should be typed in sequence on a separate page.

All abbreviated terms must be defined when first used (both in the abstract and in the text) and authors must express all quantities in SI units, with other units in parentheses if desired.

Authors in Japan please note that information about how to have the English of your paper checked, corrected and improved (before submission) is available from: Elsevier Science (Japan), 20-12 Yushima 3-chome, Bunkyo-ku, Tokyo 113; Tel: (03) 3833-3821; Fax: (03) 3836-3064.

Further information

All questions arising after the acceptance of manuscripts, especially those relating to proofs, should be directed to: Elsevier Editorial Services, Mayfield House, 256 Banbury Road, Oxford OX2 7DH, UK (tel. +44 1865 314900; fax. +44 1865 314990).

0921-5093/95/$9.50

Printed in The Netherlands

0921-5093(19950715)A198:1/2;1-3